METHODS AND MODEL ORGANISMS EDITOR'S PICK 2021

EDITED BY: Gregg E. Homanics and Stephan C. F. Neuhauss
PUBLISHED IN: Frontiers in Molecular Neuroscience

frontiers Research Topics

ISSN 1664-8714
ISBN 978-2-88966-966-0
DOI 10.3389/978-2-88966-966-0

About Frontiers

Frontiers is more than just an open-access publisher of scholarly articles: it is a pioneering approach to the world of academia, radically improving the way scholarly research is managed. The grand vision of Frontiers is a world where all people have an equal opportunity to seek, share and generate knowledge. Frontiers provides immediate and permanent online open access to all its publications, but this alone is not enough to realize our grand goals.

Frontiers Journal Series

The Frontiers Journal Series is a multi-tier and interdisciplinary set of open-access, online journals, promising a paradigm shift from the current review, selection and dissemination processes in academic publishing. All Frontiers journals are driven by researchers for researchers; therefore, they constitute a service to the scholarly community. At the same time, the Frontiers Journal Series operates on a revolutionary invention, the tiered publishing system, initially addressing specific communities of scholars, and gradually climbing up to broader public understanding, thus serving the interests of the lay society, too.

Dedication to Quality

Each Frontiers article is a landmark of the highest quality, thanks to genuinely collaborative interactions between authors and review editors, who include some of the world's best academicians. Research must be certified by peers before entering a stream of knowledge that may eventually reach the public - and shape society; therefore, Frontiers only applies the most rigorous and unbiased reviews.
Frontiers revolutionizes research publishing by freely delivering the most outstanding research, evaluated with no bias from both the academic and social point of view. By applying the most advanced information technologies, Frontiers is catapulting scholarly publishing into a new generation.

What are Frontiers Research Topics?

Frontiers Research Topics are very popular trademarks of the Frontiers Journals Series: they are collections of at least ten articles, all centered on a particular subject. With their unique mix of varied contributions from Original Research to Review Articles, Frontiers Research Topics unify the most influential researchers, the latest key findings and historical advances in a hot research area! Find out more on how to host your own Frontiers Research Topic or contribute to one as an author by contacting the Frontiers Editorial Office: frontiersin.org/about/contact

METHODS AND MODEL ORGANISMS EDITOR'S PICK 2021

Topic Editors:
Gregg E. Homanics, University of Pittsburgh, United States
Stephan C. F. Neuhauss, University of Zürich, Switzerland

Citation: Homanics, G. E., Neuhauss, S. C. F., eds. (2021). Methods and Model Organisms Editor's Pick 2021. Lausanne: Frontiers Media SA. doi: 10.3389/978-2-88966-966-0

Table of Contents

frontiers in Molecular Neuroscience

ORIGINAL RESEARCH
published: 09 January 2019
doi: 10.3389/fnmol.2018.00485

Expression and Roles of the Immunoglobulin Superfamily Recognition Molecule Sidekick1 in Mouse Retina

*Masahito Yamagata and Joshua R. Sanes**

Department of Molecular and Cellular Biology, Center for Brain Science, Harvard University, Cambridge, MA, United States

Processes of >100 types of interneurons (bipolar and amacrine cells) and projection neurons (retinal ganglion cells, RGCs) form specific and stereotyped patterns of connections in the inner plexiform layer (IPL) of the mouse retina. Four closely related homophilic immunoglobulin superfamily recognition molecules (Sidekick [Sdk] 1, Sdk 2, Dscam, and DscamL1) have been shown to play roles in patterning neuronal arbors and connections in chick retina, and all but Sdk1 have been shown to play related roles in mice. Here, we compare patterns of Sdk1 and Sdk2 expression in mouse retina and use genetic methods to assess roles of Sdk1. In adult retina, 3 neuronal types express *sdk1* but not *sdk2* at detectable levels, 5 express *sdk2* but not *sdk1* and 3 express both. Patterns of gene expression and protein localization at or near synapses are established during the first postnatal week. Dendrites of amacrine cells and RGCs that express *sdk1* but not *sdk2* arborize in the same narrow stratum in the center of the IPL. In the absence of Sdk1, this laminar restriction is degraded. Overexpression of *sdk1* in developing cells that normally express *sdk2* reorients their dendrites to resemble those of endogenously Sdk1-positive cells, indicating that Sdk1 plays an instructive role in patterning the IPL. Sdk1 fails to affect arbors when introduced after they are mature, suggesting that it is required to form but not maintain laminar restrictions. The effect of ectopically expressed sdk1 requires the presence of endogenous Sdk1, suggesting that the effect requires homophilic interactions among Sdk1-positive neurites. Together with previous results on Sdk2, Dscam, DscamL1, as well as the related Contactins, our results support the idea that an elaborate immunoglobulin superfamily code plays a prominent role in establishing neural circuits in the retina by means of tightly regulated cell type-specific expression and homophilically restricted intercellular interactions.

Keywords: laminar specificity, synapse formation, retinal ganglion cell, amacrine cell, bipolar cell

OPEN ACCESS

Edited by:
Philip Washbourne,
University of Oregon, United States

Reviewed by:
Karin Dedek,
University of Oldenburg, Germany
Andreas Faissner,
Ruhr-Universität Bochum, Germany
Johann Helmut Brandstätter,
Friedrich-Alexander-Universität Erlangen-Nürnberg, Germany

***Correspondence:**
Joshua R. Sanes
sanesj@mcb.harvard.edu

Received: *22 October 2018*
Accepted: *13 December 2018*
Published: *09 January 2019*

Citation:
Yamagata M and Sanes JR (2019) Expression and Roles of the Immunoglobulin Superfamily Recognition Molecule Sidekick1 in Mouse Retina. Front. Mol. Neurosci. 11:485. doi: 10.3389/fnmol.2018.00485

INTRODUCTION

Over the past decade, the mouse retina has emerged as a valuable model for investigating how "hard-wired" neural circuits are assembled. In one of its two synaptic layers, the inner plexiform layer (IPL), neurites of >50 types of interneurons (bipolar and amacrine cells) form synapses on dendrites of >40 types of output neurons (retinal ganglion cells, RGCs) during the first two

postnatal weeks (reviewed in Sanes and Zipursky, 2010; Hoon et al., 2014). The specific and stereotyped patterns of these connections endow each RGC type with selective sensitivity to specific visual features, such as motion in a particular direction, edges, or color contrasts (reviewed in Masland, 2012; Sanes and Masland, 2015). Analysis of these circuits has implicated a variety of recognition molecules in the cell-cell interactions that establish them; they include members of the immunoglobulin and cadherin superfamilies, the semaphorins and plexins, and others (e.g., Fuerst et al., 2008, 2009, 2012; Matsuoka et al., 2011; Kay et al., 2012; Lefebvre et al., 2012; Sun et al., 2013; Duan et al., 2014, 2018; Krishnaswamy et al., 2015; Peng et al., 2017; Liu et al., 2018; reviewed in Zhang et al., 2017). Together, these studies demonstrate that numerous recognition molecules act together to pattern neural circuitry in the IPL. Since all of these molecules are also expressed by neuronal subsets throughout the brain, insights obtained in studies of the retina are likely to be relevant to the central nervous system generally.

In this study, we focus on retinal expression and roles of two closely related immunoglobulin superfamily recognition molecules that have been implicated in retinal development, Sidekick 1 and 2 (Sdk1 and Sdk2). We isolated the Sdks in a search for genes expressed by subsets of RGCs in the developing chick retina (Yamagata et al., 2002). We named them for the related *Sdk* gene in Drosophila, which was identified in a screen for genes that affect patterning of the fly eye (Nguyen et al., 1997) and was recently shown to be required for synaptic targeting of photoreceptors (Astigarraga et al., 2018). The Sdks are large (∼250 kD), proteins, with six immunoglobulin domains, thirteen fibronectin repeats, a single transmembrane domain, and a cytoplasmic domain ending in a PDZ domain-binding motif. They are homophilic adhesion molecules (Yamagata et al., 2002; Hayashi et al., 2005; Yamagata and Sanes, 2008). Structural studies have shown that the immunoglobulin domains mediate homophilic adhesion, and defined critical residues required for adhesion *per se* and for homophilic specificity (Goodman et al., 2016; Tang et al., 2018). Their PDZ-binding motif binds scaffolding proteins of the MAGI family, an interaction that contributes to their concentration at synaptic sites (Yamagata and Sanes, 2010).

In chick retina, the Sdks are expressed by non-overlapping subsets of retinal neurons, and required for restriction of neuronal processes to specific strata within the IPL (Yamagata et al., 2002; Yamagata and Sanes, 2008). Their closest relatives, two *Dscams* (*Dscam and DscamL*) and six *contactins* (*Cntn1-6*) are also expressed by neuronal subsets in chick retina and play related roles, leading to the suggestion that they comprise an "immunoglobulin superfamily code" for laminar specificity (Yamagata and Sanes, 2008, 2012a).

Recently, we analyzed expression and roles of Sdk2 in mice (Krishnaswamy et al., 2015). We found that *sdk2* is expressed by restricted subsets of retinal neurons, including an unusual glutamatergic amacrine interneuron called VGlut3-positive amacrine cells (VG3-ACs) (Haverkamp and Wässle, 2004; Johnson et al., 2004; Grimes et al., 2011) and an RGC type called W3B, which has the unusual property of responding when the timing of the movement of a small object differs from that of the background, but not when they coincide (Kim et al., 2010, 2015; Zhang et al., 2012; Lee et al., 2014; Krishnaswamy et al., 2015). We showed that VG3-ACs synapse on W3B-RGCs, that VG3 input is essential for W3B-RGC function, that Sdk2 is required for restriction of VG3-AC and W3B-RGC processes to appropriate strata, and that the number and strength of functional connections between VG3-ACs and W3B-RGCs are dramatically reduced in the absence of Sdk2 (Krishnaswamy et al., 2015).

Here, we have analyzed expression and roles of Sdk1 in mouse retina. Confirming initial observations (Krishnaswamy et al., 2015), we show that *sdk1*, like *sdk2*, is expressed by a small number of specific interneuronal and RGC types. As in chick, types that express *sdk1* and *sdk2* are largely non-overlapping, but we also found three types that express both *sdks*. *Sdk1*, like *sdk2*, in mice and both *sdks* in chick, is expressed by interneurons and RGCs that arborize in the same strata, and neurites of these cells exhibit decreased laminar restriction in the absence of Sdk1. Finally, we use ectopic overexpression of *sdk1* in cells that normally express *sdk2* to demonstrate that it plays an instructive role in laminar targeting and that it does so by a homophilic mechanism.

MATERIALS AND METHODS

Animals

Animals were used in accordance with NIH guidelines and protocols approved by Institutional Animal Use and Care Committee at Harvard University. Production of mouse lines by genome editing was performed in the Genome Modification Facility, Harvard University.

To generate the $sdk1^{CG}$ allele, CreGFP was amplified from Addgene plasmid #13766, and inserted at the translational start site of the *Sdk1* gene using CRISPR/Cas9 nickase-mediated genome engineering (Ran et al., 2013; Wang et al., 2013). The targeting vector was modified from that reported previously (Krishnaswamy et al., 2015) by substituting CreGFP for $CreER^{T2}$. The template DNA sequences to generate the sgRNAs used to enhance homologous recombination were CGGCATGGCCCGCGCCCGGC and GGTGGCGGGCGGCGGAGTCG (see **Figure S1**). Two sgRNAs, the circular targeting construct, and the synthesized Cas9 nickase mRNA were injected into the cytoplasm of fertilized eggs. The indel mutant $sdk1^{\Delta N}$ was obtained from the same injections; in these mice, the *sdk1* gene was altered, but CreGFP was not inserted.

The $sdk1^{CE}$ (3xHA-tagged CreER) and $sdk2^{CE}$ (6xMYC-tagged CreER) mouse lines were described previously (Krishnaswamy et al., 2015). To generate $sdk2^{C}$, two sgRNAs were designed to target the junction between Cre and ER^{T2} in $sdk2^{CE}$, and coinjected with Cas9 nickase mRNA into $sdk2^{CE/CE}$ embryos. The template DNA sequences to generate the sgRNAs were GCTCTCATGTCTCCAGCAGA and GTCCCTGACGGCCGACCAGA.

To enable expression of *sdk1* or *sdk2* under Cre-dependent control, we generated three lines. A cassette encoding Venus

and Sdk1, Venus and Sdk2, or Venus plus APEX2NES (ascorbic acid peroxidase with a nuclear localization signal), separated by tripleF2A (3 tandem repeats of foot-and-mouth disease 2A peptide sequence) was cloned into a Rosa26CAG-STOP-targeting vector (Yamagata and Sanes, 2012b) to generate Rosa-CAG-LOX-STOP-LOX-Venus-3F2A-Sdk1-WPRE-FRT-neo-FRT, Rosa-CAG-LOX-STOP-LOX-Venus-3F2A-Sdk2-WPRE-FRT-neo-FRT, or Rosa-CAG-LOX-STOP-LOX-Venus-3F2A-APEX2NES-WPRE-FRT-neo-FRT. We refer to these lines as *RC-sV-Sdk1*, *RC-sV-Sdk2*, and *RC-sV-A*, respectively. Homologous recombinants were selected in the V6.5 ES cell line and chimeras were generated. Germ-line chimeras were crossed to a Flp-expressing mouse (Rodríguez et al., 2000) to remove the FRT-neo-FRT sequence.

We used several Cre-dependent reporter lines interchangeably. *Thy-STOP-YFP15* (referred to as *STOP15*) expresses YFP in a Cre-dependent manner under Thy1 regulatory elements (Buffelli et al., 2003). *Ai14* expresses tdTomato in a Cre-dependent manner (Rosa26-CAG-lox-stop-lox-tdTomato) (Madisen et al., 2010). Rosa-CAG-Lox-STOP-LOX-ChR2(H134R)-tdTomato mice (*Ai27*) expresses cell surface-localized channelrhodopsin following excision of a stop cassette by Cre recombinase (Madisen et al., 2012). *Ai14* and *Ai27* lines were obtained from The Jackson Laboratory (Bar Harbor, ME). The Rosa-CAGS-LOX-CHERRY-LOX-GFP line (referred to as *RC-FrePe*) was obtained from S. Dymecki (Harvard University) (Dymecki et al., 2010). The Cre-dependent tdTomato line *Colstd* (Collagen-CAG-loxP-STOP-loxP-tdTomato-WPRE) in the type I collagen locus (Beard et al., 2006) was generated in the V6.5 ES cells, and a mouse line was established from germ-line chimeras.

The *JamB-CreER* line to label J-RGCs was described previously (Kim et al., 2008). *ChAT-cre* (Rossi et al., 2011) was from The Jackson laboratory. *DAT-cre* mice, in which cre is targeted to the endogenous *DAT* locus (Zhuang et al., 2005) was obtained from X. Zhuang (University of Chicago) via V. Murthy (Harvard University). *Gbx2-CreERT2-IRES-GFP* (Chen et al., 2009) was a generous gift from James Y. H. Li (University of Connecticut).

To induce recombination in $CreER^{T2}$ reporter lines, animals were injected with tamoxifen as follows: P2 pups were injected with 0.5 mg tamoxifen (T5648, Sigma, St. Louis, MO) in 0.05 ml sunflower oil (S5007, Sigma). P24 animals were injected with 5 mg tamoxifen in 0.5 ml oil. In some cases, animals were injected with 1 mg tamoxifen in 0.1 ml sunflower oil at 24 and 48 h prior to sacrifice, which resulted in translocating $CreER^{T2}$ protein to the nucleus, enhancing our ability to detect it.

Plasmids, Transfection, and RT-PCR

The mouse Sdk1 (long form) cDNA in pCMVscript (Clontech, Mountain View, CA) was described previously (Yamagata and Sanes, 2008). A cDNA encoding the short form of mouse Sdk1 was modified from the long form cDNA. Each plasmid was transfected to 293T cells (ATCC, Manassas, VA) with DMRIE-C (Thermo-Fisher, Waltham, MA) as described previously (Yamagata and Sanes, 2012a).

Total RNA from animals or cultured cells was isolated using illustra RNAspin Mini (GE Heathcare Life Sciences, Marlborough, MA), which uses deoxyribonuclease I to remove DNA. cDNA was generated with Superscript III (Thermo-Fisher/Invitrogen) using random or *sdk1* specific primers (CTCTATGATGGAAAGGAAGGCTC) for the short form, and treated with RNase H (Thermo-Fisher). Primer sequences and predicted sizes after PCR were as follows (see **Figure 1** for location of each primer set).

a (161 bp): CCGGCGGGCGGCAAAGTTGAG, TGAGCACCAGGCGGTTCCCTTCC
b (243 bp): TCAAAGAAGAACGGAACCAGAT, CCGCTTCCAAGAGTTGTAGTAG
c (230 bp): AGTGATGGACAGATCAGGAGATA, ATGTCGGATTGGTGATGGTAAG
d (228 bp): AGGTATCTCCCTGGTGCAATA, GAGCCTCAAGTTGTCCTAAGATG
e (204 bp): GTAGGGACAGAATGGACACATC, CAGCTCACACAAGGAGGTAAG

EconoTaq plus green mixture (Lucigen, Middleton, WI) was used for PCR. PCR cycles were 94°C, 2 min; 42 cycles of 94°C, 30 s; 60°C, 30 s; 72°C, 1 min + 2 s extention; 72°C, 7 min, and 4°C.

Other primer sequences were as follows.

Cre: GCATTACCGGTCGATGCAACGAGTGATGAG, GAGTGAACGAACCTGGTCGAAATCAGTGCG

mouse *Gapdh*: TGAAGGTCGGTGTGAACGGATTTGGC, CATGTAGGCCATGAGGTCCACCAC.

Antibodies

Antibodies used in this study were: rabbit monoclonal antibody to estrogen receptor α (ER) (Clone SP1, from Epitomics or Abcam, Cambridge, MA); goat anti-Myc (NB600-335, from Novus, Littleton, CO); rat anti-HA (3F10, from Roche Diagnostics Co., Indianapolis, IN); anti-Brn3a (clone, 5A3.2), rabbit anti-synapsin I (AB1543P), mouse anti-calretinin (clone, 6B8.2), sheep anti-tyrosine hydroxylase and goat anti-ChAT antibodies (AB144P) from Millipore (Billerica, MA); AP2 (clone, 3B5), SV2, and anti-synaptotagmin 2 (clone, ZNP1) from Developmental Studies Hybridoma Bank (Iowa City, IA); mouse anti-VGlut1 (clone, N28/9), mouse anti-pan-MAGUK (clone, N28/86), mouse anti-HCN4 (clone, N114.10), and mouse anti-Vesicular acetylcholine transporter (clone, N6/38) from NeuroMab (Davis, CA); mouse anti-protein kinase C-α (PKCα) (clone MC5) and rabbit anti-PKCα (P4334) from Sigma; rabbit anti-Opn4 from Thermo Fisher (PA1-780), mouse monoclonal antibody to neurofilament-H (phosphorylated) SMI-34 from Covance (Princeton, NJ); goat anti-Spp1 from R&D Systems (Minneapolis, MN). Rabbit antibody to Dab1 was a kind gift from Dr. Brian Howell (SUNY Upstate, Syracuse, NY). Chicken anti-GFP (Yamagata and Sanes, 2012b), rabbit anti-mCherry/RFP (Cai et al., 2013), and mouse antibodies to mouse Sdk1 or Sdk2 (Krishnaswamy et al., 2015) were generated in our laboratory. Nuclei were labeled with NeuroTrace 640 (ThermoFisher/Invitrogen). Secondary antibodies

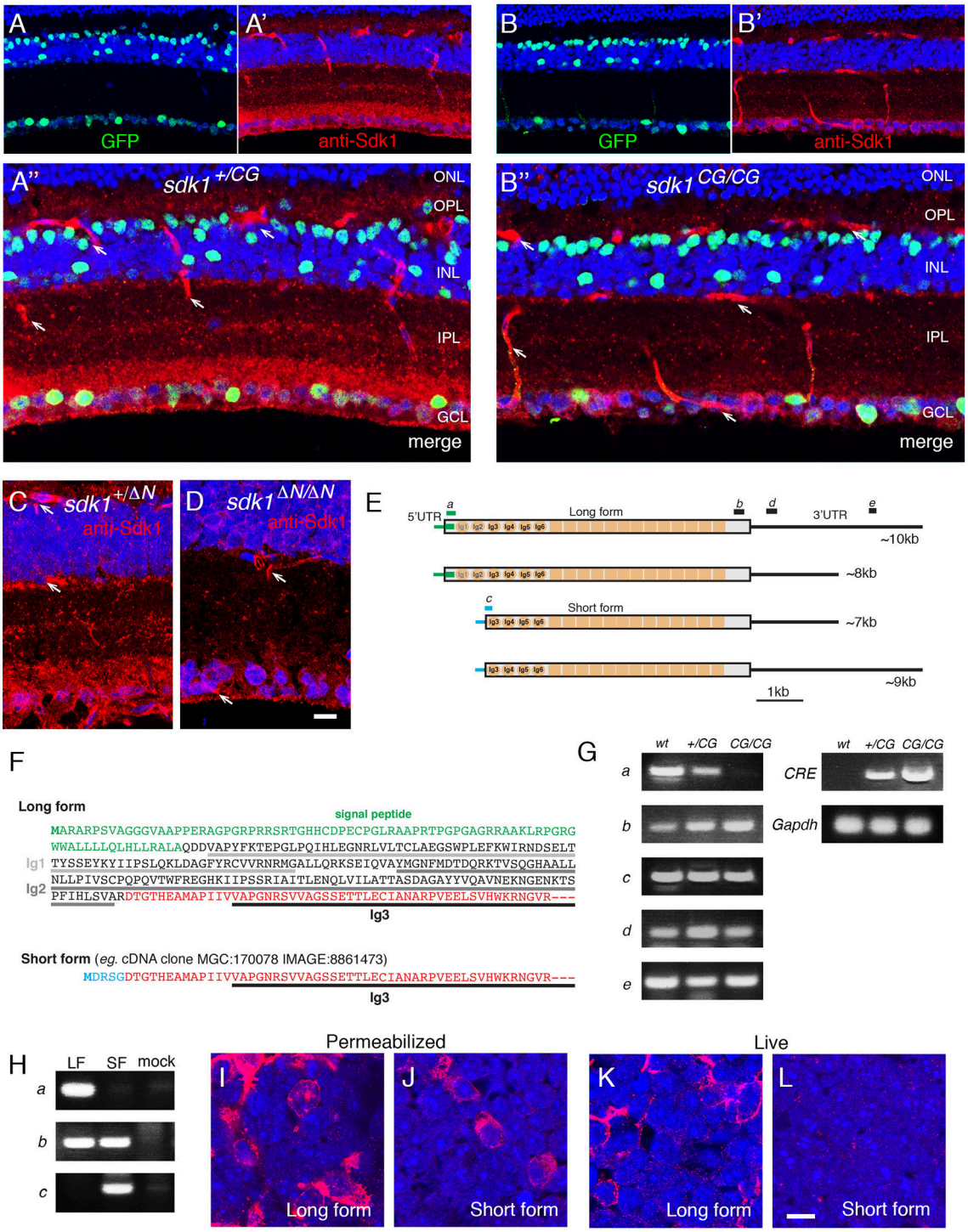

FIGURE 1 | Evidence for an intracellular Sdk1 isoform. **(A,B)** Expression of *sdk1* and localization of Sdk1 protein in retina at P30. Sections from *sdk1*$^{+/CG}$ **(A)** and *sdk1*$^{CG/CG}$ **(B)** retina were stained with antibodies to GFP (green) and Sdk1 (red). In the *sdk1*^{CG} allele, CreGFP replaces the first coding exon; GFP reports on gene expression and Cre localizes GFP to the nucleus. Expression is similar in both *sdk1*$^{+/CG}$ and *sdk1*$^{CG/CG}$ retina, with positive cells in the ganglion cell layer (GCL) and INL but not the outer nuclear layer (ONL). Sdk1 is present in the inner plexiform layer (IPL) and GCL of *sdk1*$^{+/CG}$ retina. IPL staining is absent in *sdk1*$^{CG/CG}$ retina but some GCL staining persists. Staining of blood vessels (arrows) is non-specific. **(C,D)** In the *sdk1*$^{\Delta N}$ allele, the first 46 aa of Sdk1 are deleted (see **Figure S1B**). As in the *sdk1*^{CG} allele, Sdk1 is present in the IPL of *sdk1*$^{+/\Delta N}$ retina (C) and persists in the GCL of *sdk1*$^{\Delta N/\Delta N}$ retina. Bar, 10μm for **(A–D)**. **(E)** *sdk1* transcripts, derived from entries in GenBank and the UCSC Genome browser, indicate occurrence of two 5′- and two 3′ sequences surrounding a common core. Letters a–e show positions of PCR primer pairs used in **(G)**. **(F)** 5′ coding sequence of the long and short forms. The short form lacks the signal peptide and the first two Ig domains

(Continued)

FIGURE 1 | (Ig1 and Ig2) critical for adhesion. Green, signal peptide; black, sequences in long form only; red, sequences in long and short forms; blue, sequences in short form only. Its first exon encodes five amino acids (MDRSG) absent from the long form. **(G)** Products amplified from wildtype (wt), *sdk1*$^{+/CG}$ (+/CG), and *sdk1*$^{CG/CG}$ (CG/CG) adult retinas by RT-PCR with primers shown in **(E)**, as well as *Cre* and *Gapdh* primers. The N-terminal region of the long form is not seen in *sdk1*$^{CG/CG}$ retina. The results suggest that both the long and short protein coding regions can have either a long or short 3′ UTR. **(H)** Products amplified with primer sets a–c (see **E**) from 293T cells transfected with plasmids encoding Sdk1 long (LF) or short forms (SF) and untransfected controls (mock). As expected **(E)**, primer sets a and c distinguish long and short forms. **(I–L)** Sdk1 immunoreactivity of 293T cells transfected as in **(H)**. Cells were stained live **(I,J)** or after permeabilization **(K,L)**. Only the long form is accessible extracellularly. Bar, 10μm.

conjugated to dyes were from Jackson ImmunoResearch (West Grove, PA).

Immunostaining and *in situ* Hybridization

For immunostaining, retinas were fixed with 4% (w/v) paraformaldehyde/PBS overnight at 4°C, sunk in 15%(w/v) and 30%(w/v) sucrose/PBS, and mounted in Tissue Freezing Medium (EM Sciences, Hatfield, PA). Sections were cut in a cryostat, permeabilized with 0.1% (w/v) TritonX-100/PBS for 5 min at room temperature, blocked with 5% (w/v) skim milk/PBS for 30 min at room temperature, incubated with appropriate antibodies overnight, rinsed, and incubated with appropriate secondary antibodies. After rinsing with PBS, sections were mounted in Fluoro-Gel (Electron Microscopy Sciences, Hatfield, PA, USA) and imaged with a Zeiss Meta510 confocal microscope (Oberkochen, Germany).

For double immunostaining with two mouse antibodies, we used the Zenon Horseradish Peroxidase Mouse IgG1 Labeling Kit (Life Technologies, Grand Island, NY) to label one of them, and detected reaction product with the TSA-Plus kit (Perkin-Elmer Life Sciences, Waltham, MA). For immunodetection of epitope-tagged CreER, cryosections were permeabilized in absolute methanol at −20°C overnight, treated with Image-iT FX signal enhancer (Life Technologies) by the manufacturer's protocol, and blocked with 5%(w/v) skim milk (BioRad, Hercules, CA) in PBS for 30 min at room temperature. The antibodies were diluted in Renoir Red diluent (BioCare Medical, Concord, CA), incubated at 4°C for 48 h, rinsed, and detected with secondary antibodies that had been preabsorbed with acetone powders prepared from mouse brain.

Whole-mount staining with antibodies was done as follows. Retinae were fixed with 4% (w/v) paraformaldehyde /PBS overnight at 4°C, and treated with 0.1% (w/v) TritonX-100/PBS for 30 min at 4°C. Tissues were then blocked with 1%(w/v) bovine serum albumin/PBS overnight, incubated with appropriate primary antibodies in 0.1% (w/v) TritonX-100/ 0.1%(w/v) bovine serum albumin/PBS for 48 h, rinsed with 0.1% (w/v) TritonX-100/PBS for 3 h, incubated with secondary antibodies in 0.1% (w/v) TritonX-100/ 0.1%(w/v) bovine serum albumin/PBS overnight, rinsed with 0.1% (w/v) TritonX-100/PBS overnight, mounted in glycerol-based VECTASHIELD (Vector labs, Burlingame, CA), placed on black nitrocellulose membranes (HABG01300, Millipore), and imaged with a Zeiss Meta510 confocal microscope. When anti-ER antibody was used, the retina was fixed with 4% (w/v) paraformaldehyde /PBS overnight at 4°C, and then placed in 0.1% (w/v) TritonX-100/PBS for 30 min at 4°C, 30%(v/v) methanol/0.1% (w/v) TritonX-100 for 30 min at 4°C, 50%(v/v) methanol/0.1% (w/v) TritonX-100 for 30 min at 4°C, 70%(v/v) methanol/0.1% (w/v) TritonX-100 for 30 min at 4°C, 100%(v/v) methanol overnight at −20°C, 70%(v/v) methanol/0.1% (w/v) TritonX-100 for 30 min at 4°C, 50%(v/v) methanol/0.1% (w/v) TritonX-100 for 30 min at 4°C, 30%(v/v) methanol/0.1% (w/v) TritonX-100 for 30 min at 4°C, and 0.1% (w/v) TritonX-100/PBS before blocking. Incubation with anti-ER (SP1) was done in the Renoir Red diluent supplemented with 0.1% (w/v) TritonX and 0.1%(w/v) bovine serum albumin, rinsed, and processed as described above.

Live staining of transfected 293T cells was performed as previously described (Goodman et al., 2016).

For *in situ* hybridization, riboprobes were synthesized from Sdk1cDNA using digoxigenin-labeled UTP (Roche) and hydrolyzed to around 500 bp. Probes were detected using horseradish peroxidase conjugated sheep antibodies to digoxigenin (Roche), followed by amplification with TSA-Plus system (Yamagata and Sanes, 2012a).

Imaging and Statistical Analysis

Images were processed with Adobe Photoshop, and Image-J (Version 1.47d, Fiji). Position of spots were measured using Image-J. To generate the graphs in **Figures 4F**, **7G**, **8C**, **9D**, **10J**, cells were selected based on the clarity of their dendrites: we required that only a single cell be labeled in the field, and that a broad expanse of dendrite be visible in the field. Then, all GFP+ immunopositive spots that could be assigned to the cell's arbor were measured and counted. For **Figure 5K**, immunoreactive (calbindin+) puncta were counted.

To analyze variance of measured spots, the VAR.S function and *F*-tests were used in Microsoft Excel for Mac 2011 (version 14.3.1). "Variance" was calculated by VAR.S which uses this formula.

$$\frac{\sum (x_m - x)^2}{(n-1)}$$

where x_m is the sample mean and n is the sample size. To statistically compare two variances, s1 and s2, the *F*-test was performed using the following equation.

$$F = s_1^2 / s_2^2$$

To generate box-plots, qplot function was employed in the ggplots2 package of R 3.4.4 for MacOS X GUI 1.70 (The R foundation, https://www.r-project.org/). ANOVA and Tukey *post-hoc* test were performed using R 3.4.4.

RESULTS

In a previous study (Krishnaswamy et al., 2015), we reported on the generation and use of knock-in mice in which a cDNA encoding a ligand -dependent Cre recombinase-human estrogen receptor (ER) fusion protein ($CreER^{T2}$) was targeted to the first coding exon of the *sdk1* and *sdk2* genes, thereby disrupting the gene and generating null alleles ($sdk1^{CE}$, $sdk2^{CE}$). These lines allowed us to map cells that express *sdk1* or *sdk2* by staining for ER or for epitope tags appended to the CreER (HAtag for $sdk1^{CE}$ and MYCtag for $sdk2^{CE}$) or by crossing to a cre-dependent reporter. We showed that *sdk1* and *sdk2* are expressed in largely but not entirely non-overlapping subsets of retinal cells in mice, and analyzed $sdk2^{CE/CE}$ mice to elucidate roles of Sdk2 in retinal circuitry. Here, we used these and newly generated alleles (**Figure S1**) to identify the cells that express *sdk1* and to analyze roles of Sdk1 in the retina.

Multiple Sdk1 Isoforms

We used CRISPR/Cas9 technology to generate *Sdk1* alleles in which CreGFP replaced CreER ($sdk1^{CG}$) or in which the first 46 amino acids were deleted without introduction of a reporter ($sdk1^{\Delta N}$). In characterizing these alleles, we stained retinal sections with anti-Sdk1. Immunoreactivity was present in the neuropil of the IPL of wild-type and heterozygous mice ($sdk1^{+/CG}$ and $sdk1^{+/\Delta N}$) (**Figures 1A,C**), and this immunoreactivity was greatly attenuated in homozygotes ($sdk1^{CG/CG}$ and $sdk1^{\Delta N/\Delta N}$; **Figures 1B,D**). Surprisingly, however, immunoreactivity persisted in some somata in the ganglion cell layer (GCL). In exploring the origin of the residual staining, we noted that Kaufman et al. (2004) reported multiple *sdk1* mRNAs (6–10 kb) but only a single *sdk2* mRNA (∼9 kb) by Northern analysis. Moreover, public databases report *sdk1* transcripts with at least two different 5′ ends and two different 3′ ends (**Figure 1E**). The two 5′ sequences encode different proteins. One, which we call the long form, is the previously documented Sdk1 protein, which has a signal peptide, 6 immunoglobulin (Ig) domains, 13 fibronectin type III repeats, a single-pass transmembrane, and a cytoplasmic domain. By contrast, the shorter form (e.g., IMAGE, 8861473) begins with a short exon encoding a putative initiation codon, but lacks the signal peptide and two Ig domains that are indispensable for homophilic adhesive activity of this molecule (Goodman et al., 2016) (**Figure 1F**). The $sdk1^{CE}$, $sdk1^{CG}$ $sdk1^{\Delta N}$ alleles are all predicted to inactivate the long but not the short form.

RT-PCR from retina confirmed that the long form is not expressed in $sdk1^{CG/CG}$ mice, but the short form-specific exon, as well as sequences common to both forms, are present in both $sdk1^{+/CG}$ and $sdk1^{CG/CG}$ mice (**Figure 1G**). We also generated plasmids encoding long and short forms, expressed them in heterologous cells (**Figure 1H**) and stained the cells with antibodies to the Sdk1 ectodomain. Both forms were readily detected in permeabilized cells, but staining of live cells demonstrated that only the long form is present at the extracellular face of the cell surface (**Figures 1I–L**). These results indicate that the short form is present in retina, but confined to the cytoplasm and unable to participate in intercellular recognition.

Sdk-Expressing Cells

The cells of the neural retina are divided into three cellular or "nuclear" layers, which are separated by two synaptic or "plexiform" layers. Photoreceptor somata occupy the outer nuclear layer (ONL), interneurons (horizontal, bipolar, and amacrine cells) and Müller glial cells occupy the inner nuclear layer (INL), and RGCs plus displaced amacrine cells occupy the GCL. Synapses of photoreceptors, horizontal cells and bipolar cell dendrites form the outer plexiform layer (OPL), and bipolar cell axons, amacrine cell processes and RGC dendrites synapse in the IPL.

Using reporters and antibodies, as described above, we characterized retinal cells that expressed *sdk1* or *sdk2*. Neither *sdk1* or *sdk2* was detectably expressed by photoreceptors or Müller glial cells, but horizontal cells and some bipolar, amacrine cell, and RGC types expressed *sdk1* and/or *sdk2* (**Figures 2A–C**).

Retinal Ganglion Cells

Over 40 RGC types have been described in mice (Baden et al., 2016; Bae et al., 2018; Rheaume et al., 2018). Of them, one is $sdk1^{+}sdk2^{-}$, one is $sdk1^{-}sdk2^{+}$ and two are $sdk1^{+}sdk2^{+}$.

The $sdk1^{+}sdk2^{-}$ RGC type has small somata and dendrites that ramify in a narrow sublamina at the center of S3 (**Figure 2D**). (By convention, the IPL is subdivided into 5 strata from S1 at the edge abutting the INL to S5 at the edge abutting the GCL.) This RGC type is calretinin-positive (**Figure 2E**). We provisionally call it the Sdk1+S3-RGC.

The $sdk1^{-}sdk2^{+}$ RGC type, which we characterized previously, is the W3B-RGC (Krishnaswamy et al., 2015). Like the Sdk1+S3-RGC, its soma is small, and its dendrites also ramify in S3. However, W3B dendrites are more diffuse than those of the Sdk1+S3-RGC, occupying most of the width of S3, and its somata are calretinin-negative (**Figures 2F,G**).

Both $sdk1^{+}sdk2^{+}$RGC types are large and have radial dendrites that stratify in S5 (**Figures 2H–K**). We identify one as the ONα-sustained RGC based on expression of Spp1(osteopontin) and SMI32 (Bleckert et al., 2014; Duan et al., 2015) (**Figures 2L,M**). The other is the M2 intrinsically photosensitive RGC based on its dendritic stratification, morphology and Opn4 (melanopsin) expression (**Figures 2N,O**).

Amacrine Cells

There are ∼60 amacrine cell types in mice (M. Laboulaye, W. Yan and J. R. Sanes, unpublished). Of them, two are $sdk1^{+}sdk2^{-}$ and two are $sdk1^{-}sdk2^{+}$. We found no amacrine cells that expressed both *sdk1* and *sdk2*.

One of the two $sdk1^{+}sdk2^{-}$ amacrine types has processes that ramify in S3 (**Figures 3A,B**). Most if not all of these cells are calretinin-positive type 2 catecholaminergic amacrine cells (2CA-ACs), as demonstrated by use of the *DAT-cre* line (**Figure 3A**) (Contini et al., 2010; Knop et al., 2011). The 2CA-ACs are present in both the INL and the GCL. The *DAT-cre* driver preferentially labels the group in the INL (**Figure 3A**), whereas both sets are Gbx2-positive (see below). 2CA-ACs narrowly stratify at the

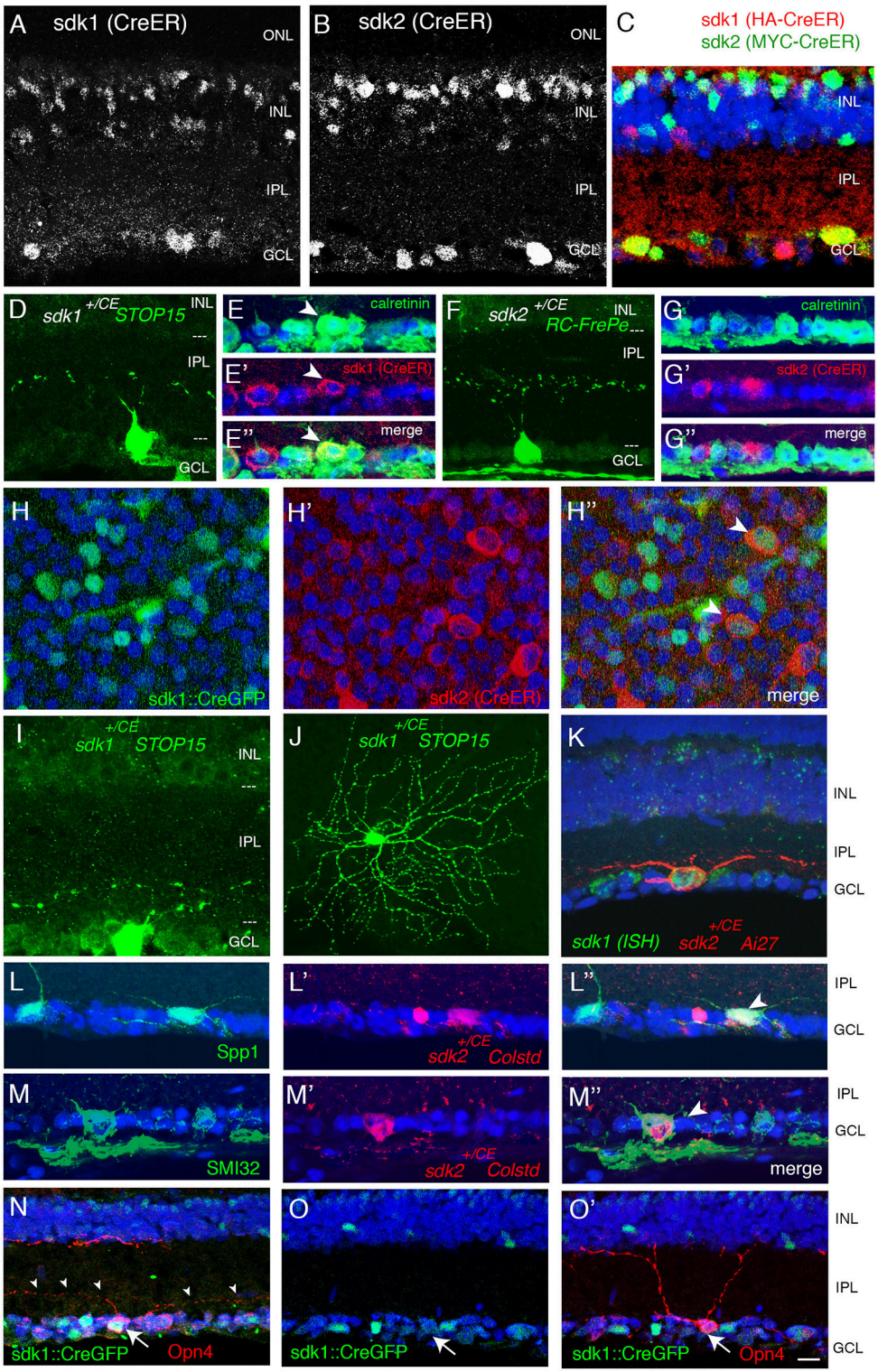

FIGURE 2 | Retinal ganglion cells that express *sdk1* and/or *sdk2*. **(A,B)** Localization of CreER in *sdk1*$^{+/CE}$ **(A)** and *sdk2*$^{+/CE}$ **(B)** retina at P30. In the CE alleles, epitope-tagged CreER^{T2} replaces the first coding exon and is detected with anti-ER. Subsets of cells express CreER^{T2} in both lines. ONL, outer nuclear layer; OPL, outer plexiform layer; INL, inner nuclear layer; IPL, inner plexiform layer; GCL, ganglion cell layer. **(C)** Expression of CreER in *sdk1*$^{+/CE}$;*sdk2*$^{+/CE}$ retina The two alleles are distinguished by staining for their epitope tags, HA in *sdk1*^{CE} and MYC in *sdk2*^{CE}. Some cell in the GCL and INL express both. **(D,F)** RGCs labeled in *sdk1*$^{+/CE}$ **(D)** or *sdk2*$^{+/CE}$ **(F)** mice mated to cre-dependent reporters (*STOP15* or *RC-FrePe*) following tamoxifen injection. Both *sdk1* and *sdk2* are expressed by RGCs with

(Continued)

FIGURE 2 | somata in the GCL and dendrites that arborize in S3 of the IPL, as shown with *sdk*$^{+/CE}$; *reporter* mice. Arbors are narrow for sdk1+ RGCs and diffuse for sdk2^{+}RGCs. **(E,G)** Many *sdk1*$^{+}$RGCs are calretinin-positive (arrowheads in **E**), whereas sdk2+RGCs are calretinin-negative **(G)** as revealed by double staining with antibodies to calretinin and ER. **(H)** GCL of P30 *sdk1*$^{+/CG}$; *sdk2*$^{+/CE}$ retina stained as flat mounts with anti-GFP **(H)** and anti-ER **(H′)** to label cells expressing *sdk1* and *sdk2*, respectively. Most of the sdk+ cells express either *sdk1* or *sdk2*, but some express both (arrowhead). **(I,J)** Large RGCs with dendrites in S5 visualized in section **(I)** and flat mount **(J)** in *sdk1*$^{+/CE}$;reporter (*STOP15*) mice following tamoxifen injection. Similar cells were observed in *sdk2*$^{+/CE}$; *STOP15*. **(K)** Large RGC with dendrites in S5 visualized in section in a *sdk2*$^{+/CE}$*; reporter* (*Ai27*) mouse (red). This RGC also expressed *sdk1*, as shown by *in situ* hybridization (green). **(L)** S5-laminating RGCs labeled in *sdk2*$^{+/CE}$*; reporter* retina are stained with anti-Spp1 (osteopontin) which marks α-RGCs and M2 RGCs (arrowhead). **(M)** Some S5-laminating RGCs labeled in *sdk2*$^{+/CE}$*;reporter* retina are stained by anti-neurofilament antibody SMI32, which labels α-RGCs but not M2-RGCs (arrowhead). **(N,O)** Some RGCs labeled in Sdk1$^{+/CG}$ retina are stained by anti-Opn4 (melanopsin), which marks M1 and M2 RGCs but not α-RGCs. The double-labeled cell in **(N)** (arrow) bears dendrites in S5, identifying it as an M2 cell. The Sdk1-negative cell in **(O)** (arrow) has dendrites in S1, identifying it as an M2 cell. Bar, 20 μm for **(J)**, and 10 μm for others.

center of S3 which corresponds to the middle of three calretinin-positive bands (**Figure 3B**).

The second sdk1^{+}sdk2^{-} amacrine type is the A17 type, identified by the striking "waterfall" shape of its arbor (**Figure 3E**), and tentatively characterized by its expression of protein kinase Cα (Puthussery and Fletcher, 2007; Downie et al., 2009) (**Figure S2A**).

We showed previously that the predominant *sdk1*$^{-}$*sdk2*$^{+}$ type is the VGlut3-positive amacrine cell (VG3-AC), an unusual excitatory amacrine cell with processes in S3 (Krishnaswamy et al., 2015; see **Figure 3C**). VG3-ACs are calretinin-negative and arborize diffusely in S3 (**Figure 3D**). We also found a small number of a second type of *sdk2*$^{+}$ amacrines that arborize in S3 but are distinct from VG3-ACs (**Figures S2B,C**). These were seldom encountered and have not been characterized further.

The *sdk1*$^{+}$*sdk2*$^{-}$ and *sdk1*$^{-}$*sdk2*$^{+}$ amacrine cells (VG3-AC and 2CA-AC) and RGCs (W3B-RGC and Sdk1+S3-RGC) are similar in that all four types have dendrites that arborize in S3. However, the fine details of their arbors differ. Our observation is consistent with our earlier observation that W3B-RGC is only weakly synaptically connected to 2CA-AC (Krishnaswamy et al., 2015), but appears to contrast an idea proposed by others (Brüggen et al., 2015) in that study, however, W3B-RGCs are not distinguished from related types.

Dendrites of the Sdk1+RGCs and the 2CA-ACs are larger in diameter and arborize in a narrow stratum in the center of S3. In contrast, dendrites of the Sdk2+ types (W3B-RGC and VG3-AC) are smaller in diameter and arborize more diffusely in S3. Sdk1^{-}+2CA cells do innervate Sdk2+W3B-RGCs (Brüggen et al., 2015), but physiological analysis indicated that the connection is far weaker than that of Sdk2+VG3-ACs with W3B-RGCs (Krishnaswamy et al., 2015).

Horizontal Cells

Horizontal cells express *sdk2* but not *sdk1* (**Figures 3F,G**). Strong punctate staining with anti-Sdk2 is seen in the outer plexiform layer (OPL), where photoreceptor synapses are abundant.

Bipolar Cells

There are 15 types of bipolar cells in mouse retina (Shekhar et al., 2016). One is *sdk1*$^{-}$*sdk2*$^{+}$ and another is *sdk1*$^{+}$*sdk2*$^{+}$.

Our recent transcriptomic analysis of mouse bipolars demonstrated selective expression of *sdk2* in type 7 bipolar cells (Shekhar et al., 2016) (**Figure 3H**). Using reporters, we confirmed expression of *sdk2* in cells with axonal arbors arborizing in IPL sublamina S4, which is characteristic of type 7 bipolars (**Figure 3I**).

Both *sdk1* and *sdk2* are expressed by rod bipolar (RB) cells (**Figures 3H–J**). Axons of these cells ramify in S5, which is strongly stained with both anti-Sdk1 and anti-Sdk2 antibodies (**Figures 4E–G**).

Patterns of *sdk1* and *sdk2* expression in mouse retina are summarized in **Figure 3K** and **Table 1**.

Localization of Sdk1 an Sdk2 in Developing Mouse Retina

To ask when Sdk proteins appear during postnatal development, we stained retinas with antibodies to Sdk1 and Sdk2. Sdk2 was present in the OPL at P0, but neither Sdk1 nor Sdk2 was present at high levels in the IPL at this stage (**Figures 4A,B**). Both Sdk1 and Sdk2 were readily detectable within the IPL by P8 (**Figures 4C,D**). Both were present at highest levels in S3-5 by this time.

By P14, the staining pattern was similar to that in adults (**Figures 4E–G**). Both Sdks were present in S3 of the IPL, but in a non-overlapping distribution, with Sdk1 concentrated in a narrow stratum in the center of S3 and Sdk2 diffusely distributed throughout this sublamina. Both Sdk1 and Sdk2 were also present in S5, with greater overlap. Both were also present in S4, but with stronger staining for Sdk2 than Sdk1 (**Figure 4E**), likely reflecting the presence of Sdk2 but not Sdk1 in type 7 bipolar cells. These patterns of localization are consistent with the cell types expressing *sdk1* and/or *sdk2*, and suggest that Sdk proteins are concentrated at or near synapses, as shown previously in chicks (Yamagata et al., 2002).

Lamination Defects in *sdk1* Mutant

Sdk1 mutants (*sdk1*$^{CE/CE}$, *sdk1*$^{CG/CG}$, and *sdk1*$^{\Delta N\Delta N}$) are viable and fertile and no abnormalities were visible on inspection of the live animal or upon inspection of major organs following euthanasia and dissection. To assess retinal structure and molecular architecture in mutants, we stained sections with a panel of antibodies to 14 cell class-specific, cell type-specific and synaptic markers (**Figure S3**). In no cases did we detect differences in level or distribution of the marker between homozygotes and controls (wild types and heterozygotes).

In a previous study, we demonstrated a role for Sdk2 in the development of Sdk2-positive VG3-ACs and W3B-RGCs. Processes of both cell types arborize in S3, and VG3-ACs synapse on W3B-RGCs. In Sdk2 mutants, the arbors of these cells extend

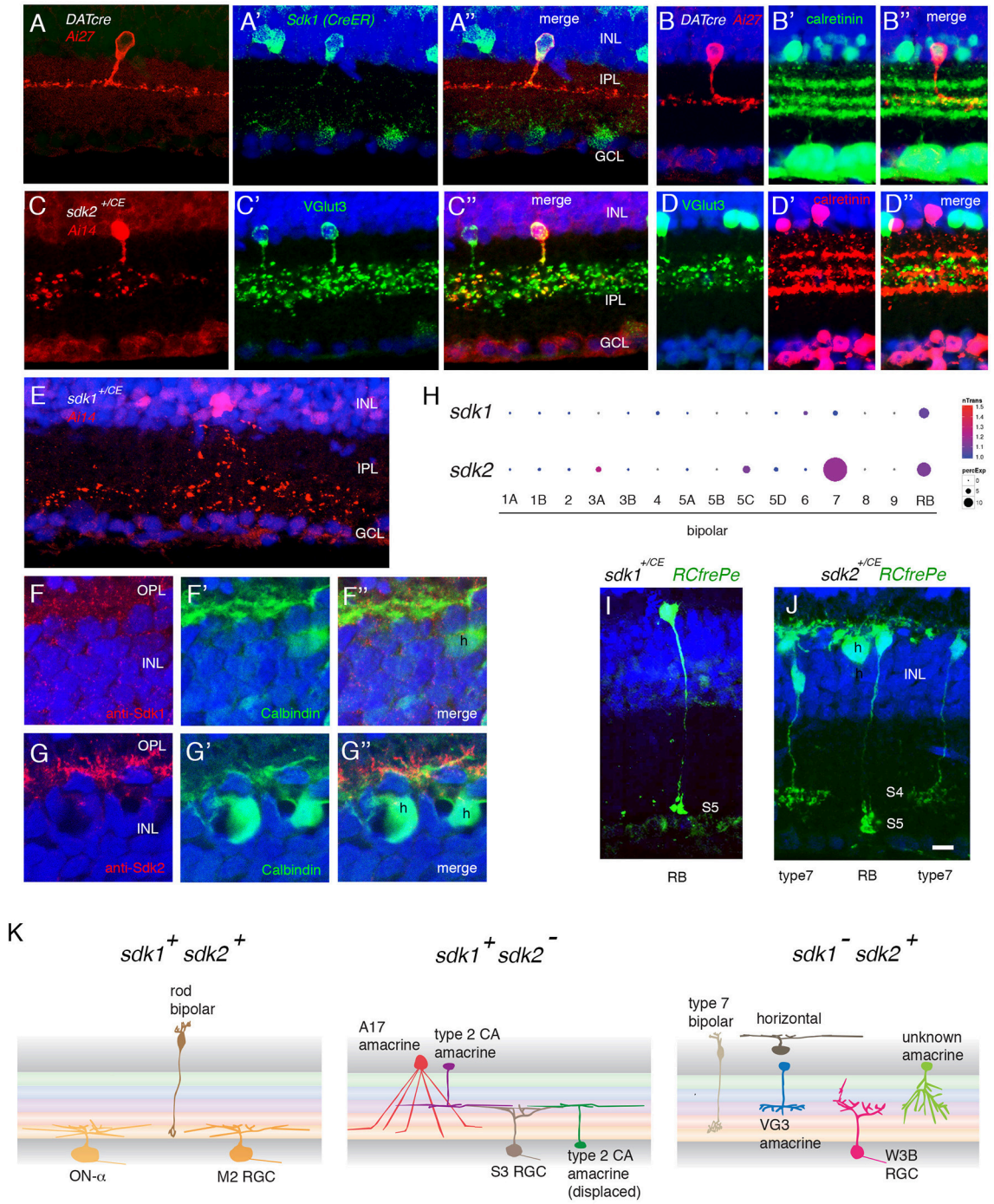

FIGURE 3 | Interneurons that express *sdk1* or *sdk2*. **(A)** *Sdk1* is expressed by type 2 catecholaminergic amacrine (2AC) cells, labeled in the *DAT-cre* line. Image from a *DAT-cre;reporter* (tdTomato *Ai27*);*sdk1*$^{+/CE}$ retina, stained for tdTomato **(A)** and ER **(A′)**; panel **(A″)** shows merge. **(B)** 2AC cells, labeled in *DAT-cre;reporter* (tdTomato *Ai27*) retina, stratify narrowly in S3, within the middle of three calretinin-positive sublaminae. **(C)** *Sdk2* is expressed by VG3 amacrine cells (*sdk1*$^{+/CE}$; *reporter* (tdTomato *Ai14*); sectioned stained with anti-VGlut3). **(D)** VG3 amacrine cells (labeled with anti-VGlut3) arborize diffusely in S3 and are calretinin-negative. **(E)** Amacrine cell labeled in *sdk1*$^{+/CE}$*;reporter* (*Ai14*) mouse following tamoxifen injection. The waterfall morphology is characteristic of A17 amacrine cells. **(F,G)** Horizontal cells (h) express Sdk2 **(F)** but not Sdk1 **(E)**. Sections were stained with anti-Sdk1 or anti-Sdk2 plus antibodies to calbindin, which marks horizontal cells. **(H)** Expression of *sdk1* and *sdk2* derived from single cell RNAseq data in Shekhar et al. (2016). RB, rod bipolar cells. *sdk2* is expressed by type 7 bipolar cells. Rod bipolar cells express both *sdk1* and *sdk2*. **(I)** Labeling of BCs in a *sdk1*$^{+/CE}$*; reporter* (*RC-FrePe*) mouse. Bulbous terminals in S5 are indicative of RBs. **(J)** Labeling of BCs in a *sdk2*$^{+/CE}$*; reporter* mouse. Broad axonal terminals in S4 are indicative of BC7. RBs are also labeled. A horizontal cell (h) is also labeled in this section. **(K)** Schematic of cell types that express *sdk1* and/or *sdk2*. Sketches summarize data from this figure, **Figure 2** and **Figure S2**. Bar, 3 μm in **(E,F)**, 10 μm for others.

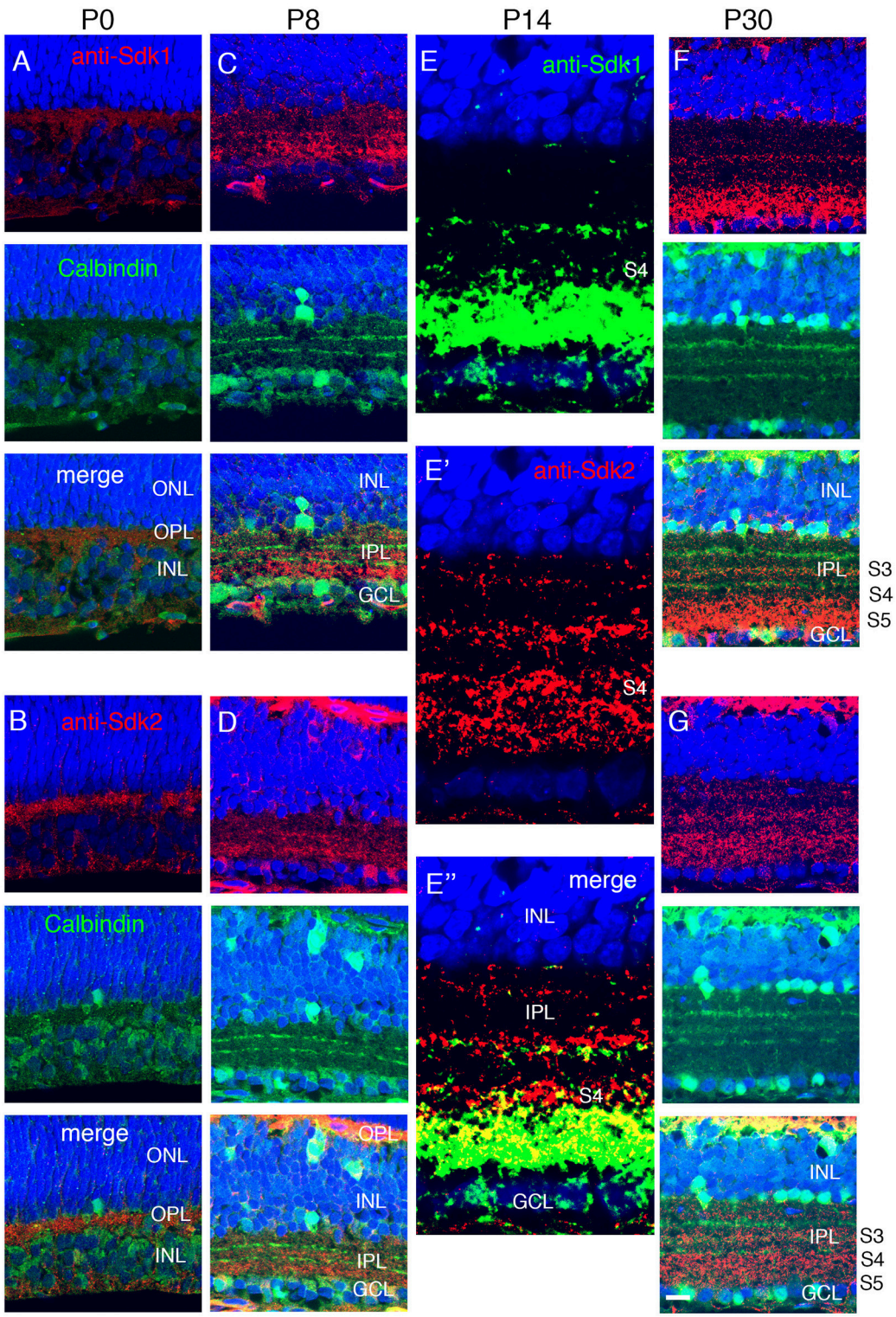

FIGURE 4 | Localization of Sdk1 and Sdk2 during retinal development. Sections from P0 **(A,B)**, P8 **(C,D)**, P14 **(E)**, or P30 **(F,G)** mice were stained with anti-Sdk1 **(A,C,E,F)** or anti-Sdk2 **(B,D,E′,G)**. Sections in **(A–D,F,G)** were double stained with anti-calbindin, which labels three narrow strata in the IPL (see **Figure 2**). Section in **(E)** was doubly stained with anti-Sdk1 and anti-Sdk2. **(A,B)** Little Sdk1 immunoreactivity is present at P0 **(A)**, but Sdk2 is present in the OPL **(B)**. **(C,D)** At P8, Sdk1 and Sdk2 are both present in S3-5 of the IPL. **(E)** By P14, Sdk1, and Sdk2 are present in a narrow band in S3 and a broader band in S4,5. Sdk1+ and Sdk2+ immunoreactive puncta overlap in S4,5 but are distinct in S3. **(F,G)** Pattern at P30 is similar to that at P14. Bar, 8 μm for **(E)**, and 25 μm for others.

TABLE 1 | Cell types expressing *sdk1* and/or *sdk2*.

Cell type	Class	Marker	IPL stratification	References
sdk1+ sdk2+				
ON-α-sustained	RGC	Spp1+, SMI32+	S4-5	Bleckert et al., 2014; Krieger et al., 2017
M2	RGC	Opn4+	S4-5	Schmidt and Kofuji, 2009; Berson et al., 2010
Rod bipolar	Bipolar	PKCα+	S5	Greferath et al., 1990
sdk1+ sdk2−				
Sdk1+S3-RGC	RGC	Calretinin+	S3 narrow	Possibly 5to in Bae et al., 2018
2CA	Amacrine	Calretinin+ *DAT-cre+*, *Gbx2+*	S3 narrow	Contini et al., 2010; Knop et al., 2011
A17	Amacrine	PKCα**+**, calretinin−, Dab1−	S5 and others	Menger and Wässle, 2000; Puthussery and Fletcher, 2007; Downie et al., 2009
sdk1− sdk2+				
W3B	RGC	*TYW3*	S3 (+S1) broad	Kim et al., 2010; Zhang et al., 2012
VG3	Amacrine	VGlut3**+**, PKCα−, calretinin−, Dab1−	S3 broad	Haverkamp and Wässle, 2004; Johnson et al., 2004; Grimes et al., 2011
Type 7 bipolar	bipolar	GUS8.4GFP	between S4 and S5	Wässle et al., 2009; Shekhar et al., 2016
Unknown	amacrine	VGlut3−, PKCα−, Dab2−	S1-S4	N/A
Horizontal	horizontal	calbindin+	N/A	Pasteels et al., 1990

beyond S3 and the strength of VG3-W3B synapses is reduced by at least an order of magnitude (Krishnaswamy et al., 2015). We were not able to selectively label Sdk1+S3-RGCs to target them for recording, because our labeling methods preferentially marked 2CA-ACs and S5-arborizing RGCs in the ganglion cell layer. We therefore used histological methods to seek defects in Sdk1 mutants.

First, we examined 2CA-ACs labeled in the *DAT-cre* line. In heterozygotes (*DAT-cre*; *reporter*; s*dk1*$^{+/CE}$) dendrites were confined to a narrow stratum in the center of S3, as shown above (**Figures 3A,B**). In the absence of sdk1, however (*DAT-cre*; *reporter*; s*dk1*$^{CE/CE}$), dendrites sprouted beyond their laminar boundary (**Figures 5A–C**). Similar results were obtained using a *Gbx2* (*Gbx2-CreER*^{T2}*-IRES-GFP*) mouse line (Chen et al., 2009) which labels 2CA-ACs in both INL and GCL. 2CA-ACs sharply stratify in S3 (**Figure 5D,E**). To quantify the effect of Sdk1 deletion on 2CA-AC arbors, we plotted the laminar position of GFP-labeled dendritic segments, which appeared as spots in the micrographs. We then calculated the variance in position as an approximation of the diffuseness of the arbors within S3 (see Materials and Methods). The "Variance" scores from each dataset are shown in **Figure 5F**. An *F*-test demonstrated that the arbors were significantly more diffuse in *sdk1* mutant homozygotes than in heterozygotes.

To analyze arbors of the Sdk1+ RGCs that laminate in S3, we compared *STOP15*; s*dk1*$^{+/CE}$) and *STOP15*;s*dk1*$^{CE/CE}$ mice following administration of tamoxifen at P0 (**Figures 5G,H**). Cells were labeled sparsely in this genotype, making satisfactory quantification infeasible, but multiple examples showed that dendrites of Sdk1+S3-RGCs sprouted beyond their laminar boundary in mutants. However, both Sdk1-postitive 2CA-ACs and Sdk1+S3-RGCs are characterized by their expression of calretinin (**Figures 2D,E**, **3A,B**), so we quantified the localization of calretinin in the IPL. The central band, which contains dendrites of Sdk1+S3-RGCs and 2CA-ACs, was more diffuse in the absence of Sdk1 than in its presence. The effect was specific in that the inner and outer bands, which contain dendrites of Sdk1-negative starburst amacrine cells, was not affected (**Figures 5I–K**). Together, these results suggest that neuronal processes of *sdk1*-expressing RGCs and amacrine cells in S3 exhibit decreased laminar restriction in the absence of Sdk1.

Lamination Defects in sdk1/sdk2 Double Mutants

We labeled ONα RGCs and rod bipolar cells, which express both *sdk1* and *sdk2*, in *sdk1*, and *sdk2* single mutants and in *sdk1sdk2* double mutants. Although the number of cells analyzed was insufficient for detailed quantification, we detected no obvious defects in the dendritic arbors of the ONα RGCs (**Figures 6A–E**). Likewise, the laminar position and size of rod bipolar terminals was unaffected in *sdk1sdk2* double mutants (**Figures 6F–L**). We also asked whether defects in VG3-ACs, which require Sdk2 for laminar restriction (Krishnaswamy et al., 2015) were more severe in double mutants, and found that they were not (**Figure S4**).

Sdk1 Acts Homophilically to Pattern Dendrites

To probe roles of Sdks further, we generated lines in which expression of *sdk1* or *sdk2*, along with a green fluorescent protein (Venus), required cre-mediated excision of a STOP cassette (**Figure 7A**). We crossed these mice to the *sdk2*$^{+/CE}$ line and delivered tamoxifen at P2, thereby expressing *sdk1* or *sdk2* plus Venus in a sparse subset of cells that normally express *sdk2*. Ectopic expression of *sdk1* in W3B-RGCs or VG3-ACs led to formation of narrowly stratified arbors,

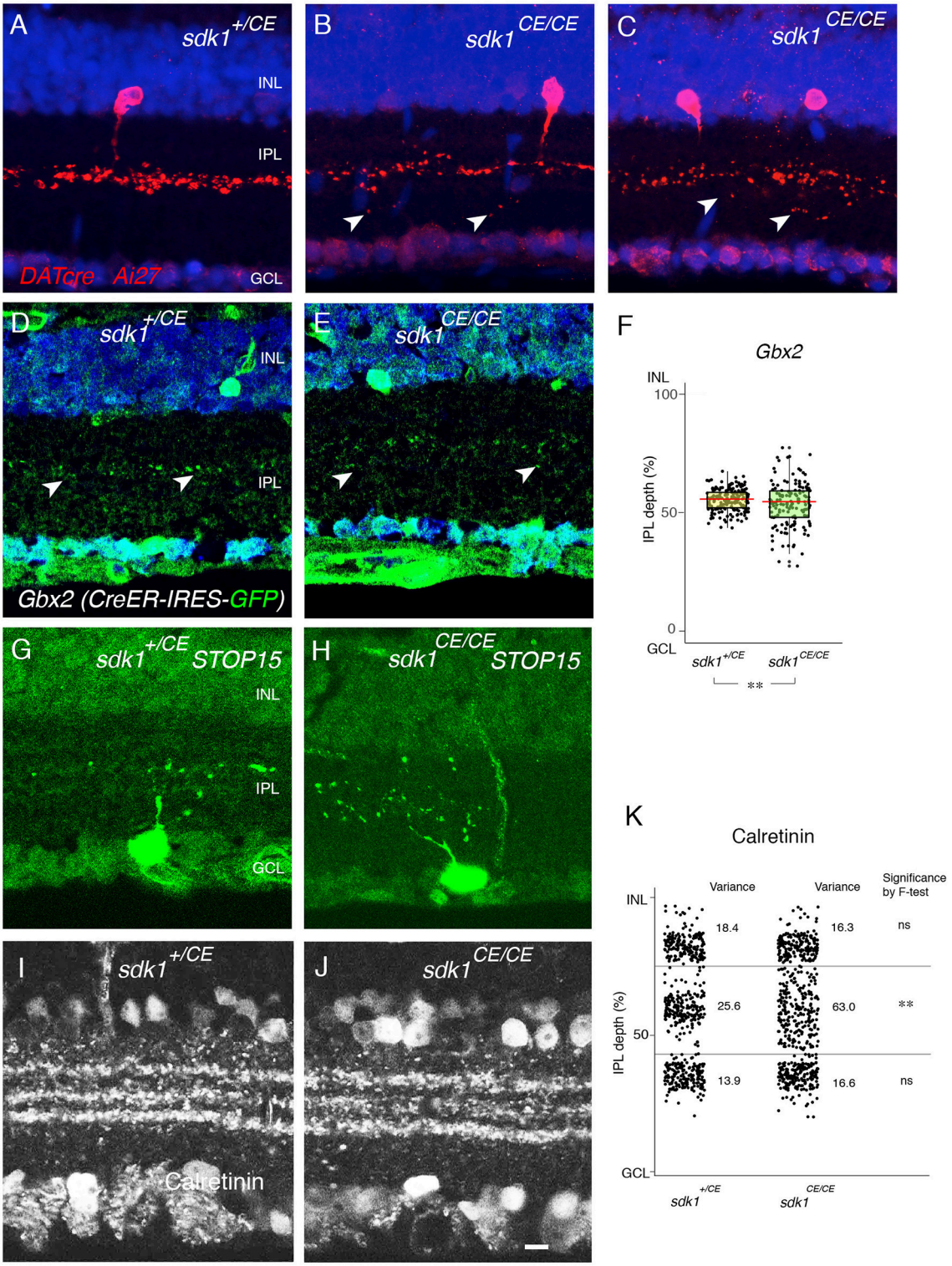

FIGURE 5 | Loss of function phenotype in *sdk1* mutants. **(A–C)** Type II catechoraminergic amacrine (2CA) cells in INL labeled in *DATcre;*reporter (*Ai27*) mice in the presence **(A)** or absence of *sdk1* **(B,C)**. In homozygotes, stratification of 2CA cells is diffuse, associated with occasional sprouting (arrows). **(D,E)** Stratification of 2CA dendrites in S3 of *Gbx2-CreERT2-IRES-GFP*; this line labels 2CA cells in both INL and GCL in $sdk1^{+/CE}$ **(D)** or $sdk1^{CE/CE}$ **(E)**. **(F)** Position of GFP-positive dendritic segments plotted from micrographs such as in **(D)** ($n = 6$ areas from 3 animals) and **(E)** ($n = 6$ areas from 3 animals). The laminar position of GFP+ spots were measured and box-plotted **(F)**. Box-plots show upper and lower quartiles (box), median (horizontal line in the box), and the highest and lowest value excluding outliers

(Continued)

FIGURE 5 | (lines). The variance score is 2.0 for $sdk1^{+/CE}$ and 8.4 for $sdk1^{CE/CE}$. *F*-test for the variation is significant (**$F < 0.0001$). **(G,H)** Cells in the GCL and their dendritic arbors were labeled by crossing $sdk1^{+/CE}$ **(D)** or $sdk1^{CE/CE}$ **(E)** to the *STOP15* reporter. Dendritic arbors in homozygotes are more diffusely distributed in the IPL than that in heterozygotes. **(I–J)** Localization of calretinin in $sdk1^{+/CE}$ **(I)** or $sdk1^{CE/CE}$ **(J)** mice. **(K)** The position of the calretinin+ spots were measured from micrographs such as those in **(I)** ($n = 3$ areas from 3 animals) and **(J)** ($n = 3$ areas from 3 animals), and box-plotted as in **(F)**. *F*-test for the variation is significant (**$F < 0.0001$) for the middle band. Variation of the outer and inner calretinin-positive bands, corresponding to sdk-negative processes including starburst amacrine cells, is unaltered. Bar, 10μm.

similar to those of Sdk1-positive Sdk1+S3-RGCs or 2CA-ACs, respectively (**Figures 7C,E,G**). In contrast, the arbors were unperturbed by expression of *sdk2* plus Venus or of Venus alone (**Figures 7B,F,G**).

As noted above, satisfactory quantification was infeasible for RGCs, but we used analysis of variance to quantify these effects for VG3-ACs, demonstrating that they were highly significant. We also showed that Sdk1 acted similarly in a Sdk2 mutant background ($sdk2^{CE/CE}$) (**Figures 7D,G**). Thus, Sdk1 can pattern dendritic arbors in cells that are normally *sdk1*-negative.

We then used this model to ask whether Sdk1 acts homophilically to pattern dendritic arbors. To this end, we expressed *sdk1* in VG3-ACs in the absence of endogenous *sdk1* (*RC-vS-Sdk1*; *sdk2-CreER*; $sdk1^{\Delta N/\Delta N}$) (**Figure 8**). In this case, ectopic Sdk1 had no significant effect on VG3-AC arbors, suggesting that the effects of Sdk1 on dendrites require homophilic interactions among arbors.

Sensitive Period for Sdk1 Function

We next used the ectopic expression model to ask whether Sdk1 can remodel dendrites after dendritic growth is over. To this end, tamoxifen was injected at P24 after IPL sublamination had been established. The morphological change documented above for P2 tamoxifen treatment was not observed at either P32 (**Figures 9A,B,D**) or P60 (**Figures 9C,D**). This result suggests that once lamination patterns are established, they are resistant to remodeling by Sdk1.

Effects of Sdk1 on Starburst Amacrines and J-RGCs

Finally, we asked whether ectopic Sdk1 could affect lamination of other cell types. We tested two types for which reliable cre drivers were available: starburst amacrine cells (*Chat-cre*) (Rossi et al., 2011) and J-RGCs (*JamCreER*) (Kim et al., 2008). Starburst amacrine cell dendrites arborize in two narrow bands in S2 and S4. Levels of ectopically expressed Sdk1 were similar to endogenous levels in S3 (**Figures 10A–D**). However, the lamination of starburst amacrine cells appeared unaffected by the ectopic expression of *sdk1*.

J-RGC dendrites ascend through the IPL, crossing S3 to arborize in S1. In this case, overexpression of Sdk1 let to formation of dendritic branches in S3 (**Figures 10E–J**). As was the case for remodeling of VG3-AC dendrites, no remodeling was observed in a $sdk1^{\Delta N/\Delta N}$ background (**Figures 10H,J**), indicating that Sdk1 acts homophilically in J-RGCs.

DISCUSSION

A group of four closely related immunoglobulin superfamily adhesion molecules has been implicated in assembly of neural circuits in chick retina: Sdk1, Sdk2, Dscam and DscamL (Yamagata et al., 2002; Yamagata and Sanes, 2008, 2010, 2012a). Of these, three have also been shown to play roles in assembly of neural circuits in mouse retina: Sidekick 2, Dscam and DscamL (Fuerst et al., 2008, 2009; Krishnaswamy et al., 2015). Here, to complete this set of studies, we investigated the expression and role of Sdk1 in developing retina.

Sdks Mediate Sublaminar Specificity in Retina

Sdk1 and *Sdk2* are each expressed by defined types of retinal neurons. Of ∼140 total retinal neuronal types in mice, 11 (∼7%) express *sdk1* and/or *sdk2* at appreciable levels. Of these, 3 express *sdk1* but not *sdk2*, 5 express *sdk2* but not *sdk1* and 3 express both *sdk1* and *sdk2* (**Figure 3K**).

Of particular note are two pairs of *sdk*-positive neurons with arbors in S3. VG3-ACs and W3B-RGCs are both *sdk2*-positive and arborize in S3. Likewise, 2CA-ACs and S3-RGCs are both *sdk1*-positive and arborize in S3. The pairs differ, however, in their sublaminar restriction: the Sdk2-positive cells arborize diffusely within S3, whereas the Sdk1-positive cells arborize in a narrow stratum at the center of S3. Moreover, VG3-ACs synapse strongly whereas 2CA-ACs synapse only weakly on W3B-RGCs (Krishnaswamy et al., 2015). Together, these results suggest that the *sdk1*- and *sdk2*-positive pairs comprise separate channels in S3.

Genetic studies indicate that *sdk1* and *sdk2* mutants not only mark these channels but are necessary for their formation. The laminar restriction of VG3-ACs and W3B-RGCs is disrupted in *sdk2* mutants, whereas there is no detectable effect on arbors of 2CA-ACs and Sdk1+S3-RGCs. Conversely, the laminar restriction of 2CA-ACs and Sdk1+S3-RGCs is disrupted in *sdk1* mutants, with no detectable effect on arbors of VG3-ACs and W3B-RGCs. Physiological studies show that functional connectivity of VG3-ACs with W3B-RGCs is dramatically reduced in *sdk2* mutants, with no effect on the weak 2CA-AC to W3B-RGC connectivity. As noted above, we have not yet been able to target Sdk1+S3-RGCs for recording, but we speculate that they will exhibit the opposite pattern—strong synapses from 2CA-ACs, weak synapses from VG3-ACs, loss of connectivity in *sdk1* mutants, and no defects in *sdk2* mutants.

We also found that $sdk1^{+}sdk2^{+}$ interneurons and RGCs share laminar restriction, with rod bipolar cells, ON-α sustained RGCs and M2 intrinsically photosensitive RGCs all of which arborize in S5. In this case, however, we detected no morphological defects

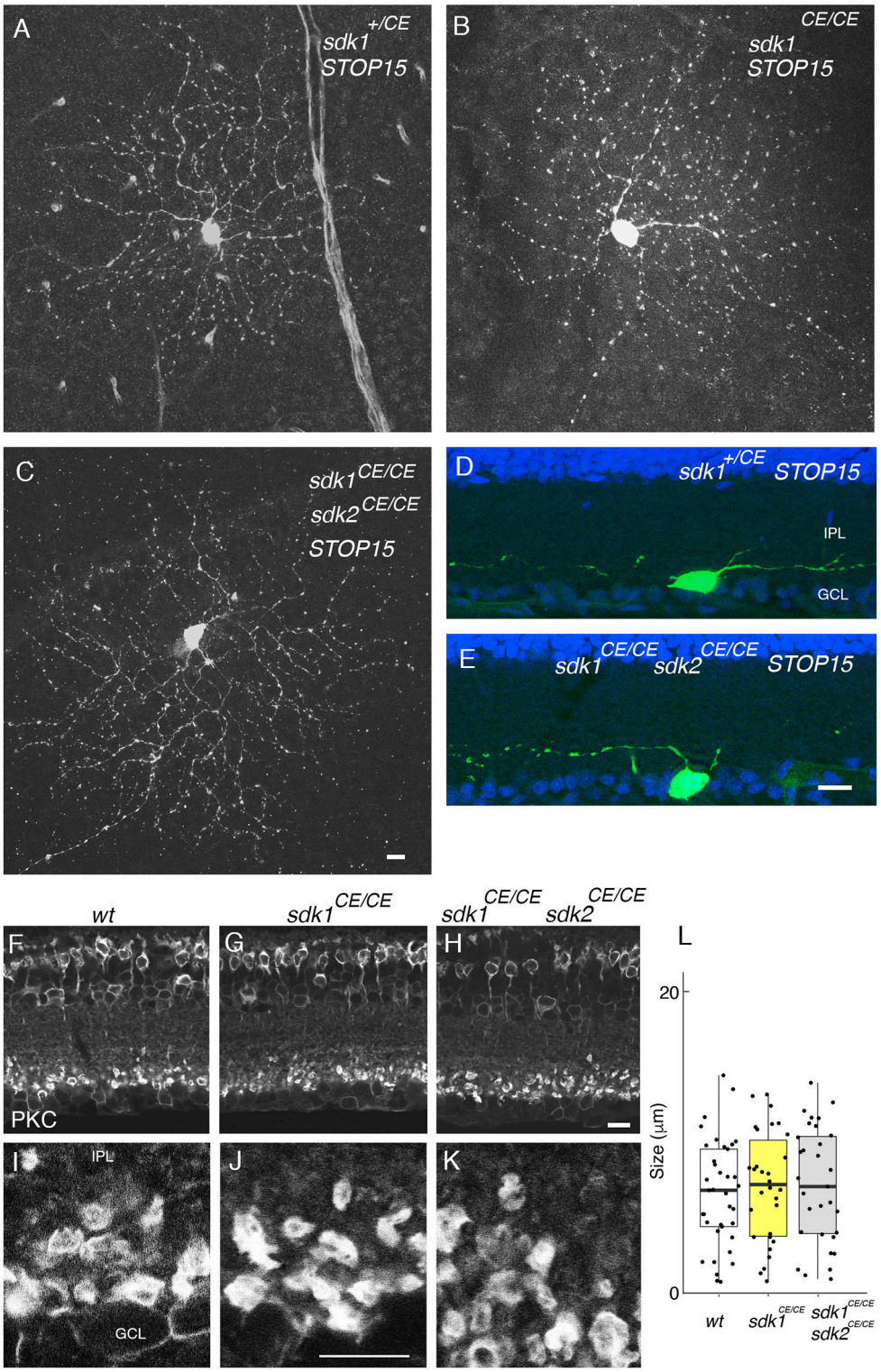

FIGURE 6 | Phenotype in *sdk1 sdk2* double knock-out retina. **(A–E)** Large RGCs with dendrites in S5, viewed in flat mounts of tamoxifen-injected $sdk1^{+/CE}$ **(A)**, $sdk1^{CE/CE}$ **(B)**, or $sdk1^{CE/CE}$ $sdk2^{CE/CE}$ **(C)** mice or in sections of $sdk1^{+/CE}$ **(D)** or $sdk1^{CE/CE}$ $sdk2^{CE/CE}$ **(E)** mice. Cell were visualized with the *STOP15* reporter. **(F–L)** Rod bipolar terminals in S5 labeled with anti-PKCα in wildtype **(F,I)** $sdk1^{CE/CE}$ **(G,J)** or $sdk1^{CE/CE}$ $sdk2^{CE/CE}$ **(H,K)** mice. Overall stratification was not affected in $sdk1^{CE/CE}$ or $sdk1^{CE/CE}$ $sdk2^{CE/CE}$ **(F–H)**. The circumference of PKCα-stained terminals **(J–K)** was measured, and plotted **(I)** ($n = 31$–38 from one animal each). Differences among genotypes were not significant by one-way ANOVA [$Pr(>F) = 0.81$; $p > 0.8$ by Tukey *post-hoc* test]. Bar, 10 μm.

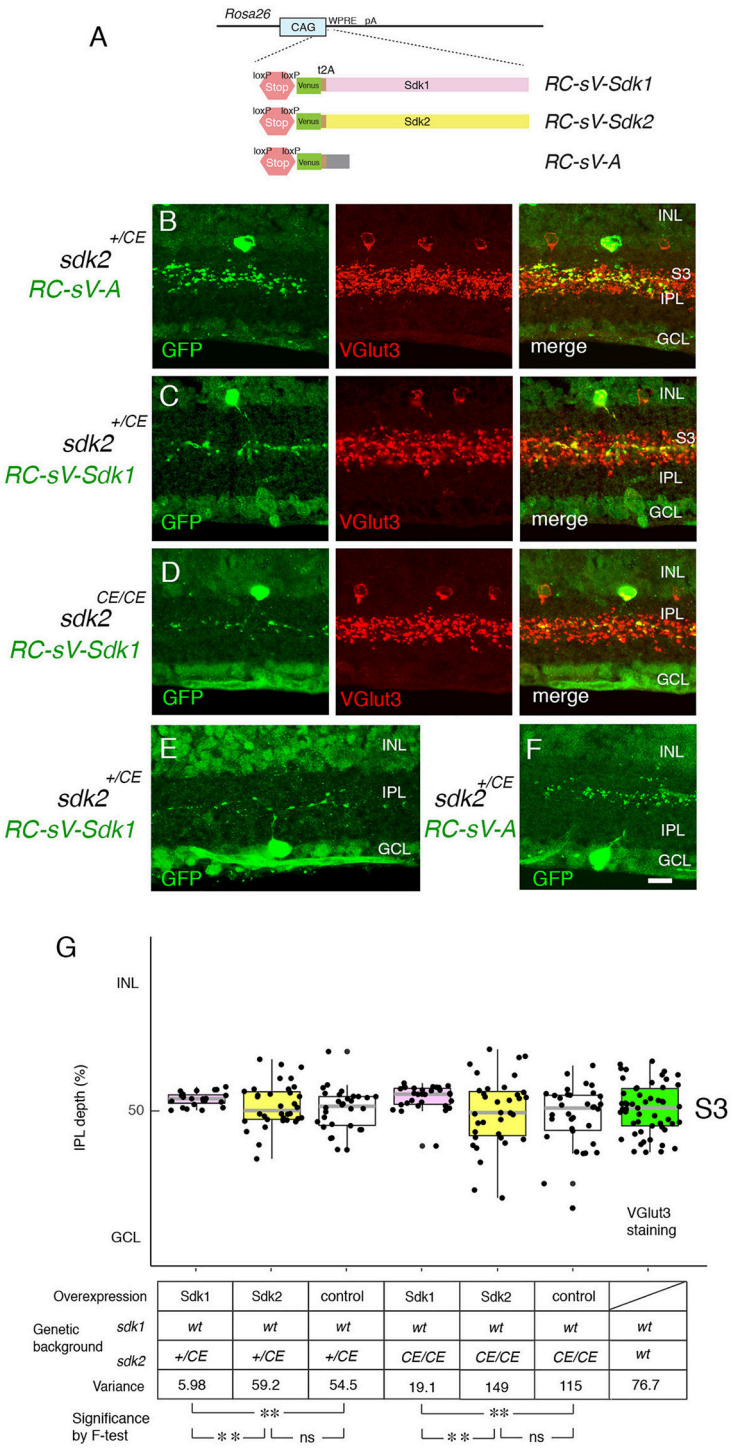

FIGURE 7 | Overexpression of Sdk1 patterns dendrites. **(A)** Design of *RC-sV-Sdk1*, *RC-sV-Sdk2*, and *RC-sV-A* mouse lines. By crossing *RC-sV-Sdk1* and *RC-sV-Sdk2* to appropriate *Cre* driver lines, Sdk1 and Sdk2 can be overexpressed. The Sdk proteins are coexpressed with Venus (GFP) via a self-cleavable F2A sequence. *RC-sV-A* expresses Venus but not Sdk following Cre-mediated recombination. **(B–D)** VG3 cells labeled in $sdk2^{+/CE}$; *RC-sV-A* mice exhibited characteristic morphology **(B)**. Expression of *sdk1* in $sdk2^{+/CE}$; *RC-sV-Sdk1* **(C)** or $sdk2^{CE/CE}$; *RC-sV-Sdk1* mice **(D)** resulted in the VG3 ACs acquiring a narrow arbor similar to that of Sdk1+ CA2 ACs. Pups were injected with tamoxifen at P2 dissected at P32, and stained with antibodies to GFP and VGlut3. **(E,F)** W3B RGCs labeled in $sdk2^{+/CE}$;*RC-sV-Sdk1* **(E)** or $sdk2^{+/CE}$;*RC-sV-A* **(F)** mice. Expression of *sdk1*resulted in the W3B RGCs acquiring a narrow dendritic arbor similar to that of the Sdk1+RGCs shown in **Figure 2**. Pups were injected with tamoxifen at P2, and dissected at P32. Bar indicates 10μm for **(A–F)**. **(G)** Laminar position of GFP+ spots from indicated genotypes was measured in micrographs such as those shown in **(B–D)**, and plotted as in **Figure 5** (n = 5–6 neurons from each of 3 animals). Plot at far right derived from VGlut3 staining. Variance scores are shown under the graph. Statistical significance of variance by F-test: ns, $F > 0.1$; $^{**}F < 0.001$.

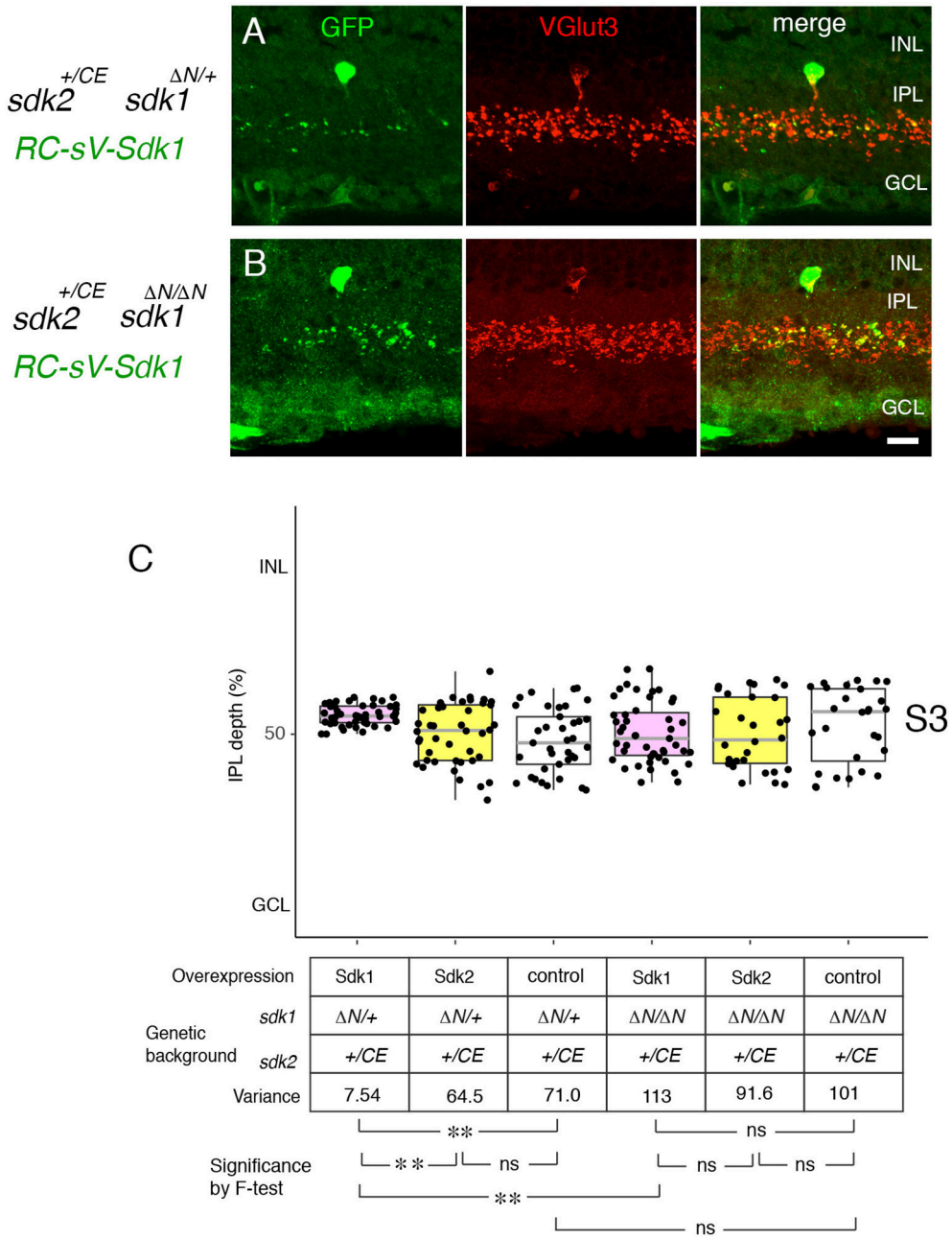

FIGURE 8 | Sdk1 patterns dendrites homophillically. **(A,B)** *Sdk1* was expressed in VG3 cells (*RC-sV-Sdk1;sdk2*$^{+/CE}$) in the presence (*sdk1*$^{+/\Delta N}$) **(A)** or absence (*sdk1* $^{\Delta N/\Delta N}$) **(B)** of endogenous Sdk1. Pups were injected with tamoxifen at P2, and dissected at P32. Narrowing of arbors elicited by ectopic expression of *sdk1* did not occur in the absence of endogenous Sdk1. Bar, 10μm. **(C)** Laminar positioning of GFP+ spots from indicated genotypes was measured in micrographs such as those shown in **(A,B)**, and presented as boxplots as in **Figure 5** ($n = 5$ neurons from each of 3 animals). Statistical significance of variance by *F*-test: ns, $F > 0.1$; $^{**}F < 0.001$.

in the arbors of these cells in *sdk1* or *sdk2* mutants or in *sdk1sdk2* double mutants. Rod bipolars also express the related recognition molecule, DscamL (Fuerst et al., 2009), and it possible that deletion of both recognition systems would be required to disrupt these arbors.

Cells that express both *sdk1* and *sdk2* can, of course, interact with cells that express either *sdk1*$^{+}$ or *sdk2*$^{+}$, generating bifurcated circuits. In this regard, it is intriguing that Sdk1-positive A17 amacrine cells also arborize extensively in S5. A circuit involving A17 amacrine cells has been characterized in rabbits, and A17 terminals contact both rod bipolar axons and ON-RGC dendrites (Diamond, 2017). Likewise, Sdk2-positive horizontal cells interact with rod bipolar dendrites in the outer plexiform layer.

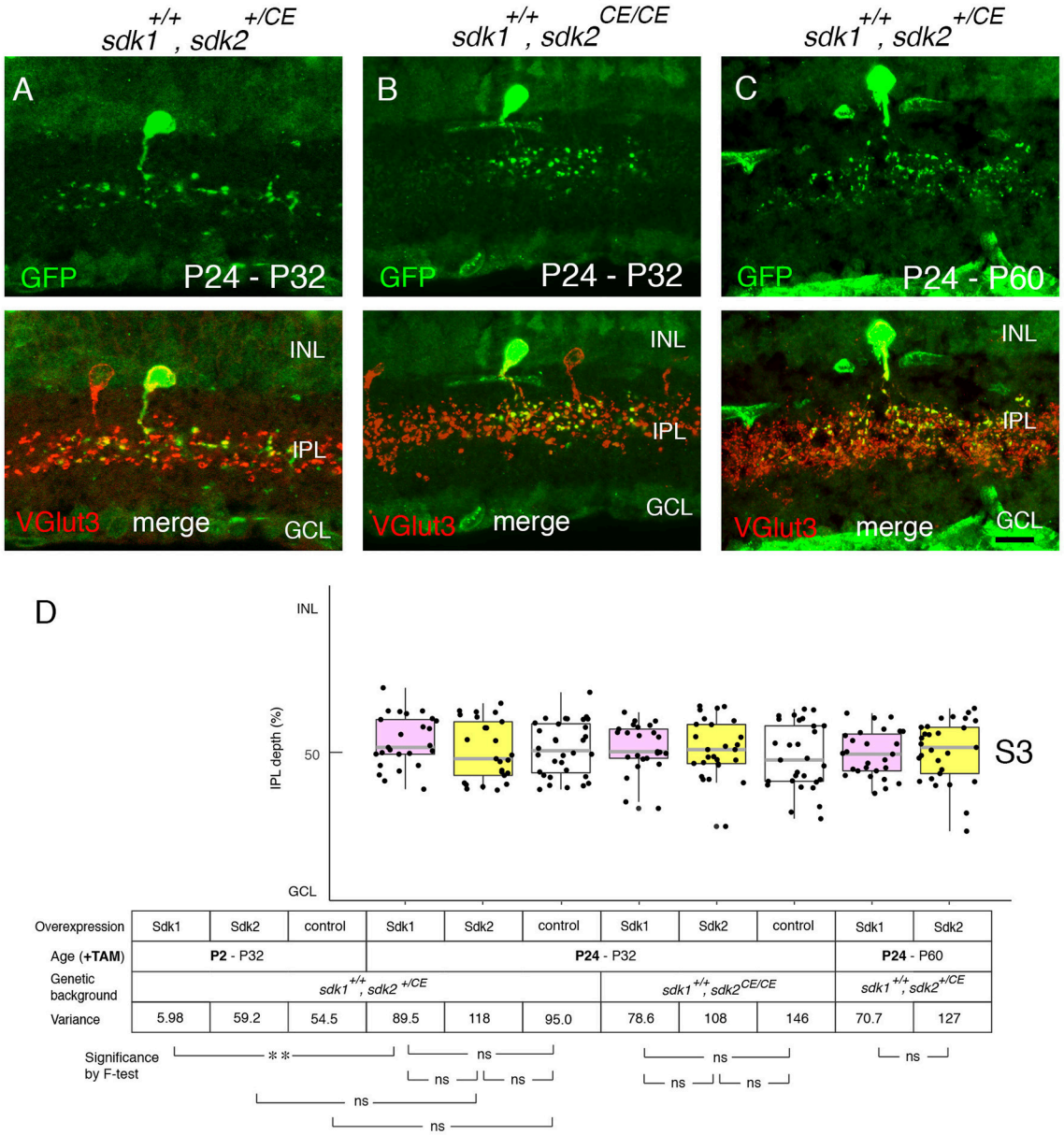

FIGURE 9 | Sensitive period for Sdk1 overexpression. **(A–C)** *RC-sV-Sdk1* was crossed to $sdk2^{+/CE}$ **(A,C)** or $sdk2^{CE/CE}$ **(B)**. In this experiment, the crosses were carried out as in **Figures 6**, **7**, but pups were injected with tamoxifen at P24 instead of P2, and dissected at P32 **(A,B)** or P60 **(C)**. Overexpression of sdk1 starting at P24 did not affect the morphology of VG3 cells. Bar, 10μm. **(D)** The laminar positioning of GFP+ spots from indicated genotypes was measured in micrographs such as those shown in **(A,C)**, and presented as boxplots as in **Figure 5** ($n = 6$ neurons from each of 2–3 animals). Statistical significance of variance by F-test: ns, $F > 0.1$; $^{**}F < 0.001$. The data for P2-P32 are from **Figure 5G** for comparison.

Sdk1 Acts Instructively and Homophilically During Arbor Formation

To analyze the mechanism by which Sdk1 acts we used a gain-of-function strategy, expressing it in cells that are normally *sdk1*-negative. From our results, we draw three conclusions. First, Sdk1 acts instructively. When expressed in VG3-ACs, it remodels their arbors in S3 from their normal diffuse pattern to the narrow, central pattern characteristic of Sdk1-positive 2CA-ACs. Likewise, expression of Sdk1 in J-RGCs, which arborize in S1, results in formation of ectopic branches in S3. Sdk1 is restricted in its potency, however; expression in starburst amacrines, with dendrites that border S3, has no detectable effect. We do not know what cell type-specific factors affect the ability of Sdk1 to pattern arbors.

Second, Sdk1 acts homophilically in that its ability to pattern arbors require that it be expressed in neighboring cells. Thus,

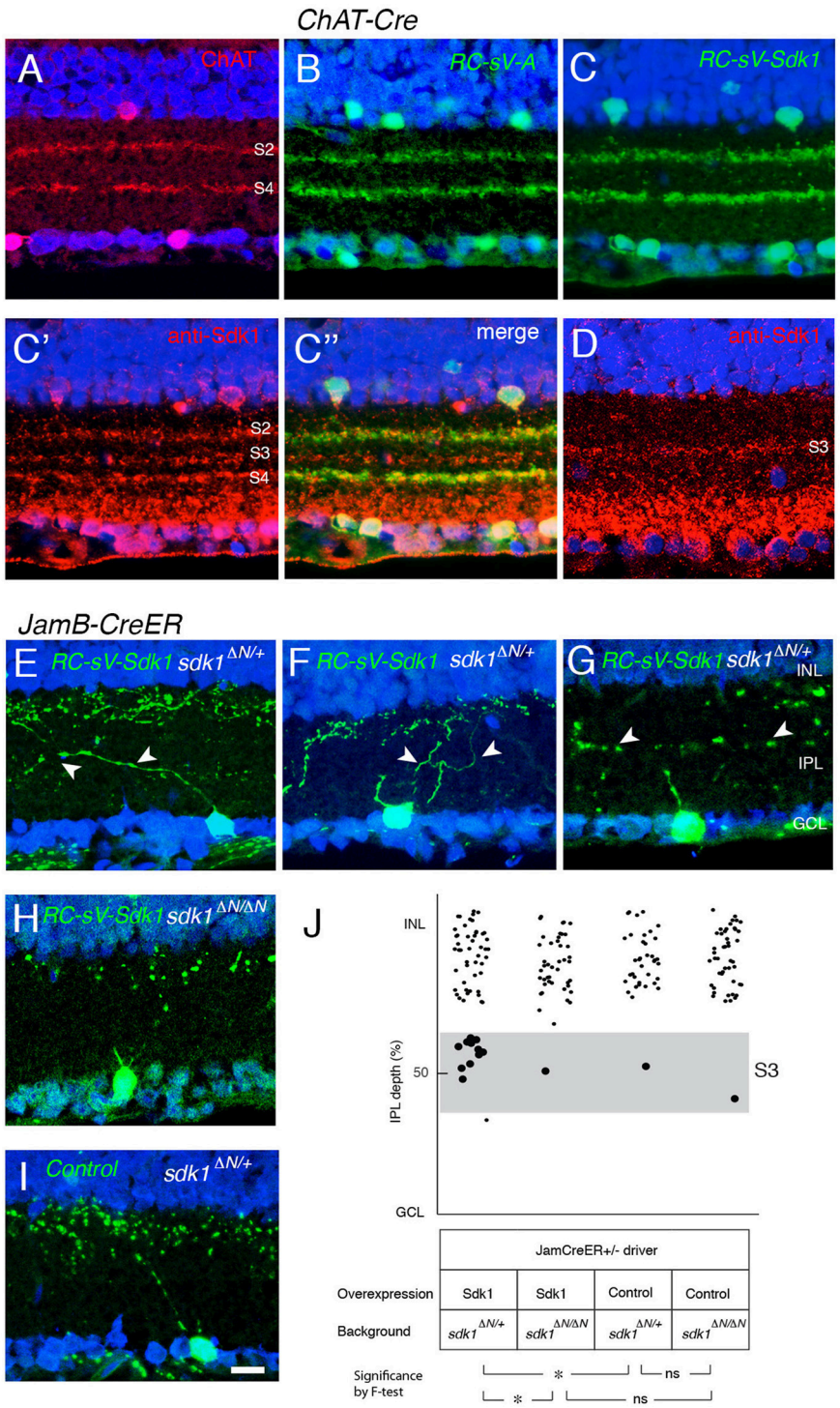

FIGURE 10 | Sdk1 overexpression in starburst amacrine cells and J-RGCs. **(A)** Starburst amacrine cell dendrites stratify in S2 and S4. P30 section stained with anti-ChAT. **(B)** Overexpression of Venus (GFP) in starburst amacrine cells (*RC-sV-A; ChAT-Cre*) labels S2 and S4. **(C)** Overexpression of Sdk1 and Venus (GFP) in starburst amacrine cells (*RC-sV-Sdk1; ChAT-Cre*) labeled tight fascicles in S2 and S4, indistinguishable from controls **(A,B)**. Staining with anti-Sdk1 confirms ectopic expression (C′,C″). **(D)** Immunostaining of wildtype P30 retina with anti-Sdk1 antibodies. Comparison with A′ indicates that recombinant Sdk1 is present at levels similar to those of endogenous Sdk1. **(E–I)** J-RGCs labeled in *JamB*^{CE} *;RC-sV-Sdk1; sdk1* $^{+/\Delta N}$**(E–G)**, *JamB*^{CE} *;RC-sV-Sdk1*; *sdk1* $^{\Delta N/\Delta N}$**(H)** or *JamB1*^{CE}*;RC-sV-A; ; sdk1* $^{+/\Delta N}$ **(I)** mice. Pups were injected with tamoxifen at P2, and dissected at P32. J-RGC dendrites normally arborize in S1 **(I)** but expression of *sdk1* led to formation of ectopic processes in S3 **(E–G)**. Mistargeting arbors elicited by ectopic expression of *sdk1* did not occur in the absence of endogenous Sdk1 (*sdk1* $^{\Delta N/\Delta N}$) **(H)**. Bar, 10μm. **(J)** Laminar position of GFP+ spots from indicated genotypes were plotted as in **Figure 5** ($n = 5$ neurons from each of 3 animals). Dots in S3 (40–60% IPL depth) were enlarged for emphasis. Statistical significance of variance by F-test: ns, $F > 0.1$; *$F < 0.01$.

expression of *sdk1* in small numbers of VG3-ACs or J-RGCs fails to affect their arbors in a *sdk1* mutant background. The simplest interpretation of this finding is that ectopically expressed *sdk1* leads to fasciculation of neurites with those of cells that express *sdk1* endogenously. This mechanism is consistent with the observation that formation of synapses between *sdk2*-positive cells requires expression of *sdk2* on both synaptic partners (Krishnaswamy et al., 2015).

Third, Sdk1 acts during a restricted period of development, as arbors are forming. When ectopic expression is initiated after arbors have already formed, it has no detectable effect over a period of at least 1 month. Apparently, once arbors have matured, they become resistant to remodeling.

Taken together, we and Fuerst, Burgess, and colleagues have now demonstrated roles for Sdk1, Sdk2, Dscam and DscamL1 in patterning the IPL in both chick and mouse retina (Yamagata et al., 2002; Fuerst et al., 2008, 2009, 2012; Yamagata and Sanes, 2008, 2010; Krishnaswamy et al., 2015; Garrett et al., 2016). There are interesting differences in phenotype among molecules and between species. For example, Dscam and DscamL1 appear to act by an inhibitory mechanism in mice but an attractive mechanism in chicks, whereas Sdks act by an attractive mechanism in both species (Fuerst et al., 2008, 2009; Yamagata and Sanes, 2008; and this paper). Also, the four relatives are expressed by almost entirely non-overlapping populations in chick retina, whereas some retinal neuronal types express both *sdks*, and/or *sdks* and *dscams* (Fuerst et al., 2008, 2009 and this paper). Despite these differences, however, results to date make a strong case that selective expression of these recognition molecules, as well as the closely related contactins (Yamagata and Sanes, 2012a; Peng et al., 2017), generates an "immunoglobulin superfamily code" critical for synaptic specificity in the vertebrate retina.

AUTHOR CONTRIBUTIONS

MY and JS planned experiments and wrote the manuscript. MY performed experiments and analyzed data.

ACKNOWLEDGMENTS

We thank the Genome Modification Facility at Harvard University for generation of mice. We thank Arjun Krishnaswarmy and Nick Tran for advice and Emily Martersteck for assistance. This work was supported by the grants from National Institute of Heath (R37NS029169 and R01EY022073).

SUPPLEMENTARY MATERIAL

The Supplementary Material for this article can be found online at: https://www.frontiersin.org/articles/10.3389/fnmol.2018.00485/full#supplementary-material

REFERENCES

Astigarraga, S., Douthit, J., Tarnogorska, D., Creamer, M. S., Mano, O., Clark, D. A., et al. (2018). Drosophila Sidekick is required in developing photoreceptors to enable visual motion detection. *Development* 145:dev158246. doi: 10.1242/dev.158246

Baden, T., Berens, P., Franke, K., Román Rosón, M., Bethge, M., and Euler, T. (2016). The functional diversity of retinal ganglion cells in the mouse. *Nature* 529, 345–350. doi: 10.1038/nature16468

Bae, J. A., Mu, S., Kim, J. S., Turner, N. L., Tartavull, I., Kemnitz, N., et al. (2018). Digital museum of retinal ganglion cells with dense anatomy and physiology. *Cell* 173, 1293–1306. doi: 10.1016/j.cell.2018.04.040

Beard, C., Hochedlinger, K., Plath, K., Wutz, A., and Jaenisch, R. (2006). Efficient method to generate single-copy transgenic mice by site-specific integration in embryonic stem cells. *Genesis* 44, 23–28. doi: 10.1002/gene.20180

Berson, D. M., Castrucci, A. M., and Provencio, I. (2010). Morphology and mosaics of melanopsin-expressing retinal ganglion cell types in mice. *J. Comp. Neurol.* 518, 2405–2422. doi: 10.1002/cne.22417

Bleckert, A., Schwartz, G. W., Turner, M. H., Rieke, F., and Wong, R. O. L. (2014). Visual space is represented by nonmatching topographies of distinct mouse retinal ganglion cell types. *Curr. Biol.* 24, 310–315. doi: 10.1016/j.cub.2013.12.020

Brüggen, B., Meyer, A., Boven, F., Weiler, R., and Dedek, K. (2015). Type 2 wide-field amacrine cells in TH::GFP mice show a homogenous synapse distribution and contact small ganglion cells. *Eur. J. Neurosci.* 41, 734–747. doi: 10.1111/ejn.12813

Buffelli, M., Burgess, R. W., Feng, G., Lobe, C. G., Lichtman, J. W., and Sanes, J. R. (2003). Genetic evidence that relative synaptic efficacy biases the outcome of synaptic competition. *Nature* 424, 430–434. doi: 10.1038/nature01844

Cai, D., Cohen, K. B., Luo, T., Lichtman, J. W., and Sanes, J. R. (2013). Improved tools for the Brainbow toolbox. *Nat. Methods* 10, 540–547. doi: 10.1038/nmeth.2450

Chen, L., Guo, Q., and Li, J. Y. H. (2009). Transcription factor Gbx2 acts cell-nonautonomously to regulate the formation of lineage-restriction boundaries of the thalamus. *Development* 136, 1317–1326. doi: 10.1242/dev.030510

Contini, M., Lin, B., Kobayashi, K., Okano, H., Masland, R. H., and Raviola, E. (2010). Synaptic input of ON-bipolar cells onto the dopaminergic neurons of the mouse retina. *J. Comp. Neurol.* 518, 2035–2050. doi: 10.1002/cne.22320

Diamond, J. S. (2017). Inhibitory interneurons in the retina: types, circuitry, and function. *Annu. Rev. Vision Sci.* 3, 1–24. doi: 10.1146/annurev-vision-102016-061345

Downie, L. E., Vessey, K., Miller, A., Ward, M. M., Pianta, M. J., Vingrys, A. J., et al. (2009). Neuronal and glial cell expression of angiotensin II type 1 (AT1) and type 2 (AT2) receptors in the rat retina. *Neuroscience* 161, 195–213. doi: 10.1016/j.neuroscience.2009.02.084

Duan, X., Krishnaswamy, A., De la Huerta, I., and Sanes, J. R. (2014). Type II cadherins guide assembly of a direction-selective retinal circuit. *Cell* 158, 793–807. doi: 10.1016/j.cell.2014.06.047

Duan, X., Krishnaswamy, A., Laboulaye, M. A., Liu, J., Peng, Y.-R., Yamagata, M., et al. (2018). Cadherin combinations recruit dendrites of distinct retinal neurons to a shared interneuronal scaffold. *Neuron* 99, 1145–1154. doi: 10.1016/j.neuron.2018.08.019

Duan, X., Qiao, M., Bei, F., Kim, I.-J., He, Z., and Sanes, J. R. (2015). Subtype-specific regeneration of retinal ganglion cells following axotomy: effects of osteopontin and mTOR signaling. *Neuron* 85, 1244–1256. doi: 10.1016/j.neuron.2015.02.017

Dymecki, S. M., Ray, R. S., and Kim, J. C. (2010). Mapping cell fate and function using recombinase-based intersectional strategies. *Methods Enzymol.* 477, 183–213. doi: 10.1016/S0076-6879(10)77011-7

Fuerst, P. G., Bruce, F., Rounds, R. P., Erskine, L., and Burgess, R. W. (2012). Cell autonomy of DSCAM function in retinal development. *Dev. Biol.* 361, 326–337. doi: 10.1016/j.ydbio.2011.10.028

Fuerst, P. G., Bruce, F., Tian, M., Wei, W., Elstrott, J., Feller, M. B., et al. (2009). DSCAM and DSCAML1 function in self-avoidance in

multiple cell types in the developing mouse retina. *Neuron* 64, 484–497. doi: 10.1016/j.neuron.2009.09.027

Fuerst, P. G., Koizumi, A., Masland, R. H., and Burgess, R. W. (2008). Neurite arborization and mosaic spacing in the mouse retina require DSCAM. *Nature* 451, 470–474. doi: 10.1038/nature06514

Garrett, A. M., Tadenev, A. L., Hammond, Y. T., Fuerst, P. G., and Burgess, R. W. (2016). Replacing the PDZ-interacting C-termini of DSCAM and DSCAML1 with epitope tags causes different phenotypic severity in different cell populations. *eLife* 5:e16144. doi: 10.7554/eLife.16144

Goodman, K. M., Yamagata, M., Jin, X., Mannepalli, S., Katsamba, P. S., Ahlsén, G., et al. (2016). Molecular basis of sidekick-mediated cell-cell adhesion and specificity. *eLife* 5:e19058. doi: 10.7554/eLife.19058

Greferath, U., Grünert, U., and Wässle, H. (1990). Rod bipolar cells in the mammalian retina show protein kinase C-like immunoreactivity. *J. Comp. Neurol.* 301, 433–442. doi: 10.1002/cne.903010308

Grimes, W. N., Seal, R. P., Oesch, N., Edwards, R. H., and Diamond, J. S. (2011). Genetic targeting and physiological features of VGLUT3+ amacrine cells. *Vis. Neurosci.* 28, 381–392. doi: 10.1017/S0952523811000290

Haverkamp, S., and Wässle, H. (2004). Characterization of an amacrine cell type of the mammalian retina immunoreactive for vesicular glutamate transporter 3. *J. Comp. Neurol.* 468, 251–263. doi: 10.1002/cne.10962

Hayashi, K., Kaufman, L., Ross, M. D., and Klotman, P. E. (2005). Definition of the critical domains required for homophilic targeting of mouse sidekick molecules. *FASEB J.* 19, 614–616. doi: 10.1096/fj.04-2947fje

Hoon, M., Okawa, H., Della Santina, L., and Wong, R. O. L. (2014). Functional architecture of the retina: development and disease. *Prog. Retinal Eye Res.* 42, 44–84. doi: 10.1016/j.preteyeres.2014.06.003

Johnson, J., Sherry, D. M., Liu, X., Fremeau, R. T., Seal, R. P., Edwards, R. H., et al. (2004). Vesicular glutamate transporter 3 expression identifies glutamatergic amacrine cells in the rodent retina. *J. Comp. Neurol.* 477, 386–398. doi: 10.1002/cne.20250

Kaufman, L., Hayashi, K., Ross, M. J., Ross, M. D., and Klotman, P. E. (2004). Sidekick-1 is upregulated in glomeruli in HIV-associated nephropathy. *J. Am. Soc. Nephrol.* 15, 1721–1730. doi: 10.1097/01.ASN.0000128975.28958.C2

Kay, J. N., Chu, M. W., and Sanes, J. R. (2012). MEGF10 and MEGF11 mediate homotypic interactions required for mosaic spacing of retinal neurons. *Nature* 483, 465–469. doi: 10.1038/nature10877

Kim, I.-J., Zhang, Y., Meister, M., and Sanes, J. R. (2010). Laminar restriction of retinal ganglion cell dendrites and axons: subtype-specific developmental patterns revealed with transgenic markers. *J. Neurosci.* 30, 1452–1462. doi: 10.1523/JNEUROSCI.4779-09.2010

Kim, I.-J., Zhang, Y., Yamagata, M., Meister, M., and Sanes, J. R. (2008). Molecular identification of a retinal cell type that responds to upward motion. *Nature* 452, 478–482. doi: 10.1038/nature06739

Kim, T., Soto, F., and Kerschensteiner, D. (2015). An excitatory amacrine cell detects object motion and provides feature-selective input to ganglion cells in the mouse retina. *eLife* 4:e08025. doi: 10.7554/eLife.08025

Knop, G. C., Feigenspan, A., Weiler, R., and Dedek, K. (2011). Inputs underlying the ON-OFF light responses of type 2 wide-field amacrine cells in TH::GFP mice. *J. Neurosci.* 31, 4780–4791. doi: 10.1523/JNEUROSCI.6235-10.2011

Krieger, B., Qiao, M., Rousso, D. L., Sanes, J. R., and Meister, M. (2017). Four alpha ganglion cell types in mouse retina: function, structure, and molecular signatures. *PLoS ONE* 12:e0180091. doi: 10.1371/journal.pone.0180091

Krishnaswamy, A., Yamagata, M., Duan, X., Hong, Y. K., and Sanes, J. R. (2015). Sidekick 2 directs formation of a retinal circuit that detects differential motion. *Nature* 524, 466–470. doi: 10.1038/nature14682

Lee, S., Chen, L., Chen, M., Ye, M., Seal, R. P., and Zhou, Z. J. (2014). An unconventional glutamatergic circuit in the retina formed by vGluT3 amacrine cells. *Neuron* 84, 708–715. doi: 10.1016/j.neuron.2014.10.021

Lefebvre, J. L., Kostadinov, D., Chen, W. V., Maniatis, T., and Sanes, J. R. (2012). Protocadherins mediate dendritic self-avoidance in the mammalian nervous system. *Nature* 488, 517–521. doi: 10.1038/nature11305

Liu, J., Reggiani, J. D. S., Laboulaye, M. A., Pandey, S., Chen, B., Rubenstein, J. L. R., et al. (2018). Tbr1 instructs laminar patterning of retinal ganglion cell dendrites. *Nat. Neurosci.* 21, 659–670. doi: 10.1038/s41593-018-0127-z

Madisen, L., Mao, T., Koch, H., Zhuo, J., Berenyi, A., Fujisawa, S., et al. (2012). A toolbox of Cre-dependent optogenetic transgenic mice for light-induced activation and silencing. *Nat. Neurosci.* 15, 793–802. doi: 10.1038/nn.3078

Madisen, L., Zwingman, T. A., Sunkin, S. M., Oh, S. W., Zariwala, H. A., Gu, H., et al. (2010). A robust and high-throughput Cre reporting and characterization system for the whole mouse brain. *Nat. Neurosci.* 13, 133–140. doi: 10.1038/nn.2467

Masland, R. H. (2012). The neuronal organization of the retina. *Neuron* 76, 266–280. doi: 10.1016/j.neuron.2012.10.002

Matsuoka, R. L., Nguyen-Ba-Charvet, K. T., Parray, A., Badea, T. C., Chédotal, A., and Kolodkin, A. L. (2011). Transmembrane semaphorin signalling controls laminar stratification in the mammalian retina. *Nature* 470, 259–263. doi: 10.1038/nature09675

Menger, N., and Wässle, H. (2000). Morphological and physiological properties of the A17 amacrine cell of the rat retina. *Vis. Neurosci.* 17, 769–780. doi: 10.1017/S0952523800175108

Nguyen, D. N., Liu, Y., Litsky, M. L., and Reinke, R. (1997). The sidekick gene, a member of the immunoglobulin superfamily, is required for pattern formation in the Drosophila eye. *Development* 124, 3303–3312.

Pasteels, B., Rogers, J., Blachier, F., and Pochet, R. (1990). Calbindin and calretinin localization in retina from different species. *Vis. Neurosci.* 5, 1–16. doi: 10.1017/S0952523800000031

Peng, Y.-R., Tran, N. M., Krishnaswamy, A., Kostadinov, D., Martersteck, E. M., and Sanes, J. R. (2017). Satb1 regulates contactin 5 to pattern dendrites of a mammalian retinal ganglion cell. *Neuron* 95, 869–883. doi: 10.1016/j.neuron.2017.07.019

Puthussery, T., and Fletcher, E. L. (2007). Neuronal expression of P2X3 purinoceptors in the rat retina. *Neuroscience* 146, 403–414. doi: 10.1016/j.neuroscience.2007.01.055

Ran, F. A., Hsu, P. D., Lin, C.-Y., Gootenberg, J. S., Konermann, S., Trevino, A. E., et al. (2013). Double nicking by RNA-guided CRISPR Cas9 for enhanced genome editing specificity. *Cell* 154, 1380–1389. doi: 10.1016/j.cell.2013.08.021

Rheaume, B. A., Jereen, A., Bolisetty, M., Sajid, M. S., Yang, Y., Renna, K., et al. (2018). Single cell transcriptome profiling of retinal ganglion cells identifies cellular subtypes. *Nat. Commun.* 9:2759. doi: 10.1038/s41467-018-05134-3

Rodríguez, C. I., Buchholz, F., Galloway, J., Sequerra, R., Kasper, J., Ayala, R., et al. (2000). High-efficiency deleter mice show that FLPe is an alternative to Cre-loxP. *Nat. Genet.* 25, 139–140. doi: 10.1038/75973

Rossi, J., Balthasar, N., Olson, D., Scott, M., Berglund, E., Lee, C. E., et al. (2011). Melanocortin-4 receptors expressed by cholinergic neurons regulate energy balance and glucose homeostasis. *Cell Metab.* 13, 195–204. doi: 10.1016/j.cmet.2011.01.010

Sanes, J. R., and Masland, R. H. (2015). The types of retinal ganglion cells: current status and implications for neuronal classification. *Annu. Rev. Neurosci.* 38, 221–246. doi: 10.1146/annurev-neuro-071714-034120

Sanes, J. R., and Zipursky, S. L. (2010). Design principles of insect and vertebrate visual systems. *Neuron* 66, 15–36. doi: 10.1016/j.neuron.2010.01.018

Schmidt, T. M., and Kofuji, P. (2009). Functional and morphological differences among intrinsically photosensitive retinal ganglion cells. *J. Neurosci.* 29, 476–482. doi: 10.1523/JNEUROSCI.4117-08.2009

Shekhar, K., Lapan, S. W., Whitney, I. E., Tran, N. M., Macosko, E. Z., Kowalczyk, M., et al. (2016). Comprehensive classification of retinal bipolar neurons by single-cell transcriptomics. *Cell* 166, 1308–1323. doi: 10.1016/j.cell.2016.07.054

Sun, L. O., Jiang, Z., Rivlin-Etzion, M., Hand, R., Brady, C. M., Matsuoka, R. L., et al. (2013). On and off retinal circuit assembly by divergent molecular mechanisms. *Science* 342:1241974. doi: 10.1126/science.1241974

Tang, H., Chang, H., Dong, Y., Guo, L., Shi, X., Wu, Y., et al. (2018). Architecture of cell-cell adhesion mediated by sidekicks. *Proc. Natl. Acad. Sci. U.S.A.* 115, 9246–9251. doi: 10.1073/pnas.1801810115

Wang, H., Yang, H., Shivalila, C. S., Dawlaty, M. M., Cheng, A. W., Zhang, F., et al. (2013). One-step generation of mice carrying mutations in multiple genes by CRISPR/Cas-mediated genome engineering. *Cell* 153, 910–918. doi: 10.1016/j.cell.2013.04.025

Wässle, H., Puller, C., Müller, F., and Haverkamp, S. (2009). Cone contacts, mosaics, and territories of bipolar cells in the mouse retina. *J Neurosci.* 29, 106–117. doi: 10.1523/JNEUROSCI.4442-08.2009

Yamagata, M., and Sanes, J. R. (2008). Dscam and Sidekick proteins direct lamina-specific synaptic connections in vertebrate retina. *Nature* 451, 465–469. doi: 10.1038/nature06469

Yamagata, M., and Sanes, J. R. (2010). Synaptic localization and function of Sidekick recognition molecules require MAGI scaffolding proteins. *J. Neurosci.* 30, 3579–3588. doi: 10.1523/JNEUROSCI.6319-09.2010

Yamagata, M., and Sanes, J. R. (2012a). Expanding the Ig superfamily code for laminar specificity in retina: expression and role of contactins. *J. Neurosci.* 32, 14402–14414.

Yamagata, M., and Sanes, J. R. (2012b). Transgenic strategy for identifying synaptic connections in mice by fluorescence complementation (GRASP). *Front. Mol. Neurosci.* 5:18. doi: 10.3389/fnmol.2012.00018

Yamagata, M., Weiner, J. A., and Sanes, J. R. (2002). Sidekicks: synaptic adhesion molecules that promote lamina-specific connectivity in the retina. *Cell* 110, 649–660. doi: 10.1016/S0092-8674(02)00910-8

Zhang, C., Kolodkin, A. L., Wong, R. O., and James, R. E. (2017). Establishing wiring specificity in visual system circuits: from the retina to the brain. *Annu. Rev. Neurosci.* 40, 395–424. doi: 10.1146/annurev-neuro-072116-031607

Zhang, Y., Kim, I.-J., Sanes, J. R., and Meister, M. (2012). The most numerous ganglion cell type of the mouse retina is a selective feature detector. *Proc. Natl. Acad. Sci. U.S.A.* 109, E2391–E2398. doi: 10.1073/pnas.12115 47109

Zhuang, X., Masson, J., Gingrich, J. A., Rayport, S., and Hen, R. (2005). Targeted gene expression in dopamine and serotonin neurons of the mouse brain. *J. Neurosci. Methods* 143, 27–32. doi: 10.1016/j.jneumeth.2004.09.020

Conflict of Interest Statement: The authors declare that the research was conducted in the absence of any commercial or financial relationships that could be construed as a potential conflict of interest.

frontiers in Molecular Neuroscience

ORIGINAL RESEARCH
published: 04 March 2019
doi: 10.3389/fnmol.2019.00054

Structure-Based Peptide Inhibitor Design of Amyloid-β Aggregation

Jinxia Lu[1†], Qin Cao[2†], Chuchu Wang[3,4†], Jing Zheng[5], Feng Luo[3,4], Jingfei Xie[3,4], Yichen Li[1], Xiaojuan Ma[3,4], Lin He[1,5], David Eisenberg[2], James Nowick[6], Lin Jiang[7] and Dan Li[1]**

[1]Key Laboratory for the Genetics of Developmental and Neuropsychiatric Disorders (Ministry of Education), Bio-X Institutes, Shanghai Jiao Tong University, Shanghai, China, [2]UCLA-DOE Institute for Genomics and Proteomics, University of California, Los Angeles, Los Angeles, CA, United States, [3]Interdisciplinary Research Center on Biology and Chemistry, Shanghai Institute of Organic Chemistry, Chinese Academy of Sciences, Shanghai, China, [4]University of Chinese Academy of Sciences, Beijing, China, [5]Shanghai Center for Women and Children's Health, Shanghai, China, [6]Department of Chemistry, University of California, Irvine, Irvine, CA, United States, [7]Department of Neurology, Easton Center for Alzheimer's Disease Research, David Geffen School of Medicine, University of California, Los Angeles, Los Angeles, CA, United States

Many human neurodegenerative diseases are associated with amyloid fibril formation. Inhibition of amyloid formation is of importance for therapeutics of the related diseases. However, the development of selective potent amyloid inhibitors remains challenging. Here based on the structures of amyloid β (Aβ) fibrils and their amyloid-forming segments, we designed a series of peptide inhibitors using RosettaDesign. We further utilized a chemical scaffold to constrain the designed peptides into β-strand conformation, which significantly improves the potency of the inhibitors against Aβ aggregation and toxicity. Furthermore, we show that by targeting different Aβ segments, the designed peptide inhibitors can selectively recognize different species of Aβ. Our study developed an approach that combines the structure-based rational design with chemical modification for the development of amyloid inhibitors, which could be applied to the development of therapeutics for different amyloid-related diseases.

Keywords: neurodegenerative diseases, Alzheimer's disease, Aβ fibril, protein misfolding, structure-based inhibitor design

OPEN ACCESS

Edited by:
Jiajie Diao,
University of Cincinnati, United States

Reviewed by:
Kailu Yang,
Stanford University, United States
Ying Lai,
Stanford University, United States
Yanmei Li,
Tsinghua University, China

****Correspondence:***
Lin Jiang
jianglin@ucla.edu
Dan Li
lidan2017@sjtu.edu.cn

[†]These authors have contributed equally to this work

Received: *12 January 2019*
Accepted: *12 February 2019*
Published: *04 March 2019*

Citation:
Lu J, Cao Q, Wang C, Zheng J, Luo F, Xie J, Li Y, Ma X, He L, Eisenberg D, Nowick J, Jiang L and Li D (2019) Structure-Based Peptide Inhibitor Design of Amyloid-β Aggregation. Front. Mol. Neurosci. 12:54. doi: 10.3389/fnmol.2019.00054

INTRODUCTION

Amyloid diseases, including many neurodegenerative diseases, are increasingly prevalent in aging societies (Eisenberg and Jucker, 2012; Dobson, 2017). The pathogenesis of these devastating diseases is closely associated with aberrant protein aggregation (Chiti and Dobson, 2006). In the progression of amyloid aggregation, soluble proteins undergo a series of conformational changes and self-assemble into insoluble amyloid fibrils (Riek and Eisenberg, 2016). Plaques containing amyloid fibrils are one of the histological hallmarks of Alzheimer's and Parkinson's diseases (Lee et al., 1991; Spillantini et al., 1997; Koo et al., 1999). Various strategies have been exploited to interfere with the process of amyloid aggregation by targeting different conformational species, including stabilizing monomers by antibodies (Ladiwala et al., 2012), redirecting monomers to nontoxic off-pathway oligomers by polyphenolic compounds (Ehrnhoefer et al., 2008), accelerating mature fibril formation by fibril binders (Bieschke et al., 2012; Jiang et al., 2013), inhibiting fibril growing by peptide blockers (Seidler et al., 2018), and disrupting amyloid assembly by nanomaterials (Hamley, 2012; Huang et al., 2014; Lee et al., 2014; Li et al., 2018; Han and He, 2018). Many of these strategies show promising inhibitory effects against toxic amyloid aggregation (Härd and Lendel, 2012; Arosio et al., 2014), but so far none has led to clinical drugs because of unsettled

issues such as target selectivity, side effects, membrane permeability and penetration of the blood-brain barrier.

Amyloid β (Aβ) has long been targeted for drug development and therapeutic treatment of Alzheimer's disease (Caputo and Salama, 1989; Haass and Selkoe, 2007; Sevigny et al., 2016). In addition to the common difficulties in targeting amyloid proteins, Aβ is especially challenging since it contains multiple species with various lengths generated by γ-secretases (Acx et al., 2014; Kummer and Heneka, 2014; Szaruga et al., 2017). Many studies have shown that $A\beta_{42}$ rather than $A\beta_{40}$ is more prone to form toxic aggregates, and the ratio of $A\beta_{42}/A\beta_{40}$ is better correlated with the pathology rather than the amount of each individual Aβ species (Lewczuk et al., 2004; Jan et al., 2008; Kuperstein et al., 2010). However, selective inhibition of $A\beta_{42}$ is very difficult because it is only two residues longer than $A\beta_{40}$ at the C-terminus. In this work, we targeted two key amyloid-forming segments of $A\beta_{42}$ (^{16}KLVFFA^{21} and ^{37}GGVVIA^{42}) based on the cryo-EM structure of $A\beta_{42}$ fibrils reported recently (Gremer et al., 2017). We designed peptide binders of these two segments using RosettaDesign with the atomic structures of these two segments as templates (Sawaya et al., 2007; Colletier et al., 2011). The designed sequences showed inhibitory effect to $A\beta_{42}$ fibril formation. We further utilized a macrocyclic β-sheet mimic scaffold (Zheng et al., 2011; Cheng et al., 2012, 2013) to constrain the designed peptide inhibitors in β-conformation, which significantly enhanced the inhibitory effect on $A\beta_{42}$ aggregation. Furthermore, we show that the peptide inhibitor designed to target the C-terminus of $A\beta_{42}$ can selectively inhibit $A\beta_{42}$ aggregation, but not to that of $A\beta_{40}$ or other amyloid proteins. Our work shed light on the application of structure-based rational design combined with chemical modification in the development of therapeutics for Alzheimer's disease and other amyloid-related diseases.

MATERIALS AND METHODS

Structure-Based Design by Rosetta Software Package

Initial Structure Model for Design

We chose two key amyloidogenic Aβ segments, ^{16}KLVFFA^{21} and ^{37}GGVVIA^{42}, for our inhibitor design. The design templates were taken from the crystal structures of KLVFFA (PDB ID: 2Y2A) and GGVVIA (PDB ID: 2ONV). The backbone of the inhibiting pentapeptide was fully extended to mimic β-conformation. This extended peptide was aligned with the N, C, and O backbone atoms of the template.

Rosetta Design of Fibril-Inhibiting Peptides

The peptide inhibitors were subsequently designed to ensure maximal interaction, while keeping the template amino acid sequence fixed. Computational designs were carried out using the RosettaDesign software package[1]. This algorithm involves building side-chain rotamers of all L-amino acids onto a fixed peptide backbone. The optimal set of side-chain rotamers at each position with the best interaction energy is then identified, with the guidance of a full-atom energy function containing a Lennard-Jones potential, an orientation-dependent hydrogen bond potential, an implicit solvation term, amino acid-dependent reference energies, and a statistical torsional potential that depends on the backbone and side-chain dihedral angles. Finally, the entire structure was refined by simultaneously optimizing degrees of freedom on: (1) the rigid-body geometry between the inhibiting peptide and template; (2) backbone torsions of each peptide; and (3) side chain torsions of each peptide. The lowest-energy model was picked and the interaction energies of each final model from different peptide inhibitors are listed in **Table 1**.

[1]https://www.rosettacommons.org

Circular Dichroism Spectroscopy (CD)

Chirascan spectrometer (Applied Photophysics) equipped with a Peltier temperature controller (Quantum Northwest) is used to acquire the CD spectra. Far UV spectra (240–180 nm) are collected in 0.05 cm path-length quartz cells. Sample concentration is 600 μM. All measurements are conducted at 23°C. Water is used as blank for subtraction from corresponding samples. Secondary structure is predicted from CD using CDPro (Eisenberg and Jucker, 2012).

Preparation of $A\beta_{42}$ and $A\beta_{40}$

Both $A\beta_{42}$ and $A\beta_{40}$ were purified from *E. coli* expression system as reported previously (Dobson, 2017). The expression constructs contain an N-terminal His-tag, followed by 19 repeats of Asn-Ala-Asn-Pro, the Tobacco etch virus (TEV) protease site, and the sequence of $A\beta_{42}$ or $A\beta_{40}$. Purification of $A\beta_{42}$ and $A\beta_{40}$ follows the same experimental procedure. Briefly, the Aβ fusion protein was overexpressed into inclusion bodies in *E. coli* BL21(DE3) cells. The inclusion bodies were solubilized in 8 M urea, followed by washing in a high salt and detergent-containing solution. The Aβ fusion proteins were purified through HisTrap^{TM} HP Columns, followed by reversed-phase high-performance liquid chromatography (RP-HPLC). After cleavage by TEV protease, Aβ was released from fusion protein, and purified through RP-HPLC followed by lyophilization. To disrupt preformed Aβ aggregates, lyophilized Aβ powder was resuspended in 100% HFIP and incubated at room temperature for 2 h. HFIP was fully removed by evaporation. Before used in ThT or MTT assay, Aβ was freshly dissolved in 10 mM NaOH, solubilized by sonication. Aβ is further diluted to 200 μM in phosphate buffer saline (PBS) as a stock solution.

Synthesis of Designed Macrocyclic Peptides

Designed macrocyclic peptides were synthesized by standard Fmoc solid-phase peptide synthesis. In brief, with Boc-Orn(Fmoc)-OH attached onto 2-chlorotrityl chloride resin, the linear peptide was elongated by standard automated Fmoc solid-phase peptide synthesis. Then, the peptide was cleaved from the resin under mildly acidic conditions, followed by being cyclized to the corresponding protected cyclic peptide by slow addition to HCTU and DIEA in dilute (ca. 0.5 mM) DMF solution. Since

TABLE 1 | Characteristics of designed peptide inhibitors.

Targeting sequence	Aβ target	Inhibitor ID	Inhibitor sequence	Predicted binding energy (kcal/mol)	Buried area ($Å^2$)	Shape complementarity (Sc; Lawrence and Colman, 1993)
^{16}KLVFFA^{21}	$Aβ_{42}$	K6A1	TLWYK	−16	280	0.65
	$Aβ_{40}$	K6A2	EHWYH	−13	278	0.7
		G6A1	HYFKY	−19	271	0.67
^{37}GGVVIA^{42}	$Aβ_{42}$	G6A2	HYYIK	−15	252	0.72
		G6A3	KYYEI	−14	270	0.66

the C-terminus of the protected linear peptide comprises an amino acid carbamate (Boc-NH-CHR-COOH), the cyclization condition efficiently avoids problematic epimerization. The final deprotection with TFA solution followed by RP-HPLC purification yielded macrocyclic peptides in 18%–43% overall yield, based on the loading of Boc- Orn(Fmoc)-OH attached onto the resin.

^{1}H NMR Spectroscopy

^{1}H NMR experiments for the designed macrocyclic peptides were performed in D_2O with the internal standard 4,4-Dimethyl-4-silapentane-1-ammonium trifluoroacetate (DSA) at 500 MHz (Brüker Avance) or 600 MHz (Brüker Avance). All peptides were studied at 2 mM in D_2O at 298 K. Sample solutions were prepared gravimetrically by dissolving the macrocyclic peptides directly in solvent. All amino groups were assumed to be protonated as the TFA salts for molecular weight calculation. The data were processed with the Brüker XwinNMR software.

ThT Fluorescence Assay

Thioflavin T (ThT) fluorescence assays were performed to monitor the real-time aggregation of $Aβ_{42}$ and $Aβ_{40}$ in the absence or presence of designed peptides. ThT assays were conducted in 96-well plates (black with flat optical bottom) in a Varioskan fluorescence plate reader (Thermo Scientific, 444 nm excitation, 484 nm emission). Each experiment was run in triplicates. The reaction solution contained 30 μM pre-disaggregated $Aβ_{42}$ or $Aβ_{40}$, 10 μM ThT, and designed peptides at indicated concentrations in PBS. The ThT assay was conducted at 37°C, without shaking for the $Aβ_{42}$ aggregation assay, and with shaking (300 rpm) for $Aβ_{40}$ aggregation assay. The fluorescence readings were collected every 2 min.

Native Gel Electrophoresis

Purified $Aβ_{42}$ powder was pre-treated by HFIP and dissolved in PBS buffer as described above. $Aβ_{42}$ solution was diluted to a final concentration of 10 μM with or without the macrocyclic peptides mcG6A1, mcG6A2, and mcK6A1 (the final concentration of the inhibitors was 50 μM), and incubated at 37°C for 7.5 h. The samples were separated by a NativePAGE 4%–16% BisTris Gel (Novex, USA) and transferred to a nitrocellulose membrane pre-packed in iBlot 2 NC Mini Stacks (Novex, USA) by iBlot 2 Dry Blotting System (Life technologies, USA). The membrane was probed by β amyloid, 1–16 (6E10) Monoclonal Antibody (Covance, USA) and secondary anti-mouse IgG-HRP (MBL, USA), and detected with SuperSignal West Pico Chemiluminescent Substrate (Thermo, USA). The freshly made $Aβ_{42}$ sample without inhibitors was loaded to a separated native gel and detected by the same method as a 0-h control. The molecular weight of the protein aggregates or monomer were accurately determined by the protein standard especially for native gel (Life technologies; cat. # LC0725).

Transmission Electron Microscopy (TEM)

For specimen preparation, 5 μl of each sample was deposited onto a glow-discharged carbon film on 400 mesh copper grids, followed by washing in water twice. The grids were then stained in 0.75% uranyl formate. A Tecnai G2 Spirit transmission electron microscope operating at an accelerating voltage of 120 kV was used to examine and visualize the samples. Images were collected by a 4k × 4k charge-coupled device camera (BM-Eagle, FEI).

Cell Viability Assay

We performed MTT-based cell viability assays to evaluate the toxicity of $Aβ_{42}$ in the absence or presence of the designed peptides. We used a CellTiter 96 aqueous non-radioactive cell proliferation assay kit (Promega cat. # G4100). PC-12 cell lines (ATCC; cat. # CRL-1721) were used to test the cytotoxicity of $Aβ_{42}$ under different conditions. PC-12 cells were cultured in ATCC-formulated RPMI 1640 medium (ATCC; cat. # 30-2001) with 5% fetal bovine serum and 10% heat-inactivated horse serum. Before the cell viability experiment, PC-12 cells were plated at 10,000 cells per well in 96-well plates (Costar; cat. # 3596), and cultured for 20 h at 37°C in 5% CO_2. For the preparation of $Aβ_{42}$ and peptide inhibitors mixture solutions, purified and pre-disaggregated $Aβ_{42}$ samples were dissolved in PBS to a final concentration of 5 μM, followed by the addition of different peptide inhibitors at indicated concentrations. The mixture solution was filtered through a 0.22 μm filter, followed by incubation at 37°C without shaking for 16 h. To initiate the cell viability assay, 10 μl of pre-incubated mixture was added to each well containing 90 μl medium. After incubation at 37°C in 5% CO_2 for 24 h. Fifteen microliter Dye solution (Promega; cat. # G4102) was applied into each well. After incubation for 4 h at 37°C, 100 μl solubilization Solution/Stop Mix (Promega; cat. # G4101) were added. After further incubation at room temperature for 12 h, the absorbance reading was collected at 570 nm with background reading at 700 nm. Four replicates were measured in parallel for each sample. The cell survival rate was normalized by using the PBS-treated cells as 100% and 0.02% SDS-treated cells as 0% viability.

RESULTS

Structure-Based Design of Peptide Inhibitors

To effectively inhibit Aβ fibril formation, we targeted two key amyloid-forming segments of $A\beta_{42}$: ^{16}KLVFFA^{21} and ^{37}GGVVIA^{42} (**Figure 1A**). The ^{16}KLVFFA^{21} segment has been identified as a key segment accounting for both $A\beta_{42}$ and $A\beta_{40}$ nucleation and fibrillation (Ahmed et al., 2010; Colletier et al., 2011; Fawzi et al., 2011; Lu et al., 2013). In the known structures of Aβ fibrils including the recent cryo-EM structure of $A\beta_{42}$ and the previous solid-state NMR structure of $A\beta_{40}$ (Paravastu et al., 2008; Ahmed et al., 2010), this segment forms extended β-strands and stacks repetitively along the fibril axis to form the Aβ fibril core (**Supplementary Figure S1**). Thus, we selected ^{16}KLVFFA^{21} as one of our design targets. In addition, the cryo-EM structure of $A\beta_{42}$ fibril shows that the C-terminal segment ^{37}GGVVIA^{42} plays an essential role in the fibril formation (**Supplementary Figure S2**). ^{37}GGVVIA^{42} of one protofilament interdigitates *via* side chains with its counterpart of the neighboring protofilament forming a steric-zipper-like interaction to compose the mature fibril. Therefore, preventing the self-assembly of either ^{16}KLVFFA^{21} or ^{37}GGVVIA^{42} may potentially inhibit the assembly of $A\beta_{42}$ fibrils.

For structure-based computational design, we used the atomic structures of ^{16}KLVFFA^{21} (PDB ID: 2Y2A) and ^{37}GGVVIA^{42} (PDB ID: 2ONV) as templates. The atomic structures of these two segments represent their conformations in the context of the full-length Aβ fibrils (**Figures 1A,B**). Based on the structures of the two targeting templates, we designed pentapeptides

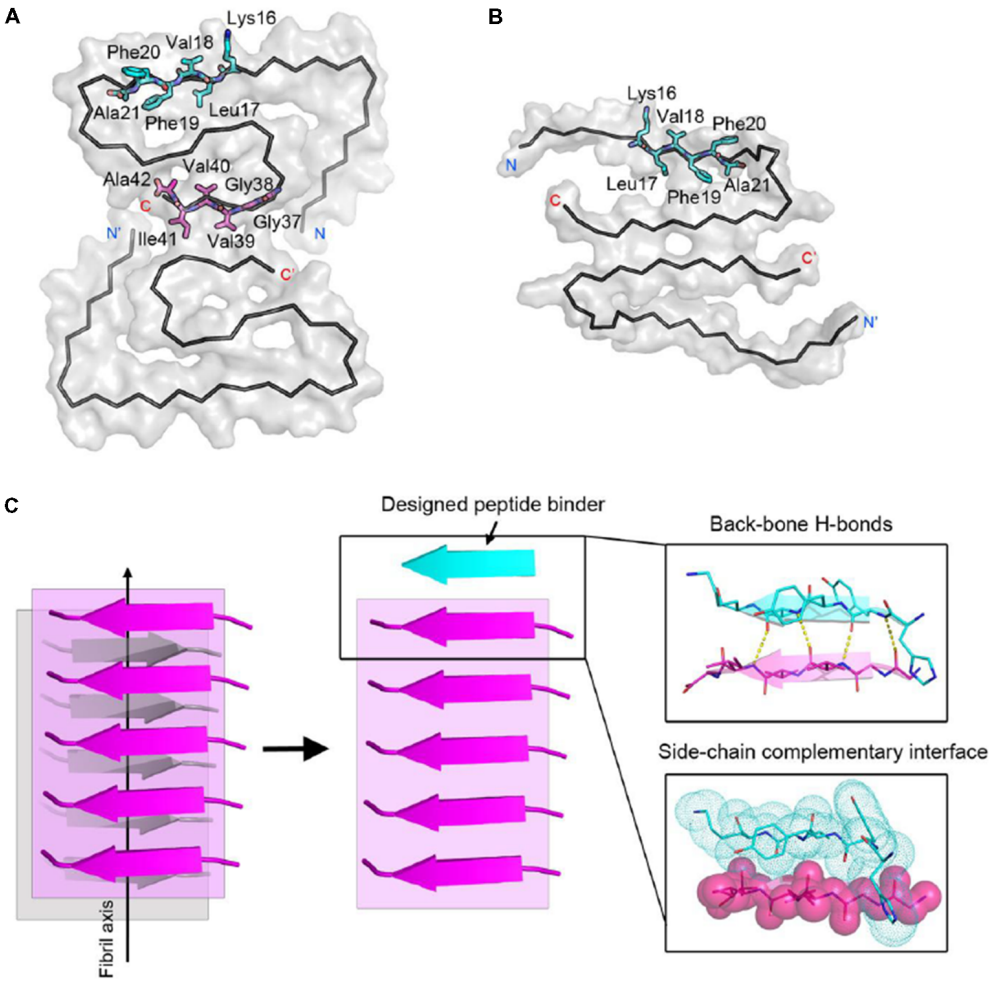

FIGURE 1 | Structure-based peptide inhibitor design of amyloid β (Aβ) amyloid aggregation. **(A)** The fibril structure of full-length $A\beta_{42}$ determined by cryo-EM (PDB ID: 5OQV) is shown as black ribbons. The atomic crystal structures of peptides KLVFFA (PDB ID: 2Y2A, cyan) and GGVVIA (PDB ID: 2ONV, magenta) are aligned on one of the two protofilaments of the full-length $A\beta_{42}$ fibril structure and shown as sticks. **(B)** The fibril structure of full-length $A\beta_{40}$ determined by solid-state NMR (PDB ID: 2LMN) is shown as black ribbons. The atomic crystal structure of peptides KLVFFA is aligned on one of the two protofilaments of the full-length $A\beta_{40}$ fibril structure and shown as sticks. **(C)** Design strategy for peptide inhibitors of amyloid fibrils. The designing template is a five-stranded sheet extracted from the fibrillar structure of the targeting segment. Peptide inhibitors (in cyan) are designed to have the optimal interactions with the target *via* backbone hydrogen bonds (yellow dashed lines) and complementary side-chain interactions (shown as spheres and dots). Oxygen atoms are in red. Nitrogen atoms are in blue.

that bind the targeting segments to block the stacking of Aβ molecules along the fibril axis, thus inhibiting fibril growth (**Figure 1C**). We extracted a five-stranded layer from the steric-zipper structure of each segment, and docked a fully extended pentapeptide backbone on one end of the β-sheet. Then, we maximized the backbone interaction with the template by forming a backbone H-bonding network. To further increase the binding affinity and selectivity, we searched for the canonical L-amino acids at each position of the pentapeptide, using RosettaDesign (Leaver-Fay et al., 2011) for the side chains and their conformations, that provide maximal interactions with the template.

Next, we calculated the binding energy, buried surface area and shape complementarity of the binding interfaces of the predicted binding models, and proceeded with experimental validation for the top-ranking designs. Using ThT fluorescence assay, we observed that the top-5 designs showed inhibitory effects on $A\beta_{42}$ amyloid aggregation by significantly delaying the aggregation lag time (Xue et al., 2008; Knowles et al., 2009; **Figure 2**). Among them, two peptide inhibitors (K6A1 and K6A2) were designed for targeting ^{16}KLVFFA^{21} and three (G6A1-G6A3) were for ^{37}GGVVIA^{42} (**Table 1**). Furthermore, unlike their targeting segments, the five designed peptides do not form amyloid fibrils by themselves (**Supplementary Figure S3**).

Constraining the Structures of Designed Peptides With a Chemical Scaffold

We next sought to enhance the potency of the peptide inhibitors. In our design, the peptide inhibitors were expected to adopt an extended β-strand conformation to maximize the interaction with the template (**Figure 1C**). However, in solution, the peptides are mainly unstructured (**Supplementary Table S1**). Thus, upon binding to the template, the peptides need to undergo conformational change to form extended β strands, which causes an entropy decrease and thus weakens the binding affinity of the peptides to the template. To overcome the entropy lost during the conformational change, we adopted a macrocyclic β-sheet mimic scaffold to fix the peptide binders into β strands (**Figure 3A**). The Nowick group has developed a series of macrocycles in different sizes as robust scaffolds for displaying peptides of interest in β-conformation (Liu et al., 2012; Cheng et al., 2013; Salveson et al., 2016; Kreutzer et al., 2017). According to the length of our designed peptides, we chose a 42-membered macrocyclic β-sheet mimic and grafted the designed sequence into the open strand of the macrocyclic scaffold with appropriate amino acids in the blocking strand for proper solubility and stability (**Figure 3B**). The β-strand conformation of the grafted sequence was validated by measuring the α-H shifts and δOrn anisotropy using ^{1}H NMR experiments (**Supplementary Figures S4, S5**) in solution. Furthermore, we confirmed that the macrocycles carrying the designed peptides do not form amyloid aggregation in solution, while those carrying native amyloid-forming sequences may form amyloid fibrils with an out-of-register packing (Lu et al., 2013; **Supplementary Figure S3**).

Next, we tested the inhibitory effects of the macrocyclic peptides on $A\beta_{42}$ amyloid aggregation. The result showed that, in comparison with the free peptides, the macrocyclic peptides remarkably enhanced the inhibition on $A\beta_{42}$ aggregation (**Figures 2B**, **4A,B**, and **Supplementary Figures S6–S10**). For instance, the macrocycle carrying K6A1 (mcK6A1) is about 10 times more potent than free K6A1 in prolonging the lag time of Aβ aggregation. The macrocyclic peptides inhibited the amyloid aggregation of $A\beta_{42}$ in a dose-dependent manner. McK6A1, mcG6A1 and mcG6A2 showed remarkably strong inhibition with a 7–10-fold increase of the lag time at sub-stoichiometric concentrations of 0.2 molar equivalence to $A\beta_{42}$ monomer (**Figure 4A**).

Moreover, we found that the designed macrocyclic peptides can inhibit the formation of $A\beta_{42}$ oligomers, the toxic intermediates of Aβ aggregation, monitored by the native gel (**Figure 4C**). This result demonstrated that targeting ^{16}KLVFFA^{21} and ^{37}GGVVIA^{42} can prevent both oligomer and fibril formation, indicating the potential important role of these two segments in the early stage of $A\beta_{42}$ aggregation. To further assess whether the designed peptides can reduce Aβ cytotoxicity,

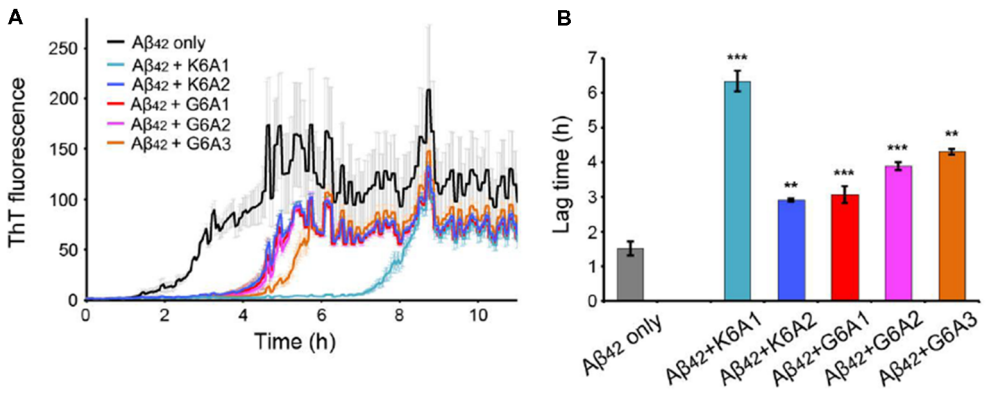

FIGURE 2 | Inhibitory effects of designed peptides on $A\beta_{42}$ amyloid aggregation measured by the thioflavin T (ThT) fluorescence assay. **(A)** The ThT fluorescence curves of $A\beta_{42}$ in the presence of designed peptide inhibitors. The molar ratio of Aβ:peptide-inhibitor is 1:5. Three replicates were measured for each curve. The lag time of $A\beta_{42}$ aggregation in the presence of peptide inhibitors is compared in **(B)**. *p-value < 0.05; **p-value < 0.01; ***p-value < 0.001.

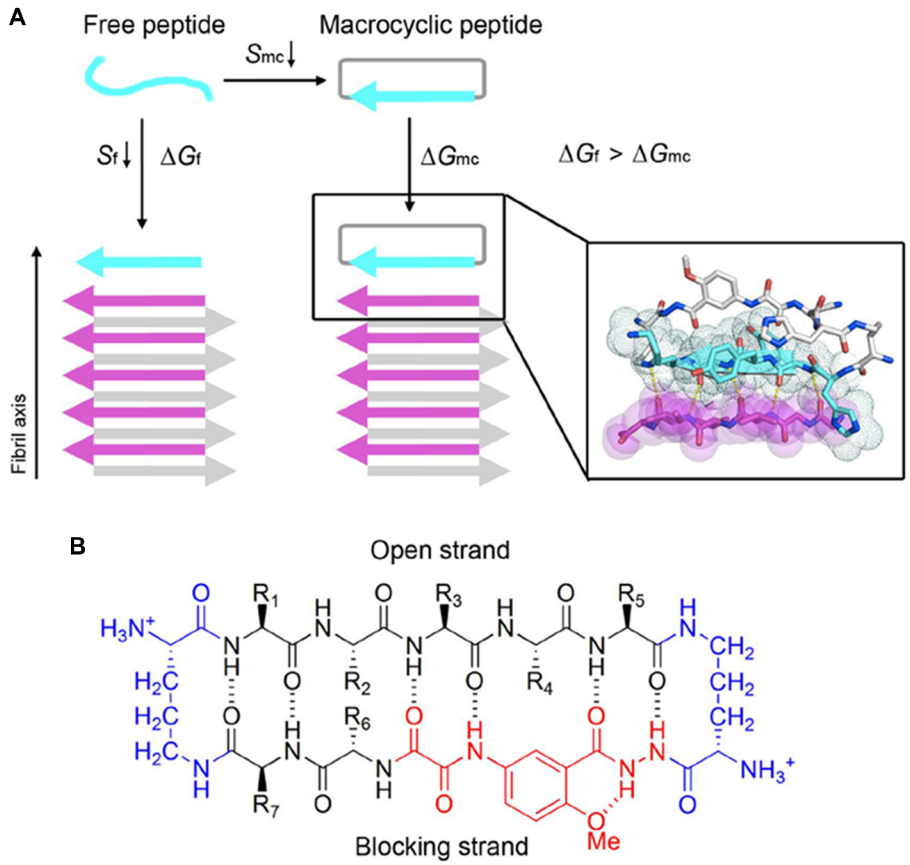

Macrocyclic peptide ID	Inserted peptide ID	R1-R5 sequence	R6-R7 sequence
mcK6A1	K6A1	TLWYK	KY
mcK6A2	K6A2	EHWYH	RY
mcG6A1	G6A1	HYFKY	KW
mcG6A2	G6A2	HYYIK	KH
mcG6A3	G6A3	KYYEI	WH

FIGURE 3 | Design of macrocyclic peptide inhibitors. **(A)** The schematic shows that as the macrocyclic β-sheet mimic scaffold constrains the designed peptide sequence into a β-strand, the entropy loss is diminished during the process of target binding. "f" represents free peptide; "mc" represents macrocyclic peptide. The zoom-in view shows the structure model of a macrocyclic inhibitor binding to the targeting segment. The targeting segment is in magenta. The designed sequence is in cyan. The macrocyclic scaffold is in gray. H-bonds between the designed sequence and the targeting sequence are labeled by yellow dotted lines. **(B)** The 42-membered macrocyclic scaffold used in this study. The open strand (positions R1 to R5) accommodates the designed peptides in β-conformation. Two δ-linked ornithine turn units are in blue. The Hao unit in the blocking strand is in red. Sequences of R1-R7 are listed in the table below.

we performed the MTT-based cell viability assay. The result showed that the designed macrocyclic peptides can significantly reduce the cytotoxicity of $A\beta_{42}$ to PC-12 cells even with a molar ratio of inhibitor to $A\beta_{42}$ as low as 0.2:1 (**Figure 4D**). Also, the designed macrocyclic peptides showed little toxicity to the PC-12 cells (**Figure 4D**). In addition, the designed inhibitors of $A\beta_{42}$ showed no inhibition of the amyloid aggregation of other amyloid proteins (e.g., α-synuclein and the K19 variant of Tau), indicating that the designed peptides are highly sequence-specific (**Supplementary Figure S11**).

Designed Peptides Selectively Inhibit the Aggregation of $A\beta_{42}$ but Not $A\beta_{40}$

Selective inhibition of $A\beta_{42}$ aggregation over that of $A\beta_{40}$ is challenging because $A\beta_{42}$ is only two residues longer than $A\beta_{40}$ at the C- terminus (**Figure 5A**). Since segment ^{37}GGVVIA^{42} exists only in $A\beta_{42}$, the designed peptides that target this segment may selectively inhibit the aggregation of $A\beta_{42}$ but not that of $A\beta_{40}$. As shown in the designed models, mcG6A1 that is designed to target ^{37}GGVVIA^{42} forms extensive side-chain interactions with ^{37}GGVVIA^{42} (**Figure 5B**). The aromatic residues Tyr

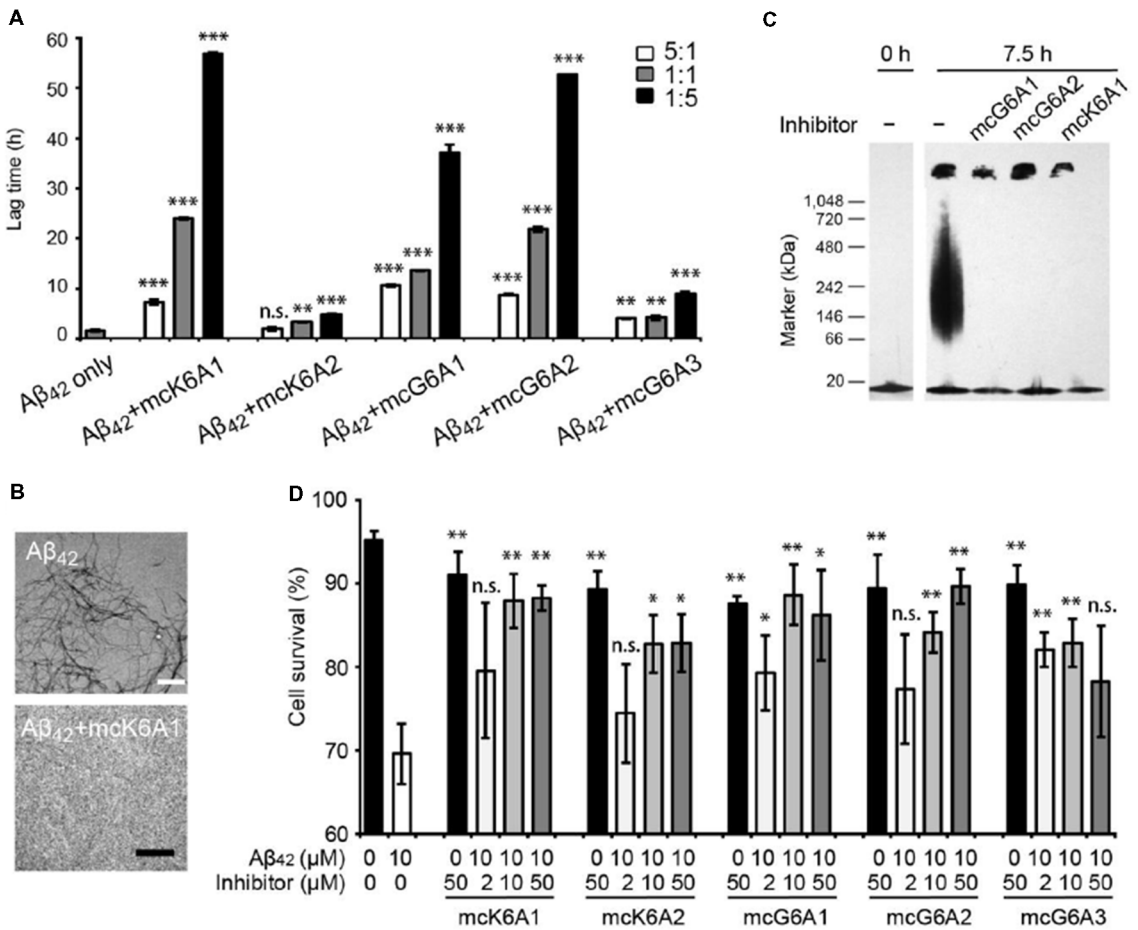

FIGURE 4 | Inhibitory effects of designed macrocyclic peptides on $A\beta_{42}$ amyloid aggregation and cytotoxicity. **(A)** The designed macrocyclic peptides, in particular mcK6A1, mcG6A1 and mcG6A2, significantly inhibit the amyloid fibril formation of $A\beta_{42}$ in a dose-dependent manner. **(B)** Transmission electron microscopy (TEM) images of $A\beta_{42}$ (20 μM) after incubation without inhibitors (top) and with 1.0 equivalent of mcK6A1 (bottom) to Aβ monome for 15 h. The scale bars are 200 nm. **(C)** Inhibition of $A\beta_{42}$ oligomers. $A\beta_{42}$ oligomers formed after 7.5 h of incubation at a concentration of 5 μM (by $A\beta_{42}$ monomer equivalence) were invisible on the native gel with the addition of five molar excess of designed macrocyclic peptides. **(D)** The designed peptide inhibitors ameliorated $A\beta_{42}$ cytotoxicity to PC-12 cells. The first column is the cells treated with 0.1 mM NaOH and phosphate buffer saline (PBS) as a positive control. Error bars correspond to standard deviations three replicates of each experiment. **p*-value < 0.05; ***p*-value < 0.01; ****p*-value < 0.001; n.s. represents "not significant".

and Phe of mcG6A1 interact with Ile41 of ^{37}GGVVIA^{42} *via* van der Waals forces. The absence of Ile41 and Ala42 in $A\beta_{40}$ diminishes the binding of mcG6A1 to $A\beta_{40}$. Indeed, the experimental data showed that mcG6A1 and mcG6A2 that strongly inhibit the amyloid aggregation of $A\beta_{42}$, cannot effectively inhibit the aggregation of $A\beta_{40}$, as measured by ThT assay (**Figure 5C**, **Supplementary Figures S12, S13**). Note that a weak inhibitory effect of mcG6A1 and mcG6A2 to $A\beta_{40}$ remains, which might come from non-specific backbone interactions between the inhibitors and $A\beta_{40}$ (**Figure 5B**). In contrast, mcK6A1 that was designed to target the ^{16}KLVFFA^{21} segment, a segment important for the amyloid aggregation of both $A\beta_{42}$ and $A\beta_{40}$, showed a dose-dependent inhibition of both $A\beta_{42}$ and $A\beta_{40}$ aggregation (**Figures 4A**, **5C,D**, and **Supplementary Figure S14**). However, the inhibitory efficiency of mcK6A1 on $A\beta_{40}$ is weaker than that on $A\beta_{42}$, indicating that ^{16}KLVFFA^{21} may play a more important role in $A\beta_{42}$ aggregation than that of $A\beta_{40}$. This implication is in agreement with the hypothesis that $A\beta_{42}$ and $A\beta_{40}$ may employ different amyloid nucleation and aggregation process (Sánchez et al., 2011; Meisl et al., 2014).

DISCUSSION

Development of peptide-based drugs is gaining greater attentions. In general, peptide-protein interactions have a high density of hydrogen bonds and highly complementary packing *via* hot-spot binding residues, leading to high binding affinity and exquisite selectivity with fewer off-target side effects (Kaspar and Reichert, 2013). Many attempts have been made to rationally design peptide inhibitors of amyloid protein aggregation, including modified internal segments of parent amyloid proteins, non-natural amino-acid inhibitors, proline substitutions, and other methods (Abedini et al.,

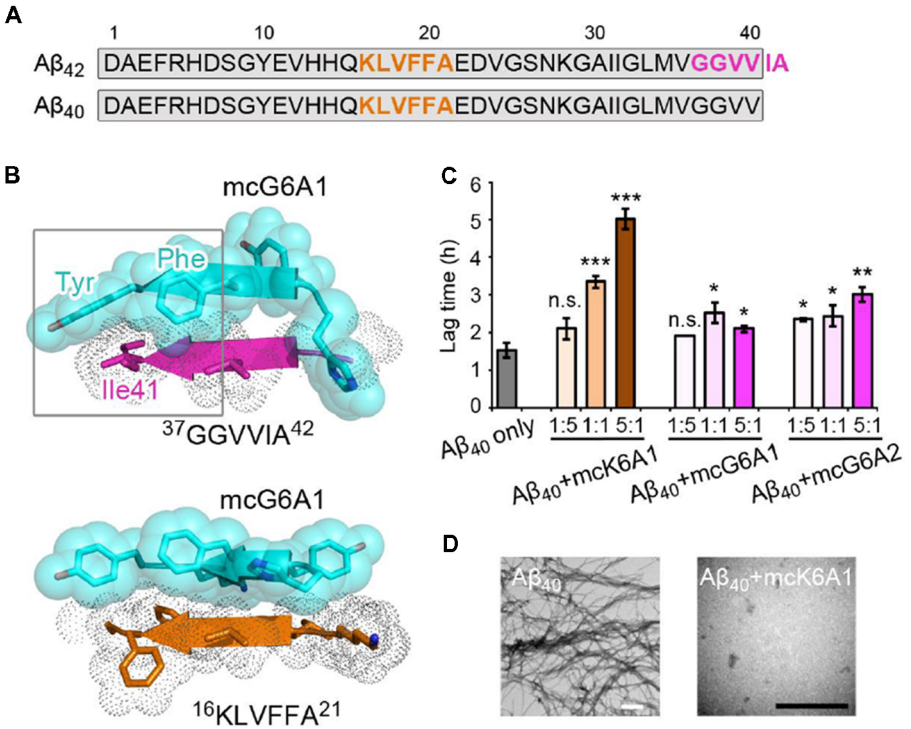

FIGURE 5 | Specificity of designed macrocyclic peptides for the inhibition of $A\beta_{42}$ and $A\beta_{40}$ aggregation. **(A)** The sequences of $A\beta_{42}$ and $A\beta_{40}$. The amyloid-forming segment ^{16}KLVFFA^{21} (highlighted in orange) is present in both $A\beta_{42}$ and $A\beta_{40}$, while segment ^{37}GGVVIA^{42} (highlighted in magenta) is present only in $A\beta_{42}$. The consensus sequence of $A\beta_{42}$ and $A\beta_{40}$ is highlighted in gray. **(B)** The structure models of mcG6A1 (cyan) in complex with ^{37}GGVVIA^{42} (magenta) and ^{16}KLVFFA^{21} (orange), respectively. McG6A1 was designed based on the structure of GGVVIA. Residues Tyr and Phe of mcG6A1, and Ile41 of GGVVIA (highlighted with a gray frame) engage in van der Waals interactions at the inhibitor-target interface. In contrast, mcG6A1 designed for GGVVIA has no specific side-chain interactions, but merely non-specific back-bone interactions with KLVFFA. **(C)** The effects of mcK6A, mcG6A1 and mcG6A2 on $A\beta_{40}$ aggregation (30 μM by $A\beta_{40}$ monomer equivalence), measured by ThT assay. Error bars correspond to standard deviations of three replicates of each experiment. *p-value < 0.05; **p-value < 0.01; ***p-value < 0.001; n.s. represents "not significant." **(D)** TEM images of $A\beta_{40}$ (30 μM) after incubation without inhibitors (left), and with 1.0 equivalent of mcK6A1 to Aβ monome (right). The scale bars are 200 nm.

2007; Sievers et al., 2011). Recently, RosettaDesign shows effectiveness for designing novel proteins and peptides with predicted structures having atomic accuracy (Bhardwaj et al., 2016; Huang et al., 2016). This technical advance has enabled the peptide inhibitor design of Tau aggregation (Abedini et al., 2007; Seidler et al., 2018). In this study, we designed peptides that can efficiently inhibit $A\beta_{42}$ aggregation. Notably, the designed peptides show selectivity for the intended amyloid target, in contrast to small molecule inhibitors (e.g., EGCG and methylene blue) that broadly interfere amyloid aggregation of many proteins (Necula et al., 2007; Jiang et al., 2013; Palhano et al., 2013). Furthermore, the designed peptides can differentiate $A\beta_{42}$ from $A\beta_{40}$, demonstrating the accuracy and potency of structure-based rational design.

Short peptides composed of natural amino acids normally form unstructured ensembles in solution. If a defined conformation is required for target binding, conformational changes may occur upon binding, at a large entropic cost. This counteracts enthalpy gain from the favorable interaction of the designed peptide and its target, and consequently reduces the binding affinity of the peptide with its target. Therefore, constraining the designed peptide in the desired conformation ("pre-organization") can minimize the entropic cost and increase the binding affinity. Chemical scaffolds provide a powerful toolbox for constraining peptides in defined secondary or tertiary structures in solution (Mowery et al., 2009; Azzarito et al., 2013; Cheng et al., 2013; Johnson and Gellman, 2013). In this work, we use a macrocyclic β-sheet mimic scaffold to constrain the designed peptides into β strands. Our results show significant enhancement of inhibition gained by the conformational constraint, which highlights the importance of conformation-constraint and the advantage of a chemical scaffold in the development of peptide binders. In addition, biopharmaceutical properties, such as degradation resistance and membrane permeability, may be achieved by modifying the chemical scaffold, rather than changing the inhibitor sequences.

Macrocyclic β-sheet mimics have been shown to be a useful model system to study the structural basis of amyloid-like oligomers and fibrils (Liu et al., 2012; Cheng et al., 2013; Zheng et al., 2013; Salveson et al., 2016). A variety of key amyloidogenic segments from different amyloid proteins (e.g., Aβ, α-synuclein and prion) were constructed into the

macrocycles (Zheng et al., 2011; Cheng et al., 2012). However, the self-assembling and potential toxic properties of macrocyclic molecules that contain native amyloid-forming sequences hinder application of macrocycles in the development of amyloid inhibitors (Liu et al., 2012; Salveson et al., 2016). In this study, by using RosettaDesign approach, we developed novel sequences and incorporated them into macrocycles. These designed macrocyclic peptides resist self-assembly and exhibit little cytotoxicity. In additional to Aβ, the structures of many other pathogenic amyloid fibrils have been determined recently (Tuttle et al., 2006; Fitzpatrick et al., 2017; Murray et al., 2017). Thus, the strategy of combining RosettaDesign and chemical scaffolds may be useful for peptide inhibitor design of different amyloid proteins for a variety of amyloid-related diseases.

DATA AVAILABILITY

All datasets generated for this study are included in the manuscript and/or the supplementary files.

AUTHOR CONTRIBUTIONS

All authors listed have made a substantial, direct and intellectual contribution to the work, and approved it for publication.

FUNDING

This work was sponsored by Shanghai Pujiang Program (18PJ1404300); the National Natural Science Foundation (NSF) of China (31872716, 91853113); National Institutes of Health (NIH; 5R01 GM097562 and R01 AG029430), the 1000 Talents Program, China; and Howard Hughes Medical Institute (HHMI), USA.

SUPPLEMENTARY MATERIAL

The Supplementary Material for this article can be found online at: https://www.frontiersin.org/articles/10.3389/fnmol.2019.00054/full#supplementary-material

REFERENCES

Abedini, A., Meng, F., and Raleigh, D. P. (2007). A single-point mutation converts the highly amyloidogenic human islet amyloid polypeptide into a potent fibrillization inhibitor. *J. Am. Chem. Soc.* 129, 11300–11301. doi: 10.1021/ja072157y

Acx, H., Chávez-Gutiérrez, L., Serneels, L., Lismont, S., Benurwar, M., Elad, N., et al. (2014). Signature amyloid β profiles are produced by different γ-secretase complexes. *J. Biol. Chem.* 289, 4346–4355. doi: 10.1074/jbc.M113.530907

Ahmed, M., Davis, J., Aucoin, D., Sato, T., Ahuja, S., Aimoto, S., et al. (2010). Structural conversion of neurotoxic amyloid-β_{1-42} oligomers to fibrils. *Nat. Struct. Mol. Biol.* 17, 561–567. doi: 10.1038/nsmb.1799

Arosio, P., Vendruscolo, M., Dobson, C. M., and Knowles, T. P. (2014). Chemical kinetics for drug discovery to combat protein aggregation diseases. *Trends Pharmacol. Sci.* 35, 127–135. doi: 10.1016/j.tips.2013.12.005

Azzarito, V., Long, K., Murphy, N. S., and Wilson, A. J. (2013). Inhibition of α-helix-mediated protein-protein interactions using designed molecules. *Nat. Chem.* 5, 161–173. doi: 10.1038/nchem.1568

Bhardwaj, G., Mulligan, V. K., Bahl, C. D., Gilmore, J. M., Harvey, P. J., Cheneval, O., et al. (2016). Accurate de novo design of hyperstable constrained peptides. *Nature* 538, 329–335. doi: 10.1038/nature19791

Bieschke, J., Herbst, M., Wiglenda, T., Friedrich, R. P., Boeddrich, A., Schiele, F., et al. (2012). Small-molecule conversion of toxic oligomers to nontoxic β-sheet-rich amyloid fibrils. *Nat. Chem. Biol.* 8, 93–101. doi: 10.1038/nchembio.719

Caputo, C. B., and Salama, A. I. (1989). The amyloid proteins of Alzheimer's disease as potential targets for drug therapy. *Neurobiol. Aging* 10, 451–461. doi: 10.1016/0197-4580(89)90096-1

Cheng, P. N., Liu, C., Zhao, M., Eisenberg, D., and Nowick, J. S. (2012). Amyloid β-sheet mimics that antagonize protein aggregation and reduce amyloid toxicity. *Nat. Chem.* 4, 927–933. doi: 10.1038/nchem.1433

Cheng, P. N., Pham, J. D., and Nowick, J. S. (2013). The supramolecular chemistry of β-sheets. *J. Am. Chem. Soc.* 135, 5477–5492. doi: 10.1021/ja3088407

Chiti, F., and Dobson, C. M. (2006). Protein misfolding, functional amyloid, and human disease. *Annu. Rev. Biochem.* 75, 333–366. doi: 10.1146/annurev.biochem.75.101304.123901

Colletier, J. P., Laganowsky, A., Landau, M., Zhao, M., Soriaga, A. B., Goldschmidt, L., et al. (2011). Molecular basis for amyloid-β polymorphism. *Proc. Natl. Acad. Sci. U S A* 108, 16938–16943. doi: 10.1073/pnas.1112600108

Dobson, C. M. (2017). The amyloid phenomenon and its links with human disease. *Cold Spring Harb. Perspect. Biol.* 9:a023648. doi: 10.1101/cshperspect.a023648

Ehrnhoefer, D. E., Bieschke, J., Boeddrich, A., Herbst, M., Masino, L., Lurz, R., et al. (2008). EGCG redirects amyloidogenic polypeptides into unstructured, off-pathway oligomers. *Nat. Struct. Mol. Biol.* 15, 558–566. doi: 10.1038/nsmb.1437

Eisenberg, D., and Jucker, M. (2012). The amyloid state of proteins in human diseases. *Cell* 148, 1188–1203. doi: 10.1016/j.cell.2012.02.022

Fawzi, N. L., Ying, J., Ghirlando, R., Torchia, D. A., and Clore, G. M. (2011). Atomic-resolution dynamics on the surface of amyloid-β protofibrils probed by solution NMR. *Nature* 480, 268–272. doi: 10.1038/nature10577

Fitzpatrick, A. W. P., Falcon, B., He, S., Murzin, A. G., Murshudov, G., Garringer, H. J., et al. (2017). Cryo-EM structures of tau filaments from Alzheimer's disease. *Nature* 547, 185–190. doi: 10.1038/nature23002

Gremer, L., Schölzel, D., Schenk, C., Reinartz, E., Labahn, J., Ravelli, R. B. G., et al. (2017). Fibril structure of amyloid-β_{1-42} by cryo-electron microscopy. *Science* 358, 116–119. doi: 10.1126/science.aao2825

Haass, C., and Selkoe, D. J. (2007). Soluble protein oligomers in neurodegeneration: lessons from the Alzheimer's amyloid β-peptide. *Nat. Rev. Mol. Cell Biol.* 8, 101–112. doi: 10.1038/nrm2101

Hamley, I. W. (2012). The amyloid β peptide: a chemist's perspective role in Alzheimer's and fibrillization. *Chem. Rev.* 112, 5147–5192. doi: 10.1021/cr3000994

Han, X., and He, G. (2018). Toward a rational design to regulate β-amyloid fibrillation for alzheimer's disease treatment. *ACS Chem. Neurosci.* 9, 198–210. doi: 10.1021/acschemneuro.7b00477

Härd, T., and Lendel, C. (2012). Inhibition of amyloid formation. *J. Mol. Biol.* 421, 441–465. doi: 10.1016/j.jmb.2011.12.062

Huang, P. S., Boyken, S. E., and Baker, D. (2016). The coming of age of de novo protein design. *Nature* 537, 320–327. doi: 10.1038/nature19946

Huang, F., Wang, J., Qu, A., Shen, L., Liu, J., Liu, J., et al. (2014). Maintenance of amyloid β peptide homeostasis by artificial chaperones based on mixed-shell polymeric micelles. *Angew. Chem. Int. Ed. Engl.* 53, 8985–8990. doi: 10.1002/anie.201400735

Jan, A., Gokce, O., Luthi-Carter, R., and Lashuel, H. A. (2008). The ratio of monomeric to aggregated forms of $A\beta_{40}$ and $A\beta_{42}$ is an important determinant of amyloid-β aggregation, fibrillogenesis, and toxicity. *J. Biol. Chem.* 283, 28176–28189. doi: 10.1074/jbc.m803159200

Jiang, L., Liu, C., Leibly, D., Landau, M., Zhao, M., Hughes, M. P., et al. (2013). Structure-based discovery of fiber-binding compounds that reduce the cytotoxicity of amyloid β. *Elife* 2:e00857. doi: 10.7554/eLife.00857

Johnson, L. M., and Gellman, S. H. (2013). α-Helix mimicry with α/β-peptides. *Methods Enzymol.* 523, 407–429. doi: 10.1016/B978-0-12-394292-0.00019-9

Kaspar, A. A., and Reichert, J. M. (2013). Future directions for peptide therapeutics development. *Drug Discov. Today* 18, 807–817. doi: 10.1016/j.drudis.2013.05.011

Knowles, T. P., Waudby, C. A., Devlin, G. L., Cohen, S. I., Aguzzi, A., Vendruscolo, M., et al. (2009). An analytical solution to the kinetics of breakable filament assembly. *Science* 326, 1533–1537. doi: 10.1126/science.1178250

Koo, E. H., Lansbury, P. T. Jr., and Kelly, J. W. (1999). Amyloid diseases: abnormal protein aggregation in neurodegeneration. *Proc. Natl. Acad. Sci. U S A* 96, 9989–9990. doi: 10.1073/pnas.96.18.9989

Kreutzer, A. G., Yoo, S., Spencer, R. K., and Nowick, J. S. (2017). Stabilization, assembly, and toxicity of trimers derived from Aβ. *J. Am. Chem. Soc.* 139, 966–975. doi: 10.1021/jacs.6b11748

Kummer, M. P., and Heneka, M. T. (2014). Truncated and modified amyloid-β species. *Alzheimers. Res. Ther.* 6:28. doi: 10.1186/alzrt258

Kuperstein, I., Broersen, K., Benilova, I., Rozenski, J., Jonckheere, W., Debulpaep, M., et al. (2010). Neurotoxicity of Alzheimer's disease Aβ peptides is induced by small changes in the $A\beta_{42}$ to $A\beta_{40}$ ratio. *EMBO J.* 29, 3408–3420. doi: 10.1038/emboj.2010.211

Ladiwala, A. R., Bhattacharya, M., Perchiacca, J. M., Cao, P., Raleigh, D. P., Abedini, A., et al. (2012). Rational design of potent domain antibody inhibitors of amyloid fibril assembly. *Proc. Natl. Acad. Sci. U S A* 109, 19965–19970. doi: 10.1073/pnas.1208797109

Lawrence, M. C., and Colman, P. M. (1993). Shape complementarity at protein/protein interfaces. *J. Mol. Biol.* 234, 946–950. doi: 10.1006/jmbi.1993.1648

Leaver-Fay, A., Tyka, M., Lewis, S. M., Lange, O. F., Thompson, J., Jacak, R., et al. (2011). ROSETTA3: an object-oriented software suite for the simulation and design of macromolecules. *Meth. Enzymol.* 487, 545–574. doi: 10.1016/B978-0-12-381270-4.00019-6

Lee, H. H., Choi, T. S., Lee, S. J., Lee, J. W., Park, J., Ko, Y. H., et al. (2014). Supramolecular inhibition of amyloid fibrillation by cucurbit[7]uril. *Angew. Chem. Int. Ed. Engl.* 53, 7461–7465. doi: 10.1002/anie.201402496

Lee, V., Balin, B., Otvos, L., and Trojanowski, J. (1991). A68: a major subunit of paired helical filaments and derivatized forms of normal tau. *Science* 251, 675–678. doi: 10.1126/science.1899488

Lewczuk, P., Esselmann, H., Otto, M., Maler, J. M., Henkel, A. W., Henkel, M. K., et al. (2004). Neurochemical diagnosis of Alzheimer's dementia by CSF $A\beta_{42}$, $A\beta_{42}/A\beta_{40}$ ratio and total tau. *Neurobiol. Aging* 25, 273–281. doi: 10.1016/S0197-4580(03)00086-1

Li, G., Yang, W.-Y., Zhao, Y.-F., Chen, Y.-X., Hong, L., and Li, Y.-M. (2018). Differentialmodulation of the aggregation of n-terminal truncated aβ via cucurbiturils. *Chem. Eur. J.* 24, 13647–13653. doi: 10.1002/chem.201802655

Liu, C., Zhao, M., Jiang, L., Cheng, P. N., Park, J., Sawaya, M. R., et al. (2012). Out-of-register β-sheets suggest a pathway to toxic amyloid aggregates. *Proc. Natl. Acad. Sci. U S A* 109, 20913–20918. doi: 10.1073/pnas.1218792109

Lu, J. X., Qiang, W., Yau, W. M., Schwieters, C. D., Meredith, S. C., and Tycko, R. (2013). Molecular structure of β-amyloid fibrils in Alzheimer's disease brain tissue. *Cell* 154, 1257–1268. doi: 10.1016/j.cell.2013.08.035

Meisl, G., Yang, X., Hellstrand, E., Frohm, B., Kirkegaard, J. B., Cohen, S. I., et al. (2014). Differences in nucleation behavior underlie the contrasting aggregation kinetics of the $A\beta_{40}$ and $A\beta_{42}$ peptides. *Proc. Natl. Acad. Sci. U S A* 111, 9384–9389. doi: 10.1073/pnas.1401564111

Mowery, B. P., Lindner, A. H., Weisblum, B., Stahl, S. S., and Gellman, S. H. (2009). Structure-activity relationships among random nylon-3 copolymers that mimic antibacterial host-defense peptides. *J. Am. Chem. Soc.* 131, 9735–9745. doi: 10.1021/ja901613g

Murray, D. T., Kato, M., Lin, Y., Thurber, K. R., Hung, I., McKnight, S. L., et al. (2017). Structure of FUS protein fibrils and its relevance to self-assembly and phase separation of low-complexity domains. *Cell* 171, 615.e16–627.e16. doi: 10.1016/j.cell.2017.08.048

Necula, M., Kayed, R., Milton, S., and Glabe, C. G. (2007). Small molecule inhibitors of aggregation indicate that amyloid β oligomerization and fibrillization pathways are independent and distinct. *J. Biol. Chem.* 282, 10311–10324. doi: 10.1074/jbc.m608207200

Palhano, F. L., Lee, J., Grimster, N. P., and Kelly, J. W. (2013). Toward the molecular mechanism(s) by which EGCG treatment remodels mature amyloid fibrils. *J. Am. Chem. Soc.* 135, 7503–7510. doi: 10.1021/ja3115696

Paravastu, A. K., Leapman, R. D., Yau, W. M., and Tycko, R. (2008). Molecular structural basis for polymorphism in Alzheimer's β-amyloid fibrils. *Proc. Natl. Acad. Sci. U S A* 105, 18349–18354. doi: 10.1073/pnas.0806270105

Riek, R., and Eisenberg, D. S. (2016). The activities of amyloids from a structural perspective. *Nature* 539, 227–235. doi: 10.1038/nature20416

Salveson, P. J., Spencer, R. K., and Nowick, J. S. (2016). X-ray crystallographic structure of oligomers formed by a toxic β-hairpin derived from α-synuclein: trimers and higher-order oligomers. *J. Am. Chem. Soc.* 138, 4458–4467. doi: 10.1021/jacs.5b13261

Sánchez, L., Madurga, S., Pukala, T., Vilaseca, M., López-Iglesias, C., Robinson, C. V., et al. (2011). $A\beta_{40}$ and $A\beta_{42}$ amyloid fibrils exhibit distinct molecular recycling properties. *J. Am. Chem. Soc.* 133, 6505–6508. doi: 10.1021/ja1117123

Sawaya, M. R., Sambashivan, S., Nelson, R., Ivanova, M. I., Sievers, S. A., Apostol, M. I., et al. (2007). Atomic structures of amyloid cross-β spines reveal varied steric zippers. *Nature* 447, 453–457. doi: 10.1038/nature05695

Seidler, P., Boyer, D. R., Rodriguez, J. A., Sawaya, M. R., Cascio, D., Murray, K., et al. (2018). Structure-based inhibitors of tau aggregation. *Nat. Chem.* 10, 170–176. doi: 10.1038/nchem.2889

Sevigny, J., Chiao, P., Bussière, T., Weinreb, P. H., Williams, L., Maier, M., et al. (2016). The antibody aducanumab reduces Aβ plaques in Alzheimer's disease. *Nature* 537, 50–56. doi: 10.1038/nature19323

Sievers, S. A., Karanicolas, J., Chang, H. W., Zhao, A., Jiang, L., Zirafi, O., et al. (2011). Structure-based design of non-natural amino-acid inhibitors of amyloid fibril formation. *Nature* 475, 96–100. doi: 10.1038/nature10154

Spillantini, M. G., Schmidt, M. L., Lee, M. Y., Trojanowski, J. Q., Jakes, R., and Goedert, M. (1997). α-synuclein in lewy bodies. *Nature* 388, 839–840. doi: 10.1038/42166

Szaruga, M., Munteanu, B., Lismont, S., Veugelen, S., Horré, K., Mercken, M., et al. (2017). Alzheimer's-causing mutations shift Aβ length by destabilizing γ-secretase-Aβn interactions. *Cell* 170, 443.e14–456.e14. doi: 10.1016/j.cell.2017.07.004

Tuttle, M. D., Comellas, G., Nieuwkoop, A. J., Covell, D. J., Berthold, D. A., Kloepper, K. D., et al. (2006). Solid-state NMR structure of a pathogenic fibril of full-length human α-synuclein. *Nat. Struct. Mol. Biol.* 23, 409–415. doi: 10.1038/nsmb.3194

Xue, W. F., Homans, S. W., and Radford, S. E. (2008). Systematic analysis of nucleation-dependent polymerization reveals new insights into the mechanism of amyloid self-assembly. *Proc. Natl. Acad. Sci. U S A* 105, 8926–8931. doi: 10.1073/pnas.0711664105

Zheng, J., Baghkhanian, A. M., and Nowick, J. S. (2013). A hydrophobic surface is essential to inhibit the aggregation of a tau-protein-derived hexapeptide. *J. Am. Chem. Soc.* 135, 6846–6852. doi: 10.1021/ja310817d

Zheng, J., Liu, C., Sawaya, M. R., Vadla, B., Khan, S., Woods, R. J., et al. (2011). Macrocyclic β-sheet peptides that inhibit the aggregation of a tau-protein-derived hexapeptide. *J. Am. Chem. Soc.* 133, 3144–3157. doi: 10.1021/ja110545h

Conflict of Interest Statement: The authors declare that the research was conducted in the absence of any commercial or financial relationships that could be construed as a potential conflict of interest.

frontiers in Molecular Neuroscience

REVIEW
published: 27 May 2019
doi: 10.3389/fnmol.2019.00110

Editing the Central Nervous System Through CRISPR/Cas9 Systems

*Agustin Cota-Coronado[1], Néstor Fabián Díaz-Martínez[2], Eduardo Padilla-Camberos[1] and N. Emmanuel Díaz-Martínez[1]**

[1]*Biotecnología Médica y Farmacéutica CONACYT, Centro de Investigación y Asistencia en Tecnología y Diseño del Estado de Jalisco (CIATEJ), Guadalajara, Mexico,* [2]*Departamento de Fisiología y Desarrollo Celular, Instituto Nacional de Perinatología, Mexico City, Mexico*

The translational gap to treatments based on gene therapy has been reduced in recent years because of improvements in gene editing tools, such as the CRISPR/Cas9 system and its variations. This has allowed the development of more precise therapies for neurodegenerative diseases, where access is privileged. As a result, engineering of complexes that can access the central nervous system (CNS) with the least potential inconvenience is fundamental. In this review article, we describe current alternatives to generate systems based on CRISPR/Cas9 that can cross the blood–brain barrier (BBB) and may be used further clinically to improve treatment for neurodegeneration in Parkinson's and Alzheimer's disease (AD).

OPEN ACCESS

Edited by:
Carlo Sala,
Institute of Neuroscience (IN), Italy

Reviewed by:
Vania Broccoli,
San Raffaele Hospital (IRCCS), Italy
Julien Rossignol,
Central Michigan University, United States

****Correspondence:***
N. Emmanuel Díaz-Martínez
ediaz@ciatej.mx

Received: *24 October 2018*
Accepted: *15 April 2019*
Published: *27 May 2019*

Citation:
Cota-Coronado A, Díaz-Martínez NF, Padilla-Camberos E and Díaz-Martínez NE (2019) Editing the Central Nervous System Through CRISPR/Cas9 Systems. Front. Mol. Neurosci. 12:110. doi: 10.3389/fnmol.2019.00110

Keywords: CRISPR/Cas9, central nervous system, blood–brain barrier, "Trojan horse" peptides, adenovirus-associated virus, d-Cas9

INTRODUCTION

The most common and prevalent worldwide neurodegenerative diseases are Alzheimer's disease (AD) and Parkinson's disease (PD). Thus far, there is no cure, nor is the etiology of either condition completely understood. Progression and ultimately death in patients with a very advanced degree of AD/PD may possibly be attributed to not having fully elucidated the molecular mechanisms that underlie these diseases (Kampmann, 2017). However, the CRISPR system and its variations open up a range of unprecedented possibilities for examining the genome and finding potential markers of early expression (Hu et al., 2018) or the development of personalized therapies that have a real impact on neurodegenerative conditions. On the other hand, research groups have developed gene therapy based on editing tools with nucleases by applying ingenious designs *in vivo*, achieving the first cases of clinical patient referrals. These achievements have shown a huge reduction in the marked gap between basic medical research and translational medicine.

In order to establish new gene therapies that could be applied in a translational way to neurodegenerative diseases, a robust design approach for gene editing systems must be considered. It should be noted that thorough *in silico* design is the fundamental basis of the performance of therapy *in vivo*, as has been demonstrated through the success of several working groups by monitoring a workflow that is the right choice of the basic elements of the CRISPR/Cas9 system (**Figure 1**).

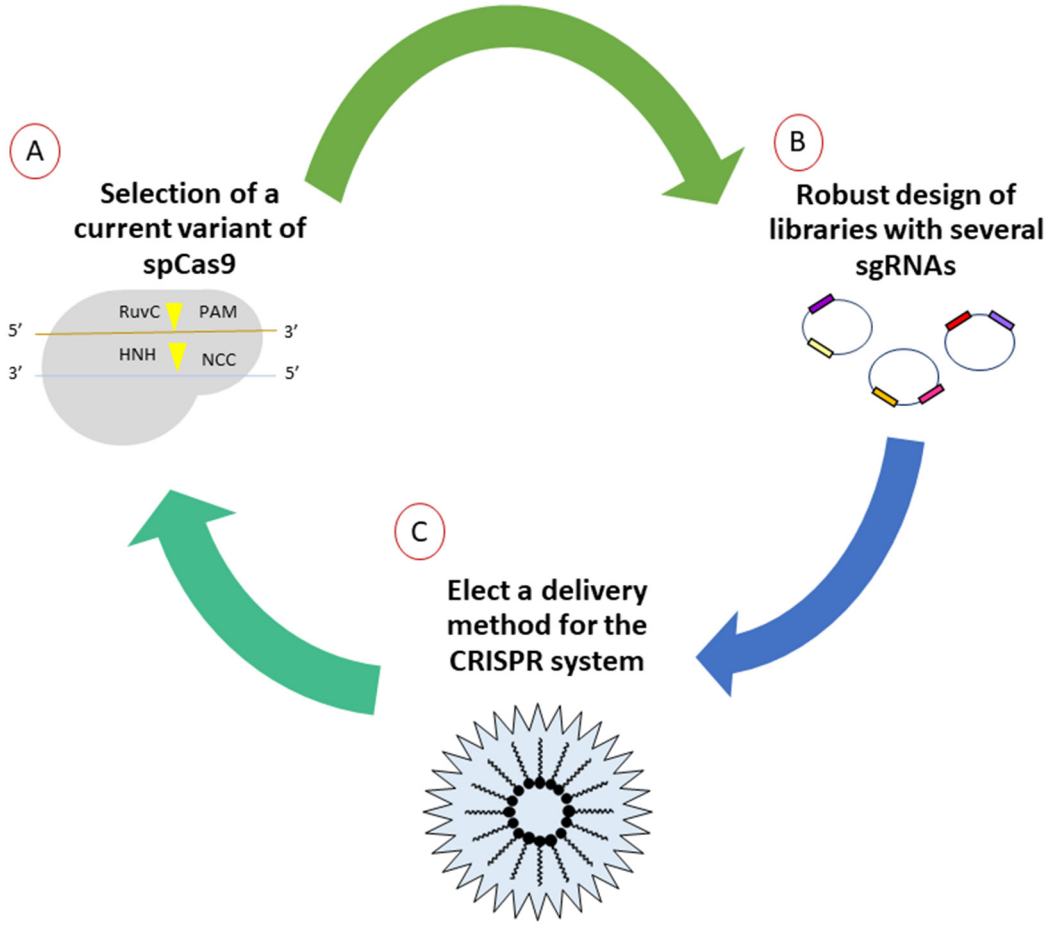

FIGURE 1 | General workflow for generation of CRISPR/Cas9 strategies for purposes of gene therapy. **(A)** First, the mutants or orthologes derived from SpCas9 evidenced by other research groups and those commercially available should be explored. Due to the emerging amount of literature, selection of the most suitable options will impact directly in the cost benefit of editing. **(B)** The elaboration of diverse libraries with thousands of single-guide RNAs (sgRNAs) allows to select those that generate real hits in the flank sequences, lowering the risk of off-target effects, verified by next-generation sequencing later. **(C)** Currently, there are various ways for the efficient delivery *in situ* of gene-editing tools. Several options are currently under investigation, especially methods that involve delivery by means of non-invasive methods.

CURRENT VARIANTS OF spCas9

Based on previous discoveries, the concept of diversifying the system by looking for other microorganisms with functional orthologous proteins and mutagenesis of the enzyme spCas9 obtained from *Streptococcus pyogenes* was raised in order to increase the percentage of efficiency and delivery when editing. Cebrian-Serrano and Davies (2017) described the structural redesign of spCas9, mutating regions of key residues and the function of the new variants of Cas9 in view of their application in mammalian gene therapy (Cebrian-Serrano and Davies, 2017). Currently, the spCas9 variants successfully used for mammalian gene editing are nCas9, dCas9-FokI, Cas9-VQR, Cas9-EQR, Cas9-VRER, Cas9-D1135E, Cas9-QQR1, SpCas9-HF1, eSpCas9 (1.0), and eSpCas9 (1.1). One of the new systems, referred to as "CRISPR 2.0," was created by Gaudelli et al. (2017). They managed to perform seventh-generation adenine base (ABEs) editing, allowing the conversion of A-T to G-C in genomic DNA by RNA adenosine deaminase to operate in DNA, through the fusion of a CRISPR-Cas9 mutant to its catalytic site. The results exhibited 50% editing efficiency in human cells with a high purity (99%) and low rates of indels ($\leq$0.01%), producing a more efficient and clean system for the introduction of specific mutations. Remarkably, it allows the direct and programmable introduction of the four mutations, A-T/G-C, without performing the classic rupture in the double-stranded DNA (Gaudelli et al., 2017). Therefore, each system has a specific purpose that is dependent on the nature of the editing to be performed. In the same way, each research group can adapt the fundamental elements of the system into their experiments. Consequently, in a few years, there will be a very diverse toolbox that includes specific Cas9 systems for each human cell lineage (somatic or stem cell), highly efficient in making the most possible changes to the genome without affecting vital functions.

ROBUST DESIGN OF SINGLE-GUIDE RNAs

Without doubt, one aspect that directly affects efficiency is the intelligent design of single-guide RNAs (sgRNAs). Previously, the guides were created without consideration for several parameters that have been identified as key factors to increase specificity over time. Several studies have shown that the off-target activity of Cas9 depends on the chemical composition of sgRNA and on the conditions in which the experiment is performed (Fu et al., 2013; Hsu et al., 2013; Ran et al., 2013; Guilinger et al., 2014; Veres et al., 2014). However, some general properties among them are difficult to determine because it is necessary to carry out an extensive series of studies that verify the interaction between DNA and RNA, making it possible to discriminate a true hit from false positives. Therefore, several platforms and algorithms have been established to optimize the generation of very wide libraries of possible sgRNAs for the same gene and are currently available online. Doench et al. (2014) discovered characteristic sequences that improve the activity of sgRNAs and optimize the site PAM for *S. pyogenes*. The study consisted of obtaining a platform that would improve the design of sgRNAs, evaluating a total of 1,841 in mammalian cells, for purposes of genetic screening and editing, culminating in an online tool for the design of highly active sgRNAs useful for any gene[1].

Based on the results of Doench et al. (2016), human libraries were generated called Avana (110, 257 sgRNAs) and Asiago (120, 453 sgRNAs) selecting six guides per gen, according to the rules to improve the design of sgRNAs (rule set 1; Doench et al., 2014), including specificity within region protein encodings and the localization of the target site within the gene. Using the cutting frequency determination (CFD) score for the most lethal sgRNA shows that a significant increase in the number of off-target sites was found. This observation suggests that guides with previously determined off-target sites exhibit more frequent depletion in negative selection screening, therefore avoiding such promiscuous sgRNAs and resulting in better performance of the designed library (Doench et al., 2016). In previous work, a better online tool was developed, increasing the efficiency in the design of sgRNAs for editing in human and mouse cells; however, the platform only included Cas9 enzymes belonging to *S. pyogenes*, which only recognizes the PAM-NGG site, and Cas from *Staphylococcus aureus*, which recognizes the PAM-NNGRR site. Therefore, it is recommended to use other tools for the design of sgRNAs directed at variants of Cas or Cas9-type enzymes that recognize different sites from PAM of the SpCas9. It should be noted that other research groups have shown that the composition and order of the sequence of the sgRNAs have a direct impact on the success of the editing. For example, Wang et al. (2014) determined that an inadequate design compromises the efficiency and specificity of the desired editing. In another study, it was observed that in the presence of guanine (G) in the first or second position with respect to PAM, the specificity increased. Likewise, Xu et al. (2015) showed that the presence of multiple T adjacent to the PAM site is not advisable because of the loss of specificity. In another work, Moreno-Mateos et al. (2015) observed that sgRNAs rich in G and poor in the presence of adenine (A) promote the increase of stability and efficiency. Another relevant aspect that has been exhaustively assessed is the tolerance of mismatches. It has been reported that there is a greater tolerance for the presence of mismatches in the terminal region of the sgRNAs. Moreover, the presence of five mismatches was defined as the limit of tolerance, because with more than five mismatches, cuts in the sequence at sites where there were no targets and consequently the presence of unwanted mutations were found (Fu et al., 2013). As described above, it is established that by following the above recommendations, large, highly specific, and efficient libraries can be obtained for editing specific target sites and avoiding false positives in gene therapy *in vivo*.

[1]https://portals.broadinstitute.org/gpp/public/analysis-tools/sgrna-design

IMPROVED METHODS FOR THE DELIVERY OF CRISPR COMPONENTS

The advantage of the CRISPR/Cas9 gene editing system in mammalian cells is the high efficiency observed when knock-out models are made by the non-homologous end joining (NHEJ) repair mechanism and the union of nonhomologous ends. However, this efficiency decreases dramatically during the production of knock-in models due to the nature of repairing with the homologous recombination mechanism (HDR; Ran et al., 2013; Rong et al., 2014). Because of the enormous implications of being able to insert fragments at will in the genome in such a specific way, several studies have suggested improvements to increase this repair mechanism. González et al. (2014) co-delivered sgRNA and a single-stranded oligodeoxynucleotide (ssODN) donor in human pluripotent cells (hPSCs) expressing Cas9, generating homozygotic knock-in clones with an efficiency of slightly more than 10%. Lin et al. (2014) synchronized HEK293T cells and hESCs in phase M using the antineoplastic agent nocodazole and introduced nucleofection of the ribonucleoproteins complexes of Cas9 (RNPs) and ssODNs, resulting in a significant increase of the insertion by the HDR mechanism of 38% for HEK293T cells and 1.6% for hESCs, contrasting with negative controls that were not synchronized (26% in HEK293T and 0% in hESCs). Schumann et al. (2015) obtained an efficiency of 20% in the delivery of RNPs-Cas9 and ssODNs in primary T-cells using an electroporation technique, obtaining human knock-in cells with a high efficiency. As previously mentioned, the techniques most used to introduce exogenous material to mammalian cells are lipofection, electroporation, and microinjection. Some of these techniques have been improved with the desire to adapt them to cells that are "tricky" to transform as stem cells. However, to prepare CRISPR technology adequately for use in gene therapy, there are some limitations that have to be overcome (Kelton et al., 2016). Among them is the use of plasmids that contain the Cas9 sequences, usually fused to a nuclear localization (NLS) signal and one or multiple sgRNAs (Sakuma et al., 2014), facilitating the intranuclear expression and securing access to the target site. Despite the remarkable results that have been generated through the use of these all-in-one plasmids, it has

been shown that this use can generate constituent expression of Cas9 due to the natural predisposition of the NHEJ repair mechanism and activation of the innate immune system because of the cut double chain (Mandal et al., 2014; Sather et al., 2015). In the same way, several studies have been reported with a therapy-oriented approach where they use some viruses with peculiar characteristics, such as the adeno-associated virus (AAV), which has a packaging capacity of about 4.5 kb and is a non-integrative virus (Senís et al., 2014). However, the number of amino acids that constitute SpCas9 is added to the sgRNA sequence, increasing the total package size. Therefore, it has been determined to divide the system between several plasmids by dividing the enzyme and sgRNAs into their own plasmids (Fine et al., 2015; Wright et al., 2015; Zetsche et al., 2015). This has been found to decrease activity due to the formation of indels after the rupture of the DNA double chain. Due to the disadvantages described, an exhaustive search of ortholog enzymes is being performed for homologies similar to SpCas9 in other microorganisms (Friedland et al., 2015). Ran et al. (2013) reported an isolated Cas9 from *S. aureus* with a size of 3.2 kb and with similar editing efficiency in mammalian cells to native SpCas9, which have 1 kb less information when encoded in the form of DNA. Furthermore, it can be packaged like Cas9 simply within the capsid of the AAV, versifying its application in clinical studies, mainly for the correction of hereditary diseases such as Duchenne muscular dystrophy (DMD), by deletion of the deficient exon to produce the dystrophin protein, a direct cause of this pathology (Nelson et al., 2016).

Another alternative used to reduce the size of Cas9 is the generation of messenger RNA (mRNA) transcript of genes, which has been adapted in embryo editing by microinjection (Wang et al., 2013; Hai et al., 2014; Niu et al., 2014), recently scaling from somatic adult cells (Liang et al., 2015) toward primary cell culture (Osborn et al., 2016) by electroporation. Another advantage of this modality of delivery is the non-integration of the enzyme in the genome. However, there is a lack of conclusive evaluation of factors, such as stability and immunogenic response, to determine whether this method is advantageous over others. Several studies are focusing on the use of lentivirus (LV) because the capsid has the capacity to store around 8 kb, which is more than the capacity of AAV, permitting the expression of Cas9 and sgRNAs at the same time (Kabadi et al., 2014; Sanjana et al., 2014). Their usefulness in the transformation of cells that are not in active division, such as neurons in adults, has also been reported (Blömer et al., 1997; Vezzani, 2007). In addition, it has been shown that gene expression using LVengineering can be sustained for years, without prompting an immune system response from host participants in some clinical trials (Palfi et al., 2014). Due to these favorable properties and the current ineffective treatment, the use of gene therapy using LV has been started in the first clinical trials for the treatment of patients with neurodegenerative disorders of the central nervous system (CNS), opening a promising new stage in the application of molecular therapies that are really effective in improving quality of life, with similar or better results than convectional drugs (Palfi et al., 2014).

GENE THERAPY TO IMPROVE NEURODEGENERATIVE PROCESS

As previously mentioned, the reason for the search for alternative therapies for treating patients with AD and PD lies in the inefficiency of the current treatment. Yiannopoulou and Papageorgiou (2013) exemplified several drugs recently used for treating AD in clinical trials around the world and directed at three main approaches: (a) anti-platelet agents targeting β-amyloid; (b) selective agents reducing Aβ42; and (c) immunotherapy. However, it has been determined that these disease-modifying drugs exhibit disappointing or doubtful results in phase IIa and III clinical studies (Yiannopoulou and Papageorgiou, 2013). On the other hand, the gold standard treatment for PD patients is the dopamine agonist levodopa (L-DOPA), which can alleviate the consistent symptoms of neurodegeneration for a few years. However, it is well documented that use for prolonged periods has direct consequences on the development of involuntary movements, such as dyskinesias, and behavioral changes (Weintraub et al., 2010). Henceforth, gene therapy is a remarkable option that offers some advantages for the treatment of progressive disorders and its adequate engineering using the CRISPR/Cas9 system displays unique opportunities to eradicate the aberrant genetic components among patients with AD and PD. In addition, the large amount of existing literature is consistent with the need for improving current delivery and release systems that can offer discriminatory properties providing specificity for both the organ and some cell lineages and, in particular, for the integral preservation of the elements that will carry out the specific editing task, regardless of whether they are biological.

NOVEL VEHICLES AND DELIVERY METHODS

The main dilemma that arises in designing a therapy directed to the brain is being able to pass through the blood–brain barrier (BBB), which has the function of isolating and protecting neural tissue, controlling the entry of molecules and therefore hindering delivery. About 7,000 drugs have been assessed in the Comprehensive Medical Chemistry database, with only 5% able to cross the BBB to enter the CNS (Pardridge, 2005). Agustín-Pavón and Isalan (2014) illustrated various strategies for the efficient delivery of components to neural tissue (Agustín-Pavón and Isalan, 2014). They divide the methods into two categories: (a) less invasive [intranasal access through nanoparticle (NP)-assisted drug delivery across the BBB is another system with mitigatory properties and the supporting NPs indicate solid colloidal particles with a size range of 1–1,000 nm (Zhou et al., 2018; polymers, lipids, magnetic), emphasizing that successful BBB passage with subsequent cellular labeling could be achieved if NPs were fabricated with non-ionic surfactants or cationic stabilizers but not when anionic compounds were added; in addition, NP's size (67–464 nm) and charge had no influence on BBB passage (Voigt et al., 2014); among others, they described exosomes, cell-penetrating peptides (CPPs), often vividly termed

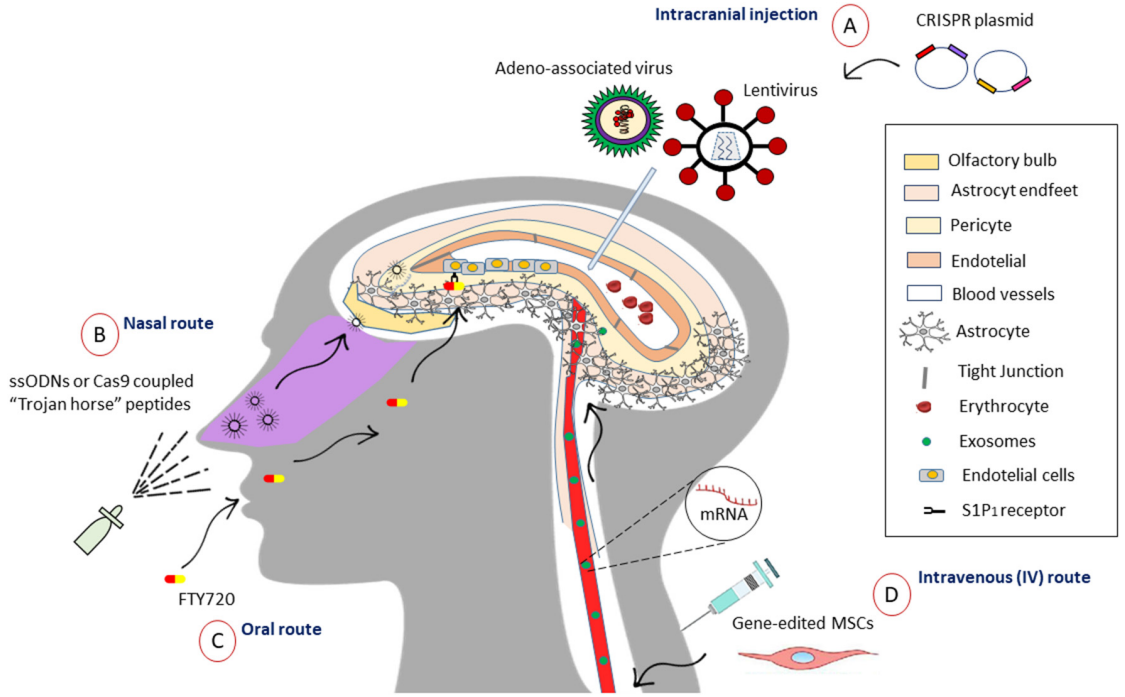

FIGURE 2 | Different strategies to access the central nervous system (CNS). **(A)** Intracranial injection allows the entry of viruses such as the adeno-associated virus (AAV) that can package the sequence of Cas9 and the sgRNA in its capsid to incorporate it in a non-integrative manner. While lentiviruses have eight times the storage capacity of AAVs, so it would be used for the co-expression of Cas9 with distinctive sgRNAs all in one. **(B)** One of noninvasive approaches used to go through BBB is the intranasal administration of "Trojan horse" peptides (5–30 amino acids), which can be coupled to nucleic acids, for example, ssODNs or the enzyme Cas9, facilitating access through the olfactory bulb. **(C)** Oral drugs like FTY720 (Fingolimod) allows inducible opening of the blood–brain barrier (BBB) through sphingosine 1-phosphate receptor-1 (S1P1) receptor in endothelial cells. This may be a promising option to control the temporary access of molecules of 10 kDa or less and larger in the future. **(D)** Mesenchymal stem cells (MSCs), for its homing properties, can travel to the site and perform the repair from the intravenous line to the CNS, acting as vehicles, and it has been shown that they do not arouse meaningful immune responses. Otherwise, the release of small vesicles called exosomes (30–150 nm) allows the transference of mRNA and other regulatory molecules among MCSs, and it has been shown to release them in cells of neural lineage. This can be an advantage for the delivery of Cas9 mRNA and sgRNAs through the BBB.

as "Trojan horse" peptides, or protein transduction domains (PTDs) as a class of diverse peptides, typically with 5–30 amino acids (4–24 nm), that can translate through the cellular plasma membrane (Shi et al., 2014)]; and (b) more invasive (direct injection into the parenchyma of the brain or ventricles during stereotactic surgery, entry of hyperosmotic solutions, microbubbles with ultrasound activation, and laser irradiation (Agustín-Pavón and Isalan, 2014). All these methods can serve as vehicles for the preservation of the integrity of CRISPR systems, improving the possibilities of editing in the target site with the enormous advantage of crossing the BBB. One novel and exciting alternative for accessing the CNS is the reversible and temporal manipulation of entry molecules that access the BBB. A study from Yanagida et al. (2017) showed that pharmacological inhibition (FTY720) and sphingosine 1-phosphate receptor-1 (S1P1) gene facilitates the selective entry of small molecules, opening the BBB, with no major signs of inflammation or CNS damage. This effect was attributed to changes in the cytoskeleton of tight junction proteins. Another pertinent finding was that the pharmacological treatment was reversible and transient, suggesting a viable alternative to intentionally opening the BBB and allowing the entry of molecules of <3–10 kDa (Yanagida et al., 2017). These results suggest another noninvasive alternative to diversifying the available therapeutic options for CNS diseases. On the other hand, subsequent studies could examine the synchronization of FTY720 activity for the introduction of molecules greater than 10 kDa, such as mRNA-Cas9 or ssODNs, for the improvement of their *in situ* action (**Figure 2**).

Another promising option lies in cell-based therapeutics, adapting mesenchymal stem cells (MSCs) due to their inherent beneficial properties, such as the release of pro-regenerative trophic factors and the generation of bilipid vesicles. These can mediate the transport of small molecules, reported in cell–cell communication and signaling, arousing a great interest as a therapeutic option (Phinney and Pittenger, 2017). Their potential lies in the size of exosomes (30–150 nm) and its form of propagation by means of horizontal transfer of mRNA, microRNAs (miRNAs), transfer RNAs (tRNAs), lipids, and proteins, modifying the cellular activities (Sarko and McKinney, 2017). In contrast to release forms, such as liposomes or nanopolymeric particles, exosomes can potentially avoid the endosomic pathway and lysosomal degradation, allowing the release of molecules directly into the cytoplasm (Lou et al., 2017). Likewise, they do

not support immunogenic problems observed in other systems of delivery for drugs such as dendrimer (Lee et al., 2005), NPs (Petros and DeSimone, 2010), and liposomes (Torchilin, 2014). Remarkably, it has been observed that these particles can be captured by nearby cells or migrate to distant tissues following circulation in the peripheral blood and through the BBB. Sarko and McKinney (2017) raised the natural reconfiguration of the secretome, allowing the use of exosomes for the controlled release of new drugs and other molecules that act *in situ*. Added to this, it has been demonstrated the release of exosomes in various neural lineages, such as astrocytes, microglia, neurons, oligodendrocytes, and neural stem cells (Sims et al., 2014; Brites and Fernandes, 2015; Budnik et al., 2016; Janas et al., 2016; Verkhratsky et al., 2016), fortifying the idea of reengineering these vesicles for therapeutic purposes in neurodegenerative diseases such as PD and AD. The incorporation of the CRISPR/Cas9 system within these biological vehicles could offer exosomic nanovesicles filled with mRNACas9, ssODNs, or saCas9 with the ability to circulate and access different regions of the brain to edit cells in a niche-specific way, having the advantage of recognizing cellular reception ligands.

Among the other biological vehicles described in the literature, work from Wang et al. (2016) demonstrated the production of self-assembly synthetic lipids, obtained from NPs belonging to bio-reduceable lipids with negatively overloaded proteins, forming Cas9 complexes: anionic sgRNAs for the efficient editing of the genome in mammalian cells and in rodent brains. The correct delivery by stereotactic injection or other noninvasive method could lead to gene correction of mature neurons *in situ*, restoring specific neural circuits through a low-toxicity delivery method (Wang et al., 2016).

Another novel strategy among nonviral approaches for examining the mammalian brain *in vivo* entails coupling the Cas9 enzyme with gold NPs. Lee et al. (2005) demonstrated that gene editing by intracranial injection of CRISPR-Gold NP ribonucleoprotein could be achieved. They performed gene editing in Thy1-YFP and Ai9 mice, in addition to targeting the metabotropic glutamate receptor 5 (*mGluR5*) gene to reduce exaggerated signaling in the striatum of a mouse model of fragile X syndrome (FXS) in a *Fmr1* KO mouse. The team observed gene editing in neurons and non-neuronal cells, including microglia. Remarkably, they inhibited 40%–50% of the expression of the autism-causing gene, *Grm5*, in the striatum after intracranial injection, leading to rescue from autism-associated behavioral phenotypes (Trenkmann, 2018).

In a recent study, Narbute et al. (2019) notably demonstrated for the first time the therapeutic effect of intranasal administration of extracellular vesicles (EVs) derived from human exfoliated deciduous teeth stem cells (SHEDs) in a unilateral 6-OHDA rat model of PD. They succeeded in reversing gait impairments and normalizing TH expression in the substantia nigra and striatum (Narbute et al., 2019). The proteomic assay demonstrates the presence of Cu/Zn superoxide dismutase 1 (SOD1) and antioxidant proteins thioredoxin (TXN) and peroxiredoxin-6 (PRDX6) within the EVs, which the authors suggest may reduce sensitivity of dopaminergic neurons to 6-OHDA-induced oxidative stress based on prior studies (Mazzio et al., 2004; Botella et al., 2008). Nonetheless, little is known about the molecular antioxidant mechanism and further studies are required to unveil the neuroprotective action of EVs, which may be an interesting nonviral approach for treating PD with fewer invasive repercussions.

Despite the novelty and growing interest in noninvasive gene-editing techniques that pass the BBB, more studies of their toxicity and efficiency are needed. In addition, the most recent reports tend to fine-tune control of key pathogenic gene expression; at the moment, this could be achieved through rational engineering-derived viruses such as AAVs, LVs, and retroviruses (RVVs).

THE GROWING PROMISE OF ADENOVIRUSES

In recent years, the manufacturing of new AAV serotypes is having an enormous effect on the field of gene therapy, especially in the neurosciences, and as a potential treatment of neurodegenerative diseases (Deverman et al., 2018). Currently, one of the most pursued objectives is the development of more efficient systems for *in vivo* gene editing. Among the most outstanding recent achievements, Suzuki et al. (2016) developed a CRISPR system homology-independent targeted integration (HITI) strategy that enabled knock-in of both dividing and nondividing cells, remarkably in the neurons of postnatal mammals, and demonstrated better efficiency than that of the HDR mechanism. The *in vivo* system consisted of HITI constructs and two AAV vectors and packaged both AAVs with serotype 8 or 9 (AAV-Cas9 and AAV-mTubb3). Afterward, they performed inducible Tubb3–GFP HITI targeting constructs, where Cre-dependent Cas9 expression was under the control of tamoxifen (TAM), by *in utero* electroporation of E15.5 fetal brain. The results revealed efficient GFP knock-in with the HITI donor and minimal knock-in with the HDR donor (Tubb3-HDR).

Furthermore, to validate their therapeutic potential, they demonstrated improvement in visual function in a rat model of retinitis pigmentosa. The *Mertk* gene was corrected using an AAV vector for inserting a copy of *Mertk* exon 2 into intron 1 (AAV-rMertk-HITI; Suzuki et al., 2016). This system promises to be a strong candidate for exploiting the *in vivo* gene-editing approach of the CNS and simultaneously overcoming the drawbacks caused by the use of the HDR repair mechanism.

The other main goal is to perform modifications among serotypes to enable a wider distribution in the large mammalian brain, enabling clinical therapeutic implementation. In another recent work, Naidoo et al. (2018) developed a novel AAV variant (AAV2-HBKO), capable of widespread CNS transduction in neurons localized in the deep cortical layers, deep cerebellar nuclei, several subcortical regions, and motor neuron transduction *via* thalamic injection and intracerebroventricular delivery. The combination resulted in the transduction of oligodendrocytes in superficial cortical layers and neurons in deeper cortical layers. They also demonstrated that the delivery route has an impact on the

cellular tropism and pattern of CNS transduction (Naidoo et al., 2018). Interestingly, vectors such as AAV1, AAV5, and AAV9 do not have affinity for heparan sulfate proteoglycans (HSPGs); therefore, they can distribute after a single injection into the brain (Pillay et al., 2016). The AAV2-HBKO serotype has been demonstrated to cope with tropism for HSPGs and showcases in particular different translation patterns in oligodendrocytes and motor neurons, depending on the delivery method of the vector (ICV or thalamic). This poses tremendous implications for providing gene therapy to humans within the next years. Furthermore, it is suitable for neurological disorders that involve many parts of the brain, such as AD, and especially those that involve the hippocampus.

Although it is widely documented that most cases of AD are sporadic, the presence of certain point mutations or deletions in the genes for amyloid precursor protein (APP), presenilin 1 (PSEN1), and presenilin 2 (PSEN2) triggers the production of beta-amyloid peptide. Therefore, the study of the familial component in AD can highlight tremendous opportunities to intervene through gene therapy. György et al. (2018) harvested fibroblasts from carriers of *APPswe* (KM670/671NL APP mutation) indigenous to Sweden (*APPswe* for the mutation and APPSW for the mutant allele) who had increased Aβ levels (Mullan et al., 1992). They mediated a CRISPR/Cas9 knockout of APP^{SW} or APP^{WT} in the human $APP^{SW/WT}$ fibroblasts. Cells treated with Cas9 and sgRNAs showed a robust reduction in unperturbed APP^{SW} reads, whereas the relative proportion of APP^{WT} reads without indels did not decrease. Thus, CRISPR-induced indels were only detected in APP^{SW} alleles and not in APP^{WT} alleles when using gRNAs against the mutation (György et al., 2018). Subsequently, they applied the system for *in vivo* disruption of the APP^{SW} allele in Tg2576 mice (mice carrying multiple copies of the APPswe mutation). AAV-mediated delivery of SW1 gRNA was applied unilaterally into the hippocampus of adult mutant mice. After 6 weeks, the results confirmed the disruption of the mutation (indels) in primary cortical neurons and in the hippocampus in the APP allele (György et al., 2018). This is the first report of AAV-CRISPR therapy in an animal model of AD. Despite the significant reduction in Aβ40 and Aβ42 in the conditioned media from patient cells treated with gRNA against the APP^{SW} allele, in the mouse model, they observed limited gene disruption efficiency as a consequence of the high number of target alleles that was not related to insufficient AAV delivery of CRISPR. Therefore, the assessment of Aβ plaque pathology was not carried out.

The study by György et al. (2018) could lead to new *in vivo* therapeutic approaches based on AAV-CRISPR correction constructs. Regardless, new variants of AAVs with greater penetration and efficiency are still needed.

Other approaches to tackling AD involve targeting the pathological process of chronic neuroinflammation. A study by Raikwar et al. (2019) proposed the glia maturation factor (GMF) as an attractive therapeutic target because of its significant upregulation in various regions of AD brains. They transduced a BV2 microglial cell line with an AAV co-expressing *S. aureus* (Sa)-Cas9 (smaller version of Cas9 than spCas9) and a GMF-specific guide RNA (GMF-sgRNA). They found a few cells expressing SaCas9 while lacking GMF expression, confirming successful GMF gene editing. Nevertheless, they achieved low transduction efficiencies. Therefore, the authors suggest the possibility of exploring transduction efficiencies in embryonic stem cells (ESCs), induced-pluripotent stem cells (iPSCs), primary neurons, astrocytes, and microglia, and also the suitability of tropism-modified AAVs (Raikwar et al., 2019). These results suggest early personalized gene therapy based on Sa-CRISPR-AAVs that includes a novel target and might help to reduce neuroinflammation/neurodegeneration not only in AD but also in PD (Khan et al., 2014).

PRECISELY FINE-TUNING EXPRESSION THROUGH dCas9 AND CRISPRa/CRISPRi TECHNOLOGY

New functions and varieties have been produced since the beginning of the exploitation of native spCas9. Among them, the nickase-dead mutant form of the Cas9 protein (dCas9), fused to a Krueppel-associated box (KRAB) domain, could achieve precise and programmed transcription activation and repression, epigenetic remodulations of local histones, DNA modifications, labeling of the genomic locus, and single-base genome mutagenesis (Dominguez et al., 2016; Nishida et al., 2016). This, therefore, represents an attractive method of performing inducible repression of target loci in neuronal cells that overexpress pathological genes when utilizing dCas9-CRISPR interference (CRISPRi) technology and may decrease toxic levels of proteins *via* fine-tunable knock-down. Recently, Zheng et al. (2018) developed two conditional CRISPRi tools to silence *Syt1* expression in either glutamatergic or GABAergic neurons with dCas9-KRAB expression under the control of pCaMKIIα and pVGAT promoters, respectively. They stereotactically infused LV encoding the *Syt1*-targeted conditional CRISPRi system into the mouse dentate gyrus (DG). They observed highly specific enrichment of the genes encoding vesicular glutamate transporter 1 (Vglut1) in pCaMKIIα::dCas9-KRAB+ neurons and glutamic acid decarboxylase 1 (Gad1) in pVGAT::dCas9-KRAB+ neurons. Remarkably, they found subtype-specific expression of the CRISPRi in the DG. Furthermore, *Syt1* expression was selectively abrogated by conditional CRISPRi within the *Syt1*-targeting glutamatergic or GABAergic neurons but not in both, emphasizing the versatility of efficient disruption in a specific subtype of neurons in living mammals (Zheng et al., 2018).

As mentioned previously, a potential strategy could be the implementation of dCas9-CRISPRi intervention to repress the levels of abnormal multiple copies of well-known pathological genes, such as *SNCA* in PD, in a reversible way. Heman-Ackah et al. (2016) demonstrated the utilization of CRISPRi as a robust tool for significantly repressing the expression *via* the transcription start site (TSS) of multiple genes involved in proteinopathy-induced neurodegeneration. They transfected HEK293T simultaneously with dCas9 sgRNAs targeting the

alpha-synuclein, microtubule-associated protein tau, APP, and huntingtin (*SNCA*, *MAPT*, *APP*, and *HTT*, respectively). Notably, they performed precise transcriptional modulation through CRISPRa of neurodegenerative disease-related genes in human iPSC-derived neurons. TSS2-2 sgRNA and dCas9-VPR transcriptional activator mediated the activation of alpha-synuclein in normal alpha-synuclein levels (NAS) iPSC-derived neurons from healthy control patient and iPSCs derived from a patient with PD caused by alpha-synuclein triplication (AST). They achieved an eightfold activation of endogenous SNCA expression in the NAS iPSC-derived neurons and through dCas9-KRAB repression, a 40% reduction in alpha-synuclein mRNA levels in the AST iPSC-derived neurons (Heman-Ackah et al., 2016). In addition, the group found that targeting the genes close to the TSS region reduced the off-target effects considerably (Heman-Ackah et al., 2016), reducing the negative side effects of using SpCas9. Overall, these findings suggest the possibility of exploiting the tunable CRISPRa/CRISPRi platform for multiplex transcriptional repression of molecular pathological signatures *in vivo* in the mammalian brain and provide enormous possibilities for addressing neurodegeneration in the familial and sporadic disease states.

SUITABILITY FOR GENE-EDITING TECHNOLOGY IN PARKINSON'S DISEASE AND ALZHEIMER'S DISEASE?

It is well known that the sporadic component is dominant in the causality of the most common neurodegenerative diseases; however, in recent years, the relevance of several genes and their participation in triggering of the pathological process have been demonstrated. Zafar et al. (2018) followed the descendant population carriers of the "Iowa-Kindred" mutation in PD and showed that triplication in the *SNCA* gene on one allele directly increased alpha-synuclein levels two-fold and lead to a rapid progression of synucleopathy, causing severe clinical and neuropathological features (Zafar et al., 2018). Therefore, the pursuit of restoring normal transcript levels of *SNCA* could have a deep clinical impact. Regarding this approach, as stated above, Heman-Ackah et al. (2016) implemented an iCRISPR-based platform to tackle this in hiPSCs and also the group of Kantor et al. (2018) recently developed an epigenetic-based approach. Using an "all-in-one" lentiviral vector encoding sgRNA-dCas9-DMNT3A directed to intron 1 hypermethylation, strikingly they restored normal levels of *SNCA* mRNA and efficiently transduced hiPSC-derived dopaminergic neurons, resulting in an effective and targeted modification of the methylation state of CpGs within *SNCA* intron 1 (Kantor et al., 2018). Taking into consideration that α-synuclein immunohistochemistry is currently the gold standard in the neuropathological evaluation of PD (Stefanis, 2012), the development of personalized treatments to reduce the levels of both SNCA and α-synuclein is imperative and now achievable. These examples are promising and demonstrate the suitability to perform CRISPR gene-editing approaches in PD, but much more has to be done toward clinical applications.

On the other hand, unfortunately in AD, multiple phase III clinical trials have failed to recover memory and cognitive function in AD patients using trial drugs, such as anti-Aβ antibody; therefore, gene therapy is an interesting option that is being supported by a few recent works. It is well known that a very small percentage of cases (<1%) are caused by known mutations in the APP protein or gene products involved in processing APP to form beta-amyloid. Despite the small percentage of cases caused by these mutations, they all trigger the production of beta-amyloid peptide (Bettens et al., 2013; Rohn et al., 2018). Notably, it has been demonstrated that they can further influence the appearance of early-onset AD before the age of 60. Among the targets described are PSEN1 and PSEN2 genes. To probe the feasibility of the CRISPR approach in AD, Ortiz-Virumbrales et al. (2017) generated human basal forebrain cholinergic neurons (BFCNs) *in vitro* from hiPSCs harboring the $PSEN2^{N141I}$ mutation, based on evidence indicating this population as one of the first cell types to be affected in all forms of AD, and that their dysfunction is clinically correlated with impaired short-term memory formation and retrieval. Interestingly, the CRISPR/Cas9 correction of the PSEN2 point mutation abolished the electrophysiological deficit, restoring both the maximal number of spikes and spike height to levels recorded in healthy controls (Ortiz-Virumbrales et al., 2017). The authors suggest that accumulation of Aβ could synergize with the altered electrophysiological mechanisms in a pathway leading to AD, but the exact mechanism and pathways remain unknown. In another exciting study, Park et al. (2019) targeted beta-secretase 1 "*Bace1*" gene (which is required for the production of Aβ peptides) through CRISPR/Cas9-loaded nanocomplexes in post-mitotic neurons *in vivo* and demonstrated their therapeutic application in five familial AD (5XFAD) and APP knock-in AD mouse models. In the present study, despite not being a viral vector-based delivery, it was nonetheless shown to have a high editing efficiency, thus highlighting the emerging technology of nonviral NPs as an interesting therapeutic option for AD. Despite that CRISPR-based gene-editing and gene-therapy approaches have been seen as powerful tools to restore monogenic diseases, new approaches have provided a compelling basis to suggest the possibility of application to the sporadic component as well. Sun et al. (2018) published in a pre-print that editing of endogenous APP at the extreme C-terminus and reciprocal manipulation of the amyloid pathway through an AAV9-APP gRNA-GFP leads to attenuation of β-cleavage and Aβ while up-regulating neuroprotective α-cleavage. These findings suggest a robust gene-editing approach in human cell lines and *in vivo* in mice[2].

Overall, although there are only a handful of recent works, they represent significant advances toward the development of more specific therapies for halting neurodegeneration in AD and PD. The most outstanding is the capacity to apply CRISPR-AAV/NP systems in the sporadic group of these diseases. With refinement of some of the current hurdles for clinical application, there is the potential for a tremendous advance for

[2]https://www.biorxiv.org/content/biorxiv/early/2018/04/28/310193

the treatment of neurodegenerative diseases, starting with the most prevalent worldwide.

DRAWBACKS TO OVERCOME

It has been demonstrated in the most recent works that a huge benefit of the implementation of treatments based on gene therapy is to cope with the drawbacks of conventional therapeutics and avoid or decrease the side effects that they cause. The age of gene therapy experienced exponential growth as a result of the adaptation of the CRISPR systems for genome-editing in mammals. However, there are still relevant drawbacks that need to be overcome before their clinical implementation in the treatment of neurodegenerative diseases. First, we have to emphasize the issue of the immune response. After the initial "CRISPR fever," there have been significant questions over the last 2 years regarding the activation of the immune response as a result of the presence of exogenous proteins such as Cas9 and their orthologs. The study from Charlesworth et al. (2019) showed the presence of humoral response and specific antigen T-cells against SaCas9 (Cas-derivative of *S. aureus*) in healthy human volunteers, presenting interesting data for the discussion of the implementation of gene therapies clinically. Nonetheless, both studies call on the international community of researchers to exercise a more rigorous assessment of the possible immunologic responses to the microbial origin of the system (Charlesworth et al., 2019).

As a way of counteracting some of the pitfalls, CRISPR/Cas9-based CNS-targeted therapies are currently being refined to increase specificity for target organs. An example is a work published by Murlidharan et al. (2016). They developed a chimeric AAV2, AAV2G9, improving the activity of AAV2 and AAV9, for the transduction of neurons within the brain, reducing glial infection (Murlidharan et al., 2016). It was also shown that a single administration of cerebrospinal fluid did not lead to the presence of the synthetic virus in off-target organs. In addition, a single intracranial injection with a vector that encodes for the gene *MIR137* (a risk gene for schizophrenia) resulted in the specific deletion of the same gene in the brain of knock-in mice, without detection of the vector in the liver (Murlidharan et al., 2016). An interesting finding of this study was the preferential neuronal tropism of AAV2g9, attributed to the presence of a greater concentration of HSPGs on the surface of the neurons greater than that of glial cells (Hsueh and Sheng, 1999). In this way, the restriction of editing to the neural lineage within the CNS is being carried out in almost exclusively, overcoming the disadvantages regarding selectivity of target organs presented by other serotypes of AAV, also demonstrated in the study mentioned for the AAV9 serotype.

Another important consideration for AAV serotypes in CNS gene therapies was addressed in a study by Long et al., where it was reported that intra-muscular, intra-peritoneal, and retro-orbital delivery form of AAV9 could not pass through the BBB in order to restore the dystrophin protein (expressed in cardiac muscle and skeletal) in the CA1/CA2 regions of the hippocampus (Long et al., 2016). Therefore, it is not possible to cross the BBB for any AAV serotype if stereotactic surgery is not performed in any specific region of the brain. In another study, Swiech et al. (2015) reported the interrogation of the genome *in vivo* by AAV containing SpCas9-sgRNAs applied *via* stereotactic injection, having *MECP2*, *DNMT1*, *Dnmt3a*, and *Dnmt3b* as target genes in the adult mice brain, efficiently achieving multiple-gene editing of post-mitotic neurons in the visual cortex.

These studies agree that with the repeated administration of doses of AAV, concomitant disturbance caused by stereotactic surgery for effective infection and the proper distribution of the virus in the different regions of the brain are necessary. Despite the low risk present during surgery, an insult is consistently generated with the perfusion of the BBB, which could increase the release of inflammatory factors, such as IFN-γ and TLR4, coupled with the inherent reaction of the glia reactive inherent, observed in disorders such as PD and AD (Booth et al., 2017; Wood, 2017). However, this same condition of the BBB is compromised by inflammation and has been shown to allow the transfer of both small and large molecules, participating as a passive mechanism for the transport of drugs to the CNS (Shlosberg et al., 2010). In addition, due to the progressive nature of PD and AD, changes in the function of age-dependent microglia have been shown. Spittau described these changes at the molecular level, including the TLR-dependent triggering of alpha-synuclein (αSyn), activation of microglia through neuromelanin, and αSyn deficient phagocytosis in PD, whereas in AD, the decrease in phagocytosis of the β-amyloid plaques (Aβ) and depletion of the microglia do not decrease the formation of plaques and neurodegeneration continues (Spittau, 2017). As described above, gene manipulation of the microglia could have interesting results in mediating inflammation or reducing hyperreactivity in the same way that it could be used in different CRISPR systems, such as dCas9 for the regulation of the release of trophic factors. On the other hand, it has been shown that the R47H mutation of the *TREM2* gene can cause a three- to four-fold increase in the risk of developing AD in a 5XFAD murine model (Wang et al., 2015). Wang et al. (2015) showed that TREM2 deficiency and haploinsufficiency increase the accumulation of β-amyloid (Aβ) due to a dysfunctional microglial response, which fails in clustering around the Aβ plaques and becomes apoptotic. However, more studies are needed to elucidate concisely the role of TREM2 in the development of AD and to evaluate the therapeutic potential of editing its gene variants. Therefore, the dissection of signaling pathways affected by variants will be essential for the design of gene-editing strategies to restore functionality *in situ*.

One of the great advantages that have been explored by some research groups is the performance of multiplex gene editing and the usefulness that CRISPR systems exhibit relative to other nucleases. Cong et al. (2013) first demonstrated the efficient editing of mammalian and human cells simultaneously; therefore, the versatility to program the enzyme and its guides was proposed, with the purpose of recognizing more regions of the genome, taking away the restriction of only being able to access every 8 bp for the SpCas9, a CRISPR system type II. Tothova et al. (2017) achieved multiple edits of CD34+ human hematopoietic stem cells from the umbilical cord and

TABLE 1 | Novel nonviral and viral systems for *in vivo* gene therapy in the mammalian brain.

	Model	Efficiency	Toxicity	Route	References
Nonviral					
Bio-reduceable lipids nanoparticles	Rosa26^{tdTomato} mouse	Highly protein delivery but minimal diffusion	Low	DM, DG, MD, cortex, BNST, LSV, paraventricular nucleus of hypothalamus (PVN), and lateral hypothalamus (LH)	Wang et al. (2016)
Complexes Ribonucleoprotein CRISPR:Gold nanoparticles	Thy1-YFP, Ai9 and *Fmr1* KO adult mice	High	Potentially accumulate but tolerated in the brain	Intracranial injection in the striatum	Lee et al. (2005)
dCas9-Suntag-TET1CD All-in-one vector	Mouse fetal brain at E14	High	No significant off-targets	*In utero* electroporation into VZ	Morita et al. (2016)
Extracellular vesicles (EVs) derived from SHEDs	Unilateral rat PD model of 6-OHDA	High	None	Intranasal administration	Narbute et al. (2019)
Viral					
AVV serotypes 8 and 9 (HITI)	Fetal brain and adult mouse model of retinitis pigmentosa	Low, partial recovery of vision	High on-target specificity of HITI (90%–95%)	*In utero* electroporation and direct injection in the visual cortex	Suzuki et al. (2016)
AAV2-HBKO serotype	Adult male *Rhesus macaques*	High number of transduced motor neurons	Perivascular cuffing and cellular infiltration in the thalamus but none presented any gross adverse clinical signs	Bilaterally thalamic injection	Naidoo et al. (2018)
Cas9/gRNA into exo-AAV1	Tg2576 mice	Insufficient AVV-delivery of CRISPR	Non-assessed	Direct injection in the hippocampus	György et al. (2018)
LVVs d-Cas9-KRAB	Mice with *Syt1* deficiency	Very high	Minimal off-target effects	Stereotactically in the DG	Zheng et al. (2018)

Currently, rationally engineered viruses are the most suitable approach for selective neural gene-therapy replacement in mammals; however, the efficiency and off-target effects of CRISPR-Cas variants still need to improve before use in clinical scenarios. Therefore, manufacturing new AAV serotypes that can easily cross the BBB and distribute broadly with a single injection will be an intense area of research in molecular neuroscience in the following years. Hopefully, identification of successful doses pre-clinically and maturation of multiplex d-Cas9 AAV-CRISPRa/CRISPRi platforms will support the introduction of carefully regulated gene editing/gene therapy to the treatment of PD and AD patients.

adult primary progenitor cells, which give rise to pre-malignant myeloid and malignant diseases, recognizing the difficulty of modeling these conditions in human cells. Other strategies highlight multiple edits at the epigenetic remodeling level. Savell and Day (2017) exemplify modular approaches for specific targeting and modification of the local chromatin environment at a single gene within the CNS across CRISPR/Cas9 systems. Moreover, they described the purpose of intervening in the regulation of crucial mechanisms that are affected in neuropsychiatric and neurologic disorders (Savell and Day, 2017). Morita et al. (2016) adapted dCas9-SunTag to demethylate a specific locus of DNA, demonstrating the demethylation of CpGs in regulatory regions of ESCs, cancer cells, and primary neural precursor cells and in mouse fetuses *in vivo*. This was the first report of epigenomic manipulation performed *in vivo* based on CRISPR technology and should promote gene modification in living organisms, including modifications in the CNS.

CONCLUSIONS AND PERSPECTIVES

The recent findings indicate that temporal and region-specific editing of gene expression *via* nonviral and viral approaches throughout the large mammalian brain *in vivo* is achievable. Nevertheless, error-prone mechanisms remain dominant after CRISPR/Cas9 execution; in the adult brain, it is virtually impossible for post-mitotic neurons to utilize the HDR mechanism efficiently for ssODN replacement integration. Therefore, the refinement of new alternatives, such as HITI (Suzuki et al., 2016), will be necessary to ensure therapeutic potential in nondividing cells. On the other hand, a new wave of nonviral delivery systems is approaching. Coupling with stable RNP complexes will allow remarkably novel ways to treat neurological disorders without the need for such invasive procedures. However, more in-depth studies are needed to elucidate its true toxicity and efficiency over prolonged periods (**Table 1**).

AUTHOR CONTRIBUTIONS

AC-C made a substantial, direct, and intellectual contribution to the work. NFD-M made an intellectual contribution and conducted manuscript review. EP-C made direct intellectual contribution and final approval to the manuscript. NED-M made a substantial intellectual contribution and performed the final revision of the manuscript.

FUNDING

This work was supported by funds from Consejo Nacional de Ciencia y Tecnología (CONACyT; 271307, 272968). This work was performed by AC-C in partial fulfillment of the requirements for the Doctorado en Ciencias en Innovación Biotecnológica, Centro de Investigación y Asistencia en Tecnología y Diseño del Estado de Jalisco.

REFERENCES

Agustín-Pavón, C., and Isalan, M. (2014). Synthetic biology and therapeutic strategies for the degenerating brain: synthetic biology approaches can transform classical cell and gene therapies, to provide new cures for neurodegenerative diseases. *Bioessays* 36, 979–990. doi: 10.1002/bies.201400094

Bettens, K., Sleegers, K., and Van Broeckhoven, C. (2013). Genetic insights in Alzheimer's disease. *Lancet Neurol.* 12, 92–104. doi: 10.1016/S1474-4422(12)70259-4

Blömer, U., Naldini, L., Kafri, T., Trono, D., Verma, I. M., and Gage, F. H. (1997). Highly efficient and sustained gene transfer in adult neurons with a lentivirus vector. *J. Virol.* 71, 6641–6649.

Booth, H. D. E., Hirst, W. D., and Wade-Martins, R. (2017). The role of astrocyte dysfunction in Parkinson's disease pathogenesis. *Trends Neurosci.* 40, 358–370. doi: 10.1016/j.tins.2017.04.001

Botella, J. A., Bayersdorfer, F., and Schneuwly, S. (2008). Superoxide dismutase overexpression protects dopaminergic neurons in a *Drosophila* model of Parkinson's disease. *Neurobiol. Dis.* 30, 65–73. doi: 10.1016/j.nbd.2007.11.013

Brites, D., and Fernandes, A. (2015). Neuroinflammation and depression: microglia activation, extracellular microvesicles and microRNA dysregulation. *Front. Cell. Neurosci.* 9:476. doi: 10.3389/fncel.2015.00476

Budnik, V., Ruiz-Cañada, C., and Wendler, F. (2016). Extracellular vesicles round off communication in the nervous system. *Nat. Rev. Neurosci.* 17, 160–172. doi: 10.1038/nrn.2015.29

Cebrian-Serrano, A., and Davies, B. (2017). CRISPR-Cas orthologues and variants: optimizing the repertoire, specificity and delivery of genome engineering tools. *Mamm. Genome* 28, 247–261. doi: 10.1007/s00335-017-9697-4

Charlesworth, C. T., Deshpande, P. S., Dever, D. P., Camarena, J., Lemgart, V. T., Cromer, M. K., et al. (2019). Identification of preexisting adaptive immunity to Cas9 proteins in humans. *Nat. Med.* 25, 249–254. doi: 10.1038/s41591-018-0326-x

Cong, L., Ran, F. A., Cox, D., Lin, S., Barretto, R., Habib, N., et al. (2013). Multiplex genome engineering using CRISPR/Cas systems. *Science* 339, 819–823. doi: 10.1126/science.1231143

Deverman, B. E., Ravina, B. M., Bankiewicz, K. S., Paul, S. M., and Sah, D. W. Y. (2018). Gene therapy for neurological disorders: progress and prospects. *Nat. Rev. Drug Discov.* 17, 641–659. doi: 10.1038/nrd.2018.110

Doench, J. G., Fusi, N., Sullender, M., Hegde, M., Vaimberg, E. W., Donovan, K. F., et al. (2016). Optimized sgRNA design to maximize activity and minimize off-target effects of CRISPR-Cas9. *Nat. Biotechnol.* 34, 184–191. doi: 10.1038/nbt.3437

Doench, J. G., Hartenian, E., Graham, D. B., Tothova, Z., Hegde, M., Smith, I., et al. (2014). Rational design of highly active sgRNAs for CRISPR-Cas9-mediated gene inactivation. *Nat. Biotechnol.* 32, 1262–1267. doi: 10.1038/nbt.3026

Dominguez, A. A., Lim, W. A., and Qi, L. S. (2016). Beyond editing: repurposing CRISPR-Cas9 for precision genome regulation and interrogation. *Nat. Rev. Mol. Cell Biol.* 17, 5–15. doi: 10.1038/nrm.2015.2

Fine, E. J., Appleton, C. M., White, D. E., Brown, M. T., Deshmukh, H., Kemp, M. L., et al. (2015). Trans-spliced Cas9 allows cleavage of HBB and CCR5 genes in human cells using compact expression cassettes. *Sci. Rep.* 5:10777. doi: 10.1038/srep10777

Friedland, A. E., Baral, R., Singhal, P., Loveluck, K., Shen, S., Sanchez, M., et al. (2015). Characterization of Staphylococcus aureus Cas9: a smaller Cas9 for all in-one adeno-associated virus delivery and paired nickase applications. *Genome Biol.* 16:257. doi: 10.1186/s13059-015-0817-8

Fu, Y., Foden, J. A., Khayter, C., Maeder, M. L., Reyon, D., Joung, J. K., et al. (2013). High-frequency off-target mutagenesis induced by CRISPR-Cas nucleases in human cells. *Nat. Biotechnol.* 31, 822–826. doi: 10.1038/nbt.2623

Gaudelli, N. M., Komor, A. C., Rees, H. A., Packer, M. S., Badran, A. H., Bryson, D. I., et al. (2017). Programmable base editing of A•T to G•C in genomic DNA without DNA cleavage. *Nature* 551, 464–471. doi: 10.1038/nature24644

González, F., Zhu, Z., Shi, Z. D., Lelli, K., Verma, N., Li, Q. V., et al. (2014). An iCRISPR platform for rapid, multiplexable, and inducible genome editing in human pluripotent stem cells. *Cell Stem Cell* 15, 215–226. doi: 10.1016/j.stem.2014.05.018

Guilinger, J. P., Thompson, D. B., and Liu, D. R. (2014). Fusion of catalytically inactive Cas9 to FokI nuclease improves the specificity of genome modification. *Nat. Biotechnol.* 32, 577–582. doi: 10.1038/nbt.2909

György, B., Lööv, C., Zaborowski, M. P., Takeda, S., Kleinstiver, B. P., Commins, C., et al. (2018). CRISPR/Cas9 mediated disruption of the swedish APP allele as a therapeutic approach for early-onset alzheimer's disease. *Mol. Ther. Nucleic Acids* 11, 429–440. doi: 10.1016/j.omtn.2018.03.007

Hai, T., Teng, F., Guo, R., Li, W., and Zhou, Q. (2014). One-step generation of knockout pigs by zygote injection of CRISPR/Cas system. *Cell Res.* 24, 372–375. doi: 10.1038/cr.2014.11

Heman-Ackah, S. M., Bassett, A. R., and Wood, M. J. (2016). Precision modulation of neurodegenerative disease-related gene expression in human iPSC-derived neurons. *Sci. Rep.* 6:28420. doi: 10.1038/srep28420

Hsu, P. D., Scott, D. A., Weinstein, J. A., Ran, F. A., Konermann, S., Agarwala, V., et al. (2013). DNA targeting specificity of RNA-guided Cas9 nucleases. *Nat. Biotechnol.* 31, 827–832. doi: 10.1038/nbt.2647

Hsueh, Y. P., and Sheng, M. (1999). Regulated expression and subcellular localization of syndecan heparan sulfate proteoglycans and the syndecan-binding protein CASK/LIN-2 during rat brain development. *J. Neurosci.* 19, 7415–7425. doi: 10.1523/JNEUROSCI.19-17-07415.1999

Hu, J. H., Miller, S. M., Geurts, M. H., Tang, W., Chen, L., Sun, N., et al. (2018). Evolved Cas9 variants with broad PAM compatibility and high DNA specificity. *Nature* 556, 57–63. doi: 10.1038/nature26155

Janas, A. M., Sapoń, K., Janas, T., Stowell, M. H., and Janas, T. (2016). Exosomes and other extracelular vesicles in neural cells and neurodegenerative diseases. *Biochim. Biophys. Acta* 1858, 1139–1151. doi: 10.1016/j.bbamem.2016.02.011

Kabadi, A. M., Ousterout, D. G., Hilton, I. B., and Gersbach, C. A. (2014). Multiplex CRISPR/Cas9-based genome engineering from a single lentiviral vector. *Nucleic Acids Res.* 42:e147. doi: 10.1093/nar/gku749

Kampmann, M. (2017). A CRISPR approach to neurodegenerative diseases. *Trends Mol. Med.* 23, 483–485. doi: 10.1016/j.molmed.2017.04.003

Kantor, B., Tagliafierro, L., Gu, J., Zamora, M. E., Ilich, E., Grenier, C., et al. (2018). Downregulation of SNCA expression by targeted editing of DNA methylation: a potential strategy for precision therapy in PD. *Mol. Ther.* 26, 2638–2649. doi: 10.1016/j.ymthe.2018.08.019

Kelton, W. J., Pesch, T., Matile, S., and Reddy, S. T. (2016). Surveying the delivery methods of CRISPR/Cas9 for *ex vivo* mammalian cell engineering. *Chimia* 70, 439–442. doi: 10.2533/chimia.2016.439

Khan, M. M., Zaheer, S., Nehman, J., and Zaheer, A. (2014). Suppression of glia maturation factor expression prevents 1-methyl-4-phenylpyridinium (MPP^+)-induced loss of mesencephalic dopaminergic neurons. *Neuroscience* 277, 196–205. doi: 10.1016/j.neuroscience.2014.07.003

Lee, C. C., MacKay, J. A., Frechet, J. M., and Szoka, F. C. (2005). Designing dendrimers for biological applications. *Nat. Biotechnol.* 23, 1517–1526. doi: 10.1038/nbt1171

Liang, X., Potter, J., Kumar, S., Zou, Y., Quintanilla, R., Sridharan, M., et al. (2015). Rapid and highly efficient mammalian cell engineering *via* Cas9 protein transfection. *J. Biotechnol.* 208, 44–53. doi: 10.1016/j.jbiotec.2015.04.024

Lin, S., Staahl, B. T., Alla, R. K., and Doudna, J. A. (2014). Enhanced homology-directed human genome engineering by controlled timing of CRISPR/Cas9 delivery. *Elife* 3:e04766. doi: 10.7554/eLife.04766

Long, C., Amoasii, L., Mireault, A. A., McAnally, J. R., Li, H., Sanchez-Ortiz, E., et al. (2016). Postnatal genome editing partially restores dystrophin expression in a mouse model of muscular dystrophy. *Science* 351, 400–403. doi: 10.1126/science.aad5725

Lou, G., Chen, Z., Zheng, M., and Liu, Y. (2017). Mesenchymal stem cell-derived exosomes as a new therapeutic strategy for liver diseases. *Exp. Mol. Med.* 49:e346. doi: 10.1038/emm.2017.63

Mandal, P. K., Ferreira, L. M. R., Collins, R., Meissner, T. B., Boutwell, C. L., Friesen, M., et al. (2014). Efficient ablation of genes in human hematopoietic stem and effector cells using CRISPR/Cas9. *Cell Stem Cell* 15, 643–652. doi: 10.1016/j.stem.2014.10.004

Mazzio, E. A., Reams, R. R., and Soliman, K. F. (2004). The role of oxidative stress, impaired glycolysis and mitochondrial respiratory redox failure in the cytotoxic effects of 6-hydroxydopamine *in vitro*. *Brain Res.* 1004, 29–44. doi: 10.1016/j.brainres.2003.12.034

Moreno-Mateos, M. A., Vejnar, C. E., Beaudoin, J.-D., Fernandez, J. P., Mis, E. K., Khokha, M. K., et al. (2015). CRISPRscan: designing highly efficient sgRNAs for CRISPR-Cas9 targeting *in vivo*. *Nat. Methods* 12, 982–988. doi: 10.1038/nmeth.3543

Morita, S., Noguchi, H., Horii, T., Nakabayashi, K., Kimura, M., Okamura, K., et al. (2016). Targeted DNA demethylation *in vivo* using dCas9-peptide repeat and scFv-TET1 catalytic domain fusions. *Nat. Biotechnol.* 34, 1060–1065. doi: 10.1038/nbt.3658

Mullan, M., Crawford, F., Axelman, K., Houlden, H., Lilius, L., Winblad, B., et al. (1992). A pathogenic mutation for probable Alzheimer's disease in the APP gene at the N-terminus of β-amyloid. *Nat. Genet.* 1, 345–347. doi: 10.1038/ng0892-345

Murlidharan, G., Sakamoto, K., Rao, L., Corriher, T., Wang, D., Gao, G., et al. (2016). CNS-restricted transduction and CRISPR/Cas9-mediated gene deletion with an engineered AAV Vector. *Mol. Ther. Nucleic Acids* 5:e338. doi: 10.1038/mtna.2016.49

Naidoo, J., Stanek, L. M., Ohno, K., Trewman, S., Samaranch, L., Hadaczek, P., et al. (2018). Extensive transduction and enhanced spread of a modified AAV2 capsid in the non-human primate CNS. *Mol. Ther.* 26, 2418–2430. doi: 10.1016/j.ymthe.2018.07.008

Narbute, K., Piļipenko, V., Pupure, J., Dzirkale, Z., Jonaviče, U., Tunaitis, V., et al. (2019). Intranasal administration of extracellular vesicles derived from human teeth stem cells improve motor symptoms and normalize tyrosine hydroxylase expression in the substantia nigra and striatum of the 6-hydroxydopamine-treated rats. *Stem Cell Transl. Med.* 8, 490–499. doi: 10.1002/sctm.18-0162

Nelson, C. E., Hakim, C. H., Ousterout, D. G., Thakore, P. I., Moreb, E. A., Castellanos Rivera, R. M., et al. (2016). *In vivo* genome editing improves muscle function in a mouse model of Duchenne muscular dystrophy. *Science* 351, 403–407. doi: 10.1126/science.aad5143

Nishida, K., Arazoe, T., Yachie, N., Banno, S., Kakimoto, M., Tabata, M., et al. (2016). Targeted nucleotide editing using hybrid prokaryotic and vertebrate adaptive immune systems. *Science* 353:aaf8729. doi: 10.1126/science.aaf8729

Niu, Y., Shen, B., Cui, Y., Chen, Y., Wang, J., Wang, L., et al. (2014). Generation of gene-modified cynomolgus monkey *via* Cas9/RNA-mediated gene targeting in one-cell embryos. *Cell* 156, 836–843. doi: 10.1016/j.cell.2014.01.027

Ortiz-Virumbrales, M., Moreno, C. L., Kruglikov, I., Marazuela, P., Sproul, A., Jacob, S., et al. (2017). CRISPR/Cas9-Correctable mutation-related molecular and physiological phenotypes in iPSC-derived Alzheimer's PSEN2 (N141I) neurons. *Acta Neuropathol. Commun.* 5:77. doi: 10.1186/s40478-017-0475-z

Osborn, M. J., Webber, B. R., Knipping, F., Lonetree, C. L., Tennis, N., DeFeo, A. P., et al. (2016). Evaluation of TCR gene editing achieved by TALENs, CRISPR/Cas9, and megaTAL nucleases. *Mol. Ther.* 24, 570–581. doi: 10.1038/mt.2015.197

Palfi, S., Gurruchaga, J. M., Ralph, G. S., Lepetit, H., Lavisse, S., Buttery, P. C., et al. (2014). Long-term safety and tolerability of ProSavin, a lentiviral vector-based gene therapy for Parkinson's disease: a dose escalation, open-label, phase 1/2 trial. *Lancet* 383, 1138–1146. doi: 10.1016/S0140-6736(13)61939-X

Pardridge, W. M. (2005). The blood-brain barrier: bottleneck in brain drug development. *NeuroRx* 2, 3–14. doi: 10.1007/bf03206638

Park, H., Oh, J., Shim, G., Cho, B., Chang, Y., Kim, S., et al. (2019). *In vivo* neuronal gene editing *via* CRISPR-Cas9 amphiphilic nanocomplexes alleviates deficits in mouse models of Alzheimer's disease. *Nat. Neurosci.* 22, 524–528. doi: 10.1038/s41593-019-0352-0

Petros, R. A., and DeSimone, J. M. (2010). Strategies in the design of nanoparticles for therapeutic applications. *Nat. Rev. Drug Discov.* 9, 615–627. doi: 10.1038/nrd2591

Phinney, D. G., and Pittenger, M. F. (2017). Concise review: MSC-derived exosomes for cell-free therapy. *Stem Cells* 35, 851–858. doi: 10.1002/stem.2575

Pillay, S., Meyer, N. L., Puschnik, A. S., Davulcu, O., Diep, J., Ishikawa, Y., et al. (2016). An essential receptor for adeno-associated virus infection. *Nature* 530, 108–112. doi: 10.1038/nature16465

Raikwar, S. P., Thangavel, R., Dubova, I., Selvakumar, G. P., Ahmed, M. E., Kempuraj, D., et al. (2019). targeted gene editing of glia maturation factor in microglia: a novel Alzheimer's disease therapeutic target. *Mol. Neurobiol.* 56, 378–393. doi: 10.1007/s12035-018-1068-y

Ran, F. A., Hsu, P. D., Lin, C.-Y., Gootenberg, J. S., Konermann, S., Trevino, A. E., et al. (2013). Double nicking by RNA-guided CRISPR Cas9 for enhanced genome editing specificity. *Cell* 154, 1380–1389. doi: 10.1016/j.cell.2013.08.021

Rohn, T. T., Kim, N., Isho, N. F., and Mack, J. M. (2018). The potential of CRISPR/Cas9 gene editing as a treatment strategy for Alzheimer's disease. *J. Alzheimers Dis. Parkinsonism* 8:439. doi: 10.4172/2161-0460.1000439

Rong, Z., Zhu, S., Xu, Y., and Fu, X. (2014). Homologous recombination in human embryonic stem cells using CRISPR/Cas9 nickase and a long DNA donor template. *Protein Cell* 5, 258–260. doi: 10.1007/s13238-014-0032-5

Sakuma, T., Nishikawa, A., Kume, S., Chayama, K., and Yamamoto, T. (2014). Multiplex genome engineering in human cells using all-in-one CRISPR/Cas9 vector system. *Sci. Rep.* 4:5400. doi: 10.1038/srep05400

Sanjana, N. E., Shalem, O., and Zhang, F. (2014). Improved vectors and genome-wide libraries for CRISPR screening. *Nat. Methods* 11, 783–784. doi: 10.1038/nmeth.3047

Sarko, D. K., and McKinney, C. E. (2017). Exosomes: origins and therapeutic potential for neurodegenerative disease. *Front. Neurosci.* 11:82. doi: 10.3389/fnins.2017.00082

Sather, B. D., Romano Ibarra, G. S., Sommer, K., Curinga, G., Hale, M., Khan, I. F., et al. (2015). Efficient modification of CCR5 in primary human hematopoietic cells using a megaTAL nuclease and AAV donor template. *Sci. Transl. Med.* 7:307ra156. doi: 10.1126/scitranslmed.aac5530

Savell, K. E., and Day, J. J. (2017). Applications of CRISPR/Cas9 in the mammalian central nervous system. *Yale J. Biol. Med.* 90, 567–581.

Schumann, K., Lin, S., Boyer, E., Simeonov, D. R., Subramaniam, M., Gate, R. E., et al. (2015). Generation of knock-in primary human T cells using Cas9 ribonucleoproteins. *Proc. Natl. Acad. Sci. U S A* 112, 10437–10442. doi: 10.1073/pnas.1512503112

Senís, E., Fatouros, C., Große, S., Wiedtke, E., Niopek, D., Mueller, A. K., et al. (2014). CRISPR/Cas9-mediated genome engineering: an adeno-associated viral (AAV) vector toolbox. *Biotechnol. J.* 9, 1402–1412. doi: 10.1002/biot.201400046

Shi, N. Q., Qi, X. R., Xiang, B., and Zhang, Y. (2014). A survey on "Trojan Horse" peptides: opportunities, issues and controlled entry to "Troy". *J. Control. Release* 194, 53–70. doi: 10.1016/j.jconrel.2014.08.014

Shlosberg, D., Benifla, M., Kaufer, D., and Friedman, A. (2010). Blood-brain barrier breakdown as a therapeutic target in traumatic brain injury. *Nat. Rev. Neurol.* 6, 393–403. doi: 10.1038/nrneurol.2010.74

Sims, B., Gu, L., Krendelchtchikov, A., and Matthews, Q. L. (2014). Neural stem cell-derived exosomes mediate viral entry. *Int. J. Nanomedicine* 9, 4893–4897. doi: 10.2147/ijn.s70999

Spittau, B. (2017). Aging microglia-phenotypes, functions and implications for age-related neurodegenerative diseases. *Front Aging Neurosci* 9:194. doi: 10.3389/fnagi.2017.00194

Stefanis, L. (2012). α-synuclein in Parkinson's disease. *Cold Spring Harb. Perspect. Med.* 2:a009399. doi: 10.1101/cshperspect.a009399

Sun, J., Carlson-Stevermer, J., Das, U., Shen, M., Delenclos, M., Snead, A. M., et al. (2018). A CRISPR/Cas9 based strategy to manipulate the Alzheimer's amyloid pathway. *bioRxiv*. doi: 10.1101/310193

Suzuki, K., Tsunekawa, Y., Hernandez-Benitez, R., Wu, J., Zhu, J., Kim, E. J., et al. (2016). *In vivo* genome editing *via* CRISPR/Cas9 mediated homology-independent targeted integration. *Nature* 540, 144–149. doi: 10.1038/nature20565

Swiech, L., Heidenreich, M., Banerjee, A., Habib, N., Li, Y., Trombetta, J., et al. (2015). *In vivo* interrogation of gene function in the mammalian brain using CRISPR-Cas9. *Nat. Biotechnol.* 33, 102–106. doi: 10.1038/nbt.3055

Torchilin, V. P. (2014). Multifunctional, stimuli-sensitive nanoparticulate systems for drug delivery. *Nat. Rev. Drug Discov.* 13, 813–827. doi: 10.1038/nrd4333

Tothova, Z., Krill-Burger, J. M., Popova, K. D., Landers, C. C., Sievers, Q. L., Yudovich, D., et al. (2017). Multiplex CRISPR/Cas9-based genome editing in human hematopoietic stem cells models clonal hematopoiesis and myeloid neoplasia. *Cell Stem Cell* 21, 547.e8–555.e8. doi: 10.1016/j.stem.2017.07.015

Trenkmann, M. (2018). Gold rush to gene-editing in the brain. *Nat. Rev. Genet.* 19, 532–533. doi: 10.1038/s41576-018-0038-6

Veres, A., Gosis, B. S., Ding, Q., Collins, R., Ragavendran, A., Brand, H., et al. (2014). Low incidence of off-target mutations in individual CRISPR-Cas9 and TALEN targeted human stem cell clones detected by whole-genome sequencing. *Cell Stem Cell* 15, 27–30. doi: 10.1016/j.stem.2014.04.020

Verkhratsky, A., Matteoli, M., Parpura, V., Mothet, J. P., and Zorec, R. (2016). Astrocytes as secretory cells of the central nervous system: idiosyncrasies of vesicular secretion. *EMBO J.* 35, 239–257. doi: 10.15252/embj.201592705

Vezzani, A. (2007). The promise of gene therapy for the treatment of epilepsy. *Expert Rev. Neurother.* 7, 1685–1692. doi: 10.1586/14737175.7.12.1685

Voigt, N., Henrich-Noack, P., Kockentiedt, S., Hintz, W., Tomas, J., and Sabel, B. A. (2014). Surfactants, not size or zeta-potential influence blood-brain barrier passage of polymeric nanoparticles. *Eur. J. Pharm. Biopharm.* 87, 19–29. doi: 10.1016/j.ejpb.2014.02.013

Wang, Y., Cella, M., Mallinson, K., Ulrich, J. D., Young, K. L., Robinette, M. L., et al. (2015). TREM2 lipid sensing sustains the microglial response in an Alzheimer's disease model. *Cell* 160, 1061–1071. doi: 10.1016/j.cell.2015.01.049

Wang, T., Wei, J. J., Sabatini, D. M., and Lander, E. S. (2014). Genetic screens in human cells using the CRISPR-Cas9 system. *Science* 343, 80–84. doi: 10.1126/science.1246981

Wang, H., Yang, H., Shivalila, C. S., Dawlaty, M. M., Cheng, A. W., Zhang, F., et al. (2013). One-step generation of mice carrying mutations in multiple genes by CRISPR/Cas-mediated genome engineering. *Cell* 153, 910–918. doi: 10.1016/j.cell.2013.04.025

Wang, M., Zuris, J. A., Meng, F., Rees, H., Sun, S., Deng, P., et al. (2016). Efficient delivery of genome-editing proteins using bioreducible lipid nanoparticles. *Proc. Natl. Acad. Sci. U S A* 113, 2868–2873. doi: 10.1073/pnas.1520244113

Weintraub, D., Koester, J., Potenza, M. N., Siderowf, A. D., Stacy, M., Voon, V., et al. (2010). Impulse control disorders in Parkinson disease: a cross-sectional study of 3090 patients. *Arch. Neurol.* 67, 589–595. doi: 10.1001/archneurol.2010.65

Wood, H. (2017). Alzheimer disease: twin peaks of microglial activation observed in Alzheimer disease. *Nat. Rev. Neurol.* 13:129. doi: 10.1038/nrneurol.2017.19

Wright, A. V., Sternberg, S. H., Taylor, D. W., Staahl, B. T., Bardales, J. A., Kornfeld, J. E., et al. (2015). Rational design of a split-Cas9 enzyme complex. *Proc. Natl. Acad. Sci. U S A* 112, 2984–2989. doi: 10.1073/pnas.1501698112

Xu, H., Xiao, T., Chen, C. H., Li, W., Meyer, C. A., Wu, Q., et al. (2015). Sequence determinants of improved CRISPR sgRNA design. *Genome Res.* 25, 1147–1157. doi: 10.1101/gr.191452.115

Yanagida, K., Liu, C. H., Faraco, G., Galvani, S., Smith, H. K., Burg, N., et al. (2017). Size-selective opening of the blood-brain barrier by targeting endotelial sphingosine 1-phosphate receptor 1. *Proc. Natl. Acad. Sci. U S A* 114, 4531–4536. doi: 10.1073/pnas.1618659114

Yiannopoulou, K. G., and Papageorgiou, S. G. (2013). Current and future treatments for Alzheimer's disease. *Ther. Adv. Neurol. Disord.* 6, 19–33. doi: 10.1177/1756285612461679

Zafar, F., Valappil, R. A., Kim, S., Johansen, K. K., Chang, A. L. S., Tetrud, J. W., et al. (2018). Genetic fine-mapping of the Iowan SNCA gene triplication in a patient with Parkinson's disease. *NPJ Parkinsons Dis.* 4:18. doi: 10.1038/s41531-018-0054-4

Zetsche, B., Volz, S. E., and Zhang, F. (2015). A split-Cas9 architecture for inducible genome editing and transcription modulation. *Nat. Biotechnol.* 33, 139–142. doi: 10.1038/nbt.3149

Zheng, Y., Shen, W., Zhang, J., Yang, B., Liu, Y. N., Qi, H., et al. (2018). CRISPR interference-based specific and efficient gene inactivation in the brain. *Nat. Neurosci.* 21, 447–454. doi: 10.1038/s41593-018-0077-5

Zhou, Y., Peng, Z., Seven, E. S., and Leblanc, R. M. (2018). Crossing the blood-brain barrier with nanoparticles. *J. Control. Release* 270, 290–303. doi: 10.1016/j.jconrel.2017.12.015

Conflict of Interest Statement: The authors declare that the research was conducted in the absence of any commercial or financial relationships that could be construed as a potential conflict of interest.

frontiers in Molecular Neuroscience

ORIGINAL RESEARCH
published: 31 July 2019
doi: 10.3389/fnmol.2019.00184

Frizzled-9+ Supporting Cells Are Progenitors for the Generation of Hair Cells in the Postnatal Mouse Cochlea

Shasha Zhang[1,2], Dingding Liu[3], Ying Dong[1], Zhong Zhang[1], Yuan Zhang[1], Han Zhou[3], Lingna Guo[1], Jieyu Qi[1], Ruiying Qiang[1], Mingliang Tang[1], Xia Gao[3], Chunjie Zhao[1], Xiaoyun Chen[4], Xiaoyun Qian[3]* and Renjie Chai[1,2,5,6,7]**

[1]Key Laboratory for Developmental Genes and Human Disease, Ministry of Education, Institute of Life Sciences, Southeast University, Nanjing, China, [2]Co-Innovation Center of Neuroregeneration, Nantong University, Nantong, China, [3]Jiangsu Provincial Key Medical Discipline (Laboratory), Department of Otolaryngology—Head and Neck Surgery, Affiliated Drum Tower Hospital of Nanjing University Medical School, Nanjing, China, [4]Department of Otolaryngology—Head and Neck Surgery, First Affiliated Hospital of Wenzhou Medical University, Wenzhou, China, [5]Institute for Stem Cell and Regeneration, Chinese Academy of Science, Beijing, China, [6]Jiangsu Province High-Tech Key Laboratory for Bio-Medical Research, Southeast University, Nanjing, China, [7]Beijing Key Laboratory of Neural Regeneration and Repair, Capital Medical University, Beijing, China

OPEN ACCESS

Edited by:
Daniel F. Gilbert,
University of Erlangen Nuremberg, Germany

Reviewed by:
Bernd Fritzsch,
The University of Iowa, United States
Guy Peel Richardson,
University of Sussex, United Kingdom

***Correspondence:**
Xiaoyun Chen
chenxiaoyun2816@163.com
Xiaoyun Qian
qxy522@163.com
Renjie Chai
renjiec@seu.edu.cn

Received: 01 April 2019
Accepted: 12 July 2019
Published: 31 July 2019

Citation:
Zhang S, Liu D, Dong Y, Zhang Z, Zhang Y, Zhou H, Guo L, Qi J, Qiang R, Tang M, Gao X, Zhao C, Chen X, Qian X and Chai R (2019) Frizzled-9+ Supporting Cells Are Progenitors for the Generation of Hair Cells in the Postnatal Mouse Cochlea. Front. Mol. Neurosci. 12:184. doi: 10.3389/fnmol.2019.00184

Lgr5+ cochlear supporting cells (SCs) have been reported to be hair cell (HC) progenitor cells that have the ability to regenerate HCs in the neonatal mouse cochlea, and these cells are regulated by Wnt signaling. Frizzled-9 (Fzd9), one of the Wnt receptors, has been reported to be used to mark neuronal stem cells in the brain together with other markers and mesenchymal stem cells from human placenta and bone marrow. Here we used Fzd9-CreER mice to lineage label and trace Fzd9+ cells in the postnatal cochlea in order to investigate the progenitor characteristic of Fzd9+ cells. Lineage labeling showed that inner phalangeal cells (IPhCs), inner border cells (IBCs), and third-row Deiters' cells (DCs) were Fzd9+ cells, but not inner pillar cells (IPCs) or greater epithelial ridge (GER) cells at postnatal day (P)3, which suggests that Fzd9+ cells are a much smaller cell population than Lgr5+ progenitors. The expression of Fzd9 progressively decreased and was too low to allow lineage tracing after P14. Lineage tracing for 6 days *in vivo* showed that Fzd9+ cells could also generate similar numbers of new HCs compared to Lgr5+ progenitors. A sphere-forming assay showed that Fzd9+ cells could form spheres after sorting by flow cytometry, and when we compared the isolated Fzd9+ cells and Lgr5+ progenitors there were no significant differences in sphere number or sphere diameter. In a differentiation assay, the same number of Fzd9+ cells could produce similar amounts of Myo7a+ cells compared to Lgr5+ progenitors after 10 days of differentiation. All these data suggest that the Fzd9+ cells have a similar capacity for proliferation, differentiation, and HC generation as Lgr5+ progenitors and that Fzd9 can be used as a more restricted marker of HC progenitors.

Keywords: Frizzled-9 (Fzd9), cochlea, hair cell progenitor, hair cell generation, self-renew

INTRODUCTION

Sensorineural hearing loss is mainly caused by hair cell (HC) loss and is one of the most common health problems around the world. HC loss is irreversible in adult mammals, whereas HCs can be regenerated from supporting cells (SCs) in the inner ear of birds and fish (Rubel et al., 2013). Recent studies have shown that HCs can also be regenerated in newborn mice (Chai et al., 2012; Shi et al., 2012; Bramhall et al., 2014; Wang et al., 2015; Li et al., 2016; You et al., 2018; Zhang et al., 2018). However, this regenerative ability is quickly lost as the mice age (Bermingham-McDonogh and Reh, 2011; Chai et al., 2012; Shi et al., 2012; Bramhall et al., 2014; Cox et al., 2014).

Several signaling pathways have been reported to play important roles in HC regeneration. The up-regulation of canonical Wnt signaling induces the proliferation of sensory precursors in the postnatal mouse cochlea (Chai et al., 2012; Shi et al., 2012; Ni et al., 2016; Waqas et al., 2016b; Wu et al., 2016; Lu et al., 2017), while Notch inhibition induces mitotically generated HCs in the mammalian cochlea *via* activation of the Wnt pathway (Li et al., 2015; Ni et al., 2016; Waqas et al., 2016b; Wu et al., 2016). Previously, *Lgr5*, a Wnt target gene, has been reported to mark the progenitors of the inner ear, and Lgr5+ progenitors have the ability to regenerate HCs in the neonatal mouse cochlea (Chai et al., 2011, 2012; Shi et al., 2012; Waqas et al., 2016a; Zhang et al., 2017). Lgr5 is expressed in third-row Deiters' cells (DCs), inner pillar cells (IPCs), inner phalangeal cells (IPhCs), and part of the lateral greater epithelial ridge (GER) cells, which is a large cell population and contains many different cell types (Chai et al., 2011, 2012; Shi et al., 2012).

Wnt signaling plays important roles in regulating HC progenitors and HC regeneration (Chai et al., 2012; Li et al., 2015; Liu et al., 2016; Ni et al., 2016; Waqas et al., 2016b; Lu et al., 2017). There are 10 Frizzled (Fzd) receptors (Fzd1-10), which are unconventional G-protein coupled receptors. Fzds contain a conserved cysteine-rich domain to which Wnt ligands bind with high affinity (MacDonald and He, 2012; Dijksterhuis et al., 2014).

Frizzled-9 (Fzd9) plays crucial roles in brain development, neuromuscular junction assembly, new bone formation, and tumor suppression (Winn et al., 2005; Zhao et al., 2005; Albers et al., 2011; Avasarala et al., 2013b; Heilmann et al., 2013; Aviles et al., 2014; Ramírez et al., 2016). In the brain, Fzd9 is selectively expressed in both the developing and adult hippocampus and is used to mark neural stem cells together with other markers (Van Raay et al., 2001; Zhao and Pleasure, 2004, 2005; Pollard et al., 2008; Trubiani et al., 2010; Zhou et al., 2010; Pedersen et al., 2012; Tian et al., 2012). In human bone marrow and chorionic placenta-derived mesenchymal stem cells, Fzd9 is also expressed on the cell surface and is used as a marker to isolate these cells (Battula et al., 2007, 2008; Buhring et al., 2007; Trubiani et al., 2010; Tran et al., 2011). Thus, we speculated that Fzd9 might also be expressed in the HC progenitors of the cochlea and thus might also be used as a HC progenitor marker in the inner ear.

Here, we used Fzd9-CreER/Rosa26-tdTomato mice to lineage trace the Fzd9+ cells in the postnatal cochlea and to investigate their HC generation ability compared to the Lgr5+ progenitors. Lineage tracing data showed that Fzd9 was expressed in IPhCs, inner border cells (IBCs), and the third-row DCs, but not in IPCs or GER cells at postnatal day (P) 3. Lineage tracing data showed that, similar to Lgr5+ progenitors, Fzd9+ cells also had HC generation ability after 6 days of lineage tracing *in vivo*. When isolated by flow cytometry and then cultured *in vitro*, Fzd9+ cells and Lgr5+ progenitors could form similar numbers of spheres in an *in vitro* sphere-forming assay. In a differentiation assay, the same number of Fzd9+ cells could generate a similar amount of HCs compared to Lgr5+ progenitors after 10 days of differentiation. Our work provides a new marker for HC progenitors and expands our knowledge of progenitor cell types in the inner ear.

MATERIALS AND METHODS

Animals

Lgr5-EGFP-IRES-creERT2 mice (Stock #008875, Jackson Laboratory) and Rosa26-tdTomato reporter mice (Stock #007914, Jackson Laboratory) of both sexes were used in the experiments (Madisen et al., 2010). The Fzd9-CreER mice were a gift from Prof Chunjie Zhao from Southeast University (Zhou et al., 2010). We performed all animal procedures according to protocols that were approved by the Animal Care and Use Committee of Southeast University and that were consistent with the National Institute of Health's Guide for the Care and Use of Laboratory Animals. We made all efforts to minimize the number of animals used and to prevent their suffering.

Genotyping PCR

Transgenic mice were genotyped using genomic DNA from tail tips by adding 180 μl 50 mM NaOH, incubating at 98°C for 1 h, and adding 20 μl 1 M Tris-HCl pH 7.0. The genotyping primers were as follows: *Lgr5*: (F) 5′-CTG CTC TCT GCT CCC AGT CT-3′; wild-type (R) 5′-ATA CCC CAT CCC TTT TGA GC-3′; mutant (R) 5′-GAA CTT CAG GGT CAG CTT GC-3′. *tdTomato*: wild-type (F) 5′-AAG GGA GCT GCA GTG GAG T-3′; wild-type (R) 5′-CCG AAA ATC TGT GGG AAG TC-3′; mutant (F) 5′-GGC ATT AAA GCA GCG TAT C-3′; mutant (R) 5′-CTG TTC CTG TAC GGC ATG G-3′. *Fzd9*: (F) 5′-CAT ACC TGG AAA ATG CTT CTG TCC-3′; (R) 5′-ATT GCT GTC ACT TGG TCG TGG C-3′.

In vivo Labeling and Lineage Tracing of Fzd9+ Cells in the Cochlea

$Fzd9^{CreER/+}$ mice and Lgr5-$EGFP^{CreER/+}$ mice were crossed with Rosa26-tdTomato mice separately to label and lineage trace Fzd9+ and Lgr5+ cells in the cochlea. To activate cre, $Fzd9^{CreER/+}$Rosa26-tdTomato and Lgr5-$EGFP^{CreER/+}$Rosa26-tdTomato double-positive mice were intraperitoneally (I.P.) injected with tamoxifen (4 mg/25 g body weight, Sigma) at P3, P7, or P14. Mice were killed at different time points, and the cochleae were examined.

Immunostaining and Image Acquisition

Cochleae were fixed in 4% (w/v) paraformaldehyde for 24 h at room temperature and washed with PBS, and the cochleae

from P7 and older mice were decalcified with 0.5 M EDTA for 1–3 days. The cochleae were then washed with PBS, dissected in HBSS, and blocked with blocking solution [5% (v/v) donkey serum, 0.5% (v/v) Triton X-100, 0.02% (w/v) sodium azide, and 1% (v/v) bovine serum albumin in PBS (pH 7.4)] for 1 h at room temperature and then incubated with primary antibodies diluted in PBT1 [2.5% (v/v) donkey serum, 0.1% (v/v) Triton X-100, 0.02% (w/v) sodium azide, and 1% (v/v) bovine serum albumin in PBS (pH 7.4)] at 4°C overnight. The cochleae were then washed with 0.1% (v/v) Triton X-100 in PBS (pH 7.4) three times and incubated with fluorescence-conjugated secondary antibody (Invitrogen), both diluted 1:400 in PBT2 [0.1% (v/v) Triton X-100 and 1% (v/v) bovine serum albumin in PBS (pH 7.4)] for 1 h at room temperature. The cochleae were mounted in anti-fade fluorescence mounting medium (DAKO) after washing three times with 0.1% (v/v) Triton X-100 in PBS (pH 7.4). The primary antibodies were anti-Myosin7a (Proteus Bioscience, #25-6790, 1:1,000 dilution in PBT1) and anti-Sox2 (Santa Cruz Biotechnology, #17320, 1:400 dilution in PBT1). A Zeiss LSM 710 confocal microscope was used to obtain the fluorescence images.

Cryosections

Isolated cochleae were fixed in 4% (w/v) paraformaldehyde in PBS (pH 7.4) at room temperature for 4 h. Decalcification with 0.5 M EDTA was performed for cochleae from P7 and older mice. For cryosectioning, tissues were equilibrated with a series of ascending concentrations of sucrose [10%–30% (w/v) in PBS] and then treated serially with a mixture of sucrose and optimum cutting temperature (OCT) compound (Sakura Finetek; 1:1, 3:7, 9:1, then 0:1) in a vacuum chamber for 1 h at room temperature. Tissues were then sectioned (10 μm thick) and processed for immunostaining.

Sphere-Forming Assay and Differentiation Assay

$Fzd9^{CreER/+}$Rosa26-tdTomato mice were I.P. injected with tamoxifen (4 mg/25 g body weight, Sigma) at P3 and killed at P5, and the cochleae were dissected and digested with trypsin into single cells for FAC sorting of Fzd9+ cells. The cochleae of P5 Lgr5-$EGFP^{CreER/+}$ mice were also dissected and digested with trypsin into single cells for FAC sorting of Lgr5+ cells. For FAC sorting, we used 2 or 3 litters of P5 mice (usually 15–30 mice) to sort the Lgr5+ and Fzd9+ cells (**Supplementary Table S1**). The sorted Fzd9+ and Lgr5+ cells were cultured in DMEM/F12 medium supplemented with N2 (1:100 dilution, Invitrogen), B27 (1:50 dilution, Invitrogen), heparin sulfate (50 ng/ml, Sigma), and the growth factors bFGF (10 ng/ml, Sigma), EGF (20 ng/ml, Sigma), and IGF-1 (50 ng/ml, Sigma). For the sphere-forming assay, the cells were cultured at a density of 2 cells/μl (200 cells per well) in Costar ultra-low attachment dishes for 5 days. Sphere number and the mean diameter of all the spheres in each well were quantified at the end of the culture. For the differentiation assay, cells were cultured at a density of 20 cells/μl (2,000 cells per well) in a 4-well dish for 10 days. EdU (10 μM, Invitrogen) was added to the culture medium from day 4 to day 7 to label proliferating cells. Immunofluorescence staining was performed at the end of the culture to quantify Myo7a+ and EdU+ cells. The Click-it EdU imaging kit (Invitrogen) was used after blocking to label proliferating cells. Consistent with previous reports (Chai et al., 2012), cell cluster with more than five cells was identified as a sphere or colony. The Myo7a+ cells inside of the colony were considered mitotically generated Myo7a+ cells, while the Myo7a+ cells outside of the colony were considered to be directly differentiated Myo7a+ cells.

RNA Extraction and RT- PCR

Approximately 20 cochleae from wild-type mice at different ages were used to extract total RNA with Trizol (Thermo). RNA was reverse transcribed into cDNA, and RT-PCR was used to quantify the gene expression levels with *β-actin* as the reference endogenous gene. The primers were as follows: *β-actin*: (F) 5′-ACG GCC AGG TCA TCA CTA TTG-3′; (R) 5′-AGG GGC CGG ACT CAT CGT A-3′; *Fzd9*: (F) 5′-CGC ACG CAC TCT GTA TGG AG-3′; (R) 5′-GCC GAG ACC AGA ACA CCT C-3′.

Statistical Analysis

For each experimental condition, at least three independent experiments were performed. Data were analyzed with GraphPad Prism6 software and presented as means ± standard errors of the means. Two-way ANOVA was used to determine the statistical significance, and a value of $p < 0.05$ was considered statistically significant. Error bars and *n* values are defined in the respective figures and legends.

RESULTS

Lineage Labeling of Fzd9+ Cells in the Neonatal Cochlea From Fzd9-CreER/Rosa26-tdTomato Mice

We used Fzd9-CreER/Rosa26-tdTomato double-positive mice to lineage label the Fzd9+ cells. Tamoxifen was I.P. injected into P3 Fzd9-CreER/Rosa26-tdTomato double-positive mice to activate cre, and thus Fzd9+ cells were labeled by tdTomato fluorescence after 48 h (**Figure 1A**). tdTomato-labeled Fzd9+ cells were observed from the apex to the base in the cochlea (**Figure 1B**), and tdTomato-labeled Fzd9+ cells were found in the SC layer (**Figures 1C,D**), including the IPhCs and IBCs and to a lesser extent the third-row DCs as shown by the high-resolution images (**Figures 1E,F**, **Supplementary Figure S2**). The cryosections showed the same results (**Figure 1G**). We also compared the lineage labeling of Lgr5+ and Fzd9+ cells in the neonatal mouse cochlea (**Figure 1H**). Lgr5+ cells have been reported to include the IPCs, IBCs, the third-row DCs, and part of the GER cells (Chai et al., 2011, 2012; Shi et al., 2012), while tdTomato-labeled Fzd9+ cells included the IPhCs, IBCs, and the third-row DCs, but did not include IPCs or GER cells. The cell types and number of Fzd9+ cells were much lower than Lgr5+ progenitors, which suggests that Fzd9+ cells might be a subset of HC progenitors.

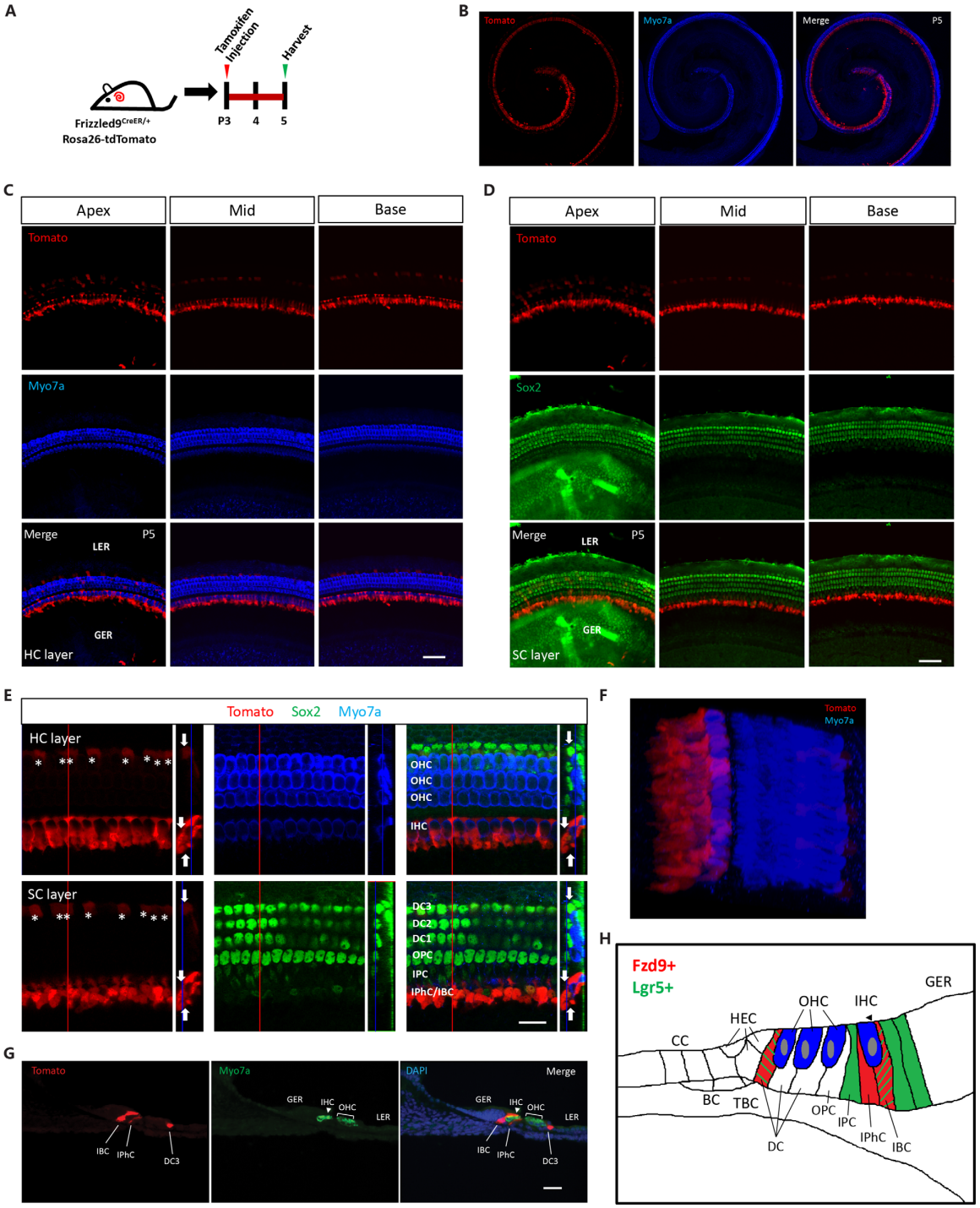

FIGURE 1 | The expression of Fzd9 in the neonatal mouse cochlea. **(A)** Tamoxifen was I.P. injected into P3 Fzd9-CreER/Rosa26-tdTomato mice to activate cre, and the cochleae were dissected 48 h later to identify the tdTomato expression pattern, which indicates Fzd9 expression. **(B–G)** Fzd9 expression was shown by tdTomato. The low-magnification images **(B)** showed that Fzd9 is expressed in the cochlea. The HC layer **(C)** and SC layer **(D)** showed that Fzd9 is expressed in the SCs, but not in the HCs. The high-magnification figures showed that Fzd9 is expressed in IPhCs, IBCs, and the third-row DCs (indicated by white *; **E**). The large square images are single XY slices, the vertical red line shows the position of the orthogonal slice that is shown to the right of each panel, and the blue line on the orthogonal slice shows the level of the XY slice to the left. Orthogonal projections of tdTomato+ cells are indicated by white arrows. A three-dimensional reconstruction of Fzd9 expression is shown in **(F)**. The cryosections also showed the same Fzd9 expression pattern **(G)**. Myo7a was used as the HC marker and Sox2 was used as the SC marker. Scale bar, 50 μm in **(C,D,G)** and 20 μm in **(E)**. **(H)** Schematic of Fzd9 expression in the neonatal mouse cochlea. HC, hair cell; SC, supporting cell; IHC, inner hair cell; OHC, outer hair cell; DC, Deiters' cell; OPC, outer pillar cell; IPC, inner pillar cell; IPhC, inner phalangeal cell; IBC, inner border cell; GER, the lateral greater epithelial ridge; LER, lesser epithelial ridge; TBC, tympanic border cells; CC, Claudius cells; HEC, Hensen's cells; BC, Boettcher cells.

The Lineage Labeling Efficiency of Cochlear Fzd9+ Cells Decreased With Age

The expression of Lgr5 decreases as the mice age and is only expressed in the third-row DCs in the adult mouse cochlea (Chai et al., 2011). Thus we speculated that the lineage labeling efficiency of cochlear Fzd9+ cells might also decrease with age, and we examined the lineage labeling efficiency of cochlear Fzd9+ cells at different time points. First, we measured the mRNA level of *Fzd9* by RT-PCR and found that the *Fzd9* mRNA level decreased dramatically with age and that very little *Fzd9* mRNA expression could be detected at P14 (**Figure 2A**). Tamoxifen was I.P. injected into P3, P7, and P14 mice, and the mice were killed 48 h later to examine the lineage labeling efficiency of cochlear Fzd9+ cells (**Figure 2B**). The results showed that consistent with the *Fzd9* mRNA expression level, tdTomato-labeled Fzd9+ cells were dramatically decreased with age, and no tdTomato+ cells could be detected in P14 mice (**Figures 2C,D**).

Fzd9+ Cells Generated Similar Numbers of New HCs Compared to Lgr5+ Progenitors in the Neonatal Mouse Cochlea *in vivo*

Next, we used lineage tracing to determine the HC generation ability of Fzd9+ cells *in vivo*. Tamoxifen was I.P. injected at P3 into Fzd9-CreER/Rosa26-tdTomato and Lgr5-EGFP-CreERT2/Rosa26-tdTomato mice to lineage trace the Fzd9+ and Lgr5+ cells, respectively, and the mice were killed at P9 to detect the newly generated tdTomato+/Myo7a+ HCs (**Figure 3A**). In both Fzd9-CreER/Rosa26-tdTomato and Lgr5-EGFP-CreERT2/Rosa26-tdTomato mice, tdTomato+/Myo7a+ HCs could be found in the apical and middle turns of P9 cochleae (**Figures 3B,C**), and Fzd9+ cells could generate similar numbers of new HCs compared to Lgr5+ progenitors (**Figure 3D**). Cryosection images showed the same results (**Figures 3E,F**). tdTomato-labeled Fzd9+ cells included the IPhCs, IBCs, and third-row DCs, and these Fzd9+ cells could generate similar numbers of new HCs compared to Lgr5+ progenitors, which included more cell types, in neonatal mice cochleae *in vivo*, which suggests that Fzd9+ cells might be HC progenitors.

Flow Cytometry-Isolated Fzd9+ Cells Have Similar Sphere-Forming Ability Compared to Lgr5+ Progenitors *in vitro*

One of the important characteristics of stem cells and progenitor cells is the ability to self-renew. Fzd9+ and Lgr5+ cells were isolated from Fzd9-CreER/Rosa26-tdTomato and Lgr5-EGFP-CreERT2 mice, respectively, by flow cytometry, and the cells were cultured *in vitro* for 5 days to form spheres (**Figure 4A**). The flow cytometry plots showed that the Lgr5+ progenitors were around 2.44% of the whole cochlear cell population, while the Fzd9+ cells were only around 0.63% of the whole cochlear cell population (**Figure 4B**). The sphere-forming assay showed that 200 Fzd9+ cells could form a similar number of spheres compared to 200 Lgr5+ progenitors (**Figures 4C,D**, **Supplementary Figure S3**), and the statistical analysis showed that the diameters of the spheres generated from Fzd9+ cells and Lgr5+ progenitors were almost the same (**Figure 4D** and **Supplementary Table S1**). Together, these results suggested that Fzd9+ cells had almost the same proliferation and sphere-forming ability as Lgr5+ progenitors.

Flow Cytometry-Isolated Fzd9+ Cells Have Similar Differentiation Ability for Generating Myo7a+ Cells Compared to Lgr5+ Progenitors *in vitro*

Next, we examined the differentiation ability of isolated Fzd9+ cells. We isolated the Fzd9+ and Lgr5+ cells, respectively, by flow cytometry and then performed a differentiation assay to culture the cells *in vitro* for 10 days, and EdU was added from day 4 to day 7 to detect the proliferating cells (**Figure 5A**). We found that 2,000 Fzd9+ cells generated similar numbers of Myo7a+ cells compared to 2,000 Lgr5+ progenitors after 10 days of differentiation and that 2,000 Fzd9+ cells also generated similar numbers of Myo7a+/EdU+ cells compared to 2,000 Lgr5+ progenitors (**Figures 5B–D**, **Supplementary Table S1**). Together this suggested that Fzd9+ cells have similar differentiation ability for generating Myo7a+ cells compared to Lgr5+ progenitors.

DISCUSSION

The loss of HCs is the main cause of sensorial hearing loss, and HC regeneration from HC progenitors has become one the most important areas of research in the field of hearing research. Lgr5 has been reported to be a marker of HC progenitors that can regenerate HCs in the neonatal mouse cochlea. However, Lgr5+ cells can be found among many cell types and in different numbers of cells. Here, we show that Fzd9 can be used as a more restricted HC progenitor marker that only marks IPhCs, IBCs, and third-row DCs. We found that Fzd9+ cells can generate HCs in the neonatal mouse cochlea *in vivo* and can form spheres and generate HCs when cultured *in vitro*.

Fzd9, one of the 10 frizzled family proteins, acts as a Wnt receptor and can activate canonical and non-canonical Wnt signaling pathways (Karasawa et al., 2002; Winn et al., 2005; Avasarala et al., 2013a,b; Heilmann et al., 2013; Aviles et al., 2014), and has been reported to interact with Wnt2, Wnt5, Wnt7, and Wnt8 to activate different downstream signaling cascades (Karasawa et al., 2002; Momoi et al., 2003; Winn et al., 2005; Avasarala et al., 2013a,b; Ramírez et al., 2016). Further research is needed to determine which Wnt proteins Fzd9 interacts within the cochlea and whether it activates the canonical or non-canonical pathway. In the brain and 293T cell line, upregulation of Fzd9 leads to the induction of Wnt signaling, while downregulation of Fzd9 inhibits Wnt signaling (Karasawa et al., 2002; Ramírez et al., 2016). In the inner ear, many previous reports, including our own findings, have shown that activation of Wnt signaling significantly promotes the proliferation of Lgr5+ progenitors both *in vitro* and *in vivo* and that inhibition of Wnt signaling significantly decreases the proliferation ability of Lgr5+ cells (Chai et al., 2012; Shi et al., 2012; Li et al., 2015; Ni et al., 2016; Wu et al., 2016). Furthermore, in 3D cultures of Lgr5+ progenitors, activation of Wnt signaling increases the formation of 3D organoids (Lenz et al., 2019). Thus

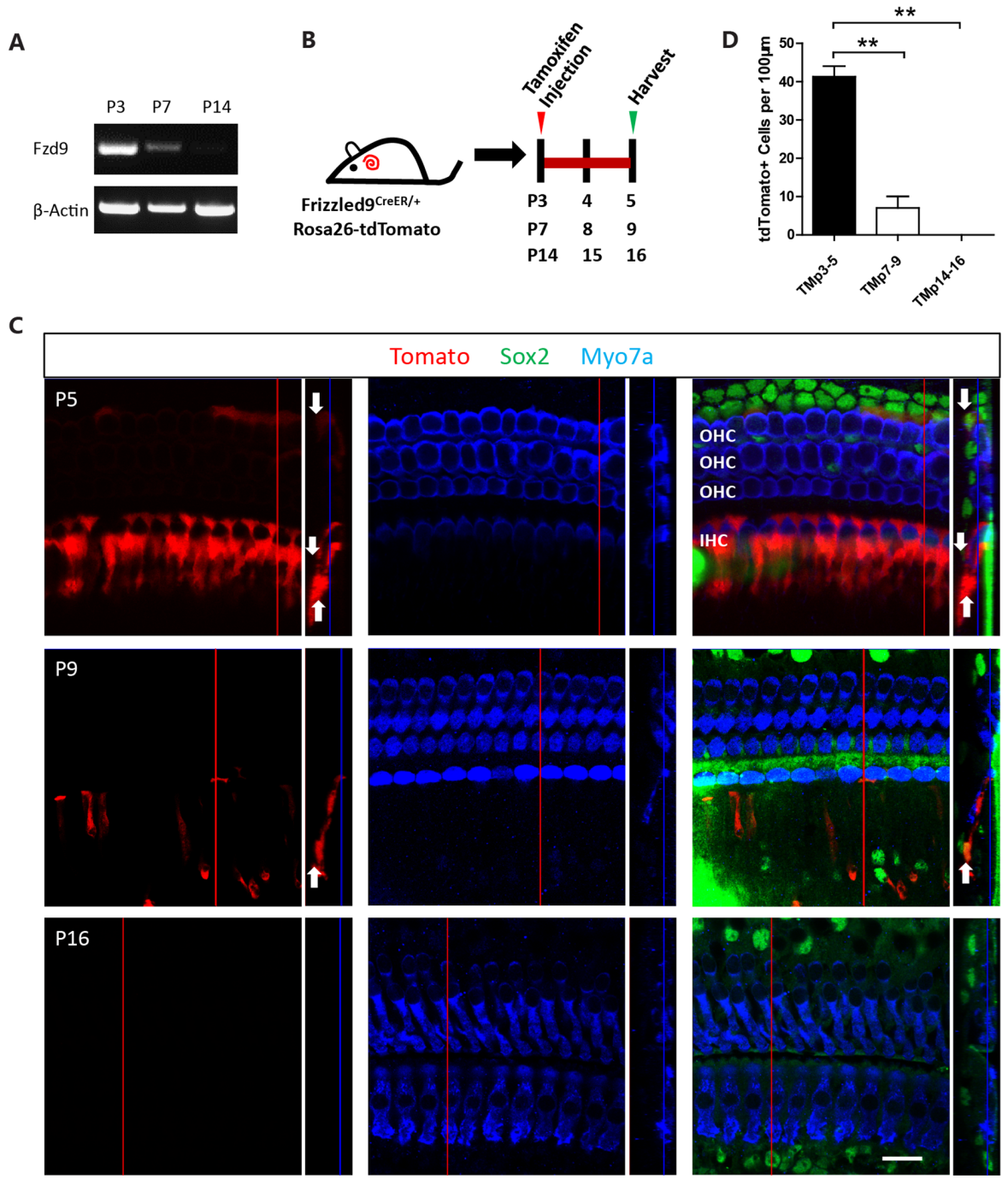

FIGURE 2 | The spatiotemporal expression of Fzd9 in the cochlea at different time points. **(A)** RT-PCR showed *Fzd9* mRNA expression at P3, P7, and P14. *β-actin* was used as the internal control. **(B)** Tamoxifen was I.P. injected into P3, P7, and P14 Fzd9-CreER/Rosa26-tdTomato mice to activate cre, and the cochleae were dissected 48 h later to determine the tdTomato expression pattern, which shows Fzd9 expression at different time points **(C)**. Myo7a was used as the HC marker, and Sox2 was used as the SC marker. The large square images are single XY slices, the vertical red line shows the position of the orthogonal slice that is shown to the right of each panel, and the blue line on the orthogonal slice shows the level of the XY slice to the left. Orthogonal projections of tdTomato+ cells are indicated by white arrows. Scale bar, 20 μm. **(D)** Quantification of tdTomato+ cells at each time point. $n = 3$ for both Lgr5 and Fzd9 mice. $^{**}p < 0.01$.

it is possible that Fzd9 might play a role in regulating Wnt signaling in the inner ear, which in turns affects the proliferation ability of Fzd9+/ Lgr5+ progenitors. And the detailed role of Fzd9 in regulating the proliferation and/or differentiation of the inner ear progenitors still need to be investigated in the future. Many other genes and signaling pathways, such as Notch,

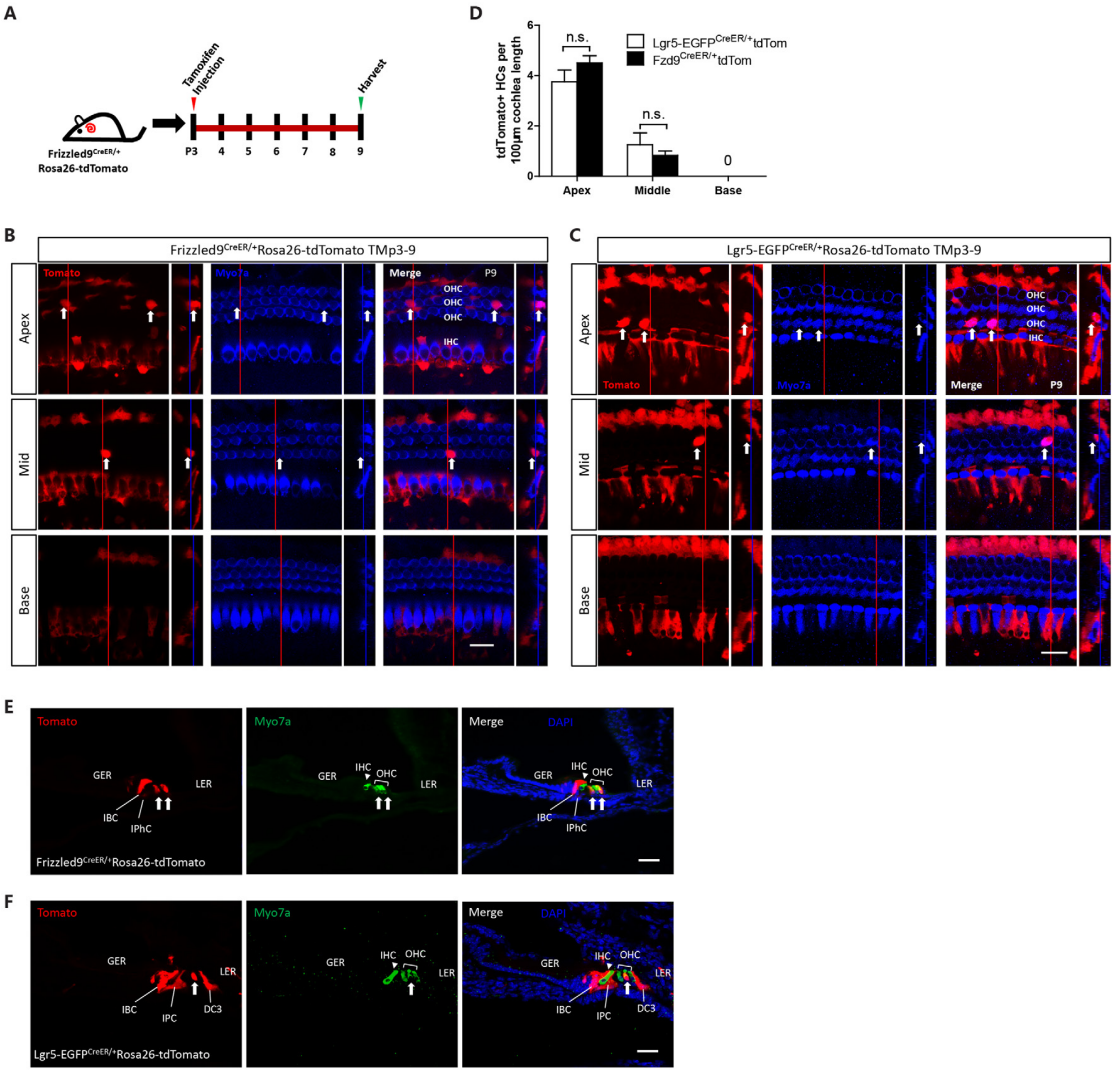

FIGURE 3 | Lineage tracing of Fzd9+ cells in the neonatal mouse cochlea. **(A)** Tamoxifen was I.P. injected into P3 Fzd9-CreER/Rosa26-tdTomato mice to activate cre, and the cochleae were dissected at P9 to lineage trace Fzd9+ cells. Lgr5-EGFP-CreER/Rosa26-tdTomato mice were treated by the same way to lineage trace Lgr5+ cells. **(B–F)** Lineage tracing results showed tdTomato+/Myo7a+ HCs (indicated by white arrows) in the apical, middle, and basal turns of the cochlea by whole-mount **(B,C)** and cryosection **(E,F)**. The large square images are single XY slices, the vertical red line shows the position of the orthogonal slice that is shown to the right of each panel, and the blue line on the orthogonal slice shows the level of the XY slice to the left. Myo7a was used as the HC marker, and Sox2 was used as the SC marker. Scale bar, 20 μm in **(B,C)** and 50 μm in **(E,F)**. Quantification of tdTomato+ HCs was shown in **(D)**. $n = 4$ for Lgr5 mice and $n = 3$ for Fzd9 mice. n.s., not significant.

Neurog1, Hedgehog, and Foxg1, have been reported to play a role in HC development and regeneration (Pauley et al., 2006; Jahan et al., 2015a,b; Li et al., 2015; Ni et al., 2016; Chen et al., 2017; He et al., 2019), and we will study their roles in Fzd9+ progenitors in the future.

Lgr5+ progenitors have been shown to include IPCs, IBCs, third-row DCs, and some of the GER cells, while Fzd9+ cells include IPhCs, IBCs, and third-row DCs (**Figure 1H**), and we used Sox2 to label SCs (**Figures 1D,E**, **Supplementary Figure S2**), including Hensen's cells (HECs), DCs, outer pillar cells (OPCs), IPCs, IPhCs, IBCs and GER (Dabdoub et al., 2008; Nichols et al., 2008; Chai et al., 2012; Li et al., 2015). In the very apical turn of the cochlea, only 4.8 ± 1.7 OPCs, first-row and second-row DCs per 100 μm of the cochlea length were labeled by tdTomato, while we did not find any tdTomato+ OPCs, first-row or second-row DCs in the rest of the apical, middle, and basal turns. The flow cytometry plots also showed that Lgr5+ progenitors made up around 2.44% of all of the cochlear cells, while the Fzd9+ cells only made up 0.63% of the total cochlear cells (**Figure 4B**). Thus the cell types and cell numbers of Fzd9+ cells were both much less than Lgr5+ cells, which means that Fzd9+ cells were a smaller cell population compared to Lgr5+ cells. Considering that the proliferation, differentiation, and HC generation ability of Fzd9+

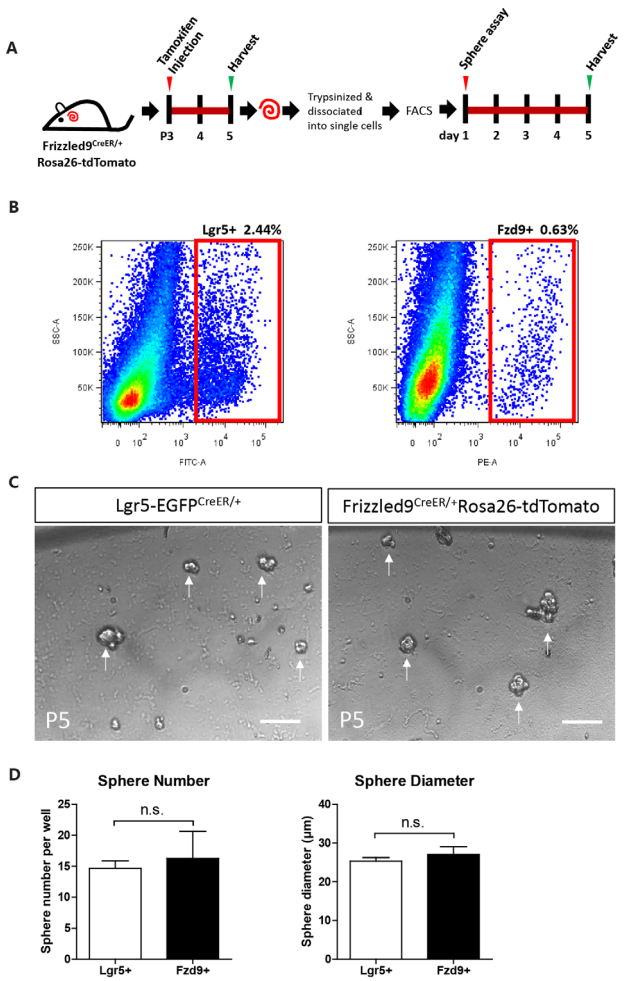

FIGURE 4 | Fzd9+ cells form spheres similarly to Lgr5+ progenitors when cultured *in vitro*. **(A,B)** Tamoxifen was I.P. injected into P3 Fzd9-CreER/Rosa26-tdTomato mice to activate cre, and the cochleae were trypsinized and dissociated into single cells 48 h later for FAC sorting of Fzd9+ cells by tdTomato fluorescence. The cochleae of P5 Lgr5-EGFP-CreER mice were also trypsinized for FAC sorting for Lgr5+ cells. FAC sorting plots are shown in **(B)**. Then Fzd9+ and Lgr5+ cells were cultured *in vitro* for 5 days to form spheres. **(C)** The spheres formed by Lgr5+ progenitors and Fzd9+ cells. Scale bar, 50 μm. **(D)** Quantification of the sphere diameter and number of Lgr5+ spheres and Fzd9+ spheres. $n = 3$ for Lgr5+ spheres and $n = 4$ for Fzd9+ spheres. n.s., not significant.

cells is similar to Lgr5+ progenitors, it is very possible that Fzd9+ cells are the main functional progenitor cell types among Lgr5+ cells, and thus our work provides a new marker for HC progenitors and narrows down the progenitor cell types and numbers compared to Lgr5+ progenitors. According to our current data, we speculated that Lgr5+/Fzd9- SCs might have very limited ability as HC progenitors, which still need further more research to prove. IBCs and the third-row DCs express both Lgr5 and Fzd9, while IPhCs only express Fzd9, and this suggests that IPhCs might also be important for HC generation. Our recent research reported that Lgr6 is expressed in the IPCs, which have higher ability for differentiation and lower ability for proliferation compared to Lgr5+ progenitors (Zhang et al., 2018). Fzd9+ IPhCs express neither Lgr5 nor Lgr6, but these cells have never been studied in terms of their ability to proliferate and differentiate. In a future study, we are planning on flow sorting the Fzd9+ IPhCs to determine their proliferation and differentiation ability.

Fzd9 expression decreased dramatically with age, which is consistent with the decreased expression of Wnt signaling with age (Chai et al., 2011; Jan et al., 2013). Fzd9 is expressed at high levels at P3, at much lower levels at P7, and is undetectable at P14, which is consistent with the rapid decrease of HC generation ability in the mouse cochlea after P7. These results also suggested that Fzd9 could serve as a marker for HC progenitors because its expression correlates with the HC generation ability of the postnatal mouse cochlea.

The sphere-forming assay showed that Fzd9+ cells could form spheres when cultured *in vitro* and that these spheres were similar in number and diameter compared to Lgr5+ progenitors. We also performed a sphere-forming assay in older mice to see if the subpopulation of Lgr5+/Fzd9+ cells loses their proliferative capacity differently. P9 Fzd9-CreER/Rosa26-tdTomato mice were injected with tamoxifen, and Fzd9+ cells were FAC sorted at P12 (**Supplementary Figure S1A**). P12 Lgr5-EGFP-CreER mice were also used for FAC sorting Lgr5+ progenitors. Both cells were cultured *in vitro* for the sphere-forming assay, and we observed fewer and smaller spheres at P12 than at P5, and the sphere numbers and mean sphere diameters generated from P12 Lgr5+ cells and Fzd9+ cells were similar after 5 days of cell culture (**Supplementary Figures S1B,C**), which was consistent with previous reports that showed the sphere-forming ability were decreasing with age (Oshima et al., 2007). This suggests that Fzd9+ cells can proliferate and renew themselves when cultured *in vitro* and that the *in vitro* proliferation ability of Fzd9+ cells and Lgr5+ cells are similar.

Differentiation results showed that Fzd9+ cells could proliferate and differentiate into Myo7a+ cells, which is consistent with our *in vivo* data. We also compared the differentiation ability of Fzd9+ cells and Lgr5+ cells and found that the numbers of Myo7a+ cells and Myo7a+/EdU+ cells were almost the same, which means that the differentiation ability of Fzd9+ cells and Lgr5+ are practically the same. Taken together, the sphere-forming assay and *in vitro* differentiation assay both showed that when cultured *in vitro* the proliferation and differentiation ability of Fzd9+ cells are similar to Lgr5+ cells and that Fzd9+ cells have similar characteristics as previously identified HC progenitors. One recent report showed that Lgr5+ progenitors could be established as a valuable *in vitro* tool for the analysis of progenitor cell manipulation and HC differentiation (Lenz et al., 2019), and this has inspired us to establish Fzd9+ progenitors for the same use in the future.

In summary, we used Fzd9-CreER/Rosa26-tdTomato mice to show that Fzd9+ cells were traced in IPhCs, IBCs, and third-row DCs, but not in IPCs or GER cells, in the neonatal mouse cochlea and that Fzd9 expression decreased with age. Fzd9+ cells have the ability to generate HCs *in vivo* and form spheres *in vitro*, and the differentiation ability of Fzd9+ cells was similar compared

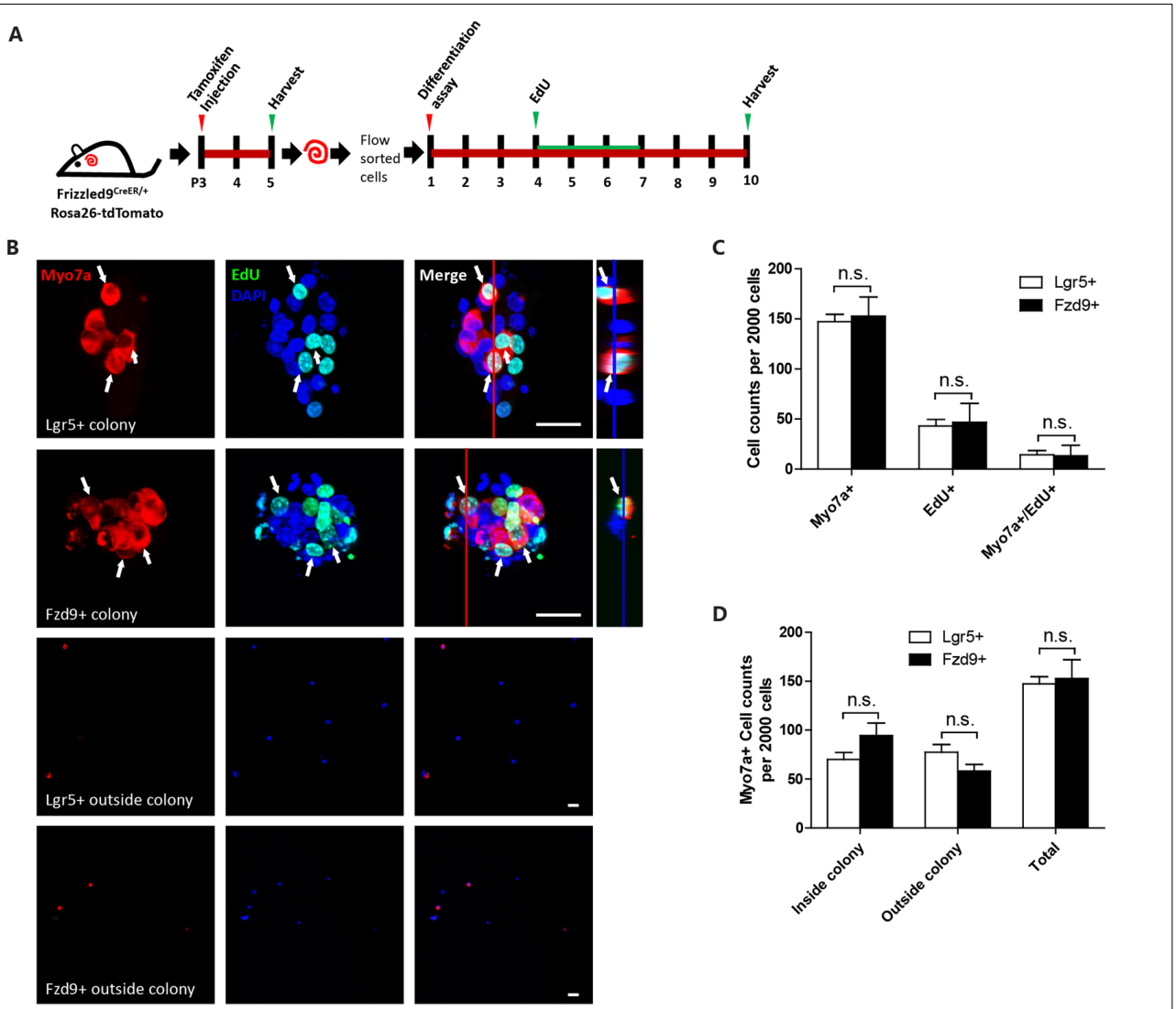

FIGURE 5 | Sphere differentiation assay of Fzd9+ and Lgr5+ cells. **(A)** The same numbers of Fzd9+ cells and Lgr5+ progenitors were cultured *in vitro* for 10 days and allowed to differentiate. **(B)** Immunofluorescence images of differentiated spheres and individual cells outside the colonies formed from Fzd9+ cells and Lgr5+ progenitors. The large square images are single XY slices, the vertical red line shows the position of the orthogonal slice that is shown to the right of each panel, and the blue line on the orthogonal slice shows the level of the XY slice to the left. Myo7a was used as the HC marker, and EdU was used to label proliferating cells. Myo7a+/EdU+ cells are indicated by white arrows. Scale bar, 20 μm. **(C,D)** Quantification of Myo7a+ and EdU+ cells in spheres **(C)** and Myo7a+ cells in inside and outside colonies **(D)** formed from Fzd9+ cells and Lgr5+ progenitors. *n* = 3 for both Lgr5+ and Fzd9+ cells. n.s., not significant.

to Lgr5+ progenitors in the *in vitro* differentiation assay. Our work thus suggests that Fzd9 is a more restricted marker for HC progenitors than Lgr5.

DATA AVAILABILITY

All datasets generated for this study are included in the manuscript and/or the **Supplementary Files**.

ETHICS STATEMENT

We performed all animal procedures according to protocols that were approved by the Animal Care and Use Committee of Southeast University and that were consistent with the National Institute of Health's Guide for the Care and Use of Laboratory Animals. We made all efforts to minimize the number of animals used and to prevent their suffering.

AUTHOR CONTRIBUTIONS

SZ, XC, XQ, and RC conceived and designed the experiments. SZ, DL, ZZ, YZ, YD, HZ, LG, JQ, and RQ performed the experiments. SZ, MT, XG, CZ, XC, XQ, and RC analyzed the data. SZ, RC, XQ, and XC wrote the article. All authors read and approved the final manuscript.

FUNDING

This work was supported by grants from the Strategic Priority Research Program of the Chinese Academy of Science (XDA16010303), the National Key R&D Program of China (2017YFA0103900, 2015CB965000), the National Natural Science Foundation of China (Nos. 31501194, 81500790, 81622013, 81771019, 81570921, 31500852, 81670938), the Jiangsu Province Natural Science Foundation (BK20150598, BK20160125), the Public Technology Application Research Foundation from the Department of Science and Technology of Zhejiang Province (2013C33241), the Wenzhou Municipal Science and Technology Bureau Foundation (Y20110090), Boehringer Ingelheim Pharma GmbH, and the Fundamental Research Funds for the Central Universities (2242017K41040, YG1705011, YG1705035).

SUPPLEMENTARY MATERIAL

The Supplementary Material for this article can be found online at: https://www.frontiersin.org/articles/10.3389/fnmol.2019.00184/full#supplementary-material

REFERENCES

Albers, J., Schulze, J., Beil, F. T., Gebauer, M., Baranowsky, A., Keller, J., et al. (2011). Control of bone formation by the serpentine receptor Frizzled-9. *J. Cell Biol.* 192, 1057–1072. doi: 10.1083/jcb.201008012

Avasarala, S., Bikkavilli, R. K., Van Scoyk, M., Zhang, W., Lapite, A., Hostetter, L., et al. (2013a). Heterotrimeric G-protein, Gα16, is a critical downstream effector of non-canonical Wnt signaling and a potent inhibitor of transformed cell growth in non small cell lung cancer. *PLoS One* 8:e76895. doi: 10.1371/journal.pone.0076895

Avasarala, S., Van Scoyk, M., Wang, J., Sechler, M., Vandervest, K., Brzezinski, C., et al. (2013b). hsa-miR29b, a critical downstream target of non-canonical Wnt signaling, plays an anti-proliferative role in non-small cell lung cancer cells *via* targeting MDM2 expression. *Biol. Open* 2, 675–685. doi: 10.1242/bio.20134507

Aviles, E. C., Pinto, C., Hanna, P., Ojeda, J., Perez, V., De Ferrari, G. V., et al. (2014). Frizzled-9 impairs acetylcholine receptor clustering in skeletal muscle cells. *Front. Cell. Neurosci.* 8:110. doi: 10.3389/fncel.2014.00110

Battula, V. L., Bareiss, P. M., Treml, S., Conrad, S., Albert, I., Hojak, S., et al. (2007). Human placenta and bone marrow derived MSC cultured in serum-free, b-FGF-containing medium express cell surface frizzled-9 and SSEA-4 and give rise to multilineage differentiation. *Differentiation* 75, 279–291. doi: 10.1111/j.1432-0436.2006.00139.x

Battula, V. L., Treml, S., Abele, H., and Bühring, H. J. (2008). Prospective isolation and characterization of mesenchymal stem cells from human placenta using a frizzled-9-specific monoclonal antibody. *Differentiation* 76, 326–336. doi: 10.1111/j.1432-0436.2007.00225.x

Bermingham-McDonogh, O., and Reh, T. A. (2011). Regulated reprogramming in the regeneration of sensory receptor cells. *Neuron* 71, 389–405. doi: 10.1016/j.neuron.2011.07.015

Bramhall, N. F., Shi, F., Arnold, K., Hochedlinger, K., and Edge, A. S. (2014). Lgr5-positive supporting cells generate new hair cells in the postnatal cochlea. *Stem Cell Rep.* 2, 311–322. doi: 10.1016/j.stemcr.2014.01.008

Buhring, H. J., Battula, V. L., Treml, S., Schewe, B., Kanz, L., and Vogel, W. (2007). Novel markers for the prospective isolation of human MSC. *Ann. N Y Acad. Sci.* 1106, 262–271. doi: 10.1196/annals.1392.000

Chai, R., Kuo, B., Wang, T., Liaw, E. J., Xia, A., Jan, T. A., et al. (2012). Wnt signaling induces proliferation of sensory precursors in the postnatal mouse cochlea. *Proc. Natl. Acad. Sci. U S A* 109, 8167–8172. doi: 10.1073/pnas.1202774109

Chai, R., Xia, A., Wang, T., Jan, T. A., Hayashi, T., Bermingham-McDonogh, O., et al. (2011). Dynamic expression of Lgr5, a Wnt target gene, in the developing and mature mouse cochlea. *J. Assoc. Res. Otolaryngol.* 12, 455–469. doi: 10.1007/s10162-011-0267-2

Chen, Y., Lu, X., Guo, L., Ni, W., Zhang, Y., Zhao, L., et al. (2017). Hedgehog signaling promotes the proliferation and subsequent hair cell formation of progenitor cells in the neonatal mouse cochlea. *Front. Mol. Neurosci.* 10:426. doi: 10.3389/fnmol.2017.00426

Cox, B. C., Chai, R., Lenoir, A., Liu, Z., Zhang, L., Nguyen, D. H., et al. (2014). Spontaneous hair cell regeneration in the neonatal mouse cochlea *in vivo*. *Development* 141, 816–829. doi: 10.1242/dev.103036

Dabdoub, A., Puligilla, C., Jones, J. M., Fritzsch, B., Cheah, K. S., Pevny, L. H., et al. (2008). Sox2 signaling in prosensory domain specification and subsequent hair cell differentiation in the developing cochlea. *Proc. Natl. Acad. Sci. U S A* 105, 18396–18401. doi: 10.1073/pnas.0808175105

Dijksterhuis, J. P., Petersen, J., and Schulte, G. (2014). WNT/Frizzled signalling: receptor-ligand selectivity with focus on FZD-G protein signalling and its physiological relevance: IUPHAR Review 3. *Br. J. Pharmacol.* 171, 1195–1209. doi: 10.1111/bph.12364

He, Z., Fang, Q., Li, H., Shao, B., Zhang, Y., Zhang, Y., et al. (2019). The role of FOXG1 in the postnatal development and survival of mouse cochlear hair cells. *Neuropharmacology* 144, 43–57. doi: 10.1016/j.neuropharm.2018.10.021

Heilmann, A., Schinke, T., Bindl, R., Wehner, T., Rapp, A., Haffner-Luntzer, M., et al. (2013). The Wnt serpentine receptor Frizzled-9 regulates new bone formation in fracture healing. *PLoS One* 8:e84232. doi: 10.1371/journal.pone.0084232

Jahan, I., Pan, N., and Fritzsch, B. (2015a). Opportunities and limits of the one gene approach: the ability of Atoh1 to differentiate and maintain hair cells depends on the molecular context. *Front. Cell. Neurosci.* 9:26. doi: 10.3389/fncel.2015.00026

Jahan, I., Pan, N., Kersigo, J., and Fritzsch, B. (2015b). Neurog1 can partially substitute for Atoh1 function in hair cell differentiation and maintenance during organ of Corti development. *Development* 142, 2810–2821. doi: 10.1242/dev.123091

Jan, T. A., Chai, R., Sayyid, Z. N., van Amerongen, R., Xia, A., Wang, T., et al. (2013). Tympanic border cells are Wnt-responsive and can act as progenitors for postnatal mouse cochlear cells. *Development* 140, 1196–1206. doi: 10.1242/dev.087528

Karasawa, T., Yokokura, H., Kitajewski, J., and Lombroso, P. J. (2002). Frizzled-9 is activated by Wnt-2 and functions in Wnt/β -catenin signaling. *J. Biol. Chem.* 277, 37479–37486. doi: 10.1074/jbc.m205658200

Lenz, D. R., Gunewardene, N., Abdul-Aziz, D. E., Wang, Q., Gibson, T. M., and Edge, A. S. B. (2019). Applications of Lgr5-positive cochlear progenitors (LCPs) to the study of hair cell differentiation. *Front. Cell Dev. Biol.* 7:14. doi: 10.3389/fcell.2019.00014

Li, W., Wu, J., Yang, J., Sun, S., Chai, R., Chen, Z. Y., et al. (2015). Notch inhibition induces mitotically generated hair cells in mammalian cochleae *via* activating the Wnt pathway. *Proc. Natl. Acad. Sci. U S A* 112, 166–171. doi: 10.1073/pnas.1415901112

Li, W., You, D., Chen, Y., Chai, R., and Li, H. (2016). Regeneration of hair cells in the mammalian vestibular system. *Front. Med.* 10, 143–151. doi: 10.1007/s11684-016-0451-1

Liu, L., Chen, Y., Qi, J., Zhang, Y., He, Y., Ni, W., et al. (2016). Wnt activation protects against neomycin-induced hair cell damage in the mouse cochlea. *Cell Death Dis.* 7:e2136. doi: 10.1038/cddis.2016.35

Lu, X., Sun, S., Qi, J., Li, W., Liu, L., Zhang, Y., et al. (2017). Bmi1 regulates the proliferation of cochlear supporting cells *via* the canonical Wnt signaling pathway. *Mol. Neurobiol.* 54, 1326–1339. doi: 10.1007/s12035-016-9686-8

MacDonald, B. T., and He, X. (2012). Frizzled and LRP5/6 receptors for Wnt/β-catenin signaling. *Cold Spring Harb. Perspect. Biol.* 4:a007880. doi: 10.1101/cshperspect.a007880

Madisen, L., Zwingman, T. A., Sunkin, S. M., Oh, S. W., Zariwala, H. A., Gu, H., et al. (2010). A robust and high-throughput Cre reporting and characterization system for the whole mouse brain. *Nat. Neurosci.* 13, 133–140. doi: 10.1038/nn.2467

Momoi, A., Yoda, H., Steinbeisser, H., Fagotto, F., Kondoh, H., Kudo, A., et al. (2003). Analysis of Wnt8 for neural posteriorizing factor by identifying Frizzled 8c and Frizzled 9 as functional receptors for Wnt8. *Mech. Dev.* 120, 477–489. doi: 10.1016/s0925-4773(03)00003-0

Ni, W., Zeng, S., Li, W., Chen, Y., Zhang, S., Tang, M., et al. (2016). Wnt activation followed by Notch inhibition promotes mitotic hair cell regeneration in the postnatal mouse cochlea. *Oncotarget* 7, 66754–66768. doi: 10.18632/oncotarget.11479

Nichols, D. H., Pauley, S., Jahan, I., Beisel, K. W., Millen, K. J., and Fritzsch, B. (2008). Lmx1a is required for segregation of sensory epithelia and normal ear histogenesis and morphogenesis. *Cell Tissue Res.* 334, 339–358. doi: 10.1007/s00441-008-0709-2

Oshima, K., Grimm, C. M., Corrales, C. E., Senn, P., Martinez Monedero, R., Geleoc, G. S., et al. (2007). Differential distribution of stem cells in the auditory and vestibular organs of the inner ear. *J. Assoc. Res. Otolaryngol.* 8, 18–31. doi: 10.1007/s10162-006-0058-3

Pauley, S., Lai, E., and Fritzsch, B. (2006). Foxg1 is required for morphogenesis and histogenesis of the mammalian inner ear. *Dev. Dyn.* 235, 2470–2482. doi: 10.1002/dvdy.20839

Pedersen, D. S., Fredericia, P. M., Pedersen, M. O., Stoltenberg, M., Penkowa, M., Danscher, G., et al. (2012). Metallic gold slows disease progression, reduces cell death and induces astrogliosis while simultaneously increasing stem cell responses in an EAE rat model of multiple sclerosis. *Histochem. Cell Biol.* 138, 787–802. doi: 10.1007/s00418-012-0996-2

Pollard, S. M., Wallbank, R., Tomlinson, S., Grotewold, L., and Smith, A. (2008). Fibroblast growth factor induces a neural stem cell phenotype in foetal forebrain progenitors and during embryonic stem cell differentiation. *Mol. Cell. Neurosci.* 38, 393–403. doi: 10.1016/j.mcn.2008.03.012

Ramírez, V. T., Ramos-Fernández, E., Henríquez, J. P., Lorenzo, A., and Inestrosa, N. C. (2016). Wnt-5a/frizzled9 receptor signaling through the Gαo-Gβγ complex regulates dendritic spine formation. *J. Biol. Chem.* 291, 19092–19107. doi: 10.1074/jbc.m116.722132

Rubel, E. W., Furrer, S. A., and Stone, J. S. (2013). A brief history of hair cell regeneration research and speculations on the future. *Hear. Res.* 297, 42–51. doi: 10.1016/j.heares.2012.12.014

Shi, F., Kempfle, J. S., and Edge, A. S. (2012). Wnt-responsive Lgr5-expressing stem cells are hair cell progenitors in the cochlea. *J. Neurosci.* 32, 9639–9648. doi: 10.1523/JNEUROSCI.1064-12.2012

Tian, C., Gong, Y., Yang, Y., Shen, W., Wang, K., Liu, J., et al. (2012). Foxg1 has an essential role in postnatal development of the dentate gyrus. *J. Neurosci.* 32, 2931–2949. doi: 10.1523/JNEUROSCI.5240-11.2012

Tran, T. C., Kimura, K., Nagano, M., Yamashita, T., Ohneda, K., Sugimori, H., et al. (2011). Identification of human placenta-derived mesenchymal stem cells involved in re-endothelialization. *J. Cell. Physiol.* 226, 224–235. doi: 10.1002/jcp.22329

Trubiani, O., Zalzal, S. F., Paganelli, R., Marchisio, M., Giancola, R., Pizzicannella, J., et al. (2010). Expression profile of the embryonic markers nanog, OCT-4, SSEA-1, SSEA-4, and frizzled-9 receptor in human periodontal ligament mesenchymal stem cells. *J. Cell. Physiol.* 225, 123–131. doi: 10.1002/jcp.22203

Van Raay, T. J., Wang, Y. K., Stark, M. R., Rasmussen, J. T., Francke, U., Vetter, M. L., et al. (2001). frizzled 9 is expressed in neural precursor cells in the developing neural tube. *Dev. Genes Evol.* 211, 453–457. doi: 10.1007/s004270100174

Wang, T., Chai, R., Kim, G., Pham, X., and Cheng, A. (2015). Damage-recruited Lgr5+ cells regenerate hair cells *via* proliferation and direct transdifferentiationin neonatal mouse utricle. *Nat. Commun.* 6:6613. doi: 10.1038/ncomms7613

Waqas, M., Guo, L., Zhang, S., Chen, Y., Zhang, X., Wang, L., et al. (2016a). Characterization of Lgr5+ progenitor cell transcriptomes in the apical and basal turns of the mouse cochlea. *Oncotarget* 7, 41123–41141. doi: 10.18632/oncotarget.8636

Waqas, M., Zhang, S., He, Z., Tang, M., and Chai, R. (2016b). Role of Wnt and Notch signaling in regulating hair cell regeneration in the cochlea. *Front. Med.* 10, 237–249. doi: 10.1007/s11684-016-0464-9

Winn, R. A., Marek, L., Han, S. Y., Rodriguez, K., Rodriguez, N., Hammond, M., et al. (2005). Restoration of Wnt-7a expression reverses non-small cell lung cancer cellular transformation through frizzled-9-mediated growth inhibition and promotion of cell differentiation. *J. Biol. Chem.* 280, 19625–19634. doi: 10.1074/jbc.m409392200

Wu, J., Li, W., Lin, C., Chen, Y., Cheng, C., Sun, S., et al. (2016). Co-regulation of the Notch and Wnt signaling pathways promotes supporting cell proliferation and hair cell regeneration in mouse utricles. *Sci. Rep.* 6:29418. doi: 10.1038/srep29418

You, D., Guo, L., Li, W., Sun, S., Chen, Y., Chai, R., et al. (2018). Characterization of Wnt and notch-responsive Lgr5+ hair cell progenitors in the striolar region of the neonatal mouse utricle. *Front. Mol. Neurosci.* 11:137. doi: 10.3389/fnmol.2018.00137

Zhang, Y., Guo, L., Lu, X., Cheng, C., Sun, S., Li, W., et al. (2018). Characterization of Lgr6+ cells as an enriched population of hair cell progenitors compared to Lgr5+ cells for hair cell generation in the neonatal mouse cochlea. *Front. Mol. Neurosci.* 11:147. doi: 10.3389/fnmol.2018.00147

Zhang, S., Zhang, Y., Yu, P., Hu, Y., Zhou, H., Guo, L., et al. (2017). Characterization of Lgr5+ progenitor cell transcriptomes after neomycin injury in the neonatal mouse cochlea. *Front. Mol. Neurosci.* 10:213. doi: 10.3389/fnmol.2017.00213

Zhao, C., Aviles, C., Abel, R. A., Almli, C. R., McQuillen, P., and Pleasure, S. J. (2005). Hippocampal and visuospatial learning defects in mice with a deletion of frizzled 9, a gene in the Williams syndrome deletion interval. *Development* 132, 2917–2927. doi: 10.1242/dev.01871

Zhao, C., and Pleasure, S. J. (2004). Frizzled-9 promoter drives expression of transgenes in the medial wall of the cortex and its chief derivative the hippocampus. *Genesis* 40, 32–39. doi: 10.1002/gene.20058

Zhao, C., and Pleasure, S. J. (2005). Frizzled9 protein is regionally expressed in the developing medial cortical wall and the cells derived from this region. *Dev. Brain Res.* 157, 93–97. doi: 10.1016/j.devbrainres.2005.02.018

Zhou, W., Zhang, Y., Li, Y., Wei, Y. S., Liu, G., Liu, D. P., et al. (2010). A transgenic Cre mouse line for the study of cortical and hippocampal development. *Genesis* 48, 343–350. doi: 10.1002/dvg.20611

Conflict of Interest Statement: The authors declare that the research was conducted in the absence of any commercial or financial relationships that could be construed as a potential conflict of interest.

frontiers in Molecular Neuroscience

METHODS
published: 20 August 2019
doi: 10.3389/fnmol.2019.00201

Development of Efficient AAV2/DJ-Based Viral Vectors to Selectively Downregulate the Expression of Neuronal or Astrocytic Target Proteins in the Rat Central Nervous System

*Charlotte Jollé[1], Nicole Déglon[2,3], Catherine Pythoud[2,3], Anne-Karine Bouzier-Sore[4] and Luc Pellerin[1,4]**

[1] Department of Physiology, Université de Lausanne, Lausanne, Switzerland, [2] Laboratory of Cellular and Molecular Neurotherapies (LCMN), Department of Clinical Neurosciences, Lausanne University Hospital, University of Lausanne, Lausanne, Switzerland, [3] LCMN, Neurosciences Research Center, Lausanne University Hospital, University of Lausanne, Lausanne, Switzerland, [4] Centre de Résonance Magnétique des Systèmes Biologiques UMR 5536, CNRS-Université de Bordeaux, Bordeaux, France

OPEN ACCESS

Edited by:
Ildikó Rácz,
Universitätsklinikum Bonn, Germany

Reviewed by:
Etiena Basner-Tschakarjan,
Independent Researcher,
Philadelphia, United States
Mitsuhiro Hashimoto,
Fukushima Medical University, Japan

***Correspondence:**
Luc Pellerin
Luc.Pellerin@unil.ch

Received: 16 May 2019
Accepted: 02 August 2019
Published: 20 August 2019

Citation:
Jollé C, Déglon N, Pythoud C, Bouzier-Sore A-K and Pellerin L (2019) Development of Efficient AAV2/DJ-Based Viral Vectors to Selectively Downregulate the Expression of Neuronal or Astrocytic Target Proteins in the Rat Central Nervous System. Front. Mol. Neurosci. 12:201. doi: 10.3389/fnmol.2019.00201

Viral vectors have become very popular to overexpress or downregulate proteins of interest in different cell types. They conveniently allow the precise targeting of well-defined tissue areas, which is particularly useful in complex organs like the brain. In theory, each vector should have its own cell specificity that can be obtained by using different strategies (e.g., using a cell-specific promoter). For the moment, there is few vectors that have been developed to alternatively target, using the same capsid, neurons and astrocytes in the central nervous system. There is even fewer examples of adeno-associated viral vectors able to efficiently transduce cells both *in vitro* and *in vivo*. The development of viral vectors allowing the cell-specific downregulation of a protein in cultured cells of the central nervous system as well as *in vivo* within a large brain area would be highly desirable to address several important questions in neurobiology. Here we report that the use of the AAV2/DJ viral vector associated to an hybrid CMV/chicken β-actin promoter (CBA) or to a modified form of the glial fibrillary acidic protein promoter (G1B3) allows a specific transduction of neurons or astrocytes in more than half of the barrel field within the rat somatosensory cortex. Moreover, the use of the miR30E-shRNA technology led to an efficient downregulation of two proteins of interest related to metabolism both *in vitro* and *in vivo*. Our results demonstrate that it is possible to downregulate the expression of different protein isoforms in a cell-specific manner using a common serotype. It is proposed that such an approach could be extended to other cell types and used to target several proteins of interest within the same brain area.

Keywords: AAV2/DJ, shRNA, neurons, astrocytes, MCT2, MCT4, miR30E, barrel cortex

INTRODUCTION

Viral vectors are used as tools to spatially and temporally regulate the expression of proteins in a wide range of cell types, including brain cells (Davidson et al., 2000; Burger et al., 2004). Adeno-associated viral vectors (AAVs) are one of the most commonly used for several reasons. AAVs are single-stranded DNA viruses with a short DNA length, about 4.7 kb (Hoggan et al., 1966). Because of their inability to replicate in the absence of a helper virus, e.g., Adenovirus or Herpesvirus, and because of their episomal form in the nucleus, working with AAVs in the laboratory is considered as safe (Dismuke et al., 2013). Moreover, this virus is not associated with any human disease (Flotte and Berns, 2005). It was shown that over 80% of the human population has been infected with the AAV2 (Calcedo et al., 2009). Because of their small size (about 20 nm), AAVs largely diffuse in the rodent brain and are widely used for *in vivo* brain studies (Aschauer et al., 2013). Unfortunately, most of the AAVs have a low efficiency *in vitro* (Ellis et al., 2013). This downside forced researchers in the past to choose different serotypes or even different viral vectors for *in vitro* and *in vivo* studies, introducing an unavoidable bias in their study.

Few years ago, the AAV2/DJ serotype was developed (Grimm et al., 2008). This serotype was created from the shuffling of capsids between eight existing serotypes (AAV2, 4, 5, 8, 9, Avian, Caprine, and Bovine). It was shown *in vitro* that the AAV2/DJ outperforms the other serotypes in terms of transduction efficiency *in vitro* (above 1,000 times depending on the cell line studied). It was also shown that the AAV2/DJ remains highly efficient *in vivo* like the other AAVs (Holehonnur et al., 2014; de Solis et al., 2017).

The ability to transduce different cell types is primarily determined by the AAV capsid proteins. Each AAV serotype has its own tropism, i.e., its own specificity for a particular cell type (Daya and Berns, 2008). Most AAVs have a prominent neuronal tropism (e.g., AAV2, AAV5) except AAV4 that targets predominantly astrocytes (Liu et al., 2005). Several years ago, it was shown that the capsid is not the only parameter that determines the cell specificity of a viral vector. Changing the promoter can modify the cell-specific expression of the transduced sequence, e.g., the use of an astrocyte-specific promoter can change the cell-specific expression from neuronal to astrocytic (Brenner et al., 1994).

Adeno-associated viral vectors are widely used to overexpress small proteins in a specific cell type. Fewer studies were conducted using AAVs to downregulate the expression of a protein in a cell-specific manner. Indeed, the AAV DNA length (4.7 kb) prevents the use of efficient knockout strategies such as the CRISPR-Cas9 system. The transgene size is usually too large, over 3 kb (Jiang and Doudna, 2017). The other commonly used strategy for protein expression downregulation is RNA interference, a post-transcriptional gene regulation mechanism that uses short hairpin RNAs (shRNAs) complementary to the targeted mRNA that will bind to it and favor its degradation (Rao et al., 2009). The incorporation of shRNAs into endogenous microRNA contexts is offering the possibility to use cell-type specific polymerase II promoter. Furthermore, Fellmann et al. (2013) showed that embedding the shRNA sequence in a miR30E backbone (miR30E-shRNA) allows the cell to recognize the sequence as its own and process it in a controlled manner, increasing the yield of downregulation.

The use of a highly efficient downregulation tool targeting different cell types could permit to conduct studies targeting different isoforms of the same protein family expressed by different cell types within the same tissue. The association of the miR30E-shRNA with the AAV2/DJ represents an interesting strategy to target different isoforms in different cell types in the same tissue. Our goal was to combine those two elements to downregulate, *in vitro* and *in vivo*, the expression of two monocarboxylate transporter isoforms (MCTs). These proteins are key players for the astrocyte-neuron lactate shuttle (ANLS), a mechanism purported to play a central role in neuroenergetics (Pellerin and Magistretti, 1994). MCTs form a small group of proton-linked carriers of energy substrates, which includes lactate, pyruvate and ketone bodies. In the central nervous system, MCT2 is predominantly expressed by neurons whereas MCT4 is found solely on astrocytes (Halestrap and Price, 1999).

To achieve our goal, we developed AAV2/DJ viral vectors with two different promoters specific for neurons or astrocytes, and injected them in the barrel field of the rat primary somatosensory cortex (S1BF). We verified that, as expected, the chicken β-actin promoter (CBA, 0.8 kbp; Wang et al., 2003; Gray et al., 2011) led to a neuronal expression of the reporter protein and the modified form of the glial fibrillary acidic protein promoter G1B3 (Merienne et al., 2017) led to an astrocytic expression. Then, derived vectors harboring a specific shRNA sequence against one of the two MCT isoforms were tested *in vitro* and *in vivo* for their capacity to selectively downregulate the expression of MCT2 and MCT4.

MATERIALS AND METHODS

Reference of materials and resources can be found in **Supplementary Table 1**.

Animals

Adult Wistar rats (over 7 weeks old, males only for *in vivo* experiments and pregnant females for *in vitro* experiments, Janvier Laboratories, RRID:RGD_13508588) were used under the protocol approved by the Swiss "Service de la Consommation et des Affaires Vétérinaires (SCAV, authorization n°3101.1) in accordance with Swiss animal welfare laws. They were housed by two and maintained on a 12 h light/dark cycle. Food and water were provided *ad libitum* throughout the experiment. Littermates of the same sex were randomly assigned to experimental groups.

Plasmids Cloning

Plasmids from Geneart (**Supplementary Table 1**, Recombinant DNA, pMK) were cloned into a pENTR (pENTR-mCherry-miR30E-shHTT6) kindly provided by Pr. Nicole Déglon (**Supplementary Table 1**, Recombinant DNA, pENTR). This pENTR already contained the reporter gene (mCherry). Then, Gateway LR Clonase reaction was performed to insert the pENTR

fragment mCherry-miR30E-miR30E-shRNA into destination vectors pAAV2ss-CBA-RFA-WPRE-bGH or pAAV2-G1B3-RFA-WPRE-bGH. Final products (**Supplementary Table 1**, Recombinant DNA, pAAV2ss) were then used to produce AAVs. The CBA promoter is a hybrid promoter corresponding to the chicken beta actin promoter with the enhancer sequence of the cytomegalovirus (Wang et al., 2003; Gray et al., 2011). The G1B3 promoter is a modified form of the GfaABC1D promoter, derived from the Glial Fibrillary Acidic Protein (GFAP) (Merienne et al., 2017). More precisely, three copies of the "B" enhancer sequence from Gfa2(b)3 (De Leeuw et al., 2006) have been cloned in the GfaABC1D promoter (Lee et al., 2008) to generate GfaABC1D(B3) (hereafter called G1B3; Merienne et al., 2017). The combination of those modifications led to a greater expression level and a more astrocyte-specific expression. The ITR (Inverted Terminal Sequence) allows the formation of episomally stable concatemers. The WPRE (Woodchuck hepatitis virus Post-Regulational Element) sequence enhances the expression of the transgene. The bGH (bovine Growth Hormone) sequence promotes polyadenylation and termination of the transgene.

AAV Production

Adeno-associated viral vectors were produced in HEK293T cells, transfected with pHelper, pAAV-DJ_Rep_Cap and pAAV2-transgene using the calcium phosphate precipitation method. Cells and supernatant were harvested 72 h post-transfection and centrifuged for 10 min at 300 *g* at 4°C. Supernatant and cell pellet were processed in parallel. Supernatant was incubated in 8% Polyethylene Glycol, 2.5 M NaCl for 2 h at 4°C. Pellets were pooled and incubated with lysis buffer (0.15 M NaCl, 50 mM Tris–HCl, pH 8.5) for three cycles of freeze/thaw steps (30 min in dry ice/ethanol followed by 30 min at 37°C). The PEG-precipitated supernatant was centrifuged at 4,000 *g* for 20 min at 4°C and the pellet was stored. The lysate was added to the pellet and incubated at 37°C for 1 h. The cellular lysate was treated with Benzonase (50 units/mL) in 1 M $MgCl_2$ for 30 min at 37°C. Then the lysate was centrifuged at 4,000 *g* for 20 min at 4°C. AAVs were separated using iodixanol gradient centrifugation at 59,000 rpm (70Ti rotor, Beckman-Coulter) for 90 min at 20°C. Phase containing AAVs was harvested and loaded on an Amicon Ultra-15PL 100 column with 0.001% Pluronic F68 D-PBS for iodixanol cleaning and viral particles concentration. Tubes were first centrifuged at 4,000 *g* at 4°C until the whole solution has passed through the column. AAVs were resuspended in 200 μL 0.001% Pluronic F68 D-PBS. The viral genome content (vg/mL) of each AAV2/DJ was assessed by Taqman®qPCR with primers recognizing Inverted Terminal Repeats of AAV2 viral genome (**Supplementary Table 1**, Oligonucleotides). AAV2/DJ was stored at −80°C until use.

Stereotaxic Surgery

Surgeries were performed on 7 weeks old animals. Animals were randomly assigned to experimental groups. Animals were anesthetized with isoflurane (5% for the induction and 3% to maintain the anesthesia). AAVs or PBS were injected in one site/hemisphere (S1BF: Anteroposterior = −2,3 mm; Mediolateral = ±5 mm; Dorsoventral = −3 mm). Viral vectors were injected with 34 G steel cannula fixed on a cannula holder and linked to a 10 μL Hamilton syringe and an infusion pump. For each site, 4 μL of viral vector were injected at 0.2 μL/min. Cannulas were left in the brain for 5 min after the injection, and then slowly removed. Skin was closed using 4.0 sterile suture thread. Sterile NaCl 0.9% solution (1 mL) was delivered to the rat by intra-peritoneal injection to avoid dehydration after surgery, and healing cream was applied on the head. Sugar-taste Paracetamol was delivered to the animal in water (1 *g*/cage for rats) during 72 h. Animals were monitored until complete awakening, and every day during 3 days after the surgery. All viral vectors were injected at a final concentration of 1×10^8 *g*/site.

Brain Samples Processing

For brain fixation, animals were anesthetized by lethal i.p. injection of Pentobarbital (150 mg/kg, 1 mL/kg). Intra-cardiac perfusion of cold PBS 1× was performed during 1 min (30 mL/min), followed by perfusion of cold fresh Paraformaldehyde 4% (PFA 4%) solution diluted in 0.15 M of Na-Phosphate buffer during 10 min (30 mL/min). The brain was quickly dissected and post-fixed in PFA 4% during 12 h, followed by cryo-protection in PBS 1×-Sucrose 20% (24 h) and PBS 1×-Sucrose 30% (24 h). Brains were conserved at –80°C until being sectioned at 25 μm with a cryostat.

For RNA and protein extractions, all procedures were performed under RNAse-free conditions. Rats were slightly anesthetized using Isoflurane and quickly decapitated. After, brain was removed and placed in a cold dissection matrix to prepare 1 mm sections. Barrel cortex area was quickly isolated and punches were immediately homogenized on ice in 1 mL of Trizol Reagent and stored at −80°C until use.

Mixed Primary Cultures of Rat Cortical Neurons and Astrocytes

The day before dissection, culture wells (6-well plates) were coated with Poly-L-Ornithine Hydrobromide 15 mg/mL. The pregnant female was sacrificed (at E17–17.5, days of gestation) by decapitation. Embryos were extracted and then cortices were isolated and minced. Minced cortices were then incubated at 37°C with a papain solution (HBSS with Penicillin-Streptomycin 1×, 1 mM L-cysteine, DNAse I 1,000 U and Papain 200 U) for 30 min. Papain activity was then quenched by 1 mL of FBS. Cortices were then finely dissociated in culture medium (High glucose DMEM, B-27 supplement 1×, FBS 10%) by gentle up and down movements in a sterile Pasteur pipette. The solution containing the dissociated cells was then centrifuged for 15 min at 1,000 *g*. Cells were resuspended in culture medium, counted and plated (200,000 cells per well). A neurons/astrocytes proportion of about 1:3 was obtained at the end of the culture time (because of astrocytes proliferation).

The MOI (Multiplicity of Infection) was calculated as the number of viral particles needed per cell (AAV number/total number of cells, Ellis et al., 2013). After 5 days of culture,

the culture medium was changed and cells were infected using increasing doses of viral vectors (MOI of 500, 2,000, 4,000 and 7,000). To avoid differences in temperature and volume of culture medium, only 40 μL of diluted vector were added per well.

After 11 days of culture, cells were incubated with 600 μM of DETA-NONOate, a NO donor, for 16 h. This exposure mimics the effect of physoxia. Indeed, at 21% of O_2, astrocytes do not express MCT4 (Marcillac et al., 2011). At day 12 *in vitro*, all cells were collected using 350 μL of RLT Buffer from the RNeasy mini kit (Qiagen) and stored at −80°C until use for mRNA extraction and in 100 μL of RIPA buffer and stored at −20°C until use for protein extraction.

Immunohistochemistry

Primary and secondary antibodies used in this study are described in the **Supplementary Table 1**. Free-floating sections of 25 μm were washed three times (5 min/wash) at RT in PBS 1×, blocked 1 h in PBS 1× containing 10% Bovine Serum Albumin Fraction V (BSA) and 0.1% of Triton x-100. Sections were incubated overnight at 4°C in PBS 1× containing 5% BSA, 0.1% Triton x-100 and primary antibodies diluted at 1/500. The following day, sections were washed three times (5 min/wash) in PBS 1× and incubated 2 h in PBS 1× containing 5% BSA, 0.1% Triton x-100 and secondary antibodies (diluted at 1/1,000). Sections were finally washed 3 times in PBS 1×, incubated in Hoechst 33342 trihydrochloride trihydrate solution (10 μg/mL) during 5 min at RT, washed three times in PBS 1× and mounted on SuperFrost Ultra Plus microscope slide in Fluoromount medium.

RNA and Protein Extraction

RNA and protein extractions were performed on ice under RNAse free conditions, with ultrapure sterile RNAse-DNAse-Protease free water. Extractions from *in vivo* experiments were performed according to the Trizol kit recommendations (mRNA and protein extraction). Extractions from *in vitro* experiments were performed according to the RNeasy mini kit recommendations. At the end, RNAs were finally resuspended in 22 μL of ultrapure sterile RNAse-DNAse-Protease free water and stored at −80°C. RNA concentration and potential chemical contamination were determined using a Nanodrop 1,000. Samples with aberrant 280/260 and 260/230 ratio were discarded.

Cells were collected in RIPA buffer. Samples were sonicated 3 times for 5 s at an intensity of 70% and centrifuged at 10,000 *g* for 5 min. Supernatants were collected and protein concentration was measured using a micro BCA assay (see below).

Reverse Transcription and qPCR

Reverse transcription was performed according to the SuperScript Transcriptase II protocol. 50 μM Random Hexamers and 10 mM dNTP mix were added to 200 ng of samples. Samples were incubated for 5 min at 65°C. Then, First Strand Buffer 5×, 0.1 M DTT and ultrapure DNAse-RNAse free water were added. Samples were incubated for 2 min at 25°C. Finally, 200 units of SuperScript Transcriptase II were added and tubes were incubated in a Thermocycler to perform the reaction (10 min at 25°C, 50 min at 42°C and 15 min at 70°C). At the end, cDNAs were diluted to obtain a final concentration of 1 ng/L.

Quantitative PCR was performed on 2 ng of cDNA following the protocol of the SensiFAST SyBr Hi-Rox kit. Samples were incubated at 95°C for 3 min then 40 cycles of 3 s at 95°C and 20 s at 60°C. For every experiment, the expression of the gene of interest was reported to RPS29 (Ribosomal Protein S29) expression.

Protein Measurement and Western Blot

Protein concentration was evaluated using the Micro BCA Protein assay kit, according to the manufacturer's recommendations. Diluted proteins were mixed with Laemmli Buffer 4×. Samples and molecular standards (PageRuler) were loaded on a SDS-PAGE 12% acrylamide gel and then transferred on a nitrocellulose membrane by semi-dry transfer (Transblot Turbo). At the end of transfer, membranes were blocked for 1 h, under agitation, at RT with Odyssey Blocking Buffer. Then, membranes were incubated with the primary antibodies in the Odyssey Blocking Buffer overnight, at 4°C, under agitation. The following day, membranes were washed in PBS-0.1% Triton x-100 and incubated with secondary antibodies diluted in Odyssey Blocking Buffer for 2 h, at RT, under agitation. After few washes in PBS-0.1% Triton x-100, membranes were revealed with the LI-COR Odyssey device. The expression of the gene of interest was reported to β-actin expression for *in vitro* experiments and to β III-tubulin expression for *in vivo* experiments.

Image Acquisition and Quantification

Images were obtained using a Zeiss LSM 710 Quasar confocal microscope. For diffusion analysis, all acquisition parameters were kept constant between sections for each animal. All analyses were performed on raw unmodified images. Colocalization analysis was performed on ImageJ (v1.44 p), using the Plugin Cell Counter[1]. To analyze the diffusion of the vector, Tile scans of 7 × 7 were taken on the confocal microscope.

Statistical Analysis

Statistical analyses were performed with GraphPad Prism (v. 7.04). For colocalization analyses and *in vivo* studies, a Student's *t*-test was applied and results were considered significant when $p < 0.05$. Results are presented as mean ± SEM. For *in vitro* studies, one-way ANOVA was used followed by a Dunnett's test that compares each condition to the non-transduced condition.

RESULTS

AAV2/DJ-based viral vectors have been recently introduced and need to be further characterized before being popularized as tools for biological studies, notably in the central nervous system. Indeed, it has already been tested in the brain to overexpress a protein as a model of Huntington's disease (Jang et al., 2018) but not to downregulate protein isoforms. In order to do so, different parameters such as their cell-specific transduction and diffusion *in vivo* were measured to validate their usefulness.

[1]Software available on: http://imagej.nih.gov/ij/index.html.

Large Diffusion in the Rat S1BF Area and Neuron-Specific Expression of the Transgene With an AAV2/DJ Viral Vector Containing a CBA Promoter

A first construct was generated with a control non-coding sequence (shUNIV) embedded in a miR30E sequence positioned after a mCherry sequence, both under the control of a CBA promoter (which was reported to promote a neuronal expression, Meunier et al., 2016; **Figure 1A**). The resulting AAV2/DJ-CBA-mCherry-mir30E-shUNIV viral vector was injected at a single site in the S1BF area of the rat (stereotaxic coordinates: anteroposterior = −2.3 mm; mediolateral = ±5 mm; dorsoventral = −3 mm). After 3 weeks, the diffusion of the viral vector was analyzed using immunofluorescence to amplify the mCherry signal and enhance its detection, especially in small neuronal elements such as fine processes. Transduced cell bodies were found in a large area of S1BF (±0.5 mm around the needle track along the anteroposterior axis) mainly localized in layers IV/V/VI (**Figure 1B**). In addition, many fibers were also transduced (**Figure 1C**) and covered a larger area than cell bodies (±1 mm around the needle track along the anteroposterior axis). Transduced fibers were found in all cortical layers. If all transduced cell bodies and fibers are taken into account, the viral vector has diffused over half of the entire S1BF area. The cellular specificity of the vector was determined by analyzing mCherry expression in the two major cell types transduced by the vector (**Figure 1D**). Co-localization between NeuN/mCherry (revealing transduced neurons) and GS/mCherry (revealing transduced astrocytes) was quantified. The vector preferentially

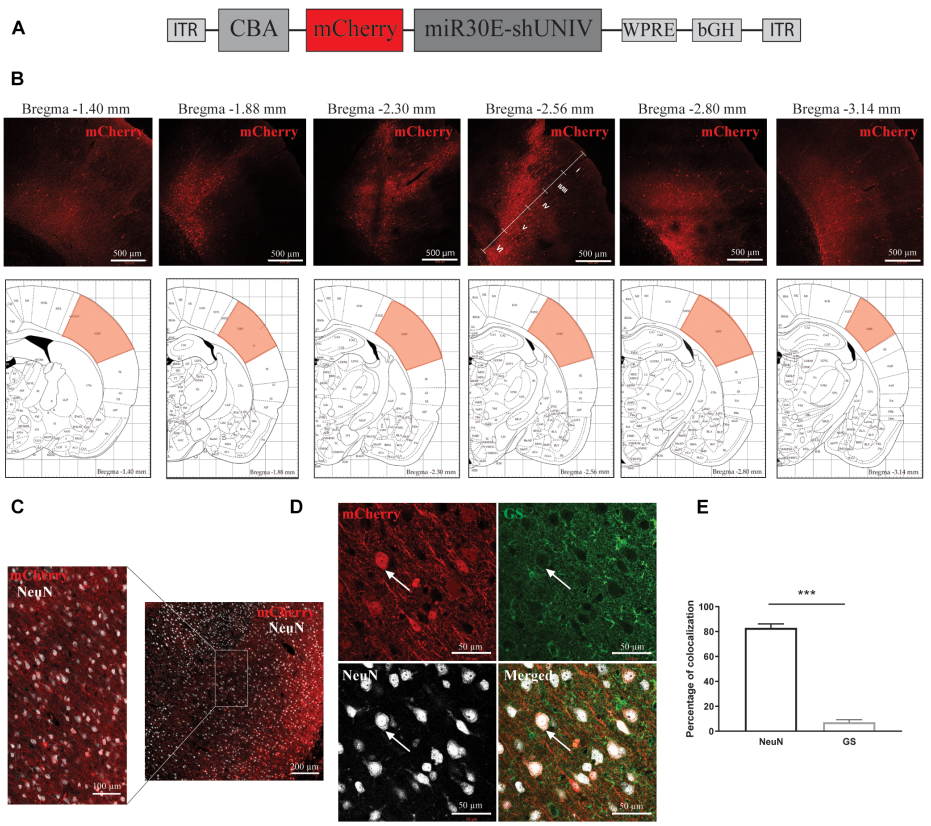

FIGURE 1 | Large diffusion and neuronal specificity of the AAV2/DJ-CBA-mCherry-miR30E-shUNIV vector within the S1BF area of the rat cerebral cortex. **(A)** Schematic representation of the viral vector construction used to target neurons. The mCherry transgene was placed under the control of a CBA promoter. The shUNIV is a non-coding sequence embedded in a miR30E sequence. **(B)** Confocal mosaic pictures of the mCherry signal (reporter protein) after immunolabeling of coronal brain sections taken at 20× magnification showing the diffusion of the viral vector in the cerebral cortex along the anteroposterior axis (upper panels). The first picture was taken from a section at Bregma –1.40 mm and the last one from a section at Bregma –3.14 mm. On the fourth picture, the position of the different cortical layers is indicated. Scale bar = 500 µm. The lower panels represent schemes taken from the Paxinos rat atlas (Paxinos and Watson, 1996). Each of the six schemes corresponds to the bregma level presented in the panel above. The area colored in red corresponds to S1BF, the targeted area. **(C)** Representative confocal pictures of the transduced area in a coronal brain section submitted to a co-immunolabeling for mCherry and the neuronal marker NeuN. The right part of the panel represents a mosaic picture (5 × 5 at 20× magnification) of the transduced area in S1BF. Scale bar = 200 µm. The left part of the panel represents a portion of the transduced area at 20× magnification. Scale bar = 100 µm. **(D)** Representative confocal pictures at high magnification (40×) of S1BF 3 weeks after the injection of the viral vector and submitted to a co-immunolabeling for mCherry, NeuN and GS. The white arrow indicates a typical transduced neuron. Scale bar = 50 µm. **(E)** Quantification of the percentage of mCherry-positive/NeuN-positive cells and mCherry-positive/GS-positive cells. Data are presented as mean ± SEM. Quantification was performed on two to six images per section, six sections per animal, from two animals. Statistical analysis was performed using a Student's *t*-test. ***$p < 0.001$.

and largely transduced neurons over astrocytes (89.44% ± 0.99 vs. 3.18% ± 0.66, respectively, **Figure 1E**). Moreover, with the dose used (see section "Materials and Methods") and a single injection, the viral vector was able to transduce 34% of NeuN-positive neurons within the transduced area.

Large Diffusion in the Rat S1BF Area and Astrocyte-Specific Expression of the Transgene With an AAV2/DJ Vector Containing a G1B3 Promoter

A second construct was made by replacing the CBA promoter with a modified version of the astrocytic promoter GfaABC1D (Merienne et al., 2017, **Figure 2A**). Three copies of the B enhancer were integrated to improve transgene expression in astrocytes [GfaABC1D(B3), hereafter called G1B3] (Merienne et al., 2017). The diffusion of this newly made AAV2/DJ-G1B3-mCherry-mir30E-shUNIV viral vector was analyzed following a single injection in the S1BF area of the rat (same stereotaxic coordinates as for the AAV2/DJ-CBA-mCherry-mir30E-shUNIV above). Three weeks after the injection, detection of the mCherry signal was made by performing immunolabeling on brain sections. Transduced cell bodies were found in a restricted part of the barrel cortex (±0.2 mm around the needle track). Transduced cell bodies were found to be mainly localized in layers V/VI of the barrel cortex (**Figure 2B**). Many transduced processes were also visible all around cell bodies (**Figure 2C**). Transduced processes were found in a larger area compared to cell bodies (±1 mm around the needle track along the anteroposterior axis). All cortical layers exhibited transduced processes. Consequently, the estimated transduced area covered half of the S1BF. Again, the cellular specificity of the vector was determined by analyzing the fluorescent signal found in the two main cell types transduced by the vector (**Figure 2D**). Co-localization between NeuN/mCherry and GS/mCherry was quantified. The vector preferentially and largely transduced astrocytes over neurons (76.99% ± 1.72 vs. 11.99% ± 1.29, respectively, **Figure 2E**). With the dose used (see section "Materials and Methods") and a single injection, approximately 70% of GS-positive cortical astrocytes were transduced by the viral vector within the transduced area.

Efficient Downregulation of Both Neuronal MCT2 mRNA and Protein Expression *in vitro* as Well as *in vivo* Using the Same AAV2/DJ-CBA-mCherry-mir30E-shMCT2 Viral Vector

A viral vector derived from the initial AAV2/DJ-CBA vector was created in order to target MCT2 in neurons. In addition to the vector used to characterize the diffusion (used here as control), one construct was made using a shRNA sequence against MCT2 (shMCT2) embedded in mir30E sequence (**Figure 3A**). Then, mixed primary cultures of rat cortical neurons and astrocytes were transduced with increasing doses of each viral vector named CBA-shUNIV and CBA-shMCT2 at day 5 *in vitro*. After 12 days of culture, both MCT2 mRNA and protein expression levels were determined. It was found that MCT2 mRNA expression significantly decreased with CBA-shMCT2 (reaching a decrease of 62% at the highest dose), while its expression level remained constant at all doses tested when cells were transduced with CBA-shUNIV (**Figure 3B**). At the protein level, both the control and the targeting vectors caused an initial decrease in expression of MCT2 at MOI 2,000 although it did not reach significance and it remained constant over doses [(F[4,23] = 1.252; p = 0.3172), **Figure 3C**]. However, at the highest dose, the decrease in MCT2 protein expression observed with CBA-shMCT2 was more important than with the control vector and became significant compared to the non-transduced condition (F[4,24] = 5.547; p = 0.0028). This difference between the two vectors was clearly visible on Western blots (**Figure 3D**). At the highest dose, the downregulation with CBA-shMCT2 reached 65% compared to the non-transduced condition. Considering the high sequence homology between MCT2 and two other MCT isoforms, MCT1 and MCT4, the specificity of the downregulation was verified by quantifying both MCT1 and MCT4 expression (**Figure 4**). The expression levels of both MCT1 mRNA (**Figure 4A**) and protein (**Figure 4B**) were not modified with both the shUNIV-containing and the shMCT2-containing vectors, at all doses tested. Representative Western blots illustrate the unchanged MCT1 protein levels in the different conditions (**Figure 4C**). The expression levels of both MCT4 mRNA (**Figure 4D**) and protein (**Figure 4E**) were unaltered with shUNIV-containing and shMCT2-containing vectors at all doses tested. Representative Western blots illustrate the unchanged MCT4 protein levels between the non-transduced condition and the highest viral dose with both vectors (**Figure 4F**).

The same vectors were then injected in the S1BF area of the rat brain. First, MCT2 mRNA levels were significantly decreased, by 26%, after the injection of the CBA-shMCT2 viral vector compared to the control CBA-shUNIV viral vector (**Figure 3E**). The downregulation at the protein level reached 54% after the injection of the CBA-shMCT2 viral vector (**Figure 3F**). The significant decrease of MCT2 protein expression obtained after injection of the CBA-shMCT2 viral vector was clearly visible on representative Western blots compared to the expression after treatment with the CBA-shUNIV viral vector (**Figure 3G**). To verify the specificity of the downregulation, expression of both MCT1 and MCT4 was quantified after the injection of either the CBA-shUNIV or the CBA-shMCT2 viral vector. No significant difference in MCT1 mRNA (**Figure 4G**) and protein (**Figure 4H**) expression was detected using each of these the two viral vectors. Representative Western blots illustrate the similar MCT1 protein levels observed with both vectors (**Figure 4I**). No significant difference in MCT4 mRNA (**Figure 4J**) and protein (**Figure 4K**) expression was found between the two viral vectors. Representative Western blots illustrate the lack of difference in MCT4 protein expression following the injection of the CBA-shUNIV and CBA-shMCT2 vectors (**Figure 4L**).

Downregulation of a protein involved in brain metabolism can cause a cellular stress and be harmful for the tissue. The presence of cell death and astrogliosis in the barrel cortex was analyzed after the injection of each viral vector in order to detect putative deleterious effects associated with the downregulation of

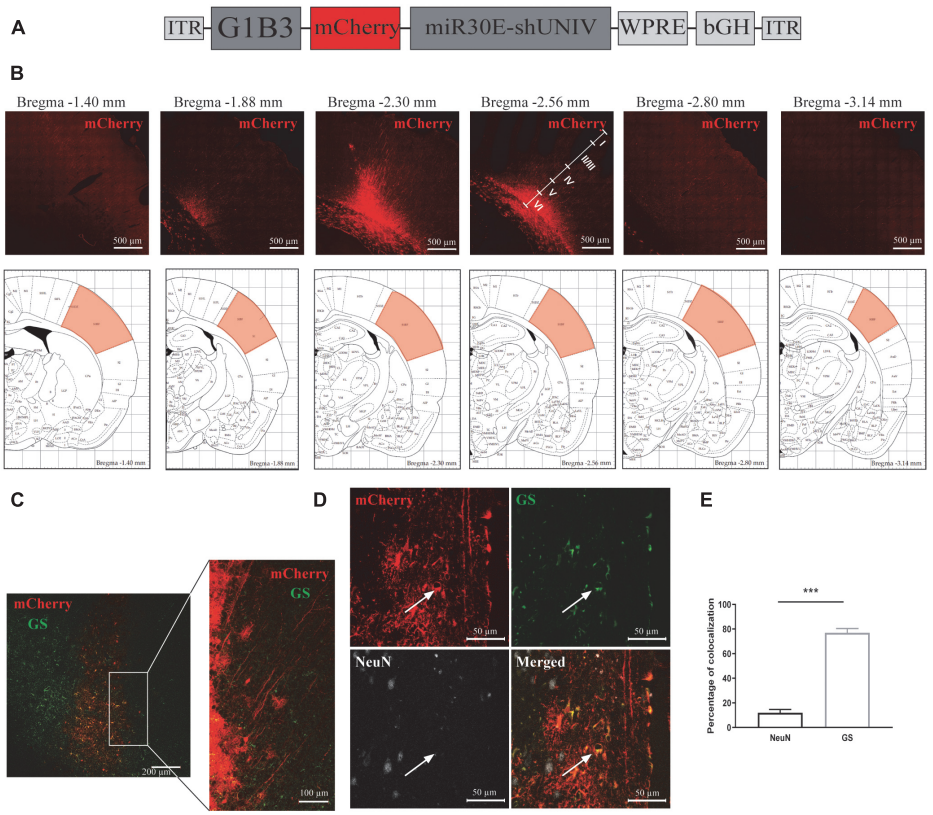

FIGURE 2 | Large diffusion and astrocytic specificity of the AAV2/DJ-G1B3-mCherry-miR30E-shUNIV vector within the S1BF area of the rat cerebral cortex. **(A)** Schematic representation of the viral vector construction used to target astrocytes. The mCherry transgene was placed under the control of a G1B3 promoter. The shUNIV is a non-coding sequence embedded in a miR30E sequence. **(B)** Confocal mosaic pictures of the mCherry signal (reporter protein) after immunolabeling of coronal brain sections taken at 20× magnification showing the diffusion of the viral vector in the cerebral cortex along the anteroposterior axis (upper panels). The first picture was taken at bregma –1.40 mm and the last one at Bregma –3.14 mm. On the fourth picture, the position of the different cortical layers is indicated. Scale bar = 500 µm. The lower panels represent schemes taken from the Paxinos rat atlas (Paxinos and Watson, 1996). Each of the six schemes corresponds to the bregma level presented in the panel above. The red area corresponds to S1BF, the targeted area. **(C)** Representative confocal pictures of the transduced area in a coronal brain section submitted to a co-immunolabeling for mCherry and the astrocytic marker GS. The left panel represents a mosaic picture (5 × 5 at 20× magnification) of the transduced area in S1BF. Scale bar = 200 µm. The right picture represents a portion of the transduced area at 20× magnification. Scale bar = 100 µm. **(D)** Representative confocal pictures at high magnification (40×) of S1BF 3 weeks after the injection of the viral vector and submitted to a co-immunolabeling for mCherry, NeuN and GS. The white arrow indicates a typical transduced astrocyte. Scale bar = 50 µm. **(E)** Quantification of the percentage of mCherry-positive/NeuN-positive cells and mCherry-positive/GS-positive cells. Data are presented as mean ± SEM. Quantification was performed on two to six images per section, six sections per animal, from two animals. Statistical analysis was performed using a Student's *t*-test. ***$p < 0.001$.

MCT2. NeuN and GS mRNA levels were quantified to verify the absence of neuronal and astrocytic death (**Figure 4M**). After the injection of the CBA-shMCT2 vector, no significant difference neither in the expression of the neuronal marker (NeuN) nor in the astrocytic marker (GS) was observed compared with the injection of the control CBA-shUNIV vector. In parallel, the presence of astrogliosis was verified with GFAP staining (**Figure 4N**). After the injection of both viral vectors, a similar pattern of astrogliosis was observed between PBS infusion, CBA-shUNIV and CBA-shMCT2 vectors. As expected, at the site of the needle track, a strong astrogliosis occurred for both viral vectors due to mechanical damage caused by the injection itself. In non-transduced areas, no sign of astrogliosis was observed, with low expression of GFAP and astrocytes exhibiting a normal, non-hypertrophied shape. In transduced areas but away from the needle track, some reactive astrocytes (i.e., GFAP-positive and hypertrophied) were observed but with a similar occurrence for both vectors.

Efficient Downregulation of Both Astrocytic MCT4 mRNA and Protein Expression *in vitro* as Well as *in vivo* Using the Same AAV2/DJ-G1B3-mCherry-miR30E-shMCT4 Viral Vector

Based on the previously described vector to target astrocytes, two viral vectors were created in order to downregulate MCT4 expression in astrocytes. Two constructs were made in which a shRNA sequence against MCT4 (called either shMCT4.1 or shMCT4.2) embedded in a miR30E sequence

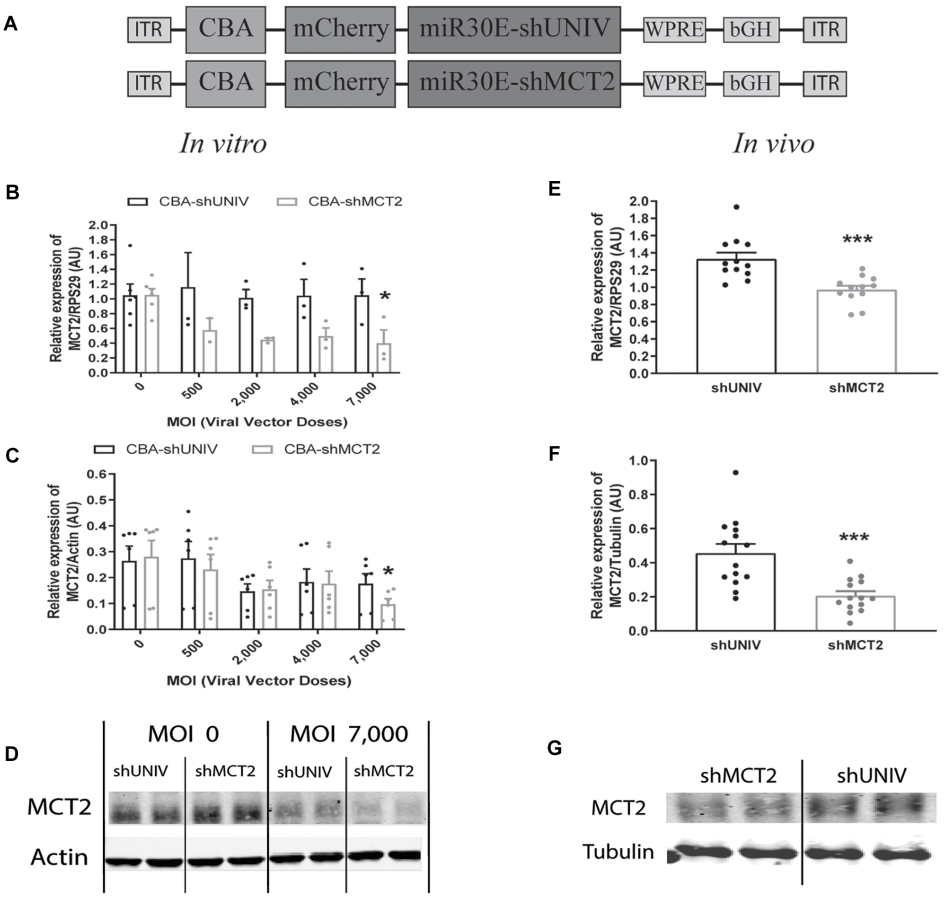

FIGURE 3 | Neuronal downregulation of MCT2 expression *in vitro* and *in vivo* using an AAV2/DJ-CBA-mCherry-miR30E-shMCT2 viral vector. **(A)** Schematic representation of the control (shUNIV) and shMCT2-containing constructs used to generate the neuron-specific AAV2/DJ-based viral vectors for MCT2 invalidation experiments. The shUNIV is a non-coding sequence embedded in a miR30E sequence. The shMCT2 sequence embedded in a miR30E sequence was designed to specifically target and downregulate rat MCT2 expression. **(B–D)** Impact of AAV2/DJ-CBA-shMCT2 vector on neuronal MCT2 expression *in vitro*. Mixed primary cultures of rat cortical neurons and astrocytes were transduced with either the shUNIV-containing or the shMCT2-contining viral vector at increasing doses. MCT2 mRNA **(B)** and protein **(C)** levels have been determined by RT-qPCR and Western blot, respectively. Representative Western blots **(D)** illustrate the downregulation of MCT2 protein expression obtained at the highest viral dose with both vectors. Data are presented as mean ± SEM. $N = 3$. $n = 6$. Statistical analysis was performed using a one-way ANOVA followed by a Dunnett's multiple comparison test for each viral condition. $^{*}p < 0.05$ (compared to the non-transduced condition for each vector). **(E–G)** Impact of AAV2/DJ-CBA-shMCT2 on MCT2 expression *in vivo*. Rats received a bilateral single injection with either the shUNIV or the shMCT2 viral vector. MCT2 mRNA **(E)** and protein **(F)** expression have been determined by RT-qPCR and Western blot, respectively. Representative Western blots **(G)** illustrate the downregulation of MCT2 protein expression with the shMCT2 viral vector *vs.* the shUNIV viral vector. Data are presented as mean ± SEM. $N = 7$. $n = 2$. Statistical analysis was performed using a Student's *t*-test. $^{***}p < 0.001$. MOI, multiplicity of infection.

was placed under the control of the G1B3 promoter while the original AAV2/DJ-G1B3-mCherry-miR30E-shUNIV viral vector was used as control (**Figure 5A**). Then, mixed primary cultures of rat cortical neurons and astrocytes were transduced at increasing doses of each viral vector. MCT4 mRNA expression levels decreased significantly and proportionally to the dose using the G1B3-shMCT4.2 vector but neither with the G1B3-shMCT4.1 vector nor with the control G1B3-shUNIV vector (**Figure 5B**). At the highest dose, the expression was decreased by 75%. The same profile of downregulation was found at the protein level (**Figure 5C**). Quantification revealed a decreased expression of the MCT4 protein proportional to the viral dose of G1B3-shMCT4.2 used, while no effect was observed with the G1B3-shMCT4.1 vector and the control G1B3-shUNIV vector. Representative Western blots illustrate the downregulation obtained at the highest dose, which reached 60% (**Figure 5D**). Considering the high sequence homology of MCT4 with MCT1 and MCT2, the downregulation specificity was verified by quantifying MCT1 and MCT2 expression after transduction with each viral vector (**Figure 6**). The levels of MCT1 mRNA (**Figure 6A**) and protein (**Figure 6B**) were not significantly modified at any dose of either G1B3-shUNIV, G1B3-shMCT4.1 or G1B3-shMCT4.2. Representative Western blots illustrate the absence of change in MCT1 protein expression at the highest dose of all vectors compared to no transduction (**Figure 6C**). In parallel, the levels of MCT2 mRNA (**Figure 6D**) and protein (**Figure 6E**) were unchanged for any tested dose of each viral

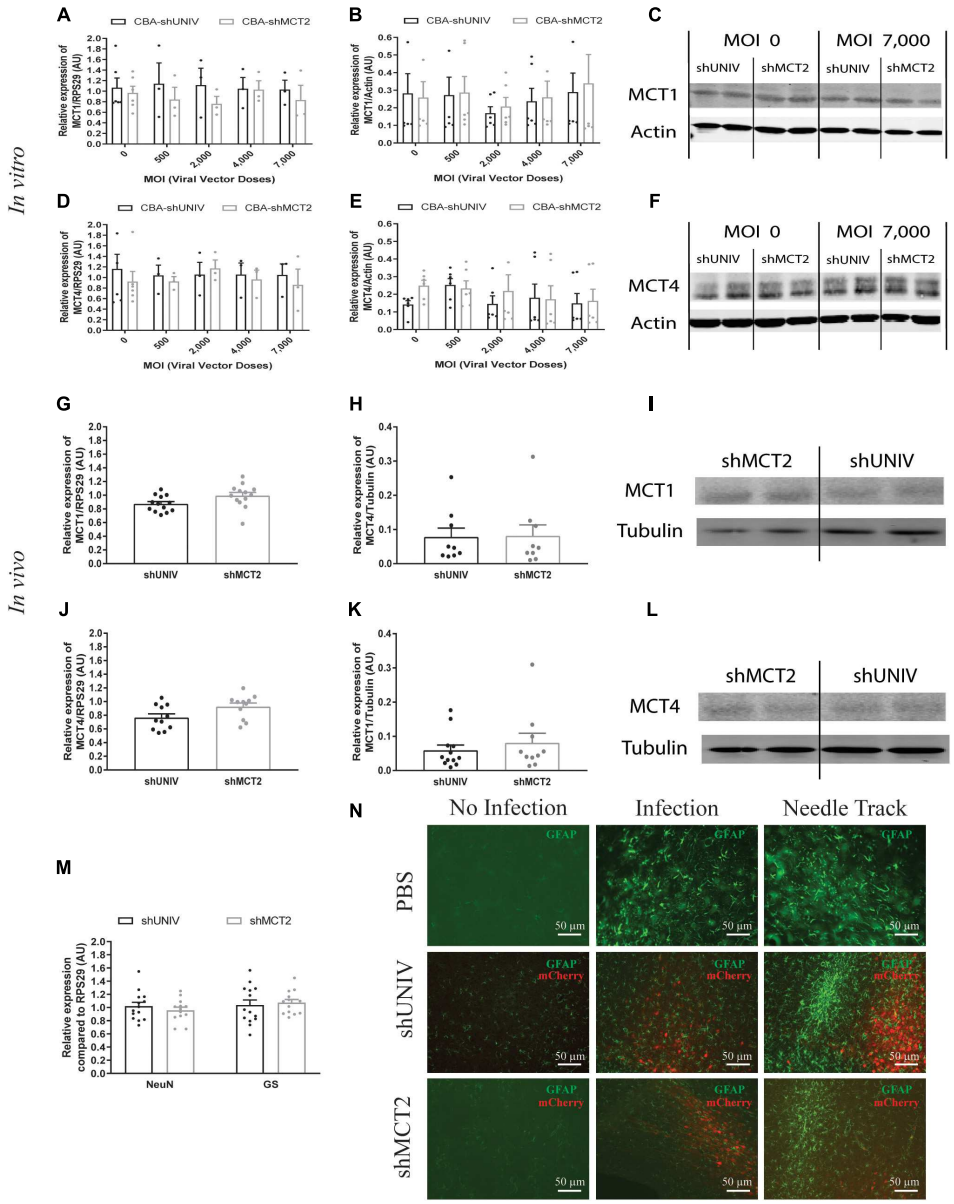

FIGURE 4 | No significant effect of the AAV2/DJ-CBA-mCherry-miR30E-shMCT2 viral vector on MCT1 and MCT4 expression as well as on cell survival or astrogliosis**. (A–C)** Impact of AAV2/DJ-CBA-shMCT2 on astrocytic MCT1 expression *in vitro*. Mixed primary cultures of rat cortical neurons and astrocytes were transduced with either the shUNIV-containing or the shMCT2-containing viral vector at increasing doses. MCT1 mRNA **(A)** and protein **(B)** levels have been determined by RT-qPCR and Western blot, respectively. Representative Western blots **(C)** illustrate the lack of effect of both vectors on MCT1 protein expression. Data are presented as mean ± SEM. $N = 3$. $n = 6$. Statistical analysis was performed using a one-way ANOVA for each viral condition. **(D–F)** Impact of AAV2/DJ-CBA-shMCT2 on MCT4 expression *in vitro*. Mixed primary cultures of neurons and astrocytes were transduced with shUNIV and shMCT2 at increasing doses. Cells were also treated with DETA-NONOate at 600 µM for 16 h to induce MCT4 expression (see section "Materials and Methods"). MCT4 mRNA **(D)** and protein **(E)** levels have been determined by RT-qPCR and Western blot, respectively. Representative Western blots **(F)** illustrate the lack of effect of both vectors on MCT4 protein expression. Data are presented as mean ± SEM. $N = 3$. $n = 6$. Statistical analysis was performed using a one-way ANOVA for each viral condition. **(G–I)** Impact of AAV2/DJ-CBA-shMCT2 on MCT1 expression *in vivo*. Rats received a bilateral single injection with either the shUNIV or the shMCT2 viral vector. MCT1 mRNA **(G)** and protein **(H)** levels have been determined by RT-qPCR and Western blot, respectively. Representative Western blots **(I)** illustrate the lack of effect of both vectors on MCT1 protein expression *in vivo*. Data are presented as mean ± SEM. $N = 7$. $n = 2$. Statistical analysis was performed using a Student's *t*-test comparing shMCT2 *vs.* shUNIV treatment. **(J–L)** Impact of AAV2/DJ-CBA-shMCT2 on MCT4 expression *in vivo*. Rats received a bilateral single injection with either the shUNIV or the shMCT2 viral vector. MCT4 mRNA **(J)** and protein **(K)** expression have been determined by RT-qPCR and Western blot, respectively. Representative Western blots **(L)** illustrate the lack of effect of both vectors on MCT4 protein expression *in vivo*. Data are represented as mean ± SEM. $N = 7$. $n = 2$. Statistical analysis was performed using a Student's *t*-test comparing shMCT2 *vs.* shUNIV treatment. **(M)** Evaluation of neuronal and astrocytic cell death after injection of AAV2/DJ-CBA-shMCT2 in the S1BF area by measuring NeuN and GS mRNA expression. Statistical analysis was performed using a Student's *t*-test comparing shMCT2 vs. shUNIV treatment. **(N)** Representative confocal images of immunolabeling performed against GFAP on brain coronal sections to detect astrogliosis following the injection of PBS, AAV2/DJ-CBA-shUNIV or AAV2/DJ-CBA-shMCT2 in the S1BF area. Scale bar = 50 µm. MOI, Multiplicity of infection.

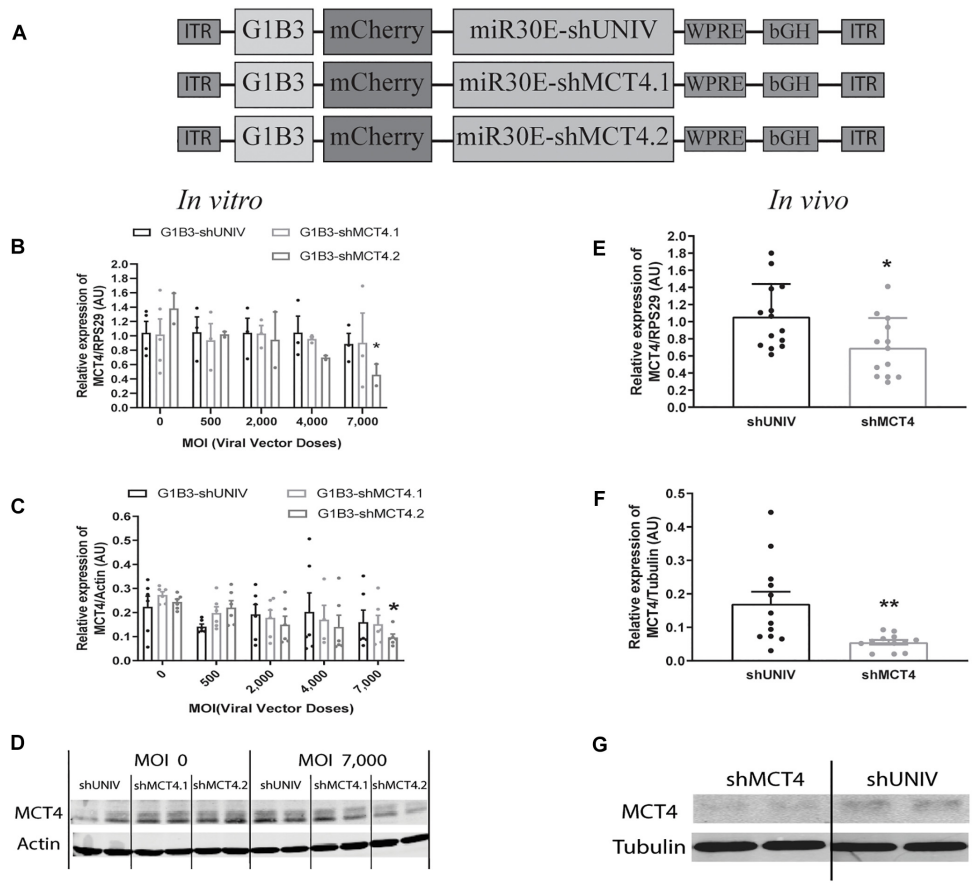

FIGURE 5 | Astrocytic downregulation of MCT4 expression *in vitro* and *in vivo* using AAV2/DJ-G1B3-mCherry-miR30E-shMCT4 viral vectors. **(A)** Schematic representation of the control (shUNIV) and two shMCT4-containing constructs used to generate the astrocyte-specific AAV2/DJ-based viral vectors for MCT4 invalidation experiments. The shUNIV is a non-coding sequence embedded in a miR30E sequence. The two shMCT4 embedded in a miR30E sequence were designed to specifically target and downregulate rat MCT4 expression. **(B–D)** Impact of AAV2/DJ-G1B3-shMCT4 vectors on astrocytic MCT4 expression *in vitro*. Mixed primary cultures of rat cortical neurons and astrocytes were transduced with either the shUNIV-containing, the shMCT4.1-containing or the shMCT4.2-containing vectors at increasing doses. Cells were treated with DETA-NONOate at 600 μM for 16 h to induce MCT4 expression (see section "Materials and Methods"). MCT4 mRNA **(B)** and protein **(C)** expression have been determined by RT-qPCR and Western blot, respectively. Representative Western blots **(D)** illustrate the downregulation of MCT4 protein expression obtained with the shMCT4.2-containing vector vs. the shUNIV-containing and shMCT4.1 vectors. Data are presented as mean ± SEM. $N = 3$. $n = 6$. Statistical analysis was performed using a one-way ANOVA followed by a Dunnett's multiple comparison test for each viral condition. $^{*}p < 0.05$ (compared to the non-transduced condition for each vector). **(E–G)** Impact of AAV2/DJ-G1B3-shMCT4 on MCT4 expression *in vivo*. Rats received a single injection in each S1BF area with either shUNIV-containing or shMCT4.2-containing (called shMCT4) viral vector at a single dose. MCT4 mRNA **(E)** and protein **(F)** levels have been determined by RT-qPCR and Western blot, respectively. Representative Western blots **(G)** illustrate the downregulation of MCT4 protein expression with the shMCT4 viral vector *vs.* the shUNIV viral vector. Data are presented as mean ± SEM. $N = 7$. $n = 2$. Statistical analysis was performed using a Student's *t*-test. $^{*}p < 0.05$; $^{**}p < 0.01$. MOI, Multiplicity of infection.

vector. Representative Western blots illustrate the absence of modification of MCT2 protein expression with either G1B3-shUNIV, G1B3-shMCT4.1, or G1B3-shMCT4.2 at the highest dose (**Figure 6F**).

The control vector (G1B3-shUNIV) and the shMCT4-containing vector showing *in vitro* efficiency in downregulating MCT4 (G1B3-shMCT4.2) were then injected at a single site in the S1BF area of the rat brain (same stereotaxic coordinates as previously indicated). It was found that MCT4 mRNA expression was significantly decreased, by 34%, after the injection of the G1B3-shMCT4.2 vector compared to the shUNIV-containing control vector (**Figure 5E**). Downregulation of the MCT4 protein reached 67% after the injection of the G1B3-shMCT4.2 vector compared to the shUNIV-containing control (**Figure 5F**). Representative Western blots illustrate the significant decrease of MCT4 protein expression obtained in the S1BF area of the rat brain (**Figure 5G**). To verify the specificity of the downregulation obtained *in vivo*, MCT1 and MCT2 expression levels were also quantified after the injection of the G1B3-shMCT4.2 viral vector in the S1BF area. The levels of MCT1 mRNA (**Figure 6G**) and protein (**Figure 6H**) were not significantly different between the two viral vectors. Representative Western blots illustrate the absence of modification of MCT1 protein levels between both vectors (**Figure 6I**). Concerning MCT2, it's mRNA (**Figure 6J**) and protein (**Figure 6K**) expression did not differ between G1B3-shMCT4.2 and G1B3-shUNIV vectors. Representative Western

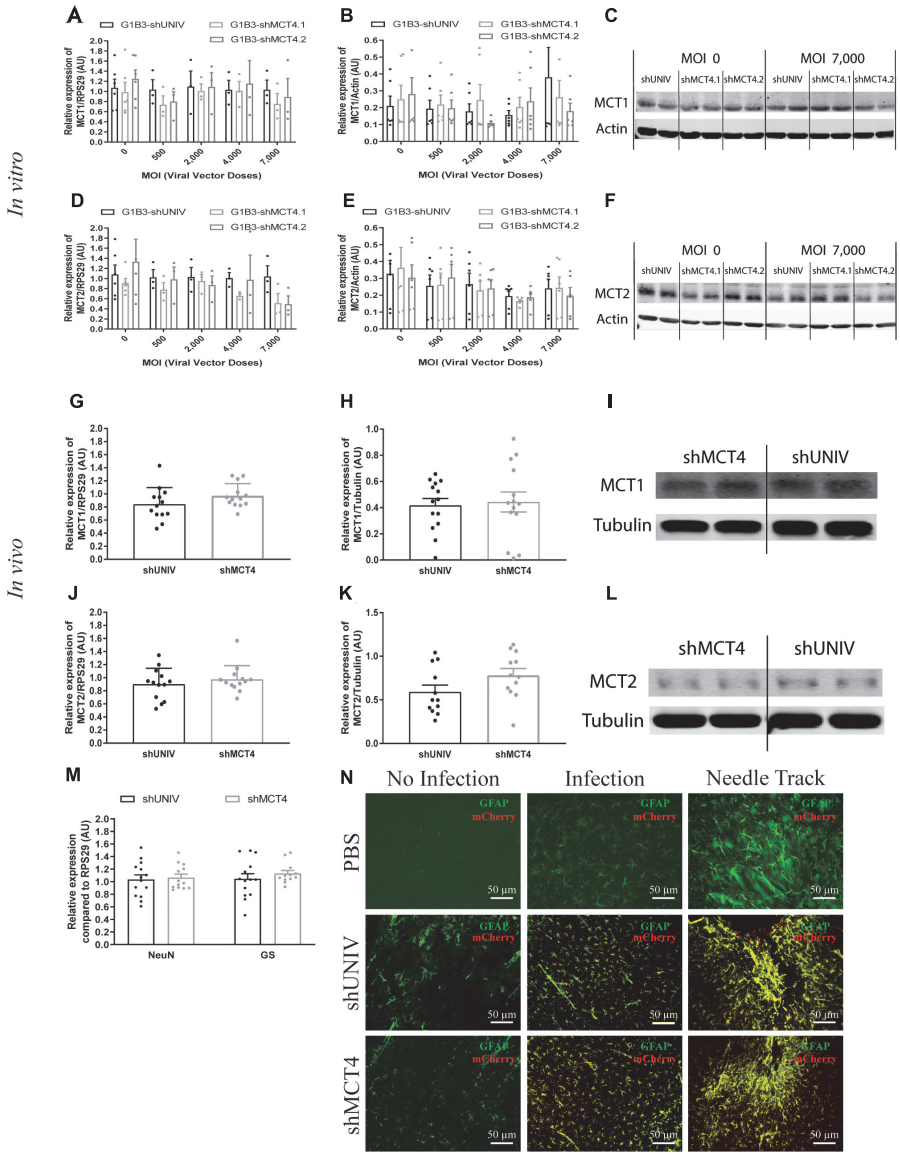

FIGURE 6 | No significant effect of the AAV2/DJ-G1B3-mCherry-miR30E-shMCT4.1 and the AAV2/DJ-G1B3-mCherry-miR30E-shMCT4.2 viral vectors on MCT1 and MCT2 expression as well as on cell survival or astrogliosis. **(A–C)** Impact of AAV2/DJ-G1B3-shMCT4.1 and AAV2/DJ-G1B3-shMCT4.2 on astrocytic MCT1 expression *in vitro*. Mixed primary cultures of rat cortical neurons and astrocytes were transduced with either the shUNIV-containing, the shMCT4.1-containing or the shMCT4.2-containing viral vector at increasing doses. MCT1 mRNA **(A)** and protein **(B)** expression have been determined by RT-qPCR and Western blot, respectively. Representative Western blots **(C)** illustrate the lack of effect of the three vectors on astrocytic MCT1 protein expression. Data are presented as mean ± SEM. $N = 3$. $n = 6$. Statistical analysis was performed using a one-way ANOVA for each viral condition. **(D–F)** Impact of AAV2/DJ-G1B3-shMCT4.1 and AAV2/DJ-G1B3-shMCT4.2 on MCT1 expression *in vitro*. Mixed primary cultures of rat cortical neurons and astrocytes were transduced with either the shUNIV-containing, the shMCT4.1-containing or the shMCT4.2-containing viral vector at increasing doses. MCT2 mRNA **(D)** and protein **(E)** levels have been determined by RT-qPCR and Western blot, respectively. Representative Western blots **(F)** illustrate the lack of effect of the three vectors on neuronal MCT2 protein expression. Data are presented as mean ± SEM. $N = 3$. $n = 6$. Statistical analysis was performed using a one-way ANOVA for each viral condition. **(G–I)** Impact of AAV2/DJ-G1B3-shMCT4.2 on MCT1 expression *in vivo*. Rats received a single injection in each S1BF area with either the shUNIV-containing or the shMCT4.2-containing viral vector at a single dose. MCT1 mRNA **(G)** and protein **(H)** expression have been determined by RT-qPCR and Western blot, respectively. Representative Western blots **(I)** illustrate the lack of effect of both vectors on MCT1 protein expression *in vivo*. Data are presented as mean ± SEM. $N = 7$. $n = 2$. Statistical analysis was performed using a Student's *t*-test comparing shMCT4.2 *vs.* shUNIV treatment. **(J–L)** Impact of AAV2/DJ-G1B3-shMCT4.2 on MCT2 expression *in vivo*. Rats received a bilateral single injection with either the shUNIV-containing or the shMCT4.2-containing viral vector. MCT2 mRNA **(J)** and protein **(K)** expression have been determined by RT-qPCR and Western blot, respectively. Representative Western blots **(L)** illustrate the lack of effect of both vectors on MCT2 protein expression *in vivo*. Data are presented as mean ± SEM. $N = 7$. $n = 2$. Statistical analysis was performed using a Student's *t*-test comparing treatments. **(M)** Evaluation of neuronal and astrocyte cell death after injection of AAV2/DJ-G1B3-shMCT4.2 in the S1BF area by measuring NeuN and GS mRNA expression. Statistical analysis was performed using a Student's *t*-test comparing shMCT4.2 *vs.* shUNIV treatment. **(N)** Representative confocal images of immunolabeling performed against GFAP on brain coronal sections to detect astrogliosis following the injection of PBS, AAV2/DJ-G1B3-shUNIV or AAV2/DJ-G1B3-shMCT4.2 in the S1BF area. Scale bar = 50 µm. MOI, Multiplicity of infection.

blots illustrate this lack of difference in MCT2 protein expression between the two vectors (**Figure 6L**).

Cell death and astrogliosis in the S1BF area were analyzed after the injection of either the G1B3-shMCT4.2 or the control G1B3-shUNIV viral vector. NeuN and GS mRNA levels were quantified to verify the absence of neuronal and astrocytic death, respectively (**Figure 6M**). No sign of neuronal death, as indicated by equivalent NeuN mRNA levels, or astrocytic death, indicated by equivalent GS mRNA levels, was observed when comparing the effect of both vectors. The presence of astrogliosis was evaluated using GFAP immunolabeling on coronal sections of the brain (**Figure 6N**). A similar pattern of astrogliosis was observed between PBS infusion, G1B3-shUNIV, and G1B3-shMCT4 vectors. In non-transduced areas, no astrogliosis was observed with low expression of GFAP and normal astrocytic shape. In transduced areas but away from the needle track, some reactive astrocytes were observed but their number did not differ between the two conditions. As expected at the site of the needle track, a strong astrogliosis occurred but to a similar extent for both viral vectors due to mechanical damage caused by the injection.

DISCUSSION

The initial goal of this study was to develop viral vectors to alternatively target two cell types by using the same capsid while modifying only the promoter of the construct. The two cell types chosen as targets were rat cortical neurons and astrocytes. Usually, viral vectors derived from either lenti- or adeno-associated viruses exhibit a preferential tropism toward either neurons or astrocytes (Wu et al., 2006; Aschauer et al., 2013). The AAV6 has already been used to selectively transduce astrocytes both *in vitro* and *in vivo* (Schober et al., 2016). However, in this study the authors used another serotype to target neurons (AAV2). Because our goal was to alternatively target a specific cell type with the same serotype, we selected the AAV2/DJ viral capsid as it was shown to efficiently transduce different cell types and cell lines (Grimm et al., 2008). Concerning the promoters, it was previously shown that the CBA promoter exhibits a neuronal specificity for expression in the brain (Burger et al., 2004; von Jonquieres et al., 2013; Meunier et al., 2016). We showed here that, in combination with an AAV2/DJ backbone, it conserved its neuronal specificity both *in vitro* and *in vivo*. The astrocytic promoter G1B3 has been shown to confer astrocyte specificity of expression in the mouse striatum (Merienne et al., 2017). Indeed, in combination with the AAV2/5, it was found to drive the expression of a transgene predominantly in astrocytes *in vivo*. The possibility to use the same viral vector to target two different cell types of the same tissue both *in vitro* and *in vivo* presents several advantages. Up to now, the use of AAV-based vectors prevented this possibility since the efficiency of infection of most AAV serotypes *in vitro* was very low (Ellis et al., 2013). It is not the case with the AAV2/DJ that permitted a significant transduction of primary cultures of both rat cortical neurons and astrocytes. It was thus possible to test *in vitro* the efficiency of our selected shRNA sequences in downregulating the expression of the target mRNAs and proteins prior to use them *in vivo*. Moreover, this approach allows to reduce the number of animals needed to assess the usefulness of such newly developed molecular tools, respecting the 3R principles (MacArthur Clarke, 2018).

In addition to their efficiency *in vitro*, the AAV2/DJ-based viral vectors were capable to efficiently transduce both neurons and astrocytes *in vivo* as demonstrated in the rat somatosensory cortex. Despite this convincing demonstration in the somatosensory cortex, it remains to be examined whether this efficiency could vary in different brain regions as previously reported for other AAV serotypes (Aschauer et al., 2013). In addition, it might be interesting to verify if this approach could be extended to other brain cell types such as oligodendrocytes or microglial cells. Although specific promoters for each of these cell types have already been identified (Goldmann et al., 2013; Georgiou et al., 2017), few AAV-based vectors have been developed to target them both *in vitro* and *in vivo*. Oligodendrocytes could be transduced *in vivo* with an AAV-based vector but it was not tested *in vitro* (von Jonquieres et al., 2013). The transduction of microglial cells *in vitro* has been reported using a modified AAV6 capsid and microglial-specific promoters but the transduction was low *in vivo* (Rosario et al., 2016). The use of the AAV2/DJ might be of interest to successfully transduce microglia and oligodendrocytes both *in vitro* and *in vivo*. Another important aspect concerns the capacity of viral vectors to diffuse over a large tissue area. Indeed, we found that AAV2/DJ-based viral vectors exhibited an important spreading capacity, sufficient to cover an area representing more than half of the entire barrel cortex with a single injection. Moreover, AAV2/DJ-based viral vectors efficiently diffused not only laterally but also throughout the cortical thickness, reaching all six cortical layers. This is also an appreciable feature since it is possible to avoid making several injections at different locations to cover the targeted area, reducing the degree of potential damage to the tissue. Interestingly, a difference in the diffusion pattern of the fluorescent signal between CBA-based and G1B3-based vectors was observed. It was recently shown that astrocytes were poorly covered by 2D imaging. Less than 10% of their true volume seemed to be covered by 2D imaging (Bindocci et al., 2017). Indeed, the soma represents only 25% of the total astrocytic volume. The diameter of a process being fine and processes being sparse, a large proportion of the processes are not captured in the focal plan. Moreover, even with the best confocal microscope, processes, and endfeet cannot be clearly seen because of resolution limitations. So, the total volume of astrocytic transduction might be underestimated although the percentage of transduced astrocytes would likely remain the same. Despite these caveats, it seems that both viral vector types based on AAV2/DJ to target alternatively neurons and astrocytes allow to express a transgene in a predominantly cell-specific manner and with a large diffusion within a brain cortical region of interest.

These new tools might be particularly useful to investigate a physiologically relevant question requiring to target the same protein or two closely related proteins in two distinct brain cell types. This is the case for two isoforms of the MCT protein

family: MCT2 and MCT4. MCT2 is specifically expressed in neurons while MCT4 is exclusively expressed by astrocytes in the cortex (Pierre and Pellerin, 2005). Both transporters have been implicated in a mechanism of lactate transfer between the two cell types to ensure an adequate energy substrate supply to neurons as a function of brain activity (Pellerin and Magistretti, 2012). In order to get further insight about the role of these transporters in this mechanism, it became necessary to develop efficient and specific viral vectors to downregulate the expression of those two isoforms in rat, because working with rats rather than mice represent an advantage in certain circumstances (e.g., perform brain imaging). Using the same AAV serotype *in vitro* and *in vivo*, we show here that a significant and specific decrease in expression could be obtained for both MCT2 and MCT4. A variance of distribution is observed for the mRNA and protein quantifications. It can be explained by several reasons. First, for the *in vitro* results, the graphs summarize quantifications from several primary cultures. Even if the basal level of each mRNA/protein could differ between cultures, the degree of down regulation after transduction is the same in every culture. Then, even if the same number of cells is plated, the same dose of viral vector is given (*in vitro* as *in vitro*), leading to a certain unavoidable variability. Moreover, this downregulation was specific of the targeted isoform, since the expression of other isoforms remained unchanged. Because of technical issues related to the sampled area of tissue that cannot be limited to the transduced area and the number of infected cells that is not 100%, the degree of downregulation is underestimated *in vivo*. The use of cell sorting to isolate only transduced cells would be required to have a more precise assessment of the downregulation. Nevertheless, a significant downregulation of MCT2 and MCT4 using AAV-based viral vectors could be evidenced directly from large punches of tissue. It represents an improvement over the previous use of a classical shRNA sequence in a lentiviral vector that led to a slight decrease of the expression of MCT2 in a small fraction of cortical neurons only detectable by immunocytochemistry at the protein level (Mazuel et al., 2017). Considering that, despite the smaller decrease in MCT2 protein expression detected previously, functional effects (notably on the BOLD fMRI response during whisker stimulation) were evidenced with the lentiviral-based vector (Mazuel et al., 2017), it is likely that the new AAV-based vectors should provide more efficient tools to explore the importance of MCTs in specific brain functions.

Apart from their higher degree of transduction efficiency, and considering the high sequence homology between the different MCTs (Halestrap, 2013), the cell specificity of each AAV-based viral vector for each MCT in each cell type is another advantage. Indeed, the use of a miR30 backbone and cell-specific promoters proved to be sufficient to obtain such a specificity.

Another important issue was the possible toxicity of the AAV-based vectors. Indeed, at high doses, viral vectors can cause cell death (Colella et al., 2018; Hinderer et al., 2018). Moreover, strong and uncontrolled shRNA expression could contribute to toxicity. Although cultured astrocytes showed no sign of toxicity for the range of doses tested, we noticed that low doses of AAV2/DJ-based viral vectors caused a partial decrease of MCT2 protein expression that does not seem related to cell death of cultured neurons (since actin expression remained constant between conditions). This effect was not dose-dependent over the range of doses tested and was independent of the transgene. Although the precise reason for this effect is uncertain, primary cultures of neurons are notoriously known to be sensitive to various stressors (Fricker et al., 2018). For example, it was shown that B27-supplement deprivation of cultured cortical neurons leads to partial neuronal cell death (Alvarez-Flores et al., 2019). Cultured neurons might also be particularly sensitive to mCherry overexpression, independently of the serotype. Indeed, expression of the fluorescent reporter protein GFP has been reported to cause toxicity (Liu et al., 1999) and even neuronal death (Detrait et al., 2002). The doses that we used are considered as classical for *in vitro* transduction (Gong et al., 2004; Shevtsova et al., 2004) but cultured neurons seem to be particularly sensitive to viral vector transduction as they modify their transcriptome (Préhaud et al., 2005) or die by apoptosis (Howard et al., 2008). In our case, it seems that neurons reacted to viral transduction by modifying their proteome and decreasing MCT2. This could reflect a modification of their metabolism. Nevertheless, it was still possible in cultured neurons to unravel a significant downregulating effect of the transgene at the highest viral vector dose used. The use of a miR30E backbone for the shRNA sequence may have contributed to the absence of cell death. Indeed, it was shown that the addition of this backbone allows the cell to process the shRNA sequence through the endogenous miR30 pathways, which decreases toxicity (Boudreau et al., 2009). Consequently, it can be concluded that the observed decrease in MCT2/MCT4 expression *in vivo* is entirely due to the specific action of the shRNA sequence on the targeted mRNA.

In parallel, the reactive state of the astrocytes in the transduced area was also verified. Indeed, astrogliosis is a protective mechanism of the brain in case of CNS injuries (Sofroniew, 2015). This natural process can become deleterious when the injury or the inflammation is too high. In addition, an uncontrolled astrogliosis can alter the function of neighboring cells. An important astrogliosis just around the needle track was observed while a moderate to low astrogliosis was found in the transduced area. The astrogliosis around the needle track is essentially due to the mechanical damages caused by the needle and the liquid flow. The same degree of astrogliosis was found between PBS and the different viral vectors, highlighting the mechanical cause of this astrogliosis. In the transduced area, it could not be excluded that astrogliosis could contribute to counterbalance the downregulation of MCT4 observed with the shMCT4, thus partly masking the effective degree of MCT4 downregulation. Indeed, it was previously shown that reactive astrocytes become more glycolytic (Iglesias et al., 2017) and thus could express more MCT4, as it was shown for astrocytes *in vitro* submitted to hypoxia (Rosafio and Pellerin, 2014) or *in vivo* after ischemia (Rosafio et al., 2016).

In conclusion, unique viral tools have been successfully created that largely diffuse in the somatosensory cortex and that can specifically target neurons or astrocytes depending on

the promoter used. Moreover, associated to a miR30E-shRNA strategy, an isoform-specific downregulation could be obtained with no sign of toxicity *in vivo*. In the present study, these tools have been used to target two isoforms of the MCT family, MCT2, and MCT4. Such tools will be particularly useful to study the precise role of MCTs in brain energy metabolism and brain functions *in vivo*, especially for aspects for which invalidation in rats represents an advantage over the use of transgenic mice. Until now, several studies have been conducted using pharmacological antagonists (Dimmer et al., 2000; Colen et al., 2006). To inhibit MCTs, CHC [2-Cyano-3-(4-hydroxyphenyl)-2-propenoic acid] has been widely used. However, CHC also targets other proteins such as the mitochondrial pyruvate carrier (Gray et al., 2015). To circumvent this problem, RNA interference has been used in the past (Maekawa et al., 2008; Suzuki et al., 2011), and later it was associated with a viral vector approach for an *in vivo* use. Recently, functional effects of the downregulation of MCT2 *in vivo* were detected using a lentiviral approach targeting MCT2 (Mazuel et al., 2017). However, the extent of the downregulation was limited and might preclude more complex investigations such as behavioral studies. Our new AAV-based viral vectors will not only allow to overcome these caveats but they could also be used in the future to target other proteins of interest in the central nervous system requiring a similar strategy.

DATA AVAILABILITY

The datasets generated for this study are available on request to the corresponding author.

AUTHOR CONTRIBUTIONS

CP and ND designed and produced the viral vectors. CJ performed the *in vivo* and *in vitro* experiments. CJ and LP wrote the manuscript. CJ, ND, A-KB-S, and LP corrected the manuscript.

FUNDING

A-KB-S and LP have received financial support from an international French (ANR)/Swiss (FNS) grant (Grant Nos. ANR-15-CE37-0012 and FNS n° 310030E-164271). LP also received financial support for this project from the program IdEx Bordeaux (Grant No. ANR-10-IDEX-03-02). A-KB-S also received financial support from the French State in the context of the "Investments for the future" Programme IdEx and the LabEx TRAIL (Grant Nos. ANR-10-IDEX and ANR-10-LABX-57).

ACKNOWLEDGMENTS

The authors would like to thank Maria Rey for producing the viral vectors.

SUPPLEMENTARY MATERIAL

The Supplementary Material for this article can be found online at: https://www.frontiersin.org/articles/10.3389/fnmol.2019.00201/full#supplementary-material

REFERENCES

Alvarez-Flores, M. P., Hébert, A., Gouelle, C., Geller, S., Chudzinski-Tavassi, A. M., and Pellerin, L. (2019). Neuroprotective effect of rLosac on supplement-deprived mouse cultured cortical neurons involves maintenance of monocarboxylate transporter MCT2 protein levels. *J. Neurochem.* 148, 80–96. doi: 10.1111/jnc.14617

Aschauer, D. F., Kreuz, S., and Rumpel, S. (2013). Analysis of transduction efficiency, tropism and axonal transport of AAV serotypes 1, 2, 5, 6, 8 and 9 in the mouse brain. *PLoS One* 8:e76310. doi: 10.1371/journal.pone.0076310

Bindocci, E., Savtchouk, I., Liaudet, N., Becker, D., Carriero, G., and Volterra, A. (2017). Three-dimensional Ca2+ imaging advances understanding of astrocyte biology. *Science* 356:eaai8185. doi: 10.1126/science.aai8185

Boudreau, R. L., Martins, I., and Davidson, B. L. (2009). Artificial MicroRNAs as siRNA shuttles: improved safety as compared to shRNAs *in vitro* and *in vivo*. *Am. Soc. Gene Ther.* 17, 169–175. doi: 10.1038/mt.2008.231

Brenner, M., Kisseberth, W. C., Su, Y., Besnard, F., and Messing, A. (1994). GFAP promoter directs astrocyte-specific expression in transgenic mice. *J. Neurosci.* 14(3 Pt 1), 1030–1037. doi: 10.1523/JNEUROSCI.14-03-01030.1994

Burger, C., Gorbatyuk, O. S., Velardo, M. J., Peden, C. S., Williams, P., and Muzyczka, N. (2004). Recombinant AAV Viral vectors pseudotyped with viral capsids from serotypes 1, 2, and 5 display differential efficiency and cell tropism after delivery to different regions of the central nervous system. *Mol. Ther.* 10, 302–317. doi: 10.1016/j.ymthe.2004.05.024

Calcedo, R., Vandenberghe, L. H., Gao, G., Lin, J., and Wilson, J. M. (2009). Worldwide epidemiology of neutralizing antibodies to adeno-associated viruses. *J. Infect. Dis.* 199, 381–390. doi: 10.1086/595830

Colella, P., Ronzitti, G., and Mingozzi, F. (2018). Emerging issued in AAV-Mediated *in Vivo* gene therapy. *Mol. Ther. Methods Clin. Dev.* 8, 87–104. doi: 10.1016/j.omtm.2017.11.007

Colen, C. B., Seraji-Bozorgzad, N., Marples, B., Galloway, M. P., Sloan, A. E., and Mathupala, S. P. (2006). Metabolic remodeling of malignant gliomas for enhanced sensitization during radiotherapy: an *in vitro* study. *Neurosurgery* 59, 1313–1324. doi: 10.1227/01.NEU.0000249218.65332.BF

Davidson, B. L., Stein, C. S., Heth, J. A., Martins, I., Kotin, R. M., and Chiorini, J. A. (2000). Recombinant adeno-associated virus type 2, 4, and 5 vectors: transduction of variant cell types and regions in the mammalian central nervous system. *Proc. Natl. Acad. Sci. U.S.A.* 97, 3428–3432. doi: 10.1073/pnas.050581197

Daya, S., and Berns, K. I. (2008). Gene therapy using adeno-associated virus vectors. *Clin. Microbiol. Rev.* 21, 583–593. doi: 10.1128/CMR.00008-08

De Leeuw, B., Su, M., ter Horst, M., Iwata, S., Rodijk, M., and Brenner, M. (2006). Increased glia-specific transgene expression with glial fibrillary acidic protein promoters containing multiple enhancer elements. *J. Neurosci. Res.* 83, 744–753. doi: 10.1002/jnr.20776

de Solis, C. A., Hosek, M. P., Holehonnur, R., Ho, A., Banerjee, A., and Ploski, J. E. (2017). Adeno-associated viral serotypes differentially transduce inhibitory neurons within the rat amygdala. *Brain Res.* 1672, 148–162. doi: 10.1016/j.brainres.2017.07.023

Detrait, E. R., Bowers, W. J., Halterman, M. W., Giuliano, R. E., Bennice, L., Federoff, H. J., et al. (2002). Reporter gene transfer induces apoptosis in primary cortical neurons. *Mol. Ther.* 5, 723–730. doi: 10.1006/mthe.2002.0609

Dimmer, K. S., Friedrich, B., Lang, F., Deitmer, J. W., and Bröer, S. (2000). The low-affinity monocarboxylate transporter MCT4 is adapted to the export of lactate in highly glycolytic cells. *Biochem. J.* 350, 219–227. doi: 10.1042/bj3500219

Dismuke, D. J., Tenenbaum, L., and Samulski, R. J. (2013). Biosafety of recombinant adeno-associated virus vectors. *Curr. Gene Ther.* 13, 1–19. doi: 10.2174/1566523211313660007

Ellis, B. L., Hirsch, M. L., Barker, J. C., Connelly, J. P., Steininger, I. I. I. R. J., and Porteus, M. H. (2013). A survey of ex vivo/in vitro transduction efficiency of mammalian primary cells and cell lines with Nine natural adeno-associated virus (AAV1-9) and one engineered adeno-associated virus serotype. *Virol. J.* 10:74. doi: 10.1186/1743-422X-10-74

Fellmann, C., Hoffmann, T., Sridhar, V., Hopfgartner, B., Muhar, M., and Zuber, J. (2013). An Optimized microRNA backbone for effective single-copy RNAi. *Cell Rep.* 5, 1704–1713. doi: 10.1016/j.celrep.2013.11.020

Flotte, T. R., and Berns, K. I. (2005). Adeno-associated virus: a ubiquitous commensal of mammals. *Hum. Gene Ther.* 16, 401–407. doi: 10.1089/hum.2005.16.401

Fricker, M., Tolkovsky, A. M., Borutaite, V., Coleman, M., and Brown, G. C. (2018). Neuronal cell death. *Physiol. Rev.* 98, 813–880. doi: 10.1152/physrev.00011.2017

Georgiou, E., Sidiropoulou, K., Richter, J., Papaneophytou, C., Sargiannidou, I., and Leopa, K. A. (2017). Gene therapy targeting oligodendrocytes provides therapeutic benefit in a leukodystrophy model. *Brain* 140, 599–616. doi: 10.1093/brain/aww351

Goldmann, T., Wieghofer, P., Müller, P. F., Wolf, Y., Varol, D., and Prinz, M. (2013). A new type of microglia gene targeting shows TAK1 to be pivotal in CNS autoimmune inflammation. *Nat. Neurosci.* 16 1618–1628. doi: 10.1038/nn.3531

Gong, Y., Chen, S., Sonntag, C. F., Sumners, C., Klein, R. L., and Meyers, E. M. (2004). Recombinant adeno-associated virus serotype 2 effectively transduces primary rat brain astrocytes and microglia. *Brain Res. Protoc.* 14, 18–24. doi: 10.1016/j.brainresprot.2004.08.001

Gray, L. R., Sultana, R., Rauckhorst, A. J., Oonthonpan, L., Tompkins, S. C., and Taylor, E. B. (2015). Hepatic mitochondrial pyruvate carrier 1 Is required for efficient regulation of gluconeogenesis and whole-body glucose homeostasis. *Cell Metabol.* 22, 669–681. doi: 10.1016/j.cmet.2015.07.027

Gray, S. J., Foti, S. B., Schwartz, J. W., Bachaboina, L., Taylor-Blake, B., and Samulski, R. J. (2011). Optimizing promoters for recombinant adeno-associated virus-mediated gene expression in the peripheral and central nervous system using self-complementary vectors. *Hum. Gene Ther.* 22, 1143–1153. doi: 10.1089/hum.2010.245

Grimm, D., Lee, J. S., Wang, L., Desai, T., Akache, B., and Kay, M. A. (2008). *In Vitro* and *in vivo* gene therapy vector evolution via multispecies interbreeding and retargeting of adeno-associated viruses. *J. Virol.* 82, 5887–5911. doi: 10.1128/JVI.00254-08

Halestrap, A. P. (2013). The SLC16 gene family – structure, role and regulation in health and disease. *Mol. Aspects Med.* 34, 337–349. doi: 10.1016/j.mam.2012.05.003

Halestrap, A. P., and Price, N. T. (1999). The proton-linked monocarboxylate transporter (MCT) family: structure, function and regulation. *Biochem. J.* 343, 281–299. doi: 10.1042/bj3430281

Hinderer, C., Katz, N., Buza, E. L., Dyer, C., Goode, T., and Wilson, J. M. (2018). Severe toxicity in nonhuman primates and piglets following high-dose intravenous administration of an adeno-associated virus vector expression human SMN. *Hum. Gene Ther.* 29, 285–298. doi: 10.1089/hum.2018.015

Hoggan, M. D., Blacklow, N. R., and Rowe, W. P. (1966). Studies of small DNA viruses found in various adenovirus preparations: physical, biological and immunological characteristics. *Proc. Natl. Acad. Sci. U.S.A.* 55, 1467–1474. doi: 10.1073/pnas.55.6.1467

Holehonnur, R., Luong, J. A., Chaturvedi, D., Ho, A., Lella, S. K., Hosek, M. P., et al. (2014). Adeno-associated viral serotypes produce differing titers and differentially transduce neurons within the rat basal and lateral amygdala. *BMC Neurosci.* 15:28. doi: 10.1186/1471-2202-15-28

Howard, D. B., Powers, K., Wang, Y., and Harvey, B. K. (2008). Tropism and toxicity of adeno-associated viral vector serotypes 1, 2, 5, 6, 7, 8, 9 in rat neurons and glia in vitro. *Virology* 372, 24–34. doi: 10.1016/j.virol.2007.10.007

Iglesias, J., Morales, L., and Barreto, G. E. (2017). Metabolic and inflammatory adaptation of reactive astrocytes: role of PPARs. *Mol. Neurobiol.* 54, 2518–2538. doi: 10.1007/s12035-016-9833-2

Jang, M., Lee, S. E., and Cho, I. H. (2018). Adeno-associated viral vector serotype DJ-mediated overexpression of N171-82Q-mutant huntingtin in the striatum of juvenile mice is a new model for huntington's disease. *Front. Cell. Neurosci.* 12:157. doi: 10.3389/fncel.2018.00157

Jiang, F., and Doudna, J. A. (2017). CRISPR – Cas9 structures and mechanisms. *Annu. Rev. Biophys.* 46, 505–529. doi: 10.1146/annurev-biophys-062215-010822

Lee, Y., Messing, A., Su, M., and Brenner, M. (2008). GFAP promoter elements required for region-specific and astrocyte-specific expression. *Glia* 56, 481–493. doi: 10.1002/glia.20622

Liu, G., Martins, I. H., Chiorini, J. A., and Davidson, B. L. (2005). Adeno-associated virus type 4 (AAV4) targets ependymal and astrocytes in the subventricular zone and RMS. *Gene Ther.* 12, 1503–1508.

Liu, H. S., Jan, M. S., Chou, C. K., Chen, P. H., and Ke, N. J. (1999). Is green fluorescent protein toxic to the living cells? *Biochem. Biophys. Res. Commun.* 260, 712–717.

MacArthur Clarke, J. (2018). The 3Rs in research: a contemporary approach to replacement, reduction and refinement. *Br. J. Nutr.* 12, S1–S7. doi: 10.1017/S0007114517002227

Maekawa, F., Minehira, K., Kadomatsu, K., and Pellerin, L. (2008). Basal and stimulated lactate fluxes in primary cultures of astrocytes are differentially controlled by distinct proteins. *J. Neurochem.* 107, 789–798. doi: 10.1111/j.1471-4159.2008.05650.x

Marcillac, F., Brix, B., Repond, C., Jöhren, O., and Pellerin, L. (2011). Nitric oxide induces the expression of the monocarboxylate transporter MCT4 in cultured astrocytes by a cGMP-independent transcriptional activation. *Glia* 59, 1987–1995. doi: 10.1002/glia.21240

Mazuel, L., Blanc, J., Repond, C., Bouchaud, V., Raffard, G., Déglon, N., et al. (2017). A neuronal MCT2 knockdown in the rat somatosensory cortex reduces both the NMR lactate signal and the BOLD response during whisker stimulation. *PLoS One* 12:e0174990. doi: 10.1371/journal.pone.0174990

Merienne, N., Vachey, G., de Longprez, L., Meunier, C., Zimmer, V., and Déglon, N. (2017). The selt-inactivating KamiCas9 system for the editing of CNS disease genes. *Cell Rep.* 20, 2980–2991. doi: 10.1016/j.celrep.2017.08.075

Meunier, C., Merienne, N., Jollé, C., Déglon, N., and Pellerin, L. (2016). Astrocytes are key but indirect contributors to the development of the symptomatology and pathophysiology of huntington's disease. *Glia* 64, 1841–1856. doi: 10.1002/glia.23022

Paxinos, G., and Watson, C. (1996). *Compact*, 3rd Edn, *The Rat Brain in Stereotaxic Coordinates*. San Diego: Academic Press.

Pellerin, L., and Magistretti, P. J. (1994). Glutamate uptake into astrocytes stimulates aerobic glycolysis: a mechanism coupling neuronal activity to glucose utilization. *Proc. Natl. Acad. Sci. U.S.A.* 91, 10625–10629. doi: 10.1073/pnas.91.22.10625

Pellerin, L., and Magistretti, P. J. (2012). Sweet sixteen for ANLS. *J. Cereb. Blood Flow Metab.* 32, 1152–1166. doi: 10.1038/jcbfm.2011.149

Pierre, K., and Pellerin, L. (2005). Monocarboxylate transporters in the central nervous system: distribution, regulation and function. *J. Neurochem.* 94, 1–14. doi: 10.1111/j.1471-4159.2005.03168.x

Préhaud, C., Mégret, F., Lafage, M., and Lafon, M. (2005). Virus infection switches TLR-3-positive human neurons to become strong producers of beta interferon. *J. Virol.* 79, 12893–12904. doi: 10.1128/JVI.79.20.12893-12904.2005

Rao, D. D., Vorhies, J. S., Senzer, N., and Nemunaitis, J. (2009). siRNA vs. shRNA: similarities and differences. *Adv. Drug Deliv. Rev.* 61, 746–759. doi: 10.1016/j.addr.2009.04.004

Rosafio, K., Castillo, X., Hirt, L., and Pellerin, L. (2016). Cell-specific modulation of monocarboxylate transporter expression contributes to the metabolic reprograming taking place following cerebral ischemia. *Neuroscience* 317, 108–120. doi: 10.1016/j.neuroscience.2015.12.052

Rosafio, K., and Pellerin, L. (2014). Oxygen tension controls the expression of the monocarboxylate transporter mct4 in cultured mouse cortical astrocytes via a hypoxia-inducible factor-1α-mediated transcriptional regulation. *Glia* 64, 477–490. doi: 10.1002/glia.22618

Rosario, A. M., Cruz, P. E., Ceballos-Diaz, C., Strickland, M. R., Siemienski, Z., and Chakrabarty, P. (2016). Microglia-specific targeting by novel capsid-modified AAV6 vectors. *Mol. Ther. Methods Clin. Dev.* 3:16026. doi: 10.1038/mtm.2016.26

Schober, A. L., Gagarkin, D. A., Chen, Y., Gao, G., Jacobson, L., and Mongin, A. A. (2016). Recombinant adeno-associated virus serotype 6 (AAV6) potently and preferentially transduced rat astrocytes *in vitro* and *in vivo*. *Front. Cell. Neurosci.* 10:262. doi: 10.3389/fncel.2016.00262

Shevtsova, Z., Malik, J. M. I., Michel, U., Bähr, M., and Kügler, S. (2004). Promoters and serotypes: targeting of adeno-associated virus vectors for gene transfer in the rat central nervous system *in vitro* and *in vivo*. *Exp. Physiol.* 90, 53–59. doi: 10.1113/expphysiol.2004.028159

Sofroniew, M. V. (2015). Astrogliosis. *Cold Spring Harb. Perspect. Biol.* 7:a020420. doi: 10.1101/cshperspect.a020420

Suzuki, A., Stern, S. A., Bozdagi, O., Huntley, G. W., Walker, R. H., and Alberini, C. M. (2011). Astrocyte-neuron lactate transport is required for long-term memory formation. *Cell* 144, 810–823. doi: 10.1016/j.cell.2011.02.018

von Jonquieres, G., Mersmann, N., Klugmann, C. B., Harasta, A. E., Lutz, B., and Klugmann, M. (2013). Glial promoter selectivity following AAV-Delivery to the immature brain. *PLoS One* 8:e65646. doi: 10.1371/journal.pone.0065646

Wang, Z., Ma, H. I., Li, J., Sun, L., Zhang, J., and Xiao, X. (2003). Rapid and highly efficient transduction by double-stranded adeno-associated virus vectors *in vitro* and *in vivo*. *Gene Ther.* 10, 2105–2111. doi: 10.1038/sj.gt.3302133

Wu, Z., Miller, E., Agbandje-McKenna, M., and Samulski, R. J. (2006). α2,3 and α2,6 N-linked sialic acids facilitate efficient binding and transduction by adeno-associated virus types 1 and 6. *J. Virol.* 80, 9093–9103. doi: 10.1128/jvi.00895-06

Conflict of Interest Statement: The authors declare that the research was conducted in the absence of any commercial or financial relationships that could be construed as a potential conflict of interest.

frontiers in Molecular Neuroscience

ORIGINAL RESEARCH
published: 11 September 2019
doi: 10.3389/fnmol.2019.00212

Generation and Characterization of Induced Pluripotent Stem Cells and Retinal Organoids From a Leber's Congenital Amaurosis Patient With Novel *RPE65* Mutations

Guilan Li[1†], Guanjie Gao[1†], Panfeng Wang[1], Xiaojing Song[1], Ping Xu[1], Bingbing Xie[1], Tiancheng Zhou[2], Guangjin Pan[2], Fuhua Peng[3], Qingjiong Zhang[1], Jian Ge[1] and Xiufeng Zhong[1]*

[1] State Key Laboratory of Ophthalmology, Zhongshan Ophthalmic Center, Sun Yat-sen University, Guangzhou, China, [2] Key Laboratory of Regenerative Biology, South China Institute for Stem Cell Biology and Regenerative Medicine, Guangzhou Institutes of Biomedicine and Health, Chinese Academy of Sciences, Guangzhou, China, [3] Department of Neurology, Third Affiliated Hospital of Sun Yat-sen University, Guangzhou, China

RPE65-associated Leber congenital amaurosis (LCA) is one of highly heterogeneous, early onset, severe retinal dystrophies with at least 130 gene mutation sites identified. Their pathogenicity has not been directly clarified due to lack of diseased cells. Here, we generated human-induced pluripotent stem cells (hiPSCs) from one putative LCA patient carrying two novel *RPE65* mutations with c.200T>G (p.L67R) and c.430T>C (p.Y144H), named RPE65-hiPSCs, which were confirmed to contain the same mutations. The RPE65-hiPSCs presented typical morphological features with normal karyotype, expressed pluripotency markers, and developed teratoma in NOD-SCID mice. Moreover, the patient hiPSCs were able to differentiate toward retinal lineage fate and self-form retinal organoids with layered neural retina. All major retinal cell types including photoreceptor and retinal pigment epithelium (RPE) cells were also acquired overtime. Compared to healthy control, RPE cells from patient iPSCs had lower expression of RPE65, but similar phagocytic activity and VEGF secretion level. This study provided the valuable patient specific, disease targeted retinal organoids containing photoreceptor and RPE cells, which would facilitate the study of personalized pathogenic mechanisms of disease, drug screening, and cell replacement therapy.

Keywords: reprogramming, differentiation, retinal organoids, *RPE65* gene mutations, retinal degeneration

OPEN ACCESS

Edited by:
Daniele Dell'Orco,
University of Verona, Italy

Reviewed by:
Knut Stieger,
University of Giessen, Germany
Breandan Kennedy,
University College Dublin, Ireland

****Correspondence:***
Xiufeng Zhong
zhongxf7@mail.sysu.edu.cn

† These authors have contributed equally to this work

Received: *21 March 2019*
Accepted: *20 August 2019*
Published: *11 September 2019*

Citation:
Li G, Gao G, Wang P, Song X, Xu P, Xie B, Zhou T, Pan G, Peng F, Zhang Q, Ge J and Zhong X (2019) Generation and Characterization of Induced Pluripotent Stem Cells and Retinal Organoids From a Leber's Congenital Amaurosis Patient With Novel RPE65 Mutations. Front. Mol. Neurosci. 12:212. doi: 10.3389/fnmol.2019.00212

INTRODUCTION

Leber's congenital amaurosis (LCA) is a group of recessively inherited retinal dystrophies (IRDs) with severe visual impairment, accounts for >5% of all retinal dystrophy and 20% of legal blindness in school-age children. The disease is characterized by vision loss from birth or the first few months of life verified by electroretinogram (ERG) recording with markedly reduced or undetectable rod and cone response, nystagmus, poor pupil light reflex, and variable fundus changes from normal

retinal appearance to severe pigmentary degeneration. The estimated prevalence is 2–3 per 100,000 people worldwide (Koenekoop, 2004; Coussa et al., 2017). To date, at least 20 mutation genes such as *CEP290*, *GUCY2D*, *CRB1*, and *RPE65* have been identified in patients with LCA. These genes were proved to express in photoreceptors or retinal pigment epithelium (RPE) cells of retina, and involved in disparate functional pathways including photoreceptor morphogenesis, visual phototransduction, and visual cycle (Wang et al., 2015; Jacobson et al., 2016; Kumaran et al., 2017).

RPE65 is a 65 kDa isomer hydrolase synthesized in RPE cells. It catalyzes isomerization of all-trans retinyl esters into the chromophore 11-*cis* retinol which is transported into photoreceptors to participate in visual phototransduction (Jin et al., 2005). This process is also called retinoid cycle or visual cycle. Mutations in this gene not only disrupt this functional visual cycle, but also lead to structural degeneration of outer neural retina (NR) and RPE over time, causing irreversible blindness, including LCA, retinal pigmentosa (RP), or cone-rod dystrophies (CORDs) (Bereta et al., 2008). Comprehensive genotyping identified *RPE65* as one of the most prevalent mutated genes in LCA patients, accounting for approximately 3–16% of all LCA cases with the highest in the Caucasian and India population. Although many variants in this gene have been documented, their pathogenicity have not been directly clarified partly due to lack of human *in vitro* disease models (Astuti et al., 2016; Bernardis et al., 2016).

So far, there is no cure for IRDs including LCA. With the advancement of gene and stem cell technology, both gene and cell therapy have been regarded as emerging, promising therapeutics for this kind of diseases (Wiley et al., 2015; Dalkara et al., 2016). RPE65 gene therapy completed phase 3 clinical trial by Russell et al. (2017), and got approved firstly by FDA for the treatment of RPE65-mediated IRD in the United States (Bainbridge et al., 2008). Although treatment effects have been observed with improved light sensitivity and mobility after subretinal administration of AAV-*RPE65* gene complex in both animal models with RPE65 mutations and RPE65-LCA patients, the improved visual function started declining 3 years after treatment and this gene therapy approach could not prevent progress of retinal degeneration with photoreceptor apoptosis, which eventually leads to retinal cell loss including RPE cells and photoreceptors. In addition, having sufficient viable retinal cells has become a prerequisite for successful gene therapy in patients with RPE65 mutations and in other retinal degenerative conditions (Dalkara et al., 2016). Therefore, cell therapy would be in demand alone or combined with gene therapy for replacing the lost or diseased retinal cells to recover the visual function and retinal structures simultaneously, especially in advanced retinal degenerative conditions.

Ten years ago, human induced pluripotent stem cells (hiPSCs) were reprogrammed from human somatic cells with Yamanaka's four transcription factors (Takahashi et al., 2007). This technology provides opportunities for study and treatment of degenerative diseases in a subject-personalized manner since hiPSCs have capacity to differentiate into almost all body cells including retinal cells (Meyer et al., 2009; Zhong et al., 2014). More importantly, human iPSCs can be directed step by step into three-dimensional (3D), laminated retinal organoids containing all major retinal cells located in proper layers with photoreceptors achieving quite high degree of maturation, resembling human retinal development *in vivo* (Reichman et al., 2014; Zhong et al., 2014; Li et al., 2018). The iPSC-3D retinal organoid induction approach provides not only unlimited cell source for retinal cell replacement therapy, but also a powerful platform for disease modeling, drug screening, and even preclinical testing of gene therapy for IRD.

In this study, we established LCA patient-specific iPSC lines with two mutations c.200T>G (p.L67R) and c.430T>C (p.Y144H) in *RPE65*, reprogrammed from urine epithelium cells. Under retinal differentiation conditions, the patient-specific iPSCs were able to differentiate into retinal organoids with laminated NR and RPE cells. Their cellular and molecular features were similar to those differentiated from control hiPSCs. However, compared with healthy control, the RPE65 expression level was decreased in patient RPE cells while phagocytosis and VEGF secretion activity were equivalent. The patient-specific retinal tissues might serve as a valuable source or disease model for personalized study and treatment.

MATERIALS AND METHODS

Case Patient

A LCA patient was diagnosed by clinical standards with compound heterozygotes *RPE65* gene mutations (c. [200T>G], p. L67R; c. [430T>C], p. Y144H) as reported by Chen et al. (2013). This study was approved by the ethics committee of the Zhongshan Ophthalmic Center of Sun Yat-sen University and was conducted in accordance with the Declaration of Helsinki. The patient agreed to take part in this experiment and signed informed consent. The clinical features and genotype of this patient have been identified before (Chen et al., 2013).

Urine Collection and Cell Expansion From a Patient With RPE65-LCA

Collection and expansion of urine cells (UCs) was performed as described previously (Zhou et al., 2011). Briefly, the mid-stream urine (100–200 ml) was collected into sterile containers from the RPE65-LCA patient. The urine samples were centrifuged at 400 × *g* for 10 min. Cell pellet was washed with PBS containing amphotericin B and 100 U/ml penicillin/streptomycin and resuspended in 2 ml of primary medium consisting of DMEM/Ham's F-12 nutrient mix (1:1) (Thermo Fisher Scientific, Waltham, MA, United States), 10% of fetal bovine serum (FBS) (Natocor, Villa Carlos Paz, Cordoba, Argentina), renal epithelial cell growth medium (REGM) SingleQuot kit supplement (Lonza, Basel, Switzerland), amphotericin B, and 100 U/ml of penicillin/streptomycin. The cells were seeded into a 12-well plate coated with 0.1% gelatin and switched to REGM (Bullet Kit, Lonza, Basel, Switzerland) 4 days later. Adherent cells/colonies appeared after

3–6 days, passaged by TrypLE express (Life Technologies, Inc., Grand Island, NY, United States) when cell density reached 80–90% confluence.

Urine Cell Reprogramming and hiPSCs Culture

The method used to reprogram UCs into human iPSCs was described previously (Xue et al., 2013) with slightly modifications. In short, 1×10^6 UCs of passage 2 were electroporated with 6 μg OriP/EBNA1-based episomal plasmid pEP4EO2SET2K (contains OCT4, SOX2, SV40LT, and KLF4) and 4 μg pCEP4-miR-302-367 cluster (contains miR-302b, c, a, d, and miR-367) by Electroporation System (Lonza, Program T-020, Basel, Switzerland). Transfected cells were plated onto Matrigel-coated six-well plates and cultured in REGM. During D2–D16, induced medium mTeSR1 (Stem Cell Technologies, Vancouver, BC, Canada) containing 0.5 μM A-83-01 (SML0788, Sigma), 3 μM CHIR99021 (S1263, Selleck), 0.5 μM Tzv (S1459, Selleck), and 0.5 μM PD0325901 (S1036, Selleck) was changed every other day. The identifiable hiPSCs colonies with clear boundary were manually picked up during 16–21 days, and cultured in mTeSR1 on Matrigel-coated surface. Cells were passaged at ∼80% confluence with 0.5 mM EDTA (Invitrogen) from passage 2. Healthy control hiPSCs lines UE022 and UE017 were gifts from Professor GP (Guangzhou Institutes of Biomedicine and Health, Chinese Academy of Sciences).

Retinal Differentiation and 3D Retinal Organoids Culture

Retinal differentiation with RPE65-hiPSCs was performed with published protocols with a slight modification (Zhong et al., 2014; Li et al., 2018). Briefly, on Day 0 (D0), hiPSCs were digested into small clumps and cultured in suspension with mTeSR1 and 10 μM Blebbistatin (Sigma-Aldrich) to form embryoid bodies (EBs). Neural induction medium (NIM) containing DMEM/F12 (1:1), 1% N2 supplement (Invitrogen), 1% non-essential amino acids (NEAA), 2 μg/ml heparin (Sigma-Aldrich) was used and changed with a 3:1 ratio of mTeSR1/NIM on D1, 1:1 on D2, and 100% NIM on D3. EBs were plated on Matrigel-coated dishes containing NIM on D5–D7. On D16, the culture medium was changed to retinal differentiation medium (RDM) [DMEM/F12 (3:1) supplemented with 2% B27 (without vitamin A, Invitrogen), 1% NEAA, and 1% antibiotic–antimycotic]. In 4–6 weeks after differentiation, horseshoe-shaped NR domains along with the surrounding RPE cells were manually detached with a sharpened Tungsten needle and subject to suspension culture for the formation of retinal organoids. For long-term culture, the organoids were switched to retinal culture medium (RCM) containing RDM, 10% FBS, 100 μM Taurine (Sigma-Aldrich), and 2 mM GlutaMAX in 1 week after detachment. Since Week (W) 13 and onward, B27 in RCM was replaced with N2. Medium was changed every 2–3 days.

Isolation and Culture of RPE Cells

After NR domains were picked out, most RPE cells were left behind and kept growing for about 1 month, and then detached from the adherent surface, digested into single cells with TrypLE Express (Life Technologies, CA, United States) for 5–10 min in a 37°C incubator. The individualized RPE cells were plated on Matrigel-coated plates containing RCM, and passaged once reaching ∼90% confluence. To promote maturation, the confluent RPE cells on D7 after passage were switched to RDM again. The control RPE derived from healthy hiPSCs line UE022 were cultured in the similar manner as described above.

Immunocytochemistry

Cells growing on coverslips were fixed in 4% paraformaldehyde (PFA, Sigma-Aldrich) for 5–10 min. Retinal organoids were fixed in 4% PFA for 30 min and dehydrated in gradient sucrose solutions 6%, 12.5%, 25% in turn. Tissue embedding, sectioning, and immunohistochemistry were performed as previously described (Zhong et al., 2014; Li et al., 2018). Briefly, cells or sections were permeabilized and blocked with 0.25% Triton X-100 and 10% donkey serum for 1 h at room temperature, then incubated with primary antibodies at 4°C overnight and incubated with the corresponding secondary antibodies with either Alexa Fluor 488 or 555 (Life Technologies, CA, United States) for 1 h at room temperature. DAPI (Sigma-Aldrich) was used to counterstain nuclei. Sections stained with the corresponding secondary antibody alone were used as negative controls. Fluorescence images were acquired with an LSM 510 confocal microscope (Zeiss, Jena, Germany). Both primary and secondary antibodies used are listed in **Table 1**.

Reverse Transcription – PCR and qRT-PCR

Total RNA was extracted using Trizol (Invitrogen), and complementary DNA (cDNA) was synthesized from 500 ng of total mRNA using Prime Script™ RT Master Mix (Takara Bio, Tokyo, Japan). PCR cycle program was: 95°C for 2 min, 35 cycles of 95°C for 30 s, 60°C for 30 s, and 72°C for 30 s, and final step was 72°C for 8 min. Subsequent PCR products were run on 2% agarose gels for 30 min. RT-PCR was performed with the primers listed in **Table 2**.

Quantitative real-time PCR (qRT-PCR) was performed using AB Applied Biosystems (step one plus). Reactions were performed in triplicate, and Ct values were calculated using the $2^{-\Delta\Delta Ct}$ method. D5 EBs were used as reference. The expression levels of target genes were normalized to that of internal control gene GAPDH. Primer sequences are listed in **Table 2**.

Alkaline Phosphatase Staining

RPE65-hiPSCs were stained according to the AKP staining kit instructions (D001-2, Nanjing Jiancheng Bioengineering Institute, China).

Karyotype Analysis

G-band staining of chromosomes was used for karyotype analysis. RPE65-hiPSCs were grown on Matrigel-coated six-well plates until reaching 70% confluence. Colchicine was added

TABLE 1 | List of antibodies used for immunofluorescence staining.

Antibody name	Company	Catalog number	Work concentration
First antibody			
E-cadherin	Abcam	ab76055	1:500
KRT7	GeneTex	GTX107343	1:500
CD44	GeneTex	GTX102111	1:500
OCT4	Bioss	bs-0830R	1:250
SOX2	Abcam	ab92494	1:100
NANOG	Abcam	ab24624	1:1000
SSEA4	Abcam	ab16287	1:200
TRA-1-81	Abcam	ab16298	1:100
TRA-1-60	Abcam	ab16288	1:100
PAX6	DSHB	3B5	1:50
SOX1	Abcam	ab109290	1:200
SIX3	Rockland	600-401-A26	1:500
OTX2	Abcam	ab21990	1:500
LHX2	Santa Cruz	sc-81311	1:200
VSX2	Millipore	ab9016	1:500
MCM2	Abcam	ab4461	1:1000
BRN3	Santa Cruz	SC-6026X	1:200
AP2	DSHB	3B5a	1:35
PROX1	Millipore	AB5475	1:2000
PKC-α	Abcam	ab32376	1:2000
CRALBP	Abcam	ab15051	1:200
Recoverin	Millipore	ab5585	1:500
Rhodopsin	Abcam	ab3267	1:200
L/M opsin	Gift from Dr Jeremy Nathans		1:5000
S opsin	Gift from Dr Jeremy Nathans		1:5000
ZO-1	Thermo Fisher	33-9100	1:400
RPE65	Abcam	ab78036	1:400
MITF	Abcam	ab12039	1:400
Second antibody			
donkey anti-rabbit (555)	invitrogen	A31572	1:500
donkey anti-rabbit (488)	invitrogen	A21206	1:500
donkey anti-mouse (488)	invitrogen	A21202	1:500
donkey anti-mouse (555)	invitrogen	A31570	1:500
donkey anti-goat (555)	invitrogen	A21432	1:500
donkey anti-sheep (488)	invitrogen	A11015	1:500

to a final concentration of 0.2 μg/ml for 2 h. Then, RPE65-hiPSCs were digested with 0.5 mM EDTA solution for 5 min, collected and centrifuged at 1000 rpm for 5 min. Cell pellets were resuspended in 8 ml of 0.075 M KCl solution, incubated for 20 min at 37°C, and then fixed with 3:1 mixture of methanol/acid acetic solution for 10 min at 37°C. After further centrifugation, the supernatant was removed, and 10 ml ice-cold fixative solution was added. Cells were dropped on a cold slide, incubated at 80°C for 2 h, trypsinized, and then stained with Giemsa. Metaphase status was observed under an Olympus BX51 Microscope and analyzed with Ikaros Karyotyping System (MetaSystems).

Sanger Sequencing

RPE65 gene mutations in hiPSCs from the patient were verified by Sanger sequencing. The genomic DNA was extracted using a DNA Midi Kit (Qiagen, Valencia, CA, United States) according to the manufacturer's protocol.

Modeling of RPE65 Structure With Mutations

The sequence of human RPE65 was obtained from UniProt[1]. The Crystal structure of bos taurus RPE65 (Protein Data Bank ID: 4RYZ) that displays 62% sequence similarity with the human protein was chosen as a template. The 3D homology model of human RPE65 was constructed using Swiss-Model (Biasini et al., 2014), and then optimized and mutated with FoldX 5.0 (Schymkowitz et al., 2005). Hydrogen bond and electrostatic potential analysis were done using VMD 1.9.3 (Humphrey et al., 1996) and PDB2PQR 2.1.1 (Dolinsky et al., 2004), respectively.

Teratoma Formation Assay

For teratoma formation, 1–2 × 10^6 hiPSCs with 30% Matrigel were injected intramuscularly into the hind limb of 6-week-old immunocompromised NOD-SCID mice. Animals were monitored each week and teratomas were dissected at W8–W10 after transplantation. The teratoma tissues were fixed in formalin, embedded in paraffin, and sectioned and stained with Hematoxylin and Eosin (HE). Images were taken with a Nikon microscope.

Phagocytosis Assay

The phagocytosis assay was performed with procedures reported (Liu et al., 2018). In short, the photoreceptor outer segments (POSs) were collected from swine retina, labeled with CM-Dil (Invitrogen, CA, United States) following the instructions. Pigmented RPE cells differentiated from both patient and control iPSCs were cultured in RDM for 10 weeks after passage, and then treated with the CM-DiI labeled POS at 37°C or 4°C for 12 h. Afterward, RPE cells were washed with PBS thoroughly, fixed by 4% PFA for 5 min, and immunostained with ZO-1, a tight junction marker, to further determine the POS internalization. Z-stack images were taken with a Zeiss LSM 880 confocal microscope (Carl Zeiss Meditec, Inc.). For quantitative analysis, POS with a minimum diameter of 0.5 μm was counted using image J software, and five random fields of view (40×) were photographed per group. Three independent experiments were conducted.

Enzyme-Linked Immunosorbent Assay

Monolayered RPE cells, grown on Matrigel-coated 24-well plates for 10 weeks, were used to evaluate VEGF secretion. After PBS washing, the cells were cultured in 500 μl DMEM-basic for 24 h, then the media were collected and centrifuged at 300 × *g* for 5 min. Total secreted VEGF in culture medium was assayed using a human VEGF Enzyme-Linked Immunosorbent Assay (ELISA) kit (QuantiCyto, China) following the manufacturer's instructions. The RPE cells in each well after medium collection were digested into single cells, and then counted. The VEGF amounts secreted by 1 × 10^6 RPE cells per well were used to compare between the patient and control groups.

[1] www.uniprot.org

TABLE 2 | Primer list.

Genes	Size (bp)	Forward	Reverse
Exogenous genes (RPE65-hiPSCs) for RT-PCR			
OCT4	657	AGTGAGAGGCAACCTGGAGA	AGGAACTGCTTCCTTCACGA
SOX2	534	ACCAGCTCGCAGACCTACAT	CCCCCTGAACCTGAAACATA
KLF4	401	CCCACACAGGTGAGAAACCT	CCCCCTGAACCTGAAACATA
SV40LT	491	TGGGGAGAAGAACATGGAAG	AGGAACTGCTTCCTTCACGA
ORIP	544	TTCCACGAGGGTAGTGAACC	TCGGGGGTGTTAGAGACAAC
EBNA-1	666	ATCGTCAAAGCTGCACACAG	CCCAGGAGTCCCAGTAGTCA
miR-302-367	322	TTTCCAAAATGTCGTAATAACCCCG	CTCCCAAAGAGTCCTGTTCTGTCCT
GAPDH	542	ACCACAGTCCATGCCATCAC	TCCACCACCCTGTTGCTGTA
Enogenous genes (RPE65-hiPSCs) for RT-PCR			
OCT4	323	CGAGCAATTTGCCAAGCTCCTGAA	TCGGGCACTGCAGGAACAAATTC
SOX2	448	CCCCCGGCGGCAATAGCA	TCGGCGCCGGGGAGATACAT
NANOG	237	AAGGTCCCGGTCAAGAAACAG	CTTCTGCGTCACACCATTGC
Genes (retinal differentiation and RPE cells) for Q-PCR			
GAPDH	120	TCGTGGAAGGACTCATGACC	AGGCAGGGATGATGTTCTGG
PAX6	120	AGT GAA TCA GCT CGG TGG TGT CTT	TGC AGA ATT CGG GAA ATG TCG CAC
VSX2	122	GGCGACACAGGACAATCTTTA	TTCCGGCAGCTCCGTTTTC
MITF	201	TGACCGCATTAAAGAACTAGGT	AGTTCCTGTATTCTGAGCAACA
RX	81	AGCGAAACTGTCAGAGGAGGAACA	TCATGCAGCTGGTACGTGGTGAAA
RPE65	259	GCCCTCCTGCACAAGTTTGACTTT	AGTTGGTCTCTGTGCAAGCGTAGT
CRALBP	173	GCTGCTGGAGAATGAGGAAACTC	GGCTGGTGGATGAAGTGGAT

Statistical Analysis

All the results are presented as the mean ± *SD*. Comparisons between two groups were analyzed using a two-tailed Student's *t*-test. $P < 0.05$ was considered statistically significant.

RESULTS

Reprogram RPE65-Patient Urine Cells Into iPSCs

To non-invasively acquire somatic cells for reprogramming, we collected 100 ml middle stream of the micturition from one 9-year old RPE65-LCA patient, from which UCs were isolated and cultured as described previously (Xue et al., 2013; **Supplementary Figure S1A**). The obtained UCs were mixed with type 1 and 2 cells. The type 1 cells were rounded and grew closely in colonies while the type 2 were elongated and grew sparsely or surrounding type 1 cells (**Supplementary Figure S1B**). They had high proliferative capacity and could expand for more than 5 passages. As assessed by immunofluorescence staining, these cells expressed UC-specific proteins E-cadherin, CD44, and the intermediate filament keratin 7 (KRT7) (**Supplementary Figure S1C**). The morphological and molecular features of UCs from the RPE65-LCA patient were similar to those from healthy individuals reported previously (Zhou et al., 2011).

To obtain non-integrating hiPSCs, we transfected OSTK factors (OCT4, SOX2, SV40T, and KLF4) along with miR-302-367 cluster expressing episomal plasmids into UCs through electroporation manner (**Figure 1A**). The transfected UCs cultured on Matrigel-coated dishes appeared a few of clonal cell clusters in 10 days, which became larger in size over time (**Figure 1B** and **Supplementary Figure S3A**). In 3 weeks after transfection, many flat and tightly packed colonies with clear boundary presented. AP staining showed that this type of colonies was positive (**Figure 1C**). To efficiently purify these good colonies, we manually picked small pitches from primary colonies one by one and plated them on Matrigel-coated 24-well plates, respectively, containing mTeSR1. With this method, the selected pitches grew and showed highly homogeneous and flat morphology with a sharp edge without obvious differentiation after only one or two round selection (**Figure 1D**). After purification, these cell colonies could be routinely passaged with EDTA solution every 4–6 days, and kept typical morphological features with a high nuclear–cytoplasmic ratio and large nucleoli (**Figure 1E**), similar with human embryonic stem cells (hESCs) and hiPSCs derived from healthy individuals. Herein, we refer to these cells as RPE65-hiPSCs. More than 20 clones were obtained from two wells of reprogrammed UCs cultured in a six-well plate and five patient-specific hiPSC lines with more than 10 passages were established.

Sanger sequencing confirmed the RPE65-hiPSCs contained two heterozygous mutations c.200T>G (p. L67R) and c.430T>C (p. Y144H) in *RPE65* gene, consistent with mutations detected in blood sample of this patient reported previously (Chen et al., 2013; **Figure 1F**). Structural analysis showed that the mutation sites L67 and Y144 were located in the blade VII and I of RPE65, respectively, which are critical to the closure of the core propeller fold (**Figure 1G**). Mutations (L67R and Y144H) had significant impacts on the local spatial volume, electrostatic potential, and/or

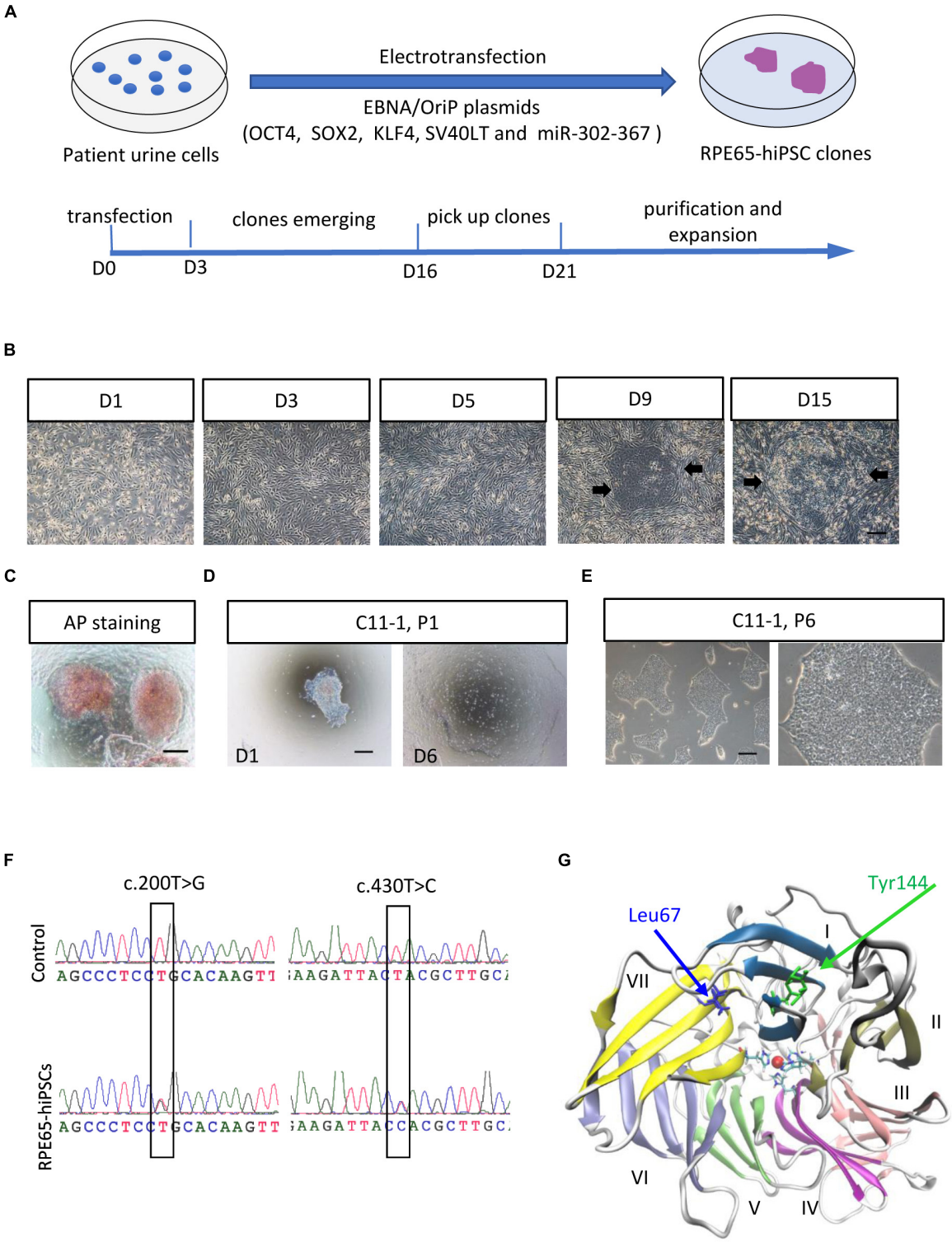

FIGURE 1 | Generation and amplification of RPE65-hiPSCs. **(A)** Schematic overview of generating integration-free RPE65-hiPSCs from UCs. **(B)** Progressive formation of RPE65-hiPSCs colonies after UCs reprogrammed. The black arrows showed emerging clones. **(C)** The emerging clones were positive for AP staining. **(D)** A manually picked small clump from primary clone gradually formed typical clones on D6. **(E)** Passaged RPE65-hiPSCs clones with EDTA treatment. Scale bars, 250 μm. **(F)** Sanger sequencing confirmed hiPSCs from the LCA patient contained compound RPE65 gene mutations with c.200T>G and c.430T>C. **(G)** Structure of human RPE65 monomer viewed from the bottom face of the seven-bladed β-propeller. Blades are numbered I–VII. Absolutely conserved His180, His241, His313, and His527 residues are shown as sticks coordinating the natively bound iron ion. The two mutation sites Leu67 (L67) and Tyr144 (Y144) are shown as blue and green sticks, respectively.

hydrogen bonds network (**Supplementary Figure S2**). These structural effects may destabilize the protein, and thus result in improper "sealing" of the propeller structure or displace the critical iron-coordinating residues such as His527 and His180, reducing the enzyme activity.

Characterization of RPE65-Patient-Specific hiPSCs

After serial passage, the established cultures of RPE65-iPS cells were subjected to stringent assessment of characteristics of human pluripotent stem cells through different assays. Immunofluorescence staining showed these cells expressed human ESC/iPSC-specific protein markers OCT4, SOX2, NANOG, SSEA4, TRA-1-81, and TRA-1-60 (**Figure 2A** and **Supplementary Figure S3C**). Meanwhile, RT-PCR verified all five RPE65 hiPSCs lines (C11–1, C4, C10, C13, and C14) were positive for endogenous pluripotent genes *OCT4*, *SOX2*, and *NANOG* (**Supplementary Figure S3B**), but negative for exogenous reprogramming factors (OCT4, SOX2, SV40T, KLF4, and miR-302-367), and episomal plasmid DNA (oriP and EBNA-1), which were detected negatively in as early as passage one (P1) cells (**Figure 2B** and **Supplementary Figure S3D**). These results indicated RPE65-LCA patient-specific hiPSCs are free of episomal DNA integration, benefiting future translational study such as cell transplantation. RPE65-hiPSCs from two lines (C11–1, C4) at different passage number were chosen to analyze karyotype. They all showed normal karyotype by G-band staining (**Figure 2C** and **Supplementary Figure S3E**). To evaluate the pluripotency, we performed teratoma formation assays. The RPE65-hiPSCs were injected into NOD/SCID mice and followed up for 2 months. The patient-specific hiPSCs developed teratoma which contained neural rosettes, cartilage, and gut-like epithelium from three germ layers, respectively (**Figure 2D**). The above results demonstrated that RPE65-LCA patient-specific hiPSCs had pluripotency features similar to hESCs *in vitro* and *in vivo*.

Generation of Patient-Specific Retinal Organoids From RPE65-hiPSCs

After stringent characterization of RPE65-hiPSCs, we asked whether they were able to differentiate into retinal organoids which were achieved with hiPSCs from healthy individuals (Zhong et al., 2014; Li et al., 2018). Using a stepwise retinal differentiation protocol reported (Li et al., 2018), the patient-specific hiPSCs recapitulated the major molecular and cellular features of retinal morphogenesis *in vivo*. Under suspension culture condition, dissociated RPE65-hiPSCs gradually formed EBs, which were then plated onto Matrigel-coated dishes for further induction (**Figures 3A–C**). Under these conditions, the RPE65-hiPSCs sequentially acquired $PAX6^+$ and $SOX1^+$ anterior neuroepithelial (AN) cell fate (**Figure 3D**) and Eye Field (EF) cell fate expressing EF transcription factors SIX3, OTX2, and LHX2 in 2 weeks after differentiation (**Figures 3E–G**). In addition, qRT-PCR showed that expression level of retinal progenitor markers (PAX6 and VSX2) and RPE cell markers (MITF) dramatically increased as differentiation progressed (**Figure 3H**). Compared to the healthy control hiPSCs, RPE65-hiPSCs presented similar mRNA expression level of retinal-specific genes *PAX6*, *VSX2*, *MITF*, and *RX* on D16 after induction ($n = 3$) (**Figures 3I–L**). Afterward, highly reflective, horseshoe shape like NR domains progressively formed, which were readily identified under inverted microscope (**Figure 3M**). Four weeks after differentiation, the domains were detached and cultured in suspension condition, under which they self-formed 3D retinal organoids with a major part of transparent NR ring attached with a small RPE ball on the other side, resembling an eye-cup (**Figure 3N**). The NR cells extensively expressed retinal progenitor markers VSX2 and MCM2 (**Figures 3O,P**). At least three RPE65-iPSCs lines (C4, C11-1, and C13) were successfully tested for their retinal differentiation ability. Collectively, these data indicated that RPE65-LCA patient-specific hiPSCs had capacity to form retinal organoids with the similar manner as hiPSCs derived from healthy individuals.

Differentiation and Lamination of Patient-Specific Neural Retina From RPE65-hiPSCs

Our pervious study showed that retinal progenitor cells (RPCs) differentiated from healthy urine-derived hiPSCs had ability to differentiate into all major retinal cell types in an ordered fashion that retinal ganglion cells are born first, followed by photoreceptor cells, amacrine cells, horizontal cells, and lastly by bipolar cells and Müller cells (Li et al., 2018). Here, we, for the first time, demonstrated that patient RPE65-hiPSCs could also recapitulate the spatiotemporal pattern of NR differentiation *in vivo*. RPE65-hiPSCs derived 3D retinal organoids comprised NR attached with more or less RPE. Retinal ganglion cells expressing BRN3 first appeared in W6 and located in the basal-most zone of the NRs (**Figure 4A**). Subsequently, the $OTX2^+$ photoreceptor progenitor cells appeared and occupied the apical part of NRs in W9 (**Figure 4B**). At the mid-term stage (W12–17) appeared interneurons, including $AP2^+$ amacrine cells and $PROX1^+$ horizontal cells lying in the intermediate layer of the NRs (**Figures 4C,D**). Finally, the developing late-born neurons appeared in W18–21, such as PKC-a^+ bipolar cells and $CRALBP^+$ Müller glial cells (**Figures 4E,F**). These results demonstrated that patient RPE65-hiPSCs kept the capacity to generate laminated NR with the similar developmental order as those from the control hiPSCs. In addition, all of three RPE65-iPSCs lines (C4, C11-1, and C13) could generate well-layered retinal organoids.

Photoreceptor Subtype Specification in Patient Retinal Organoids

After long-term culture (>20 weeks), RPE65-hiPSCs derived 3D retinal organoids kept nice structure comprising a high-reflective NR tissue attached a small RPE patch (**Figure 5A**). Immunofluorescence showed that RPCs could differentiate into recoverin positive photoreceptor cells accumulated in the apical side and forming presumptive ONL (**Figure 5B**

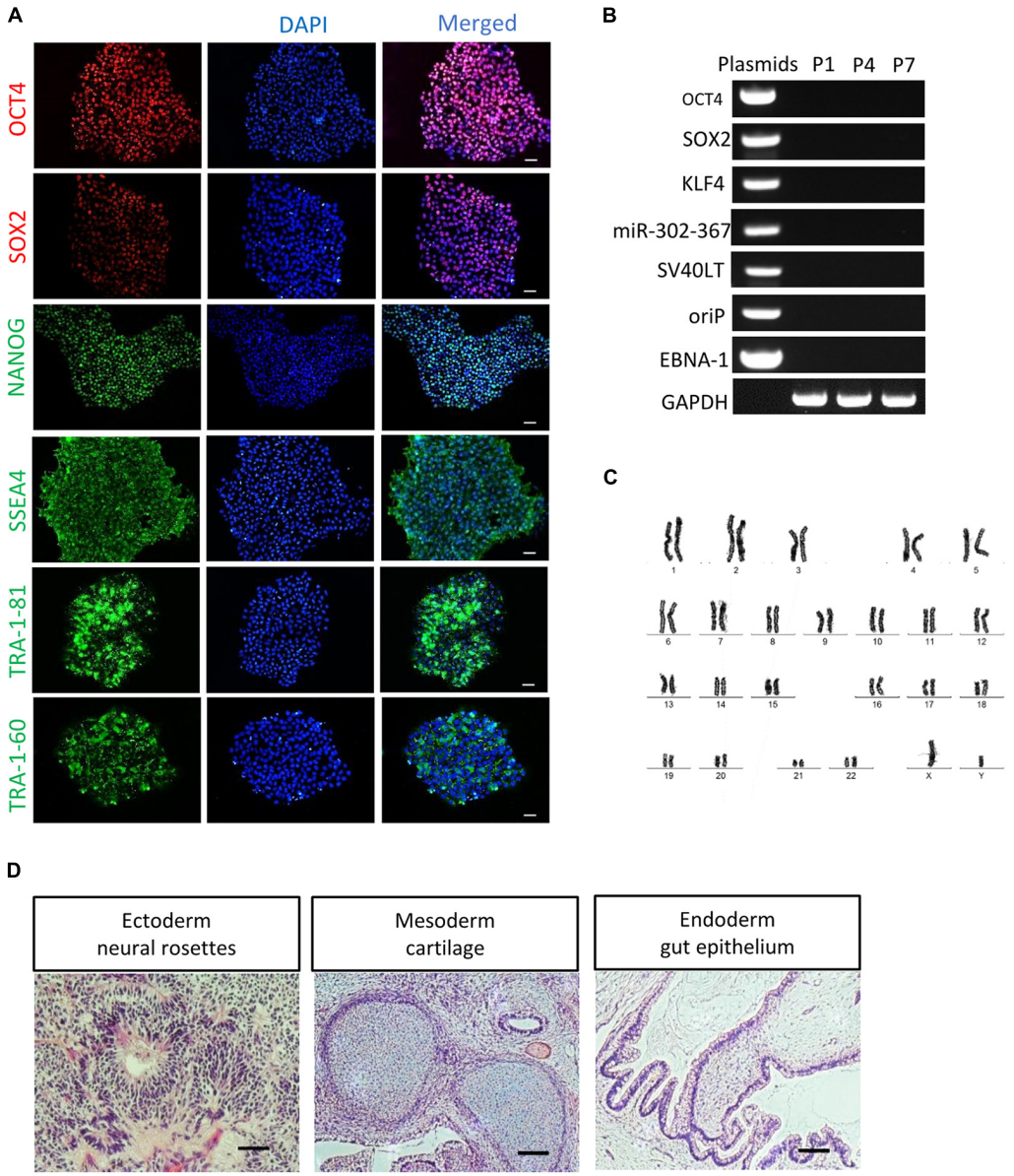

FIGURE 2 | Characterization of non-integrated RPE65-patient-specific hiPSCs. **(A)** Immunofluorescence staining of pluripotency markers (OCT4, SOX2, NANOG, SSEA4, TRA-1-81, and TRA-1-60) for RPE65-hiPSCs (C11–1, P5). Scale bars, 50 μm. **(B)** Non-integrating analysis of episomal vectors in the RPE65-hiPSCs (C11–1, P1, P4, and P7) by RT-PCR. **(C)** G-band analysis showed that RPE65-hiPSCs (representative result of C11–1) had normal karyotype. **(D)** HE staining analysis of teratomas from RPE65-hiPSC in NOD-SCID mice. Scale bars, 100 μm.

and **Supplementary Figure S4**). By W21, all subtypes of photoreceptors, including Rhodopsin$^+$ rods, L/M opsin$^+$ red/green cones, and S opsin$^+$ blue cones were also acquired and self-organized with polarization of segments toward the apical side of the NRs (**Figure 5C**). In addition, TEM demonstrated that RPE65-hiPSCs derived photoreceptors developed typical ultrastructures, including outer limiting membrane, inner segment rich of mitochondria, basal body, connecting cilium, centriole, and rudimentary outer segment (**Figures 5D–G**). These results implied that RPE65-hiPSCs could generate all subtypes of photoreceptors in organoids, similar to those derived from the healthy hiPSCs (Li et al., 2018).

Down-Regulation of RPE65 in Patient-Specific RPE Cells With Novel *RPE65* Mutations

By using the same 3D retinal differentiation protocol as described above, RPE cells were simultaneously generated with NR from hiPSCs, presented pigment and cobblestone morphology in adherent culture as early as W4 after

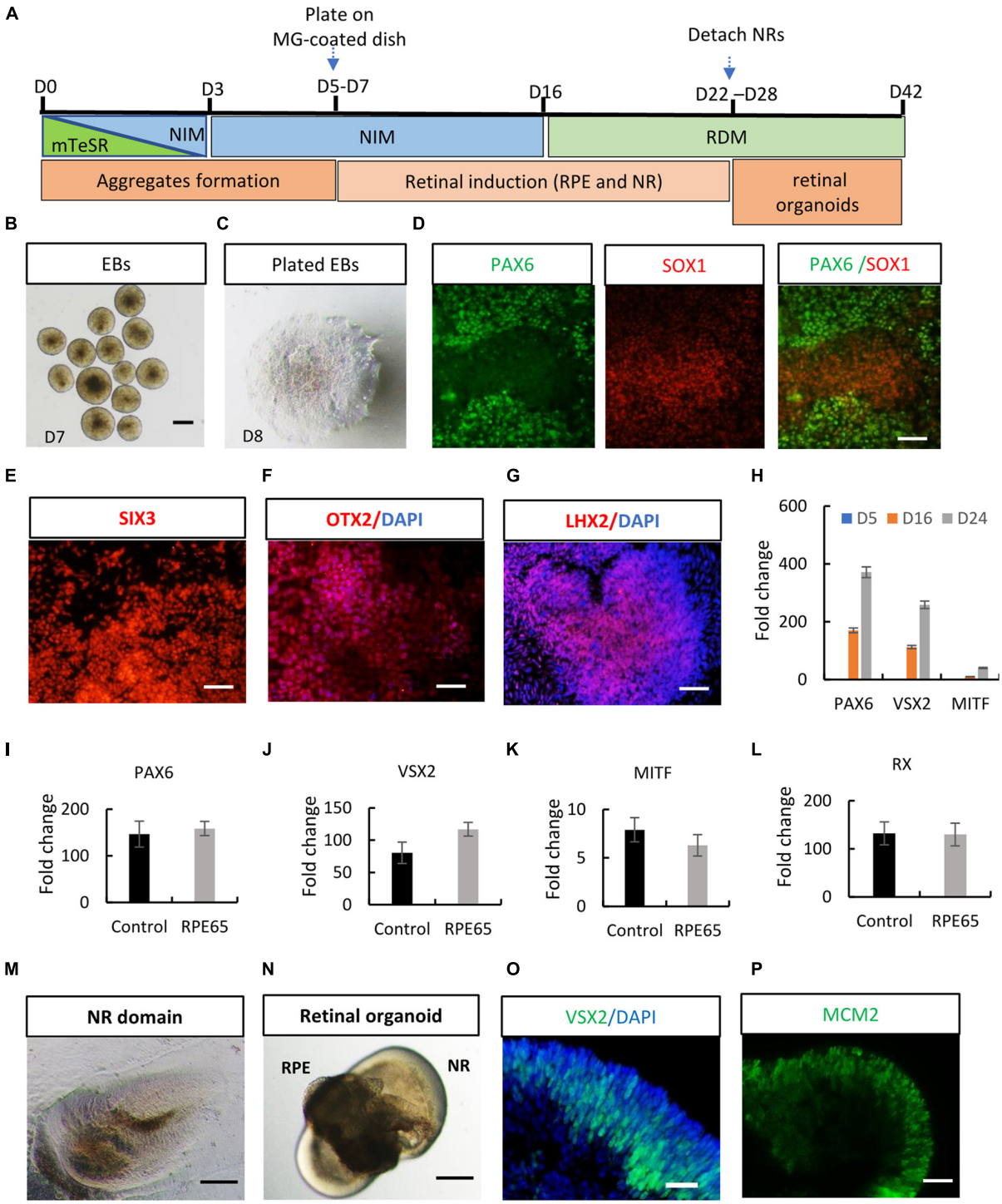

FIGURE 3 | Acquisition of retinal organoids and RPE cells from RPE65-hiPSCs. **(A)** Schematic overview of retinal differentiation protocol. **(B)** Floating embryoid bodies (EBs). **(C)** EBs plated on Matrigel-coated dishes on D7. Scale bars, 200 μm. **(D)** The adherent EBs acquired an anterior neuroepithelial fate characterized by PAX6 and SOX1 expression. Scale bar, 50 μm. **(E–G)** SIX3, OTX2, and LHX2-positive retinal progenitor cells appeared around D12. Scale bars, 20 μm. **(H)** qRT-PCR showed progressive increase of expression level of retinal progenitor markers PAX6 and VSX2 and RPE marker MITF during retinogenesis of RPE65-hiPSCs. RPE65-hiPSCs derived EBs (D5) as reference. Mean ± *SD*, $n = 3$. **(I–L)** Comparison of mRNA expression level of retinal progenitor markers (PAX6, VSX2, and RX) and RPE marker (MITF) between control and RPE65 hiPSCs on D16 after retinal differentiation. Control hiPSCs derived EBs (D5) as reference. No significant difference was disclosed between them ($P > 0.05$), mean ± *SD*, $n = 3$. **(M)** Typical morphology of horseshoe-like NR domains. Scale bar, 200 μm. **(N)** Representative image of retinal organoids containing NR and RPE. Scale bar, 200 μm. **(O,P)** Immunofluorescence staining showed retinal progenitor cells expressing VSX2 and MCM2 occupied the whole neural retina on D35 after differentiation. Scale bars, 20 μm.

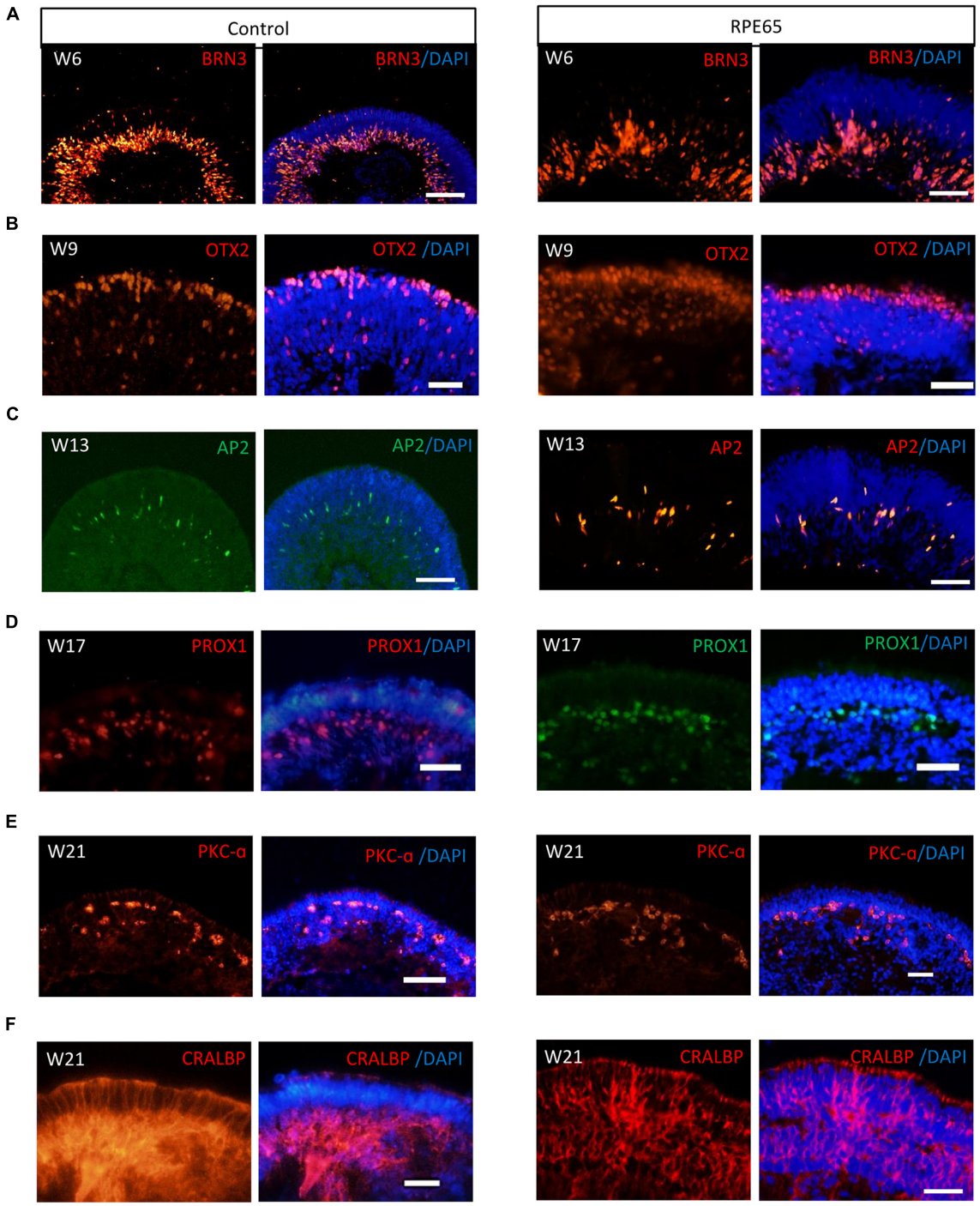

FIGURE 4 | RPE65-hiPSCs generated layered retinal organoids with all retinal cell types. Comparable to healthy control, neural retina in RPE65-hiPSCs derived retinal organoids developed laminated architecture with all major retinal cell types located in the corresponding layer. **(A)** BRN3$^+$ retinal ganglion cells located in the basal side, **(B)** OTX2$^+$ photoreceptor cells lying in the apical side, **(C,D)** AP2$^+$ amacrine cells and PROX1$^+$ horizontal cells lying in intermediate layer, **(E)** PKC-a$^+$ bipolar cells, and **(F)** CRALBP$^+$ Müller glial cells. Scale bars, 20 μm.

differentiation (**Figures 6A,B**). On W8, the pigmented RPE sheets derived from RPE65-hiPSCs and control were collected to test mRNA expression level of RPE65, MITF (the RPE cell transcription factor), and CRALBP (cellular retinaldehyde-binding protein) (**Figure 6C**). qRT-PCR showed that RPE65 expression level was significantly lower (approximately eightfold) in RPE cells from RPE65-hiPSCs than those from control hiPSCs ($P < 0.05$). However, MITF

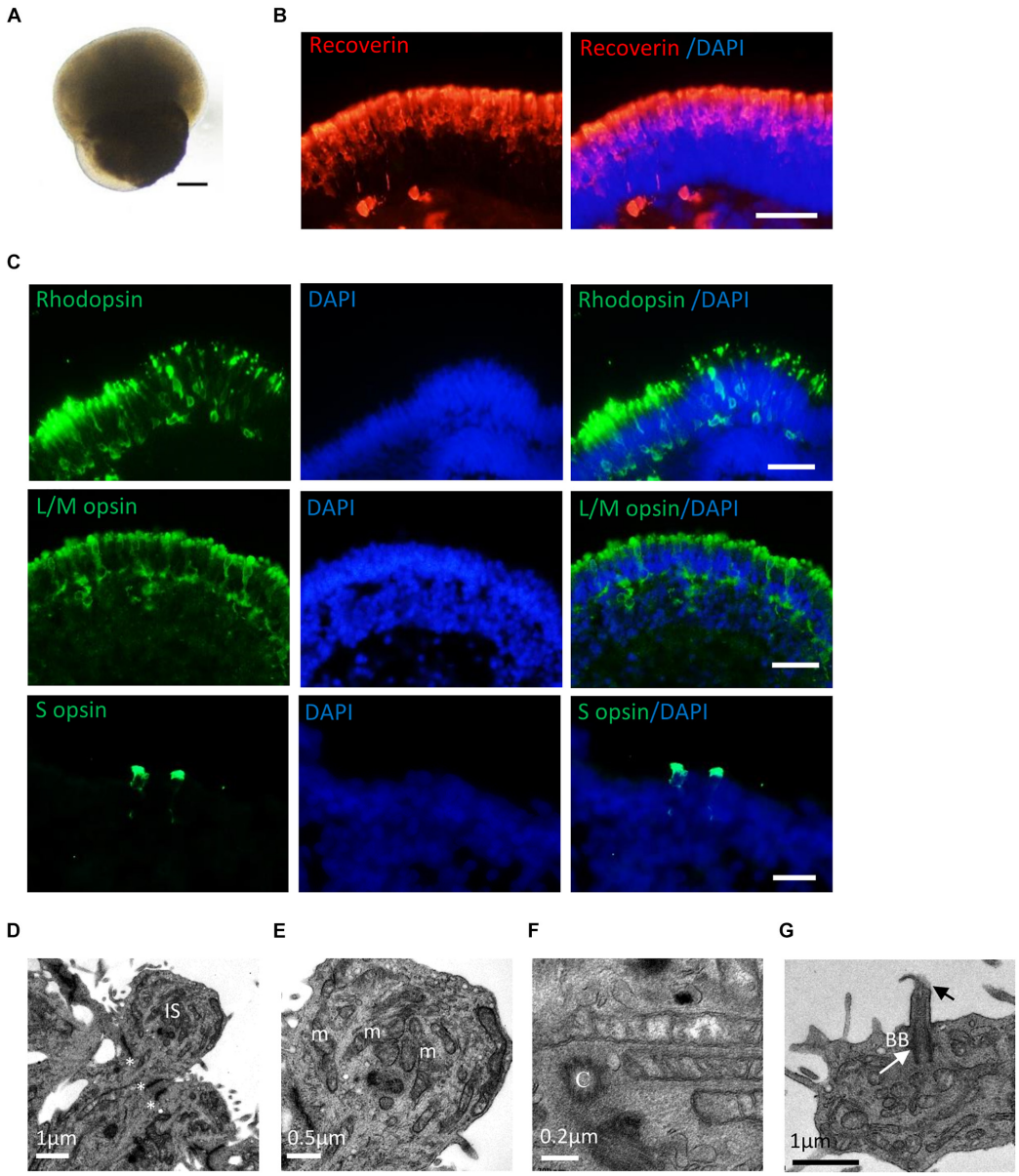

FIGURE 5 | Photoreceptor subtype specification in patient retinal organoids. **(A)** Representative images of retinal organoids derived from RPE65-hiPSCs on D150. Scale bars, 200 μm. **(B)** Photoreceptor cells developed outer nuclear layer-like structure in patient retinal organoids, expressing photoreceptor cell pan marker Recoverin. Scale bar, 20 μm. **(C)** The patient photoreceptor cells had capacity to develop all subtypes including Rhodopsin$^+$ rods, L/M opsin$^+$ red/green cones and S opsin$^+$ blue cones. Scale bars, 20 μm. **(D–G)** TEM revealed that RPE65-hiPSC-derived photoreceptors developed typical ultra-structures, outer limiting membrane (OLM, asterisks), inner segment (IS) with rich mitochondria (m), centriole (C), basal body (BB) (white arrow), and connecting cilia (black arrow). Scale bars, 1 μm **(D)**, 0.5 μm **(E)**, 0.2 μm **(F)**, and 1 μm **(G)**.

and CRALBP expression levels had no statistically significant difference between RPE65-hiPSCs and control hiPSCs derived RPE (**Figure 6D**). Moreover, immunofluorescence staining revealed that the RPE65 protein expression was hardly detected in RPE65-hiPSCs derived RPE cells at W8 after differentiation, but in control RPE cells. While CRALBP and ZO-1, a tight junction protein, were positive in RPE cells from both control and RPE65-hiPSCs (**Figure 6E**). These results indicated the compound RPE65 mutations L67R and Y144H down-regulated RPE65 mRNA and protein expression in patient-specific RPE cells.

Expansion Capacity of Patient-Specific RPE Cells

In addition, whether *RPE65* gene mutations impair the expansion capacity of patient RPE cells were evaluated. RPE sheets from control and RPE65-hiPSCs with pigmentation

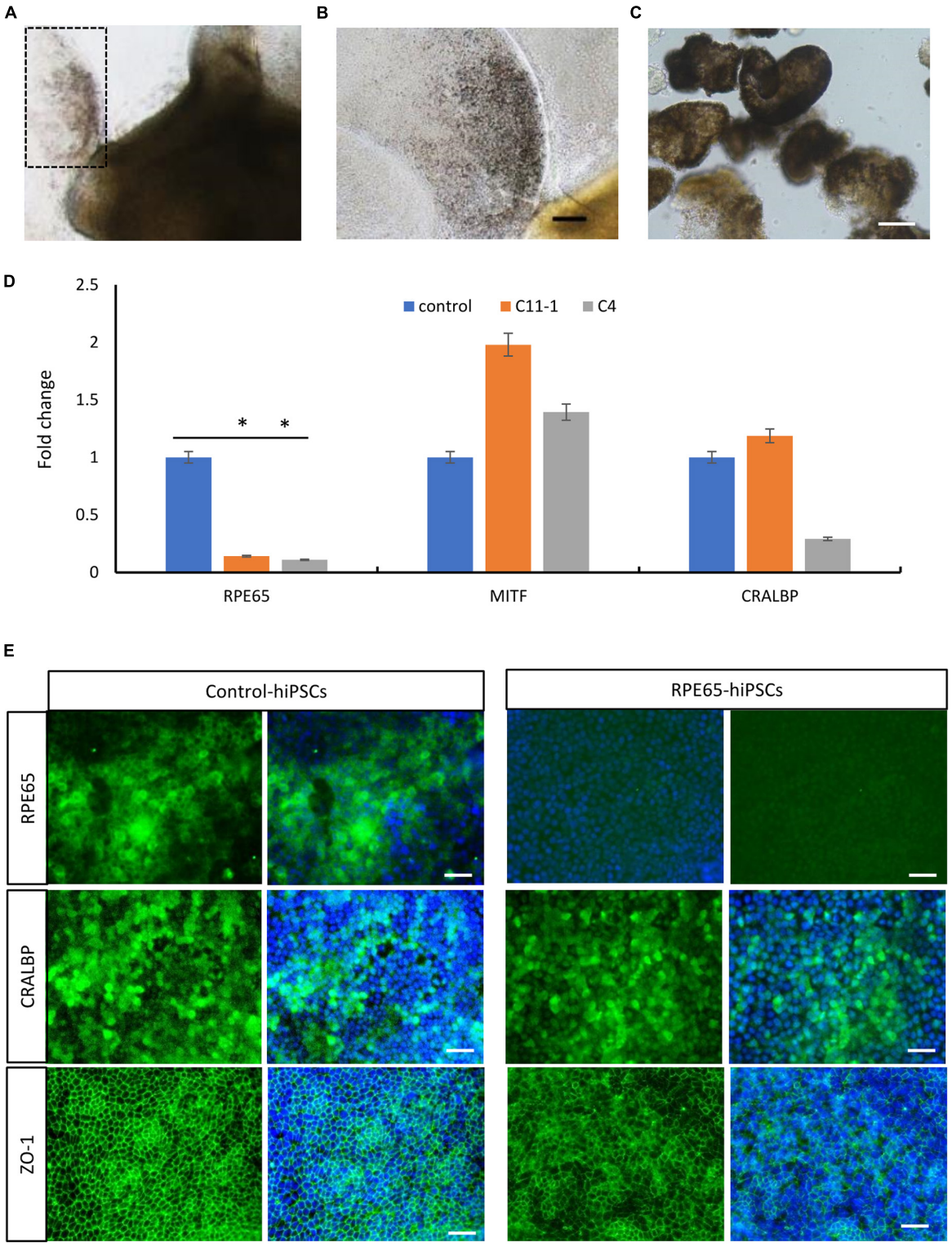

FIGURE 6 | Decreased expression of RPE65 in patient RPE cells. **(A)** Pigmented RPE cells (dashed area) differentiated from RPE65-hiPSCs. **(B)** Higher magnification of the dashed area in **A**. Scale bar, 100 μm. **(C)** The picked RPE sheets on W8 after differentiation. Scale bar, 100 μm. **(D)** qPCR analysis showed that the expression level of RPE65 was significantly lower in patient RPE cells (C11–1 and C4) than in the control (UE022), while MITF and CRALBP in patient RPE cells were comparable to the control. $^*P < 0.05$. Data presented as mean ± *SD*, $n = 3$. **(E)** Immunofluorescence staining revealed that RPE65 were negative in RPE65-hiPSCs derived RPE cells, but positive in control hiPSCs derived RPE cells, while both CRALBP and ZO-1 were strongly positive in patient and control RPE cells. Scale bars, 20 μm.

and cobblestone-like morphology were selected, and digested into single cells on W8 after differentiation, and then seeded on Matrigel-coated dishes for expansion (**Supplementary Figures S5A,B**). In RCM containing serum, RPE65-hiPSCs derived pigmented RPE cells proliferated, depigmented, and reached confluency in 1 week when cell plating density was 2–5 $\times$ 10^4/cm^2. The cells could passage every week and expanded more than three passages, yielding large populations which could be frozen and revived for future applications. When switched to RDM without serum, the expanded RPE cells regained pigmentation with typical cobblestone-like morphology, signs of mature RPE cells (**Supplementary Figure S5C**). Immunofluorescence staining showed that these RPE cells expressed RPE-specific markers PAX6, OTX2, MITF, and the tight junction marker ZO-1, comparable to the RPE cells derived from control hiPSCs (**Supplementary Figure S5D**).

Evaluation of Cell Function of Patient RPE

Next we asked whether the novel *RPE65* mutations L67R and Y144H impacted on RPE cell function. POS phagocytosis and VEGF secretion were evaluated in RPE cells derived from both control and RPE65-hiPSCs. Compared to those cultured on 4°C condition (as a negative control, normal physiological function reduced at this temperature), all RPE cells on 37°C could phagocytose POS actively. In addition, the POS number phagocytosed by the control and patient RPE cells were comparable (142.8 $\pm$ 9.4/view and 175.7 $\pm$ 7.6/view, n = 3, respectively), implying the RPE65 mutations did not change phagocytosis capacity of patient RPE cells (**Supplementary Figures S6A–C**). By ELISA analysis, the VEGF amounts secreted by patient RPE cells (547.7 $\pm$ 17.3 pg/10^6 cells, n = 3) were equivalent to the control RPE cells (585.2 $\pm$ 23.0 pg/10^6 cells, n = 3) (**Supplementary Figure S6D**). Therefore, the above data indicated that the compound RPE65 mutations L67R and Y144H had no effect on the two important biological function of patient RPE cells. However, further studies will be needed to elucidate whether the novel mutations reduce the RPE65 isomerase activity, critical for the regeneration of the visual pigment and normal vision.

DISCUSSION

In this study, we generated non-integrating hiPSCs from a presumptive LCA patient carrying novel *RPE65* mutations c.200T>G (p. L67R) and c.430T>C (p.Y144H). These patient-specific hiPSCs had typical features of healthy hiPSCs, such as clonal growth, expression of pluripotent markers, and multipotential differentiation. Moreover, RPE65-hiPSCs could differentiate into retinal organoids containing photoreceptor and RPE cells, two disease target cells. The time course of retinal differentiation and cellular and structural features of retinal organoids from RPE65-hiPSCs was similar to those from control hiPSCs. In addition, our findings disclosed that the patient RPE cells had normal biological functions, POS phagocytosis, and VEGF secretion, but lower expression of RPE65 mRNA and protein. The latter might reduce the RPE65 enzyme activity, leading to the vision loss.

The retinoid isomerase, RPE65, exclusively expressed in RPE cells, is critical for visual cycle responsible for sustaining vision. Over 130 genetic variants locating in coding or non-coding regions of this gene have been reported in LCA patients with diverse clinical phenotypes (Astuti et al., 2016). In the past decades, significant progress has been achieved in understanding normal RPE65 action and disease pathogenic mechanisms as well as developing *RPE65* gene augment therapy (Redmond et al., 1998; Jin et al., 2005; Russell et al., 2017). So far, different animal models with *RPE65* knockout, point mutations, or naturally inactivating mutations of *RPE65* (mice and dog) have been established or identified, and made huge contributions to the above achievements (Li et al., 2014; Shin et al., 2017). However, species issues in model fidelity and response to therapeutic treatments existed. Bainbridge et al. (2015) reported that gene therapy with rAAV2/2 *RPE65* vector resulted in only modest and temporary improvement in LCA patients compared with results obtained from the dog model. They postulated that there was a species difference in the amount of RPE65 required to drive the visual cycle (Bainbridge et al., 2015). Hence, there is a need to develop a human *in vitro* model of LCA caused by RPE65 for basic and translational study. With hiPSC technology, Tucker et al. (2015) created patient hiPSCs lines containing exonic leucine–toproline mutation (L408P) and intron 3 (IVS3-11) mutation in *RPE65* gene, induced them into patient-specific RPE cells from which the IVS3-11 variation was disclosed causing mis-splicing via transcriptional analysis. However, the direct impact of the above mutations on RPE65 expression, enzyme activity, and RPE cell function remains unclear. Here, we produced patient-specific hiPSCs which differentiated into retinal cells including RPE cells from a putative LCA patient containing two novel *RPE65* mutations L67R and Y144H. The pathogenicity of these two compound mutations in RPE65 gene has not determined yet. Bioinformatic analysis predicted the L67R mutation was damaging or probably damaging, while the Y144H mutation tolerated or probably damaging (Chen et al., 2013). In cellular level, our study, for the first time, revealed that these mutations decreased the expression of RPE65 mRNA and protein in patient RPE cells, which are also in agreement with the structure analysis of the mutants (**Figure 1G** and **Supplementary Figure S2**). However, further studies will be necessary to confirm the impact of these mutations on the isomerase activity.

Advance in retinal organoids induction techniques with hiPSCs provides a powerful research platform for dissecting mechanisms of retinal development and disease *in vitro*. These multi-layered retinal organoids contained nearly all major retinal cell types, especially photoreceptor and RPE cells, which are the most common, initially affected cells in retina of LCA patient. So far, retinal organoids derived from patient-specific iPSC were reported to model, at some degree, phenotypes of retinal dystrophy, such as *CEP290* and *NR2E3*

gene mutation-related LCA (Parfitt et al., 2016; Deng et al., 2018). In this study, we firstly acquired RPE65-LCA patient-specific retinal organoids containing neural retinal and RPE in different developmental stages. In patient retinal organoids, all subtypes of photoreceptors including Rhodopsin$^+$ rods, L/M opsin$^+$, and S opsin$^+$ cones developed and highly organized since W20 after differentiation. In addition, the protein expression pattern of these opsins in the organoids showed the similar spatial pattern as in the human fetal retina, with opsins first detected in the rudimentary OS, then in the entire cell membrane, and finally restricted to the elongating OS (Hendrickson et al., 2008). Especially, the typical ultrastructure of patient photoreceptors such as outer limiting membrane, inner segment, and rudimentary outer segments, a functional structure, also appeared. The success of acquiring rods and cones as well as RPE cells would provide a patient-specific cell model to dissect the pathogenic mechanisms and phenotype of the disease caused by these two mutations L67R and Y144H as well as other factors, personal factors in particular. However, a previous study showed that evident structural changes including outer segment discs were not seen in 7-week-old RPE65$^{-/-}$ mice, but in 15-week-old RPE65$^{-/-}$ mice (Redmond et al., 1998), implying the phenotype of photoreceptors presented quite late. Therefore, challenges with retinal organoids still exist in terms of modeling of photoreceptor phenotypes such as structural changes and cell loss caused by RPE65 mutations. Optimizing the retinal organoids culture system including promoting the photoreceptor maturation and long-term survival and establishing the direct contact of RPE and photoreceptors will be in demand for disease modeling of LCA.

Most of LCA patients inevitably suffer from retinal degeneration with thinning retina, which need tissue or cell replacement therapy. Although gene-based therapy could improve vision of RPE65-LCA patients, it failed to prevent degeneration process of this disease. Patient-derived retinal organoids or RPE cells can be utilized for regenerative medicine in combination with genome-editing technology (Deng et al., 2018; Zheng et al., 2018). Genome editing tools, the clustered regularly interspaced short palindromic repeats (CRISPR)/Cas9 system, zinc finger nucleases (ZFNs), and transcription activator-like effector nucleases (TALENs), are capable to correct mutations that lead to genetic diseases (Kime et al., 2016). With this technology, Soldner et al. (2011) created isogenic pairs of patient-derived iPSCs. Both RPE65-hiPSCs derived RPE cells and photoreceptor cells after mutation correction could provide unlimited seed cells for cell therapy alone or combined with gene therapy, especially in personalized therapy.

CONCLUSION

In conclusion, we obtained patient-specific, integration-free RPE65-hiPSCs, and their derivatives of retinal organoids with photoreceptors and RPE containing RPE65 mutations L67R and Y144H. The patient-specific organoids with RPE and photoreceptor cells may serve as new biomaterials or cell disease models for precision medicine including personalized pathogenic mechanisms, drug screening, gene therapy evaluation, or cell replacement therapy. Further studies will be needed to evaluate the degree to which the patient-specific retinal organoids can mimic the disease progress, phenotypes, and molecular changes.

DATA AVAILABILITY

The raw data supporting the conclusions of this manuscript will be made available by the authors, without undue reservation, to any qualified researcher.

ETHICS STATEMENT

This study was approved by the ethics committee of the Zhongshan Ophthalmic Center of Sun Yat-sen University and was conducted in accordance with the Declaration of Helsinki. The patient agreed to take part in this experiment and signed informed consent.

AUTHOR CONTRIBUTIONS

GL and GG: collection and assembly of data, data analysis and interpretation, and manuscript writing. PW and QZ: provision of study material or patients. XS, PX, BX, TZ, and GP: collection and assembly of data. FP and JG: data analysis and interpretation. XZ: conception and design, data analysis and interpretation, manuscript writing, final approval of the manuscript, and financial and administrative support.

FUNDING

This study was supported by the Natural Science Foundation of China (81570874, 81970842, and 81600746), the Science and Technology Project of Guangdong Province (2017B020230003), the National Key R&D Program of China (2017YFA0104100 and 2016YFC1101103), the Guangzhou Science and Technology Project Fund (201803010078), the Open Research Funds of the State Key Laboratory of Ophthalmology, and the Fundamental Research Funds of the State Key Laboratory of Ophthalmology.

ACKNOWLEDGMENTS

We thank Professor Jeremy Nathans (Johns Hopkins University School of Medicine) for the gifts of S opsin and L/M opsin antibodies. We also thank Dr. Guangjian Liu (Guangzhou Women and Children's Medical Center, China) for modeling of RPE65 protein structure with mutants.

SUPPLEMENTARY MATERIAL

The Supplementary Material for this article can be found online at: https://www.frontiersin.org/articles/10.3389/fnmol.2019.00212/full#supplementary-material

FIGURE S1 | Collection and culture of urine cells from a RPE65-LCA patient. **(A)** Schematic diagram of urine sample collection and cell culture. **(B)** Representative phase contrast photographs of urine epithelium cells (UCs) at passage (P) 1. Arrow, type 1 cells; arrowhead, type 2 cells. Scale bars, 100 μm. **(C)** UCs expressed epithelium markers E-cadherin, CD44, and KRT7 by immunofluorescence staining. Scale bars, 20 μm.

FIGURE S2 | Structural analysis of the *RPE65* mutations. **(A)** Hydrogen bonds analysis for the L67R mutation. Hydrogen bonds were shown as purple dash lines. There was no change in the local hydrogen bonds network when the mutation occurred. **(B,C)** The local electrostatic potentials within 3 Å of the 67th residues. Potentials less than −10 kT/e were colored in red, and those greater than +10 kT/e were depicted in blue. The positive charges around Arg67 were significantly higher than those of Leu67. **(D)** Hydrogen bonds analysis for the Y144H mutation. Y144H mutation lead to the loss of the hydrogen bond between Tyr144 and Asp 142. **(E,F)** The local electrostatic potentials within 3 Å of the 144th residues. His144 brought more positive charge than Tyr144.

FIGURE S3 | Pluripotency and free-integration of RPE65-hiPSCs demonstrated by other clones. **(A)** A primary clone (C4) with clear boundary on D20 after reprogramming. Scale bar, 200 μm. **(B)** RT-PCR showed pluripotency gene expression (OCT4, SOX2, NANOG) of RPE65-hiPSCs from five different clones. **(C)** Immunofluorescence staining of pluripotency markers (OCT4, SOX2, NANOG, SSEA4, TRA-1-81, and TRA-1-60) for RPE65-hiPSCs (C4, P6). Scale bars, 50 μm. **(D)** RT-PCR showed negative expression of exogenous episomal plasmid DNA in five RPE65-hiPSCs lines tested [C11–1 (P7), C4 (P8), C10 (P8), C13 (P9), C14 (P8)]. **(E)** G-band analysis showed RPE65-hiPSCs (C4) had normal karyotype.

FIGURE S4 | Negative controls of immunofluorescence staining (IFS) in **Figure 5**. To exclude the false positive caused by the non-specific binding of second antibodies, three types of second antibodies **(A–C)** used in **Figure 5** were tested with PBS instead of the first antibodies, Recoverin raised from rabbit **(A)**, Rhodopsin from mouse **(B)**, and S opsin from rabbit **(C)** as the negative controls. IFS were performed parallelly on serial sections of retinal organoids older than W20. All images were taken under the same exposure conditions with an LSM 510 confocal microscope (Zeiss). The detailed information of all antibodies can be found in **Table 1**. Scale bars, 20 μm.

FIGURE S5 | Propagation of RPE65-hiPSCs derived RPE cells. **(A)** Cobblestone-like RPE cells derived from RPE65-hiPSCs contained pigmentation 40 days after differentiation. Scale bar, 200 μm. **(B)** Passaged RPE cells on D2. Scale bar, 200 μm. **(C)** Passaged RPE cells presented cobblestone morphology and regained pigmentation 4 weeks after passage. Scale bar, 50 μm. **(D)** Immunostaining showed that the typical RPE markers PAX6, OTX2, MITF, and ZO-1 were positive in passaged RPE cells derived from both control and RPE65 hiPSCs. Scale bars, 20 μm.

FIGURE S6 | Functional evaluation of patient RPE cells. **(A,B)** Z-stack confocal images showing the phagocytosed CM-DiI labeled POS (red) by RPE cells derived from control **(A)** and patient **(B)** hiPSCs. During 12 h POS incubation, cells cultured in 4°C were used as negative control. **(C)** The POS phagocytosis capacity of RPE65-hiPSCs derived RPE cells was comparable to the control. Mean ± *SD*, $n = 3$. **(D)** The total VEGF secretion of both control- and patient-derived RPE cells cultured for 24 h was equivalent. Mean ± *SD*, $n = 3$.

REFERENCES

Astuti, G. D., Bertelsen, M., Preising, M. N., Ajmal, M., Lorenz, B., Faradz, S. M., et al. (2016). Comprehensive genotyping reveals RPE65 as the most frequently mutated gene in leber congenital amaurosis in Denmark. *Eur. J. Hum. Genet.* 24, 1071–1079. doi: 10.1038/ejhg.2015.241

Bainbridge, J. W., Mehat, M. S., Sundaram, V., Robbie, S. J., Barker, S. E., Ripamonti, C., et al. (2015). Long-term effect of gene therapy on Leber's congenital amaurosis. *N. Engl. J. Med.* 372, 1887–1897. doi: 10.1056/NEJMoa1414221

Bainbridge, J. W., Smith, A. J., Barker, S. S., Robbie, S., Henderson, R., Balaggan, K., et al. (2008). Effect of gene therapy on visual function in Leber's congenital amaurosis. *N. Engl. J. Med.* 358, 2231–2239. doi: 10.1056/NEJMoa0802268

Bereta, G., Kiser, P. D., Golczak, M., Sun, W., Heon, E., Saperstein, D. A., et al. (2008). Impact of retinal disease-associated RPE65 mutations on retinoid isomerization. *Biochemistry* 47, 9856–9865. doi: 10.1021/bi800905v

Bernardis, I., Chiesi, L., Tenedini, E., Artuso, L., Percesepe, A., Artusi, V., et al. (2016). Unravelling the complexity of inherited retinal dystrophies molecular testing: added value of targeted next-generation sequencing. *Biomed. Res. Int.* 2016:6341870. doi: 10.1155/2016/6341870

Biasini, M., Bienert, S., Waterhouse, A., Arnold, K., Studer, G., Schmidt, T., et al. (2014). SWISS-MODEL: modelling protein tertiary and quaternary structure using evolutionary information. *Nucleic Acids Res.* 42, W252–W258. doi: 10.1093/nar/gku340

Chen, Y., Zhang, Q., Shen, T., Xiao, X., Li, S., Guan, L., et al. (2013). Comprehensive mutation analysis by whole-exome sequencing in 41 Chinese families with Leber congenital amaurosis. *Invest. Ophthalmol. Vis. Sci.* 54, 4351–4357. doi: 10.1167/iovs.13-11606

Coussa, R. G., Lopez Solache, I., and Koenekoop, R. K. (2017). Leber congenital amaurosis, from darkness to light: an ode to Irene Maumenee. *Ophthalmic Genet.* 38, 7–15. doi: 10.1080/13816810.2016.1275021

Dalkara, D., Goureau, O., Marazova, K., and Sahel, J. A. (2016). Let there be light: gene and cell therapy for blindness. *Hum. Gene Ther.* 27, 134–147. doi: 10.1089/hum.2015.147

Deng, W. L., Gao, M. L., Lei, X. L., Lv, J. N., Zhao, H., He, K. W., et al. (2018). Gene correction reverses ciliopathy and photoreceptor loss in iPSC-derived retinal organoids from retinitis pigmentosa patients. *Stem Cell Rep.* 10:2005. doi: 10.1016/j.stemcr.2018.05.012

Dolinsky, T. J., Nielsen, J. E., McCammon, J. A., and Baker, N. A. (2004). PDB2PQR: an automated pipeline for the setup of poisson-boltzmann electrostatics calculations. *Nucleic Acids Res.* 32, W665–W667. doi: 10.1093/nar/gkh381

Hendrickson, A., Bumsted-O'Brien, K., Natoli, R., Ramamurthy, V., Possin, D., and Provis, J. (2008). Rod photoreceptor differentiation in fetal and infant human retina. *Exp. Eye Res.* 87, 415–426. doi: 10.1016/j.exer.2008.07.016

Humphrey, W., Dalke, A., and Schulten, K. (1996). VMD: visual molecular dynamics. *J. Mol. Graph.* 14, 27–38.

Jacobson, S. G., Cideciyan, A. V., Huang, W. C., Sumaroka, A., Nam, H. J., Sheplock, R., et al. (2016). Leber congenital amaurosis: genotypes and retinal structure phenotypes. *Adv. Exp. Med. Biol.* 854, 169–175. doi: 10.1007/978-3-319-17121-0_23

Jin, M., Li, S., Moghrabi, W. N., Sun, H., and Travis, G. H. (2005). Rpe65 is the retinoid isomerase in bovine retinal pigment epithelium. *Cell* 122, 449–459. doi: 10.1016/j.cell.2005.06.042

Kime, C., Mandegar, M. A., Srivastava, D., Yamanaka, S., Conklin, B. R., and Rand, T. A. (2016). Efficient CRISPR/Cas9-based genome engineering in human pluripotent stem cells. *Curr. Protoc. Hum. Genet.* 88:Unit21.4. doi: 10.1002/0471142905.hg2104s88

Koenekoop, R. K. (2004). An overview of Leber congenital amaurosis: a model to understand human retinal development. *Surv. Ophthalmol.* 49, 379–398. doi: 10.1016/j.survophthal.2004.04.003

Kumaran, N., Moore, A. T., Weleber, R. G., and Michaelides, M. (2017). Leber congenital amaurosis/early-onset severe retinal dystrophy: clinical features, molecular genetics and therapeutic interventions. *Br. J. Ophthalmol.* 101, 1147–1154. doi: 10.1136/bjophthalmol-2016-309975

Li, G., Xie, B., He, L., Zhou, T., Gao, G., Liu, S., et al. (2018). Generation of retinal organoids with mature rods and cones from urine-derived human induced pluripotent stem cells. *Stem Cells Int.* 2018:4968658. doi: 10.1155/2018/4968658

Li, S., Izumi, T., Hu, J., Jin, H. H., Siddiqui, A. A., Jacobson, S. G., et al. (2014). Rescue of enzymatic function for disease-associated RPE65 proteins containing various missense mutations in non-active sites. *J. Biol. Chem.* 289, 18943–18956. doi: 10.1074/jbc.M114.552117

Liu, S., Xie, B., Song, X., Zheng, D., He, L., Li, G., et al. (2018). Self-Formation of RPE spheroids facilitates enrichment and expansion of hiPSC-derived RPE generated on retinal organoid induction platform. *Invest. Ophthalmol. Vis. Sci.* 59, 5659–5669. doi: 10.1167/iovs.17-23613

Meyer, J. S., Shearer, R. L., Capowski, E. E., Wright, L. S., Wallace, K. A., McMillan, E. L., et al. (2009). Modeling early retinal development with human embryonic and induced pluripotent stem cells. *Proc. Natl. Acad. Sci. U.S.A.* 106, 16698–16703. doi: 10.1073/pnas.090524 5106

Parfitt, D. A., Lane, A., Ramsden, C. M., Carr, A. J., Munro, P. M., Jovanovic, K., et al. (2016). Identification and correction of mechanisms underlying inherited blindness in human ipsc-derived optic cups. *Cell Stem Cell* 18, 769–781. doi: 10.1016/j.stem.2016.03.021

Redmond, T. M., Yu, S., Lee, E., Bok, D., Hamasaki, D., Chen, N., et al. (1998). Rpe65 is necessary for production of 11-cis-vitamin A in the retinal visual cycle. *Nat. Genet.* 20, 344–351. doi: 10.1038/3813

Reichman, S., Terray, A., Slembrouck, A., Nanteau, C., Orieux, G., Habeler, W., et al. (2014). From confluent human iPS cells to self-forming neural retina and retinal pigmented epithelium. *Proc. Natl. Acad. Sci. U.S.A.* 111, 8518–8523. doi: 10.1073/pnas.1324212111

Russell, S., Bennett, J., Wellman, J. A., Chung, D. C., Yu, Z. F., Tillman, A., et al. (2017). Efficacy and safety of voretigene neparvovec (AAV2-hRPE65v2) in patients with RPE65-mediated inherited retinal dystrophy: a randomised, controlled, open-label, phase 3 trial. *Lancet* 390, 849–860. doi: 10.1016/S0140-6736(17)31868-31868

Schymkowitz, J., Borg, J., Stricher, F., Nys, R., Rousseau, F., and Serrano, L. (2005). The FoldX web server: an online force field. *Nucleic Acids Res.* 33, W382–W388. doi: 10.1093/nar/gki387

Shin, Y., Moiseyev, G., Chakraborty, D., and Ma, J. X. (2017). A dominant mutation in Rpe65, D477G, delays dark adaptation and disturbs the visual cycle in the mutant knock-in mice. *Am. J. Pathol.* 187, 517–527. doi: 10.1016/j.ajpath.2016.11.004

Soldner, F., Laganiere, J., Cheng, A. W., Hockemeyer, D., Gao, Q., Alagappan, R., et al. (2011). Generation of isogenic pluripotent stem cells differing exclusively at two early onset Parkinson point mutations. *Cell* 146, 318–331. doi: 10.1016/j.cell.2011.06.019

Takahashi, K., Tanabe, K., Ohnuki, M., Narita, M., Ichisaka, T., Tomoda, K., et al. (2007). Induction of pluripotent stem cells from adult human fibroblasts by defined factors. *Cell* 131, 861–872. doi: 10.1016/j.cell.2007.11.019

Tucker, B. A., Cranston, C. M., Anfinson, K. A., Shrestha, S., Streb, L. M., Leon, A., et al. (2015). Using patient-specific induced pluripotent stem cells to interrogate the pathogenicity of a novel retinal pigment epithelium-specific 65 kDa cryptic splice site mutation and confirm eligibility for enrollment into a clinical gene augmentation trial. *Transl. Res.* 166:740-741.e. doi: 10.1016/j.trsl.2015.08.007

Wang, H., Wang, X., Zou, X., Xu, S., Li, H., Soens, Z. T., et al. (2015). Comprehensive molecular diagnosis of a large chinese leber congenital amaurosis cohort. *Invest. Ophthalmol. Vis. Sci.* 56, 3642–3655. doi: 10.1167/iovs.14-15972

Wiley, L. A., Burnight, E. R., Songstad, A. E., Drack, A. V., Mullins, R. F., Stone, E. M., et al. (2015). Patient-specific induced pluripotent stem cells (iPSCs) for the study and treatment of retinal degenerative diseases. *Prog. Retin. Eye Res.* 44, 15–35. doi: 10.1016/j.preteyeres.2014.10.002

Xue, Y., Cai, X., Wang, L., Liao, B., Zhang, H., Shan, Y., et al. (2013). Generating a non-integrating human induced pluripotent stem cell bank from urine-derived cells. *PLoS One* 8:e70573. doi: 10.1371/journal.pone.0070573

Zheng, S. S., Han, R. Y., Xiang, L., Zhuang, Y. Y., and Jin, Z. B. (2018). Versatile genome engineering techniques advance human ocular disease researches in zebrafish. *Front. Cell Dev. Biol.* 6:75. doi: 10.3389/fcell.2018.00075

Zhong, X., Gutierrez, C., Xue, T., Hampton, C., Vergara, M. N., Cao, L. H., et al. (2014). Generation of three-dimensional retinal tissue with functional photoreceptors from human iPSCs. *Nat. Commun.* 5:4047. doi: 10.1038/ncomms5047

Zhou, T., Benda, C., Duzinger, S., Huang, Y., Li, X., Li, Y., et al. (2011). Generation of induced pluripotent stem cells from urine. *J. Am. Soc. Nephrol.* 22, 1221–1228. doi: 10.1681/ASN.2011010106

Conflict of Interest Statement: The authors declare that the research was conducted in the absence of any commercial or financial relationships that could be construed as a potential conflict of interest.

frontiers in Molecular Neuroscience

ORIGINAL RESEARCH
published: 20 December 2019
doi: 10.3389/fnmol.2019.00316

Single Cell and Single Nucleus RNA-Seq Reveal Cellular Heterogeneity and Homeostatic Regulatory Networks in Adult Mouse Stria Vascularis

*Soumya Korrapati[1†], Ian Taukulis[1†], Rafal Olszewski[1], Madeline Pyle[1], Shoujun Gu[1], Riya Singh[1], Carla Griffiths[1], Daniel Martin[2], Erich Boger[3], Robert J. Morell[3] and Michael Hoa[1]**

[1] Auditory Development and Restoration Program, National Institute on Deafness and Other Communication Disorders, National Institutes of Health, Bethesda, MD, United States, [2] Biomedical Research Informatics Office, National Institute of Dental and Craniofacial Research, National Institutes of Health, Bethesda, MD, United States, [3] Genomics and Computational Biology Core, National Institute on Deafness and Other Communication Disorders, National Institutes of Health, Bethesda, MD, United States

OPEN ACCESS

Edited by:
Fabio Mammano,
University of Padua, Italy

Reviewed by:
Karen Steel,
King's College London,
United Kingdom
Hiroshi Hibino,
Niigata University, Japan

***Correspondence:**
Michael Hoa
michael.hoa@nih.gov

[†] These authors have contributed equally to this work

Received: 02 October 2019
Accepted: 05 December 2019
Published: 20 December 2019

Citation:
Korrapati S, Taukulis I, Olszewski R, Pyle M, Gu S, Singh R, Griffiths C, Martin D, Boger E, Morell RJ and Hoa M (2019) Single Cell and Single Nucleus RNA-Seq Reveal Cellular Heterogeneity and Homeostatic Regulatory Networks in Adult Mouse Stria Vascularis. Front. Mol. Neurosci. 12:316. doi: 10.3389/fnmol.2019.00316

The stria vascularis (SV) generates the endocochlear potential (EP) in the inner ear and is necessary for proper hair cell mechanotransduction and hearing. While channels belonging to SV cell types are known to play crucial roles in EP generation, relatively little is known about gene regulatory networks that underlie the ability of the SV to generate and maintain the EP. Using single cell and single nucleus RNA-sequencing, we identify and validate known and rare cell populations in the SV. Furthermore, we establish a basis for understanding molecular mechanisms underlying SV function by identifying potential gene regulatory networks as well as druggable gene targets. Finally, we associate known deafness genes with adult SV cell types. This work establishes a basis for dissecting the genetic mechanisms underlying the role of the SV in hearing and will serve as a basis for designing therapeutic approaches to hearing loss related to SV dysfunction.

Keywords: snRNA-Seq, scRNA-Seq, adult stria vascularis, regulons, hearing, EP

INTRODUCTION

Ionic homeostasis in the endolymph-containing compartment of the cochlea, the scala media, is a critical factor in enabling proper hair cell mechanotransduction and hearing (Wangemann, 2002, 2006; Hibino et al., 2010). The endolymph is the atypical potassium rich extracellular fluid of the cochlear duct. This high potassium concentration results in a +80 millivolt (mV) positive potential known as the endocochlear potential (EP) (Wangemann, 2002; Patuzzi, 2011). The stria vascularis (SV), a non- sensory epithelial tissue in the lateral wall of the cochlea, generates and maintains this high potassium concentration and the EP.

The SV is a complex, heterogenous tissue consisting of several cell types that work together to generate and maintain the EP. Cell types identified as critical to this role thus far include

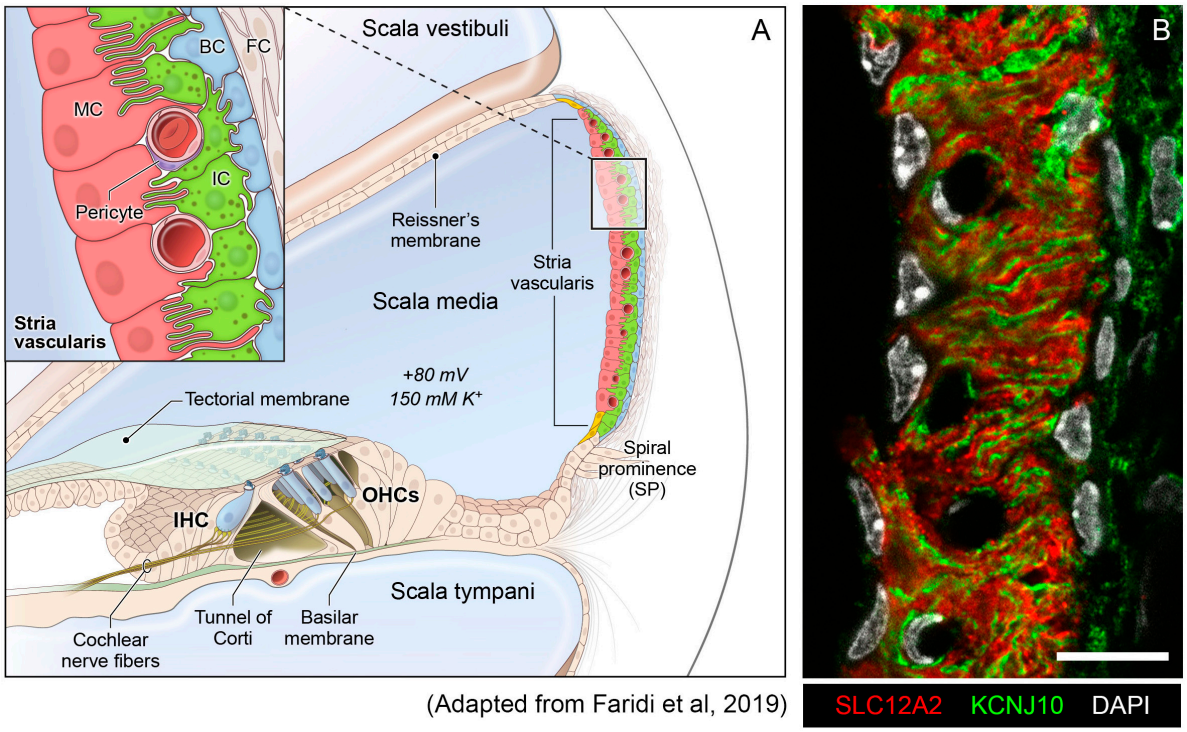

FIGURE 1 | Stria vascularis cellular heterogeneity and organization. **(A)** Schematic of the stria vascularis (SV) and its relationship to structures in the cochlea. The SV is composed of three layers of cells and is responsible for generating the +80 mV endocochlear potential (EP) and the high potassium concentration in the endolymph-containing scala media. The relationship between the marginal, intermediate and basal cells are demonstrated with the marginal cells extending basolateral projections to interdigitate with intermediate cells, which have bidirectional cellular projections that interdigitate with both marginal and basal cells. In addition to these cell types, other cell types, including spindle cells (yellow), endothelial cells, pericytes, and macrophages (not shown) are present in the SV. **(B)** Cross-section of the SV in a postnatal day 30 (P30) mouse immunostained with anti-SLC12A2 (marginal cells, red), anti-KCNJ10 (intermediate cells, green), and DAPI (4′,6-diamidino-2-phenylindole) for nuclei. Notice the interdigitation of cellular processes from both intermediate and marginal cells. Scale bar is 20 μm.

marginal cells, intermediate cells and basal cells (Wangemann, 2002; Gow, 2004; Wangemann et al., 2004; Marcus et al., 2013). The marginal cells (MCs) face the endolymph and extend basolateral projections that interdigitate with the intermediate cells (ICs) which have projections that run in both directions toward marginal cells apically and basal cells at the basolateral end (**Figure 1A**). Basal cells (BCs) are connected to each other by tight junctions (like the MCs) to prevent leakage of ions (Kitajiri S.I. et al., 2004). At least two of these cell types, marginal and intermediate cells appear to have densely interdigitating processes (**Figure 1B**) intimating at the close functional interaction between these cell types in the SV (Steel and Barkway, 1989; Nakazawa et al., 1995). In addition, other cell types in the SV include spindle cells, macrophages, pericytes and endothelial cells (Neng et al., 2013; Ito et al., 2014; Shi, 2016).

Knowledge regarding the role of the three main cell types (MCs, ICs, BCs) in the generation and maintenance of the EP is based on previous work by others. Mutations in genes expressed by marginal, intermediate and basal cells in the SV are known to cause deafness and dysfunction in EP generation. In marginal cells, mutations in Kcnq1, Kcne1 and Barttin (Bsnd) result in a loss or reduction of EP and deafness (Rickheit et al., 2008; Chang et al., 2015; Faridi et al., 2019). *Kcnq1/Kcne1* encode the voltage-gated potassium channel Kv7.1 and play a crucial role in secreting potassium and maintaining the EP. Conditional *Kcnq1* null mice exhibit collapsed Reissner's membrane, loss of EP, and are deaf (Chang et al., 2015). Barttin (*Bsnd*) is a beta subunit of chloride channel ClC-K, mutations in which cause deafness and Bartter syndrome IV in humans. Conditional null mice of barttin in the inner ear exhibit hearing loss with reduced EP (Rickheit et al., 2008; Riazuddin et al., 2009). In intermediate cells, *Kcnj10* encodes Kir4.1, an inwardly rectifying potassium channel, which is necessary for the generation of the EP. Loss or mutations in *Kcnj10* have been shown to cause hearing loss in humans and mice, accompanied by an absence of EP and loss of endolymphatic potassium (Wangemann et al., 2004; Marcus et al., 2013; Chen and Zhao, 2014). Finally, basal cells play a role in barrier formation and prevent ion leakage from the SV. Claudin 11 (*Cldn11*), a tight junction protein expressed in SV basal cells, is critical to this function as demonstrated by deafness and low EP in *Cldn11* null mice (Gow, 2004; Kitajiri S. et al., 2004).

Despite continuing interest in SV cell types, an understanding of cellular heterogeneity, including a comprehensive understanding of SV cell type-specific transcriptional profiles, is incomplete. While several *in vivo*, *in vitro*, and *in silico* studies have identified key roles for particular strial cell types in EP generation, including MCs, ICs, and BCs (Takeuchi et al., 2000; Kitajiri S. et al., 2004; Nin et al., 2008; Mori et al., 2009;

Hibino et al., 2010; Chen and Zhao, 2014; Yoshida et al., 2015; Nin et al., 2017), the mechanisms by which the various cell types work together to accomplish EP generation as well as other strial functions remains largely undefined (Ohlemiller, 2009). Furthermore, the gene regulatory networks that provide the basis for these EP-generating mechanisms remain largely undefined. Recently, both single cell and single nucleus approaches have been utilized to define transcriptional profiles of cells from organs and tissues with significant cellular heterogeneity (Zeng et al., 2016; Wu et al., 2019). Given the presence of a heterogeneous group of cell types with significant cell size and shape heterogeneity, we set out to define the transcriptional profiles of the three major cell types implicated in EP generation by utilizing single cell RNA-Seq (scRNA-Seq) and single nucleus RNA-Seq (snRNA-Seq) in the adult SV. In doing so, we seek to define transcriptional heterogeneity between SV cell types and define gene regulatory networks in the unperturbed wild type adult SV that can serve as a basis for investigating mechanisms responsible for SV functions.

MATERIALS AND METHODS

A table of key resources is provided in the **Supplementary Table S1**.

Animals

Inbred CBA/J males and females were purchased from JAX (Stock No. 000656). Breeding pairs were set up to obtain P30 mice for single cell and single nucleus RNA seq experiments, immunohistochemistry and single molecule RNA FISH.

Cell/Nucleus Isolation

Stria Vascularis Dissection

Adult mice were sacrificed and inner ears were dissected. The lateral wall of the cochlea was microdissected from the bony wall of the cochlea. Localizing the pigmented strip in the cochlear lateral wall, the SV was microdissected from the spiral ligament using fine forceps. Microdissection of the SV from 2 cochlea were accomplished in less than 4 min. Multiple lab personnel experienced with the microdissections were utilized to minimize dissection time. Samples were collected at the same time of day across individual mice and batches. For each collection, less than 1 h was spent prior to single cell or single nucleus capture on the 10x Genomics Chromium platform. A total of 10 mice and 12 mice were used for single cell and single nucleus RNA-seq experiments, respectively.

Single Cell Suspension

Inner ears from a total of ∼25 P30 mice were removed and SV from the cochleae were collected into 200 μl DMEM F-12 media. The tissue was lysed in 0.5 mg/ml trypsin at 37°C for 7 min. The media was carefully removed and replaced with 5% FBS to stop the lysis. The tissue was triturated and filtered through a 20 μm filter (pluriSelect Life Science, El Cajon, CA, United States). The filtered cells were let to sit on ice for 35 min. Hundred and fifty microliter of the supernatant was removed and cell pellet was suspended in the remaining 50 μl. Cells were counted on a Luna automated cell counter (Logos Biosystems, Annandale, VA, United States) and a cell density of 1×10^6 cells/ml was used to load onto the 10X genomics chip.

Single Nucleus Suspension

Published single nucleus suspension protocol from 10x genomics was used to isolate the nuclei. Briefly, SV from ∼10 P30 animals were isolated and collected in 3 ml DMEM F-12 media. Following collection, the media was replaced with 3 ml chilled lysis buffer (10 mM Tris-HCl, 10 mM NaCl, 3 mM $MgCl_2$,0.005% Nonidet P40 in Nuclease free water) and the tissue were lysed at 4°C for 25 min. The lysis buffer was then replaced with 1.5 ml DMEM F-12 media. The tissues were triturated and filtered through a 20 μm filter (pluriSelect Life Science, El Cajon, CA, United States). The filtrate was centrifuged at 500rcf for 5 min at 4°C. The supernatant was removed, and the cell pellet was resuspended in 1ml nuclei wash and resuspension buffer (1xPBS with 1% BSA and 0.2U/μl RNase Inhibitor). The cells were filtered through a 10 μm filter (pluriSelect Life Science, El Cajon, CA, United States) and centrifuged at 500rcf for 5 min at 4°C. The supernatant was removed, and pellet resuspended in 50 μl of nuclei wash and resuspension buffer. Nuclei were counted in a Luna cell counter (Logos Biosystems, Annandale, VA, United States) and a nuclear density of 1×10^6 cells/ml was used to load onto the 10X genomics chip.

10x Chromium Genomics Platform

Single cell or nuclei captures were performed following manufacturer's recommendations on a 10x Genomics Controller device (Pleasanton, CA, United States). The targeted number of captured cells or nuclei ranged from 6,000 to 7,000 per run. Library preparation was performed according the instructions in the 10x Genomics Chromium Single Cell 3' Chip Kit V2. Libraries were sequenced on a HiSeq 1500 or Nextseq 500 instrument (Illumina, San Diego, CA, United States) and reads were subsequently processed using 10x Genomics CellRanger analytical pipeline using default settings and 10x Genomics downloadable mm10 genome. Dataset aggregation was performed using the cellranger aggr function normalizing for total number of confidently mapped reads across libraries. For scRNA-Seq datasets, 132,866 mean reads per cell and 1,111 median genes per cell were obtained. For the snRNA-Seq dataset, 23,887 mean reads per cell and 727 genes per cell were obtained.

PCA and *t*-SNE Analysis

Selection of Genes for Clustering Analysis

Identification of the highly variable genes was performed in Seurat utilizing the MeanVarPlot function using the default settings with the aim to identify the top ∼ 2000 variable genes (Satija et al., 2015). Briefly, to control for the relationship between variability and average expression, average expression and dispersion is calculated for each gene, placing the genes into bins, and then a *z*-score for dispersion within the bins is calculated. These genes are utilized in the downstream analysis for clustering.

Clustering of Single Cells

Clustering analysis of single-cell data was performed with Seurat using a graph-based clustering approach (Satija et al., 2015). Briefly, the Jackstraw function using the default settings was used to calculate significant principal components ($p < 0.0001$) and these principal components were utilized to calculate k-nearest neighbors (KNN) graph based on the euclidean distance in PCA space. The edge weights are refined between any two cells based on the shared overlap in their local neighborhoods (Jaccard distance). Cells are then clustered according to a smart local moving algorithm (SLM), which iteratively clusters cell groupings together with the goal to optimize the standard modularity function (Blondel et al., 2008; Waltman and van Eck, 2013)[1]. Resolution in the FindClusters function was set to 0.8. High modularity networks have dense connections between the nodes within a given module but sparse connections between nodes in different modules. Clusters were then visualized using a t-distributed stochastic neighbor embedding (t-SNE) plot.

Doublet Detection and Elimination

To detect and eliminate doublets that may affect clustering analysis we used an R package called DoubletDecon described previously (DePasquale et al., 2018) that iteratively detects doublets in single-cell RNASeq data. An expression matrix of read counts, the top 50 marker genes for each cluster, and a list of cells with cluster identities are used to create "medoids" for each cluster which are averages of cell-type specific gene expression. It then compares the similarity of expression for each cluster medoid to every other medoid resulting in a binary correlation matrix. If two cluster medoids meet or exceed the similarity threshold they receive a "1" in the binary matrix, referred to as "blacklist clusters," and if they do not they receive a "0" in the binary matrix. Synthetic doublets are generated using cells from each pairwise comparison of dissimilar cluster medoids. Synthetic doublets, cells, and blacklist cluster gene expression profiles are deconvoluted and each cell is iteratively compared to both synthetic doublet profiles and blacklist clusters. If a cell is more similar in expression to synthetic doublets it is classified as a putative doublet. Putative doublets are re-clustered, and Welch's *t*-test is used to determine uniquely expressed genes. If any cells express one unique gene when compared to the blacklisted clusters they are rescued and classified as a singlet. The singlet list was used to subset our single-cell data, and the Seurat pipeline was re-run on the new doublet eliminated data.

Differential Gene Expression Analysis

Differential expression analysis was performed in Seurat utilizing the FindAllMarkers function with the default settings except that the "min.pct" and "thresh.use" parameters were utilized to identify broadly expressed (min.pct = 0.8, thresh.use = 0.01) and subpopulation-specific (min.pct = 0.5, thresh.use = 0.25) expression profiles. The parameter "min.pct" sets a minimum fraction of cells that the gene must be detected in all clusters. The parameter "thresh.use" limits testing to genes which show, on average, at least X-fold difference (log-scale) between groups of cells. The default test for differential gene expression is "bimod," a likelihood-ratio test (McDavid et al., 2013). Differentially expressed genes were then displayed on violin plots based on unbiased clustering described above.

Heatmap or Grid Violin Plot Construction of Selected Data

Heatmaps or grid violin plots were constructed using custom python scripts and utilized to display gene expression across SV cell types identified in both scRNA-Seq and snRNA-Seq datasets. Briefly, construction of heatmaps or grid violin plots was performed in the following fashion: (1) Raw counts data was processed within Seurat as previously described. (2) Normalized counts were scaled into range [0,1] by using min-max scaling method on each gene. (3) Heatmaps or violin plots were constructed by python/seaborn using the scaled data counts. Detailed code can be found in python scripts in **Supplementary Material**.

Downstream Computational Analysis

Gene Regulatory Network Inference

Two independent methods of gene regulatory network inference, Weighted gene co-expression network analysis (WGCNA) (Langfelder and Horvath, 2008) and single cell regulatory network inference and clustering (SCENIC) (Aibar et al., 2017) were utilized. Briefly, WGCNA constructs a gene co-expression matrix, uses hierarchical clustering in combination with the Pearson correlation coefficient to cluster genes into groups of closely co-expressed genes termed modules, and then uses singular value decomposition (SVD) to determine similarity between gene modules. Hierarchical clustering of modules is displayed as topological overlap matrix (TOM) plots and similarity between gene modules are displayed as adjacency plots. Briefly, SCENIC identifies potential gene regulatory networks by performing the following steps: (1) *modules* consisting of transcription factors and candidate target genes are determined on the basis of co-expression utilizing GENIE3, (2) *regulons* are constructing by filtering modules for candidate genes that are enriched for their transcription factor binding motifs utilizing RcisTarget, (3) the activity of each regulon within each cell is determined, (4) the *regulon activity matrix* is constructed utilizing these regulon activity scores and can be used to cluster cells on the basis of shared regulatory networks. In this way, SCENIC may identify cell types and cell states on the basis of shared activity of a regulatory subnetwork.

Deafness Gene Screen of Stria Vascularis Transcriptomes From scRNA-Seq and sn-RNA-Seq Datasets

In order to screen our datasets for known deafness genes, we constructed a database of known human and mouse deafness genes from the following sources: (1) Hereditary Hearing Loss page[2] (Van Camp and Smith, n.d.) and (2) Hereditary hearing loss and deafness overview (Shearer et al., 1993; Azaiez et al., 2018).

[1] https://satijalab.org/seurat/v3.1/pbmc3k_tutorial.html

[2] https://hereditaryhearingloss.org/

Gene Ontology and Gene-Set Enrichment Analysis

Gene ontology analyses and gene enrichment analyses were performed using Enrichr[3] as previously described (Chen et al., 2013; Kuleshov et al., 2016; Pazhouhandeh et al., 2017). Enrichr is an integrated web-based application that includes updated gene-set libraries, alternative approaches to ranking enriched terms, and a variety of interactive visualization approaches to display the enrichment results. Enrichr employs three approaches to compute enrichment as previously described (Jagannathan et al., 2017). The combined score approach where enrichment was calculated from the combination of the *p*-value computed using the Fisher exact test and the *z*-score was utilized. Top gene ontology (GO) terms were chosen by utilizing the combined score approach as described.

Identification of Potentially Druggable Gene Targets

To identify druggable targets within our scRNA-Seq data of the SV, genes from P30 cell-type specific SCENIC regulons were input into Pharos[4] (Nguyen et al., 2017) using their "batch search" function. Pharos is a database created by the "Illuminating the Druggable Genome" program to give users access to protein targets and the availability of drugs or small molecules for each. Pharos categorizes each protein with a "target developmental level" according to how much is known on its "druggability." Targets that are well studied are deemed "Tclin" if they can be targeted with FDA approved drugs that have a known mechanism of action on the target, "Tchem" if there are known small-molecule ligands that bind the target, or "Tbio" if the target has a known gene ontology or phenotype but no available drugs or small molecules. Targets that are currently unstudied are labeled "Tdark." To focus on the most clinically relevant targets, we filtered for only Tclin and Tchem developmental levels in our search. Tclin and Tchem targets from each cell-type specific regulon were plotted using the FeaturePlot function in Seurat to identify the most specific targets within regulons of the SV.

Fluorescent *in situ* Hybridization (smFISH) Using RNAscope Probes

In situ hybridizations were performed using the following RNAscope probes (**Supplementary Table S1**). RNAscope probes were obtained from Advanced Cell Diagnostics (Newark, CA, United States) and used with sections of cochleae from CBA/J wild type mice at P30. Adult cochleae were dissected from the head and fixed overnight at 44°C in 4% PFA in 1x PBS. Fixed adult mouse inner ears were decalcified in 150 mM EDTA for 5–7 days, transferred to 30% sucrose, and then embedded and frozen in SCEM tissue embedding medium (Section-Lab Co, Ltd.). Adhesive film (Section-Lab Co, Ltd.; Hiroshima, Japan) was fastened to the cut surface of the sample in order to support the section and cut slowly with a blade to obtain thin midmodiolar sections. The adhesive film with section attached was submerged in 100% EtOH for 60 s, then transferred to distilled water. The adhesive film consists of a thin plastic film and an adhesive and it prevents specimen shrinkage and detachment. This methodology allows for high quality anatomic preservation of the specimen. Frozen tissues were sectioned (10 μm thickness) with a CM3050S cryostat microtome (Leica, Vienna, Austria). Sections were mounted with SCMM mounting media (Section-Lab Co, Ltd., Hiroshima, Japan) and imaged using a 1.4 N.A. objective. Probe information is detailed in **Supplementary Table S1**.

Immunohistochemistry

For immunohistochemistry of cochlear sections, fixed adult mouse inner ears were prepared as previously described. Fluorescence immunohistochemistry for known SV cell-type markers was performed as follows. Mid-modiolar sections were washed in PBS then permeabilized and blocked for 1 h at room temperature in PBS with 0.2% Triton X-100 (PBS-T) with 10% fetal bovine serum (Catalog # A3840001, Thermo Fisher Scientific, Waltham, MA, United States). Samples were then incubated in the appropriate primary antibodies in PBS-T with 10% fetal bovine serum, followed by three rinses in PBS-T and labeling with AlexaFluor-conjugated secondary antibodies (1:250, Life Technologies) in PBS-T for 1 h at room temperature. Where indicated, 4,6-diamidino-2-phenylindole (1:10,000, Life Technologies) was included with the secondary antibodies to detect nuclei. Organs were rinse in PBS three times and mounted in SlowFade (Invitrogen). Specimens were imaged using a Zeiss LSM710 confocal microscope. Sections were mounted with SCEM mounting medium (Section-Lab Co, Ltd., Hiroshima, Japan). Primary antibodies used included rabbit anti-KCNJ10 (Alomone Labs, Cat# APC-035, polyclonal, dilution 1:200), rabbit anti-CLDN11 (Life Technologies, Cat# 364500, polyclonal, dilution 1:200), goat anti-SLC12A2 (Santa Cruz Biotech, Cat# sc-21545, polyclonal, dilution 1:200), goat anti-KCNQ1 (Santa Cruz Biotech, Cat# sc-10646, polyclonal, dilution 1:200), Phalloidin AlexaFluor 647 (Invitrogen, Cat# A22287, dilution 1:250).

Statistical Analysis

Statistical analysis for single-cell RNA-Seq is described in the detailed methods.

Data and Software Availability

All data generated in these studies have been deposited in the Gene Expression Omnibus (GEO) database (GEO Accession ID: GSE136196) and can be found on GEO[5]. We are also in the process of uploading the data into the gene Expression Analysis Resource (gEAR), a website for visualization and comparative analysis of multi-omic data, with an emphasis on hearing research[6].

RESULTS

Defining Cellular Heterogeneity Within the Adult Stria Vascularis (SV)

The SV is composed of a heterogeneous group of cell types that work together to generate the endocochlear potential.

[3]http://amp.pharm.mssm.edu/Enrichr/

[4]https://pharos.nih.gov

[5]https://www.ncbi.nlm.nih.gov/geo/query/acc.cgi?acc=GSE136196

[6]https://umgear.org

Defining these cell types and their respective transcriptional profiles in the adult mammalian SV is a critical first step toward understanding the genetic mechanisms that produce the EP. Cell isolation for single cell and single nucleus approaches must be optimized for the tissues they are targeting. In particular, cellular heterogeneity within a tissue can be manifested, not just by cell type heterogeneity, but also heterogeneity in size and shape, potentially necessitating different techniques to gain a comprehensive perspective on a given tissue. As can be seen in the representative image of the SV in **Figure 1B**, marginal cells (red), with cell nuclei eccentrically located closer to the endolymph (apical-medial), interdigitate with intermediate cells (green) with cell nuclei arranged so that processes extend to both the apical-medial and basolateral surfaces of the SV. The basal cells, which line the basolateral surface of the SV, appear to be relatively flat cells. The marginal, basal, and spindle cells appear to have relatively flat-appearing nuclei, while those of the intermediate cells appear more oblong in shape. For the SV, in order to address the challenge of transcriptional profiling a tissue composed of heterogeneous cell types with significant heterogeneity in cell size and shape, we utilized two methods of transcriptional profiling, single cell RNA-Seq (scRNA-Seq) and single nucleus RNA-Seq (snRNA-Seq).

An overview of the comparison between scRNA-Seq and snRNA-Seq techniques in the adult SV is provided in the **Supplementary Data and Methods** and **Supplementary Table S2**. Details of dataset aggregation for single cell captures using CellRanger is provided in the **Supplementary Data and Methods**. Briefly, distribution of cells across all clusters was analyzed and found to be equally distributed across all clusters based on cell capture date (**Supplementary Figure S1**). For these reasons, the dataset was treated as a single dataset. No other batch correction methods were used prior to analyzing these datasets. Both datasets were analyzed for dissociation-induced effects and clustering of cells was found to be minimally impacted by dissociation-induced gene expression (**Supplementary Figure S2**). Details on analysis of dissociation-induced effects have been previously detailed by others (Van Den Brink et al., 2017; Baryawno et al., 2019) and are discussed briefly in **Supplementary Data and Methods**. Due to the interdigitation of processes of the marginal and intermediate cells, it is possible that detection of ambient RNA, defined as the mRNA pool released in the cell suspensions likely by stressed or apoptotic cells (Yang et al., 2019), may affect clustering in scRNA-Seq (**Supplementary Figure S3** and **Supplementary Data and Methods**).

Stria Vascularis (SV) Cell Types Exhibit Clear Transcriptional Differences

Unbiased clustering of adult SV single cells and nuclei was performed independently. After unbiased clustering of cells by shared gene expression, known cell type-specific markers were utilized to identify these agnostically determined cell clusters. Based on these markers, marginal cell, intermediate cell, basal cell, spindle/root cell, macrophages, and immune and hematopoietic cell clusters were identified within the adult SV scRNA-Seq and snRNA-Seq datasets (**Figure 2A**). Here, we will focus the analyses on the marginal, intermediate, basal, and spindle/root cell clusters. Feature plots of both scRNA-Seq and snRNA-Seq datasets demonstrate the correlation of known gene expression for marginal cells (*Kcne1*, *Kcnq1*) (Wangemann, 2002), intermediate cells (*Cd44*, *Met*) (Shibata et al., 2016; Rohacek et al., 2017), basal cells (*Cldn11*, *Tjp1*) (Gow, 2004; Lee et al., 2017; Liu et al., 2017), and spindle/root cells (*Slc26a4*) between the two datasets (**Figures 2B,D**) (Nishio et al., 2016). Violin plots demonstrate relative expression of these known SV cell type-specific genes across the four main cell types (**Figures 2C,E**). Confirmatory smFISH and immunohistochemistry demonstrates expression of these known markers for marginal cells (*Kcne1*, *Kcnq1*), intermediate cells (*Cd44*, *Met*), basal cells (CLDN11, ZO-1), and spindle/root cells (*Slc26a4*) (**Figure 2F**). Co-expression of *Kcne1* and *Kcnq1* RNA to marginal cells of the adult SV can be seen, particularly in close proximity to marginal cell nuclei (**Figure 2F**). *Cd44* and *Met* RNA is co-expressed in intermediate cell nuclei (**Figure 2F**). CLDN11 and ZO-1 (the protein product of the *Tjp1* gene) are co-expressed in basal cells (**Figure 2F**). The confirmation of cell type clusters with known gene expression across both datasets strengthens the validity of the unbiased clustering as well as the capability of both approaches to assess transcriptome profiles in the SV.

Novel Cell Type-Specific Genes Are Identified by scRNA-Seq and snRNA-Seq of the Adult Stria Vascularis (SV)

Based on the transcriptional profiles, novel cell type-specific genes were identified and validated in adult SV. Feature plots demonstrate expression of selected novel candidate genes in marginal cells (*Abcg1*, *Heyl*), intermediate cells (*Nrp2*, *Kcnj13*), basal cells (*Sox8*, *Nr2f2*), and spindle/root cells (*P2rx2*, *Kcnj16*) in both scRNA-Seq and snRNA-Seq datasets, respectively (**Figures 3A,C**). Violin plots demonstrate the relative expression of these novel SV cell type-specific genes across the 4 main cell types (**Figures 3B,D**). The violin plots highlight aspects of shared gene expression between marginal cells and spindle cells amongst the selected candidate genes. This trend of shared gene expression was observed between marginal and spindle cells in terms of shared groups of genes (**Supplementary Figure S4**). Representative images depict co-expression of candidate gene RNA by smFISH in marginal cells (*Abcg1*, *Heyl*), intermediate cells (*Nrp2*, *Kcnj13*), basal cells (*Sox8*, *Nr2f2*) and spindle/root cells (*P2rx2*, *Kcnj16*) (**Figures 3E,F**). None of these gene transcripts have been previously identified in the mammalian SV. A discussion of the novel genes identified in this study is provided (**Supplementary Data and Methods**). Quantitation of novel cell type-specific transcript expression demonstrated transcript expression of these candidate genes in their respective cell type-specific nuclei (**Supplementary Figure 5A**).

Defining Potential Gene Regulatory Networks in SV Marginal, Intermediate and Basal Cells

Focusing on strial marginal, intermediate and basal cells, we sought to identify cell type-specific gene regulatory networks that might serve as a basis for investigating mechanisms related to

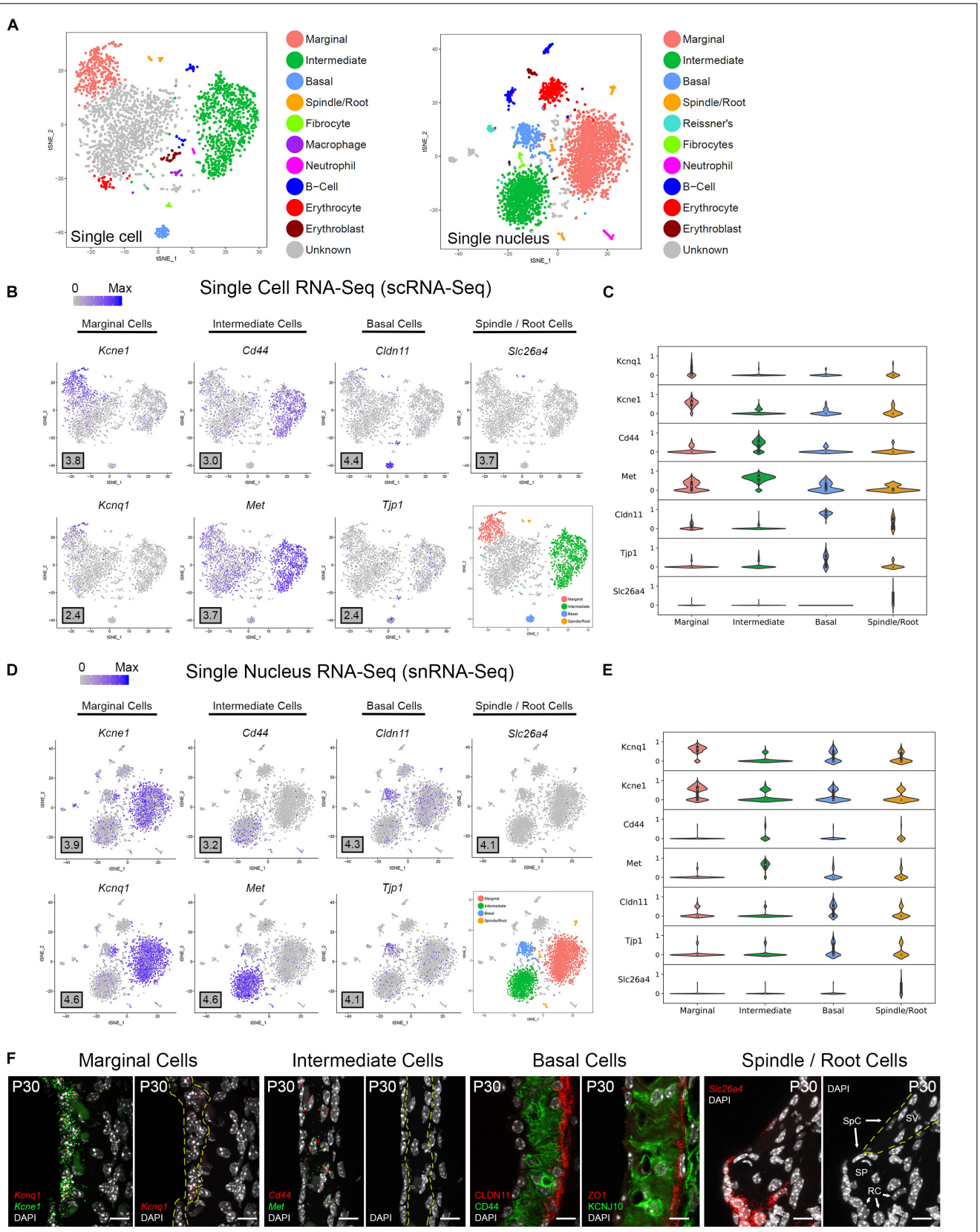

FIGURE 2 | Continued

FIGURE 2 | Stria vascularis (SV) cell types show clear transcriptional differences at the single cell and single nucleus level. **(A)** Unbiased clustering was performed on both single cell RNA-Seq (scRNA-Seq) and single nucleus RNA-Seq (snRNA-Seq) datasets from the P30 mouse SV. Known cell type-specific markers were utilized to identify these agnostically determined cell clusters. Based on these known markers, clusters consisting of marginal cells, intermediate cells, basal cells, spindle/root cells, and immune cell types, including macrophages, B cells, and neutrophils, were identified. tSNE plot of P30 mouse SV scRNA-Seq dataset demonstrates clustering of SV cell types (LEFT panel). tSNE plot of P30 mouse SV snRNA-Seq dataset demonstrates clustering of SV cell types with similar identification of cell type-specific clusters (RIGHT panel). **(B)** Feature plots for P30 SV scRNA-Seq data demonstrate expression of known markers for 4 main SV cell types: marginal cells (*Kcne1*, *Kcnq1*), intermediate cells (*Cd44*, *Met*), basal cells (*Cldn11*, *Tjp1*), and spindle/root cells (*Slc26a4*). 4 main cell types are highlighted on the inset tSNE plot of the scRNA-Seq dataset. Maximum expression (normalized counts) is noted in the black outlined gray box for each gene in the lower left corner of each feature plot. **(C)** Grid violin plot of scRNA-Seq dataset demonstrates expression of known marker genes amongst SV cell types. Normalized counts were scaled to a range of 0–1 using min-max scaling. **(D)** Feature plots for P30 SV snRNA-Seq data demonstrate expression of known markers for 4 main SV cell types: marginal cells (*Kcne1*, *Kcnq1*), intermediate cells (*Cd44*, *Met*), basal cells (*Cldn11*, *Tjp1*), and spindle/root cells (*Slc26a4*). 4 main cell types are highlighted on the inset tSNE plot of the snRNA-Seq dataset. Maximum expression (normalized counts) is noted in the black outlined gray box for each gene in the lower left corner of each feature plot. **(E),** Grid violin plot of snRNA-Seq dataset demonstrates expression of known marker genes amongst SV cell types. Normalized counts were scaled to a range of 0–1 using min-max scaling. **(F)** Validation of known gene expression was performed using single molecule fluorescent *in situ* hybridization (smFISH) and fluorescence immunohistochemistry. Known marginal cell-specific transcripts (*Kcne1*, *Kcnq1*) and intermediate cell-specific transcripts (*Cd44*, *Met*) are co-localized by smFISH. Yellow dashed lines outline the SV marginal cell layer showing Kcnq1 transcript expression in marginal cells with DAPI to label nuclei. Yellow dashed lines outline the SV intermediate cell layer in the image with DAPI only. CLDN11 and ZO-1 (protein product of *Tjp1*) are localized to the basal cell layer with anti-CD44 and anti-KCNJ10 immunostaining to label the adjacent intermediate cell layer for contrast, respectively. Finally, *Slc26a4* transcripts are localized to the spindle/root cells by smFISH. Yellow dashed lines in the image to the right with only the DAPI labeling demarcate the SV and spindle cells (SpC) and root cells (RC) in the spiral prominence (SP) are identified. DAPI (4′,6-diamidino-2-phenylindole). All scale bars 10 μm.

strial function and eventually on strial dysfunction in human disorders. To identify these potential gene regulatory networks in the adult mouse, two methods (WGCNA, SCENIC) of unbiased gene regulatory network identification were utilized as described previously. WGCNA identifies modules of co-expressed genes without making a link between transcription factors and co-expressed genes. In doing so, WGCNA casts a wider net as it relates to co-expression analysis, potentially identifying indirectly linked genes in a regulatory network. Conversely, SCENIC identifies regulons composed of co-expressed transcription factors and their downstream targets as determined by motif enrichment. This approach identifies transcription factors with potentially directly linked genes in a regulatory network.

WGCNA Identifies Cell Type-Specific Gene Regulatory Networks in the Adult Stria Vascularis

Topological overlap (TOM) plots for scRNA-Seq and snRNA-Seq datasets from the adult SV demonstrate clustering of gene modules identified in WGCNA (**Figure 4A**). The more red a box is, the higher the Pearson correlation coefficient is between modules. The adjacency plots take this adjacency matrix and display highly correlated gene modules (**Figure 4B** and **Supplementary Figures S6**, **S7**). Cell type-specific modules for marginal, intermediate and basal cells were reprojected onto the feature plots for each dataset (**Figure 4C**). The top gene ontology (GO) biological process, cellular component and molecular function are summarized in **Supplementary Figure S8**. Supplementary Tables containing all GO terms (biological process, cellular component, and molecular function) with adjusted *p*-values and the associated combined score are provided for the WGCNA modules grouped by cell type-specificity to the three major SV cell types (marginal, intermediate, and basal cells) are provided in the **Supplementary Tables S3–S5**.

GO biological process analysis revealed a significant enrichment for genes involved in positive regulation of potassium ion transport (GO:1903288) in SV marginal cells and regulation of potassium ion transport by positive regulation of transcription from RNA polymerase II promoter (GO:0097301) for SV intermediate cells. Additionally, GO biological process analysis revealed a significant enrichment in genes involved in protein stabilization (GO:0050821), neutrophil degranulation (GO:0043312), and positive regulation of rhodopsin gene expression (GO:0045872) in SV marginal, intermediate, and basal cells, respectively. GO molecular function analysis revealed a significant enrichment for genes involved in calcium-transporting ATPase activity (GO:0005388) and translation factor activity, RNA binding (GO:0008135) in SV marginal and intermediate cells, respectively. GO molecular function analysis did not reveal a significantly enriched process in SV basal cells. GO cellular component analysis revealed a significant enrichment for genes involved in G-protein coupled receptor complex (GO:0097648), interleukin-28 receptor complex (GO:0032002), and platelet alpha granule lumen (GO:0031093) for SV marginal, intermediate, and basal cells, respectively. Overall, these analyses affirm the importance of ion homeostasis amongst marginal and intermediate cells and suggest functions related to the immune system (neutrophil degranulation, interleukin-28 receptor complex).

SCENIC Identifies Cell Type-Specific Gene Regulatory Networks in the Adult Stria Vascularis

TSNE plots demonstrate a comparison between principal component analysis (PCA)-based clustering within Seurat and regulon-based clustering within SCENIC for both scRNA-Seq in the upper panel (**Figure 5A**) and snRNA-Seq in the lower panel (**Figure 5B**). Regulon-based clustering within SCENIC identifies similar clusters to those seen within Seurat based on PCA. Display of regulon activity matrix for both scRNA-Seq and snRNA-Seq datasets demonstrates cell type-specific regulons prominently within marginal, intermediate and basal cells in pink, green and blue, respectively (**Figure 5C**). The top gene ontology (GO) biological process, cellular component and molecular function are summarized in **Supplementary Figure S6**. Supplementary Tables containing all GO terms (biological process, cellular component, and molecular function) with adjusted *p*-values and the associated combined score are provided for the SCENIC

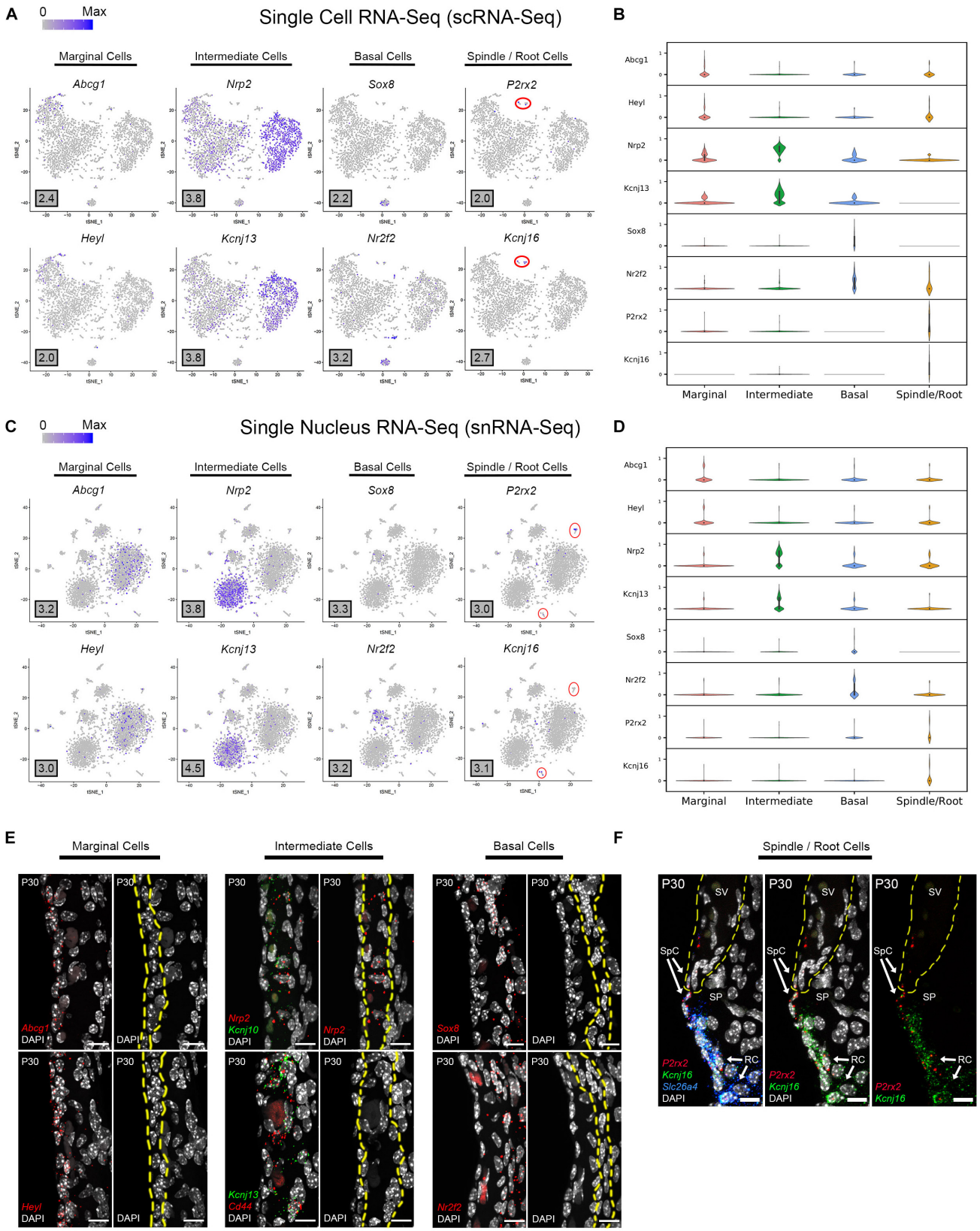

FIGURE 3 | Continued

FIGURE 3 | Single cell and single nucleus transcriptome profiles reveal common novel cell type-specific genes in the adult stria vascularis. **(A)** Feature plots for P30 SV scRNA-Seq data demonstrate expression of novel markers for 4 main SV cell types: marginal cells (*Abcg1, Heyl*), intermediate cells (*Nrp2, Kcnj13*), basal cells (*Sox8, Nr2f2*), and spindle/root cells (*P2rx2, Kcnj16*). Maximum expression (normalized counts) is noted in the black outlined gray box for each gene in the lower left corner of each feature plot. Spindle/root cell clusters are delineated by red circles. **(B)** Grid violin plot of scRNA-Seq dataset demonstrates expression of novel marker genes amongst SV cell types. Normalized counts were scaled to a range of 0–1 using min-max scaling. **(C)** Feature plots for P30 SV snRNA-Seq data demonstrate expression of novel markers for 4 main SV cell types: marginal cells (*Abcg1, Heyl*), intermediate cells (*Nrp2, Kcnj13*), basal cells (*Sox8, Nr2f2*), and spindle/root cells (*P2rx2, Kcnj16*). Maximum expression (normalized counts) is noted in the black outlined gray box for each gene in the lower left corner of each feature plot. Spindle/root cell clusters are delineated by red circles. **(D)** Grid violin plot of snRNA-Seq dataset demonstrates expression of novel marker genes amongst SV cell types. Normalized counts were scaled to a range of 0 to 1 using min-max scaling. **(E)** Validation of known gene expression was performed using single molecule fluorescent *in situ* hybridization (smFISH). Novel marginal cell-specific transcript (*Abcg1*, *Heyl*) expression in red is demonstrated in and around the marginal cell nuclei on the apical surface of the marginal cells. Novel intermediate cell-specific transcript (*Nrp2*, *Kcnj13*) expression in red is co-expressed with *Kcnj10* and *Cd44* transcripts in green, respectively. Novel basal cell-specific transcript (*Sox8*, *Nr2f2*) expression in red is localized to the basal cell layer. Yellow dashed lines in the images with only the DAPI labeling for nuclei demarcate the respective cell layers (marginal, intermediate and basal cell layers). **(F)** Novel spindle/root cell-specific transcripts, *P2rx2* (in red) and *Kcnj16* (in green) are co-expressed with *Slc26a4* transcripts to spindle and root cells (left panel). The same image without the Slc26a4 (blue) channel (center panel) and without DAPI (right panel) are shown. Note the slightly different distributions in *P2rx2* (red) versus Kcnj16 (green) transcripts amongst spindle and root cells, respectively. Yellow dashed lines demarcate the SV, spindle cells (SpC) and root cells (RC) in the spiral prominence (SP). DAPI (4′,6-diamidino-2-phenylindole). All scale bars 10 μm.

regulons grouped by cell type-specificity to the three major SV cell types (marginal, intermediate, and basal cells) are provided in the **Supplementary Tables S6–S8**.

GO biological process analysis for all SV cells reveals a significant enrichment for genes involved in the regulation of transcription from RNA polymerase II promoter (GO:0006357). GO molecular function analysis revealed a significant enrichment for genes involved in protein kinase activity (GO:0019901) and calcium channel regulator activity (GO:0005246) in SV marginal cells, for genes involved in RNA polymerase II regulatory region sequence-specific DNA binding (GO:0000977) and proton-transporting ATPase activity, rotational mechanism (GO:0046961) in SV intermediate cells, and for genes involved in RNA binding (GO:0003723) and phosphatidylinositol phosphate kinase activity (GO:0016307) in SV basal cells. GO cellular component analysis reveals a significant enrichment for genes related to mitochondrion (GO:0005739) and ruffle membrane (GO:0032587) in marginal cells, lysosome (GO:0005764) and late endosome (GO:0005770) in intermediate cells, and focal adhesion (GO:0005925) and actin cytoskeleton (GO:0015629) in SV basal cells. In addition to regulation of ion homeostasis and pH, these analyses provide some insight into additional functions and processes in which SV cell types play a role.

Gene Regulatory Network Extent Appears Related to the Number of Genes Detected per Cell or Nucleus

scRNA-Seq and snRNA-Seq datasets are subject to a phenomenon called "dropout" or detection bias, where expression of a gene may be observed in one cell but is not detected in another cell of the same type (Kharchenko et al., 2014). This phenomenon results from a combination of the low amounts of mRNA in individual cells, inefficient mRNA capture, and the stochastic nature of mRNA expression. Because of this, scRNA-Seq and snRNA-Seq datasets exhibit a high degree of sparsity resulting in the detection of a small fraction of the transcriptome in a given cell. In comparing the effect of detection bias in our scRNA-Seq and snRNA-Seq datasets, we made several observations with respect to the ability to identify potential gene regulatory networks (GRNs) and identify clusters of cells.

In general, the number of genes detected per cell was greater than the genes detected per nucleus (**Figure 6A**). When examining genes detected amongst cell type-specific cells or nuclei (marginal, intermediate, or basal cells), this observation remained consistent (**Figure 6A**). In contrast, there was a greater number of genes that demonstrated significant differential expression among the three major cell types in the snRNA-Seq dataset (**Figure 6B**). Examining the gene expression amongst cell type-specific WGCNA modules (gene regulatory networks of co-expressed genes not linked by transcription factors) revealed a trend toward a greater number of genes detected in the scRNA-Seq dataset (**Figure 6C**). An exception is that the number of marginal cell-specific WGCNA module genes per cell are lower than those detected in the nucleus data set. A technical explanation for this may be that in WGCNA analysis, genes can only be assigned to one module of co-expressed genes, which may ignore the reality that certain genes may be shared in both marginal and intermediate cells. A more detailed discussion of the potential reasons behind this observation is provided in the **Supplementary Data and Methods**. This observation of the greater number of detected genes in the single cell dataset became more definitive when examining gene expression amongst cell type-specific SCENIC regulons (gene regulatory networks of co-expressed genes linked by a common transcription factor) (**Figure 6D**). As a whole, these data suggest that gene regulatory network inference may be dependent on the number of genes detected per cell or nucleus and that nuclei-based approaches may allow for the detection of more differentially expressed genes in certain contexts.

Validation of Selected Marginal Cell- and Intermediate Cell-Specific SCENIC Regulons

In order to begin to identify critical gene regulatory networks, we identified cell type-specific SCENIC regulons identified in common between both the scRNA-Seq and snRNA-Seq datasets. We then examined these common regulons and utilized the regulon components identified in the single cell RNA-Seq dataset. Based on these parameters, two cell type-specific regulons were selected for further validation of the gene regulatory network inference approach. The estrogen-related receptor beta

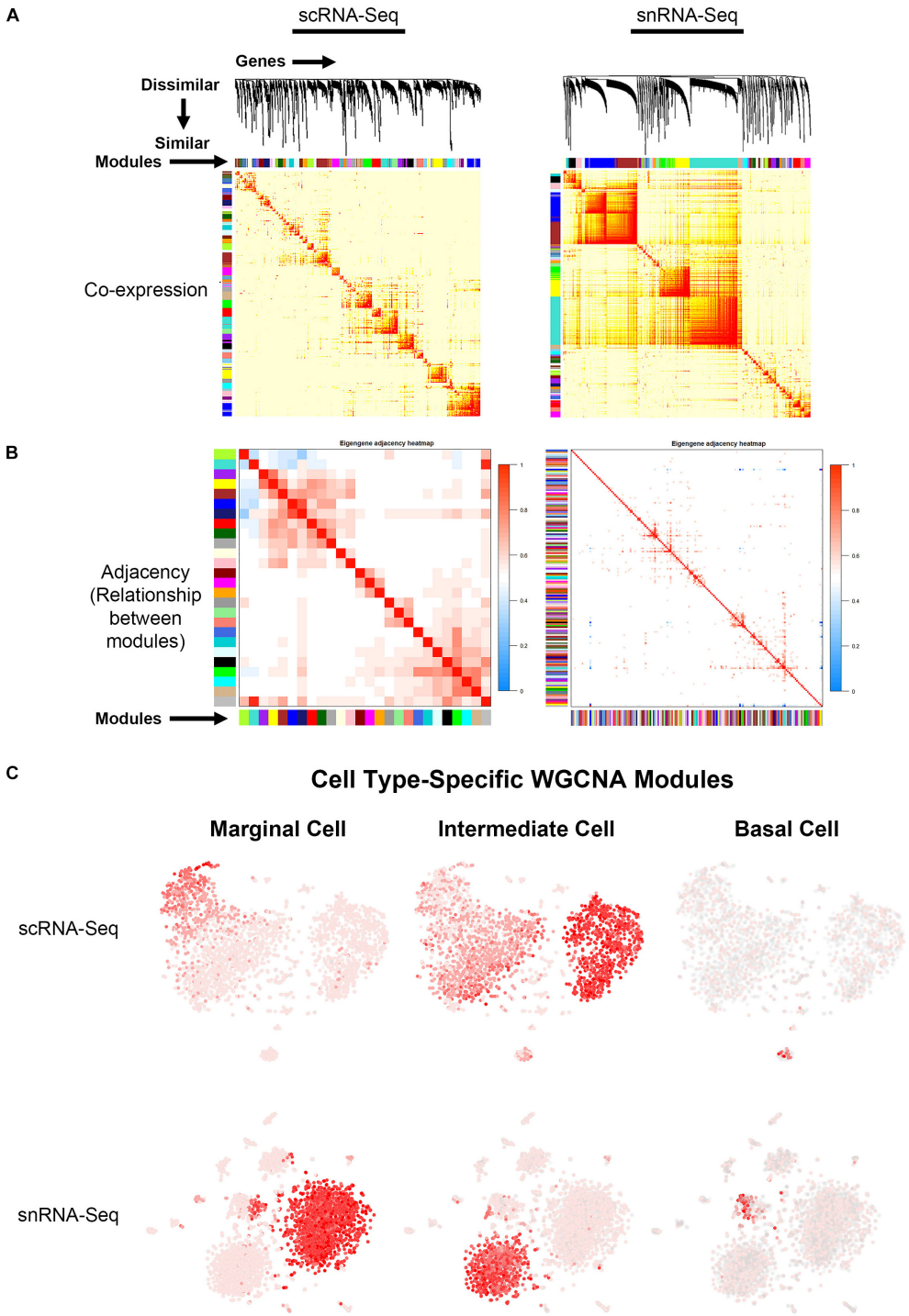

FIGURE 4 | Gene regulatory network inference using weighted gene co-expression network analysis (WGCNA) reveals cell type-specific modules. **(A)** Topological overlay map (TOM) plots demonstrate clustering of potential gene regulatory networks consisting of co-expressed genes termed modules arrayed along the horizontal and vertical axis. The more red a box is, the higher the Pearson correlation coefficient is between the respective modules. TOM plots are shown for the scRNA-Seq (LEFT) and snRNA-Seq (RIGHT) datasets. **(B)** Adjacency plots display highly correlated modules in the scRNA-Seq dataset (LEFT panel). The more red a box is, the more similar the 2 intersecting modules are to each other. Note that in the snRNA-Seq dataset (RIGHT panel), the correlation between modules is minimal. Using known cell type-specific marker genes, we focused on the cell type-specific modules identified in the scRNA-Seq dataset. **(C)** Cell type-specific WGCNA modules were then projected onto the scRNA-Seq feature plot to demonstrate aggregate cell type-specificity of these WGCNA modules for the three major cell types (marginal, intermediate, and basal cells). The more red a dot is in the feature plot, the greater the aggregate expression of the cell type-specific modules in that given cell.

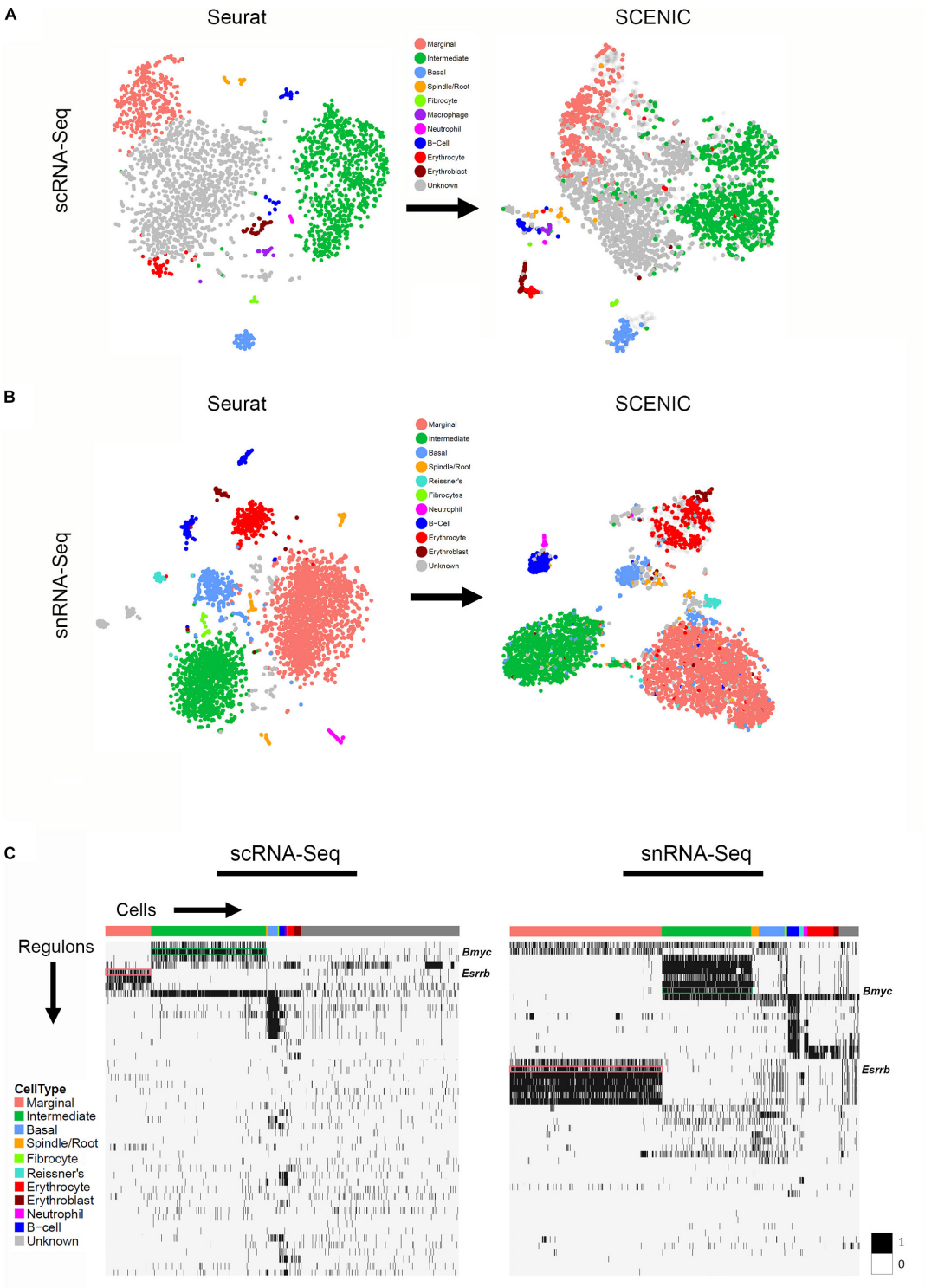

FIGURE 5 | Gene regulatory network inference with SCENIC reveals cell type-specific SCENIC regulons in both scRNA-Seq and snRNA-Seq datasets. **(A)** Unbiased clustering in Seurat (left panel) is similar to regulon-based clustering in SCENIC (right panel) for the scRNA-Seq dataset, resulting in the identification of the same cell type-specific clusters. **(B)** Unbiased clustering in Seurat (left panel) is similar to regulon-based clustering in SCENIC (right panel) for the snRNA-Seq dataset, resulting in the identification of the same cell type-specific clusters. **(C)** Regulon heatmaps display cell type-specific regulons identified from both the scRNA-Seq (left panel) and snRNA-Seq (right panel) datasets. Cells grouped by cell type are displayed along the horizontal axis and regulons organized by hierarchical clustering are displayed along the vertical axis. *Esrrb* (pink box) and *Bmyc* (green box) regulons are demarcated in both datasets (regulon labels to right of heatmap. Legend demonstrating the binarized regulon activity score (scaled as 0 or 1) is shown to right of both heatmaps.

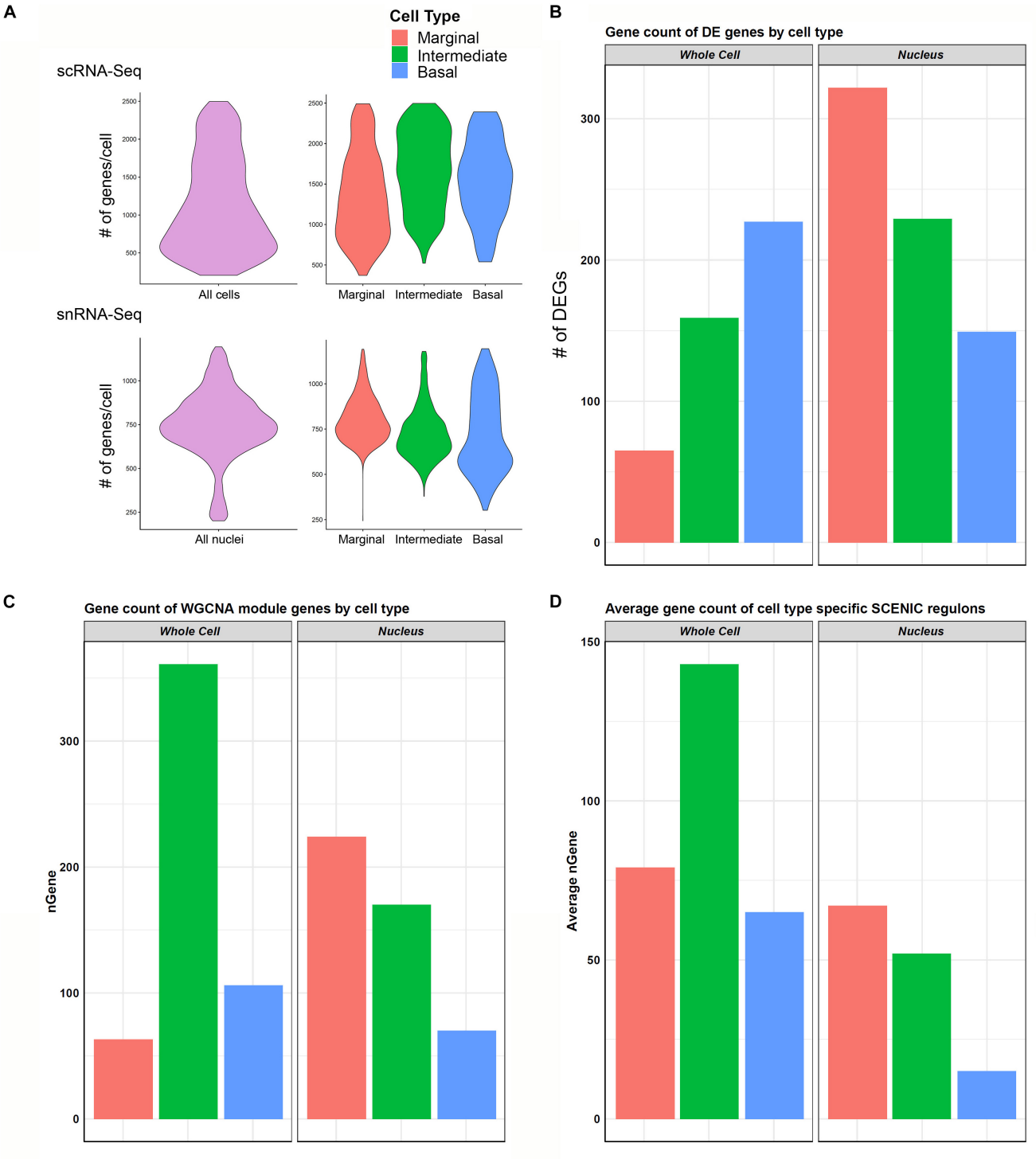

FIGURE 6 | Cell type-specific gene expression comparison between scRNA-Seq and snRNA-Seq. **(A)** Violin plots to left in upper (scRNA-Seq) and lower (snRNA-Seq) panels show the distribution of the number of genes per cell (upper panel) or nuclei (lower panel) along the vertical axis. In general, transcriptome profiles from cells exhibited a greater number of genes per cell than transcriptome profiles from nuclei. This trend continued as expected when looking at cell type-specific gene expression in marginal, intermediate, and basal cells in the panels to the right in both scRNA-Seq (upper panel) and snRNA-Seq (lower panel). **(B)** Cell type-specific expression of differentially expressed genes (DEGs) was lower in the scRNA-Seq data compared to the snRNA-Seq data in marginal, intermediate, and basal cells. nGene refers to number of differentially expression genes. **(C)** Gene counts for WGCNA cell type-specific modules did not demonstrate a consistent relationship between scRNA-Seq and snRNA-Seq datasets. **(D)** Gene counts for SCENIC cell type-specific regulons in general demonstrated a higher gene count per cell type in scRNA-Seq compared to snRNA-Seq. nGene (# of genes).

(*Esrrb*) regulon, a marginal cell-specific regulon, and the brain expressed myelocytomatosis oncogene (*Bmyc*), an intermediate cell-specific regulon, were selected for further analysis. Mutations in *Esrrb* result in autosomal recessive sensorineural hearing loss (DFNB35) (Collin et al., 2008) and missense mutations have recently been implicated in Meniere's disease (Gallego-Martinez et al., 2019). *Bmyc* has not previously been characterized as having a role in inner ear pathology or hearing loss. Selected regulons were screened for transcription factor targets with available smFISH probes, resulting in a small subset of genes from these regulons being selected.

Direct gene targets for *Esrrb* selected for validation with smFISH were *Abcg1*, *Heyl*, and *Atp13a5*. The gene activity plot shows the composite expression of the *Esrrb* regulon in SV marginal cells (**Figure 7A**). Binding motifs for *Esrrb* in each of the respective downstream targets (*Abcg1*, *Heyl*, *Atp13a5*) are shown (**Figure 7B**). Feature plots demonstrating RNA expression for *Abcg1* and *Heyl* have been previously shown in **Figures 3A,C**. Feature plots demonstrate RNA expression for *Esrrb* and *Atp13a5* in marginal cells (**Figure 7C**). smFISH demonstrates co-expression of *Esrrb* with each downstream target protein in SV marginal cells (**Figure 7D**). Using a custom MATLAB script to perform semiautomated quantitation of smFISH transcripts (see **Supplementary Data and Methods**), *Abcg1*, *Atp13a5*, and *Heyl* transcripts were noted to be co-expressed in over 90% of *Esrrb*-expressing nuclei (**Supplementary Figure S5B**).

Direct gene targets for *Bmyc* selected for validation with smFISH were *Cd44*, *Met*, *Pax3*. The gene activity plot shows the composite expression of the *Bmyc* regulon in SV intermediate cells (**Figure 8A**). Binding motifs for *Bmyc* in each of the respective downstream targets (*Cd44*, *Met*, *Pax3*) are shown (**Figure 8B**). Feature plots demonstrating RNA expression for *Cd44* and *Met* in both scRNA-Seq and snRNA-Seq datasets have been previously shown in **Figures 2B,D**. Feature plots demonstrate RNA expression for *Bmyc* and *Pax3* in intermediate cells (**Figure 8C**). smFISH demonstrates *Bmyc* co-expression with each downstream target protein in SV intermediate cells (**Figures 8D,E**). Overall, the co-expression of transcription factors with their downstream targets demonstrates the strength of the SCENIC-based approach for gene regulatory network inference as well as clustering. The identification of regulons provides a starting point for targeted modulation of gene activity within a regulon to elucidate the role of the regulon in SV function. *Cd44*, *Met*, and *Pax3* transcripts were co-expressed in over 85% of *Bmyc*-expressing nuclei (**Supplementary Figure S5C**).

Pharos Analysis Identifies Druggable Gene Targets in Cell Type-Specific Regulons

With regards to modulation of gene activity within a regulon, Pharos, a database of druggable gene targets, provides an opportunity to identify FDA-approved drugs and small molecules that could potentially be utilized to modulate gene expression[7]. Analysis with Pharos identified FDA-approved drugs with known activities against cell type-specific regulon targets. The analysis was focused on Tclin targets, which are genes whose expression can be altered by a known mechanism of action of an FDA-approved drug. As an example of this approach, the previously described *Esrrb* and *Bmyc* regulons were utilized to construct a network diagram of their direct druggable targets. Direct druggable target genes of the *Esrrb* and *Bmyc* regulons are shown (**Figures 9A,B**, respectively). For the purposes of simplifying the display, activators included receptor agonists, enzyme activators, and ion channel openers. Inhibitors included receptor antagonists, receptor inverse agonists, enzyme inhibitors, and ion channel blockers. These drugs represent potential mechanisms by which strial function might be modulated. Drugs for *Adrb2* and *Maoa* genes are provided in **Supplementary Figure S9**.

For example, in the *Esrrb* regulon, studies suggest that estrogen (estradiol) may have a role in hearing protection (Wijayaratne and McDonnell, 2001; Milon et al., 2018; Williamson et al., 2019). Milon et al. (2018) have suggested the possibility of utilizing estrogen signaling pathway effectors for hearing protection. In the *Bmyc* regulon, both metformin and acetazolamide have been associated with attenuation of hearing loss in certain settings (Sepahdari et al., 2016; Wester et al., 2018; Chen et al., 2019; Muri et al., 2019). Metformin, which inhibits *Ndufb2*, may reduce the incidence of sudden sensorineural hearing loss amongst diabetic patients (Chen et al., 2019; Muri et al., 2019). While the effects of acetazolamide in treating hearing loss associated with Meniere's disease appear to be temporary (Hoa et al., 2015; Crowson et al., 2016), recent reports suggest some utility in sudden sensorineural hearing loss associated with PDE5 inhibitors (Wester et al., 2018).

Deafness Gene Mapping Suggests a Role for SV Cell Types in Human Deafness

Finally, we screened the cellular transcriptomes from our scRNA-Seq and snRNA-Seq datasets for genes associated with human hearing loss. The database of deafness genes was constructed from resources including the Hereditary Hearing Loss Homepage as previously described (Shearer et al., 1993; Azaiez et al., 2018). Heatmaps showing gene expression for known deafness genes in the P30 SV are shown in **Figure 10**. Expression data corresponding to P30 SV scRNA-Seq is shown in the left heatmap (**Figure 10A**) and expression data corresponding to P30 SV snRNA-Seq is show in the right heatmap (**Figure 10B**). Known deafness genes are displayed along the vertical axis and SV cell types are displayed horizontally with marginal cells in pink, intermediate cells in green, basal cells in blue, and spindle cells in yellow.

We identify a subset of deafness genes that are expressed in adult SV cell types. Deafness genes expressed in marginal cells include *Lrp2*, *Esrrb*, *Hgf*, *Kcnq1*, *Kcne1*, *Ror1*, and *Eya4* (Wayne, 2001; Wangemann, 2002; Zhang et al., 2004; Collin et al., 2008; König et al., 2008; Schultz et al., 2009; Khalifa et al., 2015; Faridi et al., 2019). Deafness genes expressed in intermediate cells include *Met*, *Pde1c*, and *Pax3* (Tassabehji et al., 1993; Bondurand, 2000; Mujtaba et al., 2015; Wang et al., 2018). *Col11a2* appears to be specifically expressed in SV basal cells (McGuirt et al., 1999).

[7] https://pharos.nih.gov/

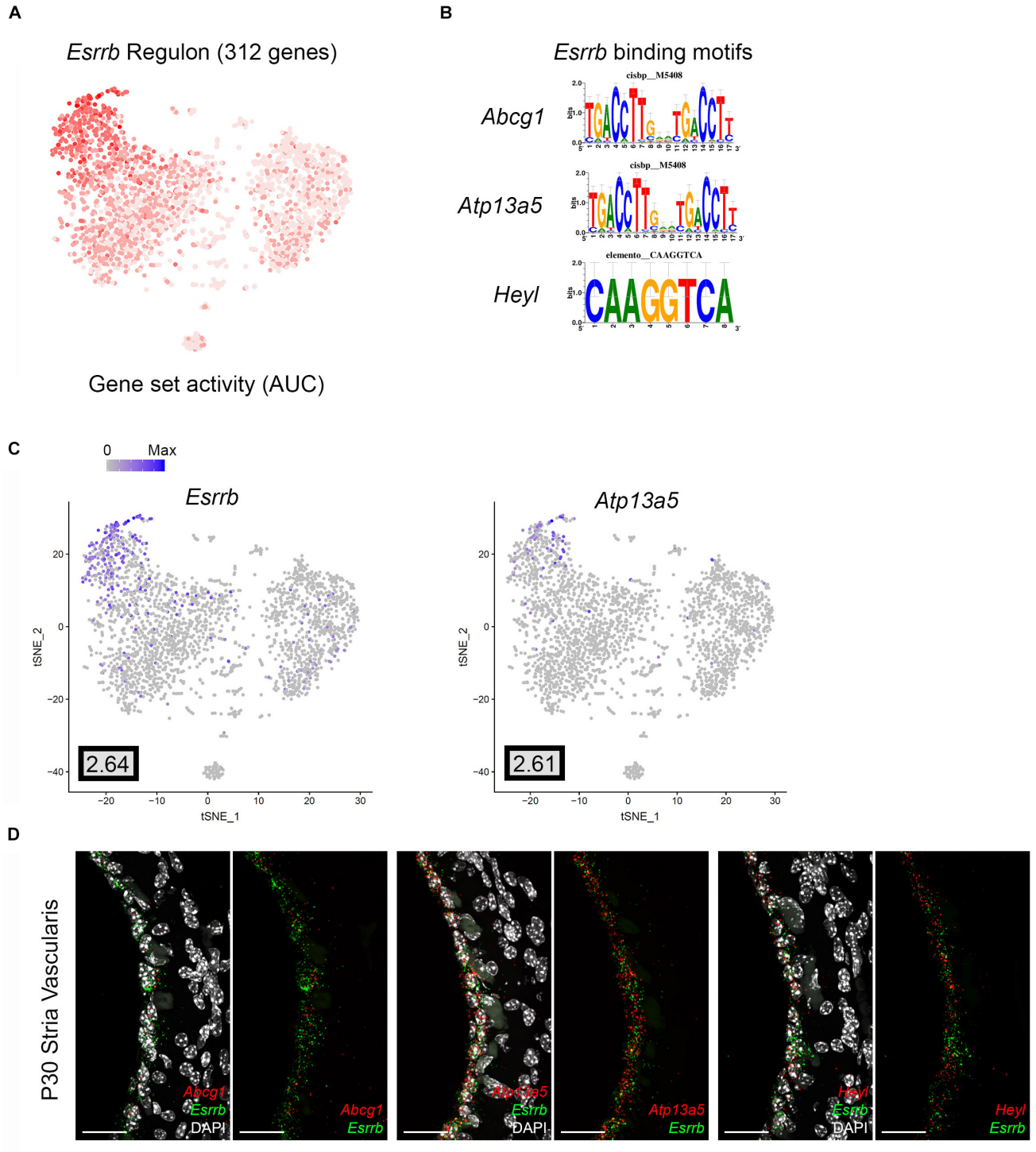

FIGURE 7 | Validation of *Esrrb* regulon. **(A)** Gene set activity plot displays *Esrrb* regulon expression in scRNA-Seq dataset. The more red a dot is, the greater the regulon activity in that given cell. **(B)** *Esrrb* binding motifs for *Esrrb* downstream targets (*Abcg1*, *Atp13a5*, *Heyl*). **(C)** Feature plots demonstrating expression of Esrrb and Atp13a5 in the marginal cell cluster in the scRNA-Seq dataset. Maximum expression (normalized counts) is noted in the black outlined gray box for each gene in the lower left corner of each feature plot. Histogram is depicted from 0 to maximum (Max) in terms of normalized counts. Feature plots for *Abcg1* and *Heyl* have been shown previously in **Figure 3**. **(D)** smFISH demonstrates co-expression of *Abcg1*, *Atp13a5*, and *Heyl* transcripts in red with *Esrrb* transcripts in green in marginal cells on representative cross-sections of the P30 mouse SV. Panels to left depict *Esrrb* transcripts (green) and downstream target transcripts (red) with DAPI. Panels to the right depict *Esrrb* transcripts (green) and downstream target transcripts (red) without DAPI. DAPI (4′,6-diamidino-2-phenylindole). All scale bars 20 μm.

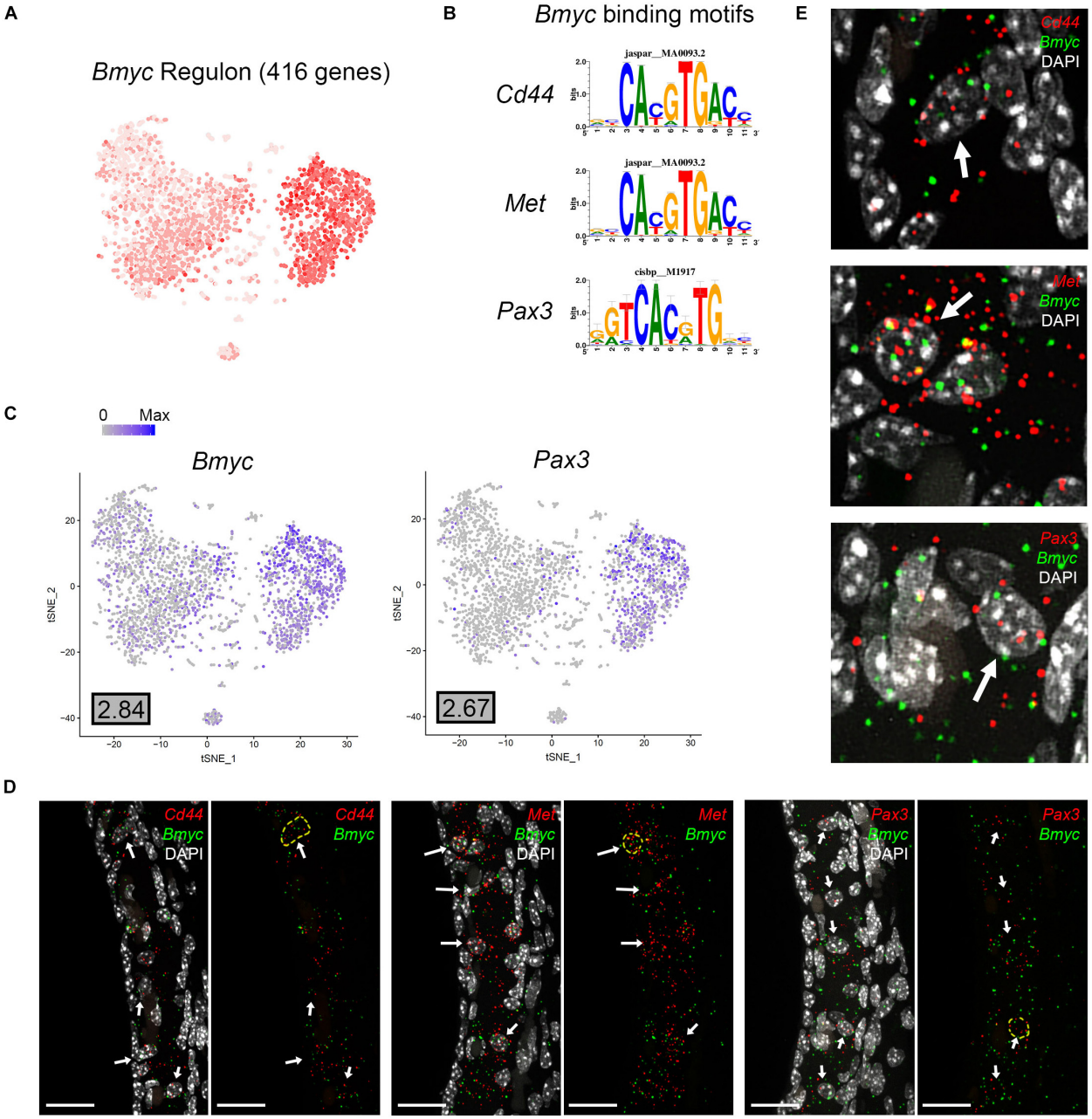

FIGURE 8 | Validation of *Bmyc* regulon. **(A)**, Gene set activity plot displays *Bmyc* regulon expression in scRNA-Seq dataset. The more red a dot is, the greater the regulon activity in that given cell. **(B)** *Bmyc* binding motifs for *Bmyc* downstream targets (*Cd44*, *Met*, *Pax3*). **(C)** Feature plots demonstrating expression of *Bmyc* and *Pax3* in the intermediate cell cluster of the scRNA-Seq dataset. Maximum expression (normalized counts) is noted in the black outlined gray box for each gene in the lower left corner of each feature plot. Histogram is depicted from 0 to maximum (Max) in terms of normalized counts. Feature plots for *Cd44* and *Met* have been shown previously in **Figure 2**. **(D)** smFISH demonstrates co-expression of *Cd44*, *Met*, and *Pax3* transcripts in red with *Bmyc* transcripts in green in intermediate cells on representative cross-sections of the P30 mouse SV. Panels to left depict *Bmyc* transcripts (green) and downstream target transcripts (red) with DAPI. Panels to the right depict *Bmyc* transcripts (green) and downstream target transcripts (red) without DAPI. DAPI (4',6-diamidino-2-phenylindole). White arrows point to examples of intermediate cells that exhibit both Bmyc and downstream target transcript expression. In the panels without DAPI, examples of cells that exhibit co-expression of *Bmyc* (green) and downstream target transcripts (red) are encircled with dashed yellow lines. All scale bars 20 μm. **(E)** Enlarged images of example cells from **(D)** are shown. White arrows in **(E)** point to encircled cells from **(D)**.

In addition to *Slc26a4*, deafness genes expressed in spindle cells include *Ceacam16*, *Cldn14*, and *P2rx2* (Wilcox et al., 2001; Ben-Yosef et al., 2003; Zheng et al., 2011; Faletra et al., 2014; Naz et al., 2017; Zhu et al., 2017; Booth et al., 2018). More importantly, these data demonstrate the possibility that some of these deafness genes affect multiple SV cell types, as in the case of *Mitf* and

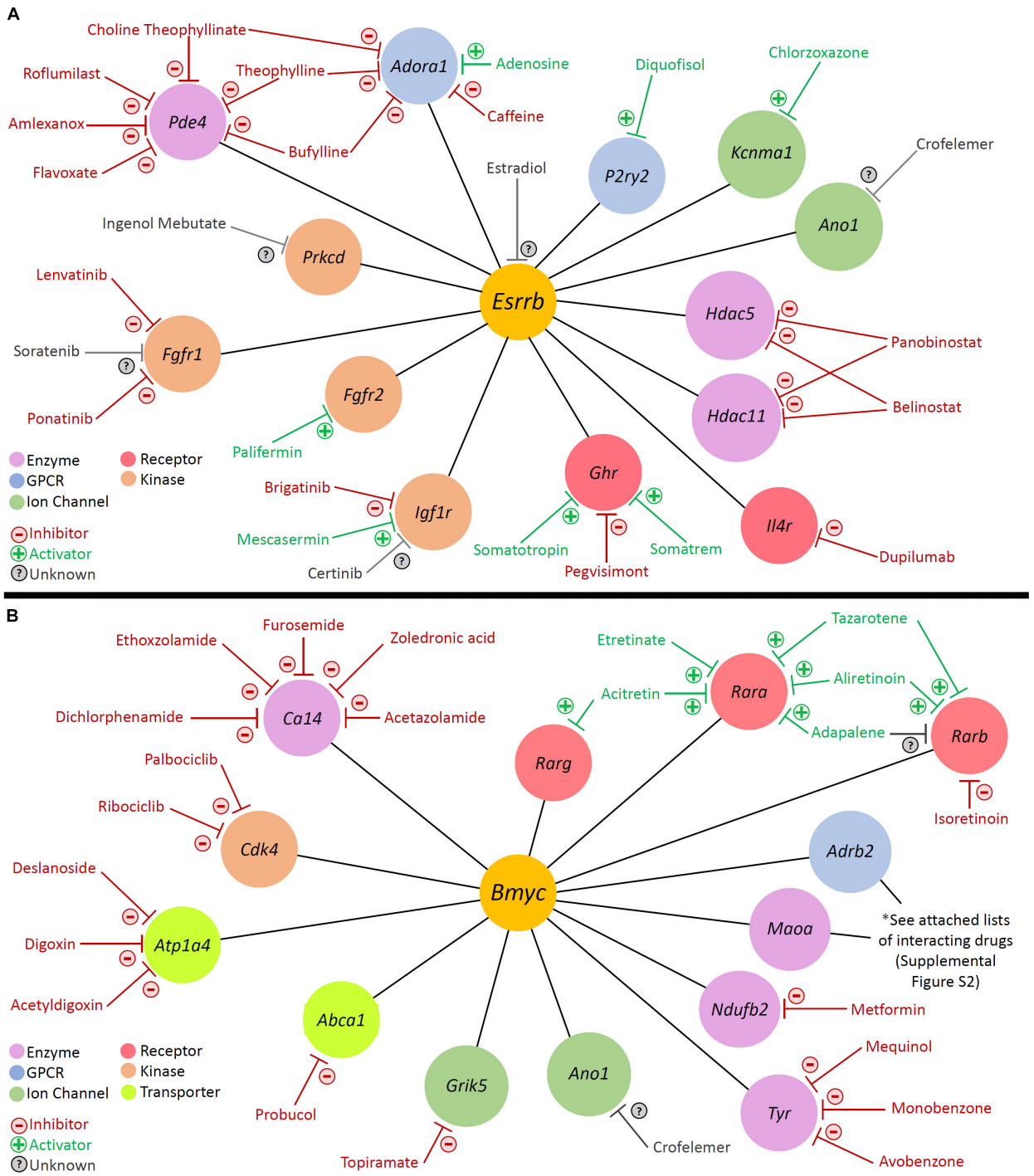

FIGURE 9 | Analysis with Pharos reveals druggable gene targets in the *Esrrb* and *Bmyc* regulons. Pharmacologic drug classes are shown in lower left corner including enzyme, G-protein coupled receptor (GPCR), ion channel, receptor, and kinase. FDA-approved drugs are classified as inhibitors (red), activators (green), or unknown (gray). **(A)** Druggable gene targets in the *Esrrb* regulon. Analysis identified 13 druggable genes with 25 FDA-approved drugs. **(B)** Druggable gene targets in the *Bmyc* regulon. Analysis identified 13 druggable genes with 68 FDA-approved drugs. Drugs for *Adrb2* and *Maoa* genes are provided in **Supplementary Figure S9**.

Sox10, which are expressed in both intermediate and marginal cells (Bondurand, 2000). Both genes are known to be expressed by neural crest cells (Potterf et al., 2001; Sommer, 2011; Locher et al., 2015). Circumstantial evidence for the origin of strial marginal cells from otic epithelium (Kikuchi and Hilding, 1966; Sher, 1971; Kuijpers et al., 1991; Sagara et al., 1995; Birkenhäger

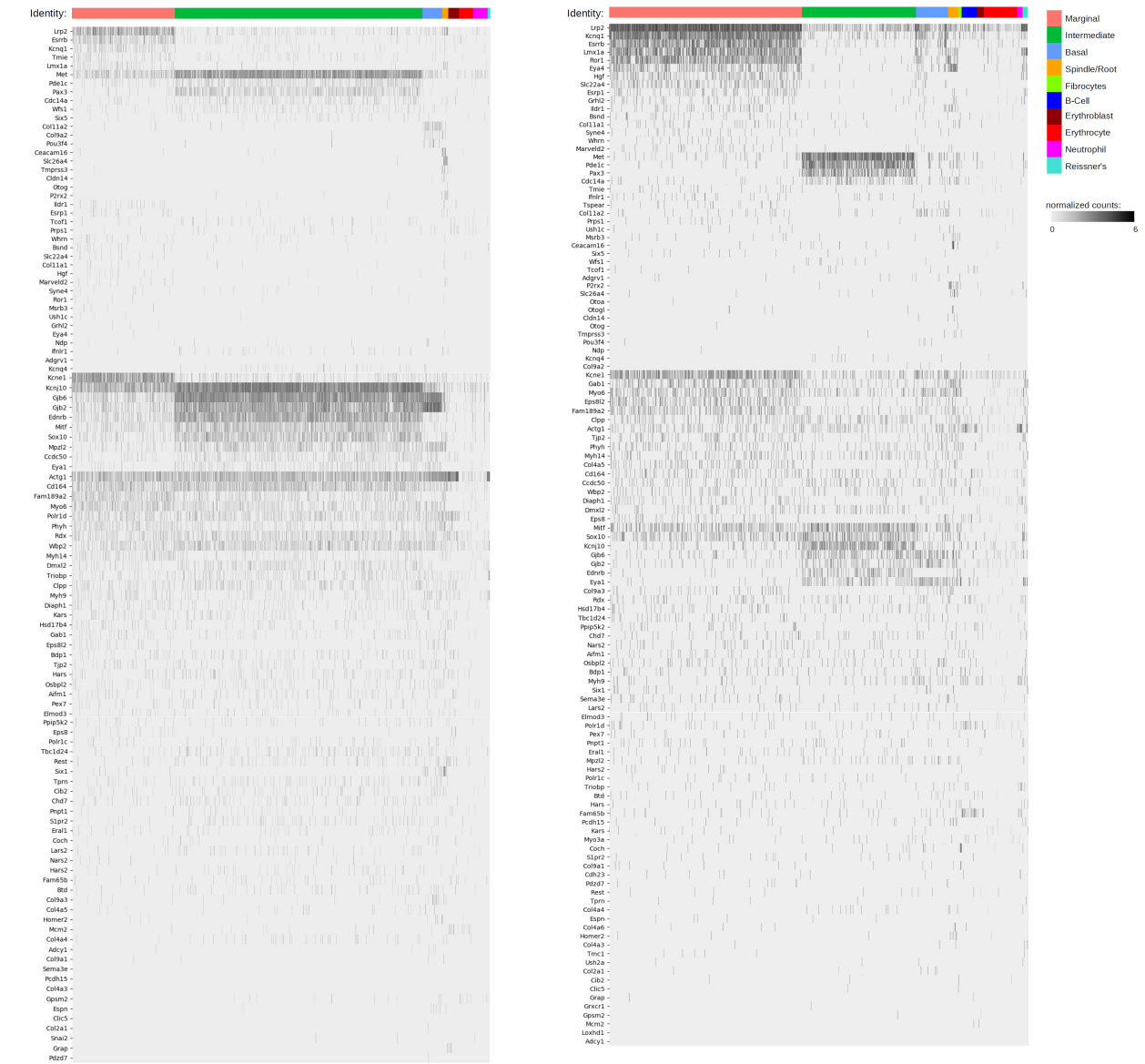

FIGURE 10 | Deafness gene mapping of adult stria vascularis single cell and single nucleus transcriptomes associates SV cell types with deafness genes. Cell types are arrayed along the horizontal axis and grouped according to cell types. Deafness genes are arrayed along the vertical axis. Deafness genes were grouped according to how specific their expression seemed to be in a given cell type. Genes with less cell type-specific expression were placed lower in the list of genes. **(A)** Expression level in normalized counts for each deafness gene (each row) across all cells in the adult SV scRNA-Seq dataset. **(B)** Expression level in normalized counts for each deafness gene (each row) across all cells in the adult SV snRNA-Seq dataset.

et al., 2001) and strial intermediate cells from neural crest cells (Steel and Barkway, 1989; Cable and Steel, 1991; Cable et al., 1992; Tachibana, 1999, 2001) has been previously supported by histochemical and immunohistochemical analyses. The role of genes expressed by neural crest cells in cells not thought to be of neural crest cell origin remains to be determined. Whether other cell types in the SV derive from neural crest cells remains to be determined by further lineage tracing experiments and have not been shown in more recent lineage tracing experiments (Shibata et al., 2016). The contribution of neurocristopathies to hearing loss is a developing area of research (Hao et al., 2014; Locher et al., 2015; Shibata et al., 2016; Ritter and Martin, 2019). Another example of hearing loss where multiple cell types may be affected includes Connexin 26 and 30 encoded by *Gjb2* and *Gjb6*, respectively, which appear to be expressed in intermediate and basal cells and, to a lesser extent, marginal cells (**Figure 10**) (Lang et al., 2007; Nickel and Forge, 2008; Liu et al., 2009; Mei et al., 2017). These data reveal expression of a subset of

human deafness genes in SV cell types and define potential opportunities for further investigation into the function of these genes in the SV.

DISCUSSION

Dual methodologies were used to develop an atlas of adult SV cell type transcriptional profiles, the most comprehensive to date. Specifically, the use of dual RNA-Seq methodologies (scRNA-Seq and snRNA-Seq) revealed similar adult SV cell type-specific transcriptional profiles. Furthermore, we demonstrate the utility of applying dual gene regulatory network inference methodologies to both corroborate cell type heterogeneity as well as define potentially critical gene regulatory networks. We provide examples of how this resource can be harnessed to identify and confirm cell type-specific gene regulatory networks, identify druggable gene targets, and implicate SV cell types in syndromic and non-syndromic hereditary deafness. We now define the implications of these data for: (1) using and developing mouse models to define the contribution of each SV cell type to SV function and hearing at the level of gene expression, (2) understanding ion homeostatic mechanisms broadly in the inner ear, (3) contributing to efforts to develop targeted SV gene therapy through the use of cell type-specific promoters, (4) identifying druggable gene targets and the potential for repurposing existing pharmacotherapies to treat inner ear disease, and (5) use of these data to identify cell type-specific contributions to disease.

Implications for Mouse Model Development to Enhance Our Understanding of Cell Type-Specific Mechanisms Related to the Loss of EP and Hearing Loss

In characterizing adult SV cellular heterogeneity using transcriptional profiling, these data provide opportunities to study adult SV cell type-specific mechanisms that contribute to EP generation and whose dysfunction results in hearing loss. Novel cell type-specific gene expression allows for the identification of existing inducible cell type-specific Cre-recombinase mouse models as well as the development of novel inducible mouse models. These mouse models will be critical to studying the effects of gene deletion in adult SV cell types, enabling a separation from the effects of gene deletion in the SV during inner ear development. Genetic mutations that affect the SV result in hearing loss that is characterized by an initial loss of EP followed by a delayed loss of hair cells (Liu et al., 2016; Huebner et al., 2019). Interpretation of the results observed in these existing mouse models is complicated by the developmental effects of genes critical to EP generation (Liu et al., 2016; Huebner et al., 2019). Conversely, mouse models of SV age-related hearing loss are complicated by incompletely defined mechanisms and time windows which make for challenging experimental conditions (Ohlemiller, 2009). Thus, the exact timing and mechanisms associated with a permanent loss of hair cells that follow the loss of EP remain incompletely defined. Use of inducible mouse models may enable insight into the timing of these mechanisms as well as insight into possible mechanisms. Understanding the critical time window for intervention as well as potential targeted interventions that might slow, halt or reverse the effects of EP loss will contribute to development of therapeutic approaches to hearing loss due to SV dysfunction.

Implications for Understanding Ionic Homeostasis in the Inner Ear

SV cell type-specific gene regulatory networks include genes critical to EP generation and ion homeostasis and as a result provide a window into inner ear ion homeostatic mechanisms. Insight into these ion homeostatic mechanisms may be important to understanding their functional contribution to hearing and hearing loss (Nickel and Forge, 2008; Zdebik et al., 2009). These gene regulatory networks within the unperturbed wild type adult mouse SV establish a basis for identifying and interpreting changes in these networks in disease settings including, but not limited to, Meniere's disease (Ishiyama et al., 2007; Collin et al., 2008; Kariya et al., 2009), autoimmune inner ear disease (Calzada et al., 2012), cisplatin-induced hearing loss (Breglio et al., 2017; Rybak et al., 2019), and enlarged vestibular aqueduct syndrome (Miyagawa et al., 2014; Ito et al., 2015).

While the consequences of dysfunctional ion homeostasis to human hearing loss are incompletely understood, ion homeostasis appears to be critical, as evident by the number of deafness genes encoding ion channels and transporters, many of which are expressed in the SV (Mittal et al., 2017). While this study demonstrates expression of these ion channels in SV cells in the cochlea, there are quite a few examples of marginal cell-specific genes that are also expressed in the vestibular portion of the inner ear (Wangemann, 1995; Chen and Nathans, 2007; Bartolami et al., 2011). The consequences of dysfunctional ion homeostasis on vestibular function remain incompletely characterized (Jones and Jones, 2014). Thus, insights gained in understanding the mechanisms regulating ion homeostasis in the SV will apply to other regions of the inner ear. The co-occurrence of hearing loss and renal disease resulting from mutations in channel and transporter genes suggests that understanding ion homeostasis in the inner ear may have broader implications to dysfunctional ion homeostasis and human disease (Lang et al., 2007).

Implications for Targeting Gene Therapy to SV Cell Types

Cell type-specific genes could be utilized to create viral vectors with cell type-specific promoters for improved therapeutic targeting to the SV. This idea is not without precedent as cell type-specific promoters have been utilized in the brain, retina and inner ear to target specific groups of cells (Praetorius et al., 2010; Kim et al., 2013; Ingusci et al., 2019; McDougald et al., 2019). Furthermore, some recent adoptive immunotherapy trials using a cell type-specific promoter for melanoma already suggest the possibility for this in relation to the SV (Johnson et al., 2009; Seaman et al., 2012; Duinkerken et al., 2019).

Specifically, these studies utilized adoptive immunotherapy using T cell receptors (TCRs) targeting MART-1, a known melanoma-associated antigen, which resulted in sensorineural hearing loss that in some cases was ameliorated by local steroid administration (Johnson et al., 2009). SV melanocytes arise from neural crest cells that migrate into the SV during development (Hilding and Ginzberg, 1977; Steel and Barkway, 1989; Cable and Steel, 1991; Cable et al., 1992; Tachibana, 1999, 2001; Matsushima et al., 2002; Shibata et al., 2016). SV melanocytes represent the future intermediate cells (Steel and Barkway, 1989; Cable and Steel, 1991; Cable et al., 1992; Shibata et al., 2016). These studies suggest the possibility that vectors utilizing the gene that encodes MART-1, Melan-A (*Mlana*), may be an effective promoter for targeting gene therapy to SV intermediate cells.

Alternatively, gene therapy for non-syndromic sensorineural hearing loss may entail targeting multiple cell types. For example, we demonstrate the expression of *Gjb2* and *Gjb6*, which encode connexin 26 and connexin 30 proteins, respectively, in SV intermediate, basal and to a lesser extent, marginal cells (**Figure 10**) (Lang et al., 2007; Nickel and Forge, 2008; Liu et al., 2009). Mutations in *Gjb2* and *Gjb6* followed by digenic mutations in these genes are among the most common causes of non-syndromic autosomal recessive sensorineural hearing loss (SNHL) in many populations around the world (Lerer et al., 2001; Del Castillo et al., 2002; Pallares-Ruiz et al., 2002; Stevenson et al., 2003; Wu et al., 2003; Bolz et al., 2004; Frei et al., 2004; Gualandi et al., 2004; Nickel and Forge, 2008; Batissoco et al., 2009; Chan et al., 2010; Asma et al., 2011; Da Silva-Costa et al., 2011; Mei et al., 2017). Mei et al. (2017) demonstrate that the loss of *Gjb2* and *Gjb6* in the SV and lateral wall result in a loss of EP and hearing loss while the loss of *Gjb2* and *Gjb6* in cochlear supporting cells does not. These data identify the loss of these genes in the SV as principal drivers of hearing loss in digenic *Gjb2* and *Gjb6* mutations. Use of SV promoters that may be capable of targeting multiple SV cell types including *Mitf* or *Sox10* could be utilized in future therapeutic attempts (**Figure 10**) (Hao et al., 2014; Walters and Zuo, 2015).

Implications for Pharmacologic Targeting of SV Cell Types

Our analyses utilizing parallel gene regulatory network inference methods (WGCNA and SCENIC) combined with a search for druggable gene targets utilizing Pharos[8] suggest a possible translational approach to utilizing scRNA-Seq and snRNA-Seq datasets (Langfelder and Horvath, 2008; Aibar et al., 2017; Nguyen et al., 2017). Through this approach, we identify genes for which FDA-approved drugs have a known effect. This agnostic *in silico* approach can potentially be utilized to identify FDA-approved medications that could be repurposed or repositioned to treat diseases in the inner ear as has been done in other areas of human disease including neurodegenerative diseases, cancer, and autoimmune disease (Ferrero and Agarwal, 2018; Paranjpe et al., 2019). This may be particularly useful in hearing and balance disorders that are characterized by onset of symptoms in adulthood (i.e., autoimmune inner ear disease, Meniere's disease). We acknowledge that there are many methods to identify drugs for repurposing or repositioning, including *in silico* methods, which have been reviewed elsewhere (Li et al., 2016; Vanhaelen et al., 2017; Ferrero and Agarwal, 2018). However, our analyses highlight the potential use of the data for drug repurposing approaches.

[8]https://pharos.nih.gov/

Implications for Identifying Cell Type-Specific Contributions to Disease

Finally, as we have alluded to previously, scRNA-Seq and snRNA-Seq approaches could potentially be utilized to associate changes in gene expression in human disease with cell types in a given tissue (Skene and Grant, 2016). Skene and Grant (2016) associated cell types with human disease by comparing human disease expression datasets for Alzheimer's disease, autism, schizophrenia, and multiple sclerosis to single cell transcriptional profiles from the mouse cortex and hippocampus. In a similar fashion, single cell and single nucleus transcriptome profiles, like the resource we have developed for the adult SV, might be utilized to associate cell types to inner ear diseases. For example, in Meniere's disease, while no single gene has been conclusively implicated in the disease, the association of gene mutations with cell type-specific expression might provide some clues to the involved cell type or types (Chiarella et al., 2015; Lopez-Escamez et al., 2018). Mutations in both *Kcne1* and *Esrrb* have been identified in patients with Meniere's disease (Lopes et al., 2016; Dai et al., 2019; Gallego-Martinez et al., 2019). Our data demonstrate expression of these genes in SV marginal cells (**Figure 10**). It is possible that marginal cells might play a role in the pathophysiology of this disease.

While this is the most comprehensive cell atlas of the adult SV to date, some limitations or caveats are worth mentioning. We did not definitively identify clusters of pericytes or endothelial cells in our dataset and chose to focus our analysis on the four main groups of cells (marginal, intermediate, basal, and spindle cells). Given the lower number of spindle and root cells, we did not definitively distinguish spindle and root cells from each other.

We believe that the utility of these datasets as resources is expansive. These datasets establish a baseline for comparison to effects on the SV related to treatment and provide a resource for identifying cell types associated with human inner ear disease. We show examples of applications of these data, including characterization of homeostatic gene regulatory networks, druggable gene target analysis with Pharos to identify potential repurposing of FDA-approved medications, and provide the most focused screen of deafness gene expression in the SV. These data will serve as a baseline for identifying key regulatory mechanisms related to genetic and acquired hearing loss, as well as, for responses to a variety of pharmacologic treatments.

DATA AVAILABILITY STATEMENT

The datasets generated for this study can be found in the Gene Expression Omnibus (GEO) database (GEO Accession ID: GSE136196) at the following link https://www.ncbi.nlm.nih.gov/geo/query/acc.cgi?acc=GSE136196.

ETHICS STATEMENT

All animal experiments and procedures were performed according to protocols approved by the Animal Care and Use Committee of the National Institute of Neurological Diseases and Stroke and the National Institute on Deafness and Other Communication Disorders, National Institutes of Health.

AUTHOR CONTRIBUTIONS

SK, RO, and MH contributed to isolation of single cells and single nuclei for single cell RNA-Seq (scRNA-Seq) and single nucleus RNA-Seq (snRNA-Seq). DM and RM were responsible for sequencing and alignment of scRNA-Seq and snRNA-Seq datasets. SK, IT, MP, SG, and MH contributed to scRNA-Seq and snRNA-Seq bioinformatic data analysis. SK, RO, and IT were responsible for smFISH and immunohistochemistry. RS, CG, IT, and RO were responsible for quantitative analysis of smFISH labeling. SK, RO, IT, and MH contributed to writing and revising the manuscript. All authors read and approved final manuscript.

FUNDING

This research was supported (in part) by the Intramural Research Program of the NIH, NIDCD to MH (ZIA DC000088), and RM (ZIC DC000086). This research was made possible through the NIH Medical Research Scholars Program (MRSP), a public–private partnership supported jointly by the NIH and contributions to the Foundation for the NIH from the Doris Duke Charitable Foundation (DDCF Grant #2014194), the American Association for Dental Research, the Colgate-Palmolive Company, Genentech, Elsevier, and other private donors. The funders of the MRSP had no role in study design, data collection and analysis, decision to publish, or preparation of the manuscript.

ACKNOWLEDGMENTS

The authors would like to acknowledge Thomas B. Friedman, Matthew W. Kelley, and Doris Wu who provided helpful feedback and review of this manuscript. The authors acknowledge Alan Hoofring for his illustrations. This study utilized the high-performance computational capabilities of the Biowulf Linux cluster at the National Institutes of Health, Bethesda, MD, United States (https://hpc.nih.gov/). This manuscript has been released as a pre-print at bioRxiv (Korrapati et al., 2019).

SUPPLEMENTARY MATERIAL

The Supplementary Material for this article can be found online at: https://www.frontiersin.org/articles/10.3389/fnmol.2019.00316/full#supplementary-material

FIGURE S1 | Distribution of single cell captures for adult SV scRNA-Seq dataset. Distribution of SV cell captures (S153 in pink, S161 in green, S171 in blue) are equally distributed across all clusters in the scRNA-Seq dataset. S153, S161, and S171 refer to batches collected on separate dates.

FIGURE S2 | Dissociation-induced gene expression in adult mouse SV scRNA-Seq and snRNA-Seq dataset has minimal effect on clustering. **(A)** Boxplot demonstrating quantification of averaged dissociation-induced gene expression across all cells in the scRNA-Seq dataset (blue box) compared to expression across all nuclei in the snRNA-Seq dataset (orange box). The average dissociation-induced gene expression represents relative level of dissociation-induced gene expression to nuclear loading controls in both single cell and single nucleus datasets. This analysis demonstrates that the level of dissociation-induced gene expression is similar between single cell and single nucleus datasets. See **Supplementary Data and Methods** for methodology and rationale. Difference in average expression is not statistically significant ($p = 0.68$). **(B)** tSNE plots demonstrate clustering of cells and nuclei before and after removal of dissociation artifact and show no difference in the number of clusters.

FIGURE S3 | snRNA-Seq resolves conflicting results in *Kcnj10* expression between scRNA-Seq and snRNA-Seq datasets in the adult mouse stria vascularis. **(A)** Feature plot from scRNA-Seq dataset demonstrating widespread *Kcnj10* expression across cell type clusters. **(B)** Feature plot from snRNA-Seq dataset demonstrating predominant expression of Kcnj10 in the intermediate cell cluster as demarcated in **Figure 2A**. **(C)** smFISH demonstrates Kcnj10 transcripts confined to intermediate cells labeled with anti-CD44 immunostaining. DAPI labels nuclei. Scale bar 20 μm.

FIGURE S4 | Shared gene expression between marginal and spindle cells. **(A)** Candidate genes identified in the scRNA-Seq dataset expressed by marginal (M) and spindle/root (S/R) cells. **(B)** Candidate genes identified in the snRNA-Seq dataset expressed by marginal (M) and spindle/root (S/R) cells. Intermediate cells (I) and basal cells **(B)** are denoted by their respective labels. Violin plots are displayed with normalized counts on the vertical axis and cell types arrayed along the horizontal axis.

FIGURE S5 | smFISH quantification of novel cell type-specific genes and regulon transcription factor with select downstream targets in SV cell types. Customized MATLAB code was utilized to determine the expression of novel gene transcripts in SV cell type nuclei and to determine the number of regulon transcription factor transcript-positive nuclei that expressed each of the downstream gene transcripts. **(A)** The percentage of cell type-specific nuclei labeled with candidate cell type-specific smFISH probes was quantified. Fifty-two of 56 (93%) and 66 of 66 (100%) of marginal cell nuclei expressed *Abcg1* and *Heyl* transcripts, respectively. One hundred thirty seven of 161 (85%) and 170 of 176 (97%) of *Kcnj10*- and *Cd44*-expressing intermediate cell nuclei expressed *Nrp2* and *Kcnj13* transcripts, respectively. 107 of 145 (73%) and 118 of 185 (64%) of basal cell nuclei express *Sox8* ($n = 145$ cells) and *Nr2f2* ($n = 185$ cells) transcripts, respectively. **(B)** The percentage of *Esrrb* transcript-positive nuclei expressing each of the downstream gene transcripts (*Abcg1*, *Atp13a5*, *Heyl*) is shown. Fifty-two of 56 (93%) *Esrrb* transcript-positive nuclei expressed *Abcg1*. Fifty-nine of 59 (100%) *Esrrb* transcript-positive nuclei expressed *Atp13a5*. Sixty-six of 66 (100%) *Esrrb* transcript-positive nuclei expressed *Heyl*. **(C)** The percentage of *Bmyc* transcript-positive nuclei expressing each of the downstream gene transcripts (*Cd44*, *Met*, *Pax3*) is shown. Forty of 43 (93%) *Bmyc* transcript-positive nuclei expressed *Cd44*. Thirty-six of 37 (97%) *Bmyc* transcript-positive nuclei expressed *Met*. Thirty-three of 38 (87%) *Bmyc* transcript-positive nuclei expressed *Pax3*.

FIGURE S6 | Enlarged image of adjacency plot for the scRNA-Seq dataset from **Figure 4B**. The more red a box is, the more similar the 2 intersecting WGCNA modules are to each other.

FIGURE S7 | Enlarged image of adjacency plot for the snRNA-Seq dataset from **Figure 4B**. The more red a box is, the more similar the 2 intersecting WGCNA modules are to each other.

FIGURE S8 | Top gene ontology (GO) terms identified by GO analysis with Enrichr in cell type-specific WGCNA modules and cell type-specific SCENIC regulons. **(A)** GO biological process, molecular function, and cellular component analysis of WGCNA modules from both the scRNA-Seq and snRNA-Seq datasets reveal gene set enrichment in marginal cells (red), intermediate cells (green), and basal cells (blue). **(B)** GO biological process, molecular function, and cellular component

analysis of SCENIC regulons from both the scRNA-Seq and snRNA-Seq datasets reveal gene set enrichment in marginal cells (red), intermediate cells (green), and basal cells (blue).

FIGURE S9 | Pharos-identified drugs with Adrb2 and Maoa gene activity. Drugs are displayed along with their mechanism of action. Activators are in green and inhibitors are in red.

TABLE S1 | Key resources.

TABLE S2 | Comparison of single-cell RNA-Seq (scRNA-Seq) and single-nucleus RNA-Seq in the adult stria vascularis.

TABLE S3 | Gene Ontology (GO) Analysis of Marginal Cell-Specific WGCNA Modules.

TABLE S4 | Gene Ontology (GO) Analysis of Intermediate Cell-Specific WGCNA Modules.

TABLE S5 | Gene Ontology (GO) Analysis of Basal Cell-Specific WGCNA Modules.

TABLE S6 | Gene Ontology (GO) Analysis of Marginal Cell-Specific SCENIC Regulons.

TABLE S7 | Gene Ontology (GO) Analysis of Intermediate Cell-Specific SCENIC Regulons.

TABLE S8 | Gene Ontology (GO) Analysis of Basal Cell-Specific SCENIC Regulons.

DATA AND METHODS | Comparative advantages between scRNA-seq and snRNA-seq in the adult stria vascularis.

REFERENCES

Aibar, S., González-Blas, C. B., Moerman, T., Huynh-Thu, V. A., Imrichova, H., Hulselmans, G., et al. (2017). SCENIC: single-cell regulatory network inference and clustering. *Nat. Methods* 14, 1083–1086. doi: 10.1038/nmeth.4463

Asma, A., Ashwaq, A., Norzana, A. G., Maizaton Atmadini, A., Ruszymah, B. H. I., Saim, L., et al. (2011). The association between GJB2 mutation and GJB6 gene in non syndromic hearing loss school children. *Med. J. Malays.* 66, 124–128.

Azaiez, H., Booth, K. T., Ephraim, S. S., Crone, B., Black-Ziegelbein, E. A., Marini, R. J., et al. (2018). Genomic landscape and mutational signatures of deafness-associated genes. *Am. J. Hum. Genet.* 103, 484–497. doi: 10.1016/j.ajhg.2018.08.006

Bartolami, S., Gaboyard, S., Quentin, J., Travo, C., Cavalier, M., Barhanin, J., et al. (2011). Critical roles of transitional cells and Na/K-ATPase in the formation of vestibular endolymph. *J. Neurosci.* 31, 16541–16549. doi: 10.1523/jneurosci.2430-11.2011

Baryawno, N., Przybylski, D., Kowalczyk, M. S., Kfoury, Y., Severe, N., Gustafsson, K., et al. (2019). A cellular taxonomy of the bone marrow stroma in homeostasis and leukemia. *Cell* 177, 1915.e16–1932.e16. doi: 10.1016/j.cell.2019.04.040

Batissoco, A. C., Abreu-Silva, R. S., Braga, M. C. C., Lezirovitz, K., Della-Rosa, V., Alfredo, T., et al. (2009). Prevalence of GJB2 (connexin-26) and GJB6 (connexin-30) mutations in a cohort of 300 Brazilian hearing-impaired individuals: implications for diagnosis and genetic counseling. *Ear Hear.* 30, 1–7. doi: 10.1097/AUD.0b013e31819144ad

Ben-Yosef, T., Belyantseva, I. A., Saunders, T. L., Hughes, E. D., Kawamoto, K., Van Itallie, C. M., et al. (2003). Claudin 14 knockout mice, a model for autosomal recessive deafness DFNB29, are deaf due to cochlear hair cell degeneration. *Hum. Mol. Genet.* 12, 2049–2061. doi: 10.1093/hmg/ddg210

Birkenhäger, R., Otto, E., Schürmann, M. J., Vollmer, M., Ruf, E. M., Maier-Lutz, I., et al. (2001). Mutation of BSND causes Bartter syndrome with sensorineural deafness and kidney failure. *Nat. Genet.* 29, 310–314. doi: 10.1038/ng752

Blondel, V. D., Guillaume, J.-L., Lambiotte, R., and Lefebvre, E. (2008). Fast unfolding of communities in large networks. *J. Stat. Mech.* 10008:12. doi: 10.1088/1742-5468/2008/10/P10008

Bolz, H., Schade, G., Ehmer, S., Kothe, C., Hess, M., and Gal, A. (2004). Phenotypic variability of non-syndromic hearing loss in patients heterozygous for both c.*35delG* of GJB2 and the 342-kb deletion involving GJB6. *Hear. Res.* 188, 42–46. doi: 10.1016/S0378-5955(03)00346-0

Bondurand, N. (2000). Interaction among SOX10, PAX3 and MITF, three genes altered in Waardenburg syndrome. *Hum. Mol. Genet.* 9, 1907–1917. doi: 10.1093/hmg/9.13.1907

Booth, K. T., Kahrizi, K., Najmabadi, H., Azaiez, H., and Smith, R. J. H. (2018). Old gene, new phenotype: splice-altering variants in CEACAM16 cause recessive non-syndromic hearing impairment. *J. Med. Genet.* 55, 555–560. doi: 10.1136/jmedgenet-2018-105349

Breglio, A. M., Rusheen, A. E., Shide, E. D., Fernandez, K. A., Spielbauer, K. K., McLachlin, K. M., et al. (2017). Cisplatin is retained in the cochlea indefinitely following chemotherapy. *Nat. Commun.* 8:1654. doi: 10.1038/s41467-017-01837-1

Cable, J., Barkway, C., and Steel, K. P. (1992). Characteristics of stria vascularis melanocytes of viable dominant spotting (Wv Wv) mouse mutants. *Hear. Res.* 64, 6–20. doi: 10.1016/0378-5955(92)90164-I

Cable, J., and Steel, K. P. (1991). Identification of two types of melanocyte within the Stria Vascularis of the mouse inner ear. *Pigment Cell Res.* 4, 87–101. doi: 10.1111/j.1600-0749.1991.tb00320.x

Calzada, A. P., Balaker, A. E., Ishiyama, G., Lopez, I. A., and Ishiyama, A. (2012). Temporal bone histopathology and immunoglobulin deposition in Sjogren's syndrome. *Otol. Neurotol.* 33, 258–266. doi: 10.1097/MAO.0b013e318241b548

Chan, D. K., Schrijver, I., and Chang, K. W. (2010). Connexin-26-associated deafness: phenotypic variability and progression of hearing loss. *Genet. Med.* 12, 174–181. doi: 10.1097/GIM.0b013e3181d0d42b

Chang, Q., Wang, J., Li, Q., Kim, Y., Zhou, B., Wang, Y., et al. (2015). Virally mediated Kcnq1 gene replacement therapy in the immature scala media restores hearing in a mouse model of human Jervell and Lange-Nielsen deafness syndrome. *EMBO Mol. Med.* 7, 1077–1086. doi: 10.15252/emmm.201404929

Chen, E. Y., Tan, C. M., Kou, Y., Duan, Q., Wang, Z., Meirelles, G., et al. (2013). Enrichr: interactive and collaborative HTML5 gene list enrichment analysis tool. *BMC Bioinformatics* 14:128. doi: 10.1186/1471-2105-14-128

Chen, H. C., Chung, C. H., Lu, C. H., and Chien, W. C. (2019). Metformin decreases the risk of sudden sensorineural hearing loss in patients with diabetes mellitus: a 14-year follow-up study. *Diab. Vasc. Dis. Res.* 16, 324–327. doi: 10.1177/1479164119826292

Chen, J., and Nathans, J. (2007). Estrogen-related receptor β/NR3B2 controls epithelial cell fate and endolymph production by the Stria Vascularis. *Dev. Cell* 13, 325–337. doi: 10.1016/j.devcel.2007.07.011

Chen, J., and Zhao, H. B. (2014). The role of an inwardly rectifying K+ channel (Kir4.1) in the inner ear and hearing loss. *Neuroscience* 265, 137–146. doi: 10.1016/j.neuroscience.2014.01.036

Chiarella, G., Petrolo, C., and Cassandro, E. (2015). The genetics of Ménière's disease. *Appl. Clin. Genet.* 8, 9–17. doi: 10.2147/TACG.S59024

Collin, R. W. J., Kalay, E., Tariq, M., Peters, T., van der Zwaag, B., Venselaar, H., et al. (2008). Mutations of ESRRB encoding estrogen-related receptor beta cause autosomal-recessive nonsyndromic hearing impairment DFNB35. *Am. J. Hum. Genet.* 82, 125–138. doi: 10.1016/j.ajhg.2007.09.008

Crowson, M. G., Patki, A., and Tucci, D. L. (2016). A systematic review of diuretics in the medical management of Ménière's disease. *Otolaryngol. Head Neck Surg.* 154, 824–834. doi: 10.1177/0194599816630733

Da Silva-Costa, S. M., Martins, F. T. A., Pereira, T., Pomilio, M. C. A., Marques-De-Faria, A. P., and Sartorato, E. L. (2011). Searching for digenic inheritance in deaf brazilian individuals using the multiplex ligation-dependent probe amplification technique. *Genet. Test. Mol. Biomark.* 15, 849–853. doi: 10.1089/gtmb.2011.0034

Dai, Q., Wang, D., and Zheng, H. (2019). The polymorphic analysis of the human potassium channel kcne gene family in meniere's disease-a preliminary study. *J. Int. Adv. Otol.* 15, 130–134. doi: 10.5152/iao.2019.5076

Del Castillo, I., Villamar, M., Moreno-Pelayo, M. A., Del Castillo, F. J., Álvarez, A., Tellería, D., et al. (2002). A deletion involving the connexin 30 gene in nonsyndromic hearing impairment. *N. Engl. J. Med.* 346, 243–249. doi: 10.1056/NEJMoa012052

DePasquale, E. A. K., Schnell, D. J., Valiente, I., Blaxall, B. C., Grimes, H. L., Singh, H., et al. (2018). DoubletDecon: cell-state aware removal of single-cell RNA-Seq doublets. *BioRxiv[Preprints].* doi: 10.1101/364810

Duinkerken, C. W., Rohaan, M. W., de Weger, V. A., Lohuis, P. J. F. M., Latenstein, M. N., Theunissen, E. A. R., et al. (2019). Sensorineural hearing loss after

adoptive cell immunotherapy for melanoma using MART-1 Specific T Cells. *Otol. Neurotol.* 40, e674–e678. doi: 10.1097/mao.0000000000002332

Faletra, F., Girotto, G., D'Adamo, A. P., Vozzi, D., Morgan, A., and Gasparini, P. (2014). A novel P2RX2 mutation in an Italian family affected by autosomal dominant nonsyndromic hearing loss. *Gene* 534, 236–239. doi: 10.1016/j.gene.2013.10.052

Faridi, R., Tona, R., Brofferio, A., Hoa, M., Olszewski, R., Schrauwen, I., et al. (2019). Mutational and phenotypic spectra of KCNE1 deficiency in Jervell and Lange-Nielsen syndrome and romano-ward syndrome. *Hum. Mutat.* 40, 162–176. doi: 10.1002/humu.23689

Ferrero, E., and Agarwal, P. (2018). Connecting genetics and gene expression data for target prioritisation and drug repositioning. *BioData Min.* 11:7. doi: 10.1186/s13040-018-0171-y

Frei, K., Ramsebner, R., Lucas, T., Baumgartner, W. D., Schoefer, C., Wachtler, F. J., et al. (2004). Screening for monogenetic del(GJB6-D13S1830) and digenic del(GJB6-D13S1830)/GJB2 patterns of inheritance in deaf individuals from Eastern Austria. *Hear. Res.* 196, 115–118. doi: 10.1016/j.heares.2004.07.001

Gallego-Martinez, A., Requena, T., Roman-Naranjo, P., and Lopez-Escamez, J. A. (2019). Excess of rare missence variants in hearing loss genes in sporadic meniere disease. *Front. Genet.* 10:76. doi: 10.3389/fgene.2019.00076

Gow, A. (2004). Deafness in Claudin 11-Null mice reveals the critical contribution of basal cell tight junctions to Stria Vascularis function. *J. Neurosci.* 24, 7051–7062. doi: 10.1523/jneurosci.1640-04.2004

Gualandi, F., Ravani, A., Berto, A., Burdo, S., Trevisi, P., Ferlini, A., et al. (2004). Occurrence of Del(GIB6-D13S1830) mutation in Italian non-syndromic hearing loss patients carrying a single GJB2 mutated allele. *Acta Oto Laryngol., Suppl.* 29–34. doi: 10.1080/03655230410017166

Hao, X., Xing, Y., Moore, M. W., Zhang, J., Han, D., Schulte, B. A., et al. (2014). Sox10 expressing cells in the lateral wall of the aged mouse and human cochlea. *PLoS One* 9:e97389. doi: 10.1371/journal.pone.0097389

Hibino, H., Nin, F., Tsuzuki, C., and Kurachi, Y. (2010). How is the highly positive endocochlear potential formed? the specific architecture of the stria vascularis and the roles of the ion-transport apparatus. *Pflugers Archiv. Eur. J. Physiol.* 459, 521–533. doi: 10.1007/s00424-009-0754-z

Hilding, D. A., and Ginzberg, R. D. (1977). Pigmentation of the stria vascularis the contribution of neural crest melanocytes. *Acta Oto-Laryngol.* 84, 24–37. doi: 10.3109/00016487709123939

Hoa, M., Friedman, R. A., Fisher, L. M., and Derebery, M. J. (2015). Prognostic implications of and audiometric evidence for hearing fluctuation in Meniere's disease. *Laryngoscope* 125(Suppl. 12), S1–S12. doi: 10.1002/lary.25579

Huebner, A. K., Maier, H., Maul, A., Nietzsche, S., Herrmann, T., Praetorius, J., et al. (2019). Early hearing loss upon disruption of Slc4a10 in C57BL/6 Mice. *JARO J. Assoc. Res. Otolaryngol.* 20, 233–245. doi: 10.1007/s10162-019-00719-1

Ingusci, S., Verlengia, G., Soukupova, M., Zucchini, S., and Simonato, M. (2019). Gene therapy tools for brain diseases. *Front. Pharmacol.* 10:724. doi: 10.3389/fphar.2019.00724

Ishiyama, G., Tokita, J., Lopez, I., Tang, Y., and Ishiyama, A. (2007). Unbiased stereological estimation of the spiral ligament and stria vascularis volumes in aging and Ménière's disease using archival human temporal bones. *JARO J. Assoc. Res. Otolaryngol.* 8, 8–17. doi: 10.1007/s10162-006-0057-4

Ito, T., Li, X., Kurima, K., Choi, B. Y., Wangemann, P., and Griffith, A. J. (2014). Slc26a4-insufficiency causes fluctuating hearing loss and stria vascularis dysfunction. *Neurobiol. Dis.* 66, 53–65. doi: 10.1016/j.nbd.2014.02.002

Ito, T., Nishio, A., Wangemann, P., and Griffith, A. J. (2015). Progressive irreversible hearing loss is caused by stria vascularis degeneration in an Slc26a4-insufficient mouse model of large vestibular aqueduct syndrome. *Neuroscience* 310, 188–197. doi: 10.1016/j.neuroscience.2015.09.016

Jagannathan, R., Seixas, A., St-Jules, D., Jagannathan, L., Rogers, A., Hu, L., et al. (2017). Systems biology genetic approach identifies serotonin pathway as a possible target for obstructive sleep apnea: results from a literature search review. *Sleep Disord.* 2017:6768323. doi: 10.1155/2017/6768323

Johnson, L. A., Morgan, R. A., Dudley, M. E., Cassard, L., Yang, J. C., Hughes, M. S., et al. (2009). Gene therapy with human and mouse T-cell receptors mediates cancer regression and targets normal tissues expressing cognate antigen. *Blood* 114, 535–546. doi: 10.1182/blood-2009-03-211714

Jones, S. M., and Jones, T. A. (2014). Genetics of peripheral vestibular dysfunction: lessons from mutant mouse strains. *J. Am. Acad. Audiol.* 25, 289–301. doi: 10.3766/jaaa.25.3.8

Kariya, S., Cureoglu, S., Fukushima, H., Nomiya, S., Nomiya, R., Schachern, P. A., et al. (2009). Vascular findings in the stria vascularis of patients with unilateral or bilateral Ménière's disease: a histopathologic temporal bone study. *Otol. Neurotol.* 30, 1006–1012. doi: 10.1097/MAO.0b013e3181b4ec89

Khalifa, O., Al-Sahlawi, Z., Imtiaz, F., Ramzan, K., Allam, R., Al-Mostafa, A., et al. (2015). Variable expression pattern in Donnai-Barrow syndrome: report of two novel LRP2 mutations and review of the literature. *Eur. J. Med. Genet.* 58, 293–299. doi: 10.1016/j.ejmg.2014.12.008

Kharchenko, P. V., Silberstein, L., and Scadden, D. T. (2014). Bayesian approach to single-cell differential expression analysis. *Nat. Methods* 11, 740–742. doi: 10.1038/nmeth.2967

Kikuchi, K., and Hilding, D. A. (1966). The development of the stria vascularis in the mouse. *Acta Oto-Laryngol.* 62, 277–291. doi: 10.3109/00016486609119573

Kim, H. J., Gratton, M. A., Lee, J.-H., Perez Flores, M. C., Wang, W., Doyle, K. J., et al. (2013). Precise toxigenic ablation of intermediate cells abolishes the "Battery" of the Cochlear Duct. *J. Neurosci.* 33, 14601–14606. doi: 10.1523/jneurosci.2147-13.2013

Kitajiri, S., Miyamoto, T., Mineharu, A., Sonoda, N., Furuse, K., Hata, M., et al. (2004). Compartmentalization established by claudin-11-based tight junctions in stria vascularis is required for hearing through generation of endocochlear potential. *J. Cell Sci.* 117(Pt 21), 5087–5096. doi: 10.1242/jcs.01393

Kitajiri, S. I., Furuse, M., Morita, K., Saishin-Kiuchi, Y., Kido, H., Ito, J., et al. (2004). Expression patterns of claudins, tight junction adhesion molecules, in the inner ear. *Hear. Res.* 187, 25–34. doi: 10.1016/S0378-5955(03)00338-1

König, O., Rüttiger, L., Müller, M., Zimmermann, U., Erdmann, B., Kalbacher, H., et al. (2008). Estrogen and the inner ear: megalin knockout mice suffer progressive hearing loss. *FASEB J.* 22, 410–417. doi: 10.1096/fj.07-9171com

Korrapati, S., Taukulis, I., Olszewski, R., Pyle, M., Gu, S., Singh, R., et al. (2019). Single cell and single nucleus RNA-Seq reveal cellular heterogeneity and homeostatic regulatory networks in adult mouse stria vascularis. *BioRxiv[Preprints]*

Kuijpers, W., Peters, T. A., Tonnaer, E. L. G. M., and Ramaekers, F. C. S. (1991). Expression of cytokeratin polypeptides during development of the rat inner ear. *Histochemistry* 96, 511–521. doi: 10.1007/BF00267077

Kuleshov, M. V., Jones, M. R., Rouillard, A. D., Fernandez, N. F., Duan, Q., Wang, Z., et al. (2016). Enrichr: a comprehensive gene set enrichment analysis web server 2016 update. *Nucleic Acids Res.* 44, W90–W97. doi: 10.1093/nar/gkw377

Lang, F., Vallon, V., Knipper, M., and Wangemann, P. (2007). Functional significance of channels and transporters expressed in the inner ear and kidney. *Am. J. Physiol. Cell Physiol.* 293, C1187–C1208. doi: 10.1152/ajpcell.00024.2007

Langfelder, P., and Horvath, S. (2008). WGCNA: an R package for weighted correlation network analysis. *BMC Bioinformatics* 9:559. doi: 10.1186/1471-2105-9-559

Lee, S., Shin, J. O., Sagong, B., Kim, U. K., and Bok, J. (2017). Spatiotemporal expression patterns of clusterin in the mouse inner ear. *Cell Tissue Res.* 370, 89–97. doi: 10.1007/s00441-017-2650-8

Lerer, I., Sagi, M., Ben-Neriah, Z., Wang, T., Levi, H., and Abeliovich, D. (2001). A deletion mutation in GJB6 cooperating with a GJB2 mutation in trans in non-syndromic deafness: a novel founder mutation in Ashkenazi Jews. *Hum. Mutat.* 18:460. doi: 10.1002/humu.1222

Li, J., Zheng, S., Chen, B., Butte, A. J., Swamidass, S. J., and Lu, Z. (2016). A survey of current trends in computational drug repositioning. *Brief. Bioinform.* 17, 2–12. doi: 10.1093/bib/bbv020

Liu, H., Li, Y., Chen, L., Zhang, Q., Pan, N., Nichols, D. H., et al. (2016). Organ of corti and stria vascularis: is there an interdependence for survival? *PLoS One* 11:e0168953. doi: 10.1371/journal.pone.0168953

Liu, W., Boström, M., Kinnefors, A., and Rask-Andersen, H. (2009). Unique expression of connexins in the human cochlea. *Hear. Res.* 250, 55–62. doi: 10.1016/j.heares.2009.01.010

Liu, W., Schrott-Fischer, A., Glueckert, R., Benav, H., and Rask-Andersen, H. (2017). The Human "Cochlear Battery" – Claudin-11 barrier and ion transport proteins in the lateral wall of the cochlea. *Front. Mol. Neurosci.* 10:239. doi: 10.3389/fnmol.2017.00239

Locher, H., de Groot, J. C., van Iperen, L., Huisman, M. A., Frijns, J. H. M., and Chuva de Sousa Lopes, S. M. (2015). Development of the stria vascularis and potassium regulation in the human fetal cochlea: insights into hereditary sensorineural hearing loss. *Dev. Neurobiol.* 75, 1219–1240. doi: 10.1002/dneu.22279

Lopes, K. D. C., Sartorato, E. L., Da Silva-Costa, S. M., De Macedo Adamov, N. S., and Ganança, F. F. (2016). Ménière's disease: molecular analysis of aquaporins 2, 3 and potassium channel KCNE1 genes in Brazilian patients. *Otol. Neurotol.* 37, 1117–1121. doi: 10.1097/MAO.0000000000001136

Lopez-Escamez, J. A., Batuecas-Caletrio, A., and Bisdorff, A. (2018). Towards personalized medicine in Ménière's disease. *F1000Research* 7:F1000Faculty Rev–1295. doi: 10.12688/f1000research.14417.1

Marcus, D. C., Wu, T., Wangemann, P., and Kofuji, P. (2013). KCNJ10 (Kir4.1) potassium channel knockout abolishes endocochlear potential. *Am. J. Physiol. Cell Physiol.* 282, C403–C407. doi: 10.1152/ajpcell.00312.2001

Matsushima, Y., Shinkai, Y., Kobayashi, Y., Sakamoto, M., Kunieda, T., and Tachibana, M. (2002). A mouse model of Waardenburg syndrome type 4 with a new spontaneous mutation of the endothelin-B receptor gene. *Mamm. Genome* 13, 30–35. doi: 10.1007/s00335-001-3038-2

McDavid, A., Finak, G., Chattopadyay, P. K., Dominguez, M., Lamoreaux, L., Ma, S. S., et al. (2013). Data exploration, quality control and testing in single-cell qPCR-based gene expression experiments. *Bioinformatics* 29, 461–467. doi: 10.1093/bioinformatics/bts714

McDougald, D. S., Duong, T. T., Palozola, K. C., Marsh, A., Papp, T. E., Mills, J. A., et al. (2019). CRISPR activation enhances in vitro potency of AAV vectors driven by tissue-specific promoters. *Mol. Therapy Methods Clin. Dev.* 13, 380–389. doi: 10.1016/j.omtm.2019.03.004

McGuirt, W. T., Prasad, S. D., Griffith, A. J., Kunst, H. P. M., Green, G. E., Shpargel, K. B., et al. (1999). Mutations in COL11A2 cause non-syndromic hearing loss (DFNA13). *Nat. Genet.* 23, 413–419. doi: 10.1038/70516

Mei, L., Chen, J., Zong, L., Zhu, Y., Liang, C., Jones, R. O., et al. (2017). A deafness mechanism of digenic Cx26 (GJB2) and Cx30 (GJB6) mutations: reduction of endocochlear potential by impairment of heterogeneous gap junctional function in the cochlear lateral wall. *Neurobiol. Dis.* 108, 195–203. doi: 10.1016/j.nbd.2017.08.002

Milon, B., Mitra, S., Song, Y., Margulies, Z., Casserly, R., Drake, V., et al. (2018). The impact of biological sex on the response to noise and otoprotective therapies against acoustic injury in mice. *Biol. Sex Differ.* 9:12. doi: 10.1186/s13293-018-0171-0

Mittal, R., Aranke, M., Debs, L. H., Nguyen, D., Patel, A. P., Grati, M., et al. (2017). Indispensable role of ion channels and transporters in the auditory system. *J. Cell. Physiol.* 232, 743–758. doi: 10.1002/jcp.25631

Miyagawa, M., Nishio, S. Y., Usami, S. I., Takeichi, N., Fukuda, S., Namba, A., et al. (2014). Mutation spectrum and genotype-phenotype correlation of hearing loss patients caused by SLC26A4 mutations in the Japanese: a large cohort study. *J. Hum. Genet.* 59, 262–268. doi: 10.1038/jhg.2014.12

Mori, Y., Watanabe, M., Inui, T., Nimura, Y., Araki, M., Miyamoto, M., et al. (2009). Ca 2+ regulation of endocochlear potential in marginal cells. *J. Physiol. Sci.* 59, 355–365. doi: 10.1007/s12576-009-0043-9

Mujtaba, G., Schultz, J. M., Imtiaz, A., Morell, R. J., Friedman, T. B., and Naz, S. (2015). A mutation of MET, encoding hepatocyte growth factor receptor, is associated with human DFNB97 hearing loss. *J. Med. Genet.* 52, 548–552. doi: 10.1136/jmedgenet-2015-103023

Muri, L., Le, N. D., Zemp, J., Grandgirard, D., and Leib, S. L. (2019). Metformin mediates neuroprotection and attenuates hearing loss in experimental pneumococcal meningitis. *J. Neuroinflamm.* 16:156. doi: 10.1186/s12974-019-1549-6

Nakazawa, K., Spicer, S. S., and Schulte, B. A. (1995). Ultrastructural localization of Na,K-ATPase in the gerbil cochlea. *J. Histochem. Cytochem.* 43, 981–991. doi: 10.1177/43.10.7560888

Naz, S., Imtiaz, A., Mujtaba, G., Maqsood, A., Bashir, R., Bukhari, I., et al. (2017). Genetic causes of moderate to severe hearing loss point to modifiers. *Clin. Genet.* 91, 589–598. doi: 10.1111/cge.12856

Neng, L., Zhang, F., Kachelmeier, A., and Shi, X. (2013). Endothelial cell, pericyte, and perivascular resident macrophage-type melanocyte interactions regulate cochlear intrastrial fluid-blood barrier permeability. *JARO J. Assoc. Res. Otolaryngol.* 14, 175–185. doi: 10.1007/s10162-012-0365-9

Nguyen, D. T., Mathias, S., Bologa, C., Brunak, S., Fernandez, N., Gaulton, A., et al. (2017). Pharos: collating protein information to shed light on the druggable genome. *Nucleic Acids Res.* 45, D995–D1002. doi: 10.1093/nar/gkw1072

Nickel, R., and Forge, A. (2008). Gap junctions and connexins in the inner ear: their roles in homeostasis and deafness. *Curr. Opin. Otolaryngol. Head Neck Surg.* 16, 452–457. doi: 10.1097/MOO.0b013e32830e20b0

Nin, F., Hibino, H., Doi, K., Suzuki, T., Hisa, Y., and Kurachi, Y. (2008). The endocochlear potential depends on two K+ diffusion potentials and an electrical barrier in the stria vascularis of the inner ear. *Proc. Natl. Acad. Sci. U.S.A.* 105, 1751–1756. doi: 10.1073/pnas.0711463105

Nin, F., Yoshida, T., Murakami, S., Ogata, G., Uetsuka, S., Choi, S., et al. (2017). Computer modeling defines the system driving a constant current crucial for homeostasis in the mammalian cochlea by integrating unique ion transports. *NPJ Syst. Biol. Appl.* 3:24. doi: 10.1038/s41540-017-0025-0

Nishio, A., Ito, T., Cheng, H., Fitzgerald, T. S., Wangemann, P., and Griffith, A. J. (2016). Slc26a4 expression prevents fluctuation of hearing in a mouse model of large vestibular aqueduct syndrome. *Neuroscience* 329, 74–82. doi: 10.1016/j.neuroscience.2016.04.042

Ohlemiller, K. K. (2009). Mechanisms and genes in human strial presbycusis from animal models. *Brain Res.* 1277, 70–83. doi: 10.1016/j.brainres.2009.02.079

Pallares-Ruiz, N., Blanchet, P., Mondain, M., Claustres, M., and Roux, A. F. (2002). A large deletion including most of GJB6 in recessive non syndromic deafness: a digenic effect? *Eur. J. Hum. Genet.* 10, 72–76. doi: 10.1038/sj.ejhg.5200762

Paranjpe, M. D., Taubes, A., and Sirota, M. (2019). Insights into computational drug repurposing for neurodegenerative disease. *Trends Pharmacol. Sci.* 40, 565–576. doi: 10.1016/j.tips.2019.06.003

Patuzzi, R. (2011). Ion flow in stria vascularis and the production and regulation of cochlear endolymph and the endolymphatic potential. *Hear. Res.* 277, 4–19. doi: 10.1016/j.heares.2011.01.010

Pazhouhandeh, M., Samiee, F., Boniadi, T., Khedmat, A. F., Vahedi, E., Mirdamadi, M., et al. (2017). Comparative network analysis of patients with non-small cell lung cancer and smokers for representing potential therapeutic targets. *Sci. Rep* 7:13812. doi: 10.1038/s41598-017-14195-1

Potterf, S. B., Mollaaghababa, R., Hou, L., Southard-Smith, E. M., Hornyak, T. J., Arnheiter, H., et al. (2001). Analysis of SOX10 function in neural crest-derived melanocyte development: SOX10-dependent transcriptional control of dopachrome tautomerase. *Dev. Biol.* 237, 245–257. doi: 10.1006/dbio.2001.0372

Praetorius, M., Hsu, C., Baker, K., Brough, D. E., Plinkert, P., and Staecker, H. (2010). Adenovector-mediated hair cell regeneration is affected by promoter type. *Acta Oto-Laryngol.* 130, 215–222. doi: 10.3109/00016480903019251

Riazuddin, S., Anwar, S., Fischer, M., Ahmed, Z. M., Khan, S. Y., Janssen, A. G. H., et al. (2009). Molecular basis of DFNB73: mutations of BSND can cause nonsyndromic deafness or bartter syndrome. *Am. J. Hum. Genet.* 85, 273–280. doi: 10.1016/j.ajhg.2009.07.003

Rickheit, G., Maier, H., Strenzke, N., Andreescu, C. E., De Zeeuw, C. I., Muenscher, A., et al. (2008). Endocochlear potential depends on Cl- channels: mechanism underlying deafness in Bartter syndrome IV. *EMBO J.* 27, 2907–2917. doi: 10.1038/emboj.2008.203

Ritter, K. E., and Martin, D. M. (2019). Neural crest contributions to the ear: implications for congenital hearing disorders. *Hear. Res.* 376, 22–32. doi: 10.1016/j.heares.2018.11.005

Rohacek, A. M., Bebee, T. W., Tilton, R. K., Radens, C. M., McDermott-Roe, C., Peart, N., et al. (2017). ESRP1 mutations cause hearing loss due to defects in alternative splicing that disrupt cochlear development. *Dev. Cell* 43, 318.e5–331.e5. doi: 10.1016/j.devcel.2017.09.026

Rybak, L. P., Mukherjea, D., and Ramkumar, V. (2019). Mechanisms of cisplatin-induced ototoxicity and prevention. *Semin. Hear.* 40, 197–204. doi: 10.1055/s-0039-1684048

Sagara, T., Furukawa, H., Makishima, K., and Fujimoto, S. (1995). Differentiation of the rat stria vascularis. *Hear. Res.* 83, 121–132. doi: 10.1016/0378-5955(94)00195-V

Satija, R., Farrell, J. A., Gennert, D., Schier, A. F., and Regev, A. (2015). Spatial reconstruction of single-cell gene expression data. *Nat. Biotechnol.* 33, 495–502. doi: 10.1038/nbt.3192

Schultz, J. M., Khan, S. N., Ahmed, Z. M., Riazuddin, S., Waryah, A. M., Chhatre, D., et al. (2009). Noncoding mutations of HGF are associated with nonsyndromic hearing loss. DFNB39. *Am. J. Hum. Genet.* 85, 25–39. doi: 10.1016/j.ajhg.2009.06.003

Seaman, B. J., Guardiani, E. A., Brewer, C. C., Zalewski, C. K., King, K. A., Rudy, S., et al. (2012). Audiovestibular dysfunction associated with adoptive cell immunotherapy for melanoma. *Otolaryngol. Head Neck Surg.* 147, 744–749. doi: 10.1177/0194599812448356

Sepahdari, A., Vorasubin, N., Ishiyama, G., and Ishiyama, A. (2016). Endolymphatic hydrops reversal following acetazolamide therapy:

demonstration with delayed intravenous contrast-enhanced 3D-FLAIR MRI. *Am. J. Neuroradiol.* 37, 151–154. doi: 10.3174/ajnr.A4462

Shearer, A. E., Hildebrand, M. S., and Smith, R. J. (1993). "Hereditary hearing loss and deafness overview," in *GeneReviews®*, eds M. P. Adam, H. H. Ardinger, R. A. Pagon, S. E. Wallace, L. J. H. Bean, K. Stephens, et al. (Seattle, WA: University of Washington).

Sher, A. E. (1971). The embryonic and postnatal development of the inner ear of the mouse. *Acta Oto-Laryngol. Suppl.* 285, 1–77.

Shi, X. (2016). Pathophysiology of the cochlear intrastrial fluid-blood barrier (review). *Hearing Res.* 338, 52–63. doi: 10.1016/j.heares.2016.01.010

Shibata, S., Miwa, T., Wu, H.-H., Levitt, P., and Ohyama, T. (2016). Hepatocyte growth factor-c-met signaling mediates the development of nonsensory structures of the mammalian cochlea and hearing. *J. Neurosci.* 36, 8200–8209. doi: 10.1523/jneurosci.4410-15.2016

Skene, N. G., and Grant, S. G. N. (2016). Identification of vulnerable cell types in major brain disorders using single cell transcriptomes and expression weighted cell type enrichment. *Front. Neurosci.* 10:16. doi: 10.3389/fnins.2016.00016

Sommer, L. (2011). Generation of melanocytes from neural crest cells. *Pigment Cell Melanoma Res.* 24, 411–421. doi: 10.1111/j.1755-148X.2011.00834.x

Steel, K. P., and Barkway, C. (1989). Another role for melanocytes: their importance for normal stria vascularis development in the mammalian inner ear. *Development* 107, 453–463.

Stevenson, V. A., Ito, M., and Milunsky, J. M. (2003). Connexin-30 deletion analysis in Connexin-26 heterozygotes. *Genet. Test.* 7, 151–154. doi: 10.1089/109065703322146867

Tachibana, M. (1999). Sound needs sound melanocytes to be heard. *Pigment Cell Res.* 12, 344–354. doi: 10.1111/j.1600-0749.1999.tb00518.x

Tachibana, M. (2001). Cochlear melanocytes and MITF signaling. *J. Investig. Dermatol. Symp. Proc.* 6, 95–98. doi: 10.1046/j.0022-202x.2001.00017.x

Takeuchi, S., Ando, M., and Kakigi, A. (2000). Mechanism generating endocochlear potential: role played by intermediate cells in stria vascularis. *Biophys. J.* 79, 2572–2582. doi: 10.1016/S0006-3495(00)76497-6

Tassabehji, M., Read, A. P., Newton, V. E., Patton, M., Gruss, P., Harris, R., et al. (1993). Mutations in the PAX3 gene causing Waardenburg syndrome type 1 and type 2. *Nat. Genet.* 3, 26–30. doi: 10.1038/ng0193-26

Van Camp, G., and Smith, R. J. (n. d.). *Hereditary Hearing Loss Homepage*. Available at: https://hereditaryhearingloss.org/ (accessed August 11, 2019).

Van Den Brink, S. C., Sage, F., Vértesy, Á, Spanjaard, B., Peterson-Maduro, J., Baron, C. S., et al. (2017). Single-cell sequencing reveals dissociation-induced gene expression in tissue subpopulations. *Nat. Methods* 14, 935–936. doi: 10.1038/nmeth.4437

Vanhaelen, Q., Mamoshina, P., Aliper, A. M., Artemov, A., Lezhnina, K., Ozerov, I., et al. (2017). Design of efficient computational workflows for in silico drug repurposing. *Drug Discov. Today* 22, 210–222. doi: 10.1016/j.drudis.2016.09.019

Walters, B. J., and Zuo, J. (2015). A Sox10rtTA/+ mouse line allows for inducible gene expression in the auditory and balance organs of the inner ear. *JARO J. Assoc. Res. Otolaryngol.* 16, 331–345. doi: 10.1007/s10162-015-0517-9

Waltman, L., and van Eck, N. J. (2013). A smart local moving algorithm for large-scale modularity-based community detection. *Eur. Phys. J. B* 86:471. doi: 10.1140/epjb/e2013-40829-0

Wang, L., Feng, Y., Yan, D., Qin, L., Grati, M., Mittal, R., et al. (2018). A dominant variant in the PDE1C gene is associated with nonsyndromic hearing loss. *Hum. Genet.* 137, 437–446. doi: 10.1007/s00439-018-1895-y

Wangemann, P. (1995). Comparison of ion transport mechanisms between vestibular dark cells and strial marginal cells. *Hear. Res.* 90, 149–157. doi: 10.1016/0378-5955(95)00157-2

Wangemann, P. (2002). K+ cycling and the endocochlear potential. *Hear. Res.* 165, 1–9. doi: 10.1016/S0378-5955(02)00279-4

Wangemann, P. (2006). Supporting sensory transduction: cochlear fluid homeostasis and the endocochlear potential. *J. Physiol.* 576(Pt 1), 11–21. doi: 10.1113/jphysiol.2006.112888

Wangemann, P., Itza, E. M., Albrecht, B., Wu, T., Jabba, S. V., Maganti, R. J., et al. (2004). Loss of KCNJ10 protein expression abolishes endocochlear potential and causes deafness in Pendred syndrome mouse model. *BMC Med.* 2:30. doi: 10.1186/1741-7015-2-30

Wayne, S. (2001). Mutations in the transcriptional activator EYA4 cause late-onset deafness at the DFNA10 locus. *Hum. Mol. Genet.* 10, 195–200. doi: 10.1093/hmg/10.3.195

Wester, J. L., Ishiyama, G., Karnezis, S., and Ishiyama, A. (2018). Sudden hearing loss after cialis (tadalafil) use: a unique case of cochlear hydrops. *Laryngoscope* 128, 2615–2618. doi: 10.1002/lary.27428

Wijayaratne, A. L., and McDonnell, D. P. (2001). The human estrogen receptor-α is a ubiquitinated protein whose stability is affected differentially by agonists, antagonists, and selective estrogen receptor modulators. *J. Biol. Chem.* 276, 35684–35692. doi: 10.1074/jbc.M101097200

Wilcox, E. R., Burton, Q. L., Naz, S., Riazuddin, S., Smith, T. N., Ploplis, B., et al. (2001). Mutations in the gene encoding tight junction claudin-14 cause autosomal recessive deafness DFNB29. *Cell* 104, 165–172. doi: 10.1016/S0092-8674(01)00200-8

Williamson, T. T., Ding, B., Zhu, X., and Frisina, R. D. (2019). Hormone replacement therapy attenuates hearing loss: mechanisms involving estrogen and the IGF-1 pathway. *Aging Cell* 18:e12939. doi: 10.1111/acel.12939

Wu, B.-L., Kenna, M., Lip, V., Irons, M., and Platt, O. (2003). Use of a multiplex PCR/sequencing strategy to detect both connexin 30 (GJB6) 342 kb deletion and connexin 26 (GJB2) mutations in cases of childhood deafness. *Am. J. Med. Genet.* 121A, 102–108. doi: 10.1002/ajmg.a.20210

Wu, H., Kirita, Y., Donnelly, E. L., and Humphreys, B. D. (2019). Advantages of single-nucleus over single-cell RNA sequencing of adult kidney: rare cell types and novel cell states revealed in fibrosis. *J. Am. Soc. Nephrol.* 30, 23–32. doi: 10.1681/asn.2018090912

Yang, S., Corbett, S. E., Koga, Y., Wang, Z., Johnson, W. E., Yajima, M., et al. (2019). Decontamination of ambient RNA in single-cell RNA-seq with DecontX. *BioRxiv[Preprints]*

Yoshida, T., Nin, F., Ogata, G., Uetsuka, S., Kitahara, T., Inohara, H., et al. (2015). NKCCs in the fibrocytes of the spiral ligament are silent on the unidirectional K+ transport that controls the electrochemical properties in the mammalian cochlea. *Pflugers Archiv. Eur. J. Physiol.* 467, 1577–1589. doi: 10.1007/s00424-014-1597-9

Zdebik, A. A., Wangemann, P., and Jentsch, T. J. (2009). Potassium ion movement in the inner ear: insights from genetic disease and mouse models. *Physiology* 24, 307–316. doi: 10.1152/physiol.00018.2009

Zeng, W., Jiang, S., Kong, X., El-Ali, N., Ball, A. R., Ma, C. I. H., et al. (2016). Single-nucleus RNA-seq of differentiating human myoblasts reveals the extent of fate heterogeneity. *Nucleic Acids Res.* 44:e158. doi: 10.1093/nar/gkw739

Zhang, Y., Knosp, B. M., Maconochie, M., Friedman, R. A., and Smith, R. J. H. (2004). A comparative study of Eya1 and Eya4 protein function and its implication in branchio-oto-renal syndrome and DFNA10. *JARO J. Assoc. Res. Otolaryngol.* 5, 295–304. doi: 10.1007/s10162-004-4044-3

Zheng, J., Miller, K. K., Yang, T., Hildebrand, M. S., Shearer, A. E., DeLuca, A. P., et al. (2011). Carcinoembryonic antigen-related cell adhesion molecule 16 interacts with α-tectorin and is mutated in autosomal dominant hearing loss (DFNA4). *Proc. Natl. Acad. Sci. U.S.A.* 108, 4218–4223. doi: 10.1073/pnas.1005842108

Zhu, Y., Beudez, J., Yu, N., Grutter, T., and Zhao, H. B. (2017). P2x2 dominant deafness mutations have no negative effect on wild-type isoform: implications for functional rescue and in deafness mechanism. *Front. Mol. Neurosci.* 10:371. doi: 10.3389/fnmol.2017.00371

Conflict of Interest: The authors declare that the research was conducted in the absence of any commercial or financial relationships that could be construed as a potential conflict of interest.

frontiers in Molecular Neuroscience

ORIGINAL RESEARCH
published: 15 January 2020
doi: 10.3389/fnmol.2019.00320

The *lhfpl5* Ohnologs *lhfpl5a* and *lhfpl5b* Are Required for Mechanotransduction in Distinct Populations of Sensory Hair Cells in Zebrafish

Timothy Erickson[1,2], Itallia V. Pacentine[2], Alexandra Venuto[1], Rachel Clemens[2] and Teresa Nicolson[2†]*

[1] Department of Biology, East Carolina University, Greenville, NC, United States, [2] Oregon Hearing Research Center and Vollum Institute, Oregon Health and Science University, Portland, OR, United States

Hair cells sense and transmit auditory, vestibular, and hydrodynamic information by converting mechanical stimuli into electrical signals. This process of mechano-electrical transduction (MET) requires a mechanically gated channel localized in the apical stereocilia of hair cells. In mice, lipoma HMGIC fusion partner-like 5 (LHFPL5) acts as an auxiliary subunit of the MET channel whose primary role is to correctly localize PCDH15 and TMC1 to the mechanotransduction complex. Zebrafish have two *lhfpl5* genes (*lhfpl5a* and *lhfpl5b*), but their individual contributions to MET channel assembly and function have not been analyzed. Here we show that the zebrafish *lhfpl5* genes are expressed in discrete populations of hair cells: *lhfpl5a* expression is restricted to auditory and vestibular hair cells in the inner ear, while *lhfpl5b* expression is specific to hair cells of the lateral line organ. Consequently, *lhfpl5a* mutants exhibit defects in auditory and vestibular function, while disruption of *lhfpl5b* affects hair cells only in the lateral line neuromasts. In contrast to previous reports in mice, localization of Tmc1 does not depend upon Lhfpl5 function in either the inner ear or lateral line organ. In both *lhfpl5a* and *lhfpl5b* mutants, GFP-tagged Tmc1 and Tmc2b proteins still localize to the stereocilia of hair cells. Using a stably integrated GFP-Lhfpl5a transgene, we show that the tip link cadherins Pcdh15a and Cdh23, along with the Myo7aa motor protein, are required for correct Lhfpl5a localization at the tips of stereocilia. Our work corroborates the evolutionarily conserved co-dependence between Lhfpl5 and Pcdh15, but also reveals novel requirements for Cdh23 and Myo7aa to correctly localize Lhfpl5a. In addition, our data suggest that targeting of Tmc1 and Tmc2b proteins to stereocilia in zebrafish hair cells occurs independently of Lhfpl5 proteins.

Keywords: hair cell, mechanotransduction, deafness, lateral line, zebrafish, LHFPL5, TMC1, PCDH15

OPEN ACCESS

Edited by:
Isabel Varela-Nieto, Spanish National Research Council (CSIC), Spain

Reviewed by:
Hiroshi Hibino, Niigata University, Japan
*Sangyong Jung, Singapore Bioimaging Consortium (A*STAR), Singapore*
Gwenaelle Geleoc, Harvard Medical School, United States

****Correspondence:***
Timothy Erickson
ericksonti17@ecu.edu

†Present address:
Teresa Nicolson, Otolaryngology-Head and Neck Surgery, Stanford School of Medicine, Stanford, CA, United States

Received: *11 September 2019*
Accepted: *16 December 2019*
Published: *15 January 2020*

Citation:
Erickson T, Pacentine IV, Venuto A, Clemens R and Nicolson T (2020) The lhfpl5 Ohnologs lhfpl5a and lhfpl5b Are Required for Mechanotransduction in Distinct Populations of Sensory Hair Cells in Zebrafish. Front. Mol. Neurosci. 12:320. doi: 10.3389/fnmol.2019.00320

INTRODUCTION

The mechano-electrical transduction (MET) complex of sensory hair cells is an assembly of proteins and lipids that facilitate the conversion of auditory, vestibular and hydrodynamic stimuli into electrical signals. Our current understanding is that the proteins of the MET complex consist of the tip link proteins cadherin 23 (CDH23) and protocadherin 15 (PCDH15) at the upper

and lower ends of the tip link respectively (Kazmierczak et al., 2007), the pore-forming subunits transmembrane channel-like proteins TMC1 and TMC2 (Kawashima et al., 2011; Pan et al., 2013, 2018), and the accessory subunits transmembrane inner ear (TMIE) and lipoma HMGIC fusion partner-like 5 (LHFPL5) (Xiong et al., 2012; Zhao et al., 2014; Cunningham and Müller, 2019). How these proteins are correctly localized to the sensory hair bundle and assemble into a functional complex is a fundamental question for understanding the molecular basis of how mechanotransduction occurs.

Recent studies have revealed extensive biochemical interactions between the MET complex proteins that are required for the function and/or stable integration of each component in the complex. In particular, LHFPL5 is a central player in MET complex formation, stability, and function. LHFPL5 (a.k.a. tetraspan membrane protein of the hair cell stereocilia/TMHS) is a four transmembrane domain protein from the superfamily of tetraspan junctional complex proteins. This superfamily includes junctional proteins like claudins and connexins, as well as ion channel auxiliary subunits such as transmembrane α-amino-3-hydroxy-5-methyl-4-isoxazole propionic acid receptor (AMPAR) regulatory proteins (TARPs) and the gamma subunits of voltage gated calcium channels. Pathogenic mutations in LHFPL5 are a cause of non-syndromic sensorineural hearing loss in humans (DFNB67), mice and zebrafish (Nicolson et al., 1998; Longo-Guess et al., 2005; Shabbir et al., 2006; Obholzer et al., 2012). LHFPL5 localizes to the tips of stereocilia (Xiong et al., 2012; Mahendrasingam et al., 2017; Li et al., 2019) where it directly interacts with other MET complex components. Co-immunoprecipitation experiments in heterologous cells suggests that LHFPL5 can directly interact with PCDH15 and TMIE (Xiong et al., 2012; Zhao et al., 2014). A structure of the PCDH15 – LHFPL5 complex has also been reported (Ge et al., 2018).

A precise role for LHFPL5 has yet to be defined. One current hypothesis is that LHFPL5 acts as an auxiliary subunit of the MET channel to stabilize the complex, similar to TARPs and the gamma subunits of voltage-gated calcium channels. In mouse cochlear hair cells, PCDH15 and LHFPL5 require each other for stable localization at the tips of stereocilia (Xiong et al., 2012; Mahendrasingam et al., 2017), consistent with their well-defined biochemical interaction. The partial loss of PCDH15 from the stereocilia explains the observed reduction in the number of tip links and the dysmorphic hair bundles in *Lhfpl5*$^{-/-}$ hair cells. Interestingly, although experiments have failed to demonstrate a biochemical interaction between LHFPL5 and the TMCs, LHFPL5 is required for the localization of TMC1, but not TMC2, in the hair bundle of mouse cochlear hair cells (Beurg et al., 2015). Consistent with this finding, the researchers identified a residual TMC2-dependent MET current in *Lhfpl5* mutant mice. The basis for the selective loss of TMC1 is not known.

In zebrafish, Lhfpl5a plays a similar role in mechanotransduction as its mammalian counterparts. A mutation in zebrafish *lhfpl5a* was reported in a forward genetic screen for genes required for hearing and balance (Nicolson et al., 1998; Obholzer et al., 2012). The loss of Lhfpl5a disrupts the targeting of Pcdh15a to stereocilia and results in splayed hair bundles (Maeda et al., 2017). However, Lhfpl5a is not required to correctly localize Tmie and vice versa (Pacentine and Nicolson, 2019), in spite of their biochemical interaction in cultured cells (Xiong et al., 2012). Lhfpl5 still localizes to the tips of stereocilia in *Tmc1*/*Tmc2* double mutants (Beurg et al., 2015), as well as *transmembrane O-methyltransferase* (*tomt*) mouse and zebrafish mutants, which fail to traffic TMCs to the hair bundle (Cunningham et al., 2017; Erickson et al., 2017). This phenotype suggests that Lhfpl5 localization does not require the TMCs. However, a number of questions regarding the functions of Lhfpl5 remain unanswered: (1) In zebrafish, what are the molecular requirements for targeting Lhfpl5a to the hair bundle? (2) Is the Lhfpl5-dependent targeting of Tmc1 to the hair bundle an evolutionarily conserved aspect of their interaction? (3) *lhfpl5a* mutants have defects in auditory and vestibular behaviors, yet sensory hair cells of the lateral line are unaffected (Nicolson et al., 1998). What is the genetic basis for the persistence of lateral line function in *lhfpl5a* mutants?

In this work, we report that teleost fish have two *lhfpl5* genes, *lhfpl5a* and *lhfpl5b*. The zebrafish *lhfpl5* ohnologs are expressed in distinct populations of larval sensory hair cells: *lhfpl5a* in the auditory and vestibular system; *lhfpl5b* in the hair cells of the lateral line organ. Their divergent expression patterns explain why lateral line hair cells are still mechanically sensitive in *lhfpl5a* mutants. CRISPR-Cas 9 knockout of *lhfpl5b* alone silences the lateral line organ but has no effect on otic hair cell function. We also show that neither Lhfpl5a nor Lhfpl5b are required for Tmc localization in stereocilia. Additionally, we use a GFP-tagged Lhfpl5a to demonstrate that Myo7aa and the tip link proteins Cdh23 and Pcdh15a are required for proper Lhfpl5a localization in otic hair cell bundles. This study reveals the subfunctionalization of the zebrafish *lhfpl5* ohnologs through the divergence in their expression patterns. Furthermore, our work complements previous results from murine cochlear hair cells by highlighting a conserved association between Lhfpl5 and Pcdh15, but also demonstrating novel requirements for Cdh23 and Myo7aa in localizing Lhfpl5a. Lastly, our work indicates that Lhfpl5-dependent localization of Tmc1 is not a universal feature of sensory hair cells and that Lhfpl5 proteins are required for mechanotransduction independently of a role in localizing the Tmc channel subunits to stereocilia.

MATERIALS AND METHODS

Ethics Statement

Animal research complied with guidelines stipulated by the Institutional Animal Care and Use Committees at Oregon Health and Science University (Portland, OR, United States) and East Carolina University (Greenville, NC, United States). Zebrafish (*Danio rerio*) were maintained and bred using standard procedures (Westerfield, 2000).

Mutant and Transgenic Fish Lines

The following zebrafish mutant alleles were used for this study: *cdh23*^{nl9}, *cdh23*^{tj264}, *lhfpl5a*^{tm290d}, *lhfpl5b*^{vo35}, *myo7aa*^{ty220},

pcdh15a^{psi7}, *pcdh15a*^{th263b} (Nicolson et al., 1998; Ernest et al., 2000; Obholzer et al., 2012; Erickson et al., 2017; Maeda et al., 2017). The transgenic lines used in this study were *Tg(-6myo6b:eGFP-lhfpl5a)vo23Tg*, *Tg(-6myo6b:tmc1-emGFP)vo27Tg*, *Tg(-6myo6b:tmc2b-emGFP)vo28Tg* (Erickson et al., 2017), and *Tg(-6myo6b:eGFP-pA)vo68Tg*. All experiments used larvae at 1–7 dpf, which are of indeterminate sex at this stage.

Genotyping

Standard genomic PCR followed by Sanger sequencing was used to identify *cdh23*^{tj264}, *cdh23*^{nl9}, *lhfpl5a*^{tm290d}, *pcdh15a*^{psi7}, and *pcdh15a*^{th263b} alleles. The *lhfpl5b*^{vo35} mutation disrupts a MluCI restriction site (AATT) and we are able to identify *lhfpl5b*^{vo35} hetero- and homozygotes based on the different sizes of MluCI-digested PCR products resolved on a 1.5% agarose gel. The following primers were used for genotyping:

cdh23^{nl9}: Fwd – CCACAGGAATTCTGGTGTCC, Rvs – GAAAGTGGGCGTCTCATCAT;
cdh23^{tj264}: Fwd – GGACGTCAGTGTTCATGGTG, Rvs – TTTTCTGACCGTGGCATTAAC;
lhfpl5a^{tm290d}: Fwd – GGACCATCATCTCCAGCAAAC, Rvs – CACGAAACATATTTTCACTCACCAG;
lhfpl5b^{vo35}: Fwd – GCGTCATGTGGGCAGTTTTC, Rvs – TAGACACTAGCGGCGTTGC;
myo7aa^{ty220}: Fwd – TAGGTCCTCTTTAATGCATA, Rvs – GTCTGTCTGTCTGTCTATCTGTCTCGCT;
pcdh15a^{psi7}: Fwd – TTGGCACCACTATCTTTACCG, Rvs – ACAGAAGGCACCTGGAAAAC;
pcdh15a^{th263b}: Fwd – AGGGACTAAGCCGAAGGAAG, Rvs – CACTCATCTTCACAGCCATACAG.

Phylogeny

Lhfpl5 protein sequences retrieved from either NCBI or Ensembl (**Supplementary Table 1**). Phylogenetic analysis was done on www.phylogeny.fr using T-Coffee (multiple sequence alignment), GBlocks (alignment curation), PhyML (maximum likelihood tree construction with 100 replicates to estimate bootstrap values), and TreeDyn (visualization) (Dereeper et al., 2008).

mRNA *in situ* Hybridization

lhfpl5a and *lhfpl5b* probe templates were amplified from total RNA using the following primers: *lhfpl5a* Fwd: AATATTGGTGCATAGACTCAAGGAGG; Rvs: GACTCCAA AATGACCTTTTAACAAACGC. *lhfpl5b* Fwd: TGAAGAT CAGCTACGATATAACCGG; Rvs: ACTGTGATTGGTGTA TTTCCAGC. The inserts were cloned into the pCR4 vector for use in probe synthesis. mRNA *in situ* probe synthesis and hybridization was performed essentially as previously described (Thisse and Thisse, 2008; Erickson et al., 2010). Stained specimens were mounted on a depression slide in 1.2% low-melting point agarose and imaged on a Leica DMLB microscope fitted with a Zeiss AxioCam MRc 5 camera using Zeiss AxioVision acquisition software (Version 4.5).

Immunofluorescent Staining, FM Dye Labeling, and Fluorescence Microscopy

Anti-Pcdh15a immunostaining and FM dye labeling of inner ear and lateral line hair cells were performed as previously described (Erickson et al., 2017). All fluorescent imaging was done on Zeiss LSM 700 or LSM 800 laser scanning confocal microscopes. Z-stacks were analyzed using ImageJ (Schneider et al., 2012). All related control and experimental images were adjusted equally for brightness and contrast in Adobe Photoshop CC.

CRISPR-Cas9 Knockout of *lhfpl5b*

An sgRNA targeting the *lhfpl5b* sequence 5′-CAACCCAATCACCTCGGAAT-3′ was synthesized essentially as described (Gagnon et al., 2014). For microinjection, 1 μg of sgRNA was mixed with 1 μg of Cas9 protein and warmed to 37°C for 5 min to promote the formation of the Cas9-sgRNA complex. Approximately 2 nl of this solution was injected into wild type embryos at the single-cell stage. Efficacy of cutting was determined in two ways: (1) Single larvae genotyping - Amplification of the target genomic region by PCR and running the products on 2.5% agarose gels to assay for disruption of a homogenous amplicon. (2) Assaying for disruption of the mechanotransduction channel in lateral line hair cells by FM 1-43 dye uptake. Larvae displaying a non-wild type pattern of FM 1-43 dye uptake were raised to adulthood. Progeny from in-crosses of F0 adults were exposed to FM 1-43 dye to identify founders. By outcrossing founder adults, we established a line of fish carrying a 5 base pair deletion in the *lhfpl5b* coding region that causes a S77FfsX48 mutation (*lhfpl5b*^{vo35}). This mutation disrupts the protein in the first extracellular loop and deletes the final three of four transmembrane helices in Lhfpl5b.

Acoustic Startle Response

Quantification of the larval acoustic startle response was performed using the Zebrabox monitoring system (ViewPoint Life Sciences, Montreal, Canada) as previously described (Maeda et al., 2017) with the following modifications. Each trial included six larvae which were subjected to two or three trials of 6 acoustic stimuli. For each individual larva, the trial with best AEBR performance was used for quantification. Positive responses where spontaneous movement occurred in the second prior to the stimulus were excluded from analysis. Trials where spontaneous movement occurred for more than 6 of the 12 stimuli were also excluded from analysis.

Microphonics

We performed the microphonic measurements as previously described (Pacentine and Nicolson, 2019). In brief, we anesthetized 3 dpf larvae in extracellular solution [140 mM NaCl, 2 mM KCl, 2 mM $CaCl_2$, 1 mM $MgCl_2$, and 10 mM 4-(2-hydroxyethyl)-1-piperazineethanesulfonic acid (HEPES); pH 7.4] containing 0.02% 3-amino benzoic acid ethylester (MESAB; Western Chemical). We pinned the larvae with two glass fibers straddling the yolk and a third perpendicular fiber to prevent sliding. For pipettes, we used borosilicate glass with filament,

O.D.: 1.5 mm, O.D.: 0.86 mm, 10 cm length (Sutter, item # BF150-86-10, fire polished). Using a Sutter Puller (model P-97), we created recording pipettes with a long shank with a resistance of 10–20 MΩ, after which we beveled the edges to a resistance of 4–5 MΩ using a Sutter Beveler with impedance meter (model BV-10C). For the glass probe delivering the piezo stimulus, we pulled a long shank pipette and fire polished to a closed bulb. We shielded the apparatus with tin foil to completely ground the piezo actuator. To maintain consistent delivery of stimulus, we always pressed the probe to the front of the head behind the lower eye, level with the otoliths in the ear of interest. We also maintained a consistent entry point dorsal to the anterior crista and lateral to the posterior crista. During delivery of stimulus, the piezo probe made light contact with the head. We drove the piezo with a High Power Amplifier (piezosystem jena, System ENT/ENV, serial # E18605), and recorded responses in current clamp mode with a patch-clamp amplifier (HEKA, EPC 10 usb double, serial # 550089). Voltage responses were amplified 1000x and filtered between 0.1 – 3000 Hz by the Brownlee Precision Instrumentation Amplifier (Model 440). We used a 200 Hz sine wave stimulus at 10 V and recorded at 20 kHz, collecting 200 traces per experiment. Each stimulus was of 40 ms duration, with 20 ms pre- and post-stimulus periods. The piezo signal was low-pass filtered at 500 Hz using the Low-Pass Bessel Filter 8 Pole (Warner Instruments). In Igor Pro, we averaged each set of 200 traces to generate one wave response per larva. To quantify hair cell activity, we calculated the amplitude from base-to-peak of the first peak. Larvae were genotyped as described above.

Hair Cell Counts

lhfpl5b$^{vo35/+}$ fish were crossed with *Tg(myo6b:eGFP-pA)vo68Tg; lhfpl5b*$^{vo35/+}$ fish to produce wild type and *lhfpl5b*^{vo35} siblings expressing green fluorescent protein in hair cells. Wild type and *lhfpl5b* mutant larvae were sorted by FM 4-64 labeling (n = 11 each). In experiment 1, larvae (n = 5 each genotype) were fixed in 4% paraformaldehyde at 5 dpf. In experiment 2, larvae (n = 6 each genotype) were imaged immediately. *lhfpl5a*$^{tm290d/+}$ fish were in-crossed to produce wild type and *lhfpl5a*^{tm290d} siblings. Larvae were sorted based on the auditory and vestibular defects associated with the *lhfpl5a*^{tm290d} homozygous mutants. Larvae were labeled with FM 1-43 (n = 6 each). For all experiments, specimens were mounted in low melting point agarose and the L1, MI1, and O2 neuromasts were imaged on a Zeiss LSM 800 confocal. Cell counts were performed using the Z-stack data.

Statistics

Statistical analyses were done using the R stats package in RStudio (RStudio Team, 2018; R Core Team, 2019). P-values of less than 0.05 were considered to be statistically significant. Plots were made with ggplot2 (Wickham, 2016).

Data Availability

The raw data supporting the conclusions of this article will be made available by the corresponding author, without undue reservation, to any qualified researcher.

RESULTS

Teleost Fish Have Ohnologous *lhfpl5* Genes

Genes that have been duplicated as a result of a whole genome duplication (WGD) event are known as *ohnologs* (Ohno, 1970; Wolfe, 2000). Due to the teleost-specific WGD, it is not uncommon to find ohnologous genes in teleost fish where other vertebrate classes possess a single gene. The *Danio rerio* (zebrafish) genome contains two *lhfpl5* genes: *lhfpl5a* (ENSDARG00000045023) and *lhfpl5b* (ENSDARG00000056458). To determine if *lhfpl5* duplication is general to the teleost lineage, we queried either GenBank or Ensembl databases to collect Lhfpl5 protein sequences for humans, mice, chick, frogs, and representative sequences from 14 phylogenetic orders of ray-finned fish (Actinopterygii), including 13 orders from the Teleostei infraclass and one from the Holostei infraclass (**Supplementary Table 1**). The latter (Spotted gar, *Lepisosteus oculatus*) is commonly used to infer the consequences of the teleost WGD, since the Holostei and Teleostei infraclasses diverged before the teleost WGD (Braasch et al., 2016). Phylogenetic analysis of the Lhfpl5 protein sequences supports the idea that duplicate *lhfpl5* genes originated from the teleost WGD event (**Figure 1A**). In all 13 teleost orders surveyed, there are two *lhfpl5* genes whose protein products cluster with either the *lhfpl5a* or *lhfpl5b* ohnolog groups. Based on available genomic data, there is no evidence that spotted gar fish have duplicated *lhfpl5* genes. Nor is there evidence that the Salmonid-specific WGD (Allendorf and Thorgaard, 1984) lead to further expansion of the *lhfpl5* family. These analyses suggest that the ancestral *lhfpl5* gene was duplicated in the teleost WGD and that the *lhfpl5* ohnologs were retained in all teleost species examined here.

Alignment of the zebrafish Lhfpl5a and Lhfpl5b proteins with those from human, mouse and chicken reveals that both zebrafish ohnologs retain the same protein structure (**Figure 1B**). Zebrafish Lhfpl5a and Lhfpl5b are 76% identical and 86% similar to one another (Needleman-Wunsch alignment). Compared to human LHFPL5, Lhfpl5a and Lhfpl5b are 70/65% identical and 86/81% similar respectively. The ENU-generated mutation in *lhfpl5a* (*tm290d*) (Obholzer et al., 2012) is indicated by the red triangle (K80X). To investigate the function of *lhfpl5b*, we generated a Cas9-induced lesion in the *lhfpl5b* gene in a similar location as the *tm290d* mutation. We recovered a line with a 5 base pair deletion leading to a frameshift mutation (*lhfpl5b*^{vo35}, red square; S77FfsX48).

lhfpl5a and *lhfpl5b* Are Expressed in Distinct Populations of Sensory Hair Cells

To characterize the spatial and temporal patterns of *lhfpl5a/b* gene expression, we performed whole mount mRNA *in situ* hybridization on zebrafish larvae at 1, 2, and 5-days post-fertilization (dpf) (**Figure 2**). After 1 day of development, there are nascent hair cells of the presumptive anterior and posterior maculae in the developing ear, but no lateral line hair cells at this stage. We detect *lhfpl5a* expression in the presumptive anterior

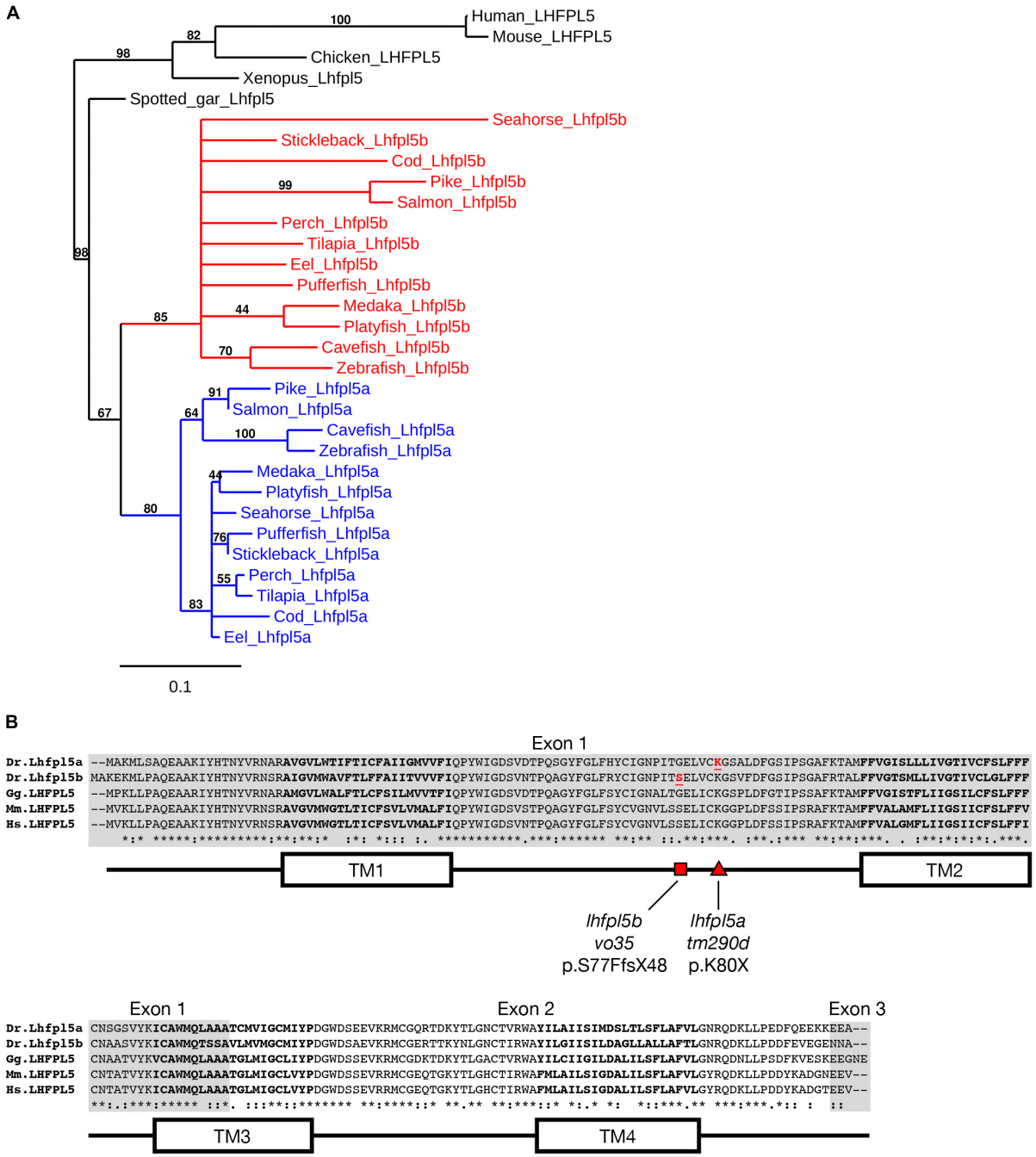

FIGURE 1 | Duplicated *lhfpl5* genes in teleost fish. **(A)** Phylogenic tree of representative teleost and vertebrate Lhfpl5 protein sequences. See **Supplementary Table S1** for species' names and protein accession numbers. **(B)** Sequence alignment of Lhfpl5 proteins from zebrafish (*Danio rerio*, Dr), chicken (*Gallus gallus*, Gg), mouse (*Mus musculus*, Mm), and humans (*Homo sapiens*, Hs). Regions of the proteins coded for by exons 1 and 3 are shaded gray. Locations of the transmembrane (TM) helices 1–4 are shown in the linear protein structure diagram. The *lhfpl5a*^{tm290d} and *lhfpl5b*^{vo35} mutations are indicated by the red triangle and red square, respectively.

and posterior maculae at 1 dpf (**Figure 2A**). No signal for *lhfpl5b* was observed at this time point (**Figure 2B**). At 2 dpf, we observe a clear distinction in the expression patterns of the *lhfpl5a* and *lhfpl5b* genes (**Figures 2C,D**). *lhfpl5a* continues to be expressed in the ear, but expression is not observed in the newly deposited neuromasts. Conversely, we detect *lhfpl5b* expression exclusively in neuromasts at this stage, both on the head (**Figure 2D**) and trunk (data not shown). This divergence in *lhfpl5* ohnolog expression continues at 5 dpf, with *lhfpl5a* found exclusively in the sensory patches of the ear and *lhfpl5b* restricted to lateral line

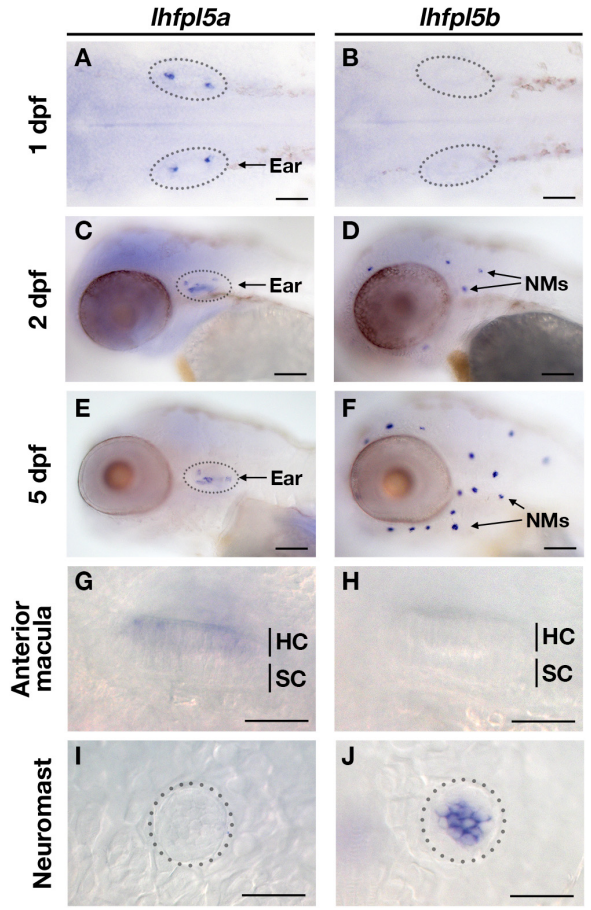

FIGURE 2 | Zebrafish *lhfpl5a* and *lhfpl5b* genes are expressed in distinct populations of sensory hair cells. Whole mount mRNA *in situ* hybridization for *lhfpl5a* **(A,C,E,G,I)** and *lhfpl5b* **(B,D,F,H,J)** at 1, 2, and 5 days post-fertilization (dpf). **(G–J)** Are details from 5 dpf larvae. NMs, neuromasts; HC, hair cell; SC, support cell. Scale bars: **(A,B)** = 50 μm; **(C–F)** = 100 μm; **(G–J)** = 25 μm.

hair cells (**Figures 2E–J**). Taken together, our results suggest that both *lhfpl5a* and *lhfpl5b* have been retained since the teleost WGD because of their non-overlapping mRNA expression patterns.

lhfpl5a Mediates Mechanosensitivity of Otic Hair Cells

lhfpl5a^{tm290d} (*astronaut/asn*) mutants were initially characterized by balance defects, an absence of the acoustic startle reflex, and a lack of brainstem Ca^{2+} signals after acoustic startle. However, neuromast microphonic potentials were normal (Nicolson et al., 1998). In light of our *in situ* hybridization data (**Figure 2**), these results suggest that *lhfpl5a* is required for auditory and vestibular hair cell function only. To test this possibility, we performed several functional assays measuring the activity of hair cells in the otic capsule. First, we tested macular hair cell activity (Lu and DeSmidt, 2013; Yao et al., 2016) by recording extracellular microphonic potentials from the inner ears of *lhfpl5a*^{tm290d} mutants, along with wild type and *lhfpl5b*^{vo35} larvae at 3 dpf. We then measured baseline-to-peak amplitude of the first peak to quantify activity (**Supplementary Figures 1A–D**). Consistent with the initial characterization of the behavioral defects in *lhfpl5a*^{tm290d} mutants, we did not detect robust microphonic potentials from the inner ear of *lhfpl5a*^{tm290d} mutants (**Figure 3A**). We measured an average first peak microphonic of 53.1 μV from *lhfpl5a*^{tm290d} mutants (n = 7), which was significantly less than the 296.2 μV average value of their WT siblings (n = 5; p = 0.01, Welch's t-test). We believe that at least some of the signal detected in *lhfpl5a*^{tm290d} mutants may be a stimulus artifact due the unusual rise time and similar observations we have made in other known transduction-null mutants.

For the *lhfpl5b*^{vo35} mutants (n = 6), we measured an average first peak microphonic potential of 280.9 μV. These values were not significantly different from their WT siblings (n = 4, average 243.8 μV; p = 0.7) but were significantly greater than the *lhfpl5a*^{tm290d} mutants (p = 0.036). Thus, *lhfpl5a*^{tm290d} mutants exhibit defects in inner ear function, while the *lhfpl5b*^{vo35} mutation has no effect on these hair cells. To further confirm the lack of inner ear function in *lhfpl5a*^{tm290d} mutants, we performed an acoustic startle test on larvae at 6 dpf (**Figure 3B**). Results confirm that *lhfpl5a*^{tm290d} mutants are profoundly deaf, displaying little to no response to acoustic stimuli ($p < 0.001$ compared to all other genotypes). Finally, we examined the basal MET channel activity of hair cells of the inner ear by injecting FM 4–64 into the otic capsule and imaging the lateral cristae sensory patch. WT hair cells readily labeled with FM 4–64 whereas *lhfpl5a*^{tm290d} mutant cells showed no sign of dye internalization (**Figures 3C,D**). These three tests confirmed that all sensory patches in the otic capsule are inactive in *lhfpl5a*^{tm290d} mutants.

A *GFP-lhfpl5a* transgenic line of zebrafish – *Tg(myo6b:eGFP-lhfpl5a)vo23Tg* – has been reported previously (Erickson et al., 2017). GFP-Lhfpl5a is present at the tips of stereocilia, similar to the localization observed for mouse LHFPL5 (Xiong et al., 2012; Mahendrasingam et al., 2017). To demonstrate that the GFP-Lhfpl5a protein is functional, we assayed for rescue of the acoustic startle reflex and MET channel activity in homozygous *lhfpl5a*^{tm290d} mutants expressing the transgene. The startle reflex of *lhfpl5a*^{tm290d} mutants expressing GFP-Lhfpl5a were statistically indistinguishable from non-transgenic and transgenic WT siblings (p = 0.48 and 0.26 respectively; **Figure 3B**). Likewise, FM 4–64 dye-labeling in the inner ear was restored to *lhfpl5a*^{tm290d} mutants expressing GFP-Lhfpl5a (**Figures 3E–F'**). From these results we conclude that the hair bundle-localized GFP-Lhfpl5a protein is functional and can rescue the behavioral and MET channel defects in *lhfpl5a*^{tm290d} mutants.

lhfpl5b Mediates Mechanosensitivity of Lateral Line Hair Cells

The divergent expression patterns of the *lhfpl5* ohnologs suggests that *lhfpl5b* alone may be mediating mechanosensitivity of lateral line hair cells. To test this, we compared basal MET channel activity in neuromast hair cells of WT, *lhfpl5a*^{tm290d} and *lhfpl5b*^{vo35} larvae using an FM 1–43 dye uptake assay (**Figures 4A–C**). Strikingly, lateral line hair cells in *lhfpl5b*^{vo35}

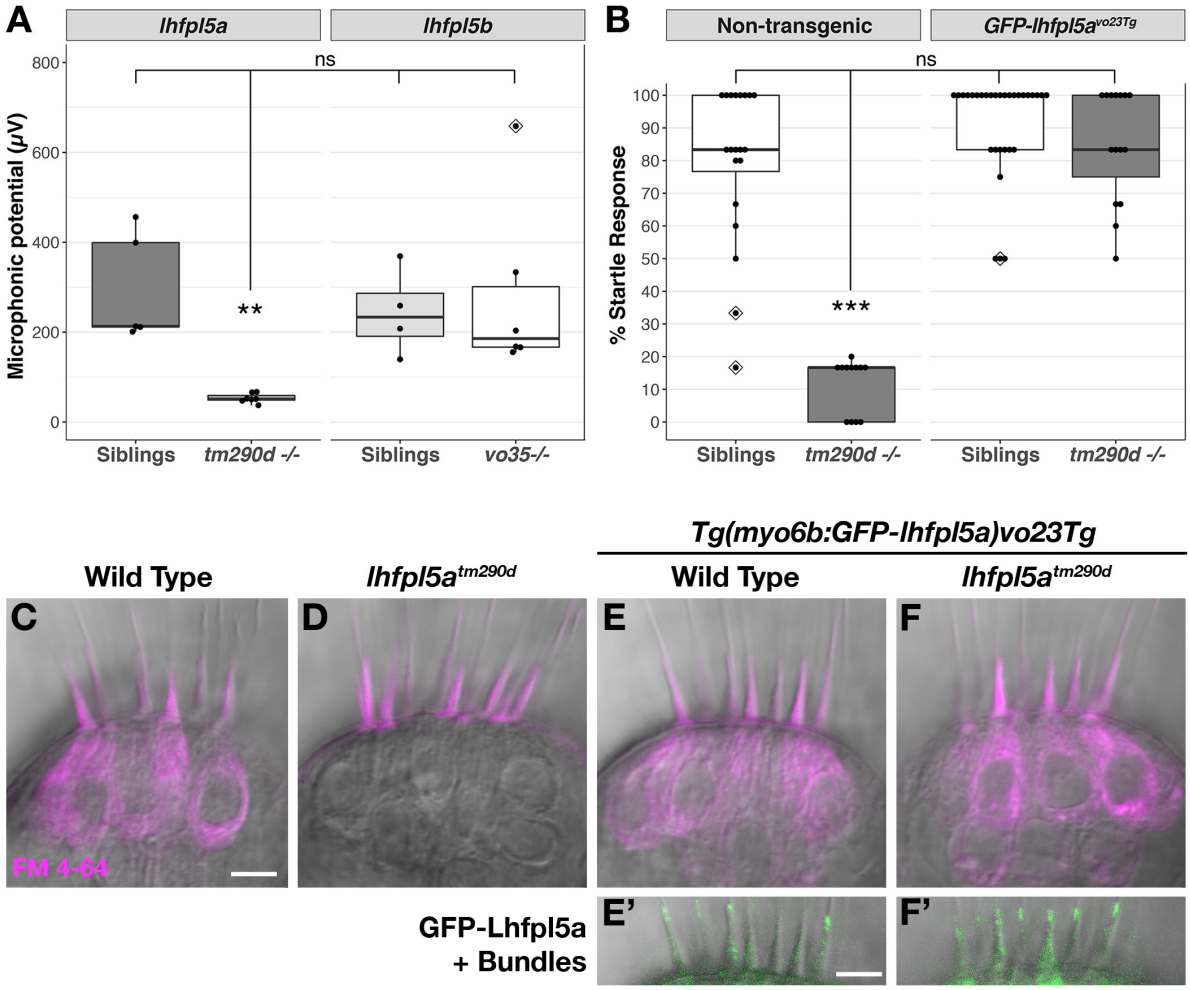

FIGURE 3 | *lhfpl5a* is required for auditory and vestibular hair cell function. **(A)** Boxplot showing the first peak amplitude (μV) of microphonic recordings from the inner ear of 3 dpf wild type, *lhfpl5a*^{tm290d}, and *lhfpl5b*^{vo35} larvae. The boxes cover the inter-quartile range (IQR), and the whiskers represent the minimum and maximum datapoints within 1.5 times the IQR. Values from individual larvae are indicated by the black dots and outliers indicated by a diamond. Asterisks indicate $p < 0.01$ (**) by Welch's *t*-test. ns, not significant. **(B)** Boxplot of the acoustic startle response in 6 dpf wild type and *lhfpl5a*^{tm290d} mutants, with or without the *GFP-lhfpl5a vo23Tg* transgene. Values from individual larvae are indicated by the black dots and outliers indicated by a diamond. Asterisks indicate $p < 0.001$ (***) by Welch's *t*-test. ns, not significant. **(C–F')** FM 4–64 dye labeling assay for MET channel activity of inner ear hair cells from 6 dpf larvae [**C** – Wild type (+/+ *or*±), **D** – *lhfpl5a*^{tm290d} mutants, **E** – Wild type *GFP-lhfpl5a vo23Tg*, **F** – GFP-*lhfpl5a vo23Tg; lhfpl5a*^{tm290}]. **(E',F')** Are images of GFP-Lhfpl5a protein in the bundle of the hair cells shown above in **(E,F)**. *n* = 2, 3, 12, and 4 for the genotypes in **(C–F)**, respectively. Scale bars = 5 μm and apply to all images.

mutants do not label with FM 1–43 while there is no difference in the intensity of FM 1–43 labeling of hair cells between WT and *lhfpl5a*^{tm290d} mutants (**Figures 4A–C** and **Supplementary Figures 2A–C**). We quantified this loss of lateral line function in *lhfpl5b* mutants by measuring the average FM 1–43 fluorescence intensity per hair cell in each imaged neuromast of *lhfpl5b*^{vo35} mutants and wild type siblings at 2 dpf (**Figures 4D,E,H**) and 5 dpf (**Figures 4F–H**). *lhfpl5b*^{vo35} mutants exhibit a statistically significant decrease in FM 1–43 uptake at both 2 and 5 dpf (Welch's *t*-test, $p < 0.001$ both time points). While there is negligible FM dye labeling in the vast majority of *lhfpl5b*^{vo35} mutant neuromasts, we occasionally observe labeling in some hair cells, most reproducibly in the SO3 neuromast. Occasional labeling persists in *lhfpl5a*/*lhfpl5b* double mutants, indicating that *lhfpl5a* is not partially compensating for the loss of *lhfpl5b* (**Supplementary Figures 3A–D**). The loss of MET channel activity in *lhfpl5b*^{vo35} neuromasts is rescued by expression of the *GFP-lhfpl5a vo23Tg* transgene (**Figures 4I,J**; $n = 7/7$ mutant individuals). This result indicates that Lhfpl5a and Lhfpl5b are functionally interchangeable in this context.

We have previously reported a reduced number of neuromast hair cells in other transduction mutants such as *myo7aa (mariner)*, *pcdh15a (orbiter)*, and *tomt (mercury)* (Seiler et al., 2005; Erickson et al., 2017). The ultimate cause for this reduction in hair cell number is not known. If *lhfpl5b*^{vo35} mutants are defective in mechanotransduction, we would expect a similar decrease in the number of neuromast hair cells. To test this idea, we compared hair cell counts between wild type, *lhfpl5a*^{tm290d},

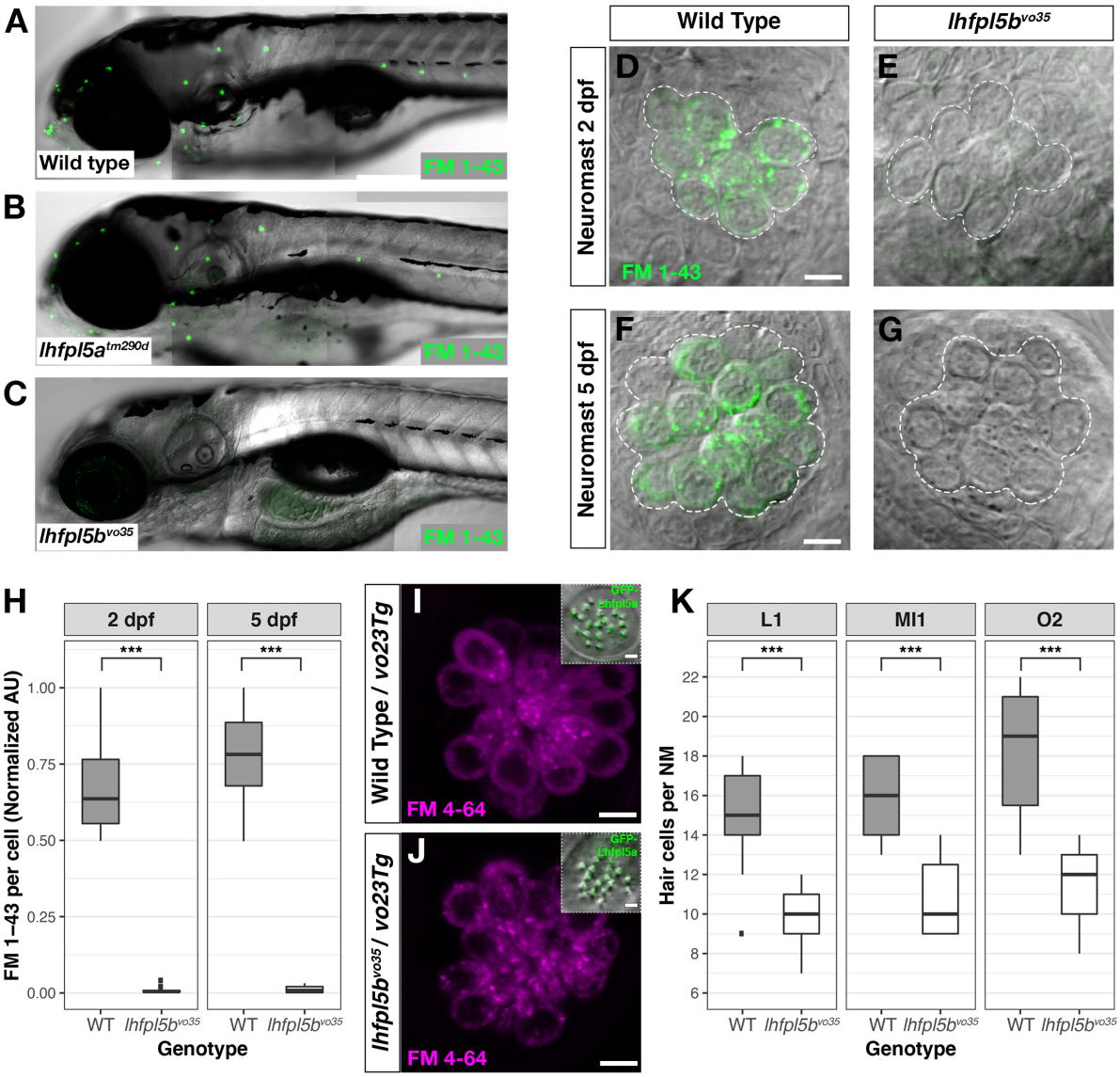

FIGURE 4 | *lhfpl5b* is required for lateral line hair cell function. **(A–C)** Representative images of 5 dpf zebrafish larvae (**A** – Wild type; **B** – *lhfpl5a*^{tm290d}; **C** – *lhfpl5b*^{vo35}) labeled with the MET channel-permeant dye FM 1–43. **(D–G)** Representative images of individual neuromasts from 2 and 5 dpf wild type and *lhfpl5b*^{vo35} larvae labeled with FM 1–43. Dashed lines outline the cluster of hair cells in each neuromast. **(H)** Quantification of normalized FM 1–43 fluorescence intensity per hair cell of 2 and 5 dpf neuromasts (n = 10 WT, 14 *lhfpl5b*^{vo35} NMs at 2 dpf; n = 6 WT, 13 *lhfpl5b*^{vo35} NMs each genotype at 5 dpf). The box plots cover the inter-quartile range (IQR), and the whiskers represent the minimum and maximum datapoints within 1.5 times the IQR. Asterisks indicate $p < 0.001$ (***) by Welch's t-test. **(I,J)** Rescue of FM dye labeling in *lhfpl5b*^{vo35} mutants (n = 7) by the *GFP-lhfpl5a* (*vo23Tg*) transgene. The GFP-Lhfpl5a bundle and FM 4–64 images are from the same NM for each genotype. **(K)** Quantification of hair cell number in L1, MI1, and O2 neuromasts from 5 dpf *lhfpl5b*^{vo35} mutants (n = 11) and wild-type siblings (n = 11). The box plots are the same as in **(H)**. Asterisks indicate $p < 0.001$ (***) by Welch's t-test. Scale bars = 5 μm, applies to **(D–G,I,J)**; 2 μm in **(I,J)** insets.

and *lhfpl5b*^{vo35} larvae at 5 dpf. As expected, wild type and *lhfpl5a*^{tm290d} mutants have statistically equivalent numbers of hair cells in the neuromasts surveyed (**Supplementary Figure 2D**, p = 0.58). In *lhfpl5b*^{vo35} mutant neuromasts, we observe a statistically significant decrease in the number of hair cells (**Figure 4K**, n = 11 individuals per genotype, 3 NM each, $p < 0.001$ each NM type by Welch's t-test; representative neuromasts are shown in **Supplementary Figure 4**). This decrease in the number of neuromast hair cells is consistent with *lhfpl5b* mutants being deficient in mechanotransduction in this cell type.

lhfpl5 Is Not Required for Tmc Localization to the Hair Bundle in Zebrafish Hair Cells

Previous studies have demonstrated that loss of LHFPL5 leads to a ∼90% reduction in the peak amplitude of the transduction

current in mouse cochlear outer hair cells (Xiong et al., 2012). Single channel recordings from *Lhfpl5* mutants revealed that the remaining transduction current in *Lhfpl5* mutants was mediated by TMC2 (Beurg et al., 2015). Using antibodies to detect endogenous protein, TMC1 was found to be absent from the bundle of *Lhfpl5* mouse mutants. However, injectoporated Myc-TMC2 was still able to localize to the hair bundle, supporting the idea that LHFPL5 is required for the targeting of TMC1, but not TMC2. The localization of exogenously expressed TMC1 in *Lhfpl5* mutants was not reported.

To determine if the Tmcs require Lhfpl5a for localization to the hair bundle of zebrafish hair cells, we bred stable transgenic lines expressing GFP-tagged versions of Tmc1 (*vo27Tg*) and Tmc2b (*vo28Tg*) (Erickson et al., 2017) into the *lhfpl5a*^{tm290d} mutant background and imaged Tmc localization in the lateral cristae of the ear. In contrast to what was observed in mouse cochlear hair cells, both Tmc1-GFP and Tmc2b-GFP are still targeted to the hair bundle in *lhfpl5a*^{tm290d} mutants (n = 11/11 and 9/9 individuals respectively; **Figures 5A–D'**). We also observe Tmc2b-GFP localization in the neuromast hair bundles of *lhfpl5b*^{vo35} mutants (n = 7/7 individuals; **Figures 5E–F'**). Additionally, we do not observe any rescue of hair cell function in *lhfpl5b* mutants expressing the Tmc2b-GFP protein (**Supplementary Figures 5A–C**). As such, these results suggest that GFP-tagged Tmc1 and Tmc2b do not require Lhfpl5 for hair bundle localization in zebrafish hair cells.

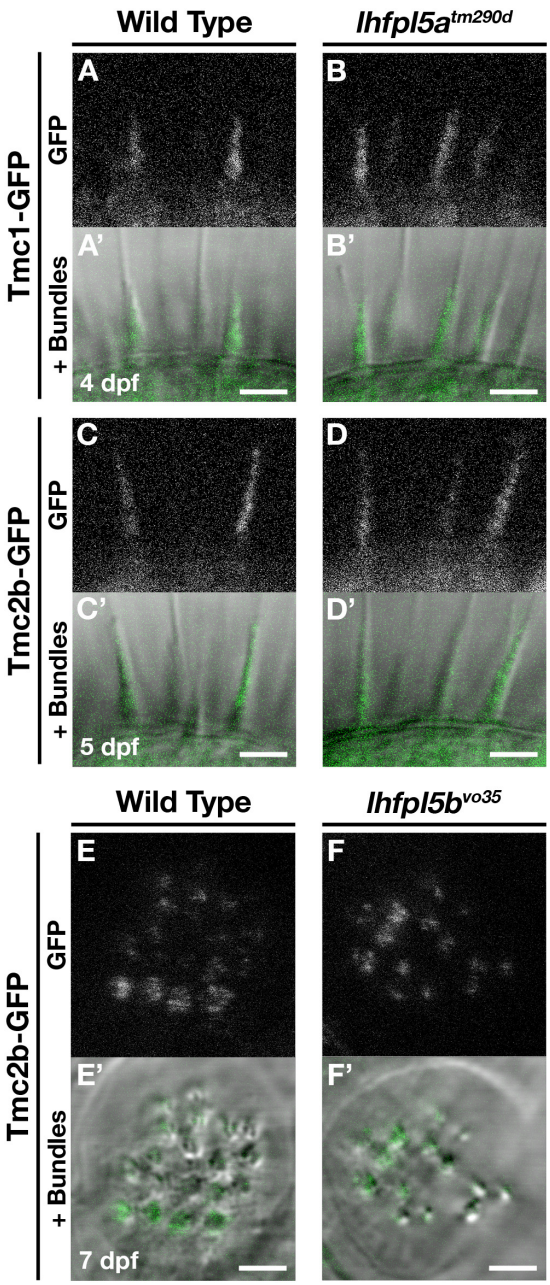

FIGURE 5 | Tmc proteins do not require Lhfpl5a or Lhfpl5b for localization to the stereocilia of zebrafish hair cells. **(A–D')** Representative images of Tmc1-GFP (*vo27Tg*) or Tmc2b-GFP (*vo28Tg*) in the lateral cristae of wild type **(A,A',C,C')** and *lhfpl5a*^{tm290d} **(B,B',D,D')** larvae. The GFP-only channel is shown in **(A–D)** and overlaid with a light image of the bundles in **(A'–D')**. **(E–F')** Representative images of Tmc2b-GFP (*vo28Tg*) in the neuromasts of wild type **(E,E')** and *lhfpl5b*^{vo35} **(F,F')** larvae. The GFP-only channel is shown in **(E,F)** and overlaid with a light image of the bundles in **(E',F')**. Scale bars = 3 μm in all panels.

GFP-Lhfpl5a Localization in Stereocilia Requires Pcdh15a, Cdh23, and Myo7aa

Previous work has shown that PCDH15 and LHFPL5 are mutually dependent on one another to correctly localize to the site of mechanotransduction in mouse cochlear hair cells (Xiong et al., 2012; Mahendrasingam et al., 2017). Likewise in zebrafish, Lhfpl5a is required for proper Pcdh15a localization in the hair bundle, as determined Pcdh15a immunostaining and the expression of a Pcdh15a-GFP transgene in *lhfpl5a*^{tm290d} mutants (Maeda et al., 2017). Using the previously characterized antibody against Pcdh15a, we observe the highest level of Pcdh15a staining at the apical part of the hair bundle, with less intense punctate staining throughout the stereocilia in 3 dpf wild type larvae (**Figure 6A**). *lhfpl5a*^{tm290d} mutants exhibit splayed hair bundles, with low levels of Pcdh15a staining restricted to the tip of each stereocilium (n = 5/5 individuals; **Figure 6B**), confirming our previous report.

To determine if Lhfpl5a also depends on Pcdh15a for its localization, we imaged GFP-Lhfpl5 in the lateral cristae of *pcdh15a*^{psi7} homozygous mutants. In wild type larvae, GFP-Lhfpl5a is distributed throughout the hair bundle at the tips of stereocilia (yellow arrow heads), with a higher intensity of GFP evident in the tallest rows, possibly at the sites of kinociliary links (**Figures 6C,C'**, arrow). In *pcdh15a*^{psi7} mutants, GFP-Lhfpl5a is absent from the hair bundle except for the tallest rows of stereocilia adjacent to the kinocilium (n = 4 individuals; **Figures 6D,D'**, arrow). We observed similar results using the *pcdh15a*^{th263b} allele (n = 6/6 individuals; **Supplementary Figures 6A,B'**). Consistent with our earlier studies (Seiler et al., 2005; Maeda et al., 2017), we observe splayed hair bundles in both *pcdh15a* alleles suggesting a loss of connections and tip links between the stereocilia. These results

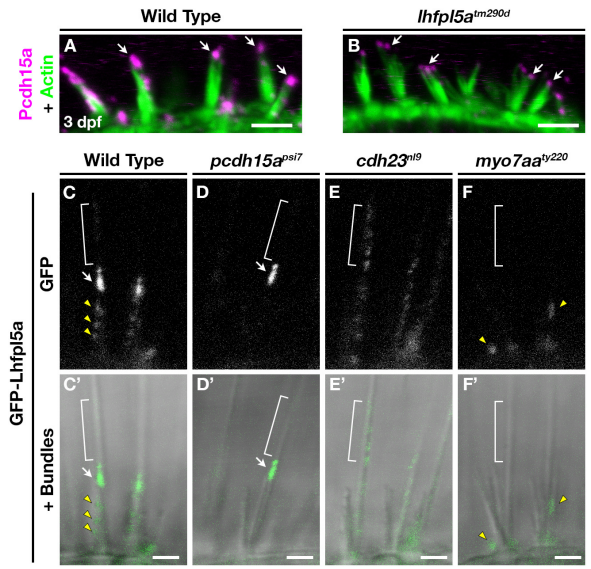

FIGURE 6 | Lhfpl5a requires MET complex proteins Pcdh15a, Cdh23, and Myo7a for normal localization in the stereocilia of zebrafish hair cells. **(A,B)** Immunostain of Pcdh15a (magenta) in the lateral cristae of wild type and *lhfpl5a*^{tm290d} mutants at 3 dpf. Phalloidin-stained actin of the hair bundle is shown in green. Arrows indicate areas of Pcdh15a accumulation. **(C–F')** Representative images of GFP-Lhfpl5a (*vo23Tg*) in the lateral cristae hair bundles of wild type **(C,C')** and *pcdh15a*^{psi7} **(D,D')**, *cdh23*^{nl9} **(E,E')**, and *myo7aa*^{ty220} **(F,F')** mutants. White arrows indicate GFP signal in the presumptive kinocilial linkages, yellow arrow heads indicate GFP signal in the stereocilia or the base of the hair bundle, and brackets indicate GFP signal in the kinocilium. Scale bars = 3 μm in **(A,B)**; 2 μm in **(C–F')**.

indicate that GFP-Lhfpl5a requires Pcdh15a for stable targeting to the shorter stereocilia, but Pcdh15a is not required for retaining GFP-Lhfpl5a in the tallest rows of stereocilia adjacent to the kinocilium.

The observation that some GFP-Lhfpl5a signal remains in the tallest stereocilia of *pcdh15a* mutants suggests that additional proteins are involved in targeting Lhfpl5a to these sites in zebrafish vestibular hair cells. Previous research has shown that mouse CDH23 still localizes to tips of stereocilia in PCDH15-deficient mice (Boëda et al., 2002; Senften et al., 2006) and that CDH23 is a component of kinociliary links (Siemens et al., 2004; Goodyear et al., 2010). Based on these reports, we tested whether Cdh23 was required for GFP-Lhfpl5a localization. In *cdh23*^{nl9} mutants, GFP-Lhfpl5 is sparsely distributed throughout the length of the kinocilium (n = 4/4 individuals, **Figures 6E,E'**). We also observe a redistribution of GFP-Lhfpl5a into the kinocilium using the *cdh23*^{tj264} allele (n = 4/4 individuals; **Supplementary Figures 6C,C'**). In both *cdh23* alleles, we see occasional GFP signal in the stereocilia as well, though this localization is not as robust. Interestingly, these results contrast with those from mouse cochlear hair cells which showed that Lhfpl5 does not require Cdh23 for bundle localization (Zhao et al., 2014). The same study also could not detect any biochemical interaction between LHFPL5 and proteins of the upper tip link density including CDH23, USH1C/Harmonin, or USH1G/Sans. Together, our data indicate an unexpected role for Cdh23 in the localization of GFP-Lhfpl5a to the region of kinocilial links in zebrafish vestibular hair cells.

Myosin 7A (MYO7A) is an actin-based motor protein required for the localization of many proteins of the hair bundle, including PCDH15 and USH1C/Harmonin, along with several proteins of the Usher type 2 complex (Boëda et al., 2002; Senften et al., 2006; Lefevre et al., 2008; Morgan et al., 2016; Maeda et al., 2017; Zou et al., 2017). Results in both mice and zebrafish suggest that MYO7A is not required for CDH23 bundle localization (Senften et al., 2006; Blanco-Sanchez et al., 2014). However, its role in Lhfpl5 localization has not been examined. In *myo7aa*^{ty220} (*mariner*) mutant hair cells, GFP-Lhfpl5a localization in hair bundle is severely disrupted (n = 5/5 individuals; **Figures 6F,F'**). We observe GFP signal near the base of hair bundles and occasionally in stereocilia (yellow arrowheads), but do not see robust Lhfpl5a localization in the presumptive kinocilial links nor to the kinocilium itself. Taken together, our results using the GFP-Lhfpl5a transgene suggest that Pcdh15a, Cdh23, and Myo7aa all play distinct roles in Lhfpl5 localization in the bundle of zebrafish vestibular hair cells.

DISCUSSION

In this study, we provide support for the following points: (1) The ancestral *lhfpl5* gene was likely duplicated as a result of the teleost WGD, leading to the *lhfpl5a* and *lhfpl5b* ohnologs described in this paper. (2) In zebrafish, there has been subfunctionalization of these genes as a result of their divergent expression patterns. As determined by mRNA *in situ* hybridization, *lhfpl5a* is expressed only in auditory and vestibular hair cells of the ear while *lhfpl5b* is expressed solely in hair cells of the lateral line organ. Consistent with their expression patterns, we show that each ohnolog mediates mechanotransduction in the corresponding populations of sensory hair cells in zebrafish. (3) Targeting of GFP-tagged Tmcs to the hair bundle is independent of Lhfpl5a function. (4) Proper targeting of GFP-tagged Lhfpl5a to the hair bundle requires the tip link protein Pcdh15a, but as in mice, Lhfpl5a can localize to regions of the hair bundle independently of Pcdh15 function. Additionally, we demonstrate novel requirements for Cdh23 and the Myo7aa motor protein in Lhfpl5 localization.

Duplicated Zebrafish Genes in Hair Cell Function

With regards to genes involved in hair cell function, the zebrafish duplicates of *calcium channel, voltage-dependent, L type, alpha 1D* (*cacna1d*/*cav1.3*), *C-terminal binding protein 2* (*ctbp2*/*ribeye*), *myosin 6* (*myo6*), *otoferlin* (*otof*), *pcdh15*, and *tmc2* have been analyzed genetically. In the cases of *cacna1db*, *pcdh15b* and *myo6a*, these ohnologs are no longer functional in hair cells (Seiler et al., 2004, 2005; Sidi et al., 2004). For the *ctbp2*, *otoferlin*, and *tmc2* duplicates, both genes are required in at least partially overlapping populations of hair cells (Sheets et al., 2011; Maeda et al., 2014; Lv et al., 2016; Chou et al., 2017). In contrast, our results for the *lhfpl5* ohnologs suggest that each gene is

expressed and functionally required in distinct, non-overlapping hair cell lineages. To our knowledge, this is the first description of duplicated genes whose expression patterns have cleanly partitioned between inner ear and lateral line hair cells.

Subfunctionalization of Zebrafish *lhfpl5* Ohnologs

We constructed a phylogenetic tree using publicly available Lhfpl5 protein sequence data (**Figure 1**) Our results suggest that the ancestral *lhfpl5* gene was duplicated during the teleost WGD event and that both genes have been retained throughout the teleost lineage (**Figure 1**). Our conclusion that *lhfpl5a* and *lhfpl5b* are ohnologs is substantiated by a recent study of ohnologs in teleosts (Singh and Isambert, 2019). In all four teleost species surveyed, Singh and Isambert show that *lhfpl5a* and *lhfpl5b* are true ohnologs that arose from the teleost-specific WGD under the strictest criteria used in their study.

Some kind of selection pressure is required for the retention of both gene ohnologs (Glasauer and Neuhauss, 2014). Our *in situ* hybridization results show that *lhfpl5a* and *lhfpl5b* are expressed in distinct populations of hair cells and support the idea that the zebrafish *lhfpl5* ohnologs were retained because of their divergent expression patterns (**Figure 2**). Analysis of hair cell function in the different *lhfpl5* mutants agrees with the gene expression results, showing that *lhfpl5a* is required for transduction in the ear while *lhfpl5b* plays the same role in the lateral line organs. However, rescue of the MET channel defects in *lhfpl5b*^{vo35} mutants by GFP-tagged Lhfpl5a suggests that the functions of these ohnologs are at least partially interchangeable. This result is not surprising given the high degree of similarity between the Lhfpl5a and 5b proteins. As such, the subfunctionalization of the *lhfpl5* ohnologs appears to be caused by the divergence in their expression patterns rather than functional differences in their protein products. It is possible that a similar mechanism is responsible for the retention of both genes in other teleost species as well, though the expression patterns of the *lhfpl5* ohnologs have not been examined in other fish.

The non-overlapping expression of the *lhfpl5* ohnologs provides us with a unique genetic tool to study lateral line function. Most mechanotransduction mutants in zebrafish disrupt both inner ear and lateral line hair cell function (Nicolson, 2017). As such, we are unable to assess the role of the lateral line independently of auditory and vestibular defects, which are lethal for larval fish. The *lhfpl5b* mutants are adult viable (data not shown) and represent a possible genetic model for understanding the lateral line in both larval and adult fish. Future studies on adults will determine whether the lateral line remains non-functional and whether *lhfpl5b* contributes to inner ear function in the mature auditory and vestibular systems.

The Molecular Requirements for Bundle Localization of MET Complex Proteins Differs Between Mouse and Zebrafish Hair Cells

Our understanding of mechanotransduction at the molecular level is heavily informed by work done using mouse cochlear hair cells. However, analysis of zebrafish inner ear and lateral line hair cells can lead to a more complete picture of how vertebrate sensory hair cells form the MET complex. At their core, the genetic and molecular bases for mechanotransduction are well conserved between mouse and zebrafish hair cells. For example, the tip link proteins Cdh23 and Pcdh15a, MET channel subunits Tmc1/2, Tmie, and Lhfpl5, along with additional factors such as Tomt, Cib2, and Myo7aa are all necessary for MET channel function in both mice and fish (Nicolson et al., 1998; Siemens et al., 2004; Söllner et al., 2004; Senften et al., 2006; Gleason et al., 2009; Kawashima et al., 2011; Xiong et al., 2012; Zhao et al., 2014; Cunningham et al., 2017; Erickson et al., 2017; Giese et al., 2017; Pacentine and Nicolson, 2019). However, while each of these factors are required for mechanotransduction in vertebrate hair cells, the details of how they contribute to MET channel function may differ depending on the particular type of hair cell or the vertebrate species. For example, Tmie is required for Tmc localization to the hair bundle in zebrafish (Pacentine and Nicolson, 2019), but this does not appear to be the case in mouse cochlear hair cells (Zhao et al., 2014). The evolutionary pressures that lead to these differences between mouse and zebrafish hair cells are not understood.

Based on multiple lines of evidence gathered from mice, TMC1 and TMC2 have different requirements for LHFPL5 regarding localization to the hair bundle (Beurg et al., 2015). Endogenous TMC1 is absent from the bundle in LHFPL5-deficient cochlear hair cells with the remaining MET current mediated through TMC2. Exogenously expressed TMC2 is still targeted correctly in *Lhfpl5* mutants, but it was not reported whether the same is true for exogenous TMC1, nor whether similar requirements hold for vestibular hair cells. As such, the role of LHFPL5 in mechanotransduction is not clear: is LHFPL5 required primarily for targeting TMC1 to the hair bundle, or does LHFPL5 mediate MET channel function in other ways?

For our study, we used stable transgenic lines expressing GFP-tagged Tmc1 and Tmc2b to show that the Tmcs do not require Lhfpl5a for targeting to the stereocilia of zebrafish vestibular hair cells. Nor is Lhfpl5b required for Tmc2b-GFP localization in the hair bundle of neuromast hair cells. The occasional FM labeled-hair cell in *lhfpl5b* and *lhfpl5a/5b* mutant neuromasts is consistent with the continued ability of the Tmcs to localize to the hair bundle. This observation is reminiscent of the sporadic, low level of FM dye labeling in the cochlear hair cells of *Lhfpl5* mutant mice (György et al., 2017). Partial compensation by yet another member of the *lhfpl* family remains as a possible explanation for the remaining basal channel function. Lastly, we find that exogenous Tmc expression does not rescue MET channel activity in either *lhfpl5* mutant zebrafish. Taken together, our results support a Tmc-independent role for Lhfpl5 proteins in mechanotransduction.

What then is the role of LHFPL5 in vertebrate mechanotransduction? LHFPL5 and PCDH15 are known to form a protein complex and regulate each other's localization to the site of mechanotransduction in mouse cochlear hair cells (Xiong et al., 2012; Mahendrasingam et al., 2017; Ge et al., 2018).

However, their localization to the hair bundle is not completely dependent on one another. For example, tips links are not completely lost in *Lhfpl5*$^{-/-}$ cochlear hair cells and exogenous overexpression of PCDH15 partially rescues the transduction defects in *Lhfpl5* mutant mice (Xiong et al., 2012). Similarly, a detailed immunogold study in wild type and *Pcdh15*$^{-/-}$ cochlear hair cells showed that there are PCDH15-dependent and PCDH15-independent sites of LHFPL5 localization (Mahendrasingam et al., 2017). PCDH15 is required for stable LHFPL5 localization at the tips of ranked stereocilia in association with the MET channel complex. However, LHFPL5 is still targeted to shaft and ankle links, unranked stereocilia, and the kinocilium in P0-P3 inner and outer hair cells from both wild type and *Pcdh15*$^{-/-}$ mutant mice (Mahendrasingam et al., 2017). Whether the kinocilial localization would remain in mature cochlear hair cells is not known because the kinocilia degenerate by P8 in mice and detailed LHFPL5 localization in vestibular hair cells (which retain their kinocilium) has not been reported.

Zebrafish hair cells retain a kinocilium throughout their life, thus providing a different context in which to examine Lhfpl5 localization. In wild type hair cells, GFP-Lhfpl5a is present at the tips of the shorter ranked stereocilia, but the most robust signal is detected in the tallest stereocilia adjacent to the kinocilium. In *pcdh15a* mutants, only this "kinocilial link"-like signal remains in the hair bundle. This result is similar to the LHFPL5 localization reported at the tips of the tallest stereocilia of P3 cochlear hair cells from wild type mice, a region where LHFPL5 would presumably not be associated with either PCDH15 or the TMCs (Mahendrasingam et al., 2017). Since the kinocilium does not degenerate in zebrafish hair cells, our results suggest that Lhfpl5a is normally targeted to these kinocilial links in wild type cells and that its retention at this site does not require Pcdh15a. Thus, there are PCDH15-dependent and PCDH15-independent mechanisms of LHFPL5 localization in both mouse and zebrafish hair cells. These results suggest that LHFPL5 performs as-of-yet uncharacterized PCDH15-independent functions as well.

Cdh23 is thought to form part of the linkages between the kinocilium and adjacent stereocilia, and therefore may play a role in retaining Lhfpl5a at these sites. Consistent with this hypothesis, *cdh23* mutants do not exhibit GFP-Lhfpl5a accumulation in stereocilia. Instead, GFP-Lhfpl5a is diffusely distributed throughout the kinocilium. These data suggest that normal Lhfpl5a localization requires both Pcdh15a and Cdh23 function, albeit in distinct ways. This result differs from previous reports which found that Lhfpl5 still localized to the tips of stereocilia in CDH23-deficient cochlear hair cells of mice. The same study also could not detect a biochemical interaction between Lhfpl5 and CDH23 via co-IP in heterologous cells (Xiong et al., 2012). Given these contrasting results for mouse and zebrafish hair cells, it seems that the requirement for Cdh23 in the localization of LHFPL5 is not a universal one.

Given the available biochemical evidence, it is possible that the association between Lhfpl5a and Cdh23 is indirect through an as-of-yet unidentified protein or protein complex. Based on the defects in GFP-Lhfpl5a localization in *myo7aa* mutants, Myo7aa is a candidate member of this uncharacterized protein complex. Taken together, these results highlight the fact that, although all sensory hair cells share many core genetic and biochemical features, there are important details that differ between the various types of hair cells and between vertebrate species. Analyzing these differences will allow for a more comprehensive understanding of vertebrate hair cell function and the underlying principles of mechanotransduction.

DATA AVAILABILITY STATEMENT

The datasets generated for this study are available on request to the corresponding author.

ETHICS STATEMENT

The animal study was reviewed and approved by the Institutional Animal Care and Use Committee, Oregon Health & Science University Institutional Animal Care and Use Committee, East Carolina University.

AUTHOR CONTRIBUTIONS

TE and TN conceived and designed the study. TE, IP, AV, and RC collected and analyzed the data. TE wrote the manuscript with Materials and Methods sections contributed by IP and AV and editorial input from TN and IP.

FUNDING

This study was supported by funding from the NIDCD (R01 DC013572 and DC013531 to TN) and from East Carolina University's Division of Research, Economic Development and Engagement (REDE), Thomas Harriot College of Arts and Science (THCAS), and Department of Biology (to TE).

ACKNOWLEDGMENTS

We thank Eliot Smith for assistance with CRISPR-Cas9 knockout of *lhfpl5b*. We also thank Leah Snyder, Matthew Esqueda, and members of the Erickson lab for their assistance with animal husbandry.

SUPPLEMENTARY MATERIAL

The Supplementary Material for this article can be found online at: https://www.frontiersin.org/articles/10.3389/fnmol.2019.00320/full#supplementary-material

REFERENCES

Allendorf, F. W., and Thorgaard, G. H. (1984). "Tetraploidy and the evolution of salmonid fishes," in *Evolutionary Genetics of Fishes*, ed. B. J. Turner, (Boston, MA: Springer), 1–53. doi: 10.1007/978-1-4684-4652-4_1

Beurg, M., Xiong, W., Zhao, B., Müller, U., and Fettiplace, R. (2015). Subunit determination of the conductance of hair-cell mechanotransducer channels. *Proc. Natl. Acad. Sci. U.S.A.* 112, 1589–1594. doi: 10.1073/pnas.1420906112

Blanco-Sanchez, B., Clement, A., Fierro, J., Washbourne, P., and Westerfield, M. (2014). Complexes of Usher proteins preassemble at the endoplasmic reticulum and are required for trafficking and ER homeostasis. *Dis. Model. Mech.* 7, 547–559. doi: 10.1242/dmm.014068

Boëda, B., El-Amraoui, A., Bahloul, A., Goodyear, R., Daviet, L., Blanchard, S., et al. (2002). Myosin VIIa, harmonin and cadherin 23, three Usher I gene products that cooperate to shape the sensory hair cell bundle. *EMBO J.* 21, 6689–6699. doi: 10.1093/emboj/cdf689

Braasch, I., Gehrke, A. R., Smith, J. J., Kawasaki, K., Manousaki, T., Pasquier, J., et al. (2016). The spotted gar genome illuminates vertebrate evolution and facilitates human-teleost comparisons. *Nat. Genet.* 48, 427–437. doi: 10.1038/ng.3526

Chou, S.-W., Chen, Z., Zhu, S., Davis, R. W., Hu, J., Liu, L., et al. (2017). A molecular basis for water motion detection by the mechanosensory lateral line of Zebrafish. *Nat. Commun.* 8:2234. doi: 10.1038/s41467-017-01604-1602

Cunningham, C. L., and Müller, U. (2019). Molecular structure of the hair cell mechanoelectrical transduction complex. *Cold Spring Harb. Perspect. Med.* 9:a033167. doi: 10.1101/cshperspect.a033167

Cunningham, C. L., Wu, Z., Jafari, A., Zhao, B., Schrode, K., Harkins-Perry, S., et al. (2017). The murine catecholamine methyltransferase mTOMT is essential for mechanotransduction by cochlear hair cells. *Elife* 6:e33307. doi: 10.7554/eLife.24318

Dereeper, A., Guignon, V., Blanc, G., Audic, S., Buffet, S., Chevenet, F., et al. (2008). Phylogeny.fr: robust phylogenetic analysis for the non-specialist. *Nucleic Acids Res.* 36, W465–W469. doi: 10.1093/nar/gkn180

Erickson, T., French, C. R., and Waskiewicz, A. J. (2010). Meis1 specifies positional information in the retina and tectum to organize the Zebrafish visual system. *Neural Dev.* 5:22. doi: 10.1186/1749-8104-5-22

Erickson, T., Morgan, C. P., Olt, J., Hardy, K., Busch-Nentwich, E., Maeda, R., et al. (2017). Integration of Tmc1/2 into the mechanotransduction complex in Zebrafish hair cells is regulated by Transmembrane O-methyltransferase (Tomt). *Elife* 6:e28474. doi: 10.7554/eLife.28474

Ernest, S., Rauch, G.-J., Haffter, P., Geisler, R., Petit, C., and Nicolson, T. (2000). Mariner is defective in myosin VIIA: a Zebrafish model for human hereditary deafness. *Hum. Mol. Genet.* 9, 2189–2196. doi: 10.1093/hmg/9.14.2189

Gagnon, J. A., Valen, E., Thyme, S. B., Huang, P., Ahkmetova, L., Pauli, A., et al. (2014). Efficient mutagenesis by Cas9 protein-mediated oligonucleotide insertion and large-scale assessment of single-guide RNAs. *PLoS One* 9:e98186. doi: 10.1371/journal.pone.0098186

Ge, J., Elferich, J., Goehring, A., Zhao, H., Schuck, P., and Gouaux, E. (2018). Structure of mouse protocadherin 15 of the stereocilia tip link in complex with LHFPL5. *Elife* 7:e38770. doi: 10.7554/eLife.38770

Giese, A. P. J., Tang, Y.-Q., Sinha, G. P., Bowl, M. R., Goldring, A. C., Parker, A., et al. (2017). CIB2 interacts with TMC1 and TMC2 and is essential for mechanotransduction in auditory hair cells. *Nat. Commun.* 8:43. doi: 10.1038/s41467-017-00061-61

Glasauer, S. M. K., and Neuhauss, S. C. F. (2014). Whole-genome duplication in teleost fishes and its evolutionary consequences. *Mol. Genet. Genomics* 289, 1045–1060. doi: 10.1007/s00438-014-0889-882

Gleason, M. R., Nagiel, A., Jamet, S., Vologodskaia, M., López-Schier, H., and Hudspeth, A. J. (2009). The transmembrane inner ear (Tmie) protein is essential for normal hearing and balance in the Zebrafish. *Proc. Natl. Acad. Sci. U.S.A.* 106, 21347–21352. doi: 10.1073/pnas.0911632106

Goodyear, R. J., Forge, A., Legan, P. K., and Richardson, G. P. (2010). Asymmetric distribution of cadherin 23 and protocadherin 15 in the kinocilial links of avian sensory hair cells. *J. Comp. Neurol.* 518, 4288–4297. doi: 10.1002/cne.22456

György, B., Sage, C., Indzhykulian, A. A., Scheffer, D. I., Brisson, A. R., Tan, S., et al. (2017). Rescue of hearing by gene delivery to inner-ear hair cells using exosome-associated AAV. *Mol. Ther.* 25, 379–391. doi: 10.1016/j.ymthe.2016.12.010

Kawashima, Y., Géléoc, G. S. G., Kurima, K., Labay, V., Lelli, A., Asai, Y., et al. (2011). Mechanotransduction in mouse inner ear hair cells requires transmembrane channel-like genes. *J. Clin. Invest.* 121, 4796–4809. doi: 10.1172/JCI60405

Kazmierczak, P., Sakaguchi, H., Tokita, J., Wilson-Kubalek, E. M., Milligan, R. A., Müller, U., et al. (2007). Cadherin 23 and protocadherin 15 interact to form tip-link filaments in sensory hair cells. *Nature* 449, 87–91. doi: 10.1038/nature06091

Lefevre, G., Michel, V., Weil, D., Lepelletier, L., Bizard, E., Wolfrum, U., et al. (2008). A core cochlear phenotype in USH1 mouse mutants implicates fibrous links of the hair bundle in its cohesion, orientation and differential growth. *Development* 135, 1427–1437. doi: 10.1242/dev.012922

Li, X., Yu, X., Chen, X., Liu, Z., Wang, G., Li, C., et al. (2019). Localization of TMC1 and LHFPL5 in auditory hair cells in neonatal and adult mice. *FASEB J.* 33, 6838–6851. doi: 10.1096/fj.201802155RR

Longo-Guess, C. M., Gagnon, L. H., Cook, S. A., Wu, J., Zheng, Q. Y., and Johnson, K. R. (2005). A missense mutation in the previously undescribed gene Tmhs underlies deafness in hurry-scurry (hscy) mice. *Proc. Natl. Acad. Sci. U.S.A.* 102, 7894–7899. doi: 10.1073/pnas.0500760102

Lu, Z., and DeSmidt, A. A. (2013). Early development of hearing in Zebrafish. *JARO J. Assoc. Res. Otolaryngol.* 14:509. doi: 10.1007/S10162-013-0386-Z

Lv, C., Stewart, W. J., Akanyeti, O., Frederick, C., Zhu, J., Santos-Sacchi, J., et al. (2016). Synaptic ribbons require ribeye for electron density. proper synaptic localization, and recruitment of calcium channels. *Cell Rep.* 15, 2784–2795. doi: 10.1016/j.celrep.2016.05.045

Maeda, R., Kindt, K. S., Mo, W., Morgan, C. P., Erickson, T., Zhao, H., et al. (2014). Tip-link protein protocadherin 15 interacts with transmembrane channel-like proteins TMC1 and TMC2. *Proc. Natl. Acad. Sci. U.S.A.* 111, 12907–12912. doi: 10.1073/pnas.1402152111

Maeda, R., Pacentine, I. V., Erickson, T., and Nicolson, T. (2017). Functional analysis of the transmembrane and cytoplasmic domains of pcdh15a in Zebrafish hair cells. *J. Neurosci.* 37, 3231–3245. doi: 10.1523/JNEUROSCI.2216-16.2017

Mahendrasingam, S., Fettiplace, R., Alagramam, K. N., Cross, E., and Furness, D. N. (2017). Spatiotemporal changes in the distribution of LHFPL5 in mice cochlear hair bundles during development and in the absence of PCDH15. *PLoS One* 12:e0185285. doi: 10.1371/journal.pone.0185285

Morgan, C. P., Krey, J. F., Grati, M., Zhao, B., Fallen, S., Kannan-Sundhari, A., et al. (2016). PDZD7-MYO7A complex identified in enriched stereocilia membranes. *Elife* 5:e18312. doi: 10.7554/eLife.18312

Nicolson, T. (2017). The genetics of hair-cell function in Zebrafish. *J. Neurogenet.* 31, 102–112. doi: 10.1080/01677063.2017.1342246

Nicolson, T., Rüsch, A., Friedrich, R. W., Granato, M., Ruppersberg, J. P., and Nüsslein-Volhard, C. (1998). Genetic analysis of vertebrate sensory hair cell mechanosensation: the Zebrafish circler mutants. *Neuron* 20, 271–283. doi: 10.1016/S0896-6273(00)80455-80459

Obholzer, N., Swinburne, I. A., Schwab, E., Nechiporuk, A. V., Nicolson, T., and Megason, S. G. (2012). Rapid positional cloning of Zebrafish mutations by linkage and homozygosity mapping using whole-genome sequencing. *Development* 139, 4280–4290. doi: 10.1242/dev.083931

Ohno, S. (1970). *Evolution by Gene Duplication. Berlin, Heidelberg.* Berlin: Springer.

Pacentine, I. V., and Nicolson, T. (2019). Subunits of the mechano-electrical transduction channel, Tmc1/2b, require Tmie to localize in Zebrafish sensory hair cells. *PLoS Genet.* 15:e1007635. doi: 10.1371/journal.pgen.1007635

Pan, B., Akyuz, N., Liu, X.-P., Asai, Y., Nist-Lund, C., Kurima, K., et al. (2018). TMC1 forms the pore of mechanosensory transduction channels in vertebrate inner ear hair cells. *Neuron* 99, 736.e6–753.e6. doi: 10.1016/j.neuron.2018.07.033

Pan, B., Géléoc, G. S., Asai, Y., Horwitz, G. C., Kurima, K., Ishikawa, K., et al. (2013). TMC1 and TMC2 Are components of the mechanotransduction channel in hair cells of the mammalian inner ear. *Neuron* 79, 504–515. doi: 10.1016/j.neuron.2013.06.019

R Core Team (2019). *). R: A Language and Environment for Statistical Computing*. Vienna: R Core Team.

RStudio Team (2018). *RStudio: Integrated Development Environment for R*. Vienna: RStudio Team.

Schneider, C. A., Rasband, W. S., and Eliceiri, K. W. (2012). NIH Image to ImageJ: 25 years of image analysis. *Nat. Methods* 9, 671–675. doi: 10.1038/nmeth.2089

Seiler, C., Ben-David, O., Sidi, S., Hendrich, O., Rusch, A., Burnside, B., et al. (2004). Myosin VI is required for structural integrity of the apical surface of sensory hair cells in Zebrafish. *Dev. Biol.* 272, 328–338. doi: 10.1016/j.ydbio.2004.05.004

Seiler, C., Finger-Baier, K. C., Rinner, O., Makhankov, Y. V., Schwarz, H., Neuhauss, S. C. F., et al. (2005). Duplicated genes with split functions: independent roles of protocadherin15 orthologues in Zebrafish hearing and vision. *Development* 132, 615–623. doi: 10.1242/dev.01591

Senften, M., Schwander, M., and Kazmierczak, P. (2006). Physical and functional interaction between protocadherin 15 and myosin VIIa in mechanosensory hair cells. *J.* Neurosci. 26, 2060–2071. doi: 10.1523/JNEUROSCI.4251-05.2006

Shabbir, M. I., Ahmed, Z. M., Khan, S. Y., Riazuddin, S., Waryah, A. M., Khan, S. N., et al. (2006). Mutations of human TMHS cause recessively inherited non-syndromic hearing loss. *J. Med. Genet.* 43, 634–640. doi: 10.1136/jmg.2005.039834

Sheets, L., Trapani, J. G., Mo, W., Obholzer, N., and Nicolson, T. (2011). Ribeye is required for presynaptic CaV1.3a channel localization and afferent innervation of sensory hair cells. *Development* 138, 1309–1319. doi: 10.1242/dev.059451

Sidi, S., Busch-Nentwich, E., Friedrich, R., Schoenberger, U., and Nicolson, T. (2004). gemini encodes a Zebrafish L-type calcium channel that localizes at sensory hair cell ribbon synapses. *J. Neurosci.* 24, 4213–4223. doi: 10.1523/JNEUROSCI.0223-04.2004

Siemens, J., Lillo, C., Dumont, R. A., Reynolds, A., Williams, D. S., Gillespie, P. G., et al. (2004). Cadherin 23 is a component of the tip link in hair-cell stereocilia. *Nature* 428, 950–955. doi: 10.1038/nature02483

Singh, P. P., and Isambert, H. (2019). OHNOLOGS v2: a comprehensive resource for the genes retained from whole genome duplication in vertebrates. *Nucleic Acids Res.* gkz909 doi: 10.1093/nar/gkz909

Söllner, C., Rauch, G.-J., Siemens, J., Geisler, R., Schuster, S. C., Müller, U., et al. (2004). Mutations in cadherin 23 affect tip links in Zebrafish sensory hair cells. *Nature* 428, 955–959. doi: 10.1038/nature02484

Thisse, C., and Thisse, B. (2008). High-resolution in situ hybridization to whole-mount Zebrafish embryos. *Nat. Protoc.* 3, 59–69. doi: 10.1038/nprot.2007.514

Westerfield, M. (2000). *The Zebrafish Book. A Guide for the Laboratory use of Zebrafish (Danio Rerio)*, 4th Edn. Eugene OR: University of Oregon.

Wickham, H. (2016). *Ggplot2: Elegant Graphics for Data Analysis*. New York, NY: Springer-Verlag.

Wolfe, K. (2000). Robustness—it's not where you think it is. *Nat. Genet.* 25, 3–4. doi: 10.1038/75560

Xiong, W., Grillet, N., Elledge, H. M., Wagner, T. F. J., Zhao, B., Johnson, K. R., et al. (2012). TMHS is an integral component of the mechanotransduction machinery of cochlear hair cells. *Cell* 151, 1283–1295. doi: 10.1016/j.cell.2012.10.041

Yao, Q., DeSmidt, A. A., Tekin, M., Liu, X., and Lu, Z. (2016). Hearing assessment in Zebrafish during the first week postfertilization. *Zebrafish* 13, 79–86. doi: 10.1089/ZEB.2015.1166

Zhao, B., Wu, Z., Grillet, N., Yan, L., Xiong, W., Harkins-Perry, S., et al. (2014). TMIE Is an essential component of the mechanotransduction machinery of cochlear hair cells. *Neuron* 84, 954–967. doi: 10.1016/j.neuron.2014.10.041

Zou, J., Chen, Q., Almishaal, A., Mathur, P. D., Zheng, T., Tian, C., et al. (2017). The roles of USH1 proteins and PDZ domain-containing USH proteins in USH2 complex integrity in cochlear hair cells. *Hum. Mol. Genet.* 26, 624–636. doi: 10.1093/hmg/ddw421

Conflict of Interest: The authors declare that the research was conducted in the absence of any commercial or financial relationships that could be construed as a potential conflict of interest.

frontiers in Molecular Neuroscience

METHODS
published: 12 May 2020
doi: 10.3389/fnmol.2020.00075

Modified *in situ* Hybridization Chain Reaction Using Short Hairpin DNAs

Yousuke Tsuneoka[1]* *and Hiromasa Funato*[1,2]*

[1]*Department of Anatomy, Faculty of Medicine, Toho University, Tokyo, Japan,* [2]*International Institutes for Integrative Sleep Medicine (WPI-IIIS), University of Tsukuba, Ibaraki, Japan*

The visualization of multiple gene expressions in well-preserved tissues is crucial for the elucidation of physiological and pathological processes. *In situ* hybridization chain reaction (HCR) is a method to visualize specific mRNAs in diverse organisms by applying a HCR that is an isothermal enzyme-free nucleotide polymerization method using hairpin DNAs. Although *in situ* HCR is a versatile method, this method is not widely used by researchers because of their higher cost than conventional *in situ* hybridization (ISH). Here, we redesigned hairpin DNAs so that their lengths were half the length of commonly used hairpin DNAs. We also optimized the conjugated fluorophores and linkers. Modified *in situ* HCR showed sufficient fluorescent signals to detect various mRNAs such as *Penk*, *Oxtr*, *Vglut2*, *Drd1*, *Drd2*, and *Moxd1* in mouse neural tissues with a high signal-to-noise ratio. The sensitivity of modified *in situ* HCR in detecting the *Oxtr* mRNA was better than that of fluorescent ISH using tyramide signal amplification. Notably, the modified *in situ* HCR does not require proteinase K treatment so that it enables the preservation of morphological structures and antigenicity. The modified *in situ* HCR simultaneously detected the distributions of c-Fos immunoreactivity and *Vglut2* mRNA, and detected multiple mRNAs with a high signal-noise ratio at subcellular resolution in mouse brains. These results suggest that the modified *in situ* HCR using short hairpin DNAs is cost-effective and useful for the visualization of multiple mRNAs and proteins.

Keywords: short hairpin DNA, hybridization chain reaction, *in situ* hybridization, fluorophore, mouse brain, striatum, medial preoptic area

OPEN ACCESS

Edited by:
Jean-Marc Taymans, Institut National de la Santé et de la Recherche Médicale (INSERM), France

Reviewed by:
Dagmar Galter, Karolinska Institutet (KI), Sweden
Françoise Gofflot, Catholic University of Louvain, Belgium

***Correspondence:**
Yousuke Tsuneoka
yousuke.tsuneoka@med.toho-u.ac.jp
Hiromasa Funato
hiromasa.funato@med.toho-u.ac.jp

Received: *28 January 2020*
Accepted: *16 April 2020*
Published: *12 May 2020*

Citation:
Tsuneoka Y and Funato H (2020) Modified in situ Hybridization Chain Reaction Using Short Hairpin DNAs. Front. Mol. Neurosci. 13:75. doi: 10.3389/fnmol.2020.00075

INTRODUCTION

To elucidate physiological and pathological processes in living organisms, it is crucial to visualize gene expression at good spatial resolution in a well-preserved morphological context. *In situ* hybridization (ISH) is a commonly used technique for detecting specific mRNAs in cells, tissues or whole bodies (Jensen, 2014). ISH was originally developed with the use of a radioisotope-labeled antisense nucleotide (Krumlauf et al., 1987; Marcus et al., 2001), which was subsequently replaced by a digoxigenin-labeled probe that enabled alkaline phosphatase- or peroxidase-based chromogenic reactions (Funato et al., 2000; Moorman et al., 2001). The use of two or more chromogens or fluorophores in combination enables the visualization of more than one mRNA. To increase the sensitivity of the ISH method to detect less abundant mRNAs, a method called tyramide signal amplification has been developed (Zaidi et al., 2000). Recent progress in ISH includes locked nucleic acid probes that are commonly applied for the detection of small RNAs (Urbanek et al., 2015), and rolling cycle amplification that has been reported to detect a single mRNA *in situ* (Larsson et al., 2010).

Currently, enzyme-based amplification using digoxigenin-labeled probes is the most used detection technique. To visualize multiple mRNAs, however, the procedures from probe hybridization to the chromogenic reaction generally need to be conducted twice serially, which takes a substantial amount of time and requires great labor. Also, when detecting low abundance mRNAs, artificial signals are inevitably produced due to nonspecific probe hybridization and nonspecific chromogenic enzyme reactions (Jensen, 2014).

The hybridization chain reaction (HCR) is an isothermal enzyme-free polymerization method that uses two different hairpin nucleotides: H1 and H2 (**Figure 1A**; Dirks and Pierce, 2004). The hairpin molecules are composed of toehold, stem, and loop domains and are self-assembling and metastable in the absence of initiator nucleotides that have a specific sequence complementary to the toehold and stem domains of an H1 hairpin (**Figure 1A**). In the presence of an initiator nucleotide, the toehold and stem domains of an H1 hairpin hybridize with the initiator through strand displacement. The remaining single-strand part of the opened H1 hairpin that was originally the loop and stem domains, hybridizes with H2 hairpin and produces a single strand part that has a sequence identical to the initiator, which in turn hybridizes with an H1 hairpin. Therefore, once an H1 hairpin is hybridized with an initiator, the polymerization of H1 and H2 hairpins continues and forms long nicked double-helices (**Figures 1A,D** and **Supplementary Figure S1**; Dirks and Pierce, 2004).

In situ HCR is a method that applies the HCR technique to the visualization of a specific nucleotide in cells, tissues, and whole-mount samples using an RNA probe that has a sequence enabling the hybridization to a target mRNA and a sequence to work as an initiator of HCR (Choi et al., 2010). Choi et al. (2010) successfully visualized the localization of target mRNA in zebrafish using HCR with fluorescently labeled RNA hairpins. *In situ* HCR has been further advanced by the use of a DNA hairpin (Choi et al., 2014; Yamaguchi et al., 2015), and the use of different fluorophore-labeled DNA hairpins for the detection of multiple mRNAs (Choi et al., 2016). Although *in situ* HCR frequently has been accompanied by false-positive signals and background signals due to nonspecific probe bindings, the "third-generation" *in situ* HCR method using a pair of split probes successfully reduced nonspecific signals (Choi et al., 2018). The advantages of *in situ* HCR using split probes are a high signal-to-noise ratio, a high sensitivity that enables single-molecule imaging, and an easy protocol for multiplex staining. *In situ* HCR using split-probes does not require stringent conditions for probe hybridization, and both prehybridization and hybridization are conducted under a mild condition of 37°C, which leads to decreased damage to tissues and well-preserved morphology.

Despite the technical advantages of *in situ* HCR, this method has not become standard procedure to detect mRNAs because *in situ* HCR that uses 72-nucleotide (nt)-long DNA hairpins costs more than conventional ISH methods. The cost of oligonucleotides increases in proportion to their length, and the yield of full-length oligos decreases as their lengths increase. Thus, shorter DNA hairpins are favorable as long as they progress HCR.

In this study, we optimized and shortened DNA hairpins and initiators for *in situ* HCR with split probes. We also simplified *the in situ* HCR protocol by removing proteinase K treatment. Our modified *in situ* HCR protocol is sensitive to a low abundance mRNA, is easier to handle and enables better antigenicity preservation for immunohistochemistry at a decreased cost.

MATERIALS AND METHODS

Design and Synthesis of DNA Probes

All nonlabeled oligo DNAs were synthesized as standard desalted oligos (Integrated DNA Technologies). We modified and optimized the design of DNA probes using short hairpin DNAs from previous studies (Choi et al., 2014, 2018) as follows. Split-initiator DNA probes were designed to minimize off-target complementarity using a homology search by NCBI Blastn[1], and they were designed to have 45–55% GC content in their mRNA binding sites. A pair of split-initiator probes were a 39-nt long DNA (25-nt long binding sites, 2-nt long spacer, and 12-nt long split-initiator sequence) and a 36-nt long DNA (25-nt long binding sites, 2-nt-long spacer, and 9-nt-long split-initiator sequence). The split-initiator sequence of the 39-nt-long DNA has a 9-nt-long toehold and a 3-nt-long sequence that is complementary to the first 3-nt of the stem domain of the hairpins. The split-initiator sequence of the 36-nt-long DNA probe has a 9-nt-long sequence that is complementary to the following 9-nt of the stem domain of the hairpins (**Figure 1B** and **Supplementary Figure S1**). Five or 10 sets of 36-nt and 39-nt DNA probes were designed for each target mRNA (**Supplementary Table S2**). All probe sets for each target mRNA were prepared, mixed, and stored in TE (10 mM Tris-HCl pH 8.0 and 1 mM EDTA). Each probe mixture was subsequently purified by denaturing polyacrylamide gel electrophoresis (PAGE) using 20% polyacrylamide gels (1:40 bis and linear acrylamide). After purification, the probes were diluted in TE to 2 μM.

Design and Synthesis of DNA Hairpin Amplifiers

To find the shortest sequences of DNA for hairpins that reliably trigger and continue HCR, we tested 36-44-nt long hairpins containing a 12-nt long stem sequence (**Supplementary Table S1**). The hairpin DNAs were designed using the multistate sequence design feature of NUPACK[2], to produce target secondary structures shown in **Figure 1A**. After the NUPACK random design, the sequences were manually edited according to the previously reported criteria: less than 40% GC content in a toehold domain and greater than 60% GC content in a stem (Ang and Yung, 2016). The manually adjusted hairpin sequences were subsequently assessed by a NUPACK simulation to avoid undesirable secondary structures.

DNA hairpins labeled at the 5′ end with an amino linker, ssH, were synthesized (FASMAC). ssH-labeling of the 5′ end of DNAs enables subsequent coupling to a fluorophore

[1]https://blast.ncbi.nlm.nih.gov
[2]http://www.nupack.org/

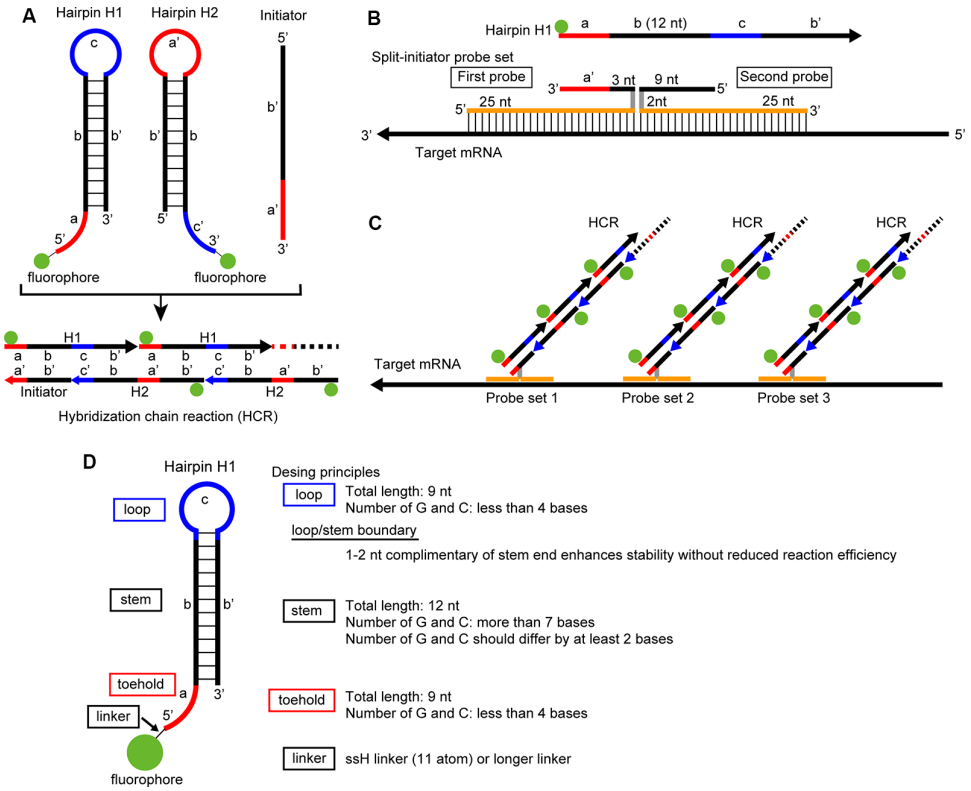

FIGURE 1 | Principle of *in situ* hybridization chain reaction (HCR) and short hairpin design. **(A)** Each hairpin DNA (H1, H2) has toehold, stem and loop domains and is conjugated to a fluorophore. Whereas the sequence of the toehold domain of H1 (a) is complementary to that of the loop domain of H2 (a'), the sequence of the loop domain of H1 (c) is complementary to that of the toehold domain of H2 (c'). In the presence of an initiator that is composed of a' and b', the initiator hybridizes with the toehold and stem domains (a,b) of H1. Then, the remaining part of H1 (c,b') hybridizes with the toehold and stem domains (c',b) of H2. Thereafter, H1 and H2 continue to hybridizes with each other (lower). **(B)** Split-initiator probe set. One probe has sequence a', first 3 nucleotide (nt) of sequence b', 2 nt spacer sequence, and 25 nt sequence complementary to the target mRNA. Another probe has 25 nt sequence complementary to the target mRNA, 2 nt spacer sequence and the last 9 nt of sequence b'. **(C)** *In situ* HCR using split-initiator probes. Three sets of split-initiator probes hybridize with the target mRNA and lead to HCR. **(D)** Design principles of short hairpin DNA. A set of short hairpin DNAs and split-initiator probes with actual nucleotide sequences are shown in **Supplementary Figure S1**.

(Komatsu et al., 2008). For comparison, C6-amino linker-labeled DNAs were also prepared (FASMAC). The fluorophores that were conjugated with succinimidyl esters were FAM (Sigma–Aldrich #21878), ATTO390, ATTO488, ATTO550, ATTO565 (ATTO-TEC), Alexa Fluor488, Alexa Fluor568, and Alexa Fluor647 (Thermo Fisher Scientific; **Figures 2D–K**). Following chloroform purification and ethanol precipitation with MgCl2, ssH-labeled DNAs were dissolved in 0.1 M borate buffer, pH 9.0, at 1 mM concentration of the DNA. One-third volume of fluorophore-conjugated succinimidyl ester (10 mg/ml in dimethylformamide) was mixed with the DNA solution and incubated for 4 h at room temperature to allow the coupling reaction of succinimidyl ester with the ssH-amino linker conjugated to the DNA. Fluorophore-conjugated DNAs were purified by denaturing PAGE using 20% polyacrylamide gels to remove incorporated fluorophores and incorrectly synthesized shorter oligonucleotides. The fluorescence of DNA bands corresponding to expected sizes was visualized by a hand-made LED illuminator (OptoSupply) and filter sets (LEE filters) to minimize DNA damage caused by UV light; then the bands were excised from the gel. The excised gel bands were crushed and soaked in TE at 4°C overnight, and the DNA recovered by ethanol precipitation as described above. The fluorophore-labeled DNAs were eluted in TE with 150 mM NaCl, and the concentration was adjusted to 3 μM based on the 260 nm absorbance. It is noted that the exact concentration of fluorophore-labeled DNAs cannot be determined because the fluorophores absorb 260 nm light to some extent, and the stem domain (double-strand) has a lower 260 nm absorbance per nucleotide than the toehold and loop domains (single strand).

Nonlabeled DNA hairpins were used only for *in vitro* study in microtubes, not for *in situ* HCR. Nonlabeled DNAs were purified by denaturing PAGE like the process used for the labeled DNAs, except for post staining of the polyacrylamide gel using GelGreen (Biotium).

HCR Verification of Hairpin DNAs in Microtubes

All hairpin DNAs were snap-cooled (heated to 95°C for 2 min and cooled to room temperature for 30 min) to form a hairpin

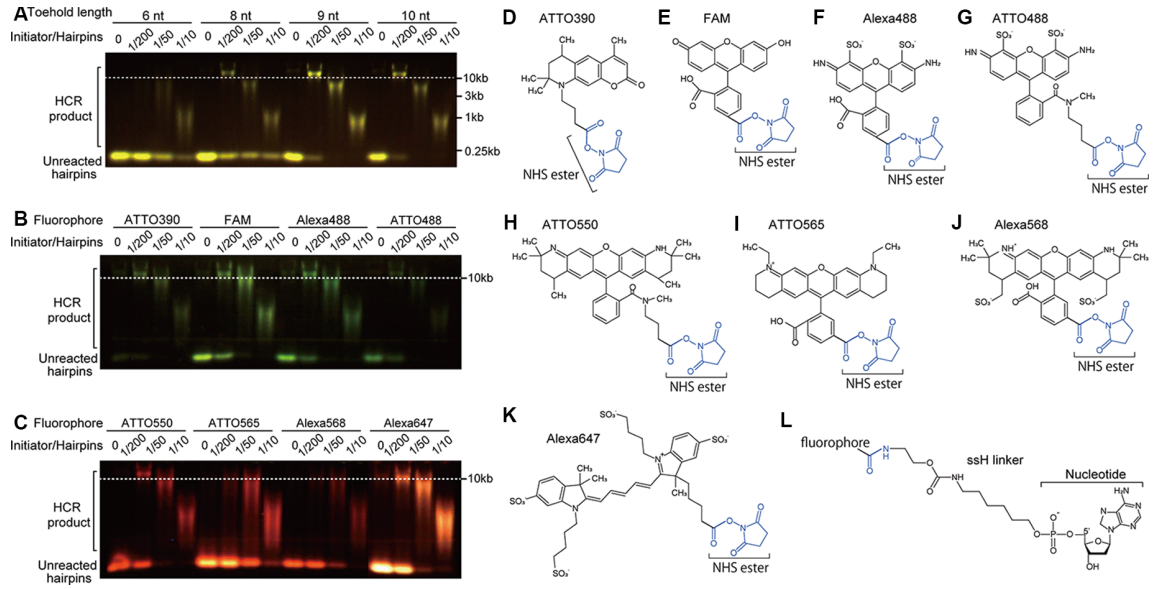

FIGURE 2 | Effect of toehold length and fluorophores on HCR. **(A)** Effect of toehold length of hairpin DNAs on HCR efficiency. Short hairpin DNAs with a toehold length of 6, 8, 9, and 10 nt were examined. The ratios of initiator's concentration to hairpin DNAs' concentration were 0, 1/200, 1/50, and 1/10 with a constant concentration of 0.5 μM hairpin DNAs. HCR products were visualized after agarose gel electrophoresis. HCR product bands longer than 10 kb indicate efficient HCR. Unreacted hairpin DNAs were recognized as bands shorter than the position of 0.25 kb. Used hairpin DNAs were #S4 (6-nt toehold), #S8 (8-nt toehold), #S41 (9-nt toehold), and #S9 (10-nt toehold; **Supplementary Table S2**). **(B,C)** Effect of fluorophores on HCR efficiency. Hairpin DNAs with 9-nt toehold (#S41) conjugated with either ATTO390, FAM, Alexa488, ATTO488, ATTO550, ATTO565, ATTO568 or Alexa647 were used with different initiator/hairpin concentration ratios. Captured images taken with appropriate filter sets were overlaid based on the loading position. Dashed lines indicate a band size of 10 kb dsDNA. **(D–K)** Chemical structures of N-hydroxysuccinimide (NHS) ester (blue)-conjugated fluorophores. **(L)** Chemical structure of ssH linker that is conjugated with a fluorophore *via* an amido bond and with a nucleotide *via* a phosphoric acid.

structure before use. HCR was performed in 5× standard saline citrate (SSC) with 0.1% Tween 20 (5× SSCT). Each microtube was prepared by adding 2 μl of 3 μM hairpin DNAs, 6 μl of 0, 0.005, 0.02 or 0.1 μM initiator DNA, and an appropriate amount of 20× SSC with 10% Tween 20 to bring the reaction volume to 12 μl. Two hours after mixing the DNAs, the samples were supplemented with prestained loading dye (Bio-craft) and loaded into native 1% agarose gels. The gels were electrophoresed in sodium borate buffer (10 mM NaOH and 35 mM boric acid) at 135 V for 30 min and then were imaged. The intensity of each band was analyzed by ImageJ to quantify the amount of HCR products.

We determined that a pair of hairpins showed strong amplification when HCR products exceeded 10 kb with 1/200 of the initiator-to-short hairpin ratio. We also judged that initiator-independent HCR (leakage) was low when a very weak signal of the HCR product was observed after 2 h of HCR without initiator nucleotides. Also, HCR efficiency was evaluated based on the amount of unreacted hairpin (see **Figure 2**).

In situ Hybridization

All animal procedures were conducted following the Guidelines for Animal Experiments of Toho University and were approved by the Institutional Animal Care and Use Committee of Toho University (Approved protocol ID #19-51-405). Breeding pairs of C57BL/6J mice were obtained from Japan SLC and CLEA Japan. Mice were raised in our breeding colony under controlled conditions (12 h light/dark cycle; lights on at 8:00 A.M., 23 ± 2°C, 55 ± 5% humidity; and ad libitum access to water and food). Male mice (20–30 weeks old) were used except for c-Fos staining after maternal behavior. Female mice (20–30 weeks old) were sacrificed 2 h after pup presentation for c-Fos immunohistochemistry (Tsuneoka et al., 2013). At least three mice were used for each experiment to confirm reproducibility. Mice were anesthetized with sodium pentobarbital (50 mg/kg, i.p.), and then were transcardially perfused with 4% paraformaldehyde (PFA) in phosphate-buffered saline (PBS). The brains were postfixed in 4% PFA at 4°C overnight, which was followed by cryoprotection in 30% sucrose in PBS for 2 days, embedded in Surgipath (FSC22, Leica Biosystems), and were stored at −80°C until use. The brains were cryosectioned coronally at a thickness of 40 μm.

All the sections were stained by the free-floating method, which enables better preservation of tissue morphology and uniform staining of the sections. The handling and prehybridization procedures were the same as those in our published protocol (Tsuneoka et al., 2015, 2017b). Briefly, the sections were washed with PBS containing 0.1% Tween-20 (PBST), treated with or without proteinase K (Roche, 10 mg/ml in PBST) for 10 min and postfixed with 4% PFA in PBS for 10 min at 37°C. The sections were immersed in methanol containing 0.3% H_2O_2 for 10 min, followed by acetylation with 0.25% acetic anhydride in 0.1 M triethanolamine (pH 8.0) for 20 min. After washing, the sections were prehybridized

for 10 min at 37°C in a hybridization buffer containing 30% formamide, 10% dextran sulfate, 5× SSC, 10 mM citric acid, 0.1% Tween 20, 50 μg/ml heparin, 1× Denhardt's solution as described (Choi et al., 2018). The sections were moved to another hybridization solution containing a mixture of 1 nM split-initiator probes, and incubated overnight at 37°C. In the case of staining for multiple targets, the probes were added simultaneously. After hybridization, the sections were washed three times for 10 min in 5× SSCT with 30% formamide at 37°C, followed by three washes for 10 min in 5× SSCT without formamide at room temperature.

For *in situ* HCR (**Figure 1C**), 3 μM hairpin DNA solutions were separately snap-cooled before use. The sections were incubated in amplification buffer (10% dextran sulfate in 5× SSCT) with 60 nM hairpin DNA pairs for 45 min, 2 h or overnight at 25°C. In the case of multiple staining, the hairpin DNAs were added simultaneously. Then, the samples were washed with 5× SSCT and PBST three times at room temperature.

In the case of combined ISH and immunohistochemistry, the sections were blocked using 0.8% Block Ace/PBST (Dainihon-Seiyaku), which was followed by overnight incubation with rabbit anti-c-Fos antibody (1:2,500, sc-52, Santa Cruz) in 0.4% Block Ace/PBST at 4°C. After washing three times with PBST, sections were incubated with an Alexa488-conjugated donkey anti-rabbit goat antibody (1:500, 711-545-152, Jackson ImmunoResearch) with Hoechst 33342 (1 μg/ml) for an hour at room temperature. The sections were mounted on the slide glass and cover-slipped with mounting media containing antifade (1% n-propyl gallate and 10% Mowiol4–88 in PBS).

To compare the sensitivity between *in situ* HCR and enzyme-based ISH, we also performed chromogenic ISH and fluorescent ISH using tyramide signal amplification. The cDNA fragment of *oxytocin receptor* (*Oxtr*) mRNA (GenBank ID: NM_001081147,1869-3843) was amplified, inserted into the pGEM-T plasmid (A3600, Promega), which was used into DH5α *E. coli*. After confirmation that the DNA sequence was correct, template cDNA was produced using polymerase chain reaction with specific primers (5′-ATTTAGGTGACACTATAG-3′) and (5′-TAATACGACTCACTATAGGG-3′). The probe was transcribed by SP6 RNA polymerase (P1085; Promega) in the presence of digoxigenin-labeled UTP (Dig labeling mix; Roche Diagnostics, Switzerland), which was followed by precipitation with LiCl with ethanol. The riboprobe was digested by alkaline hydrolysis to reduce the average size to 500 bases. Although hydrolyzed riboprobes sometimes increase nonspecific hybridization, our ISH protocol using a stringent wash, RNase A treatment, and non-excessive hydrolysis suppresses the background.

The prehybridization procedure was identical to that of *in situ* HCR. After acetylation, sections were washed with PBST, which was followed by incubation at 57°C overnight in a hybridization mixture containing 1 μg/ml riboprobe, 50% deionized formamide, 5× SSC (pH 7.0), 5 mM EDTA (pH 8.0), 0.2 mg/ml yeast tRNA, 0.2% Tween-20, 0.2% sodium dodecyl sulfate, 10% dextran sulfate, and 0.1 mg/ml heparin. After hybridization, the sections were washed twice with 2× SSC containing 50% formamide at 57°C for 10 min, incubated with RNAse A solution (20 μg/ml) at 37°C for 30 min, rinsed twice with 2× SSC and 0.2× SSC at 37°C (10 min each), and incubated in an alkaline phosphatase-conjugated or peroxidase-conjugated anti-digoxigenin antiserum (1:5,000 and 1:10,000, respectively; Roche) for 2 h at room temperature. Then the alkaline phosphatase-labeled sections were washed with 100 mM Tris-HCl (pH 8.0) and 150 mM NaCl and were incubated with BCIP/NBT (Roche) in 100 mM Tris-HCl (pH 9.5), 150 mM NaCl, 1 mM $MgCl_2$ and 10% polyvinyl alcohol for 3 days at room temperature. The sections were dehydrated by treatment with methanol, ethanol, and xylene, and were mounted with Marinol (Muto Pure Chemical). The peroxidase-labeled sections were washed and immersed in 0.1 M boric buffer (pH 8.5) containing 10 μM Alexa568-labeled tyramide, 10% dextran sulfate, 0.05 mg/ml iodophenol and 0.003% H_2O_2 for 30 min. After washing, the sections were mounted as they were in the *in situ* HCR experiments.

Histological Analysis

Fluorescent photomicrographs were obtained using a Nikon Eclipse Ni microscope equipped with the A1R confocal detection system under 20×, 40× and 100× objective lenses (Nikon Instruments Inc., Tokyo, Japan). The photomicrographs for the bright field observation were taken by a Nikon AZ-100 microscope equipped with a digital camera (Sony α7s). Images were analyzed using ImageJ software (version 1.50i, NIH, USA). Quantification of the fluorescent photographs was performed at the same threshold and adjustment of contrast.

RESULTS

Reliable HCR Using 42-nt-long DNA Hairpins

To find the shortest sequences of DNA hairpins that reliably proceed with the HCR, we systematically examined hairpin DNAs with different lengths for their HCR efficiency based on the appearance of HCR products larger than 10 kb and the intensity of the unreacted hairpin DNA band. Because the commonly used DNA hairpins have toehold and loop domains of equal length and are 72-nt long containing 12-nt toehold, 24-nt stem and 12-nt loop domains (Choi et al., 2014, 2016, 2018), we first tested 7 pairs of nonlabeled 36-nt hairpin DNAs containing 6-nt toehold, 12-nt stem, and 6-nt loop domains. However, they all showed low HCR efficiency (#S1-S7 in **Supplementary Table S1**). Even in the presence of a high concentration of an initiator DNA, an HCR that was allowed to occur for 2 h left a majority of hairpin DNAs unreacted (**Figure 2A**). Thus, 36-nt hairpin DNAs were not suitable for HCR.

Next, we tested non-labeled hairpin DNAs which have 8-nt, 9-nt, or 10-nt long toehold and loop domains and 12-nt stem domains (8-nt: #S8, 9-nt: #S41, and 10-nt: #S9 in **Supplementary Table S1**). HCR with 8-nt long toehold and loop domains successfully produced ∼10 kb products, but unreacted hairpin DNAs remained in all initiator concentrations.

HCR with 9-nt and 10-nt long toehold and loop domains produced ∼10 kb products, and only a small amount of hairpin DNA was unreacted (**Figure 2A**). There was no apparent difference in the amount of incorporated hairpin DNA between the 9-nt and 10-nt toehold/loop after a 2-h HCR, indicating that the 9-nt-long toehold and loop domains were sufficient for efficient HCR (**Figure 2A**, #S4, #S8–9, and #S41 in **Supplementary Table S1**), which is consistent with our NUPACK simulation (data not shown). Thus, we used 42-nt hairpins containing 9-nt toehold, 12-nt stem, and 9-nt loop domains thereafter.

The Sequence of the Stem and Transition Between the Stem and Loop Affected Hairpin Stability

Since insufficient stability of hairpin DNAs leads to initiator-independent HCR, we optimized the sequence of the stem domains of short hairpin pair based on the abundance of initiator-independent HCR. Through this optimization using short hairpins with different nucleotide contents, we noticed that short hairpin pair with a similar number of G and C on one strand of the stem domain tended to result in frequent initiator-independent HCR (**Table 1**). In contrast, when the number difference between G and C on one strand of the stem domain is 4 or 5, the incidence of initiator-independent HCR was low (**Table 1**). The difference between the numbers of G and C on one strand of the stem domain significantly correlated with the initiator-independent HCR as evaluated by band intensity (Spearman's rank correlation test, rho = −0.40, S = 6941.8, p = 0.026).

Also, we noticed that the shift of the transition site between the stem and loop domains by one or two nucleotides sometimes decreased initiator-independent HCR (**Figure 1D**). For example, the shift by one nucleotide produces a hairpin containing 9-nt toehold, 13-nt stem, and 7-nt loop domains, in which the toehold sequence hybridized with the loop domain and a part of the stem domain. However, the shift of the transition site sometimes led to decreased HCR efficiency due to the higher stability of the hairpin. Thus, the 42-nt DNA hairpins used in this study have some differences in the length of the stem and loop domains. Because of the high HCR efficiency and a small amount of initiator-independent HCR, we used #S41 hairpin DNAs to examine eight fluorophores and two linkers thereafter.

Conjugated Fluorophores Affected HCR Efficiency

We examined which fluorophore to use affects HCR efficiency in microtubes. The conjugation of ATTO390, FAM, ATTO488, Alexa488, ATTO550, and Alexa647 (**Figures 2D–K**) to 42-nt DNA hairpins did not interfere with HCR, while that of ATTO565 and Alexa568 resulted in decreased HCR efficiency (**Figures 2B,C**). ATTO565- or Alexa568-conjugated hairpin DNAs produced a small amount of ∼10 kb products with a 1:200 ratio of initiator and hairpin DNAs and left a large amount of hairpin DNAs unreacted (**Figure 2C**). When compared with the C6 linker, the ssH linker showed higher HCR efficiency. C6-linked ATTO550-conjugated hairpin DNA did not form ∼10 kb long products with 1/200 amount of initiator DNA (**Supplementary Figure S2**), indicating that ssH linker is better at least for ATTO550.

In situ HCR Using Short Hairpin DNAs

Next, we performed *in situ* HCR for mouse brain using the fluorophore-labeled short hairpin DNAs described above and the reagents and buffers with reaction conditions reported in previous studies (Choi et al., 2014, 2018). Consistent with *in vitro* HCR, 42-nt hairpin DNAs provided stronger *in situ* HCR signals for *Proenkephalin* (*Penk*) mRNA than 36-nt hairpin DNA (**Supplementary Figure S3**). Thus, 42-nt hairpin DNAs were used for *in situ* HCR to detect mRNAs in this study. *Penk* mRNA-positive cells were abundantly detected in the striatum after HCR amplification initiated by five split-initiator probe sets for *Penk* mRNA (**Figure 3**). Extending the incubation time with Alexa647-conjugated hairpin pairs (#S41 in **Supplementary Table S1**) from 45 min to overnight enhanced the fluorescence signal for *Penk* mRNA. The incubation of split-initiator probes with one of the hairpin pairs (H1) or the incubation of hairpin pairs (H1, H2) without split-initiator probes did not generate any signals, indicating the *in situ* HCR specific to *Penk* mRNA (**Figure 3**). In the absence of initiator probes, background signals slightly increased as the incubation continued.

Since conjugated fluorophores and linkers affected the HCR efficiency in microtubes, we examined the effect of fluorophores and linkers on *in situ* HCR for *Penk* mRNA using the same

TABLE 1 | Number of short hairpin pairs with different G and C number on one strand of the stem domain and their initiator-independent hybridization chain reaction (HCR).

Number difference between G and C in the stem domain*	Initiator-independent HCR				Total
	Not recognized	Faint	Mild**	Abundant***	
0	0	0	2	1	3
1	0	0	3	2	5
2	2	1	1	0	4
3	1	0	0	1	2
4	2	4	2	2	10
5	2	4	1	0	7
Total	7	9	9	6	31

*Note: *For example, the stem domain sequence of GCGAGGACCACG comes to 1 because the sequence has five Gs and four Cs. **The abundance of initiator-independent HCR was less than that of unreacted hairpins. ***The abundance of initiator-independent HCR was the same or more than that of unreacted hairpins.*

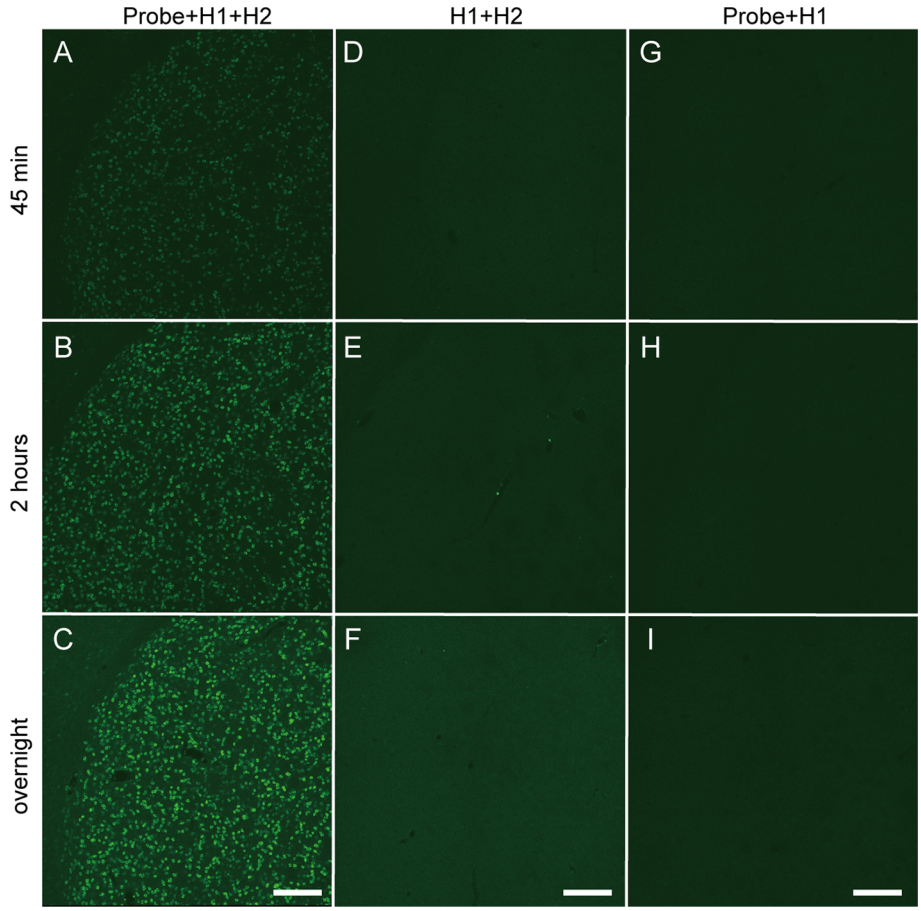

FIGURE 3 | Time-dependent increase in fluorescence of *in situ* HCR using short hairpin DNAs. *Penk* mRNA expression in the mouse striatum was detected by Alexa647-conjugated hairpin DNA (#S41) and corresponding probe sets. Background signals were not subtracted. **(A–C)** Sections were hybridized with split-initiator probes followed by HCR amplification. **(D–F)** Sections were treated without probes, which was followed by HCR amplification. **(G–I)** Sections were hybridized with probes followed by only H1 hairpin DNA hybridization. **(A,D,G)** Incubation for 45 min with hairpin DNAs. **(B,E,H)** Incubation for 2 h with hairpin DNAs. **(C,F,I)** Overnight incubation with hairpin DNAs. Scale bars: 200 μm.

five probe sets. Although the autofluorescence and detection conditions differed among the color spectra, *Penk*-positive neurons were observed using hairpins labeled with ATTO390, Alexa488, ATTO488, ATTO550, ATTO565, and Alexa647, but the signal intensity of ATTO390, ATTO488 and ATTO565 was weak (**Figure 4**). We obtained the best and brightest signals with the conjugation of ATTO550, and Alexa647, which is consistent with HCR efficiencies observed in microtubes (**Figures 2B,C**).

Consistent with *in vitro* HCR (**Supplementary Figure S2**), ssH-linked ATTO550 produced higher signal intensity for *Penk*-positive neurons than C6-linked ATTO550 (**Supplementary Figure S4**). The use of the ssH linker for Alexa488 or Alexa647 resulted in slightly stronger signals for *Penk* mRNA than that of the C6 linker (**Supplementary Figure S4**). PAGE purification of split-initiator probes for *Penk* mRNA increased fluorescent intensity compared with that of unpurified probes (data not shown).

We compared the sensitivity of *in situ* HCR using short hairpins with other ISH methods by detecting *Oxtr* mRNA, which we selected as an example of very low abundance mRNAs. After hybridization of 10 split-initiator probe sets for *Oxtr* mRNA, *in situ* HCR detected *Oxtr* mRNA signals in the rhomboid nucleus of the bed nucleus of the stria terminalis (BNST) and the magnocellular nucleus (MN) and weak signals in the principal nucleus of the BNST and the medial preoptic area (MPOA; **Figures 5A,D**; Young et al., 1997; Okabe et al., 2017). ISH with tyramide signal amplification failed to visualize *Oxtr*-positive cells in the BNST (**Figures 5B,E**). ISH using BCIP/NBT as chromogens demonstrated the distribution of *Oxtr* mRNA-positive cells consistent with that of *in situ* HCR, but there were much weaker and imprecise signals (**Figures 5C,F,I**). Almost all the HCR signals were observed near cell nuclei (**Figure 5G**). ISH with tyramide signal amplification produced a low signal-to-noise ratio results in cells at the BNST (**Figure 5H**).

Proteinase K treatment has been used for ISH and *in situ* HCR to improve the penetration of RNA/DNA probes and fluorophore-labeled hairpins by digesting proteins. However,

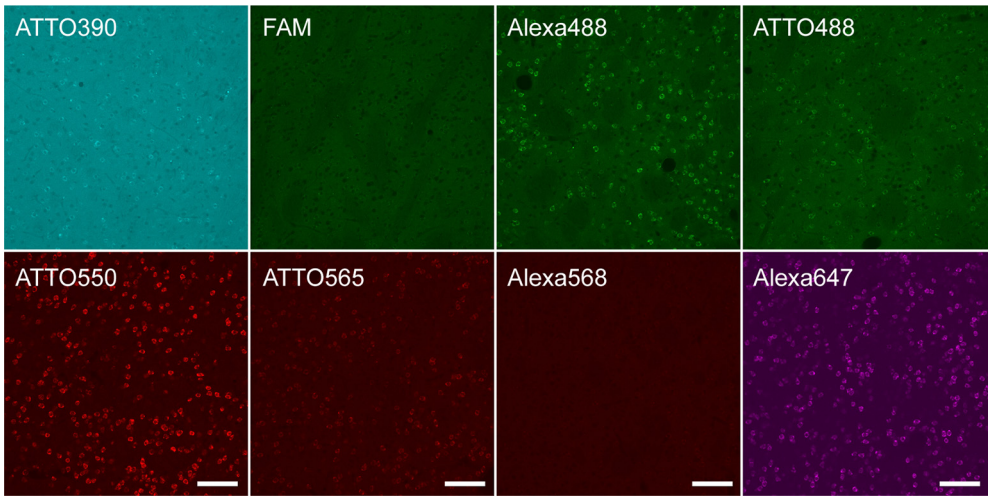

FIGURE 4 | Fluorophores conjugated to hairpin DNAs affect *in situ* HCR signal intensity. *in situ* HCR for *Penk* mRNAs in the mouse striatum using #S41 hairpin DNA. Various fluorophores were conjugated to the hairpin DNAs. All tissue sections were prepared from the same mouse. Background signals were not subtracted. Scale bars: 100 μm.

proteinase K treatment damages endogenous proteins such as c-Fos, which is a commonly used marker of neural activity, which limits the usefulness of ISH combined with immunohistochemistry. Since our modified *in situ* HCR uses shorter probes than what has been previously used, proteinase K treatment may not be necessary. As predicted, *in situ* HCR using 42-nt hairpins and five sets of 39- and 36-nt split-initiator probes without proteinase K treatment detected *vesicular glutamate transporter* (*Vglut*) *2* in the MPOA (**Figure 6C**) and the paraventricular thalamus (PVT; **Figure 6D**) with the same or slightly decreased signal levels as tissues that did undergo proteinase K treatment.

Female mice induced c-Fos expression in the MPOA after the retrieval of pups (Tsuneoka et al., 2013, 2017b; Moffitt et al., 2018). *In situ* HCR without proteinase K treatment successfully detected abundant c-Fos-positive cells in the MPOA and PVT (**Figures 6C,D**), whereas the number of c-Fos-positive cells and the intensity of c-Fos immunoreactivity were drastically decreased after proteinase K treatment (**Figures 6A,B**). *Vglut2*-positive neurons were scattered in the MPOA, but most of them were not c-Fos positive (**Figures 6E,F**).

Multiplex *in situ* HCR

To test whether the hairpin DNAs separately detect different mRNAs in a single tissue section, we performed multiplexed *in situ* HCR. After 2 h of HCR amplification, *dopamine receptor d1* (*Drd1*), *Drd2* and *Penk* mRNAs were simultaneously detected in the mouse striatum using the corresponding probes (five probe sets for each mRNA) and hairpin DNA pairs conjugated to different fluorophores (**Figure 7**). Although *Drd1* and *Drd2* mRNA were abundantly expressed in the striatum, double-positive cells for *Drd1* and *Drd2* mRNAs were rarely observed (**Figure 7**). In contrast, most of the *Drd2*-positive cells were also *Penk*-positive. When observed at higher magnification, the subcellular distribution and abundance of fluorescence for *Drd2* mRNA were distinct from those for *Penk* mRNA.

We next examined the sensitivity and resolution of modified *in situ* HCR using two different probe sets for *Moxd1* mRNA (**Supplementary Table S2**), which is a marker of sexually dimorphic nuclei (Tsuneoka et al., 2017a). One of them was five split-initiator probes containing #S41 initiator sequence and detected by ATTO550-conjugated hairpin pairs (#S41) and another was five split-initiator probes containing #S25 initiator sequence and detected by Alexa647-conjugated hairpin pairs (#S25). Both probe-hairpin combinations successfully detected *Moxd1*-positive cells in the BNST by 45-min HCR amplification (**Figure 8A**), which is consistent with the previous report (Tsuneoka et al., 2017a). At the highest magnification, almost all the ATTO550 and Alexa647 signals were observed as granules that colocalized within the cell (**Figure 8B**). Whereas 76.9% of ATTO550-positive granules were Alexa647-positive, 74.8% of Alexa647-positive granules were ATTO550-positive (247 and 254 granules in the total count, respectively).

DISCUSSION

In this study, we designed new short hairpin DNAs and corresponding split initiator probe sets to achieve sensitive detection of various mRNAs. This study proposed short hairpin design rules as well as linker types and fluorophores suitable for *in situ* HCR. These hairpin sets successfully performed HCR both *in vitro* and *in situ* and detected multiple mRNAs simultaneously with virtually the same procedures for a single mRNA. Short probes and hairpin DNAs can penetrate tissues without proteinase K treatment as well as they can tissues with proteinase K treatment. Also, our modified *in situ* HCR technique provided highly sensitive mRNA detection for the visualization of less abundant mRNAs such as *Oxtr*.

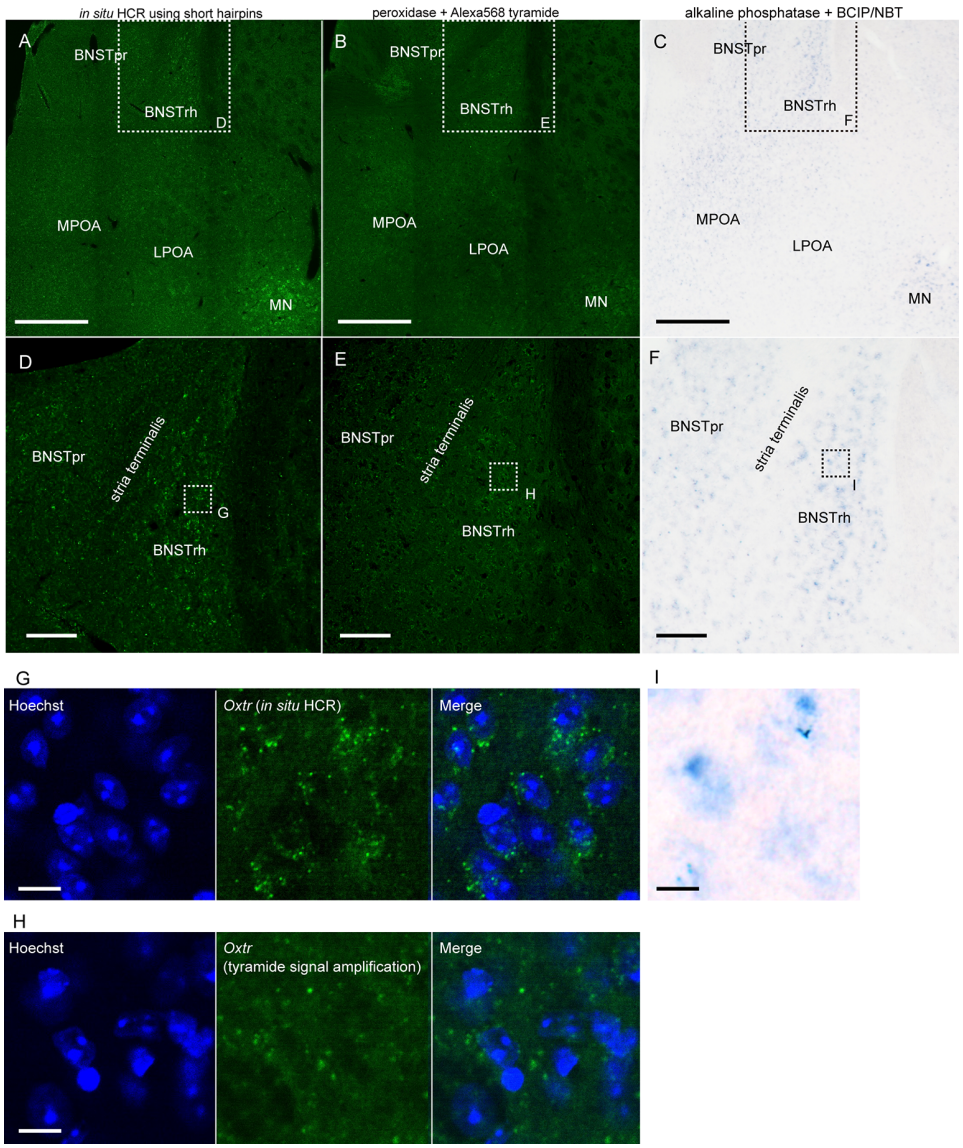

FIGURE 5 | Detection of low abundance mRNA using *in situ* HCR. **(A,D)** *In situ* HCR using ATTO550-conjugated hairpin DNA (#S23) detected *Oxtr* mRNA in mouse brain. Amplification was performed overnight. **(B,E)** Fluorescent ISH with tyramide signal amplification for *Oxtr* mRNA. *Oxtr* mRNA was visualized by a combination of DIG-labeled probe, peroxidase-conjugated anti-DIG antibody, and tyramide Alexa568. **(C,F)** Chromogenic ISH for *Oxtr* mRNA by a combination of DIG-labeled probe, alkaline phosphatase-conjugated anti-DIG antibody, and BCIP/NBT. Color development was performed for 3 days. Panels **(D–F)** corresponds to dashed squares in panels **(A–C)**, respectively. Panels **(G–I)** corresponds to dashed squares in **(D–F)**. Scale bars: 400 μm **(A–C)**, 100 μm **(D–F)** and 10 μm **(G–I)**. BNST, bed nucleus of stria terminalis; BNSTpr, principal nucleus of BNST; BNSTrh, rhomboid nucleus of BNST; LPOA, lateral preoptic area; MN, magnocellular nucleus; MPOA, medial preoptic area.

Design of Short Hairpin DNA

To achieve efficient and optimal HCR, the lengths of the total hairpin and each domain are crucial. HCR progresses using the difference in free energy between a long double-strand formed by hairpin pairs and a short double strand of the stem domain of each monomer hairpin. Therefore, longer toehold/loop domains enhance HCR. The HCR efficiency was increased by the extension of the toehold sequence and was independent of the stem sequences shown in **Figure 2A**. The difference in free energy also depended on the GC contents in the toehold/loop domain. However, increased GC content in the toehold/loop and longer toehold/loop may lead to initiator-independent HCR (Ang and Yung, 2016).

The stability of each hairpin largely depends on the stem length and its sequence. In general, increased stem length and GC content enhance hairpin stability due to an increased number of hydrogen bonds. In this respect, we extended the stem length from 12-nt to 13- or 14-nt by shifting the transition between the stem and loop by one or two nucleotides [e.g., S23-H1: toehold (9 nt) -stem (12 nt)—A—loop (7 nt)—T—stem

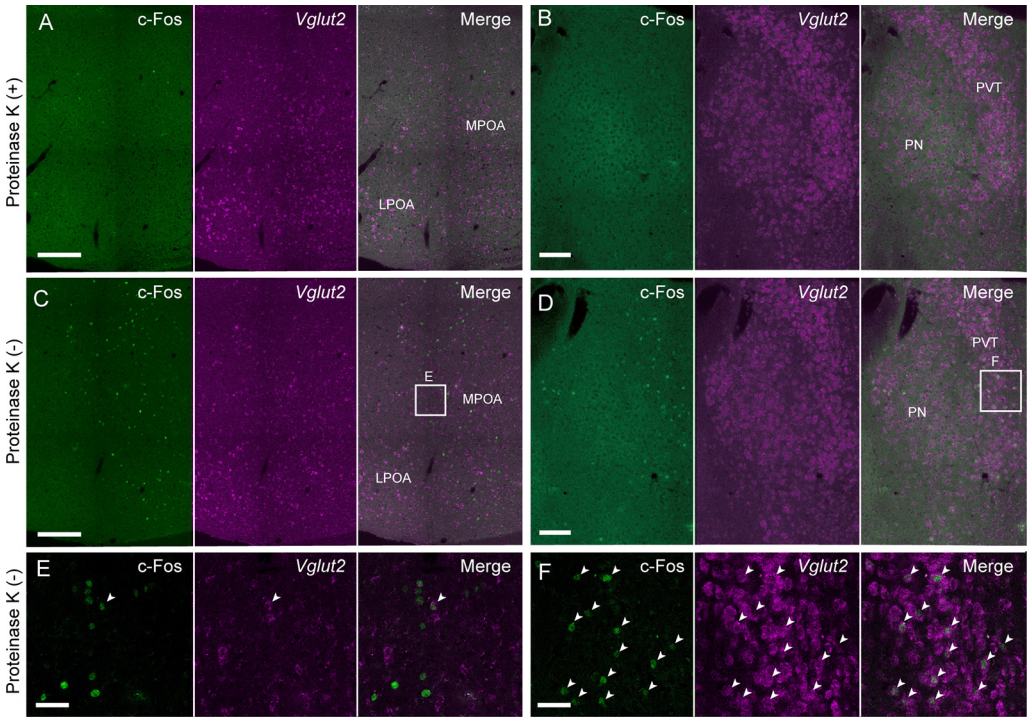

FIGURE 6 | Modified *in situ* HCR without proteinase K treatment. *Vglut2* mRNAs were detected in the mouse medial preoptic area **(A,C,E)** and PVT **(B,D,F)** using Alexa647-conjugated hairpin DNA (#S41). Amplification was performed for 2 h. **(A,B)** Sections were pretreated with proteinase K. **(C,D)** Sections were not treated with proteinase K. Maternal behavior-induced c-Fos immunoreactivity that was diminished by proteinase K treatment before hybridization. Panels **(E,F)** correspond to dashed areas in panels **(C,D)**. Arrowheads indicate double-positive cells of c-Fos protein and *Vglut2* mRNA. LPOA, lateral preoptic area; MPOA, medial preoptic area; PN, parataenial nucleus; PVT, paraventricular thalamus. Scale bars: 200 μm **(A,C)**, 100 μm **(B,D)** and 40 μm **(E,F)**.

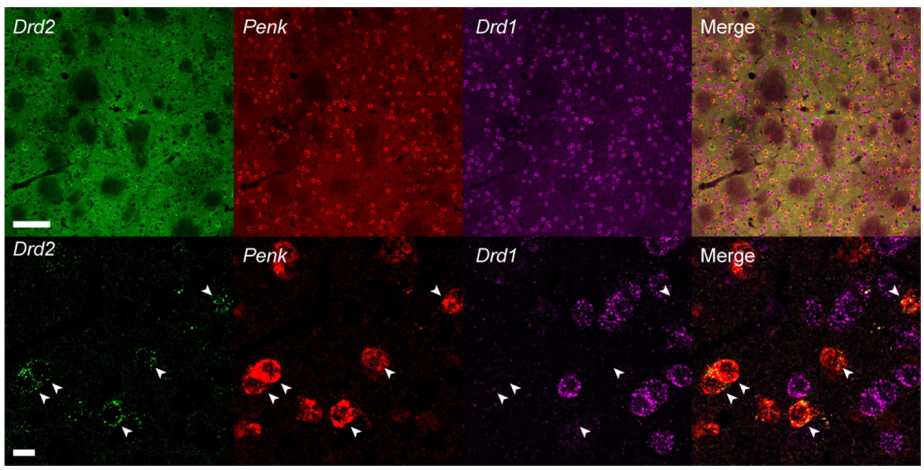

FIGURE 7 | Multiplex *in situ* HCR in the mouse striatum. *Drd2, Penk* and *Drd1* mRNAs were detected by 2-h HCR that simultaneously used different probe-hairpin pairs: Alexa488-conjugated hairpin DNA (#S23) for *Drd2*, ATTO565-conjugated hairpin DNA (#S10) for *Penk*, and Alexa647-conjugated hairpin DNA (#S25) for *Drd1*. In the upper panels, background signals were not subtracted. *Drd2*-positive cells were also *Penk*-positive (arrowheads). Scale bars: 100 μm (Upper panel) and 10 μm (Lower panel).

(12-nt); A and T are transition bases], which often decreased initiator-independent HCR but did not exhibit a decrease in HCR efficiency. Many designed hairpins showed a certain level of initiator-independent HCR, polymerization without an initiator. Many factors cause initiator-independent HCR (Chen et al., 2013). Practically, the purification of synthesized oligos is effective for reducing initiator-independent HCR, although the HPLC purification of DNA hairpins sometimes led to a

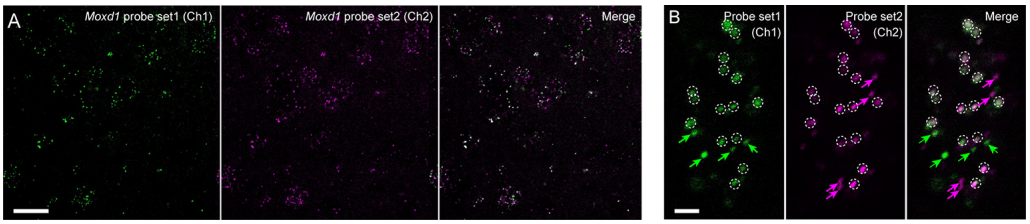

FIGURE 8 | Redundant detection of *Moxd1* mRNA using different probes. **(A)** *In situ* HCR using different probe-hairpin sets designed for different regions of the *Moxd1* mRNAs. HCR for 45 min detected *Moxd1* mRNAs in the bed nucleus of the stria terminalis. Five probe pairs were used for each channel. Fluorescent signals in Ch1 and Ch2 were detected using ATTO550-conjugated hairpin DNA (#S41) and Alexa647-conjugated hairpin DNA (#S25), respectively. **(B)** Representative photomicrograph showing subcellular resolution using the same probe-hairpin sets as in panel **(A)**. Dotted circles indicate granules detected in both channels, and arrows indicate granules detected in one of the two channels. Scale bars: 20 μm **(A)** and 2 μm **(B)**.

low HCR efficiency compared with that of PAGE purification (data not shown). We also found that a biased abundance of G or C on one side of the stem domain decreased the stability of the hairpin monomer (**Table 1**). Although further investigation of the hairpin stability is needed, these data provide useful information regarding the design of new hairpin-based nonenzymatic circuits.

We also found that fluorophores conjugated with hairpin DNAs affect HCR, and the linker length between hairpin DNAs and fluorophores and the structure of fluorophores may be involved in this effect. When a C6-amino linker (6 carbon atom-length) was used to link hairpin DNAs with ATTO550 succinimidyl ester, HCR did not form long products (**Supplementary Figure S2**). In contrast, the ssH-amino linker (11 atom-length) enabled the HCR using the same hairpin DNA conjugated with ATTO550 (**Figure 2** and **Supplementary Figure S2**), indicating that the use of a longer linker enhances the HCR. Similarly, the signal intensity of ATTO550-labeled hairpin DNAs *via* the ssH linker was brighter than *via* the C6 linker *in situ* (**Supplementary Figure S4**). Also, the ssH-amino linker achieves a high conjugation efficiency with succinimidyl esters and easy purification (Komatsu et al., 2008). We found efficient HCR amplification with fluorophore-labeled hairpin DNAs conjugated through an ssH-amino linker.

The presence of a linker-like linear structure in fluorophores is an additional factor to be considered for higher signal gain. Among the fluorophores examined, Alexa647, ATTO550, and ATTO488 have a linker-like linear structure (**Figure 2**). Hairpin DNAs conjugated with Alexa647 using the C6-amino linker led to over 10 kb HCR products (**Supplementary Figure S2**). Many fluorophores, such as the Alexa and ATTO series, have a comparable molecular structure and steric size to a single nucleotide molecule. Therefore, the use of a long linker and fluorophore with a linker-like linear structure is preferred because it is unlikely to cause steric hindrance against forming double-strands between hairpin DNA pairs. We found efficient HCR amplification with fluorophore-labeled hairpin DNAs conjugated through an ssH-amino linker, except ATTO565 and Alexa568 (**Figure 2B**), which have a very large molecular structure without any linker-like structure, although Alexa568 is widely used bright fluorophore in the immunohistochemistry and ISH. Such steric hindrance was further suggested in performing *in situ* HCR (**Figure 4**). The molecular structures of ATTO550 and Alexa647 succinimidyl esters are also very large, but they have a linker-like structure near the binding site, enabling efficient HCR amplification.

In situ HCR Using Short Hairpin DNA

The signal gain of HCR amplification by short hairpin DNAs was also confirmed in the mouse brain. *In situ* HCR showed that *Penk* mRNA was uniformly expressed in the mouse striatum (**Figure 3**), which was consistent with the results from previous ISH studies (Turchan et al., 1997; Lobo et al., 2006; Labouesse et al., 2018). The signal for *Penk* developed intensely after an overnight incubation as HCR amplification proceeded, although the overnight incubation also resulted in slight background staining. Such *Penk*-positive cells were never observed in the reaction buffer without H2 hairpin DNA, suggesting that simple hybridization of H1 with a probe for *Penk* mRNA was not enough to visualize *Penk* mRNA-positive cells.

Although modification and adoption of the short hairpin *in situ* HCR was reported to detect very abundant neuropeptide mRNAs (Sui et al., 2016), the amplification reached a plateau within an hour and the polymerized products were much smaller (approximately 1 kb) than those observed in the current study.

The gel electrophoresis of our short hairpin DNAs showed at least 400-fold amplification to develop more than 10 kb double-strand products from 42 nt single-strand hairpin DNAs (**Figure 2**). Compared with 42-nt hairpin DNAs, 36-nt hairpin DNAs exhibited lower HCR efficiency *in vitro* (**Figure 2A**) and *in situ* (**Supplementary Figure S3**), which may be due to a short toehold/loop length that renders hairpin monomer stable.

Such strong amplification by HCR using our short hairpin DNAs enabled us to visualize low abundance mRNAs such as *Oxtr* mRNA. Although G-protein-coupled receptors are often difficult to visualize by enzyme-based fluorescent ISH because of their low abundance, *in situ* HCR successfully detected weak *Oxtr* mRNA expression in the MPOA and BNST, consistent with previous studies (Young et al., 1997; Okabe et al., 2017) and

Allen brain atlas[3]. *Oxtr* mRNA was detected using chromogenic ISH (CISH) using alkaline phosphatase and BCIP/NBT after a long chromogenic reaction which is thought to be most sensitive among enzyme-based conventional ISH (Bonn et al., 2012). We also confirmed that the sensitivity of CISH was superior to that of ISH with tyramide signal amplification for low abundance mRNA. Importantly, the distribution of *Oxtr* mRNA detected by *in situ* HCR was largely matched with the result of CISH, suggesting that the sensitivity of *in situ* HCR was comparable to that of CISH. Furthermore, *in situ* HCR has several advantages over CISH such as simultaneous multiplex imaging and an elevated ability for the probes to penetrate.

Probe Design

In this study, we detected six genes using five or ten sets of split probes per gene. In the original report of split probes (Choi et al., 2018), the authors recommended more than 20 sets of probes to increase signal/noise ratio and precision, because the number of probes theoretically correlates signal intensity. As shown in **Figure 8**, five sets of probes can visualize a single mRNA, although the imaging of a single-molecule requires a high N.A. lens (e.g., >1.3). Ten sets of probes allowed us to visualize low abundance mRNA such as *Oxtr* at a relatively low magnification using a 20× objective lens with 0.75 N.A. (**Figure 5**). Additional probe sets may increase signal/noise ratio and precision, while it costs more. The minimum number of probes for appropriate imaging needs to be determined by users based on many factors including the imaging environment, the intensity of autofluorescence, conjugated fluorophore, required resolution, and precision.

We designed split probes according to Choi et al. (2018). The sequence for probes were chosen in consideration of GC contents and homology without further optimization and evaluation, because the split probes were very robust for non-specific hybridization (Choi et al., 2018). Gene expressions shown in this study were consistent with previous studies. Therefore, the design of new probes for target genes is as easy and fast as probes for conventional ISH.

Probe penetration is a key factor for the sensitivity of ISH. To enhance penetration, proteinase K treatment has been widely used in ISH in addition to the fragmentation of long probes, although some endogenous proteins are degraded by proteinase K treatment. Some reports proposed organic solvents as an alternative to proteinase K treatment in the *Drosophila* embryo (Nagaso et al., 2001; Jaeger et al., 2004), but these techniques were not as effective as the proteinase K treatment in mouse neural tissue (data not shown). Therefore, in the case of ISH with immunohistochemistry, there was a trade-off in the use of proteinase K between better ISH probe penetration and better preservation of antigens, such as c-Fos, for immunohistochemistry of mouse neural tissue. There was a report on the combined use of *in situ* HCR with immunohistochemistry to detect both mRNA and proteins (Zhuang et al., 2020). However, the authors adopted proteinase K treatment, which requires additional optimization of immunohistochemistry such as adjusting the concentration of antibodies. *In situ* HCR using short hairpins overcomes these issues. *In situ* HCR without proteinase K treatment showed *Vglut2* mRNA signals comparable to those observed following proteinase K treatment (**Figure 6**).

Multiplex *in situ* HCR

Using three hairpin DNA sets, *in situ* HCR demonstrated that *Penk*-positive cells in the mouse striatum were also *Drd2*-positive, but *Drd1*-negative (**Figure 7**). Almost all striatal neurons in mice express either *Drd1* or *Drd2* mRNA, and *Drd2*-positive neurons express *Penk* mRNA, as demonstrated by ISH, cell-assembly microarray using transgenic reporter mice and single-cell RNA-seq (Lobo et al., 2006; Heiman et al., 2008; Gokce et al., 2016; Labouesse et al., 2018). *In situ* HCR in this study exactly reproduced cell data revealed by the previous studies. Thus, multiplex *in situ* HCR works to visualize different sets of mRNAs simultaneously with a high signal-to-noise ratio. Tyramide signal amplification has been a popular approach for performing multiplexed fluorescent ISH (Zaidi et al., 2000; Lauter et al., 2011a,b; Bonn et al., 2012; Tsuneoka et al., 2015, 2017b). It has been used with different hapten-labeled probes, peroxidase-conjugated anti-hapten antibodies, and fluorophore-conjugated tyramides. ISH using tyramide signal amplification requires optimization for each step, requiring substantial labor from researchers. Also, antibody reactions and subsequent amplification steps should be performed separately for each target mRNA after the deactivation of the enzyme. In contrast, the *in situ* HCR system can simultaneously develop multiple colors and show autonomous suppression of noise without further optimization per target mRNA (Choi et al., 2014, 2018). Such advantages were also observed with the short hairpin DNAs designed in this study. Moreover, the current modification for the short hairpin DNA design implies further signal amplification by modifying the hairpin sequence, such as is used in the branched HCR system (Xu and Zheng, 2016; Bi et al., 2017; Liu et al., 2018; Wu et al., 2019).

Single-molecule fluorescent ISH has become a powerful technique not only for analyzing subcellular localization of specific mRNAs (Chen et al., 2016; Samacoits et al., 2018) but also for demonstrating the presence of low abundance mutant mRNAs (Haimovich and Gerst, 2018; Marras et al., 2019), long noncoding RNAs (Chen et al., 2016), ribosome-mRNA interactions (Burke et al., 2017) and comprehensive transcriptional analyses *in situ* (Shah et al., 2016; Moffitt et al., 2018). The signals from two different probes designed for detection of *Moxd1* mRNA were largely matched to each other at subcellular resolution (**Figure 8**). This suggests that *in situ* HCR using short hairpin DNAs is also applicable for single-molecule fluorescent ISH with a specific imaging device, similar to the original hairpin *in situ* HCR methods (Choi et al., 2014, 2018). Because, we used a small number of probe sets (five probe sets) and the thresholds were determined to minimize false-positive signals derived from tissue autofluorescence, not all the signal from one channel coincide with those from another channel. Increasing the number of probe sets will gain a higher signal/noise ratio and precision.

[3]http://mouse.brain-map.org

Summary and Advantage of Short Hairpin DNA

In summary, our short hairpin *in situ* HCR enables the visualization of low abundance mRNA and multiple mRNAs and the simultaneous detection of mRNA and protein without proteinase K treatment. When designing short hairpins, the following points should be taken into account; length of toehold/loop, end bases of toehold/loop, the number of G and C on one strand of the stem domain, structures of fluorophores and linker length. The advantages of short hairpin DNAs are low cost and high permeability without proteinase K treatment. Given that the length of DNA decreases from 72 nt to 42 nt, the cost for oligo DNA synthesis per mole decreases by 66% ($1–42^2/72^2$). Also, as the oligos get longer, mis-synthesized oligos increase exponentially, which further makes short hairpins cost-effective.

DATA AVAILABILITY STATEMENT

All data are available from the corresponding authors upon reasonable request.

ETHICS STATEMENT

The animal study was reviewed and approved by Institutional Animal Care and Use Committee of Toho University.

AUTHOR CONTRIBUTIONS

YT: conceptualization, methodology and formal analysis. YT and HF: writing, funding acquisition and supervision.

FUNDING

This work was supported by Takeda Science Foundation (to YT), Grant for Basic Science Research Projects from the Sumitomo Foundation (to YT), Uehara Memorial Foundation (to HF) and Japan Society for the Promotion of Science (JSPS) Kakenhi (18K06509 to YT and 17H05583 to HF).

ACKNOWLEDGMENTS

We are grateful to Hiroko Arai, Akane Iijima, Naomi Ohno, Moana Ohnishi and Haruka Arai for excellent technical assistance for this study, and Sachine Yoshida and Mayuko Oka for helpful discussions.

SUPPLEMENTARY MATERIAL

The Supplementary Material for this article can be found online at: https://www.frontiersin.org/articles/10.3389/fnmol.2020.00075/full#supplementary-material.

REFERENCES

Ang, Y. S., and Yung, L. L. (2016). Rational design of hybridization chain reaction monomers for robust signal amplification. *Chem. Commun.* 52, 4219–4222. doi: 10.1039/c5cc08907g

Bi, S., Yue, S., and Zhang, S. (2017). Hybridization chain reaction: a versatile molecular tool for biosensing, bioimaging, and biomedicine. *Chem. Soc. Rev.* 46, 4281–4298. doi: 10.1039/c7cs00055c

Bonn, M., Schmitt, A., and Asan, E. (2012). Double and triple *in situ* hybridization for coexpression studies: combined fluorescent and chromogenic detection of neuropeptide Y (NPY) and serotonin receptor subtype mRNAs expressed at different abundance levels. *Histochem. Cell Biol.* 137, 11–24. doi: 10.1007/s00418-011-0882-3

Burke, K. S., Antilla, K. A., and Tirrell, D. A. (2017). A fluorescence *in situ* hybridization method to quantify mRNA translation by visualizing ribosome-mRNA interactions in single cells. *ACS Cent. Sci.* 3, 425–433. doi: 10.1021/acscentsci.7b00048

Chen, X., Briggs, N., McLain, J. R., and Ellington, A. D. (2013). Stacking nonenzymatic circuits for high signal gain. *Proc. Natl. Acad. Sci. U S A* 110, 5386–5391. doi: 10.1073/pnas.1222807110

Chen, F., Wassie, A. T., Cote, A. J., Sinha, A., Alon, S., Asano, S., et al. (2016). Nanoscale imaging of RNA with expansion microscopy. *Nat. Methods* 13, 679–684. doi: 10.1038/nmeth.3899

Choi, H. M. T., Beck, V. A., and Pierce, N. A. (2014). Next-generation *in situ* hybridization chain reaction: higher gain, lower cost, greater durability. *ACS Nano* 8, 4284–4294. doi: 10.1021/nn405717p

Choi, H. M. T., Calvert, C. R., Husain, N., Huss, D., Barsi, J. C., Deverman, B. E., et al. (2016). Mapping a multiplexed zoo of mRNA expression. *Development* 143, 3632–3637. doi: 10.1242/dev.140137

Choi, H. M. T., Chang, J. Y., Trinh, L. A., Padilla, J. E., Fraser, S. E., and Pierce, N. A. (2010). Programmable *in situ* amplification for multiplexed imaging of mRNA expression. *Nat. Biotechnol.* 28, 1208–1212. doi: 10.1038/nbt.1692

Choi, H. M. T., Schwarzkopf, M., Fornace, M. E., Acharya, A., Artavanis, G., Stegmaier, J., et al. (2018). Third-generation *in situ* hybridization chain reaction: multiplexed, quantitative, sensitive, versatile, robust. *Development* 145:dev165753. doi: 10.1242/dev.165753

Dirks, R. M., and Pierce, N. A. (2004). Triggered amplification by hybridization chain reaction. *Proc. Natl. Acad. Sci. U S A* 101, 15275–15278. doi: 10.1073/pnas.0407024101

Funato, H., Saito-Nakazato, Y., and Takahashi, H. (2000). Axonal growth from the habenular nucleus along the neuromere boundary region of the diencephalon is regulated by semaphorin 3F and netrin-1. *Mol. Cell. Neurosci.* 16, 206–220. doi: 10.1006/mcne.2000.0870

Gokce, O., Stanley, G. M., Treutlein, B., Neff, N. F., Camp, J. G., Malenka, R. C., et al. (2016). Cellular taxonomy of the mouse striatum as revealed by single-Cell RNA-seq. *Cell Rep.* 16, 1126–1137. doi: 10.1016/j.celrep.2016.06.059

Haimovich, G., and Gerst, J. E. (2018). Single-molecule fluorescence *in situ* hybridization (smFISH) for RNA detection in adherent animal cells. *Bioprotocol* 8:21. doi: 10.21769/bioprotoc.3070

Heiman, M., Schaefer, A., Gong, S., Peterson, J. D., Day, M., Ramsey, K. E., et al. (2008). A translational profiling approach for the molecular characterization of CNS cell types. *Cell* 135, 738–748. doi: 10.1016/j.cell.2008.10.028

Jaeger, J., Surkova, S., Blagov, M., Janssens, H., Kosman, D., Kozlov, K. N., et al. (2004). Dynamic control of positional information in the early *Drosophila* embryo. *Nature* 430, 368–371. doi: 10.1038/nature02678

Jensen, E. (2014). Technical review: *in situ* hybridization. *Anat. Rec.* 297, 1349–1353. doi: 10.1002/ar.22944

Komatsu, Y., Kojima, N., Sugino, M., Mikami, A., Nonaka, K., Fujinawa, Y., et al. (2008). Novel amino linkers enabling efficient labeling and convenient purification of amino-modified oligonucleotides. *Bioorg. Med. Chem.* 16, 941–949. doi: 10.1016/j.bmc.2007.10.011

Krumlauf, R., Holland, P. W. H., McVey, J. H., and Hogan, B. L. M. (1987). Developmental and spatial patterns of expression of the mouse homeobox gene, Hox 2.1. *Development* 99, 603–617.

Labouesse, M. A., Sartori, A. M., Weinmann, O., Simpson, E. H., Kellendonk, C., and Weber-Stadlbauer, U. (2018). Striatal dopamine 2 receptor upregulation during development predisposes to diet-induced obesity by reducing

energy output in mice. *Proc. Natl. Acad. Sci. U S A* 115, 10493–10498. doi: 10.1073/pnas.1800171115

Larsson, C., Grundberg, I., Söderberg, O., and Nilsson, M. (2010). *in situ* detection and genotyping of individual mRNA molecules. *Nat. Methods* 7, 395–397. doi: 10.1038/nmeth.1448

Lauter, G., Soll, I., and Hauptmann, G. (2011a). Multicolor fluorescent *in situ* hybridization to define abutting and overlapping gene expression in the embryonic zebrafish brain. *Neural Dev.* 6:10. doi: 10.1186/1749-8104-6-10

Lauter, G., Söll, I., and Hauptmann, G. (2011b). Two-color fluorescent *in situ* hybridization in the embryonic zebrafish brain using differential detection systems. *BMC Dev. Biol.* 11:43. doi: 10.1186/1471-213x-11-43

Liu, L., Liu, J.-W., Wu, H., Wang, X.-N., Yu, R.-Q., and Jiang, J.-H. (2018). Branched hybridization chain reaction circuit for ultrasensitive localizable imaging of mRNA in living cells. *Anal. Chem.* 90, 1502–1505. doi: 10.1021/acs.analchem.7b04848

Lobo, M. K., Karsten, S. L., Gray, M., Geschwind, D. H., and Yang, X. W. (2006). FACS-array profiling of striatal projection neuron subtypes in juvenile and adult mouse brains. *Nat. Neurosci.* 9, 443–452. doi: 10.1038/nn1654

Marcus, J. N., Aschkenasi, C. J., Lee, C. E., Chemelli, R. M., Saper, C. B., Yanagisawa, M., et al. (2001). Differential expression of orexin receptors 1 and 2 in the rat brain. *J. Comp. Neurol.* 435, 6–25. doi: 10.1002/cne.1190

Marras, S. A. E., Bushkin, Y., and Tyagi, S. (2019). High-fidelity amplified FISH for the detection and allelic discrimination of single mRNA molecules. *Proc. Natl. Acad. Sci. U S A* 116, 13921–13926. doi: 10.1073/pnas.1814463116

Moffitt, J. R., Bambah-Mukku, D., Eichhorn, S. W., Vaughn, E., Shekhar, K., Perez, J. D., et al. (2018). Molecular, spatial, and functional single-cell profiling of the hypothalamic preoptic region. *Science* 5324:eaau5324. doi: 10.1126/science.aau5324

Moorman, A. F. M., Houweling, A. C., de Boer, P. A. J., and Christoffels, V. M. (2001). Sensitive nonradioactive detection of mRNA in tissue sections: novel application of the whole-mount *in situ* hybridization protocol. *J. Histochem. Cytochem.* 49, 1–8. doi: 10.1177/002215540104900101

Nagaso, H., Murata, T., Day, N., and Yokoyama, K. K. (2001). Simultaneous detection of RNA and protein by *in situ* hybridization and immunological staining. *J. Histochem. Cytochem.* 49, 1177–1182. doi: 10.1177/002215540104900911

Okabe, S., Tsuneoka, Y., Takahashi, A., Ooyama, R., Watarai, A., Maeda, S., et al. (2017). Pup exposure facilitates retrieving behavior *via* the oxytocin neural system in female mice. *Psychoneuroendocrinology* 79, 20–30. doi: 10.1016/j.psyneuen.2017.01.036

Samacoits, A., Chouaib, R., Safieddine, A., Traboulsi, A.-M., Ouyang, W., Zimmer, C., et al. (2018). A computational framework to study sub-cellular RNA localization. *Nat. Commun.* 9:4584. doi: 10.1038/s41467-018-06868-w

Shah, S., Lubeck, E., Schwarzkopf, M., He, T. F., Greenbaum, A., Sohn, C. H., et al. (2016). Single-molecule RNA detection at depth by hybridization chain reaction and tissue hydrogel embedding and clearing. *Development* 143, 2862–2867. doi: 10.1242/dev.138560

Sui, Q.-Q., Zhu, J., Li, X., Knight, G. E., He, C., Burnstock, G., et al. (2016). A modified protocol for the detection of three different mRNAs with a new-generation *in situ* hybridization chain reaction on frozen sections. *J. Mol. Histol.* 47, 511–529. doi: 10.1007/s10735-016-9696-x

Tsuneoka, Y., Maruyama, T., Yoshida, S., Nishimori, K., Kato, T., Kuroda, K. O., et al. (2013). Functional, anatomical, and neurochemical differentiation of medial preoptic area subregions in relation to maternal behavior in the mouse. *J. Comp. Neurol.* 521, 1633–1663. doi: 10.1002/cne.23251

Tsuneoka, Y., Tokita, K., Yoshihara, C., Amano, T., Esposito, G., Huang, A. J., et al. (2015). Distinct preoptic-BST nuclei dissociate paternal and infanticidal behavior in mice. *EMBO J.* 34, 2652–2670. doi: 10.15252/embj.201591942

Tsuneoka, Y., Tsukahara, S., Yoshida, S., Takase, K., Oda, S., Kuroda, M., et al. (2017a). Moxd1 is a marker for sexual dimorphism in the medial preoptic area, bed nucleus of the stria terminalis and medial amygdala. *Front. Neuroanat.* 11:26. doi: 10.3389/fnana.2017.00026

Tsuneoka, Y., Yoshida, S., Takase, K., Oda, S., Kuroda, M., and Funato, H. (2017b). Neurotransmitters and neuropeptides in gonadal steroid receptor-expressing cells in medial preoptic area subregions of the male mouse. *Sci. Rep.* 7:9809. doi: 10.1038/s41598-017-10213-4

Turchan, J., Lasoń, W., Budziszewska, B., and Przewocka, B. (1997). Effects of single and repeated morphine administration on the prodynorphin, proenkephalin and dopamine D2 receptor gene expression in the mouse brain. *Neuropeptides* 31, 24–28. doi: 10.1016/s0143-4179(97)90015-9

Urbanek, M. O., Nawrocka, A. U., and Krzyzosiak, W. J. (2015). Small RNA detection by *in situ* hybridization methods. *Int. J. Mol. Sci.* 16, 13259–13286. doi: 10.3390/ijms160613259

Wu, Q., Wang, H., Gong, K., Shang, J., Liu, X., and Wang, F. (2019). Construction of an autonomous nonlinear hybridization chain reaction for extracellular vesicles-associated MicroRNAs discrimination. *Anal. Chem.* 91, 10172–10179. doi: 10.1021/acs.analchem.9b02181

Xu, Y., and Zheng, Z. (2016). Direct RNA detection without nucleic acid purification and PCR: combining sandwich hybridization with signal amplification based on branched hybridization chain reaction. *Biosens. Bioelectron.* 79, 593–599. doi: 10.1016/j.bios.2015.12.057

Yamaguchi, T., Kawakami, S., Hatamoto, M., Imachi, H., Takahashi, M., Araki, N., et al. (2015). *In situ* DNA-hybridization chain reaction (HCR): a facilitated *in situ* HCR system for the detection of environmental microorganisms. *Environ. Microbiol.* 17, 2532–2541. doi: 10.1111/1462-2920.12745

Young, L. J., Muns, S., Wang, Z., and Insel, T. R. (1997). Changes in oxytocin receptor mRNA in rat brain during pregnancy and the effects of estrogen and interleukin-6. *J. Neuroendocrinol.* 9, 859–865. doi: 10.1046/j.1365-2826.1997.00654.x

Zaidi, A. U., Enomoto, H., Milbrandt, J., and Roth, K. A. (2000). Dual fluorescent *in situ* hybridization and immunohistochemical detection with tyramide signal amplification. *J. Histochem. Cytochem.* 48, 1369–1375. doi: 10.1177/002215540004801007

Zhuang, P., Zhang, H., Welchko, R. M., Thompson, R. C., Xu, S., and Turner, D. L. (2020). Combined microRNA and mRNA detection in mammalian retinas by *in situ* hybridization chain reaction. *Sci. Rep.* 10:351. doi: 10.1038/s41598-019-57194-0

Conflict of Interest: The authors declare that the research was conducted in the absence of any commercial or financial relationships that could be construed as a potential conflict of interest.

frontiers in Molecular Neuroscience

ORIGINAL RESEARCH
published: 08 September 2020
doi: 10.3389/fnmol.2020.00168

Development and Validation of CRISPR Activator Systems for Overexpression of CB1 Receptors in Neurons

*Valentina Di Maria[1], Marine Moindrot[1], Martin Ryde[1], Antonino Bono[1], Luis Quintino[2] and Marco Ledri[1]**

[1] *Laboratory of Molecular Neurophysiology and Epilepsy, Department of Clinical Sciences, Epilepsy Center, Lund University, Lund, Sweden,* [2] *Laboratory of CNS Gene Therapy, Department of Experimental Medical Sciences, Lund University, Lund, Sweden*

Gene therapy approaches using viral vectors for the overexpression of target genes have been for several years the focus of gene therapy research against neurological disorders. These approaches deliver robust expression of therapeutic genes, but are typically limited to the delivery of single genes and often do not manipulate the expression of the endogenous locus. In the last years, the advent of CRISPR-Cas9 technologies have revolutionized many areas of scientific research by providing novel tools that allow simple and efficient manipulation of endogenous genes. One of the applications of CRISPR-Cas9, termed CRISPRa, based on the use of a nuclease-null Cas9 protein (dCas9) fused to transcriptional activators, enables quick and efficient increase in target endogenous gene expression. CRISPRa approaches are varied, and different alternatives exist with regards to the type of Cas9 protein and transcriptional activator used. Several of these approaches have been successfully used in neurons *in vitro* and *in vivo*, but have not been so far extensively applied for the overexpression of genes involved in synaptic transmission. Here we describe the development and application of two different CRISPRa systems, based on single or dual Lentiviral and Adeno-Associated viral vectors and VP64 or VPR transcriptional activators, and demonstrate their efficiency in increasing mRNA and protein expression of the *Cnr1* gene, coding for neuronal CB1 receptors. Both approaches were similarly efficient in primary neuronal cultures, and achieved a 2–5-fold increase in *Cnr1* expression, but the AAV-based approach was more efficient *in vivo.* Our dual AAV-based VPR system in particular, based on *Staphylococcus aureus* dCas9, when injected in the hippocampus, displayed almost complete simultaneous expression of both vectors, high levels of dCas9 expression, and good efficiency in increasing *Cnr1* mRNA as measured by *in situ* hybridization. In addition, we also show significant upregulation of CB1 receptor protein *in vivo*, which is reflected by an increased ability in reducing neurotransmitter release, as measured by electrophysiology. Our results show that CRISPRa techniques could be successfully used in neurons to target overexpression of genes involved in synaptic transmission, and can potentially represent a next-generation gene therapy approach against neurological disorders.

Keywords: CRISPR, CB1, Cas9 activators, AAV (Adeno-Associated virus), lentivirus, gene therapy

OPEN ACCESS

Edited by:
Felix Viana,
Institute of Neurosciences of Alicante (IN), Spain

Reviewed by:
Stephane Pelletier,
Indiana University Bloomington, United States
Gabriele Lignani,
University College London, United Kingdom

****Correspondence:***
Marco Ledri
marco.ledri@med.lu.se

Received: *14 January 2020*
Accepted: *11 August 2020*
Published: *08 September 2020*

Citation:
Di Maria V, Moindrot M, Ryde M, Bono A, Quintino L and Ledri M (2020) Development and Validation of CRISPR Activator Systems for Overexpression of CB1 Receptors in Neurons. Front. Mol. Neurosci. 13:168. doi: 10.3389/fnmol.2020.00168

INTRODUCTION

Gene therapy approaches using engineered viral vectors have been for many years the focus of developing alternative treatment strategies against several neurological disorders, such as Parkinson's disease, Alzheimer's Disease and epilepsy. These strategies rely on the delivery of therapeutic genes in specific areas of interest and aim to interfere with disease processes or restore pathological alterations in brain networks key to the development of disease symptoms (Simonato et al., 2013; Simonato, 2014; Combs et al., 2016; Axelsen and Woldbye, 2018; Ingusci et al., 2019). Similar approaches, including also the use of transgenic animals or knock-down approaches, have also been used extensively to interrogate the function of specific genes in particular disease states. While valuable, these techniques often do not manipulate the expression of the endogenous gene locus and are mostly limited to affecting one target gene at a time (Kunieda et al., 2002; Götz and Ittner, 2008; Harvey et al., 2008, 2012; Dawson et al., 2018).

In the last years, CRISPR-Cas9 (clustered regularly interspaced short palindromic repeats (CRISPR) associated nuclease 9) has revolutionized many areas of scientific research by aiding the development of advanced tools addressing certain limitations of traditional gene therapy approaches (Jie et al., 2015; Dai et al., 2016; Koo and Kim, 2016; Lino et al., 2018; Jacinto et al., 2020). Specifically, the development of inducible CRISPR-Cas9 transcriptional activator methods (CRISPRa) shows great potential toward studying the impact of upregulating genes that are involved in neuronal activity and synaptic function, particularly during disease states. These activator methods are based on the use of the nuclease-null (or "dead" dCas9) variants fused to transcriptional activator domains, allowing Cas9 to be used as a tool for modulate transcription activity (Gilbert et al., 2013; Maeder et al., 2013; Mali et al., 2013; Perez-Pinera et al., 2013; Chavez et al., 2015). The most popular of such CRISPR-Cas9 activator methods involves the use of VP64 (and combinations) transcriptional activator domains fused to the C-terminus of *Streptococcus pyogenes* (SP)-dCas9, and were shown to be able to increase endogenous expression (Gilbert et al., 2013; Mali et al., 2013; Perez-Pinera et al., 2013) of genes such as human *VEGFA* (Maeder et al., 2013), *L1RN*, *SOX2*, and *OCT4* genes (Cheng et al., 2013). However, the large size of such constructs only allowed their insertion into Lentiviral (LV) particles. These viral vectors have limited distribution from injection sites, when compared to the more widely-used Adeno Associated Virus (AAV). More recently, several other transcriptional activator domains have been described, such as VPR (Chavez et al., 2015), a tripartite effector composed of VP64, p65, and Rta transcription activator domains showing much increased induction of gene expression compared to traditional VP64-based approaches. Chavez et al. (2015) demonstrated the possibility to strongly activate the expression of *MIAT*, *NeuroD1*, *Ascl1*, *RhoxF2* genes using a dCas9-VPR activator system. In addition, an *Sp*dCas9-VPR based approach has been recently shown to be effective in inducing Brain Derived Neurotrophic Factor (BDNF) gene expression in neurons (Savell et al., 2019). But, as stated above, the limited coverage area associated with LV injections in the brain renders this approach less ideal for studies requiring delivery of target genes in larger brain areas.

To package a VPR-based activator system in AAV vectors, Ma et al. (2018) were able to modify the canonical *Sp*dCas9-VPR structure with a smaller ortholog from *Staphylococcus aureus* (*Sa*dCas9) and shorten the VPR domain. Although *Sp*dCas9 and *Sa*dCas9 derive from different bacterial species, when fused to VPR they induce the same transcriptional activator mechanisms. This alternative *Sa*dCas9-based system when delivered in several cell lines, was able to induce overexpression of several target genes.

In the recent years, various combinations of dCas9 proteins and transcriptional activators have been used successfully to increase gene expression *in vitro* and *in vivo* (Chavez et al., 2016; Zhou et al., 2018). Single and dual AAV vector systems have proven functional in overexpressing a variety of target genes, but the possibility of changing neurotransmission by altering the expression of synaptic proteins *in vivo* with CRISPRa has not been fully explored yet.

In this study, we added to the growing toolbox of CRISPRa systems by developing and verifying the performance of different *Sp*dCas9 and *Sa*dCas9-based activator approaches. To upregulate the expression of genes directly involved in neuronal and network activity, we aimed to adapt these technologies for the overexpression of *Cnr1,* the gene coding for Cannabinoid Receptor 1 (CB1), an endocannabinoid receptor expressed pre-synaptically in both excitatory and inhibitory neurons, responsible for feedback control of neurotransmitter release (Mackie, 2006).

MATERIALS AND METHODS

Design of sgRNAs

The sgRNAs were designed to bind the promoter region of the mouse *Cnr1* gene. Using CHOPCHOP web tool[1], we were able to select the optimum target site for CRISPR-Cas9 activation system. Four different sgRNAs were identified to bind 400 bp upstream to the transcription starting site (TSS) of the Cnr1 promoter. Each sgRNAs consist of 20-21 nucleotide followed by specific *Sa*Cas9 or *Sp*Cas9 sgRNA scaffolds. The sgRNAs sequences are provided in **Supplementary Table 1**.

Screening of gRNAs

Approximately 16000 HEK293T cells/well were plated in 96 well-plates. After 6 h, cells were co-transfected with a mixture polyethyleneimine (PEI) transfection reagent and *Sa*dCas9-VPR, sgRNAs-Cnr1, CMV-BFP and Cnr1-tdTomato expressing plasmids with a DNA molar ratio of 2:1:1:0.1, respectively in a total of 200 ng per well using PEI:DNA ratio of 5:1. For the control conditions, cells were transfected using the same conditions described before and a random sgRNA expressing plasmid instead of sgRNAs-Cnr1 plasmid. Forty eight hours after co-transfection, cell well fixed with 1% PFA and the fluorescent intensity of BFP and tdTomato were measured. The fluorescent

[1]https://chopchop.cbu.uib.no/

intensity of BFP, tdTomato, and the ratio tdTomato/BFP were normalized with the control condition.

Molecular Cloning Methods

The molecular cloning methods (e.g., restriction digestion, ligation, and DNA electrophoresis in agarose gel) were performed according to standard procedures. DNA inserts and back bones were separately digested with restriction enzymes provided by Thermo Fisher Scientific and the ligation was performed according to the instruction provided by Anza T4 DNA ligase (Thermo Fisher Scientific). Zero Blunt TOPO PCR Cloning (Invitrogen) was used for the direct insertion of the sgRNAs-CNR1 blunt-end PCR product in a plasmid vector. The Golden Gate assembly method was used to accommodate the sgRNAs into the destination vector. The fragments were previously designed to have compatible 4 base overhangs in order to create circular vector (Engler et al., 2008; Potapov et al., 2018). The DNA was digested with restriction enzymes and the fragments were ligated with T4 DNA ligase (Thermo Fischer Scientific) in the same reaction. After the ligation reactions, the DNA was used to transform One Shot TOP10 (Invitrogen) or One Shot Stbl3 chemically competent bacteria (Invitrogen) using the heat-shock procedures. Plasmid DNA extraction and purification was done by using GeneJET Plasmid Miniprep Kit (Thermo Fischer Scientific) or PureLink™ HiPure Plasmid Maxiprep Kit (Thermo Fisher Scientific) in other to obtain high number copies of transfection-grade plasmid. DNA fragments were isolated and purified from 1% agarose gel with the QIAquick Gel Extraction Kit (Qiagen).

Lentivirus and AAV Productions

Recombinant lentiviruses were produced by co-transfection of HEK 293T cells with the transgene vector and the packaging plasmids pBR8.91 and pMD2G using the standard PEI method (Zufferey et al., 1997; Quintino et al., 2018). The lentivirus were harvested 48 h post-transfection and the pellet was obtained by ultracentrifugation of the medium containing lentivirus at 77,000 g for 90 min. Subsequently, the lentivirus were titered by infecting the HEK293T cells and after 72 h the DNA was extracted from the cells using DNeasy blood and tissue kit (Qiagen). qPCR was performed to amplify the woodchuck hepatitis virus post regulatory element (WPRE) and the human albumin (Alb). Relative quantification of WPRE and Alb expression was calculated by ΔΔCT method (Livak and Schmittgen, 2001). The resulting values were then used to estimate the titer of each lentiviral vector produced (Quintino et al., 2013, 2018; **Supplementary Table 2**).

Recombinant AAV vectors were produced by co-transfection of HEK 293T cells with the transgene plasmid and AAV8 plasmid from Plasmid Factory (pdp8), using PEI transfection method (Gray et al., 2011). The AAVs were harvested 72 h after transfection using polyethylene glycol 8000 (PEG8000) for the AAVs precipitation and chloroform for AAVs extraction (Davidsson et al., 2019). The AAV were collected and resuspended in PBS using Amicon Ultra-0.5 Centrifugal filters (Merck Millipore) (Wu et al., 2001). To calculate the number of genome-containing particles of the AAVs, we first made a standard curve using 10^2–10^8 copies of linearized plasmid. Subsequently, purified AAV vectors and standard curve DNA samples were quantified by qPCR using WPRE primers.

Animals

P0-P1 animals of both sexes and 6–8 weeks old male C57BL/6 were used for *in vitro* and *in vivo* experiments, respectively. The experiments were conducted according to the Swedish Animal Welfare Agency as well as the international guidelines on the use of experimental animals.

Primary Neuronal Isolation and Transduction

Cortical primary neurons were obtained from P0-P1 day old C57BL/6 mice. The entire brain was removed from the skull and the cortical areas were dissected in a petri dish containing cold Hibernate-E media supplemented with B-27 serum. The tissue was subsequently digested in a solution containing Papain (Sigma) and HBSS (Gibco) for 30 min at 37°C and a single cell resuspension was formed. The cells were centrifuged at 150 g for 5 min and the pellet was resuspended by adding 2 mL of Neurobasal medium supplemented with B27, Glutamax and Pen/Strep. 110,000 cells/well were plated on Poly-D-Lysine coated coverslips in 24-well plates and incubated at 37°C in 5% CO_2. Half of the medium was changed 24 h after isolation and then every 2 days. Primary neurons were transduced with lentiviral viral vectors at a multiplicity of infection (MOI) 5 for a single viral vector transduction and MOI 10 for a dual viral vector transduction. 110,000 cortical primary neurons were also transduced with AAVs at an MOI of 10,000. Control cells transduced with vectors without sgRNAs (Empty) and non-treated cells were in some cases pooled and are referred to as "controls," as no difference was found in any of the analyzed parameters.

MEF Cell Culture and Transduction

Mouse Embryonic Fibroblast (MEF) were purchased from ATTC (ATCC® SCRC-1040 TM). The cells were cultured according to the standard procedures provided from the company. For the cell's transduction, approximately 50,000 cells were plated in a 6 well plate. After 3 h, the cells were transduced at a multiplicity of infection (MOI) 5 for a single viral vector transduction and MOI 10 (5 for each virus) for a dual viral vector transduction. As for primary neurons, control cells transduced with vectors without sgRNAs and non-treated cells were pooled and are referred to as "controls," as no difference was found in any of the analyzed parameters.

RNA Extraction and RT-qPCR

Animals used for RT-qPCR experiments were sacrificed by decapitation 3 weeks after lentivirus injection and 2 weeks after AAV injection. In correspondence to the injection site, the hippocampal hemisphere was removed and processed for total RNA extraction. Primary neurons an MEFs cultures were first washed with PBS to remove the residual medium, then there were processed for total RNA extraction. The RNA was extracted from

hippocampal tissue, primary neurons and MEFs by Trizol reagent (Invitrogen) and purified using GeneJET RNA Purification Kit (Thermo Fisher Scientific), according to the manufacturer's instructions. On-column digestion of DNA was performed using the DNAse digestion Kit (Invitrogen). Approximately 70–300 ng of total RNA were retrotranscribed into cDNA using High-Capacity RNA-to-cDNA™ Kit (Applied Biosystems) according to the manufacturer's instructions provided. RT-qPCR using Taqman assay, was used to amplify the mouse *Cnr1*, *Cas9,* and *Gapdh* genes. The thermal cycle conditions included a denaturation cycle of 95°C for 10 min, followed by 40 cycle of amplification at 95°C for 15 s and 60°C for 1 min. The experiments of gene expression profiling were done in triplicate in three independent experiments. The results were analyzed using the 2-ΔΔCT method described by Livak and Schmittgen (2001) and the *Gapdh* gene was used to normalize the data.

RNASeq

RNA libraries from primary neuronal cultures were generated starting from 15 ng of total RNA at 10 DIV, 7 days after virus transduction. RNA was processed using the SMART-Seq v4 Ultra low input RNA kit (Takara) followed by Nextera XT DNA library kit. Samples were analyzed on Nextseq500 using NSQ 500/550 Mid Output KT v2 (150 CYS).

Western Blot

Total proteins were extracted using N-PER™ Neuronal Protein Extraction agents (Thermo Fisher Scientific). After extraction, the lysate was subsequently centrifuged at 10,000 × g for 10 min at 4°C and the supernatant containing the proteins was used for protein quantification by Bradford assay. Five to twenty microgram of proteins were separated in a Bolt™ 4–12% Bis-Tris precast polyacrylamide gel (Thermo Fisher Scientific) and subsequently transferred to PVDF membranes using a Trans-Blot Turbo Transfer system (BioRad). Membranes were incubated about 6 h with a TBST solution (10 mM Tris, pH 8.0, 150 mM NaCl, 0.5% Tween 20) supplemented with 5% skim milk (Sigma-Adrich). Membranes were washed three times for 10 min with a TBST solution and incubated over-night with the primary antibody anti-CB1 (Rabbit, Immunogenes, 1:1000 or Cayman Chemicals, 1:200) in TBST and 5% skim milk. Subsequently, the secondary antibody was added in a concentration of 1:1000 (anti-rabbit HRP; Abcam) for 2 h at room temperature. The blots were subsequently developed with the ECL substrate (Pierce™ ECL western blotting substrate) according to the manufacturer's protocols. After protein detection, the membrane was treated with a stripping solution (1M Tris-HCL, 20% SDS and β-Mercaptoethanol) and incubate with the anti-β-actin antibody conjugated with HRP (Sigma-Aldrich 1:50,000) for 1 h at room temperature. The blots were washed and developed with the ECL method described before. Image capture was performed with a ChemiDoc XRS + camera from BioRad. Expression levels were calculated with ImageLab software and normalized to β-Actin.

Immunocytochemistry

Primary neurons were rinsed in PBS and rapidly fixed in 4% PFA for 15 min at room temperature (RT). Cells were permeabilized using a PBS solution containing 0.25% Triton X-100 (PBST) for 15 min at RT and then blocked for 2 h in PBST containing 5% Donkey serum. Primary antibodies were diluted in a PBST supplemented with 5% Donkey serum and incubated over night at 4°C. The primary antibody used were mouse anti-Map2 (Immunogene, 1:500) and rabbit anti HA-Tag (Thermo Fisher Scientific, 1:500). The secondary antibodies anti-mouse CY5 and anti-rabbit CY3 were added in a concentration of 1:500 an incubated for 2 h at RT in the dark. Primary neurons were washed with PBS for three times and subsequently loaded on a glass slide using a DABCO containing Hoechst diluted 1:1000. Images were taken on a Olympus BX51 upright fluorescent microscope. Quantification of markers was carried out manually by examining randomly three fields from three independent experiments and presented as percentage of double labeled cells.

Lentiviral and AAV Injections in Mouse Hippocampus

C57BL/6 mice were anesthetized using ∼2.5% Isoflurane and subsequently fixed into a stereotactic frame. The lentiviral resuspension was injected into two different points according to the following coordinates: Medio-Lateral (ML) 2,9, Antero-Posterior (AP) -3,6, Dorso-Ventral (DV) -3,6 and -2,8 (from Dura) and ML 3,6; AP -3,2 and DV -3,5 and -1,5 (from Dura). The AAV resuspension was also injected into two different positions according to the following coordinates: AP -2,2, ML -1,7, DV-1,9 and -1,3 (from Dura) and AP -3,3, ML -3,0 and DV -3,7 and -2,7 (from Dura). Two different injection points were used to reach both dorsal and ventral hippocampus. 0,5 μL of lentiviral resuspension and 0,4 μL of AAVs resuspension were injected for each injection point at rate of 0,1 μL/min using a glass capillary.

In situ Hybridization

The *in situ* hybridization was performed using the RNAScope method from Advanced Cell Diagnostics (ACD). According to the standard procedures, the mouse brain was removed from the skull and immediately frozen in liquid nitrogen. Before sectioning, the frozen brain was equilibrated for ∼1 h at −20°C. Subsequently, 15 μm thick sections were mounted onto Superfrost Plus Slides and kept drying at −20°C for 1 h. The slides were fixed in a chill 4% PFA for 15 min and immediately used for alcoholic dehydration procedure. The slides were kept drying at room temperature for 2 min before to proceed with the *in situ* hybridization protocol provided. The ZZ RNAScope probes used were the murine Cnr1, saCas9, EGFP, positive control Mm-Ppib and negative control DapB probes. The **Supplementary Table 3** shows the details of the probes used in these experiments. TSA Plus Cyanine 5 (Cy5) or FITC detection kit in a concentration 1:750 were used for signal amplification. At the end of the procedures, approximately 4 drops of DAPI were added to each slide. The slides were quickly covered with a ProLong Antifade Mountant (Invitrogen) and closed using a glass coverslip. The samples were kept dry and processed for confocal imaging the day after using a Nikon

A1 + confocal microscope equipped with 405, 488, 561, and 640 nm laser lines.

Analysis for quantification of RNAScope signals was performed using the Spot Detection algorithm in NIS Elements Advanced software (Nikon). Settings were selected to detect bright spots, clustered, with a typical diameter of 0.7 μm and contrast at 68.1. A region of interest (ROI) was drawn around the DG, CA3 and CA1 principal cell layers from images obtained with a 20 × 0.75 N.A. objective at Nyquist resolution (pixel size 0.14 μm), and detected spots were counted and normalized by the ROI area.

Electrophysiology

Three to six weeks after viral vector injections, animals were briefly anesthetized with isofluorane and decapitated. The brains were quickly removed and immersed into ice-cold cutting solution, containing, in mM: sucrose 75, NaCl 67, $NaHCO_3$ 26, glucose 25, KCl 2.5, NaH_2PO_4 1.25, $CaCl_2$ 0.5, and $MgCl_2$ 7 (pH 7.4, osmolarity 305–310 mOsm). The cerebellum was discarded, the hemispheres were separated by a single midline cut and transverse 400 μm slices were cut with a vibratome (VT1200S, Leica microsystems). Three to four slices per hemisphere were collected and stored into a submerged recovery chamber filled with cutting solution for 30 min at 34°C, before being transferred to a second maintenance chamber filled with recording aCSF, containing in mM: NaCl 119, $NaHCO_3$ 26, glucose 11, KCl 2.5, NaH_2PO_4 1.25, $CaCl_2$ 2, and $MgSO_4$ 1.3 (pH 7.4, osmolarity 295–305 mOsm). All solutions were constantly bubbled with carbogen gas (95% O_2 and 5% CO_2).

For recordings, individual slices were transferred to a dual superfusion recording chamber (Supertech, Hungary) where they were perfused on both sides with recording aCSF at a speed of 2.5 mL/min/channel, heated to 38°C by an in-line heater placed 10–20 cm before the recording chamber and a bubble trap. This assures a constant temperature in the chamber of 34°C. GFP fluorescence was inspected by illuminating the slices with a 488 nm LED light source (Prizmatix, Israel) while observing the image through a camera. Only slices where GFP expression was deemed sufficient and covered the whole hippocampal formation were used for recordings. At this stage, some of the slices showing good GFP expression were immediately and quickly frozen in dry ice for western blot experiments.

Glass capillaries pulled from borosilicate glass and back-filled with recording aCSF were used as both stimulation and recording electrodes. Stimulating electrodes were placed in the middle portion of the stratum radiatum in CA1 to stimulate Schaffer collaterals originating from CA3 pyramidal neurons, and were connected to a current stimulator, where single 0.1 ms, 20–150 μA square pulses were delivered through the electrode every 15 s. Field excitatory post-synaptic potentials (fEPSPs) were monitored from the stratum radiatum of CA1 through the recording electrode connected to a EPC-10 amplifier (HEKA, Germany) and PatchMaster software (HEKA), and sampled at 20 kHz. Only recordings showing clear separation between the stimulation artifact, the pre-synaptic fiber volley and the fEPSP were used for further analysis. An input-output analysis was performed on each slice to assess slice quality, and slices responding with fEPSPs of <1 mV amplitude at maximal stimulation (typically 120–150 μA) were discarded. Baseline stimulation strength was set at 40% of the maximum. After recording a stable baseline period of 20 min, WIN 55,212-2 (Sigma-Aldrich, Sweden) was dissolved in DMSO and added to the perfusion aCSF to reach a final concentration of 1 μM and a DMSO dilution of at least 1:10,000. While recording baseline, DMSO without WIN in aCSF was used as recording solution.

After recordings, slices were fixed in 4% PFA overnight, and GFP expression was once again confirmed by fluorescence microscopy the day after.

Statistical Analysis

All data are presented as the mean ± SEM, and *n* values indicate the number of independent experiments performed, the number of individual mice or slices. Significant differences were evaluated using an unpaired Student's *t*-test with Welch's correction or Mann-Whitney test where two groups were compared, or one-way analysis of variance (ANOVA) with Dunnett's *post hoc* test for multiple comparisons. Electrophysiological data was analyzed with two-way repeated measures ANOVA followed by Sidak's multiple comparison test to test for differences between time points over time. Statistical analyses were performed using Prism software (GraphPad). Group differences were considered statistically significant at $^*p < 0.05$.

RESULTS

*Sp*dCas9 Based Lentiviral System for the Spatial Control of *Cnr1* Gene Expression

We first generated two different Lentivirus-based CRISPR-dCas9 activator systems able to induce spatial control of *Cnr1* expression in mammalian target cells (**Figures 1A,E**). Both technologies are based on guide RNAs components, targeting the promoter region of the *Cnr1* gene, and the inactivated version of the Cas9 enzyme derived from *Streptococcus pyogenes* (*Sp*dCas9). The first system consists in a single vector carrying *Sp*dCas9 fused to the transcriptional activator domain VP64, a reporter gene GFP separated by a 2A sequence and four sgRNAs (LV-*Sp*dCas9-VP64-Cnr1, **Figure 1A**). The general promoter UbC drives the expression of *Sp*dCas9-VP64-2A-GFP, while the four gRNAs are driven by the human or murine hH1, h7SK, hU6 and mU6 promoters (**Figure 1A**). The second system is composed by *Sp*dCas9 fused to the transcriptional activator domain VPR in one vector (driven by the human Synapsin promoter, LV-*Sp*dCas9-VPR), and sgRNA components together with a reporter gene GFP in a second vector (LV-Cnr1-gRNA, **Figure 1E**).

We first evaluated constructs efficiency in MEFs cultures that do not normally express high level of *Cnr1*. MEFs were transduced with lentivirus carrying the single construct and after 72 h we validated gene activation by RT-PCR. Gene expression analysis showed a significant upregulation of *Cnr1* gene in MEFs transduced with LV-*Sp*dCas9-VP64-Cnr1 compared with controls (Fold Change (FC) 50.7 ± 0.57; Ctrl vs. Cnr1-gRNA; $p < 0.001$; $n = 6$) (**Supplementary Figure 1A**).

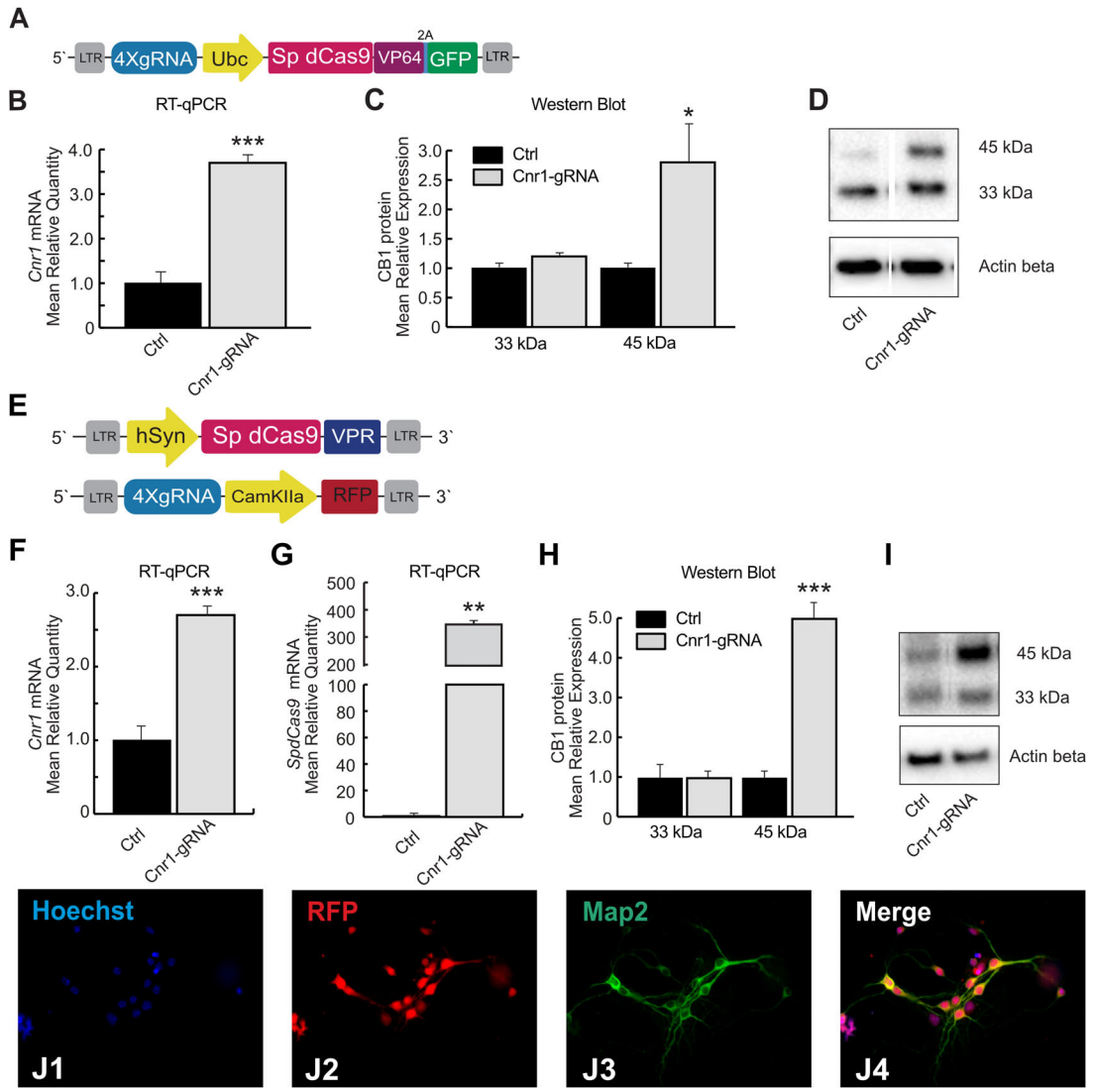

FIGURE 1 | *Sp*dCas9 based lentiviral system and modulation of *Cnr1* gene expression *in vitro*. **(A)** Schematic illustrating the main components of the single lentiviral vector LV-*Sp*dCas9-VP64-Cnr1. **(B)** mRNA expression level of the *Cnr1* gene in primary neurons transduced with the single lentiviral vector LV-*Sp*dCas9-VP64-Cnr1 (Cnr1-gRNA) compared with controls (Ctrl) (Unpaired Student's *t*-test, ***$p < 0.001$). **(C)** Expression level of the two immunoreactive CB_1 bands (~33 and 45 kDa) in primary neurons (Cnr1-gRNA vs. Ctrl, Unpaired Student's *t*-test, *$p < 0.05$). **(D)** WB analyses of total protein lysates from primary neurons. The upper panel shows the detection of the immunoreactive CB_1 bands (~33 and 45 kDa) and the lower panel shows β-actin detection for loading control. **(E)** Schematic of the main components of the dual viral vector system LV-*Sp*dCas9-VPR and LV-Cnr1-gRNA. **(F)** mRNA expression level of the *Cnr1* gene in primary neurons transduced with the dual viral vector system LV-*Sp*dCas9-VPR and LV-Cnr1-gRNA (Cnr1-gRNA) compared with controls (Ctrl) (Unpaired Student's *t*-test, ***$p < 0.001$). **(G)** mRNA expression level of the *spdCas9* gene in primary neurons (Unpaired Student's *t*-test, **$p < 0.01$). **(H)** Expression level of the two immunoreactive CB_1 bands (~33 and 45 kDa) in primary neurons (Cnr1-gRNA vs. Ctrl, Unpaired Student's *t*-test, ***$p < 0.001$). **(I)** WB analyses of total protein lysates from primary neurons. **(J1–J4)** Representative micrographs obtained with fluorescence microscopy of cortical primary neurons. The images show the Hoechst nuclear staining (Blue; **J1**), RFP expression (Red; **J2**) and GFP (Green; **J3**) expression. Scale bar: 80 μm.

To evaluate the efficiency of the single lentiviral vector in neurons, we used cortical primary neurons from early post-natal mice. Primary neurons were transduced with lentivirus 3 days after neuronal isolation (DIV 3) and 10 days after, we validated the efficiency of the vector by RT-PCR and WB analysis. Gene expression profiling using RT-PCR revealed a significant upregulation of *Cnr1* gene in cortical primary neurons transduced with the LV-*Sp*dCas9-VP64-Cnr1, compared with controls (FC 3.6 ± 0.17; Ctrl vs. Cnr1-gRNA; $p < 0.001$; $n = 6$) (**Figure 1B**). Western blot analysis revealed two immunoreactive CB_1 bands in primary neurons. The most prominent immunoreactive band had a molecular mass of ~33 kDa and the additional band a molecular mass of ~45 kDa. Protein expression analysis showed an increased expression of the immunoreactive CB_1 band with a molecular mass ~45 kDa in primary neurons transduced with LV-*Sp*dCas9-VP64-Cnr1,

compared with controls (FC 2.7 ± 0.82; Ctrl vs. Cnr1-gRNA ∼45 kDa, $p < 0.05$, $n = 6$ and FC 1.2 ± 0.36, Ctrl vs. Cnr1-gRNA ∼33 kDa; $p > 0,05$; $n = 6$) (**Figures 1C,D**).

Taken together, these data show that using this strategy, we were able to increase the expression of CB1 receptors in MEF and in primary neurons at both mRNA and protein levels.

To ensure the highest possible expression levels of both *Sp*dCas9 and sgRNAs components, and selectively direct *Sp*dCas9 expression into neurons, we designed instead a dual lentiviral vector system (**Figure 1E**). Compared to the single-vector strategy, this approach involves the transcriptional activator domain VPR that it is noted to greatly increase gene expression compared to VP64 domain (Chavez et al., 2015). To validate the performance of the dual-vector system in neurons, primary neuronal cells from postnatal mice were transduced with LV-*Sp*dCas9-VPR and LV-Cnr1-gRNA at DIV3, and RT-PCR, WB and immunofluorescent (IF) analysis was performed 10 days after.

Similar to the single-vector system, RT-PCR analysis showed a significant upregulation of the *Cnr1* gene in cortical primary neurons transduced with the vector combination compared with controls (FC 2.7 ± 0.07; Ctrl vs. Cnr1-gRNA; $p < 0.001$; $n = 6$) (**Figure 1F**). Using the same method, we also evaluated the *Sp*dCas9 gene expression and detected a significant presence of *Sp*dCas9 in primary neurons transduced with LV-*Sp*dCas9-VPR and LV-Cnr1-gRNA compared with non-treated controls (FC 342.0 ± 50.9; Ctrl vs. Cnr1-gRNA; $p < 0.001$; $n = 6$) (**Figure 1G**).

In parallel, WB analysis showed an increased expression of the immunoreactive CB_1 band with a molecular mass ∼45 kDa in treated primary neurons compared with controls (FC 4.98 ± 0.12; Ctrl vs. Cnr1-gRNA ∼45 kDa; $p < 0.001$; $n = 6$ and FC 0.96 ± 0.25 Ctrl vs. Cnr1-gRNA ∼33 kDa; $p > 0,05$; $n = 6$) (**Figures 1H,I**), and IF analysis revealed co-localization of the mature neuronal marker Map2 and RFP (**Figures 1J1–4**), indicating that the constructs were expressed correctly in mature neurons.

These results indicate that the dual lentiviral viral vector system can infect primary neurons and most importantly is able to upregulate *Cnr1* gene expression at mRNA and protein level. Using these strategies, we were able to continuously express *Sp*dCas9 and modulate *Cnr1* gene expression immediately after the viral vector treatment.

*Sp*dCas9 Based Lentiviral System for the Temporal Control of *Cnr1* Gene Expression

Specific gene expression modulation in neuronal cell populations could be a powerful tool to analyze the mechanisms underlying neuronal circuits, and the CRISPR-Cas9 based technologies described above are able to continuously upregulate the expression of *Cnr1* in all neurons. However, *Cnr1* expression in the brain is highly dynamic and plastic, and differently responds to distinct network states. *Cnr1* expression is for example highly and consistently downregulated during the early stages of epileptogenesis, and therefore designing an overexpression system with precise temporal control might be more appropriate when considering CRISPR/Cas9 gene therapy for disease modification.

Toward this goal, we generated a dual lentiviral vector CRISPR-Cas9 system for temporal control of *Sp*dCas9-VPR and *Cnr1* gene expression. In these constructs, the *Sp*dCas9-VPR transgene is under the control of the Tetracycline Responsive Element (LV-TRE-*Sp*dCas9-VPR), while in the second vector the promoter CamKIIa1.3 controls expression of the Doxycycline-sensitive transcriptional activator rtTA and the reporter gene GFP, separated by a 2A sequence (LV-Cnr1-gRNA-rtTA-GFP). This second vector also expresses four sgRNAs under the control the human or murine hH1, h7SK, hU6 and mU6 promoters (**Figure 2A**). With this strategy, *Sp*dCas9-VPR is expressed only during periods of Doxycycline (Dox) administration.

We evaluated the efficiency of the DoxCRISPR-Cas9 dual lentiviral system in both MEFs and in cortical primary neurons under different conditions of Dox administration. Dox was administered for 1 or 6 days after lentiviral co-transduction, and *Cnr1* gene upregulation was evaluated by RT-PCR and WB analysis. RT-PCR showed a significant upregulation of *Cnr1* in MEFs after 1 day (FC 7.38 ± 0.73; Cnr1-gRNA + Dox 1 day; $p < 0.05$; $n = 6$) and 6 days (FC 10.04 ± 0.72; Cnr1-gRNA + Dox 6 days; $p < 0.001$; $n = 6$) exposure to Dox compared to both non-transduced (Ctrl) and non-treated (-Dox) controls, or cells transduced with an empty gRNA vector and exposed to Dox (Empty + Dox, **Supplementary Figure 1B**). Similarly, RT-qPCR showed a significant upregulation of *Cnr1* gene (FC 4.22 ± 0.43; Ctrl vs. Cnr1-gRNA + Dox 6 days; $p < 0.001$, $n = 6$; FC 3.25 ± 0.33; Ctrl vs. Cnr1-gRNA + Dox 1 day; $p < 0.001$, $n = 6$) (**Figure 2B**) in cortical primary neurons.

CB1 protein expression analysis by WB in primary neurons showed the same expression patterns obtained in the single and dual lentiviral vector system described before. The analysis showed an increased expression of the immunoreactive CB_1 band with a molecular mass ∼45 kDa in samples co-transduced with LV-TRE-*Sp*dCas9-VPR and LV-Cnr1-gRNA-rtTA-GFP by 1 and 6 days exposure to Dox (FC 2.58 ± 0.18 Ctrl vs. Cnr1-gRNA + Dox 6 days ∼45 kDa; $p < 0.05$, $n = 3$; FC 1.72 ± 0.21 Ctrl vs. Cnr1-gRNA + Dox 1 day ∼45 kDa; $p < 0.05$, $n = 3$) (**Figures 2C,D**).

Taken together, these data show that it is possible to achieve temporal control of *Cnr1* gene expression by Dox administration, with significant increases in both mRNA and protein levels with as little as 1 day of Dox exposure.

*Sp*dCas9-VPR Expression in the Mouse Hippocampus

Our *in vitro* data shows that we are able to induce expression of CB1 receptors in neuronal cultures, but to potentially apply this technology for disease modeling or modulation, we needed to confirm its function also *in vivo*. We therefore injected adult C57BL/6J mice with the combination of LV-*Sp*dCas9-VPR and LV-Cnr1-gRNA, previously described in **Figure 1E**, in the hippocampus. After 3 weeks, we analyzed the mouse brains for both histological and molecular evaluations.

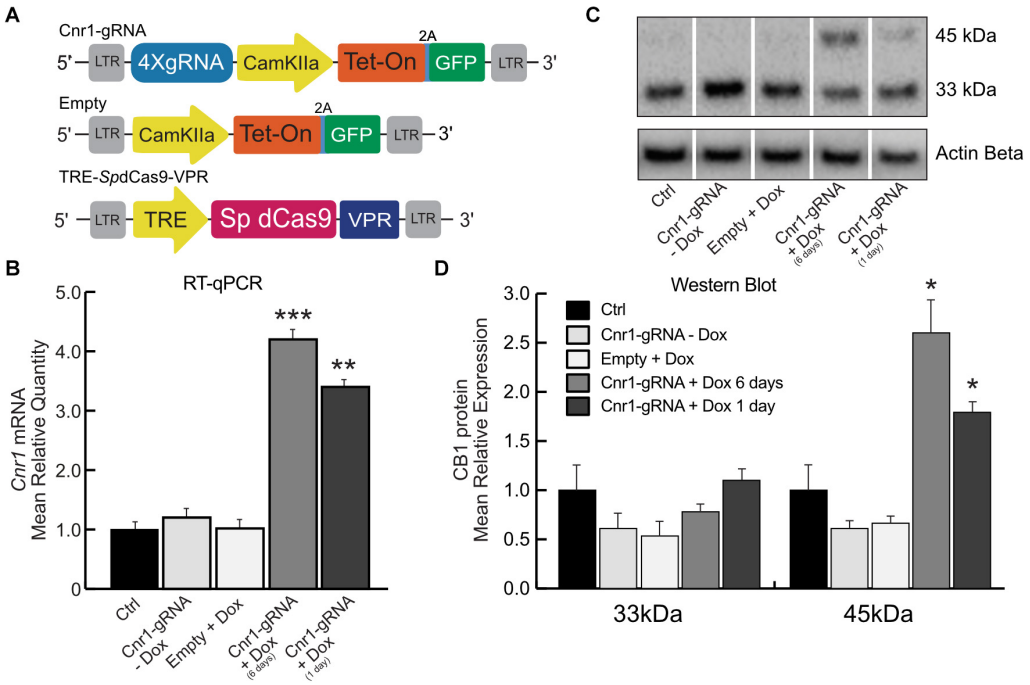

FIGURE 2 | Doxycycline-inducible *Sp*dCas9-VPR system. **(A)** Schematic illustrating the main components of the DoxCRISPR-Cas9 dual lentiviral system LV-TRE-*Sp*dCas9-VPR, LV-Cnr1-gRNA-rtTA-GFP, and LV-Empty. **(B)** The bar graphs show the mRNA expression level of the *Cnr1* gene in primary neurons transduced with the DoxCRISPR-Cas9 dual lentiviral system at two different time points (Cnr1-gRNA + Dox 1 and 6 days), compared to non-transduced (Ctrl), non-treated (Cnr1-gRNA -Dox) controls and cells transduced with LV-Empty and receiving Dox (Empty + Dox) (One-way ANOVA followed by Dunnett's multiple comparison test, $^{**}p < 0.01$ and $^{***}p < 0.001$). **(C)** WB analyses of total protein lysates from primary neurons. The upper panel shows the detection of the immunoreactive CB_1 bands (~33and 45 kDa) and the lower panel shows β-actin detection for loading control. **(D)** Expression level of the two immunoreactive CB_1 bands (~33 and 45 kDa) in primary neurons (One-way ANOVA followed by Dunnett's multiple comparison test, $^{*}p < 0.05$).

Histological analysis of hippocampal slices showed only a very limited expression of RFP in all major principal cell layers (**Figure 3A**), and RT-PCR showed no significant upregulation of the *Cnr1* gene in the injected hippocampi compared with non-treated controls (FC 1.43 ± 0.43; $p > 0.05$; $n = 4$), despite *Sp*dCas9 being expressed at significant levels ($p < 0.05$; $n = 4$) (**Figure 3B**).

These data suggest that although the dual viral vector system is able to increase the expression of the neuronal gene in *in vitro* models such as in primary neurons and MEF, the same system is not able to upregulate *Cnr1* gene expression in *in vivo* mouse brain.

Generation of *Sa*dCas9-VPR Viral Vector Technology for the Overexpression of *Cnr1* Gene

The limited hippocampal expression of the lentivirus based *Sp*dCas9 system *in vivo* prompted us to refine this technology for a better translation into animal models. Lentiviruses have the advantage of a large transgene capacity, but their spread into brain tissue outside of the injection site is limited. In addition, after transduction, the transgene is integrated randomly into the host cell genome, with unpredictable outcome on potential integration on silenced genomic regions. To ensure the highest possible expression levels of dCas9-VPR and sgRNAs, as well as optimize the spread of viral vector in target brain areas, we assembled different constructs for Adeno-Associated vectors (AAVs). The main limitation of AAV vectors consists on their limited packaging capacity, which is around 4.8 kb, including 300 bp of their Inverted Terminal Repeats (ITRs). Since the size of the *Sp*dCas9 transgene is substantial (4.1 kb) there is limited space left for promoter and the VPR transcriptional activator on the same vector. The use of a smaller dCas9 variant is therefore necessary. A recent report has described the development of a "mini-dCas9-VPR" variant based on the dCas9 protein from *Staphylococcus aureus* (Sa) and a modified, shortened version of the VPR activator (Ma et al., 2018). We adapted this system and integrated it with a second vector carrying the necessary gRNAs and a reporter gene. Our modified CRISPRa *Sa*dCas9-VPR vector system is composed of two vectors: first, the *Sa*dCas9 variant fused to the transcriptional activator domain VPR under the control of the human Synapsin 1 gene promoter (hSyn1), to confer highly neuron-specific transgene expression (Kügler et al., 2003) as well as the hemagglutinin tag (HA-tag) for construct expression validation trough immunohistochemical analysis (AAV-*Sa*dCas9-VPR). Preliminary data (data not shown) suggested that the nuclear import of the mini VPR system was suboptimal in neurons. Therefore, we further reengineered the mini-dCas-VPR system by removing the original nuclear localization signals and adding synthetic ones (Ma et al., 2018).

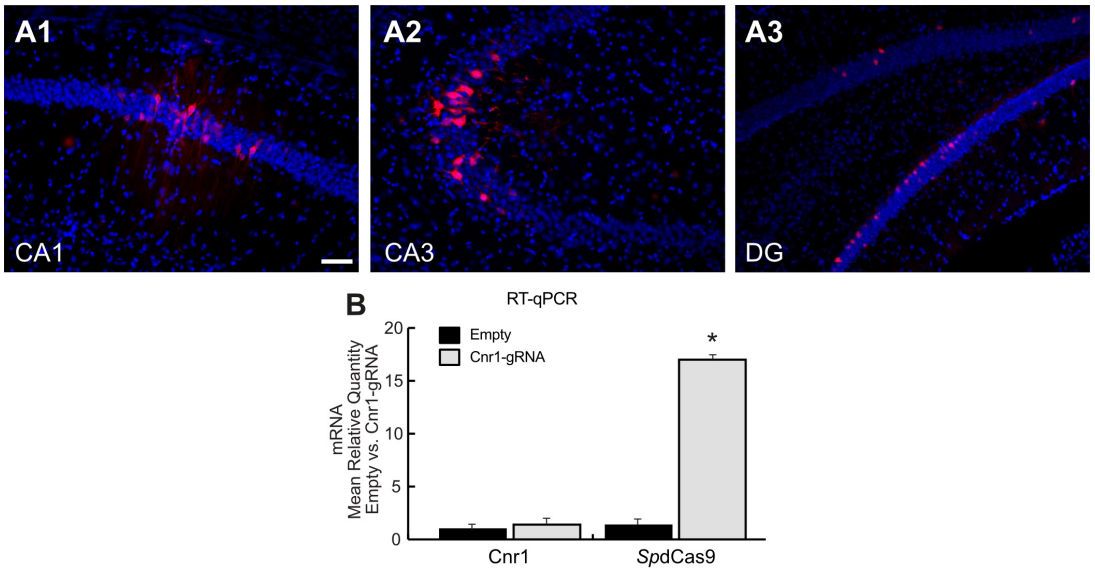

FIGURE 3 | Histological and molecular evaluation of *spd*Cas9-VPR and *Cnr1* expression in the mouse hippocampus. **(A1–A3)** The images show coronal sections (30 μm) of mouse hippocampus injected with the combination of LV-*Spd*Cas9-VPR and LV-Cnr1-gRNA. Representative images of RFP expression (Red) and Hoechst nuclear staining (Blue) in CA1 **(A1)**, CA3 **(A2)**, and DG **(A3)**. Scale bar: 50 μm. **(B)** The bar graphs show the mRNA expression level of the *Cnr1* and *spdCas9* genes in mouse hippocampus (Cnr1-gRNA vs. Empty, Mann-Whitney test, $^*p < 0.05$).

Second, the sgRNA vector contained a reporter gene GFP under the control of the CamKIIa1.3 promoter to selectively identify the expression in the excitatory neurons and up to 4 sgRNA designed selectively to target the promoter region of the *Cnr1* gene (AAV-Cnr1-gRNA). Each sgRNA is expressed separately as earlier, and driven by hH1, h7SK, hU6 and mU6 promoters. Lastly, we also designed a non-targeting control vector using the same AAV-CamKIIa-GFP construct but without the sgRNAs (AAV-Empty) for the determination of baseline cellular responses in the different experimental conditions (**Figure 5A**).

Validating sgRNAs for the *Sa*dCas9 CRISPRa System

We engineered four independent sgRNA to selectively bind the mouse promoter *Cnr1*, using the *in silico* tool CHOPCHOP[2] and selected the best sgRNAs based on their predicted scores for specificity to minimize off-target binding (**Figure 4A**). However, although *in silico* methods such as these are highly efficient, the validation of individual sgRNAs is still necessary, especially for a system based on *Sa*dCas9.

We used HEK293T cells transfected with several plasmids: one is carrying the target mouse genomic sequence *Cnr1* (−500 to −50 bp from the TSS), ahead of tdTomato; the second is coding *Sa*dCas9-VPR; the third carries CMV-BFP for normalization of expression levels and the last plasmids carry individual sgRNAs (**Figures 4A,B**, sequences in **Supplementary Table 1**). An increase in tdTomato intensity is used as a performance marker for single sgRNAs, meaning that the particular sgRNA is capable of binding to the *Cnr1* genomic sequence ahead of tdTomato and drive expression of the fluorescent protein.

Using this tool, we detected a significant up-regulation of tdTomato intensity when cells were co-transfected with the combination of all four sgRNAs (sgRNA 1/2/3 and 4 vs. all individual sgRNA1–4; FC 1.53 ± 0.08, $p < 0.05$; $n = 4$), but not with individual sgRNAs (**Figure 4C**). These results suggest that the engineered sgRNA are able to bind the target mouse genomic sequence before the *Cnr1* TSS and modulate the expression of the reporter gene tdTomato, but only when acting in concert. This is in line with other reports showing a synergistic action of multiple sgRNAs acting on the same genomic target (Cheng et al., 2013).

*Sa*dCas9-VPR Induces an Overexpression of *Cnr1* Gene in Cortical Primary Neurons

To evaluate the specificity and the efficiency of the dual AAV viral vector system (**Figure 5A**) on *Cnr1* gene expression, we first validated both constructs in an *in vitro* model, as earlier. Cortical primary neurons were transduced at DIV3 with a combination of AAV-*Sa*dCas9-VPR and AAV-Cnr1-gRNA or AAV-empty. Seven days after we evaluated vectors specificity and efficiency by next generation sequencing (NGS), RT-qPCR and ICC.

To evaluate the specificity of our designed sgRNAs (packaged in AAV-Cnr1-gRNA) in targeting only the promoter region of the *Cnr1* gene in the mouse genome, we first determined potential off-target sites with a maximum of four base pair mismatch using the online CasOFF Finder tool (Bae et al., 2014). This returned a list of 171 potential off-target sites (full list in **Supplementary Table 4**), of which 14 were within 2 kb of a TSS and only 2 were in a promoter region, specifically in the promoter of *Pdss1* and

[2]https://chopchop.cbu.uib.no

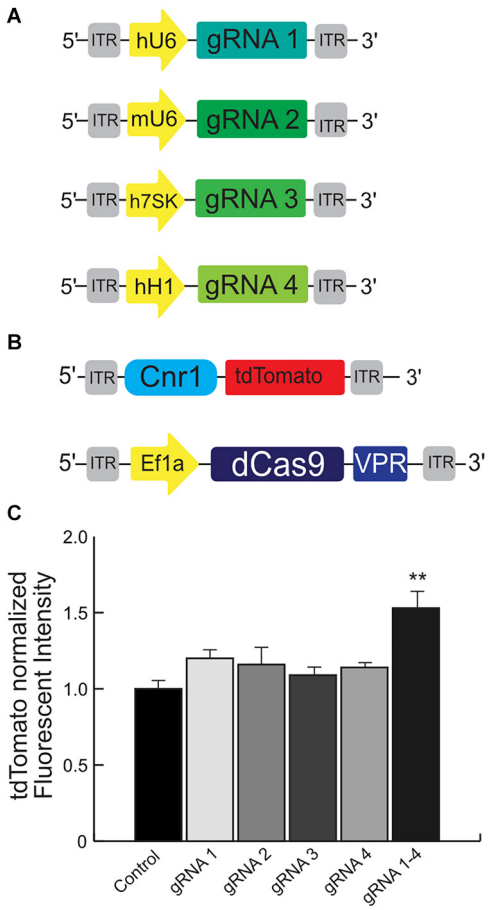

FIGURE 4 | Schematic illustrating the main components used for the validation of the mouse Cnr1-sgRNA for the CRISPR-Cas9 transcriptional activator system. The illustration **(A)** show the plasmids carrying four independent sgRNAs to selectively bind the mouse promoter *Cnr1*. The illustration **(B)** show the plasmid carrying the target mouse genomic sequence Cnr1 and the plasmid coding the *Sa*dCas9-VPR. **(C)** The combination of all four independent sgRNAs can induce a significant up-regulation of tdTomato intensity. (One-way ANOVA followed Dunnett's multiple comparison test, gRNA vs. Ctrl, $^{**}p < 0.01$) compared to single sgRNAs.

Mrps6 (**Figure 5B**, green dots). RNASeq analysis from primary neurons showed that none of these 16 genes were significantly altered in cells treated with the AAV-*Sa*dCas9-VPR and AAV-Cnr1-gRNA vector combination, but indicated that *Cnr1* was significantly upregulated (**Figure 5B**).

To further confirm *Cnr1* upregulation, we performned RT-qPCR on a separate set of cultures, and confirmed a significant upregulation of *Cnr1* in cortical primary neurons transduced with AAV-*Sa*dCas9-VPR and AAV-Cnr1-gRNA compared with non-treated controls (Ctrl vs. AAV-gRNA-Cnr1; FC 3.92 ± 0.45, $p < 0.0001$; $n = 9$) and with the non-targeting controls (AAV-Empty; $p < 0.0001$; $n = 9$, **Figure 5C**). RT-qPCR also confirmed the presence of *Sa*dCas9 in the cortical primary neurons transduced with AAV-*Sa*dCas9-VPR compared with non-treated controls (Ctrl vs. AAV-gRNA-Cnr1 and Ctrl vs. Empty, $p < 0.0001$, $n = 6$, **Figure 5D**). Western blot experiments further showed that also CB1 protein levels were increased in cells treated with the AAV-gRNA-Cnr1 vector compared to AAV-Empty (FC 2.73 ± 0.55, $p < 0.05$, $n = 5$, **Figure 5E**).

Immunocytochemistry analysis revealed co-localization of mature neuronal marker Map2 and GFP in cortical primary neurons transduced with AAV-*Sa*dCas9-VPR and AAV-Cnr1-gRNA, where 96.31% of primary neurons expressing Map2 co-localized with GFP. These results indicate that the vectors are able to infect mature excitatory neurons (**Figures 5F1–4**). ICC analysis also revealed a high co-localization of HA-Tag and GFP (86.59% of GFP positive neurons co-localized with the HA-Tag), indicating that *Sa*dCas9 protein is expressed in targeted neurons. These results show additionally that AAV-*Sa*dCas9-VPR and AAV-Cnr1-gRNA (GFP) are expressed in the same neuronal population confirming the efficiency and applicability of this dual viral vector system (**Figures 5G1–4**).

*Sa*dCas9-VPR and *Cnr1* Expression in the Mouse Hippocampus

After confirming the functionality of our system in primary neurons, we injected the same mixture of AAVs into the hippocampus of adult mice. Histological evaluation of hippocampal slices revealed extensive expression of GFP throughout all hippocampal layers, as well as significant dorso-ventral coverage. Because of the lack of well-performing antibodies against *Sa*Cas9 or the HA-tag in slices, we used a dual RNAscope *in situ* hybridization to simultaneously evaluate the expression of the *Sa*dCas9 and GFP mRNAs *in vivo*. Probing with a specific probe against *Sa*dCas9 revealed expression of the mRNA in all principal cell layers of the hippocampus, as well as in putative interneurons (**Figure 6**) only on the ipsilateral side, confirming that our AAV-*Sa*dCas9-VPR can efficiently infect target neurons and induce expression of the *Sa*dCas9 mRNA. In addition, GFP mRNA expression was also seen in all principal layers of the hippocampus (GFP in the second vector is driven by the CaMKIIa promoter), and the GFP and *Sa*dCas9 *in situ* signals were overlapping in virtually all expressing cells (*Sa*dCas9 expression in GFP positive cells: 97.5 ± 2.1% in DG, 98.2 ± 1.8% in CA1 and 97.9 ± 2.1% in CA3, **Figure 6**), indicating the simultaneous expression of both AAVs in all transduced cells also *in vivo*.

CB1 receptors are expressed on both excitatory and inhibitory synaptic terminals, but at very different levels. While their expression and localization on pre-synaptic boutons in GABAergic terminals is easily visualized by immunohistochemistry, their expression level on glutamatergic synapses is very low and cannot be reliably visualized and measured by antibody-based techniques (Marsicano and Lutz, 1999; Katona, unpublished). We therefore applied the RNAscope technology also for visualizing and quantifying the amount of *Cnr1* mRNA *in situ* in hippocampal slices from animals injected with our vector combinations.

In animals injected with AAV-*Sa*dCas9-VPR and AAV-empty, *Cnr1* mRNA was easily visualized in all principal layers of the hippocampus, with higher expression in CA1 and CA3 compared to the DG, where only few positive signals were detected

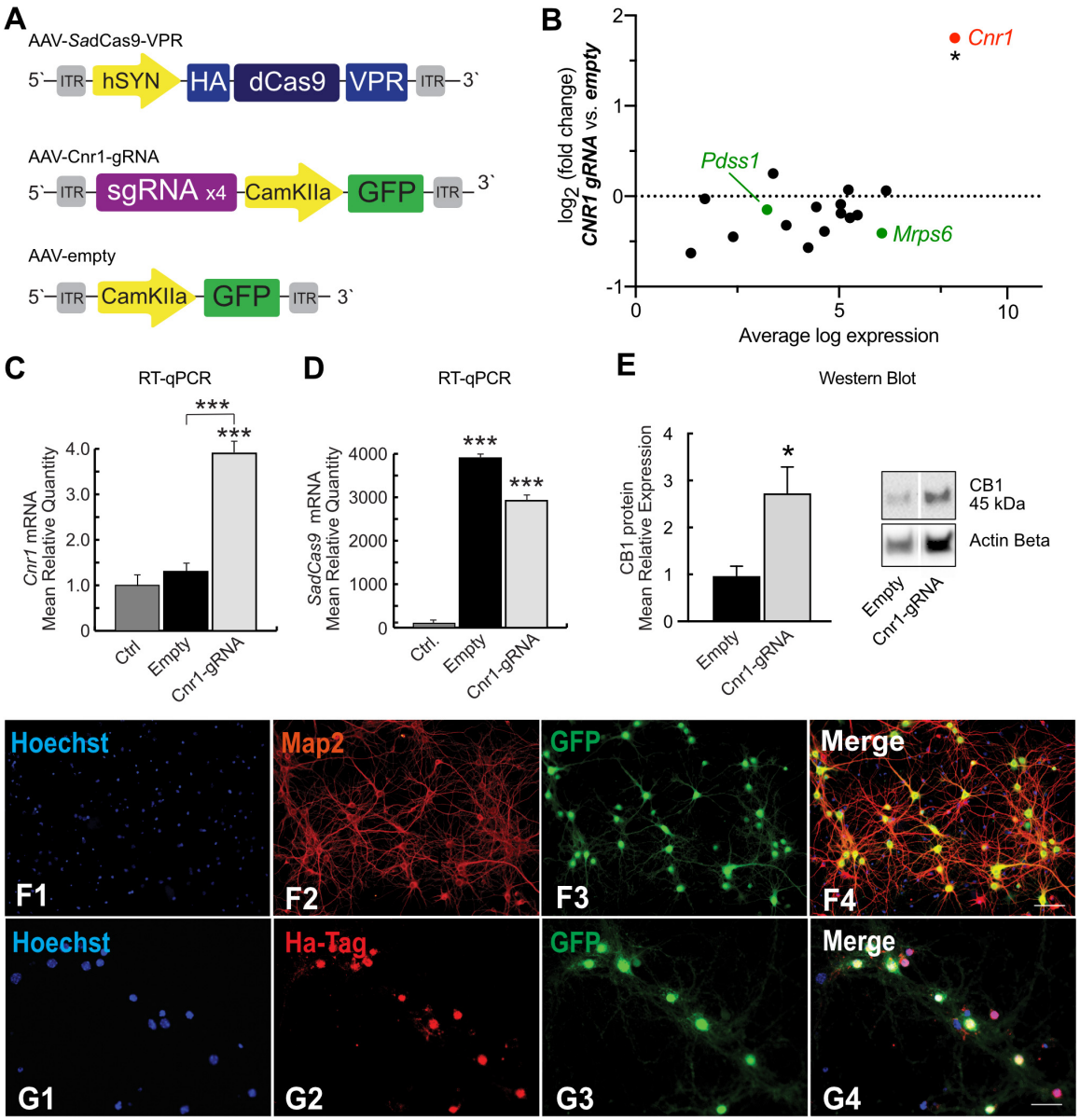

FIGURE 5 | *Sad*Cas9-VPR based AAV vector system and modulation of *Cnr1* gene expression in cortical primary neurons. **(A)** Schematic illustrating the main components of the CRISPRa *Sad*Cas9-VPR vectors system. The first vector expresses the *Sad*Cas9 variant fused to the transcriptional activator domain VPR under the control of the hSyn1 promoter (AAV-*Sad*Cas9-VPR), the second vector carrying the individual sgRNAs contains the reporter gene GFP under the control of the CamKIIa1.3 promoter (AAV-Cnr1-gRNA), and the third vector represents the empty control (AAV-empty). **(B)** Fold change expression in mRNA levels plotted against baseline expression for potential off-target genes where sgRNAs designed for *Cnr1* bind within 2kb of the TSS (black) or within promoter regions (green) (Unpaired *t*-test $*p < 0.05$). **(C)** mRNA expression levels of the *Cnr1* gene in primary neurons transduced with AAV-*Sad*Cas9-VPR and AAV-Cnr1-gRNA (Cnr1-gRNA) compared with non-treated controls and empty controls (Empty) (One-way ANOVA followed Dunnett's multiple comparison test, $***p < 0.001$). **(D)** mRNA expression level of the *saCas9* gene in primary neurons (One-way ANOVA followed Dunnett's multiple comparison test, $***p < 0.001$). **(E)** Total protein western blot from primary neurons showing increased CB1 expression in cells treated with AAV-*Sad*Cas9-VPR and AAV-*Sad*Cas9-VPR (Cnr1-gRNA) compared to Empty vector controls (Cnr1-gRNA vs. Empty, Mann-Whitney test, $*p < 0.05$). **(F1–F4,G1–G4)** Representative micrographs obtained with fluorescence microscopy of cortical primary neurons transduced with CRISPRa *Sad*Cas9-VPR vectors system to up regulate *Cnr1* gene expression. **(F1–4)** The images show the Hoechst nuclear staining (Blue; **F1**), Microtubule associate protein 2 staining (Map2; Red; **F2**) and GFP (Green; **F3**) expression. Scale bar: 50 μm. **(G1–G4)** The images show the Hoechst nuclear staining (Blu; **G1**), Hemagglutinin Tag staining (Ha-Tag; Red; **G2**) and GFP (Green; **G3**) expression. Scale bar: 80 μm.

in granule cells (**Figure 7**). This is according to previously published reports showing that DG mossy fibers are less sensitive than Schaffer collaterals to CB1 receptor agonists (Hofmann et al., 2008; Caiati et al., 2012). In animals injected with the AAV-Cnr1-gRNA vector and AAV-*Sad*Cas9-VPR, a significant fivefold upregulation of *Cnr1* mRNA was observed particularly

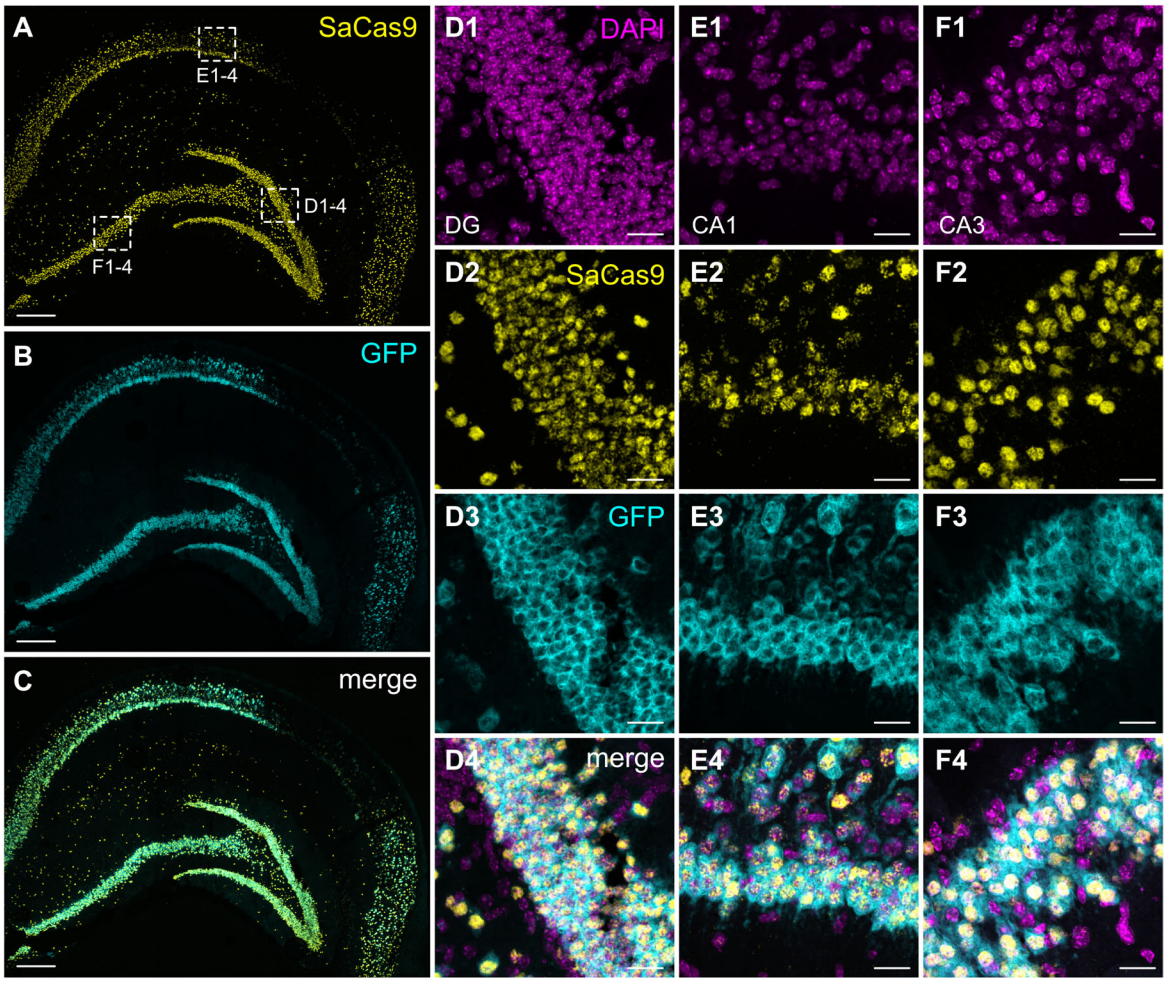

FIGURE 6 | Expression of *Sad*Cas9 and GFP mRNAs in the mouse hippocampus. *In situ* hybridization was performed with a two RNAscope probes targeting *Sad*Cas9 and GFP mRNA. The images show coronal sections (15 μm) of mouse hippocampus injected with AAV-*Sad*Cas9-VPR and AAV-Cnr1-gRNA. Representative images for *Sad*Cas9 (**A**; Yellow dots), GFP mRNA (**B**; Cyan dots) and DAPI (**C**; Magenta dots). High magnification images show *Sad*Cas9 and GFP mRNA expression in the DG **(D1–D4)**, CA1 **(E1–E4)** and CA3 **(F1–F4)**. Scale bar in **(A–C)** is 250 μm, **(D–F)** 25 μm.

in DG granule cells (from 21,549 ± 2,257 in AAV-Empty to 114,343 ± 22,675 in AAV-Cnr1-gRNA, density of particles per mm^2, $p < 0.05$, **Figures 7A–D,M**), but also to a lesser extent in the CA3 area (from 253,322 ± 11,107 to 331,531 ± 24,530, $p < 0.05$, **Figures 7E–H,M**). Quantification of *Cnr1* mRNA signal on putative interneurons was not possible due to the very high basal level of expression even in control conditions.

Taken together, these data show that our dual AAV-based system can be successfully expressed in the brain of adult animals and is able to significantly upregulate the expression of *Cnr1*.

Functional Evaluation of *Cnr1* Upregulation in the Hippocampus

The *in situ* hybridization data indicates that our AAV-based CRISPRa system can significantly upregulate *Cnr1* mRNA *in vivo*, but this does not necessarily translate into increased protein levels and does not offer any insight into the function of the upregulated gene. Toward these aims, we injected unilaterally another cohort of animals with AAV-*Sad*Cas9-VPR and AAV-Cnr1-gRNA or AAV-empty vector combinations, and 3–6 weeks later performed western blot and electrophysiological investigations to confirm CB1 upregulation and gain-of-function. After the slicing procedure for electrophysiology, some of the slices in the ipsilateral side were immediately frozen in dry ice, before proceeding with protein extraction and western blot analysis. Immunoblot quantification, similarly to what observed in primary cultures, showed two distinct bands and a significant upregulation of the 45 kDa band in slices animals injected with AAV-Cnr1-gRNA compared to AAV-empty (Empty vs. Cnr1-gRNA, FC 1.80 ± 0.28, $p < 0.05$, $n = 6$ animals) but no change in the 33 kDa band (**Figure 8A**).

The remaining hippocampal slices that were not processed for western blot were used for electrophysiological investigations of CB1-mediated decrease in synaptic transmission. Activation of CB1 receptors by endocannabinoids or other agonists induces

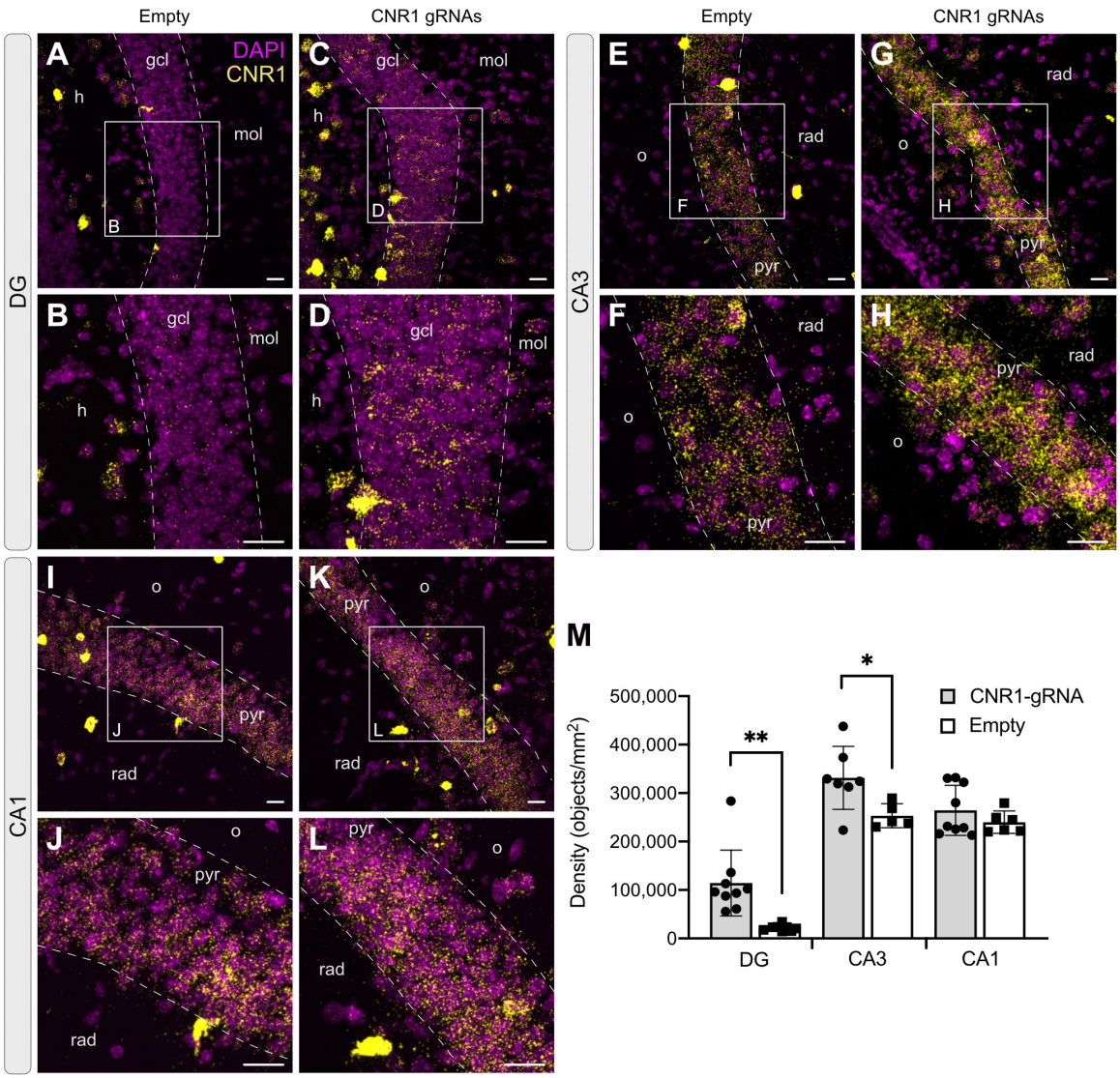

FIGURE 7 | Expression of the Cnr1 mRNA in the mouse hippocampus. *In situ* hybridization was performed with the RNAscope probe targeting Cnr1 mRNA. The images show coronal sections (15 μm) of mouse hippocampus injected with AAV-*Sa*dCas9-VPR and AAV-Cnr1-gRNA (Cnr1-gRNA) or AAV-*Sa*dCas9-VPR and AAV-empty (Empty). Representative images for Cnr1 mRNA (Yellow dots) and Dapi (Magenta dots) in the DG **(A–D)**, CA3 **(E–H)**, and CA1 **(I–L)**. Scale bars are 25 μm. gcl: granular cell layer; mol: molecular layer; h: hilus; o: stratum oriens; pyr: pyramidal layer; rad: stratum radiatum. **(M)** Bar graphs showing the quantification of Cnr1 mRNA signal expressed in density of particles per mm^2 in the DG, CA3, and CA1 hippocampal regions of the experimental groups CNR1 gRNAs and Empty. N = 5–9 slices from 3 animals per group. (Cnr1-gRNA vs. Empty, Unpaired t-test $^{**}p < 0.01$; $^{*}p < 0.05$).

downstream the inhibition of voltage-gated calcium channels and therefore reduces the release of neurotransmitters at the synapses on which it is expressed (Godino et al., 2007). A stimulating and a recording electrodes were placed in the stratum radiatum of area CA1, and field excitatory post-synaptic potentials (fEPSPs) were induced by electrical stimulation of Schaffer collaterals every 15 s. Representative traces are shown in **Figure 8B**. To quantify the CB1-mediated impact on synaptic transmission in these synapses, after measuring a 20 min baseline period, we applied in the bath the CB1 receptor agonist WIN 55,212-2 at a concentration of 1 μM and continuously monitored the pre-synaptic fiber volley and slope of the fEPSPs. In both slices from animals injected with AAV-*Sa*dCas9-VPR and AAV-Cnr1-gRNA (Cnr1-gRNA group) or AAV-*Sa*dCas9-VPR and AAV-empty (Empty group), we could observe a constant decrease in the slope amplitude starting from approximately 10 min after WIN application, peaking at 25 min. When comparing the relative decrease in slope over time between the two groups, we could observe that WIN had a stronger effect in the Cnr1-gRNA group starting from approximately 18 min after WIN application (**Figure 8C**, $^{*}p < 0.05$, n = 6 slices from 6 animals per group), indicating that potentially an increased number of CB1 receptors at these synapses would induce a stronger reduction in pre-synaptic neurotransmitter release. Importantly, WIN effects in

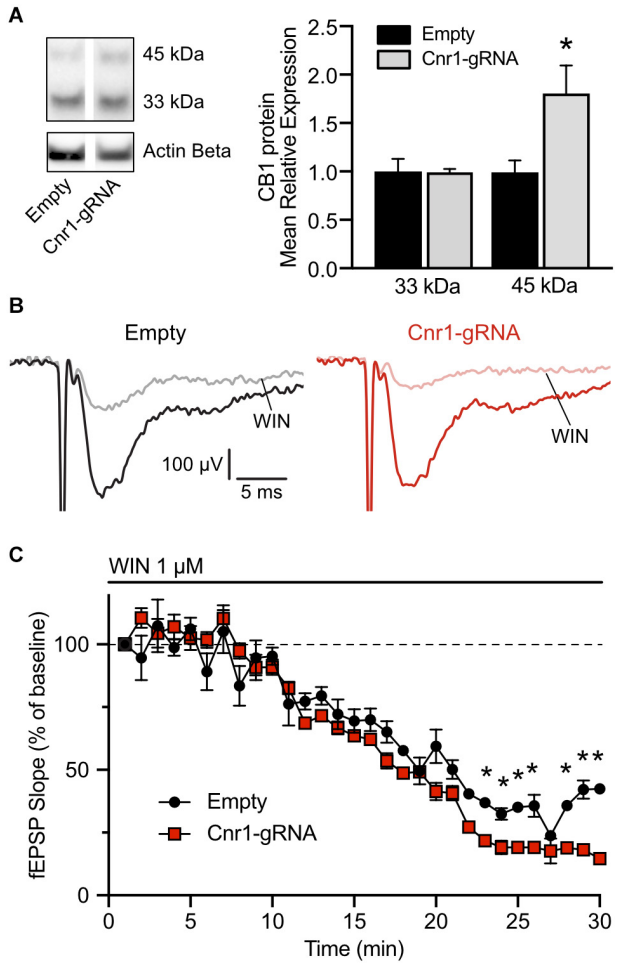

FIGURE 8 | Expression of CB1 protein in the mouse hippocampus and functional validation of overexpression. **(A)** Total protein western blot from hippocampal tissue showing increased CB1 expression in animals treated with AAV-*Sad*Cas9-VPR and AAV-*Sad*Cas9-VPR (Cnr1-gRNA) compared to Empty vector controls (Cnr1-gRNA vs. Empty, Mann-Whitney test, $*p < 0.05$). **(B)** Representative traces showing fEPSPs recorded from CA1, before (black and dark red) and 25 min after WIN 55,212-22 application (WIN, gray and light red), in hippocampal slices from the Empty (left) and Cnr1-gRNA groups (right). Stimulation artifacts were cropped. **(C)** Quantification of fEPSP slope over time, displayed as percentage from baseline, during the period of WIN application (Cnr1-gRNA vs. Empty, Two-way repeated measures ANOVA followed by Sidak's multiple comparison test, $*p < 0.05$).

both groups were completely abolished by co-application of the CB1 receptor antagonist/inverse agonist AM251, and fiber volley amplitudes were constant over time (data not shown), confirming the specificity of this approach.

DISCUSSION

The study of complex neuronal function sometimes requires the use of tools able to specifically increase expression of target genes. In this study, we describe two flexible and efficient approaches for overexpressing target gene expression in neurons, and we demonstrate their ability to increase CB1 expression both *in vitro* and *in vivo*.

Classic gene overexpression approaches rely on the ability of lentiviruses or AAVs to deliver transgenes in target neurons, but are affected by several limitations. The packaging size of viral vectors in particular is limited, and does not allow the incorporation of long genes or combination of genes. These limitations could be largely overcome by using a CRISPRa system, where the transgene cargo size is fixed and gene targets are determined solely by altering sgRNAs sequences. Here, we packaged different variants of CRISPRa systems in both lentiviruses and AAVs and show that while both systems are similarly effective in overexpressing CB1 receptors *in vitro*, there is a significant difference in performance when injected in the brain *in vivo*.

Our first lentiviral based approach is based on a single-vector system where the "dead" Cas9 protein from *Streptococcus pyogenes (Sp)*, transcriptional activators and sgRNAs are packaged together in one virus. Using the EF1a promoter or CamKIIa promoter, this design only allows the insertion of smaller transcriptional activator modules, such as VP64, and not larger but theoretically more efficient fusion activators such as VPR (Chavez et al., 2015). To incorporate the VPR activator, and restrict expression the excitatory neurons, we developed a dual-vector system where expression of dCas9 and sgRNAs are confined to separate lentiviruses. Both systems were successful in inducing the expression of *Cnr1* mRNA and protein in MEFs and primary neuronal cultures, but surprisingly, we did not notice major differences in efficiency and gene induction strength between VP64 and VPR-based systems, as was instead previously described (Chavez et al., 2015; Bao et al., 2017), with both approaches able to increase expression by 3–4-fold in neurons. The amount of upregulation achieved by our system is similar to what previously observed by other research groups using both AAV and Lentivirus based approaches (Savell et al., 2019; Colasante et al., 2020), despite the use of different activator domains or target genes. This observation raises the interesting possibility that different activator domains might be more efficient in inducing expression of certain genes but not others, and even if multiple domains are used in concert to theoretically increase output, some genes cannot be overexpressed more than a given amount. In line with this concept, induction of *Cnr1* mRNA was significantly higher in MEFs (∼50-fold). This suggests, as previously described by others as well (Konermann et al., 2015; Chavez et al., 2016), that CRISPRa efficiency could be dependent on basal expression levels of the target genes, since MEFs do not normally express CB1 receptors while primary neurons physiologically do. In addition, at least for our AAV system based on *Sa*dCas9, multiple sgRNAs targeting the same gene at different locations are required to significantly increase mRNA transcription, as previously shown (Lau et al., 2019). Whether sgRNA synergy is required or not could, however, also be dependent on the specific gene targeted as in some cases one individual sgRNA is sufficient for significant gene induction of other typically neuronal genes (Colasante et al., 2020).

One notable observation from our western blot experiments was the presence of two discrete bands after immunodetection,

one at approximately 30–35 kDa and the other at 45–50 kDa. CB1 receptors are glycosylated proteins, and different levels of glycosylation could explain the different apparent molecular weight observed on the membranes (Song and Howlett, 1995). In addition, CB1 mRNA could also undergo different splicing alternatives, resulting in an N-terminal modified isoform which is shorter than full length CB1 (Shire et al., 1995). However, this does not explain why our CRISPRa-induced overexpression only affected the larger molecular weight receptors, as increasing mRNA expression would theoretically result in proportional increase in protein levels from all alternative splicing forms, unless the splicing machinery would become overwhelmed and not able to process mRNAs as effectively when there are increased amounts present. This seems, however, unlikely as the mRNA increase was only 3–5-fold, but it's a possibility that cannot be excluded. Alternatively, the presence of two bands could be explained by poor antibody performance and specificity, as it was only observed in western blots performed with the Immunogenes primary antibody and not with the Cayman antibody (which was used in **Figure 5E**). However, the Immunogenes antibody we used did not detect any protein in membranes loaded with samples from CB1 knock-out animal brains (data not shown), rendering this possible explanation highly unlikely. In addition, similar results have also been observed in other laboratories using the same primary antibody (Katona, unpublished observation), but the true nature of the two separate putative CB1 isoforms remains to be clearly elucidated.

To further extend the potential applications of our CRISPRa systems, we modified the dual vector approach for temporal control of target gene induction, by incorporating a Doxycycline sensitive induction control (TetON). In primary neurons transfected with the two lentiviruses, we were able to significantly induce CB1 expression by exposing cells to Dox for 1 or 6 days, and importantly, we did not detect significant induction of gene expression in the absence of Dox, validating the possibility that our CRISPRa dCas9-VPR system can be used when temporal control of gene induction is necessary. Similar systems have been used recently in the brain, for both CRISPRa and gene editing (Kumar et al., 2018; Colasante et al., 2020), indicating that such an approach could represent a robust strategy for temporal control of gene regulation.

To assess the functionality of the lentivirus-based dual vector system *in vivo*, we injected the viral combination in the hippocampus of wild type mice, and observed only a very limited expression of the reporter gene RFP in principal cell layers. Real time PCR analysis in the whole hippocampus revealed the expression of the dCas9 mRNA but failed to detect differences in *Cnr1* expression levels between groups. This was most likely due to the limited number of cells transduced by our viral combination, where non-transduced neurons masked the effect of a potential successful upregulation of *Cnr1* in transduced cells. The limited expression of transgene in the injected hippocampi, despite the injection of a combined 2 μL in four sites and a relatively high viral titer, is in line with what has been recently shown in other studies using similar CRISPRa approaches (Savell et al., 2019), and the reason has to be found on the intrinsic properties of the viral particles themselves. Lentiviruses have a medium-high packaging capacity but their larger size limits the viral spread from the injection sites, thereby resulting in a limited target area coverage. However, the use of lentiviruses could still be desirable for situations where the modification of only a limited number of neurons is necessary, as for the investigation of the impact of few cells on behavior (Zheng et al., 2018) or for interfering with small epileptic foci.

Our results with lentiviruses have prompted us to explore the possibility of applying an AAV-based CRISPRa approach to increase hippocampal coverage and thereby render the system more applicable for cases in which large areas need to be transduced. However, the *Sp*dCas9 protein fused to the VPR activator cannot be introduced into AAV particles due to the large size of their coding DNA, which exceeds the packaging capacity of AAVs. We therefore turned to CRISPRa system based on dCas9 from *Streptococcus aureus (Sa)*, a Cas9 ortholog with much smaller size and a smaller VPR domain (Ma et al., 2018). By modifying both the dCas9 protein and the VPR activator, we were able to fit the whole construct, including a neuron specific hSyn promoter, into AAV particles and produce viruses with high titer capable of transducing neurons both *in vitro* and *in vivo*.

In vitro performance of the AAV-based CRISPRa system was comparable to what we have seen with lentiviruses, but the coverage of hippocampal areas *in vivo* was significantly larger. With two injection sites and four total deposits of viral particles we were able to cover most of the dorso-ventral axis of the hippocampus. In addition, we demonstrate that using a dual viral vector approach does not present significant drawbacks, at least in the case of AAVs, as both *in vitro* and *in vivo* we observed very high co-transduction rates, indicating using two separate viral vectors to maximize expression of dCas9-VPR and sgRNAs separately can be used to activate genes as there is robust colocalization. However, when thinking about potential clinical applications of CRISPRa strategies, a dual vector system might not satisfy biosafety regulations for the use of AAVs in humans. In this case, continuous engineering of promoters, activator domains and regulatory sequences would be required to fit all components into a single AAV, in the cases where one sgRNA is sufficient to drive enough overexpression, as recently shown (Lau et al., 2019).

To quantify *Cnr1* mRNA expression in different hippocampal subregions we turned to RNAScope *in situ* hybridization, and observed a significant upregulation of *Cnr1* in the dentate gyrus and CA3 areas, but not in CA1. In particular, the upregulation was more pronounced in the DG, where basal expression levels of *Cnr1* are lower (Monory et al., 2006; Frazier, 2007), again confirming that CRISPRa tools are more efficient in inducing genes with low basal expression levels. In addition, western blot experiments confirmed that mRNA upregulation was reflected in protein expression, indicating that our system was functional *in vivo*, and could be used for interfering with CB1 expression in the hippocampus.

Nevertheless, increased CB1 protein levels at the western blot level does not necessarily mean that a gain-of-function can be achieved at the synaptic level, where CB1 receptors are normally expressed. It is possible that overexpressed receptors might not position correctly at synapses and could not be exerting their

physiological function. It was previously shown, however, that overexpression of CB1 by AAV vectors was able to protect against seizure-induced excitotoxicity (Guggenhuber et al., 2010), indicating that overexpressed CB1 receptors should position and function correctly. To confirm the functionality of CB1 receptor overexpression, we performed field recordings in the CA1 area of the hippocampus from mice, and found that application of the CB1 agonist WIN 55,212-2 induced a bigger decrease in synaptic transmission in slices from animals injected with the vector combination containing *Cnr1* sgRNAs compared to those receiving the Empty vector. The observed decrease in synaptic transmission is in line with what previously observed by others in similar experimental setups (Kawamura et al., 2006; Takahashi and Castillo, 2006). Importantly, fiber volley amplitude was not affected, confirming that the effect was dependent on decrease in synaptic transmission and not on decreased afferent fiber stimulation over time.

The AAV-based system we describe here is made for constitutive expression, but could be easily adapted for temporal control of gene expression, using a similar approach as we described for our lentivirus-based CRISPRa vectors (Savell et al., 2019). In addition, it could be even made responsive to intrinsic neuronal activity, but incorporating activity-dependent promoters, or limited in expression to selective cell populations by adapting it for Cre-lox recombination strategies. These modifications will enable cell-type or circuit specific targeting to study the impact of target gene overexpression in more details.

The potential of CRISPRa gene therapy approaches for the treatment of neurological diseases is immense, also considering the relative ease of use and transferability to other models or even species. However, there are still several unknowns about the long-term use and safety of such approach. While it is certain that with time research will properly investigate this, at present the major drawback is represented by the uncertainty around the potential immunogenicity of bacterial proteins in human cells. It has been in fact previously shown that injection of AAVs encoding non-self-proteins (including the seemingly innocuous GFP) in non-human primates can elicit immune response and inflammation (Ciesielska et al., 2013; Yang et al., 2016), but whether that is the case for Cas9 and its derivates is presently unknown. Another concern revolves around the potential off-target effects of sgRNAs, but in this case the likelihood of deleterious effects is lower in CRISPRa approaches compared to CRISPR gene editing, as no DNA cleavage is involved.

CONCLUSION

In conclusion, we show that gene modulation by CRISPRa *in vivo* in the brain can be successfully adapted to increase expression of synaptic proteins, and add to the growing CRISPRa toolbox for the potential development of gene therapy approaches against neurological disorders.

DATA AVAILABILITY STATEMENT

The original contributions presented in the study are included in the article/**Supplementary Material**, further inquiries can be directed to the corresponding author.

ETHICS STATEMENT

The animal study was reviewed and approved by the Swedish Animal Welfare Agency.

AUTHOR CONTRIBUTIONS

VDM contributed to the design, performance and analysis of all the experiments. MR contributed to cloning lentiviral vectors. AB performed some Western Blot experiments. MM and LQ contributed to designing and performing the sgRNA validation. LQ contributed to designing the AAV-based *Sa*dCas9-VPR constructs. ML overseen all work, designed, performed, and analyzed the experiments. VDM and ML wrote the manuscript. All authors contributed to the article and approved the submitted version.

FUNDING

This work was supported by the Swedish Research Council (ML, Grant No. 2015-00353), Marie Skłodowska Curie Actions (ML, INCA 600398), the Crafoord Foundation, the Segerfalk Foundation, the Jeansson Foundation, and the Åke-Wibergs Foundation.

ACKNOWLEDGMENTS

We are grateful to Nora Pernaa and Susanne Jonsson for technical assistance, Spencer Stong, Bianca Ana Zaharia, and Danilo Gambino for help with experiments.

SUPPLEMENTARY MATERIAL

The Supplementary Material for this article can be found online at: https://www.frontiersin.org/articles/10.3389/fnmol.2020.00168/full#supplementary-material

REFERENCES

Axelsen, T. M., and Woldbye, D. P. D. (2018). Gene therapy for Parkinson's disease, an update. *J. Parkinsons Dis.* 8, 195–215. doi: 10.3233/JPD-181331

Bae, S., Park, J., and Kim, J. S. (2014). Cas-OFFinder: a fast and versatile algorithm that searches for potential off-target sites of Cas9 RNAguided endonucleases. *Bioinformatics* 30, 1473–1475. doi: 10.1093/bioinformatics/btu048

Bao, Z., Jain, S., Jaroenpuntaruk, V., and Zhao, H. (2017). Orthogonal regulation in human cell using chemically induced CRISPR/Cas9 activators. *ACS Synth. Biol.* 6, 686–693. doi: 10.1021/acssynbio.6b00313

Caiati, M. D., Sivakumaran, S., Lanore, F., Mulle, C., Richard, E., Verrier, D., et al. (2012). Developmental regulation of CB1-mediated spike-time dependent depression at immature mossy fiber-CA3 synapses. *Sci. Rep.* 2:285. doi: 10.1038/srep00285

Chavez, A., Scheiman, J., Vora, S., Pruitt, B. W., Tuttle, M. P. R., Iyer, E., et al. (2015). Highly efficient Cas9-mediated transcriptional programming. *Nat. Methods* 12, 326–328. doi: 10.1038/nmeth.3312

Chavez, A., Tuttle, M., Pruitt, B. W., Ewen-Campen, B., Chari, R., Ter-Ovanesyan, D., et al. (2016). Comparison of Cas9 activators in multiple species. *Nat. Methods* 13, 563–567. doi: 10.1038/nmeth.3871

Cheng, A. W., Wang, H., Yang, H., Shi, L., Katz, Y., Theunissen, T. W., et al. (2013). Multiplexed activation of endogenous genes by CRISPR-on, an RNA-guided transcriptional activator system. *Cell Res.* 23, 1163–1171. doi: 10.1038/cr.2013.122

Ciesielska, A., Hadaczek, P., Mittermeyer, G., Zhou, S., Wright, F., Bankiewicz, K. S., et al. (2013). Cerebral infusion of AAV9 vector-encoding non-self proteins can elicit cell-mediated immune responses. *Mol. Ther.* 21, 158–166. doi: 10.1038/mt.2012.16

Colasante, G., Qiu, Y., Massimino, L., Di Berardino, C., Cornford, J. H., Snowball, A., et al. (2020). In vivo CRISPRa decreases seizures and rescues cognitive deficits in a rodent model of epilepsy. *Brain* 143, 891–905. doi: 10.1093/brain/awaa04

Combs, B., Kneynsberg, A., and Kanaan, N. M. (2016). Gene therapy models of Alzheimer's disease and other dementias. *Methods Mol. Biol.* 1382, 339–366. doi: 10.1007/978-1-4939-3271-9_25

Dai, W. J., Zhu, L. J., Yan, Z. Y., Xu, Y., Wang, Q. L., and Lu, X. J. (2016). CRISPR-Cas9 for in vivo gene therapy: promise and hurdles. *Mol. Ther. Nucleic Acids* 5:349. doi: 10.1038/mtna.2016.58

Davidsson, M., Wang, G., Aldrin-Kirk, P., Cardoso, T., Nolbrant, S., Hartnor, M., et al. (2019). A systematic capsid evolution approach performed in vivo for the design of AAV vectors with tailored properties and tropism. *Proc. Natl. Acad. Sci. U.S.A.* 116, 27053–27062. doi: 10.1073/pnas.1910061116

Dawson, T. M., Golde, T. E., and Lagier-Tourenne, C. (2018). Animal models of neurodegenerative diseases. *Nat. Neurosci.* 21, 1370–1379. doi: 10.1038/s41593-018-0236-8

Engler, C., Kandzia, R., and Marillonnet, S. (2008). A one pot, one step, precision cloning method with high throughput capability. *PLoS One* 3:e3647. doi: 10.1371/journal.pone.0003647

Frazier, C. J. (2007). Endocannabinoids in the Dentate Gyrus. *Prog. Brain Res.* 163, 319–337. doi: 10.1016/S0079-6123(07)63019-2

Gilbert, L. A., Larson, M. H., Morsut, L., Liu, Z., Brar, G. A., Torres, S. E., et al. (2013). CRISPR-mediated modular RNA-guided regulation of transcription in eukaryotes. *Cell* 154, 442–451. doi: 10.1016/j.cell.2013.06.044

Godino, M. D. C., Torres, M., and Sánchez-Prieto, J. (2007).). CB1 receptors diminish both Ca(2+) influx and glutamate release through two different mechanisms active in distinct populations of cerebrocortical nerve terminals. *J. Neurochem.* 101, 1471–1482. doi: 10.1111/j.1471-4159.2006.04422.x

Götz, J., and Ittner, L. M. (2008). Animal models of Alzheimer's disease and frontotemporal dementia. *Nat. Rev. Neurosci.* 9, 532–544. doi: 10.1038/nrn2420

Gray, S. J., Choi, V. W., Asokan, A., Haberman, R. A., McCown, T. J., and Samulski, R. J. (2011). Production of recombinant adeno-associated viral vectors and use in in vitro and in vivo administration. *Curr. Protoc. Neurosci.* Chapter 4:Unit4.17. doi: 10.1002/0471142301.ns0417s57

Guggenhuber, S., Monory, K., Lutz, B., and Klugmann, M. (2010). AAV vector-mediated overexpression of CB1 cannabinoid receptor in pyramidal neurons of the hippocampus protects against seizure-induced excitoxicity. *PLoS One* 5:e15707. doi: 10.1371/journal.pone.0015707

Harvey, B. K., Richie, C. T., Hoffer, B. J., and Airavaara, M. (2012). Transgenic animal models of neurodegeneration based on human genetic studies. *J. Neural Transm.* 118, 27–45. doi: 10.1007/s00702-010-0476-6

Harvey, B. K., Wang, Y., and Hoffer, B. J. (2008). Transgenic rodent models of Parkinson's disease. *Acta Neurochir. Suppl.* 101, 89–92. doi: 10.1007/978-3-211-78205-7_15

Hofmann, M. E., Nahir, B., and Frazier, C. J. (2008). Excitatory afferents to CA3 pyramidal cells display differential sensitivity to CB1 dependent inhibition of synaptic transmission. *Neuropharmacology* 55, 1140–1146. doi: 10.1016/j.neuropharm.2008.07.007

Ingusci, S., Verlengia, G., Soukupova, M., Zucchini, S., and Simonato, M. (2019). Gene therapy tools for brain diseases. *Front. Pharmacol.* 10:724. doi: 10.3389/fphar.2019.00724

Jacinto, F. V., Link, W., and Ferreira, B. I. (2020). CRISPR/Cas9-mediated genome editing: from basic research to translational medicine. *J. Cell. Mol. Med.* 24, 3766–3778. doi: 10.1111/jcmm.14916

Jie, L. K., Ying, X. H., Ping, K. Z., Lian, C. J., and Juan, J. L. (2015). CRISPR-Cas9: a new and promising player in gene therapy. *J. Med. Genet.* 52, 289–296. doi: 10.1136/jmedgenet-2014-102968

Katona, I., Sperlágh, B., Maglóczky, Z., Sántha, E., Köfalvi, A., Czirják, S., et al. (2000). GABAergic interneurons are the targets of cannabinoid actions in the human hippocampus. *Neuroscience* 100, 797–804. doi: 10.1016/s0306-4522(00)00286-4

Kawamura, Y., Fukaya, M., Maejima, T., Yoshida, T., Miura, E., Waranabe, M., et al. (2006). The CB1 cannabinoid receptor is the major cannabinoid receptor at excitatory presynaptic sites in the hippocampus and cerebellum. *J. Neurosci.* 26, 2991–3001. doi: 10.1523/JNEUROSCI.4872-05.2006

Konermann, S., Brigham, M. D., Trevino, A. E., Joung, J., Abudayyeh, O. O., Barcena, C., et al. (2015). Genome-scale transcriptional activation by an engineered CRISPR-Cas9 complex. *Nature* 517, 583–588. doi: 10.1038/nature14136

Koo, T., and Kim, J. S. (2016). Therapeutic applications of CRISPR RNA-guided genome editing. *Brief. Funct. Genomics* 16, 38–45. doi: 10.1093/bfgp/elw032

Kügler, S., Kilic, E., and Bähr, M. (2003). Human synapsin 1 gene promoter confers highly neuron-specific long-term transgene expression from an adenoviral vector in the adult rat brain depending on the transduced area. *Gene Ther.* 10, 337–347. doi: 10.1038/sj.gt.3301905

Kumar, N., Stanford, W., de Solis, C., Aradhana, Abraham, N. D., Dao, T. M. J., et al. (2018). The development of an AAV-based CRISPR SaCas9 genome editing system that can be delivered to neurons in vivo and regulated via doxycycline and cre-recombinase. *Front. Mol. Neurosci.* 11:413. doi: 10.3389/fnmol.2018.00413

Kunieda, T., Zuscik, M. J., Boongrid, A., Perez, D. M., Lüders, H. O., and Najim, I. N. (2002). Systemic overexpression of the Alpha 1B-adrenergic receptor in mice: an animal model of epilepsy. *Eilepsia* 43, 1324–1329. doi: 10.1046/j.1528-1157.2002.13202.x

Lau, C. H., Ho, J. W., Lo, P. K., and Tin, C. (2019). Targeted transgene activation in the brain tissue by systemic delivery of engineered AAV1 expressing CRISPRa. *Mol. Ther. Nucleic Acids* 16, 637–649. doi: 10.1016/j.omtn.2019.04.015

Lino, C. A., Harper, J. C., Carney, J. P., and Timlin, J. A. (2018). Delivering CRISPR: a review of the challenges and approaches. *Drug. Deliv.* 25, 1234–1257. doi: 10.1080/10717544.2018.1474964

Livak, K. J., and Schmittgen, T. D. (2001). Analysis of relative gene expression data using real-time quantitative PCR and the 2(-Delta Delta C(T)) method. *Methods* 25, 402–408. doi: 10.1006/meth.2001.1262

Ma, D., Peng, S., Huang, W., Cai, Z., and Xie, Z. (2018). Rational design of mini-Cas9 for transcriptional activation. *ACS Synth. Biol.* 7, 978–985. doi: 10.1021/acssynbio.7b00404

Mackie, K. (2006). Mechanisms of CB1 receptor signaling: endocannabinoid modulation of synaptic strength. *Int. J. Obes. (Lond.)* 30 Suppl 1, S19–S23. doi: 10.1038/sj.ijo.0803273

Maeder, M. L., Linder, S. J., Cascio, V. M., Fu, Y., Ho, Q. H., and Joung, J. K. (2013). CRISPR RNA-guided activation of endogenous human genes. *Nat. Methods* 10, 977–981. doi: 10.1038/nmeth.2598

Mali, P., Aach, J., Stranges, P. B., Esvelt, K. M., Moosburner, M., Kosuri, S., et al. (2013). CAS9 transcriptional activators for target specificity screening and paired nickases for cooperative genome engineering. *Nat. Biotechnol.* 31, 833–838. doi: 10.1038/nbt.2675

Marsicano, G., and Lutz, B. (1999). Expression of the cannabinoid receptor CB1 in distinct neuronal subpopulations in the adult mouse forebrain. *Eur. J. Neurosci.* 11, 4213–4225. doi: 10.1046/j.1460-9568.1999.00847.x

Monory, K., Massa, F., Egertová, M., Eder, M., Blaudzun, H., Westenbroek, R., et al. (2006). The endocannabinoid system controls key epileptogenic circuits in the hippocampus. *Neuron* 51, 455–466. doi: 10.1016/j.neuron.2006.07.00

Perez-Pinera, P., Kocak, D. D., Vockley, C. M., Adler, A. F., Kabadi, A. M., Polstein, L. R., et al. (2013). RNA-guided gene activation by CRISPR-Cas9-based transcription factors. *Nat. Methods* 10, 973–976. doi: 10.1038/nmeth.2600

Potapov, V., Ong, J. L., Kucera, R. B., Langhorst, B. W., Bilotti, K., Pryor, J. M., et al. (2018). Comprehensive profiling of four base overhang ligation fidelity by T4 DNA ligase and application to DNA assembly. *ACS Synth. Biol.* 7, 2665–2674. doi: 10.1021/acssynbio.8b00333

Quintino, L., Manfre, G., Wettergren, E. E., Namislo, A., Isaksson, C., and Lundberg, C. (2013). Functional neuroprotection and efficient regulation of GDNF using destabilizing domains in a rodent model of Parkinson's disease. *Mol. Ther.* 21, 2169–2180. doi: 10.1038/mt.2013.169

Quintino, L., Namislo, A., Davidsson, M., Breger, L. S., Kavanagh, P., Avallone, M., et al. (2018). Destabilizing domains enable long-term and inert regulation of GDNF expression in the brain. *Mol. Ther. Methods Clin. Dev.* 11, 29–39. doi: 10.1016/j.omtm.2018.08.008

Savell, K. E., Bach, S. V., Zipperly, M. E., Revanna, J. S., Goska, N. A., Tuscher, J. J., et al. (2019). A neuron-optimized CRISPR/dCas9 Activation system for robust and specific gene regulation. *eNeuro* 6:ENEURO.0495-18.2019. doi: 10.1523/ENEURO.0495-18.2019

Shire, D., Carillon, C., Kaghad, M., Calandra, B., Rinaldi-Carmona, M., Le Fur, G., et al. (1995). An amino-terminal variant of the central cannabinoid receptor resulting from alternative splicing. *J. Biol. Chem.* 270, 3726–3731. doi: 10.1074/jbc.270.8.3726

Simonato, M. (2014). Gene therapy for Epilepsy. *Epilepsy Behav.* 38, 125–130. doi: 10.1016/j.yebeh.2013.09.013

Simonato, M., Bennett, J., Boulis, N. M., Castro, M. G., Fink, D. J., Goins, W. F., et al. (2013). Progress in gene therapy for neurological disorders. *Nat. Rev. Neurol.* 9, 277–291. doi: 10.1038/nrneurol.2013.56

Song, C., and Howlett, A. C. (1995). Rat brain cannabinoid receptors are N-linked glycosylated proteins. *Life Sci.* 56, 1983–1989. doi: 10.1016/0024-3205(95)00179-a

Takahashi, K. A., and Castillo, P. E. (2006). The CB1 cannabinoid receptor mediates glutamatergic synaptic suppression in the hippocampus. *Neuroscience* 139, 795–802. doi: 10.1016/j.neuroscience.2006.01.024

Wu, X., Dong, X., Wu, Z., Cao, H., Niu, D., Qu, J., et al. (2001). A novel method for purification of recombinant adenoassociated virus vectors on a large scale. *Chin. Sci. Bull.* 46, 485–488. doi: 10.1007/bf03187263

Yang, C., Hao, F., He, J., Lu, T., Klein, R. L., Zhao, L. R., et al. (2016). Sequential adeno-associated viral vector serotype 9-green fluorescent protein gene transfer causes massive inflammation and intense immune response in rat striatum. *Hum. Gene Ther.* 27, 528–543. doi: 10.1089/hum.2015.083

Zheng, Y., Shen, W., Zhang, J., Yang, B., Liu, Y. N., Qi, H., et al. (2018). CRISPR interference-based specific and efficient gene inactivation in the brain. *Nat. Neurosci.* 21, 447–454. doi: 10.1038/s41593-018-0077-5

Zhou, H., Liu, J., Zhou, C., Gao, N., Hu, X., Li, X., et al. (2018). In vivo simultaneous transcriptional activation of multiple genes in the brain using CRISPR–dCas9-activator transgenic mice. *Nat. Neurosci.* 21, 440–446. doi: 10.1038/s41593-017-0060-6

Zufferey, R., Nagy, D., Mandel, R. J., Naldini, L., and Trono, D. (1997). Multiply attenuated lentiviral vector achieves efficient gene delivery in vivo. *Nat. Biotechnol.* 15, 871–875. doi: 10.1038/nbt0997-871

Conflict of Interest: The authors declare that the research was conducted in the absence of any commercial or financial relationships that could be construed as a potential conflict of interest.

Advantages of publishing in Frontiers

OPEN ACCESS
Articles are free to read for greatest visibility and readership

FAST PUBLICATION
Around 90 days from submission to decision

HIGH QUALITY PEER-REVIEW
Rigorous, collaborative, and constructive peer-review

TRANSPARENT PEER-REVIEW
Editors and reviewers acknowledged by name on published articles

Frontiers
Avenue du Tribunal-Fédéral 34
1005 Lausanne | Switzerland

Visit us: www.frontiersin.org
Contact us: frontiersin.org/about/contact

REPRODUCIBILITY OF RESEARCH
Support open data and methods to enhance research reproducibility

DIGITAL PUBLISHING
Articles designed for optimal readership across devices

FOLLOW US
@frontiersin

IMPACT METRICS
Advanced article metrics track visibility across digital media

EXTENSIVE PROMOTION
Marketing and promotion of impactful research

LOOP RESEARCH NETWORK
Our network increases your article's readership